

SEARCHES FOR SUPERSYMMETRIC PARTICLES WITH THE ATLAS DETECTOR  
USING BOOSTED DECAY TREE TOPOLOGIES

by

DANIEL BULLOCK

DISSERTATION

Submitted in partial fulfillment of the requirements  
for the degree of Doctor of Philosophy at  
The University of Texas at Arlington  
August 2016

Arlington, Texas

Supervising Committee:

Amir Farbin  
Kaushik De  
Haleh Hadavand  
Zdzislaw Musielak  
Andrew White

## ABSTRACT

Searches for Supersymmetric Particles with the ATLAS Detector using Boosted Decay  
Tree Topologies

Daniel Bullock, Ph.D.

The University of Texas at Arlington, 2016

Supervising Professor: Amir Farbin

The existence of a scalar Higgs particle poses a challenge to the Standard Model through an unnatural hierarchy problem with quadratic divergence. A supersymmetric framework, proposing heavy partners to every Standard Model particle, can solve this problem by introducing new loop diagrams that involve a new fermion-boson symmetry. The LHC has the potential to probe the energy scale necessary for creation of these particles and the ATLAS experiment is poised for discovery. The detected particles are studied by reconstructing the detected events in boosted frames that approximate each decay frame of the interaction with pairs of heavy, invisible particles. This Razor method was used in the analysis of data from 2011 and 2012 and then generalized to the Recursive Jigsaw method in 2015.

Copyright by  
Daniel Bullock  
2016

This work is licensed under the Creative Commons  
Attribution-NonCommercial-ShareAlike 4.0 International License.  
To view a copy of this license, visit <http://creativecommons.org/licenses/by-nc-sa/4.0/>.

## ACKNOWLEDGEMENTS

This research was made possible through funding from the U.S. Department of Energy Early Career Research Program and the U.S. Department of Energy base grant. The Office of Graduate Studies at the University of Texas at Arlington funded the writing portion of this dissertation through the Dissertation Fellowship grant.

## DEDICATION

To the inspired, the inspiring, and the inspiration itself...

I would like to thank the science teachers that helped me develop my interest in science through middle and high school: Mr. Arguello, Ms. Bunting, Ms. Combs, Mr. Desiato, Ms. Kafig, and Ms. Pannabecker. I would also like to thank my guidance counselor, D. McLaughlin for helping me explore the paths of my future. And I thank my band directors from middle school and high school, H. Perez and R. Wilson, for showing me encouragement even when I knew my future lay along a different path.

I owe a lot to my undergraduate professors for making physics both approachable and digestible: C. Aars, C. Allen, D. Bixler, C. Poppeliers, D. Lloyd, J. Satterfield, T. Sauncy, and A. Wallace.

I thank my academic professors from graduate school, from whom I learned to admire a complete and clear answer to a question: N. Fazleev, R. Lopez, Z. Musielak, A. Ray, A. Weiss, and Q. Zhang. I would like to thank those from the HEP group who gave me advice and indulged my ponderings: K. De, A. Farbin, C. Jackson, A. White, J. Yu.

I thank the administrative assistants that have helped me greatly with paperwork including the daunting task of international relocation: S. Cody, B. Harris, M. Jackymack, J. Johnston, A. Leyval, and A. Winter.

I have to thank all my colleagues in the ATLAS collaboration, but especially those I worked with closely: T. Bain, L. Heelan, P. Jackson, E. Kuwertz, L. Lee, Z. Marshall, C. Rogan, R. Smith, C. Solans, and G. Usai.

It's important to take a break and have friends that can help you make the most of it: J. Conn, S. Darmora, J. Hendryx, H.Y. Kim, T. Lawrence, M. Lynch, D. Parsons, A. Valva, and M. Wilkinson.

I would like to extend a special thank you to the outstanding professionals that helped in the part of this dissertation that I neglected the most: R. Mitchell and others from UTA Medical Clinic; Y.A. Yankov from Neurology and Sleep; D. Atkins, C. Bogaev, and others, from Methodist Stone Oak Hospital; L. Fichtel and others from The START Center; K.

Eyre and others from STRIC; and S. Ernst, A. Krejci, J. Milliken, and others from Smithsonian Physical Therapy.

And lastly, I want to thank my brother and my parents. It can actually be fortunate to have a catastrophic experience if you rediscover the strength of support you've always had at home.

## TABLE OF CONTENTS

ABSTRACT . . . . .	ii
ACKNOWLEDGEMENTS . . . . .	iv
LIST OF FIGURES . . . . .	xiv
LIST OF TABLES . . . . .	xxvi
LIST OF ABBREVIATIONS . . . . .	xxx
1. Introduction . . . . .	1
2. The Fundamental Theory of Particle Physics . . . . .	5
2.1 Quantum Field Theory . . . . .	5
2.2 Model Building from Symmetry . . . . .	7
2.2.1 Symmetries and Conservation . . . . .	8
2.2.2 Building the Model . . . . .	10
2.3 Feynman Diagrams . . . . .	20
2.4 The Standard Model . . . . .	22
2.5 Beyond the Standard Model . . . . .	26
3. Supersymmetry . . . . .	29
3.1 The Hierarchy Problem . . . . .	29
3.1.1 Photon Mass . . . . .	29
3.1.2 Electron Mass . . . . .	30
3.1.3 Higgs Mass . . . . .	31
3.1.4 Fixing the Higgs Mass Problem . . . . .	32
3.2 Fermion-Boson Supersymmetry . . . . .	33
3.2.1 Building SUSY . . . . .	33
3.2.2 Unification of Scales . . . . .	36
3.3 Broken Supersymmetry . . . . .	38

3.4	R-Parity . . . . .	38
3.5	Supersymmetry as a Framework . . . . .	40
3.6	Simplified Models . . . . .	42
4.	Detection and Instrumentation . . . . .	45
4.1	Overview of the LHC . . . . .	45
4.1.1	Design of the LHC . . . . .	46
4.1.2	Filling the Beams . . . . .	48
4.1.3	LHC Detectors . . . . .	51
4.2	The ATLAS Detector . . . . .	52
4.2.1	Design Philosophies . . . . .	54
4.2.2	Performance of ATLAS . . . . .	55
4.3	Kinematics and Measurables . . . . .	57
4.3.1	Transverse Variables . . . . .	59
4.3.2	Relativistic Boosts . . . . .	59
4.3.3	Consistency Checks . . . . .	60
4.4	The Magnetic Systems . . . . .	62
4.5	The Inner Detector . . . . .	63
4.6	The Calorimeters . . . . .	64
4.6.1	Calorimeter Principles . . . . .	65
4.6.2	LAr Calorimeters . . . . .	65
4.6.3	TileCal . . . . .	66
4.7	The Muon Spectrometers . . . . .	68
4.8	Forward Detectors . . . . .	70
4.9	Missing Momentum . . . . .	70
4.9.1	Simulated SUSY Event . . . . .	72
5.	Online Triggering . . . . .	74
5.1	Calorimeter Electronics and Diagnostics . . . . .	75
5.1.1	MobiDick . . . . .	78



5.1.2	Phase I Upgrades . . . . .	80
5.1.3	Demonstrator . . . . .	84
5.1.4	Prometeo . . . . .	85
5.2	Event Triggers . . . . .	89
5.2.1	Level 1 . . . . .	90
5.2.2	Common Time . . . . .	90
5.2.3	High-Level Trigger . . . . .	91
5.2.4	Trigger Nomenclature . . . . .	92
5.3	Detector Status and Control . . . . .	93
5.4	Prescaling . . . . .	94
5.5	Trigger Efficiency . . . . .	95
6.	Simulation and Reconstruction . . . . .	98
6.1	Monte Carlo . . . . .	98
6.1.1	Scatter Evolution . . . . .	99
6.1.2	Pileup . . . . .	100
6.1.3	Generators . . . . .	101
6.1.4	Detector Simulation . . . . .	102
6.2	Reconstruction . . . . .	102
6.2.1	Tracking . . . . .	103
6.2.2	Electrons and Photons . . . . .	103
6.2.3	Muons . . . . .	104
6.2.4	Jets . . . . .	105
6.2.5	Flavor Tagging . . . . .	107
6.2.6	Taus . . . . .	107
6.2.7	Missing Transverse Momentum . . . . .	108
7.	Offline Analysis . . . . .	109
7.1	Background Processes . . . . .	110
7.2	Event Selection . . . . .	111

7.3	Overlap Removal . . . . .	113
7.4	Systematic Uncertainties . . . . .	114
7.4.1	Energy Scale . . . . .	116
7.4.2	Energy Resolution . . . . .	117
7.5	Jet Smearing . . . . .	119
7.6	Variable Comparisons . . . . .	120
7.7	Control, Validation, and Signal Regions . . . . .	124
7.8	Event Complementarity . . . . .	125
7.9	Likelihood Function . . . . .	127
7.10	Exclusions and Discovery . . . . .	128
7.11	HistFitter . . . . .	132
8.	Global and Topological Variables . . . . .	133
8.1	Energy Scale Variables . . . . .	135
8.1.1	Hadronic Momentum . . . . .	135
8.1.2	The Effective Mass . . . . .	135
8.1.3	Dijet Invariant Mass . . . . .	136
8.1.4	Transverse Mass . . . . .	136
8.1.5	Stransverse Mass . . . . .	136
8.2	Event Shape . . . . .	137
8.2.1	Delta Phi . . . . .	137
8.2.2	Sphericity . . . . .	138
8.2.3	Jet Thrust . . . . .	139
8.3	Cotransverse and Contransverse Mass . . . . .	140
8.4	Alpha T . . . . .	141
8.5	Razor and Super-Razor . . . . .	141
8.5.1	Event Frames . . . . .	144
8.5.2	Razor . . . . .	144
8.5.3	Super-Razor . . . . .	146

8.6	Recursive Jigsaw Reconstruction . . . . .	148
8.6.1	Inclusive Disparticle Reconstruction . . . . .	149
8.6.2	Digluino Reconstruction . . . . .	156
8.6.3	Compressed Sparticle Reconstruction . . . . .	159
8.6.4	Hadronic Scale Reconstruction . . . . .	160
8.6.5	QCD Multijet Rejection Method . . . . .	165
8.7	Trigger Evolution . . . . .	169
8.7.1	L1 Seed . . . . .	170
8.7.2	Predictions of Performance . . . . .	173
8.7.3	Trigger Validation . . . . .	175
8.7.4	Trigger Performance . . . . .	178
9.	2011 Razor Analysis . . . . .	181
9.1	Trigger Choice . . . . .	182
9.2	Object Definitions and Event Selection . . . . .	183
9.3	Monte Carlo Samples . . . . .	186
9.4	Systematic Uncertainties . . . . .	186
9.5	Definition of Signal Regions . . . . .	188
9.6	Definition of Control and Validation Regions . . . . .	193
9.7	Prescaled Data Validation . . . . .	196
9.7.1	CMS Data-Driven Estimate . . . . .	196
9.7.2	Prescaled Data . . . . .	197
9.7.3	Modified ABCD . . . . .	198
9.7.4	MC Cleaning . . . . .	201
9.7.5	Data Scaling . . . . .	201
9.7.6	Comparison to Other Methods . . . . .	202
9.8	Background CR Fit . . . . .	203
9.9	Signal Region Extrapolation . . . . .	211
9.10	Exclusion Results . . . . .	216

9.11	Comments on the 2011 Analysis . . . . .	219
10.	2012 Razor Analysis . . . . .	221
10.1	Trigger Choice . . . . .	222
10.2	Object Definitions and Event Selections . . . . .	224
10.3	Monte Carlo Samples . . . . .	226
10.4	Systematic Uncertainties . . . . .	227
10.5	Definition of Signal Regions . . . . .	228
10.6	Definition of Control and Validation Regions . . . . .	229
10.7	QCD MC Cleaning . . . . .	232
10.7.1	Nested Exponential Model . . . . .	232
10.7.2	Three Fit Methods . . . . .	233
10.7.3	Removing Spikes . . . . .	236
10.8	Background CR Fit . . . . .	238
10.9	Signal Region Extrapolation . . . . .	243
10.10	Exclusion Results . . . . .	251
10.11	Event Overlap . . . . .	252
10.12	Comments on 2012 Analysis . . . . .	255
11.	2015 Recursive Jigsaw Analysis . . . . .	257
11.1	Trigger Choice . . . . .	257
11.2	Object Definitions and Event Selections . . . . .	259
11.3	Monte Carlo Samples . . . . .	262
11.4	Systematic Uncertainties . . . . .	263
11.5	Definition of Signal Regions . . . . .	263
11.6	QCD Multijet Rejection . . . . .	266
11.7	Definition of Control and Validation Regions . . . . .	269
11.8	Background CR Fit . . . . .	271
11.9	Signal Region Extrapolation . . . . .	271
11.10	Meff Comparisons . . . . .	275

11.10.1 SR Overlap . . . . .	278
11.10.2 Variable Relations . . . . .	280
11.10.3 Systematic Variations . . . . .	283
11.11 Exclusion Reach . . . . .	285
12. Conclusions . . . . .	288
REFERENCES . . . . .	290
APPENDIX	
A. Mathematical Notation . . . . .	305
B. Feynman Rules for the Standard Model . . . . .	316
C. Radiative Corrections in SUSY . . . . .	324
D. Variable Correlations . . . . .	329

## LIST OF FIGURES

Figure	Page
2.1 An arbitrary equation used to demonstrate the effectiveness of symmetries . . . . .	8
2.2 A representation of the Higgs potential exhibiting its “broken” symmetry . . . . .	15
2.3 A Feynman diagram of charged attraction via exchange of a photon . . . . .	21
2.4 A Feynman diagram of strong force attraction via exchange of a pion . . . . .	21
2.5 A Feynman diagram of the weak decay of a neutron . . . . .	22
2.6 A diagrammatic representation of the SM showing its (a) particles and (b) forces . . . . .	26
2.7 A Feynman diagram for the exchange of a new heavy particle . . . . .	28
3.1 A Feynman diagram for photon self-energy with a one-loop electron correction	29
3.2 A Feynman diagram for electron self-energy with a one-loop photon correction	30
3.3 A Feynman diagram for Higgs self-energy with a one-loop fermion correction	31
3.4 Two Feynman diagrams for Higgs self-energy with one-loop sfermion corrections with (a) cubic and (b) quartic vertices . . . . .	34
3.5 The running gauge couplings with and without SUSY . . . . .	37
3.6 A comparison of (a) cMSSM to (b) simplified model gluino decay . . . . .	43
3.7 Examples of the simplified model decay of a gluino: (a) direct two-body decay $\tilde{q} \rightarrow q \tilde{\chi}_1^0$ , (b) direct three-body decay $\tilde{g} \rightarrow qq \tilde{\chi}_1^0$ , (c) two-step cascade $\tilde{g} \rightarrow qqW \tilde{\chi}_1^0$ , and (d) three-step cascade $\tilde{g} \rightarrow qqWW \tilde{\chi}_1^0$ . . . . .	44
4.1 A timeline of important dates and schedule of the LHC, ATLAS, and planned upgrades . . . . .	46
4.2 The LHC magnetic dipole field . . . . .	47
4.3 A view of the LHC tunnel . . . . .	48
4.4 A schematic layout of the LHC components and main detectors . . . . .	49

4.5	A schematic map of the accelerator facilities at CERN . . . . .	49
4.6	The integrated luminosity taken during 2011, 2012, and 2015. This figure is a combination of three plots that have been scaled manually to the same timescale and luminosity scale . . . . .	52
4.7	A schematic cross-section of the ATLAS detector showing how particles interact with the sub-detectors . . . . .	53
4.8	A distribution of energy deposition versus momentum used in particle identification by the ALICE collaboration . . . . .	54
4.9	A plot of stopping power versus muon momentum . . . . .	55
4.10	A schematic for the ATLAS detector indicating the major subsystems . . .	56
4.11	A view of the ATLAS detector with the TileCal extended barrel pulled out	56
4.12	Confirmation of the SM cross-sections by ATLAS . . . . .	57
4.13	Confirmation of the SM cross-sections by ATLAS with varying $\sqrt{s}$ . . . . .	58
4.14	The magnetic systems of ATLAS showing (a) the geometry of the solenoid and toroids, and (b) a photograph of the toroids during construction . . . . .	62
4.15	A schematic of the ID (a) components and (b) transverse cutaway . . . . .	63
4.16	A schematic layout of the TileCal and LAr calorimeters . . . . .	65
4.17	A schematic view of a barrel section of LAr . . . . .	66
4.18	A breakdown of TileCal showing the boosted geometry of its cells . . . . .	67
4.19	A schematic of the MS . . . . .	69
4.20	A simulation of SUSY production in an event display . . . . .	72
5.1	The production cross-sections of multiple processes at varying $\sqrt{s}$ . . . . .	75
5.2	A cesium scan of TileCal showing the effect of particles traveling through alternating layers of scintillators and steel . . . . .	76
5.3	A photograph of the TileCal FEBs during maintenance. The super-drawer is rectangular in shape and is shown sitting in a temporary aluminum cradle for stability, rotation, and ease of access . . . . .	77
5.4	A diagram of the FEB electronics of TileCal . . . . .	77

5.5	The embedded system of MobiDick uses an ML507 motherboard to process data and control daughterboards that interface with the FEBs . . . . .	79
5.6	The DigShape test is used to fit and evaluate a pulse for each 3-in-1 and diagnose any problems with the electronics . . . . .	80
5.7	A photograph of MobiDick (lower left) in use for TileCal maintenance. The inset shows two workers reading the test results . . . . .	81
5.8	A representation of (a) fully saturated values and (b) partially saturated values in a 12-bit sampler . . . . .	82
5.9	The various time constants of integrator circuits plotted to show the amount of time needed to reach a plateau value . . . . .	82
5.10	A timeline of masked cells in TileCal . . . . .	84
5.11	A diagram of the upgraded FEBs of TileCal . . . . .	85
5.12	A diagram of the hybrid FEBs of the upgrade Demonstrator . . . . .	85
5.13	A block diagram of the Prometeo test-bench . . . . .	86
5.14	Distributions of BiasNoise for PMT 10 and high-gain presented as (a) a 2D plot versus event number and (b) the 1D projection . . . . .	87
5.15	A full 48-channel summary of the Gaussian fit parameters for BiasNoise for low-gain . . . . .	87
5.16	Plots of (a) the correlation of values for gain configuration 12 and (b) an unstable integrator response for PMT 2 and gain configuration 12 . . . . .	88
5.17	The definition of parameters used in the pulse shape fit . . . . .	89
5.18	The trigger efficiency for single-jet triggers for (a) L1 with $ \eta  < 2.6$ and (b) HLT with $ \eta  < 2.8$ . . . . .	96
6.1	The evolution of a scatter from (a) collision to (b) parton showering and (c) hadronization. Red particles represent the evolution of a primary event, purple particles represent an underlying event, blue particles represent ISR, and orange particles represent beam remnants . . . . .	99



6.2	A distribution of the average number of interactions per bunch crossing for (a) 2011 and 2012 and (b) 2015 . . . . .	101
7.1	The production cross-section of (a) QCD multijets, (b) photons, and (c) $W$ and $Z$ BGs as estimated under various experimental production and detection conditions . . . . .	112
7.2	A diagram of the major effects of systematic variations on a distribution: (left) a change in mean, (middle) a change in uncertainty, and (right) a change in normalization . . . . .	115
7.3	A diagram of “Mercedes” events where one of the jets is colinear with large $E_T^{\text{miss}}$ . . . . .	120
7.4	A scatter between generic variables $A$ and $B$ with 1 million points to illustrate covariance (+0.3) and correlation (+67%) . . . . .	121
7.5	A hypocycloid ( $r_1 = 3.8, r_2 = 1$ ) drawn with 1 million points to illustrate the difference between correlation ( $-0.1\%$ ) and mutual information (34%) . . . . .	122
7.6	A diagram of generic CR extrapolation into VR and SR . . . . .	125
7.7	A diagram of the ABCD method. Transfer functions (TM or TD) are calcu- lated to extrapolate the CR estimate into the SR . . . . .	126
7.8	A diagram defining the complementarity between variables $A$ and $B$ . . . . .	126
7.9	A demonstration of the 95% CL for the hypothesis tests of BG-only and signal+BG . . . . .	129
7.10	A demonstration of the 95% CL sensitivity issue . . . . .	130
7.11	The look-elsewhere effect of data excess using a Likelihood ratio test statistic	131
8.1	A diagram showing a signature involving pair production and subsequent decay to jets/leptons and invisible particles . . . . .	133
8.2	A distribution of $M_{T2}$ for SUSY, $Z$ , and QCD events . . . . .	137
8.3	A distribution of $\Delta\phi(\vec{p}_T, \vec{E}_T^{\text{miss}})$ for SUSY, $Z$ , and QCD events . . . . .	138
8.4	A diagrammatic representation of thrust variables . . . . .	140
8.5	A distribution of $\alpha_T$ . . . . .	142

8.6	The cross-section for SUSY pair-production at $\sqrt{s} = 8$ TeV . . . . .	143
8.7	The cross-sections for SUSY production at $\sqrt{s} = 8$ TeV (dashed lines) and $\sqrt{s} = 13$ TeV (solid lines) . . . . .	144
8.8	The definition of $R$ and $R + 1$ frames by approximate boosts . . . . .	145
8.9	The decay tree used for reconstructing $pp \rightarrow \tilde{q}\tilde{q} \rightarrow qq \tilde{\chi}_1^0 \tilde{\chi}_1^0$ . . . . .	150
8.10	A distribution of $M_P$ for (a) $\tilde{q}\tilde{q} \rightarrow qq \tilde{\chi}_1^0 \tilde{\chi}_1^0$ and (b) $\tilde{g}\tilde{g} \rightarrow qq\tilde{q}\tilde{q} \tilde{\chi}_1^0 \tilde{\chi}_1^0$ . . . . .	151
8.11	A distribution of $1/\gamma_P^{PP}$ for (a) $\tilde{q}\tilde{q} \rightarrow qq \tilde{\chi}_1^0 \tilde{\chi}_1^0$ and (b) $\tilde{g}\tilde{g} \rightarrow qq\tilde{q}\tilde{q} \tilde{\chi}_1^0 \tilde{\chi}_1^0$ . . . . .	151
8.12	A distribution of $VS_{PP}$ for (a) $\tilde{q}\tilde{q} \rightarrow qq \tilde{\chi}_1^0 \tilde{\chi}_1^0$ and (b) $\tilde{g}\tilde{g} \rightarrow qq\tilde{q}\tilde{q} \tilde{\chi}_1^0 \tilde{\chi}_1^0$ . . . . .	152
8.13	A distribution of $M_\Delta^R$ for (a) $\tilde{q}\tilde{q} \rightarrow qq \tilde{\chi}_1^0 \tilde{\chi}_1^0$ and (b) $\tilde{g}\tilde{g} \rightarrow qq\tilde{q}\tilde{q} \tilde{\chi}_1^0 \tilde{\chi}_1^0$ . . . . .	153
8.14	A distribution of $\cos \theta_{PP}$ for (a) $\tilde{q}\tilde{q} \rightarrow qq \tilde{\chi}_1^0 \tilde{\chi}_1^0$ and (b) $\tilde{g}\tilde{g} \rightarrow qq\tilde{q}\tilde{q} \tilde{\chi}_1^0 \tilde{\chi}_1^0$ . . . . .	154
8.15	A distribution of $\cos \theta_P$ for (a) $\tilde{q}\tilde{q} \rightarrow qq \tilde{\chi}_1^0 \tilde{\chi}_1^0$ and (b) $\tilde{g}\tilde{g} \rightarrow qq\tilde{q}\tilde{q} \tilde{\chi}_1^0 \tilde{\chi}_1^0$ . . . . .	154
8.16	A distribution of $\Delta\phi_{PP,V}$ for (a) $\tilde{q}\tilde{q} \rightarrow qq \tilde{\chi}_1^0 \tilde{\chi}_1^0$ and (b) $\tilde{g}\tilde{g} \rightarrow qq\tilde{q}\tilde{q} \tilde{\chi}_1^0 \tilde{\chi}_1^0$ . . . . .	155
8.17	A distribution of $\Delta\phi_{VP}$ for (a) $\tilde{q}\tilde{q} \rightarrow qq \tilde{\chi}_1^0 \tilde{\chi}_1^0$ and (b) $\tilde{g}\tilde{g} \rightarrow qq\tilde{q}\tilde{q} \tilde{\chi}_1^0 \tilde{\chi}_1^0$ . . . . .	155
8.18	The decay tree used for reconstructing $pp \rightarrow \tilde{g}\tilde{g} \rightarrow qq \tilde{q}\tilde{q} \rightarrow qq\tilde{q}\tilde{q} \tilde{\chi}_1^0 \tilde{\chi}_1^0$ . . . . .	156
8.19	A distribution of $\Delta\phi_{P_i,C_i}$ for (a) $\tilde{q}\tilde{q} \rightarrow qq \tilde{\chi}_1^0 \tilde{\chi}_1^0$ and (b) $\tilde{g}\tilde{g} \rightarrow qq\tilde{q}\tilde{q} \tilde{\chi}_1^0 \tilde{\chi}_1^0$ . . . . .	157
8.20	A distribution of $R_{P_i}^{P_i}$ for (a) $\tilde{q}\tilde{q} \rightarrow qq \tilde{\chi}_1^0 \tilde{\chi}_1^0$ and (b) $\tilde{g}\tilde{g} \rightarrow qq\tilde{q}\tilde{q} \tilde{\chi}_1^0 \tilde{\chi}_1^0$ . . . . .	158
8.21	A distribution of $VS_P$ for (a) $\tilde{q}\tilde{q} \rightarrow qq \tilde{\chi}_1^0 \tilde{\chi}_1^0$ and (b) $\tilde{g}\tilde{g} \rightarrow qq\tilde{q}\tilde{q} \tilde{\chi}_1^0 \tilde{\chi}_1^0$ . . . . .	158
8.22	The decay tree used for reconstructing compressed SUSY points . . . . .	159
8.23	Correlation between $\vec{p}_I^{CM} \cdot \hat{p}_{TS}^{CM}/p_{TS}^{CM}$ and $p_{TS}^{ISR}$ for (top) BG and (bottom) signal. The BG processes are (a) QCD multijets, (b) $ZS$ +jets, and (c) top. The signal models are $\tilde{g}$ events with (d) $m_{\tilde{g}} = 812$ GeV and $m_{\tilde{\chi}_1^0} = 787$ GeV, (e) $m_{\tilde{g}} = 825$ GeV and $m_{\tilde{\chi}_1^0} = 7775$ GeV, and (f) $m_{\tilde{g}} = 900$ GeV and $m_{\tilde{\chi}_1^0} = 700$ GeV . . . . .	160
8.24	A distribution of $H_{1,1}^{PP}$ for (a) BG, (b) disquark, and (c) digluino . . . . .	161
8.25	A distribution of (top) $H_{T2,1}^{PP}$ and (bottom) $H_{T4,1}^{PP}$ for (left) BG, (b) disquark, and (d) digluino . . . . .	162
8.26	A distribution of $H_{1,1}^{PP}/H_{2,1}^{PP}$ for (a) BG, (b) large mass-splitting disquark, and (c) intermediate mass-splitting disquark . . . . .	163

8.27	A distribution of $H_{1,1}^{PP} / H_{4,1}^{PP}$ for (a) BG, (b) large mass-splitting digluino, and (c) intermediate mass-splitting digluino . . . . .	163
8.28	A distribution of $p_z^{Lab} / (p_z^{Lab} / H_{T2,1}^{PP})$ for (a) BG, (b) large mass-splitting disquark, and (c) intermediate mass-splitting disquark . . . . .	164
8.29	A distribution of $p_z^{Lab} / (p_z^{Lab} / H_{T4,1}^{PP})$ for (a) BG, (b) large mass-splitting digluino, and (c) intermediate mass-splitting digluino . . . . .	164
8.30	A distribution of $H_{T4,1}^{PP} / H_{4,1}^{PP}$ for (a) BG, (b) large mass-splitting digluino, and (c) intermediate mass-splitting digluino . . . . .	164
8.31	A distribution of $p_{Tj_2}^{PP} / H_{T2,1}^{PP}$ for (a) BG, (b) large mass-splitting disquark, and (c) intermediate mass-splitting disquark . . . . .	165
8.32	A distribution of $p_{Tj_2}^{PP} / H_{T2,1}^{PP}$ for (a) BG, (b) large mass-splitting digluino, and (c) intermediate mass-splitting digluino . . . . .	165
8.33	Three possible decay trees for reconstructing $pp \rightarrow 2j + E_T^{\text{miss}}$ . . . . .	166
8.34	An example of a decay tree for reconstructing $pp \rightarrow 8j + E_T^{\text{miss}}$ . . . . .	167
8.35	A distribution of $R_{p_T^{PP}, M_{PP}}$ for (a) $\tilde{q} \rightarrow q \tilde{\chi}_1^0$ and (b) $\tilde{g} \rightarrow qq \tilde{\chi}_1^0$ . . . . .	168
8.36	A distribution of $R_{p_z^{PP}, M_{PP}}$ for (a) $\tilde{q} \rightarrow q \tilde{\chi}_1^0$ and (b) $\tilde{g} \rightarrow qq \tilde{\chi}_1^0$ . . . . .	168
8.37	The trigger is based on the $M_{\Delta}^R$ contours of the Super-Razor analysis plane (a) determined by the hyperbolic shape of enriched bias data and (b) discriminant to compressed SUSY . . . . .	170
8.38	The correlation between HLT and offline definitions of $M_{\Delta}^R$ . . . . .	171
8.39	A comparison of the rates after various $H_T$ and $\bar{\Pi}$ cuts expected for (a) unique events selected by $H_T$ , (b) unique events selected by $\bar{\Pi}$ , and (c) an overlap of events . . . . .	172
8.40	A comparison of the rates of $E_T^{\text{miss}} / \sqrt{H_T}$ of various cuts to (a) $H_T$ and (b) $\bar{\Pi}$	172
8.41	A comparison of the rates of acceptance $\times$ efficiency after applying cuts (left) $H_T > 800$ GeV and (right) $\bar{\Pi} > 250$ GeV for (top) $\tilde{q} \rightarrow q \tilde{\chi}_1^0$ and (bottom) $\tilde{g} \rightarrow qq \tilde{\chi}_1^0$ . . . . .	173

8.42	A distribution of the reconstructed prescaled data for (a) $p_T$ and (b) $E_T^{\text{miss}}$ for a preliminary validation of the trigger . . . . .	174
8.43	The unique rate for triggers in the jet+MET category for a compressed gluino model. Events that pass Trigger Y do not pass Trigger X . . . . .	175
8.44	The acceptance $\times$ efficiency increase if <b>xe100</b> and <b>razor170</b> (left) compete for rate and (right) complement each other for (top) $\tilde{q} \rightarrow q \tilde{\chi}_1^0$ and (bottom) $\tilde{g} \rightarrow qq \tilde{\chi}_1^0$ . . . . .	176
8.45	The distribution of $M_{\Delta}^R$ using (black) all jets as compared to (red) only the leading $N$ jets: (a) $N > 5$ (b) $N > 7$ (c) $N > 10$ . . . . .	177
8.46	The efficiency of <b>razor170</b> in the (a) the $M_{\Delta}^R$ versus $E_T^{\text{miss}}$ plane and (b) the $M_{PP}$ versus $VS_{PP}$ plane . . . . .	178
8.47	The efficiency of <b>razor170</b> with and without a $E_T^{\text{miss}} > 100$ GeV cut . . . . .	179
8.48	The efficiency of Razor and <b>xe100</b> triggers . . . . .	179
8.49	The acceptance $\times$ efficiency of <b>razor170</b> OR <b>xe100</b> for $\tilde{g} \rightarrow qq \tilde{\chi}_1^0$ . . . . .	180
9.1	Timeline of integrated luminosity during 2011 data-taking run . . . . .	181
9.2	The efficiency of <b>EF_j100_a4tc_EFFS_ht400</b> for increasing $R$ : (a) $R > 0.0$ , (b) $R > 0.1$ , (c) $R > 0.2$ , (d) $R > 0.3$ , (e) $R > 0.4$ , (f) $R > 0.5$ . . . . .	182
9.3	Schematic of CR, VR, and SR configurations used in the fit for 0-lepton in 2011 . . . . .	194
9.4	Schematic of CR, VR, and SR configurations used in the fit for 1-lepton in 2011 . . . . .	195
9.5	Schematic of CR, VR, and SR configurations used in the fit for 2-lepton in 2011 . . . . .	195
9.6	The QCD multijet estimate employed by CMS. In (a), the distribution of $M_R$ is shown for increasing $R$ cuts and (b) the slope of the exponential decay is plotted as a function of $R^2$ . . . . .	197
9.7	The $p_T$ spectrum built from prescaled single-jet triggers for (a) $b$ -veto and (b) $b$ -tag . . . . .	198

9.8	The $M_R$ spectrum comparing single-jet trigger preselections with the 0-lepton signal trigger for (a) $b$ -veto and (b) $b$ -tag . . . . .	199
9.9	The percentage of events passing the 0-lepton signal trigger compared to the single-jet trigger preselections for (a) $b$ -veto and (b) $b$ -tag . . . . .	199
9.10	A validation of the prescaled data estimate of multijet BG events using a modified ABCD method . . . . .	200
9.11	The BG estimate of the multijet CRs (left) before and (right) after fit for (top) $b$ -veto and (bottom) $b$ -tag . . . . .	203
9.12	A comparison of MC to data in multijet CRs for (top) $b$ -veto and (bottom) $b$ -tag (left) before and (right) after the CR BG fit . . . . .	204
9.13	A comparison of MC to data in $W + jets$ $b$ -veto CRs for (top) $e$ and (bottom) $\mu$ (left) before and (right) after the CR BG fit . . . . .	205
9.14	A comparison of MC to data in $Z + jets$ $b$ -tag CRs for (top) $e$ and (bottom) $\mu$ (left) before and (right) after the CR BG fit . . . . .	206
9.15	A comparison of MC to data in $t\bar{t}$ $b$ -tag CRs for (top) $e$ and (bottom) $\mu$ (left) before and (right) after the CR BG fit . . . . .	207
9.16	A comparison of MC to data in $t\bar{t}$ $b$ -tag CRs for (top) $e$ and (bottom) $\mu$ (left) before and (right) after the CR BG fit . . . . .	208
9.17	A comparison of MC to data in a charge-flip $ee$ CR for (left) before and (right) after the CR BG fit . . . . .	209
9.18	A distribution of $M_R$ in the 0-lepton channel for (a) $b$ -veto and (b) $b$ -tag SRs after the combined fit comparing data and MC . . . . .	211
9.19	A distribution of $M_R$ in the 1-lepton channel for (top) $e$ and (bottom) $\mu$ SRs with (left) $b$ -veto and (right) $b$ -tag comparing data and MC . . . . .	212
9.20	A distribution of $M_R$ in the 2-lepton channel for (top) $ee$ , (middle) $\mu\mu$ , and (bottom) $e\mu$ SRs with (left) OS and (right) SS comparing data and MC . . .	213
9.21	A correlation matrix of all free-floating parameters used in the combined fit	214
9.22	The pull on BG weights after the combined fit . . . . .	215

9.23	An exclusion plot in the $m_{1/2}$ versus $m_0$ plane in the mSUGRA model . . .	217
9.24	An exclusion plot in the $m_{\tilde{\chi}_1^0}$ versus $m_{\tilde{g}}$ plane in the $\tilde{g} \rightarrow t\bar{t} \tilde{\chi}_1^0$ simplified model	217
9.25	An exclusion plot in the $m_{\tilde{\chi}_1^0}$ versus $m_{\tilde{g}}$ plane in the $\tilde{q} \rightarrow q\bar{q}W \tilde{\chi}_1^0$ simplified model . . . . .	218
9.26	An exclusion plot in the $\tan \beta$ versus $\Lambda$ plane in the GMSB model . . . . .	218
9.27	An exclusion plot in the $m_{frac}$ versus $m_{\tilde{g}}$ plane . . . . .	220
10.1	Timeline of integrated luminosity during 2012 data-taking run . . . . .	221
10.2	The complementary coverage of a $E_T^{miss}$ trigger and an $H_T$ trigger . . . . .	222
10.3	The efficiency of EF_xe75.tclcw OR EF_xe80.tclcw for increasing cuts on $R$ : (a) $R > 0.0$ , (b) $R > 0.2$ , (c) $R > 0.3$ , (d) $R > 0.4$ , (e) $R > 0.5$ , and (f) $R > 0.5$	224
10.4	Schematic of CR, VR, and SR configurations for the (a) loose and (b) tight regions . . . . .	231
10.5	Schematic of CR and VR configurations for (a) $W + jets$ , (b) $Z + jets$ , and (c) top regions . . . . .	231
10.6	Stacked distributions of QCD multijet BG for (a) the full range of $p_T$ and (b) low $p_T$ . . . . .	232
10.7	The distribution of QCD multijet events while varying the number of bins from (a) 3 bins to (b) 20 bins and (c) 500 bins . . . . .	233
10.8	A “1.5” dimensional fit of mean values with uncertainty determined by distributions shown in (a) a 2D histogram and (b) a 3D perspective . . . . .	234
10.9	A bootstrapped fit of the jet $p_T$ distribution for (a) the full spectrum and (b) a windowed view. The ratio is an MC count divided by the fit . . . . .	235
10.10	A combination of fits showing the strong agreement between push-pull, “1.5D”, and bootstrap methods for the (a) full view and (b) a windowed view . . . . .	236
10.11	A comparison of the leading jet $p_T$ spectrum (a) before and (b) after truth cleaning . . . . .	238
10.12	A comparison of MC to data in multijet CRs (left) before and (right) after the fit for (top) CRtight and (bottom) CRloose . . . . .	240

10.13	A comparison of MC to data (left) before and (right) after the fit for (top) $W$ and (bottom) $Z$ CRs . . . . .	241
10.14	A comparison of MC to data (left) before and (right) after the fit for top CRs	242
10.15	A distribution of (left) $M_R$ and (right) $R$ in (top) SRloose and (bottom) SRtight after the combined fit comparing data and MC . . . . .	246
10.16	A correlation matrix of all free-floating parameters used in the combined fit for SRloose . . . . .	247
10.17	A correlation matrix of all free-floating parameters used in the combined fit for SRtight . . . . .	248
10.18	The systematic variation after the combined fit for (a) SRloose and (b) SRtight	249
10.19	The pull on BG weights after the combined fit for (a) SRloose and (b) SRtight	250
10.20	The combined exclusion results for the $m_{\tilde{\chi}_1^0}$ versus $m_{\tilde{q}}$ in the $\tilde{q}\tilde{q}$ direct decay simplified model . . . . .	251
10.21	The component exclusion results for the $m_{\tilde{\chi}_1^0}$ versus $m_{\tilde{q}}$ in the $\tilde{q}\tilde{q}$ direct decay simplified model . . . . .	252
10.22	A study of event overlap between SRs for (a) $m_{\tilde{q}} = 850$ GeV $m_{\tilde{\chi}_1^0} = 100$ GeV (b) $m_{\tilde{q}} = 450$ GeV $m_{\tilde{\chi}_1^0} = 400$ GeV, and (c) BG . . . . .	254
11.1	Timeline of integrated luminosity during 2015 data-taking run . . . . .	257
11.2	The distribution of $\Delta_{QCD}$ versus $R_{p_{sib}, E_T^{miss}}$ for (top) QCD multijets, (middle) $\tilde{q}$ , and (bottom) $\tilde{g}$ decays with (left) $M_{Delta} < 300$ GeV and (right) $M_{\Delta} > 1000$	267
11.3	The distribution of $R_{p_T^{PP}, M_{PP}}$ versus $\Delta\phi_{PP,V}$ for (top) QCD multijets, (middle) $\tilde{q}$ , and (bottom) $\tilde{g}$ decays with (left) $M_{Delta} < 300$ GeV and (right) $M_{\Delta} > 1000$ . . . . .	268
11.4	ROC curves for the BG rejection method for (top) squark and (bottom) gluino with (left) intermediate and (right) large mass splittings . . . . .	269
11.5	Pull plots after the combined fit to SRS1 . . . . .	272
11.6	Pull plots after the combined fit to SRS2 . . . . .	272
11.7	Pull plots after the combined fit to SRS3 . . . . .	272

11.8	Pull plots after the combined fit to SRG1 . . . . .	273
11.9	Pull plots after the combined fit to SRG2 . . . . .	273
11.10	Pull plots after the combined fit to SRG3 . . . . .	273
11.11	Pull plots after the combined fit to SRC1 . . . . .	274
11.12	Pull plots after the combined fit to SRC2 . . . . .	274
11.13	Pull plots after the combined fit to SRC3 . . . . .	274
11.14	Pull plots after the combined fit to SRC4 . . . . .	275
11.15	SR complementarity between $M_{\text{eff}}$ and RJ for all squark grid points showing (a) unique rate for $M_{\text{eff}}$ , (b) unique rate for RJ, and (c) overlapping rate . .	277
11.16	SR complementarity between $M_{\text{eff}}$ and RJ for all gluino grid points showing (a) unique rate for $M_{\text{eff}}$ , (b) unique rate for RJ, and (c) overlapping rate . .	277
11.17	SR complementarity between $M_{\text{eff}}$ and RJ for QCD BG showing (a) overlapping rate and (b) unique rate . . . . .	278
11.18	SR complementarity between $M_{\text{eff}}$ and RJ for an intermediate mass-splitting squark simplified model showing (a) overlapping rate and (b) unique rate . .	279
11.19	SR complementarity between $M_{\text{eff}}$ and RJ for a large mass-splitting squark simplified model showing (a) overlapping rate and (b) unique rate . . . . .	279
11.20	SR complementarity between $M_{\text{eff}}$ and RJ for a compressed mass-splitting gluino simplified model showing (a) overlapping rate and (b) unique rate . .	279
11.21	SR complementarity between $M_{\text{eff}}$ and RJ for an intermediate mass-splitting gluino simplified model showing (a) overlapping rate and (b) unique rate . .	280
11.22	SR complementarity between $M_{\text{eff}}$ and RJ for a large mass-splitting gluino simplified model showing (a) overlapping rate and (b) unique rate . . . . .	280
11.23	Variable (a) correlation and (b) mutual information used for $M_{\text{eff}}$ and RJ analyses for QCD BG . . . . .	281
11.24	Variable (a) correlation and (b) mutual information used for $M_{\text{eff}}$ and RJ analyses for an intermediate mass-splitting squark simplified model . . . . .	281



11.25	Variable (a) correlation and (b) mutual information used for $M_{\text{eff}}$ and RJ analyses for a large mass-splitting squark simplified model . . . . .	281
11.26	Variable (a) correlation and (b) mutual information used for $M_{\text{eff}}$ and RJ analyses for a compressed mass-splitting gluino simplified model . . . . .	282
11.27	Variable (a) correlation and (b) mutual information used for $M_{\text{eff}}$ and RJ analyses for an intermediate mass-splitting gluino simplified model . . . . .	282
11.28	Variable (a) correlation and (b) mutual information used for $M_{\text{eff}}$ and RJ analyses for a large mass-splitting gluino simplified model . . . . .	282
11.29	Systematic variations to (a) shape and (b) normalization used for $M_{\text{eff}}$ and RJ analyses for QCD BG . . . . .	283
11.30	Systematic variations to (a) shape and (b) normalization used for $M_{\text{eff}}$ and RJ analyses for an intermediate mass-splitting squark simplified model . . .	284
11.31	Systematic variations to (a) shape and (b) normalization used for $M_{\text{eff}}$ and RJ analyses for a large mass-splitting squark simplified model . . . . .	284
11.32	Systematic variations to (a) shape and (b) normalization used for $M_{\text{eff}}$ and RJ analyses for a compressed mass-splitting gluino simplified model . . . . .	284
11.33	Systematic variations to (a) shape and (b) normalization used for $M_{\text{eff}}$ and RJ analyses for an intermediate mass-splitting gluino simplified model . . .	285
11.34	Systematic variations to (a) shape and (b) normalization used for $M_{\text{eff}}$ and RJ analyses for a large mass-splitting gluino simplified model . . . . .	285
11.35	Expected exclusion sensitivity to the $\tilde{q}$ direct decay mass plane comparing the most performant (left) $M_{\text{eff}}$ SRs and (right) RJ SRs . . . . .	286
11.36	Expected exclusion sensitivity to the $\tilde{q}$ direct decay mass plane comparing the most performant (left) $M_{\text{eff}}$ SRs and (right) RJ SRs . . . . .	286
11.37	Expected and observed limits of the 2015 $M_{\text{eff}}$ analysis for (left) squark and (right) gluino simplified models . . . . .	287

## LIST OF TABLES

Table	Page
2.1 A table connecting SM Lagrangian terms to their respective diagrams . . .	23
2.2 The particle content of the SM . . . . .	25
2.3 The interactions of the SM . . . . .	26
3.1 The particles of the MSSM . . . . .	36
4.1 Nominal beam parameters for the LHC . . . . .	51
5.1 The representation of objects in the standardized naming of triggers . . . .	92
5.2 The representation of algorithms in the standardized naming of triggers . .	93
7.1 The energy resolution, $\sigma_E/E$ , of the ATLAS calorimeters . . . . .	118
7.2 A table of $p$ -values as a significance of fluctuation. The $p$ -value is given in units of a Gaussian $\sigma$ and the equivalent confidence level . . . . .	130
9.1 Trigger selection for the 2011 analysis . . . . .	183
9.2 Summary of the electron definitions used in the 2011 analysis . . . . .	184
9.3 Summary of the muon definitions used in the 2011 analysis . . . . .	184
9.4 Summary of the jet definitions used in the 2011 analysis . . . . .	185
9.5 Summary of the $E_T^{\text{miss}}$ definition used in the 2011 analysis . . . . .	185
9.6 Summary of MC generators used in the 2011 analysis . . . . .	187
9.7 SR definitions for 0-, 1-, and 2-lepton in 2011 . . . . .	189
9.8 Estimated number of events in each signal region for 0-lepton in 2011 . . . .	190
9.9 Estimated number of events in each signal region for 1- $e$ in 2011 . . . . .	190
9.10 Estimated number of events in each signal region for 1- $\mu$ in 2011 . . . . .	191
9.11 Estimated number of events in each signal region for $e$ - $e$ in 2011 . . . . .	191
9.12 Estimated number of events in each signal region for $\mu$ - $\mu$ in 2011 . . . . .	192
9.13 Estimated number of events in each signal region for $e$ - $\mu$ in 2011 . . . . .	192

9.14	Multijet CR and VR definitions in 2011 . . . . .	193
9.15	$W \rightarrow jets$ CR and VR definitions in 2011 . . . . .	193
9.16	$Z \rightarrow jets$ CR definitions in 2011 . . . . .	194
9.17	Top CR and VR definitions in 2011 . . . . .	194
9.18	Prescaled triggers and their 99% efficiency bins in $p_T$ . . . . .	198
9.19	A CR using prescaled data designed for QCD multijets . . . . .	199
9.20	Estimated number of multijet events in the 0-lepton SRs with and without MC cleaning . . . . .	201
9.21	Data scale factors used for the estimate of multijet events in the 0-lepton SR	201
9.22	Estimated number of multijet events in the 0-lepton SR with and without data scaling . . . . .	202
9.23	Estimations of multijet event counts in SRs by various methods . . . . .	202
9.24	Estimation methods used in the BG fit in 2011 . . . . .	204
9.25	BG fit result for 0- and 1-lepton for 2011 . . . . .	209
9.26	BG fit result for 2-lepton for 2011 . . . . .	210
9.27	SR extrapolation result for 0- and 1-lepton for 2011 . . . . .	211
9.28	SR extrapolation result for 2-lepton for 2011 . . . . .	214
9.29	The free-floating parameter values after the BG combined fit for 2011 . . . .	215
9.30	SR exclusion for 0- and 1-lepton after the combined fit . . . . .	216
9.31	SR exclusion for 2-lepton after the combined fit . . . . .	216
10.1	Trigger selection for the 2012 analysis . . . . .	223
10.2	Luminosity from individual periods for the 2012 analysis . . . . .	223
10.3	Summary of the electron definitions used in the 2012 analysis . . . . .	225
10.4	Summary of the muon definitions used in the 2012 analysis . . . . .	225
10.5	Summary of the jet definitions used in the 2012 analysis . . . . .	226
10.6	Summary of MC generators used in the 2012 analysis . . . . .	227
10.7	SR definitions for loose and tight regions in 2012 . . . . .	229
10.8	CR and VR definitions for QCD loose and tight regions in 2012 . . . . .	230

10.9	CR and VR definitions for $W + jets$ in 2012 . . . . .	230
10.10	CR and VR definitions for $Z + jets$ in 2012 . . . . .	230
10.11	CR and VR definitions for $t\bar{t}$ in 2012 . . . . .	231
10.12	Bins for the truth jet $p_T$ used in the 2012 analysis . . . . .	237
10.13	Estimation methods used in the BG fit in 2012 . . . . .	238
10.14	BG fit result for SRloose . . . . .	239
10.15	BG fit result for SRtight . . . . .	239
10.16	Systematic uncertainties of SRloose . . . . .	244
10.17	Systematic uncertainties of SRtight . . . . .	245
10.18	Standard SR definitions for 2012 . . . . .	253
11.1	Trigger selection for the 2015 analysis . . . . .	259
11.2	Summary of the electron definitions used in the 2015 analysis . . . . .	259
11.3	Summary of the photon definitions used in the 2015 analysis . . . . .	260
11.4	Summary of the muon definitions used in the 2015 analysis . . . . .	260
11.5	Summary of the jet definitions used in the 2015 analysis . . . . .	260
11.6	Summary of the event preselections used in the 2015 analysis . . . . .	261
11.7	Summary of MC generators used in the 2015 analysis . . . . .	262
11.8	Summary of MC systematics used in the 2015 analysis . . . . .	263
11.9	SR target mass-splittings for the 2015 analysis . . . . .	263
11.10	SR definitions for $\tilde{q}$ -like events for the 2015 analysis . . . . .	264
11.11	SR definitions for $\tilde{g}$ -like events for the 2015 analysis . . . . .	264
11.12	SR definitions for compressed spectra for the 2015 analysis . . . . .	265
11.13	CR definitions for the 2015 analysis . . . . .	270
11.14	VR definitions . . . . .	270
11.15	CR loose definitions for SRS in the 2015 analysis . . . . .	270
11.16	CR loose definitions for SRG in the 2015 analysis . . . . .	271
11.17	BG fit result for 2015 . . . . .	271
11.18	Standard 2 jet SR definitions for 2015 . . . . .	276

11.19 Standard 3+ jet SR definitions for 2015 . . . . . 276

## LIST OF ABBREVIATIONS

- ADC** Analog-to-Digital Conversion: automatic conversion of analog signals into digital bits.
- ALFA** Absolute Luminosity For ATLAS: a forward detector in ATLAS used for calibrating luminosity measurements.
- ALICE** A Large Ion Collider Experiment: a detector for the LHC focused on heavy ion collisions.
- AMSB** Anomaly-Mediated Supersymmetry Breaking: a SUSY model that is a special case of supergravity.
- ATLAS** A Toroidal Large Hadron Collider Apparatus: a detector for the LHC focused on new physics.
- BCID** Bunch Crossing Identification: a unique identifier of events that is defined by the unique bunch crossing number of the collision.
- BDT** Boosted Decision Tree: an algorithm of alternating decisions to categorize an event.
- BE** Back-End: electronics used to gather data from the FEBs or the network servers that hold the data external to the detector volume.
- BF** Branching Fraction: the probabilistic ratio of two interaction possibilities, also known as Branching Ratio.
- BG** Background: refers to events that do not correspond to new physics.
- BR** Branching Ratio: the probabilistic ratio of two interaction possibilities, also known as Branching Fraction.
- BSM** Beyond the Standard Model: any model of new physics that challenges assumptions central to the construction of the SM.
- CAN** Controller Area Network: a communication protocol that controls the settings and operation of the FEBs.

**CC** Charged Current: weak interactions involving a change in EM charge.

**CERN** Conseil Européen pour la Recherche Nucléaire: a science laboratory along the French-Swiss border.

**CIS** Charge Injection System: a system that uses capacitance to deliver a test of FEB pulse reponse.

**CKM** Cabibbo-Kobayashi-Maskawa: refers to the matrix describing  $CP$  violation.

**CL** Confidence Level: a statistical evaluation of how many events are inconsistent with a null hypothesis.

**CM** Center of Mass: defines a frame that is unboosted with respect to the particle scatter.

**CMS** Compact Muon Solenoid: a detector for the LHC focused on new physics.

**cMSSM** Constrained Minimal Supersymmetric Standard Model: an MSSM reduced to 5 additional parameters, also known as mSUGRA.

**CR** Control Region: a region defined for enriched BG events with low signal contamination.

**CSC** Cathode Strip Chamber: a tracking sensor used in a subcomponent of the MS in ATLAS.

**CTP** Central Trigger Processor: a system that manages individual triggers.

**DCS** Detector Control System: a system that reads information about the status of the detector and controls its support systems.

**EBA** Extended Barrel A: a subcomponent of TileCal in ATLAS.

**EBC** Extended Barrel C: a subcomponent of TileCal in ATLAS.

**EER** Electron Energy Resolution: the energy spread of electron energy deposits in the EM calorimeters.

**EES** Electron Energy Scale: the scale at which electron energy is normalized for response to energy deposits in the EM calorimeters.

**EF** Event Filter: the third (and most refined) level of ATLAS TDAQ that was used in Run I of the LHC.

**EFT** Effective Field Theory: a model that is adequate for some predictions, particularly at lower energies.

**EM** Electromagnetic: pertaining to electrically-charged particles.

**EMB** Electromagnetic Barrel: a subcomponent of LAr in ATLAS.

**EMEC** Electromagnetic End-Cap: a subcomponent of LAr in ATLAS.

**EW** Electroweak, a combination of EM and weak theories.

**EWSB** Electroweak Symmetry Breaking: the broken local symmetry that leads to massive gauge bosons.

**FCAL** Forward Calorimeter: a subcomponent of LAr in ATLAS.

**FCNC** Flavor-Changing Neutral Current: weak interactions with no change in EM charge that mix particle flavors.

**FEB** Front-End Boards: electronics for each subcomponent of the detector that are situated inside the detector volume.

**FEX** Feature Extraction: identifies objects in a triggered event.

**FPGA** Field Programmable Gate Array: a programmable integrated circuit.

**FSR** Final-State Radiation: parton radiation after the PV.

**FWHM** Full Width Half Maximum: a measure of the width of a pulse shape by measuring the width between two points at half of the maximum value.

**GCW** Global Cluster Weighting: a scale at which jets are corrected for a normalized response to energy deposits in the hadronic calorimeters.

**GMSB** Gauge-Mediated Supersymmetry Breaking: a SUSY model associated with gauge mediation.

**GRL** Good Runs List: a list of runs and LBs that pass DAQ standards.

**GS** Global Sequential: a scale at which jets are corrected for a normalized response to energy deposits in the hadronic calorimeters.

**GUI** Graphical User Interface: an interactive component of software designed for visual interface.

**GUT** Grand Unified Theory: a union between EW and the strong force.

**HE-LHC** High-Energy Large Hadron Collider: a planned upgrade or replacement of the LHC that uses higher energy no earlier than Run V.



**HEC** Hadronic End-Cap: a subcomponent of LAr in ATLAS.

**HEP** High-Energy Physics: the branch of physics associated with fundamental particles.

**HL-LHC** High-Luminosity Large Hadron Collider: a planned upgrade of the LHC in Run IV that is radiation-hardened for higher luminosities.

**HLT** High-Level Trigger: the second (and most refined) level of ATLAS TDAQ that is used in Run II of the LHC.

**HV** High Voltage: voltages in the  $\mathcal{O}(800\text{ V})$  range providing bias voltage.

**HYPO** Hypothesis: algorithms that define quantities that determine if an event is triggered.

**I/O** Input/Output: an interface that controls incoming and outgoing information.

**IBL** Insertable B-Layer: an extra subcomponent added outside the Pixel layer in the ID of ATLAS.

**ID** Inner Detector: the innermost subsystem in the detector for vertexing, tracking, and particle identification.

**IP** Impact Parameter: the closest approach between two particles in a scatter.

**ISR** Initial-State Radiation: parton radiation prior to the PV.

**ITC** Intermediate Tile Calorimeter: a subcomponent of TileCal in ATLAS added between the long barrel and the end-caps.

**JER** Jet Energy Resolution: the energy spread of jet energy deposits in the EM calorimeters.

**JES** Jet Energy Scale: a scale at which jets are corrected for a normalized response to energy deposits in the hadronic calorimeters.

**JVF** Jet Vertex Fraction: a fraction used to determine how much activity in the event is due to a PV.

**JVT** Jet Vertex Tagger: a multivariate discriminant for determining hard-scatter events.

**L1** Level 1: the first and coarsest trigger used in ATLAS TDAQ.

**L1A** Level 1 Acceptance: a system by which the BE servers can request FEB buffered data after a trigger decision is made to keep an event.

**L2** Level 2: the second level of ATLAS TDAQ that was used in Run I of the LHC.

**LAr** Liquid Argon: EM and hadronic calorimeter subsystems of ATLAS.

**LB** Luminosity Blocks: segments of data separated into units of time durations.

**LBA** Long Barrel A: a subcomponent of TileCal in ATLAS.

**LBC** Long Barrel C: a subcomponent of TileCal in ATLAS.

**LCW** Local Cluster Weighting: a scale at which jets are corrected for a normalized response to energy deposits in the hadronic calorimeters.

**LED** Light-Emitting Diode: a circuit device that can pulse light.

**LEP** Large Electron-Positron: a collider previously at CERN.

**LHC** Large Hadron Collider: a particle collider at CERN.

**LHCb** Large Hadron Collider Beauty: a detector for the LHC focused on precision EW measurements.

**LL** Leading Log: a correction estimate to tree level calculations.

**LO** Leading Order: scatter calculation at tree level.

**LS1** Long Shutdown 1: a planned shutdown of all detectors at CERN for management and upgrades.

**LSP** Lightest Supersymmetric Particle: the least massive BSM particle required by SUSY.

**LUCID** Luminosity measurement using Cherenkov Integrating Detector: a forward detector in ATLAS used for luminosity measurements.

**LV** Low Voltage: voltages in the 4,  $\pm 5$ , and 9 V range to activate circuits.

**MBTS** Minimum Bias Trigger System: a trigger system that identifies MIPs that represents the loosest possible trigger definitions.

**MC** Monte Carlo: an estimation technique that is often used to describe scatter simulation.

**MDT** Monitored Drift Tube: a tracking sensor used in a subcomponent of the MS in ATLAS.

**MIP** Minimally-Interacting Particle: a particle that interacts minimally with a medium as determined by its momentum.

**MobiDick** Mobile Data Acquisition: a diagnostic system that can certify individual modules in TileCal.

**MS** Muon System: a series of spectrometers used to detect muons in ATLAS.

**MSSM** Minimal Supersymmetric Standard Model: a minimal extension of the MSSM to incorporate SUSY.

**mSUGRA** Minimal Supergravity: an MSSM reduced to 5 additional parameters, also known as cMSSM.

**NC** Neutral Current: weak interactions with no change in EM charge.

**NLL** Next-to-Leading Log: a correction to loop corrections to tree-level calculations.

**NLO** Next-to-Leading Order: a loop correction to tree-level calculations.

**NLSP** Next-to-Lightest Supersymmetric Particle: the lightest particle (after the LSP) required by SUSY.

**PDF** Probability Density Function or Parton Distribution Function: the first term refers to a normalized probability distribution while the second refers to the relative sharing of momenta between the quarks within a hadron.

**pMSSM** Phenomenological Minimal Supersymmetric Standard Model: an MSSM reduced to 19 additional parameters.

**PMT** Photo-Multiplier Tube: a sensor that amplifies photon production to create a large electrical signal.

**Prometeo** Prometeo: an upgrade to MobiDick for use with the upgraded TileCal FEBs and BE electronics.

**PS** Proton Synchrotron: an accelerator at CERN supporting the LHC.

**PSB** Proton Synchrotron Booster: an accelerator at CERN supporting the LHC.

**PU** Pileup: more than one event present in a particle collision.

**PV** Primary Vertex: the vertex of the initial particle collision for an event.

**QCD** Quantum Chromodynamics: a QFT that describes the strong force.

**QED** Quantum Electrodynamics: a QFT that describes the interactions of EM charged particles.

**QFD** Quantum Flavordynamics: a QFT that describes the weak force.

**QFT** Quantum Field Theory: the mathematical basis of HEP that combines quantum mechanics and special relativity.

**RJ** Recursive Jigsaw: a reconstruction technique that attempts to approximate the missing degrees of freedom in a BSM event.

**RMS** Root Mean Square: a statistical measure of a spread in values, often calculated relative to an average (standard deviation).

**ROD** Read Out Driver: a system that retrieves the buffered data from the FEBS.

**ROI** Regions Of Interest: sections of the detector identified during trigger for further study of the object features.

**RPC** *R*-Parity Conservation: a symmetry common to many SUSY models.

**SCT** Semiconductor Tracker: a subcomponent of the ID in ATLAS.

**SFP** Small Form-factor Pluggable: an optical communication for fast transfers.

**SM** Standard Model: the current and successful model of experimental HEP.

**SPS** Super Proton Synchrotron: an accelerator at CERN supporting the LHC.

**SR** Signal Region: a region defined for enriched signal events optimized against BG contamination.

**ST** Simplified Topologies: a generalization of SUSY interactions, also known as Simplified Models.

**STACO** Statistical Combination: an algorithm for reconstructing muons.

**SUSY** Supersymmetry: a model that proposes a BSM spin symmetry between fermions and bosons.

**SV** Secondary Vertex: a subsequent vertex created by the decay of an unstable particle.

**TBJC** Track-Based Correction to the Jet Calibration: a scale at which jets are corrected for a normalized response to energy deposits in the hadronic calorimeters.

**TDAQ** Trigger and Data Acquisition: a system designed to reduce the rate of data recording.

**TGC** Thin Gap Chamber: a triggering sensor used in a subcomponent of the MS in ATLAS.

**TileCal** Tile Calorimeter: a hadronic calorimeter subsystem of ATLAS.

**TRT** Transition Radiation Tracker: a subcomponent of the ID in ATLAS.

**TTC** Trigger and Timing Control: refers to a TDAQ cable that delivers the LHC clock to individual FEBs and transmits trigger requests.

**UDP** User Datagram Protocol: a policy for connecting to an FPGA.

**UE** Underlying Event: a collision between quarks other than the hard scatter that presents a background to rare processes.

**VEV** Vacuum Expectation Value: the minimum potential of quantized fields.

**VHDL** VHASIC Hardware Description Language: a programming language used to configure an FPGA.

**VHSIC** Very High Speed Integrated Circuit: a fast processing circuit.

**VME** Versa Module Europa: a server technology previously used in MobiDick.

**VR** Validation Region: a region defined for evaluating the performance of a BG fit between data and MC.

**WIMP** Weakly-Interactive Massive Particle: a generic name for a heavy particle that is difficult to detect.

**WLS** Wavelength-Shifting: fibers that smear sharp optical pulses into a more useful pulse shape.

**ZDC** Zero Degree Calorimeter: a forward detector in ATLAS used for nuclear measurements.

## CHAPTER 1

### Introduction

Particle physics (or high-energy physics; HEP) has developed from an insatiable quest to dissect the nature of the universe down to its bare fundamentals. The motion of molecules can unite the seemingly disparate phenomena of sound and heat. Optics, electricity, and magnetism can be written in terms of Maxwell's equations. Quantum mechanics can describe particle motion at a very small scale (distance, energy, time, etc.), where existing theories would otherwise fail.

Field equations describe how some physical quantity, such as temperature, at some point in space and time influences another point with a value of its own. Classical field theories such as Maxwell's equations and Newton's theory of gravity can even be expanded to incorporate special relativity. The quantum field theory of HEP unites a simultaneous understanding of both quantum mechanics and special relativity to describe particles as quantized excitations of the underlying field. This formalism even allows electromagnetism to be united with a quantum description of nature, while gravity is curiously incompatible.

Symmetry is what makes a theory "beautiful". The equations are not merely a collection of symbols and numbers written on a page for educated guessing. Instead, something physical in nature is being described by geometrical relations or spatial propagation. For a set of particles used as input, another set of particles is predicted because they are required by symmetry.

One observant question is to ask how the boundary between "high" energy and "low" energy physics is being used in this discipline. "High" energy physics refers to physics at its most fundamental or smallest scale, where quantum and relativistic effects cannot be ignored. The creation of exotic particles through collisions, for example, requires ordinary matter to have very high kinetic energy to spontaneously produce something heavier.

To bring the conceptual understanding down to this scale, consider how “mass” is defined. A typical definition of “mass” may refer to how much matter is contained within an object. By holding two objects for comparison, one can determine which object has more matter by moving them around. An object with large mass will require a greater force to change its inertia than the object with less mass.

This definition subtly relies on treating matter as a collective whole. Rather than being infinitely cuttable, matter is composed of molecules or atoms. This was an idea espoused since Democritus and ancient times, but Einstein conclusively showed that the random collision of discrete atoms, rather than continuous waves, is responsible for the effect of Brownian motion. Furthermore, these atoms bind themselves together through the electromagnetic force, allowing them to clump together in the classical definition of matter.

The binding of atoms is possible through electric charge. In fact, the Periodic Table can be organized by intrinsic properties such as this, suggesting that there is a substructure to the atom. Thompson showed the existence of negatively charged electrons in beta rays, while Rutherford revealed the nucleus with alpha scattering. The X-ray spectra of Moseley’s experiment showed that the number of protons in a nucleus is the best way to organize the elements. Chadwick then completed the atomic mass with the proposal of neutrons after studying nuclear decay.

Protons and neutrons can be further dissected with the deep inelastic scattering of electrons to expose a substructure of quarks and gluons. This exploration leads to a quantum realm where the definition of mass as an amount of matter is hopelessly lost. The effective mass of the proton is much greater ( $\sim 100x$ ) than the sum of its three constituent quarks (and massless gluons). Instead, the gluons takes up a significant kinetic energy to confine these quarks together. This is a quintessential case of why the mass-energy effects of relativity cannot be ignored.

It is true that an atom is slightly heavier when one electron gains kinetic excitation, but the effect is so small that it is often ignored. Nuclear decay can be achieved with thermal energy, or neutrons that are not very energetic. In HEP, the luxury of Galilean

relativity is inapt because Einstein's relativity is required. It is not uncommon to measure electrons with 100 GeV of energy ( $p \gg m_e$ ) in HEP. The definition of "mass" has to be adjusted to reflect this inescapable reality. The intrinsic "mass" of a fundamental particle is perturbed by spontaneous interactions with its surrounding vacuum energy. The definition of "mass" is the strength of a particle's couplings, or the resulting probabilistic sum of all these possible interactions.

By increasing the amount of energy in particle interactions, HEP was able reach new particles that could otherwise not be seen. Particle physics experiments led to a "zoo" of many particles in the mid-20th century that seemed arbitrarily complex, and perhaps even a little "ugly". Quantum electrodynamics, electroweak theory, and quantum chromodynamics eventually began to converge into the formulation of the Standard Model. This model is something very "pretty" indeed, but there are limitations where it fails. Supersymmetry posits another symmetry that has not been incorporated yet in order to fix a few of these problems.

Supersymmetry is appealing because of its simplistic reliance on the same idea of imposed symmetries that went into the creation of the Standard Model, but it can pose a few experimental difficulties. The first is that supersymmetry needs many more free parameters to completely define itself. Each one of these would have to be measured (or scanned through guesses) before the hypothesis can be predictive. The second issue is that measuring these parameters is difficult because they often involve particles that elude detection. Finally, these events are rare and existing physics creates a super-abundance of events that can cloud the existence of new physics.

The scattered particles in high-energy events are detected in numerous ways by very large and specialized equipment. Exactly how matter passes through the multiple layers of these detectors must be understood very well. The limitation of data recording poses more challenges and care is devoted to efficiently capture the most new physics events.

Simplified Models of supersymmetry and certain topological variables could provide sufficient discrimination to new physics. The Recursive Jigsaw method in particular at-



tempts to resolve the unconstrained masses and decay angles of “invisible” particles that could be produced by supersymmetric interactions. This method of reconstruction has several advantages to select these new physics events when compared to the more standard approaches.

This dissertation covers work performed at CERN with the ATLAS collaboration between summer 2011 and spring 2016. Chapter 2 describes the Standard Model of particle physics and addresses some of its shortcomings before offering supersymmetry (Chapter 3) as a viable candidate for physics beyond the Standard Model. Chapter 4 introduces the LHC and the ATLAS detector as tools for discovery, including work that was performed on diagnostic equipment. Chapter 5 discusses the triggering system that is used to reduce the rate of recorded events. Chapter 7 delves into some of the steps taken to increase confidence in the particle content and reconstruction of events and introduces the statistical estimation concepts that will be used to interpret the results. Chapter 8 details topological variables and the progress that has been made in defining the Recursive Jigsaw reconstruction method and a trigger based on it. Chapters 9 and 10 contain studies of the Run I data using an early prototype of Recursive Jigsaw called Razor. Chapter 11 contains a study of 2015 data using the Recursive Jigsaw method with some projections for early 2016 data. Finally, Chapter 12 wraps up a status of the method in the overall view of particle physics.

## CHAPTER 2

### The Fundamental Theory of Particle Physics

The search for new physics starts with establishing the basis of a practical theory or model. The extraordinary claim of new physical evidence must compete with the best existing ideas. This allows the search to compare new results against discovered results, but it also allows an opportunity to identify missing pieces in the theory. The Standard Model (SM) represents the most empirically successful theory used in HEP. New physics could modify the predictions of the SM, include more features that lead to new predictions, fix problems of the existing features, or even suggest a completely different basis.

The fundamental theory of HEP will need at least four components:

- field theory
- quantum mechanics
- special relativity
- symmetries

#### 2.1 Quantum Field Theory

The mathematical description of the SM is written in terms of a field theory. A field theory description of classical mechanics facilitates an approach to the complex nature of continuous, or  $n$ -body, systems. For example, the simple harmonic oscillation of a mass on a spring is very well understood, but a large grid of springs (such as a galaxy-size mattress) is notationally difficult to write and computationally intractable even if the same basic principles apply. It is simpler to treat each point in the grid as being its own entity with measurable responses to each other. Pushing against one side of the grid of springs will create a packet of compression and extension that can travel as waves throughout the medium and perturb the field points into vibration modes. Harmonic modes can pass

through each other (linear terms) but anharmonic modes can couple to each other (nonlinear terms) and scatter to make new modes. Such a model could also describe how sound travels through a steel slab.

Describing the nature of fundamental physics runs into another problem. A hallmark of quantum mechanics is the fluctuation of energy. The uncertainty principle asserts that the precision of measurement is fundamentally limited by the nature of the system, which is accessible by complementary variables, and not on the tools of measurement. An increase in the precision of a positional measurement reduces the precision of a momentum measurement. The increase in timing precision reduces the precision of energy measurement. Quantum mechanics can describe something very small if it does not move very fast. In special relativity, energy can be transformed into mass and mass can transform into energy. Special relativity can describe the mechanics of large objects (e.g. a very powerful rocket) that move very fast. If something small is moving very fast, an imprecision in energy conflicts with the relativistic treatment of mass. If the energy measurement can fluctuate in quantum mechanics, then particles can appear or disappear in special relativity.

In quantum mechanics, energy levels are quantized in a potential (such as an electromagnetic – EM – potential). An electron with negative charge can exist at discrete energy levels (quanta) around a nucleus of positive charge. When incident EM radiation is introduced, atomic electrons can be promoted (e.g. fluorescent lamps) or demoted (e.g. lasers). The Schrödinger equation that describes these interactions is based on a Hamiltonian eigenfunction that governs how a particle (e.g. the electron) is affected by the EM fields. The quantization of the EM field allows the EM radiation scattering problem to be written in terms of creation and annihilation operators. These operators can be used to define a number operator that describes how many particles exist at a certain state, but the total number of particles is conserved. Photons can be created or destroyed, but the electron cannot. This suggests that quantum mechanics is not giving mass and energy the equal treatment that is established in special relativity. Quantum field theory (QFT) is a quantum treatment of nature that obeys special relativity, and it is written in the mathe-

mathematical language of fields. All *possibilities* are allowed, but they are not all *probable*. The probability amplitude of each interaction is at the center of making the SM predictive.

The SM takes a set of particles as an input and predicts another set. The input particles are the fermions, defined as spin-1/2 particles. “Spin” is a quantum number that allows two electrons to exist at the same energy quanta, because one is “spin-up” and the other is “spin-down”. These fermions are the six massive quarks exclusively participating in the strong force ( $u, d, s, c, b, t$ ) and three massive leptons ( $e, \mu, \tau$ ) and their associated massless neutrinos ( $\nu_e, \nu_\mu, \nu_\tau$ ) participating in EM and weak forces. The output particles are spin-1 particles called “bosons” that mediate these interactions (no Pauli spin exclusion). The massless photon ( $\gamma$  or sometimes  $A$  to avoid notation confusion) mediates the EM force, eight massless gluons ( $g$ ) mediate the strong force, and three massive bosons ( $W^+, W^-, Z^0$ ) mediate the weak force. Each one of these particles has an antimatter partner, which for a charged particle is just a particle with opposite sign and is identical otherwise.

## 2.2 Model Building from Symmetry

The SM is an approximation of nature. As is the case with the galactic mattress described in Section 2.1, the exact form of fundamental physics is not directly revealed. Instead, the foundation of the model is built from features of nature that were discovered. For example, consider the function shown in Figure 2.1. The exact form of this function does not have to be known before several descriptions can be made about it.

It is an odd function, which means that  $f(-x) = -f(x)$ , or mirror values across the  $x$ -axis have function values mirrored across the  $y$ -axis. The absolute value of this function is an even function, and the odd-ordered derivatives of this function are even. Its Maclaurin series expansion only includes odd terms and a Fourier expansion of this function can only contain sine terms. If the function is integrated over symmetric limits, the answer will be zero. Integrating its square over symmetric limits is equal to twice the integration over one side. Values near zero appear to be modeled well by  $x^3$ . A lot can be known about this function by studying its properties without explicitly defining it.

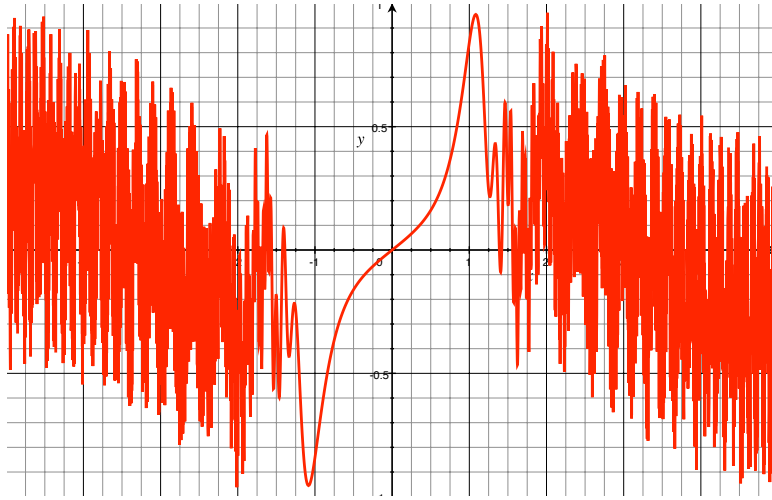


Figure 2.1. An arbitrary equation used to demonstrate the effectiveness of symmetries.

### 2.2.1 Symmetries and Conservation

For every apparent conservation law observed in nature, there is an underlying symmetry in the theory that describes nature. This is Noether’s theorem, which also states that a model built upon these symmetries correctly describes those conservation laws. A symmetry transformation is invariant if changes allowed within its symmetry group leave the system unchanged. For example, an equilateral triangle can be rotated by  $120^\circ$ , which would be indistinguishable from a rotation of  $0^\circ$ ,  $240^\circ$ , or  $-120^\circ$ . A  $\mathbb{Z}_2$  symmetry ensures that there is a symmetry to a discrete change in field sign ( $\phi \rightarrow -\phi$ ). Symmetries can also occur in continuous transformations, such as space or time.

A theory cannot be fundamental if it depends on where or when the experiment is performed. Any variations to position or initiation must bear out as a consequence of the theory. Symmetry to translations in time results in a conservation of energy. An invariance to spacial translations leads to a conservation of momentum. Angular momentum is the result of a symmetry to rotational transformations. Charge is conserved since the fields are invariant to gauge transformations ( $\partial_\mu A^\mu = 0$ ).

“Global” symmetries are defined as symmetries that act at every point in spacetime. If the transformations are applied separately with different values to the fields, the symmetry

is “local”. The global and local symmetries need to be communicated across spacetime, which means that “mediators” are needed. For example, if one spring in the galactic mattress were to break, the rest of the mattress would have to be “informed” of the change through wave packets.

The local symmetry of the SM is represented by unitary matrices, which are the choice representations of group symmetry in quantum theories because they preserve probability amplitude; the total probability should always be 1.  $U(1)$  is a unitary group related to a circle group in the complex plane, where the only parameter is a rotation angle that repeats itself every  $2\pi$  radians. Each element of the group is characterized by its phase and the generator is  $\exp(i\theta)$ . In the SM, this corresponds to the EM charge of the fields and is denoted  $U(1)$ .  $SU(n)$  is a group of “special”  $n \times n$  unitary matrices for which the determinant equals unity. The symmetry group of weak interactions is  $SU(2)$ , which is generated by three Pauli matrices (Appendix A.4). The symmetry group of strong interactions is  $SU(3)$ , which is generated by eight Gell-Mann matrices (Appendix A.5).

The formalism that describes the SM features several instances of “broken” symmetry. The symmetry is preserved in the SM Lagrangian and not in its particular solutions. Exact global symmetries can be broken, which would result in massless Goldstone *scalars* (spin-0). Exact local symmetries produce *massless* spin-1 (boson) mediators, but they can also produce *massive* spin-1 (boson) mediators if the symmetry is broken.

As a simple example, consider human left hands versus right hands. They look identical in most respects; they each have a thumb and four fingers. By placing the two hands together, the thumbs point in the same direction, but the fingers curl in opposite directions. If these hands are rotated so that the thumbs point toward each other (opposite each other), the fingers curl in the same direction. At no orientation can the two hands exhibit exactly the same behavior. This effect can also be observed by comparing one hand to a mirrored hand. There is a fundamental difference between “left” and “right” even if, for many applications, they appear identical in form and function. In HEP, a particle may

have its spin aligned with its momentum vector, or anti-aligned. Transformations involving the symmetry of spin interactions are called parity operations (Appendix A.6).

This parity interaction works well for EM and strong interactions, but it is violated maximally in weak interactions. Only left-handed neutrinos participate in weak interactions, and right-handed neutrinos may not exist as far as any empirical study that can be designed. Conversely, *antineutrinos* are all right-handed. To understand this in terms of the “hand” analogy, some people never use their right hand for writing. Charge conjugation describes a transformation of charge sign, which means that there is a realm of antimatter particles as well. If the parity transformation is combined with a charge conjugation to form a charge-parity (*CP*) transformation, the symmetry very nearly recovers. Yet, *CP* violation is a cornerstone of the SM (Section 2.2.2.5).

### 2.2.2 Building the Model

The model is formulated using a Lagrangian density, which is ideal for explicitly revealing the symmetries and conservations of the system. The coordinate system can be chosen as desired to conveniently exploit the symmetries of the system or its constraints. The equations of motion can be solved, but the extra work may not be necessary since the symmetries and conservation can often be read plainly. The basic form of the Lagrangian includes individual fields and their derivatives:

$$\mathcal{L}[\phi_i(x), \partial_\mu \phi_i(x)] \tag{2.1}$$

The most general theory that can be written down is:

$$\mathcal{L}(\phi, \psi) = \mathcal{L}_{kinetic} + \mathcal{L}_{fermion} + \mathcal{L}_{scalar} + \mathcal{L}_{Yukawa} \tag{2.2}$$

The Lagrangian takes fermions (spin-1/2,  $\psi$ ) and scalars (spin-0,  $\phi$ ) as input. The kinetic terms are included to allow propagation, and the Yukawa term allows an interac-

tion between the scalars and fermions. From this point, models can be built by inserting experimental observations into this Lagrangian.

### 2.2.2.1 QED

The  $U(1)$  local gauge symmetry needs an electromagnetic (EM) propagator to keep the theory continuously invariant for complex fields. The resulting force communicates the global symmetry of charge across spacetime to keep the fields locally gauge invariant. This EM interaction is known as quantum electrodynamics (QED). The EM field is a gauge field of photons that mediate the interaction between charged fermion fields. QED interactions are invariant under parity and charge transformations.

The leptons ( $e, \mu, \tau$ ) are all charged fermions with  $-1$  EM charge. Anti-particle partners exist for each of the leptons, but they have a  $+1$  EM charge. The anti-electron has a special name – positron – because of its historical context in the development of QED. The mediating boson is a photon ( $\gamma$ ), which is EM neutral, so it does not interact with itself. If two charged particles approach each other, they are repelled if the charges are the same sign, or attracted to each other if they are of opposite sign. Under low-energy interactions, QED also applies to protons, but these are not fundamental particles. For this reason, the Lagrangian is written with a generalized  $f$  for fermions:

$$\mathcal{L}_{QED} = \frac{1}{4}F^{\mu\nu}F_{\mu\nu} + \bar{f}(i\not{D} - m)f \quad (2.3)$$

The EM field tensor is:

$$F^{\mu\nu} = \partial^\mu A^\nu - \partial^\nu A^\mu \quad (2.4)$$

The field must be gauge invariant, so its covariant derivative is:

$$D^\mu = \partial^\mu + ieq_f A^\mu \quad (2.5)$$



The coupling constant ( $e$ ) is the EM charge and  $q$  is the magnitude of the charge, which could be something other than 1.

#### 2.2.2.2 QCD

A local  $SU(3)$  symmetry needs a strong propagator, which is the gluon ( $g$ ). The theory of the strong force is called quantum chromodynamics (QCD) because a “color” field of bosonic gluons mediates the interaction between fermionic quarks. These particles are confined into hadrons (baryons with  $qqq$  or mesons with  $q\bar{q}$  – perhaps also tetraquarks  $q\bar{q}q\bar{q}$  and pentaquarks  $qqqq\bar{q}$ ), even though the individual quarks and gluons are the basis of the interactions. When hadrons are given enough energy, they spontaneously shower into more hadrons rather than releasing their quark content. Leptons have no interaction with the strong force, but because the gluons have color charge, gluon-gluon interactions are possible. QCD interactions are invariant under parity and charge transformations.

The quarks ( $u, d, s, c, b, t$ ) are all fermions. Up-quarks ( $u, c, t$ ) have  $+2/3$  EM charge and down-quarks ( $d, s, b$ ) have  $-1/3$  EM charge. The six quarks are triplets because they each can be designated as red, green, or blue. Gluons are color octets because there are eight combinations of color-anti-color. All color particles exist in singlets ( $R + G + B$ ), and a gluon singlet ( $(R\bar{R} + G\bar{G} + B\bar{B})/\sqrt{3}$ ) is possible. The Lagrangian for QCD is given by:

$$\mathcal{L}_{QCD} = \frac{1}{4}G_a^{\mu\nu}G_{\mu\nu}^a + i\bar{q}\not{D}q - m_q\bar{q}q \quad (2.6)$$

The field strength is given by:

$$G_a^{\mu\nu} = \partial^\mu G_a^\nu - \partial^\nu G_a^\mu + g_S f_{abc}G_b^\mu G_c^\nu \quad (2.7)$$

The covariant derivative of the field is:

$$D^\mu = \partial^\mu + ig_S G_a^\mu L_a \quad (2.8)$$

The  $L_a$  term includes the generators of the  $SU(3)$  symmetry group (Appendix A.5):

$$L_a = \frac{1}{2}\lambda_a \quad (2.9)$$

### 2.2.2.3 QFD

Quantum flavordynamics (QFD) is a field theory for weak interactions based on a local  $SU(2)$  symmetry. This force governs nuclear decay as well as cosmic showers involving muons. Weak interactions introduce neutral fermionic neutrinos, which are associated with lepton flavor ( $\nu_e, \nu_\mu, \nu_\tau$ ). For nuclear decay, the nucleons ( $p$  and  $n$ ) are still hadronically confined, so the model is ignorant of the individual quarks unlike QCD (or EW; Section 2.2.2.5).

Originally starting from the Dirac equation, the theory (which steps through Fermi theory and vector-axial theory) is built on Hamiltonian mechanics. QFD interactions are *not* invariant under parity transformations (Appendix A.6), which is a hallmark of the theory. Experiments have not discovered *any* right-handed neutrinos or *any* left-handed antineutrinos, either because they do not exist or because their interactions are still unknown. Two operators are defined to describe left-handed and right-handed spinors separately:

$$P_L = \frac{1 - \gamma^5}{2} \quad (2.10a)$$

$$P_R = \frac{1 + \gamma^5}{2} \quad (2.10b)$$

$$(2.10c)$$

Since neutrinos can only be left-handed, the only terms in the Hamiltonian should be the vector ( $\gamma^\mu$ ) and pseudovector or axial-vector terms ( $\gamma^5$ ) (Appendix A.6).

$$\mathcal{H}_W = \frac{1}{\sqrt{2}}G_F [\bar{u}_p \gamma_\mu (1 - g_A \gamma^5) u_n] [\bar{u}_e \gamma^\mu (1 - \gamma^5) u_\nu] + h.c. \quad (2.11)$$

$G_F$  is known as the Fermi constant and  $g_A = 1.26$ . QFD clashes with QED because the massive bosons would violate gauge symmetry unless a mechanism (Higgs) is developed to spontaneously break the symmetry of the local group.

#### 2.2.2.4 Higgs

The Brout-Engler-Higgs mechanism is one of the most important features of the SM because it is necessary for the completion of the union between the EM and weak forces. In a Lagrangian, the general form is  $\mathcal{L} = T - U$  and the equations of motion are obtained by the Euler-Lagrange relationship:

$$\frac{\partial \mathcal{L}}{\partial q_i} - \frac{d}{dt} \left( \frac{\partial \mathcal{L}}{\partial \dot{q}_i} \right) = 0 \quad (2.12)$$

The Hamiltonian is a Legendre transformation of the Lagrangian:

$$\begin{aligned} \mathcal{H} &\equiv \sum_i \dot{q}_i \frac{\partial \mathcal{L}}{\partial \dot{q}_i} \\ &= \sum_i \dot{q}_i p_i - \mathcal{L} \end{aligned} \quad (2.13)$$

The time evolution of the Hamiltonian is given by:

$$\frac{dp}{dt} = - \frac{\partial \mathcal{H}}{\partial q} \quad (2.14a)$$

$$\frac{dq}{dt} = + \frac{\partial \mathcal{H}}{\partial p} \quad (2.14b)$$

One might assume that equations derived through the Hamiltonian formalism can also be described in the Lagrange formalism, which is only partially correct because the equations are *equivalent*. The Hamiltonian is often thought of as  $\mathcal{H} = T + V$ , but this relationship is not always true. The Lagrangian can be formed from the Hamiltonian equations of motion, but the vital description of its symmetries could be obscured. Consider encountering an equation such as:

$$\mathcal{L}_\phi = \partial_\mu \phi \partial^\mu \phi^* + \mu^2 \phi \phi^* + \lambda (\phi \phi^*)^2 \quad (2.15)$$

This equation actually looks more like a Hamiltonian. From a Lagrangian perspective, the second term looks like a mass term, but it would have to be an *imaginary* mass ( $m = \pm\sqrt{2}i\mu$ ). At first glance, it may even appear to be a simple sign error, but it cannot be dismissed so easily. Evidently, the potential term in the Lagrangian is not centered at its ground state.

$$\begin{aligned} \frac{\partial^2 V(\phi)}{\partial \phi^2} &= 0 \\ \mu^2 &= -2\lambda \phi \phi^* \end{aligned} \quad (2.16)$$

If  $\mu^2 > 0$ , the form of the potential would be a paraboloid, but since  $\mu^2 < 0$  the potential has a “Mexican hat” or “champagne bottle” shape (Figure 2.2). There is a minimum vacuum expectation value (VEV) that occurs in this potential:

$$\begin{aligned} v &= \sqrt{\frac{-\mu^2}{2\lambda}} \\ \mu^2 &= -2\lambda v^2 \end{aligned} \quad (2.17)$$

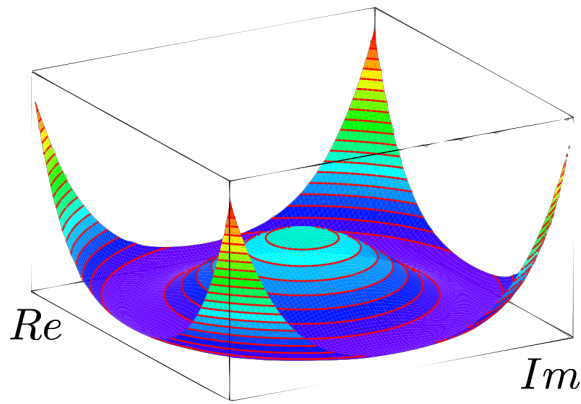


Figure 2.2. A representation of the Higgs potential exhibiting its “broken” symmetry.

To get a Lagrangian that looks more familiar, the field can be written as a complex field with real components  $\eta$  and  $\xi$  shifted by the VEV:

$$\phi(x) = [v + \eta(x)] \exp[i\xi(x)] \quad (2.18)$$

Plugging this complex field back into the Lagrangian results in some new terms:

$$\begin{aligned} \mathcal{L} &= \partial^\mu \eta \partial_\mu \eta + (v + \eta)^2 \partial^\mu \xi \partial_\mu \xi - \mu^2 (v + \eta)^2 - \lambda (v + \eta)^4 \\ &= \partial^\mu \eta \partial_\mu \eta + (v + \eta)^2 \partial^\mu \xi \partial_\mu \xi - 4\lambda v^2 \eta^2 - 4\lambda v \eta^3 - \lambda \eta^4 + \lambda v^4 \end{aligned} \quad (2.19)$$

The mass term has the correct sign ( $m_\eta^2 = 4\lambda v^2$ ) and a new term ( $\sim \eta^3$ ) describing a 3-point vertex has appeared. The problem is that this 3-point vertex is now violating the  $\mathbb{Z}_2$  symmetry ( $\phi \rightarrow -\phi$ ) that appeared in the original Lagrangian because it is an odd term. Only the notation has changed, so this *should* be the same physical system, but a symmetry has been broken *spontaneously*; nothing outside the system caused it to break. It seems that the symmetry does exist, but it is obscured because the potential is not centered at the ground level.

It is also strange that there are now kinetic terms for  $\xi$  but no mass term for it. The Higgs mechanism is able to give a real mass to  $\eta$ , but zero mass to  $\xi$ . This massless field creates Goldstone bosons, and it represents the freedom for a particle to rotate in  $\theta$  along the VEV. Since the theory is locally gauge invariant, a clever choice would be to fix it to a “unitary gauge” that sets  $\xi(x) = 0$ .

#### 2.2.2.5 EW

A combination of QED and QFD is expressed by a  $SU(2) \times U(1)$  symmetry that needs weak operators:  $W^\pm$  for charged current (CC) and  $Z^0$  for neutral current (NC). The combination of weak forces and EM forces is called electroweak (EW) theory. Because the Higgs field is coupled to gauge fields, the model exhibits electroweak symmetry breaking (EWSB). The vector mixing causes the weak mediators to become massive while leaving

the photon massless. With its remaining degree of freedom, the Higgs scalar also acquires a mass. The electroweak symmetry breaking (EWSB)

$$\mathcal{L}_{VM} = \frac{1}{8} \begin{pmatrix} 0 & v \end{pmatrix} \begin{pmatrix} gW_3 + g'B & g(W_1 - iW_2) \\ g(W_1 + iW_2) & -gW_3 + g'B \end{pmatrix}^\dagger \begin{pmatrix} gW_3 + g'B & g(W_1 - iW_2) \\ g(W_1 + iW_2) & -gW_3 + g'B \end{pmatrix} \begin{pmatrix} 0 \\ v \end{pmatrix} \quad (2.20)$$

This motivates writing a different basis to define the CC boson:

$$W^\pm = \frac{1}{\sqrt{2}}(W_1 \mp iW_2) \quad (2.21)$$

To express the remaining bosons, the mixing angle is given a shorthand notation:

$$t_W \equiv \tan \theta_W = \frac{g'}{g} \quad (2.22a)$$

$$s_W \equiv \sin \theta_W = \sqrt{1 - \left(\frac{m_W}{m_Z}\right)^2} \quad (2.22b)$$

$$c_W \equiv \cos \theta_W = \frac{m_W}{m_Z} \quad (2.22c)$$

The NC and photon terms can then be written nicely:

$$Z^0 = c_W W_3 - s_W B \quad (2.23a)$$

$$A^0 = s_W W_e + c_W B \quad (2.23b)$$

In this basis, the vector bosons can then be decoupled:

$$\mathcal{L}_{VM} = \frac{1}{4}g^2v^2W^+W^- + \frac{1}{8}(g^2 + g'^2)v^2Z^0Z^0 \quad (2.24)$$

There is a “flavor” or fermion “generation” symmetry for leptons that requires them to have the same flavor:

$$\begin{aligned} n^0 + p^- &\rightarrow e^- + \bar{\nu}_e \\ n^0 + p^- &\not\rightarrow e^- + \bar{\nu}_\mu \end{aligned} \tag{2.25}$$

In other words, if the flavor symmetry was not required, the two processes should occur at the same frequency. However, the first one *does* occur, while the second one *does not*. The net equation reveals that no vertex exists where an electron and a muon neutrino meet.

$$\begin{aligned} W^- &\rightarrow e^- + \bar{\nu}_e \\ W^- &\not\rightarrow e^- + \bar{\nu}_\mu \end{aligned} \tag{2.26}$$

Another example is that flavor symmetry requires the decay of a muon to have two neutrinos:

$$\begin{aligned} \mu^- &\rightarrow e^- + \bar{\nu}_e + \nu_\mu \\ \mu^- &\not\rightarrow e^- + \bar{\nu}_e \end{aligned} \tag{2.27}$$

The flavor symmetry works so well for leptons that it is a wonder why it does not work for quarks. If it did, there would be a lightest, stable, “strange” meson ( $K^\pm$ ) and a lightest, stable, “beauty” meson ( $B^\pm$ ). The  $\beta$ -decay of a neutron manages to conserve flavor:

$$\begin{aligned} n^0 &\rightarrow p^+ + e^- + \bar{\nu}_e \\ d^{-1/3} &\rightarrow u^{+2/3} + W^- \end{aligned} \tag{2.28}$$

The decay of a  $\Lambda^0$  baryon *does not* conserve flavor:

$$\begin{aligned} \Lambda^0 &\rightarrow p^+ + \pi^- \\ s^{-1/3} &\rightarrow u^{+2/3} + W^- \end{aligned} \tag{2.29}$$

The quarks are able to mix flavors while the leptons do not. Flavor-changing neutral currents (FCNC) are highly suppressed and represent a beacon for new physics. There is no  $Z$  vertex that can accomplish this, but CC loops do not entirely cancel each other due to the spectrum of quark masses. If the fermions are all treated as flavor doublets, then the eigenstates must have the form:

$$\begin{pmatrix} \nu_e \\ e \end{pmatrix}, \begin{pmatrix} \nu_\mu \\ \mu \end{pmatrix}, \begin{pmatrix} \nu_\tau \\ \tau \end{pmatrix}, \begin{pmatrix} u \\ d' \end{pmatrix}, \begin{pmatrix} c \\ s' \end{pmatrix}, \begin{pmatrix} t \\ b' \end{pmatrix} \quad (2.30)$$

The quarks are mixed by a transformation matrix that defines the primed quark basis. This Cabibbo-Kobayashi-Maskawa (CKM) matrix (Appendix A.7) is defined such that:

$$\begin{aligned} \begin{pmatrix} d' \\ s' \\ b' \end{pmatrix} &= \begin{pmatrix} V_{ud} & V_{us} & V_{ub} \\ V_{cd} & V_{cs} & V_{cb} \\ V_{td} & V_{ts} & V_{tb} \end{pmatrix} \begin{pmatrix} d \\ s \\ b \end{pmatrix} \\ &= V_{CKM} \begin{pmatrix} d \\ s \\ b \end{pmatrix} \end{aligned} \quad (2.31)$$

The Lagrangian for EW can now unite all these pieces:

$$\begin{aligned} \mathcal{L}_{EW} &= \frac{1}{4} W_a^{\mu\nu} W_{\mu\nu}^a + \frac{1}{4} B^{\mu\nu} B_{\mu\nu} \\ &+ \bar{Q}_i i \not{D} Q_i + \bar{U}_i i \not{D} U_i + \bar{D}_i i \not{D} D_i \\ &+ \bar{L}_i i \not{D} L_i + \bar{E}_i i \not{D} E_i \\ &+ V_{ij}^U \bar{Q}_{Li} U_{Rj} \tilde{\phi} + V_{ij}^D \bar{Q}_{Li} D_{Rj} \phi + V_{ij}^E \bar{L}_{Li} E_{Rj} \phi + h.c. \\ &- \lambda \left( \phi^\dagger \phi - \frac{1}{2} v^2 \right)^2 \end{aligned} \quad (2.32)$$

The field strengths are given by:



$$W_a^{\mu\nu} = \partial^\mu W_a^\nu - \partial^\nu W_a^\mu - g\epsilon_{abc}W_b^\mu W_c^\nu \quad (2.33a)$$

$$B^{\mu\nu} = \partial^\mu B^\nu - \partial^\nu B^\mu \quad (2.33b)$$

The covariants of the fields are:

$$\begin{aligned} D^\mu L_L &= \left( \partial^\mu + \frac{1}{2}igW_a^\mu \sigma_a - \frac{1}{2}ig'B^\mu \right) L_L \\ D^\mu E_R &= (\partial^\mu - ig'B^\mu) E_R \\ D^\mu \phi &= \left( \partial^\mu + \frac{1}{2}igW_a^\mu \sigma_a + \frac{1}{2}ig'B^\mu \right) \phi \end{aligned} \quad (2.34)$$

The SM is

### 2.3 Feynman Diagrams

The meaning of the equations can be lost in the expression of its mathematical intricacy, but the key is that its development is targeted at describing discovered processes. Luckily, a visually simplistic view of the interactions can be recovered with Feynman diagrams. All of the mathematical basis explained in Section 2.2.2 is preserved in these diagrams, but they are much more intuitive to grasp. These diagrams are built from deceptively easy “tinker-toys” that represent the limited number of pieces that are needed for every possible solution. If a diagram can be constructed using these pieces, then calculations of probability become a matter of tabulation. A list of Feynman rules for the SM can be found in Appendix B.

The particles exchanged in Feynman diagrams are called propagators. These are usually particles that facilitate the interaction, but they are virtual, meaning that they are not observable. They are also referred to as “internal” while visible particles are called “external”. Wherever two or more particles meet, a vertex interaction is formed. A vertex factor is applied and momentum is conserved. The diagrams simply represent the existence of particles and the emission of mediators, but they do not imply any spatial relation. The

familiar situation of two charged particles exerting an EM force on each other is presented in Figure 2.3.

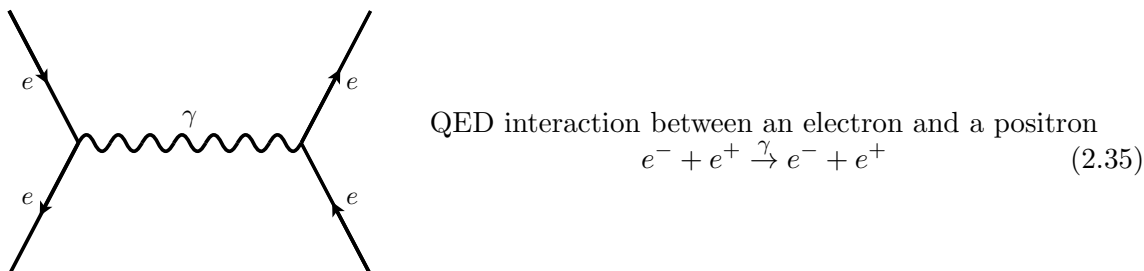


Figure 2.3. A Feynman diagram of charged attraction via exchange of a photon.

One of the questions that a chemistry course might leave unanswered is why a nucleus can be packed with protons when the protons should repulse each other. Figure 2.4 shows how the strong interaction between quarks creates a residual effect via the exchange of a  $\pi^0$  meson. This exchange is strong enough to stabilize some heavy nuclei.

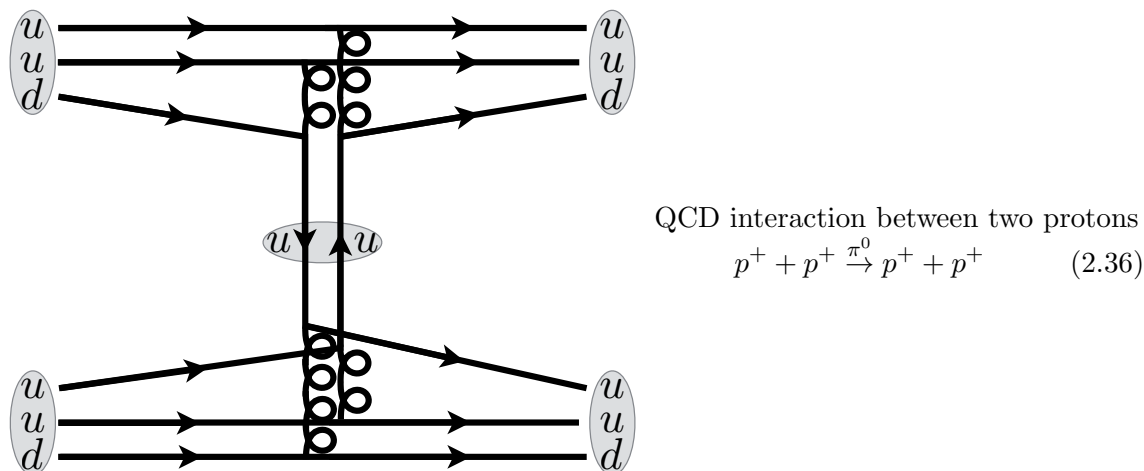


Figure 2.4. A Feynman diagram of strong force attraction via exchange of a pion.

The last of the fundamental forces that are shown in this section is the weak force. Some radioactive nuclei can undergo  $\beta$ -decay, which explains how a neutron can spontaneously change into a proton. The  $\beta$  ray emitted by this change is an electron, and

conservation of lepton number requires an antineutrino to be paired with it. This process is shown by the  $W^-$  exchange in Figure 2.5.

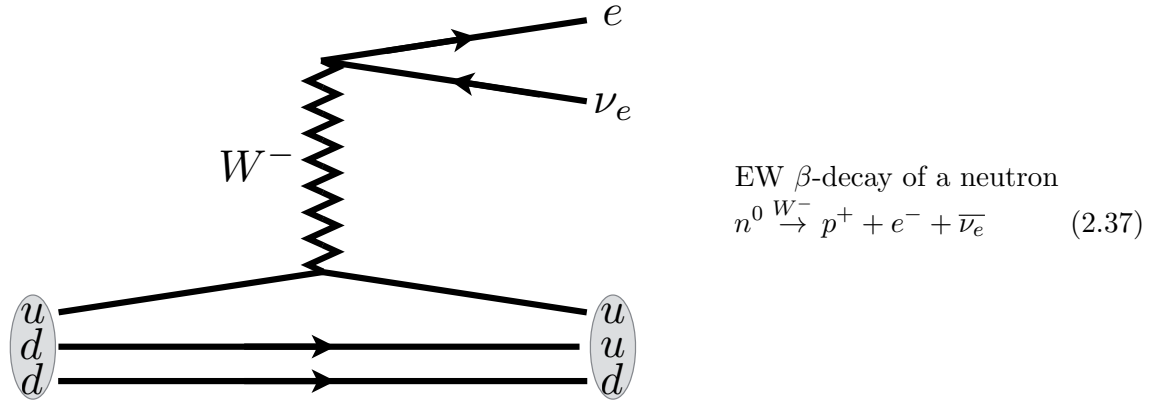


Figure 2.5. A Feynman diagram of the weak decay of a neutron.

## 2.4 The Standard Model

The local symmetry of the SM is  $SU(3) \times SU(2) \times U(1)$  or a direct product of QCD and EW. Constructing the SM following the outline of Section 2.2.2 could be as simple as writing the sum of equations 2.3, 2.6, and 2.32. After considering the usefulness of the Feynman diagrams in Section 2.3, it would be more appropriate to present the SM in terms of the natural predictions of its interactions.

$$\begin{aligned} \mathcal{L}_{SM} = & \mathcal{L}_{kinetic} + \mathcal{L}_{QCD} + \mathcal{L}_{NC} + \mathcal{L}_{CC} \\ & + \mathcal{L}_H + \mathcal{L}_{HV} + \mathcal{L}_{3V} + \mathcal{L}_{4V} + \mathcal{L}_{Yukawa} \end{aligned} \quad (2.38)$$

The terms in this Lagrangian describe different types of Feynman diagrams. A table locating the corresponding diagrams in Appendix B is provided in Table 2.1.

The kinetic terms are given by:

Table 2.1. A table connecting SM Lagrangian terms to their respective diagrams

SM term	Lagrangian	diagrams
kinetic	Equation 2.39	Appendix B.2
QCD	Equation 2.41	Figure B.13
NC	Equation 2.42	Figures B.7, B.11
CC	Equation 2.43	Figures B.8, B.9, B.10
H	Equation 2.44	Figures B.26, B.27
HV	Equation 2.45	Figures B.22, B.23, B.24, B.25
3V	Equation 2.46	Figures B.14, B.15
4V	Equation 2.47	Figures B.17, B.18, B.19, B.20
Yukawa	Equation 2.48	Figure B.12

$$\begin{aligned}
\mathcal{L}_{kinetic} = & \frac{1}{4} G_a^{\mu\nu} G_{\mu\nu}^a + \frac{1}{2} W^{\mu\nu+} W_{\mu\nu}^- + \frac{1}{4} Z^{\mu\nu} Z_{\mu\nu} + \frac{1}{4} F^{\mu\nu} F_{\mu\nu} + \frac{1}{2} (\partial^\mu H)(\partial_\mu H) \\
& - m_W^2 W^{\mu+} W_\mu^- - \frac{1}{2} m_Z^2 Z^\mu Z_\mu - \frac{1}{2} m_H^2 H^2
\end{aligned} \tag{2.39}$$

The covariant derivatives are given by:

$$\begin{aligned}
D^\mu Q_L &= \left( \partial^\mu + \frac{1}{2} i g_S G_a^\mu \lambda_a + \frac{1}{2} i g W_b^\mu \sigma_b + \frac{1}{6} i g' B^\mu \right) Q_L \\
D^\mu U_R &= \left( \partial^\mu + \frac{1}{2} i g_S G_a^\mu \lambda_a + \frac{2}{3} i g' B^\mu \right) U_R \\
D^\mu D_R &= \left( \partial^\mu + \frac{1}{2} i g_S G_a^\mu \lambda_a - \frac{1}{3} i g' B^\mu \right) D_R \\
D^\mu L_L &= \left( \partial^\mu + \frac{1}{2} i g W_a^\mu \sigma_a - \frac{1}{2} i g' B^\mu \right) L_L \\
D^\mu E_R &= (\partial^\mu - i g' B^\mu) E_R \\
D^\mu \phi &= \left( \partial^\mu + \frac{1}{2} i g W_a^\mu \sigma_a + \frac{1}{2} i g' B^\mu \right) \phi
\end{aligned} \tag{2.40}$$

The QCD interaction from Section 2.2.2.2 is also added:

$$\mathcal{L}_{QCD} = i \bar{q} \not{D} q - m_q \bar{q} q \tag{2.41}$$

The first term describing EW interactions is due to NC:

$$\mathcal{L}_{NC} = eq_f \bar{f} \gamma_\mu f A^\mu + \frac{g}{c_W} \left( I_f^3 \bar{f} \gamma^\mu \frac{1-\gamma^5}{2} f - s_W^2 q_f \bar{f} \gamma_\mu f \right) Z^\mu \quad (2.42)$$

In this notation,  $I_f^3$  is the ‘‘isospin’’, which is a term that expresses the degeneracy of hadrons from the content of  $u$  and  $d$  quarks. Similarly, the charged current (CC) is:

$$\mathcal{L}_{CC} = -\frac{1}{\sqrt{2}} g \left( \bar{U} \gamma^\mu \frac{1-\gamma^5}{2} V_{CKMD} + \bar{\nu} \gamma^\mu \frac{1-\gamma^5}{2} e \right) W_\mu^+ + h.c. \quad (2.43)$$

The three-point and four-point Higgs vertices describe two terms:

$$\mathcal{L}_H = -\frac{1}{4} g \frac{m_H^2}{m_W} H^3 - \frac{1}{32} g^2 \left( \frac{m_H}{m_W} \right)^2 H^4 \quad (2.44)$$

The Higgs particle can interact with the vector bosons:

$$\mathcal{L}_{HV} = \left( gm_W H + \frac{1}{4} g^2 H^2 \right) \left( W^{\mu+} W_\mu^- + \frac{1}{2 c_W} Z^\mu Z_\mu \right) \quad (2.45)$$

Three-point vertices can be formed from the bosons:

$$\mathcal{L}_{3V} = -ig \left[ (W^{\mu\nu+} W_\mu^- - W^{\mu+} W_{\mu\nu}^-) (A_\nu s_W - Z_\nu c_W) + W^{\nu-} W^{\mu+} (A_{\mu\nu} s_W - Z_{\mu\nu} c_W) \right] \quad (2.46)$$

Four-point vertices can also be formed from the bosons:

$$\begin{aligned} \mathcal{L}_{4V} = & -\frac{1}{4} g^2 \left[ 2W^{\mu+} W^{\mu-} + (A_\mu s_W - Z_\mu c_W)^2 \right]^2 \\ & -\frac{1}{4} g^2 \left[ W^{\mu+} W^{\nu-} + W^{\nu+} W^{\mu-} + (A_\mu s_W - Z_\mu c_W) (A_\nu s_W - Z_\nu c_W) \right]^2 \end{aligned} \quad (2.47)$$

Lastly, the Yukawa term is an interaction between the fermions and the scalar Higgs potential:

$$\mathcal{L}_{Yukawa} = V_{ij}^U \bar{Q}_{Li} U_{Rj} \tilde{\phi} + V_{ij}^D \bar{Q}_{Li} D_{Rj} \phi + V_{ij}^E \bar{L}_{Li} E_{Rj} \phi + h.c. \quad (2.48)$$

There are 19 free parameters of the SM that need to be measured for it to truly be predictive. Nine of them are the masses of fermions, one is the mass of the Higgs particle, four are CKM mixing angles and the  $CP$ -violating phase, three are gauge couplings, one is the QCD vacuum angle, and one is the Higgs VEV.

Table 2.2 summarizes the properties of the particles in the SM. Their masses as predicted by theory are compared to their experimentally measured values. Table 2.3 lists the interaction basis with their couplings and range.

Table 2.2. The particle content of the SM

particle	spin	color	charge	mass (th.)	mass (exp.)
$u, \bar{u}$	1/2	(3)	$\pm 2/3$	–	$2.3^{+0.7}_{-0.5}$ MeV
$c, \bar{c}$	1/2	(3)	$\pm 2/3$	–	$1.275 \pm 0.025$ GeV
$t, \bar{t}$	1/2	(3)	$\pm 2/3$	–	$173.21 \pm 0.51 \pm 0.71$ GeV
$d, \bar{d}$	1/2	(3)	$\mp 1/3$	–	$4.8^{+0.5}_{-0.3}$ MeV
$s, \bar{s}$	1/2	(3)	$\mp 1/3$	–	$95 \pm 5$ MeV
$b, \bar{b}$	1/2	(3)	$\mp 1/3$	–	$4.18 \pm 0.03$ GeV
$e^\mp$	1/2	–	$\mp 1$	$y_e/\sqrt{2}$	$0.510998928 \pm 0.000000011$ MeV
$\mu^\mp$	1/2	–	$\mp 1$	$y_\mu/\sqrt{2}$	$105.6583715 \pm 0.0000035$ MeV
$\tau^\mp$	1/2	–	$\mp 1$	$y_\tau/\sqrt{2}$	$1776.86 \pm 0.1$ MeV
$\nu_e, \bar{\nu}_e$	1/2	–	0	0	$< 2$ eV
$\nu_\mu, \bar{\nu}_\mu$	1/2	–	0	0	$< 0.17$ MeV
$\nu_\tau, \bar{\nu}_\tau$	1/2	–	0	0	$< 15.5$ MeV
$\gamma^0$	1	–	0	0	$< 1 \times 10^{-18}$ eV
$W^\pm$	1	–	$\pm 1$	$\frac{1}{2}g$	$80.385 \pm 0.015$ GeV
$Z^0$	1	–	0	$\frac{1}{2}\sqrt{g^2 + g'^2}$	$91.1876 \pm 0.0021$ GeV
$g$	1	(8)	0	0	–
$H^0$	0	–	0	$\sqrt{2}\lambda$	$125.09 \pm 0.21 \pm 0.11$ GeV

The SM is perhaps best described in the diagrams shown in Figure 2.6. This emphasizes the fact that quarks and leptons have the same number of flavors, and each flavor is associated to a pair of fermions and a pair of leptons. There are also four boson mediators and one scalar. This presents the mass basis of the SM, but it can also be helpful to see the interaction basis, which is shown on the right of the figure.

Table 2.3. The interactions of the SM

interaction	mediator	coupling	range
EM	$\gamma^0$	$eQ$	long
NC	$Z^0$	$\frac{e(T_3 - s_W^2 Q)}{s_W c_W}$	short
CC	$W^\pm$	$gV$	short
Yukawa	$H$	$y_q$	short
strong	$g$	$gs$	long

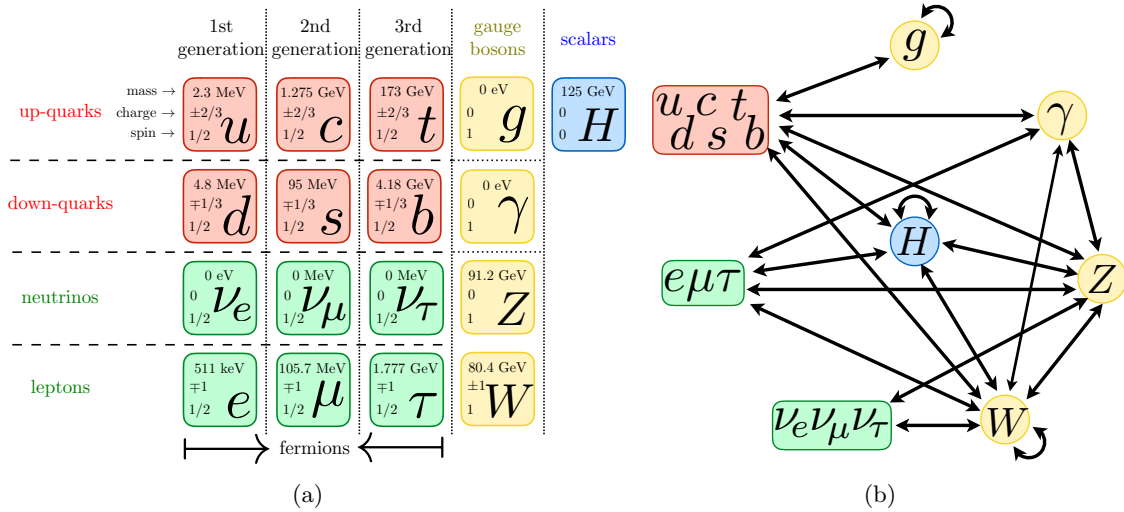


Figure 2.6. A diagrammatic representation of the SM showing its (a) particles and (b) forces.

## 2.5 Beyond the Standard Model

The SM has been tested with great experimental success. It took about 46 years after Weinberg and Salam incorporated the Higgs mechanism into EW theory to form the SM before the Higgs particle was discovered. In the intervening years, physicists were able to discover the  $W$  and  $Z$  bosons, confirm that hadrons are composed of quarks and gluons, and discover the bottom and top quarks as well as the tau neutrino. Despite the undiscovered particles necessary to the theory of EW interactions, the model correctly anticipated their discovery as a way of strengthening the SM. However, in the strictest parlance, the SM is not a complete theory. Despite its sheer power of prediction, it works best when questions are ignored for which it was not designed to answer.

For example, neutrinos should not have any mass, but observation of oscillations between neutrino flavors suggests that they do. An analysis of the relic cosmic microwave background, the orbital velocity of stars in a galaxy, and large red-shifts in supernovae have established that the SM cannot account for a vast amount of mass-energy in the universe.  $CP$  violation can allow an imbalance of matter and antimatter, but perhaps there is *too much* matter in the universe compared to antimatter for the SM to explain. The introduction of a Higgs boson ties many concepts together in the SM, but its mass creates a hierarchy problem as well (Section 3.1).

Gravity, perhaps the first fundamental force observed by humans, is considered far too weak to make an appearance in the SM because it eludes a quantum description. The existence of neutron stars, where gravity is strong enough to prevent the spontaneous decay of neutrons, shows that this is not something that can always be overlooked. A large-scale relativistic theory of gravity and a theory of small-scale quantum dynamics must combine somehow in a universe that contains black holes.

The SM holds the status of a fundamental “theory” in HEP, but there are always things to look at beyond the Standard Model (BSM). Instead of treating it as a solid theory, the SM is often seen as a very successful effective field theory (EFT). The SM is not yet relegated to a historical artifact preserving the old ways of thinking, but consider how anyone would ever look at the world beyond the elements of the Periodic Table without asking ever-refined questions. The success in the forefront cannot be ignored even if the description is limited by technology and incremental progress. The next answers will be better than the ones current and present, but not truly contradictory.

To recover the QFT description of BSM physics, consider the exchange of a new heavy particle with mass  $M$  given in Figure 2.7. If the incoming momentum is much less than  $M$ , then the exchange is suppressed by the cutoff scale ( $\Lambda$ ). Below some scale ( $\Lambda < E_{EW}$ ), the SM works very well. Above this energy level, the Lagrangian should be expanded to be perturbative in mass couplings.



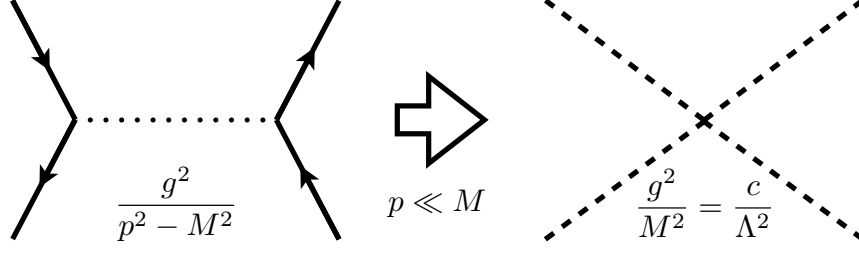


Figure 2.7. A Feynman diagram for the exchange of a new heavy particle.

Remembering that the Lagrangian is built from its observed symmetries, this EFT can be split up into different processes, and a possible expansion is shown below. Equation 2.49a is a term for the cosmological constant and Equation 2.49b is a term for the Higgs mass hierarchy problem (Section 3.1). Equation 2.49c is the SM with dimensionless couplings. Equation 2.49d is a term that can allow the neutrinos to have mass. Equations 2.49e and 2.49f are a few terms involving other new particles. There could, of course, be more terms here as needed. At low  $E$ , the terms with higher mass dimension become negligible. These are characteristics of the terms of new physics that are sought, although their exact form may yield different terms in this Lagrangian.

$$\mathcal{L}_{eff} \sim c_4 \Lambda^4 \tag{2.49a}$$

$$+ c_2 \Lambda^2 H^\dagger H \tag{2.49b}$$

$$+ \lambda (H^\dagger H)^2 + \mathcal{L}_{kin}^{SM} + \mathcal{L}_{Yuk}^{SM} \tag{2.49c}$$

$$+ \frac{(L_L H)^2}{\Lambda} \tag{2.49d}$$

$$+ \frac{H^\dagger D_\mu H H^\dagger D^\mu H}{\Lambda^2} + \frac{H^\dagger D_\mu H \bar{e}_R \gamma^\mu e_R}{\Lambda^2} + \frac{H^\dagger \sigma^a H W_{\mu\nu}^a B^{\mu\nu}}{\Lambda^2} \tag{2.49e}$$

$$+ \frac{H^\dagger H B_{\mu\nu} B^{\mu\nu}}{\Lambda^2} + \frac{H^\dagger H W_{\mu\nu}^a W_a^{\mu\nu}}{\Lambda^2} + \dots \tag{2.49f}$$

$$+ \dots \tag{2.49g}$$

## CHAPTER 3

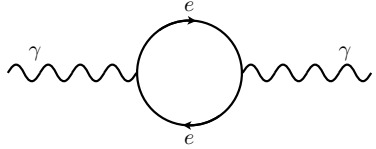
### Supersymmetry

#### 3.1 The Hierarchy Problem

Despite providing the completion of the SM, the discovery of the Higgs mechanism also puts it in danger of catastrophic failure. The Higgs boson is a neutral, massive scalar that can couple to any of the other particles that have mass. All of the Higgs couplings are determined by the masses of the particle it couples to; the heavier a particle is, the stronger the Higgs coupling is. This is the term in Equation 2.49b which confronts the SM as in Reference [2,3].

##### 3.1.1 Photon Mass

Suppose the mass of a photon is to be calculated from a one-loop correction (“self-energy”). The photon spontaneously creates an electron-positron pair, which then annihilate into a photon (Figure 3.1). To simplify, the limit in which the photon has no momentum of its own is taken, which would mean it has a very long wavelength. The Feynman rule in Figure B.7 is applied twice to get the correct terms.



$$\begin{aligned}
 \pi(0) &= - \int \frac{d^4k}{(2\pi)^4} \text{Tr} \left[ (-ie\gamma^\mu) \frac{i}{\not{k} - m_e} (-ie\gamma^\mu) \frac{i}{\not{k} - m_e} \right] \\
 &= -4e^2 \int \frac{d^4k}{(2\pi)^4} \frac{2k^\mu k^\nu - g^{\mu\nu}(k^2 - m_e^2)}{(k^2 - m_e^2)^2} \\
 &= 0
 \end{aligned}$$

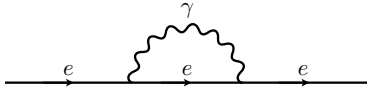
(3.1)

Figure 3.1. A Feynman diagram for photon self-energy with a one-loop electron correction.

The momentum of the loop is not limited by the external momentum in this case. For example, the electron could have an infinite energy as long as the positron then takes it back. The diagram must be integrated over all possible momenta in the loop. However, since the photon must be gauge invariant, both Dirac ( $m\bar{A}A$ ) and Majorana ( $mAA$ ) mass terms are forbidden. Formally, the mass of the photon is zero because the coupling runs with the energy scale.

### 3.1.2 Electron Mass

On the contrary, the self-energy of an electron (Figure 3.2), although it uses the same Feynman rules, provides a chance to examine the details of the integration with allowed Dirac mass. The integral over energy from zero to infinity diverges because it reaches a singularity ( $d^4k$  to  $k^{-4}$ ). Instead of taking the limit to infinity, a cutoff energy ( $\Lambda$ ) is substituted.



$$\begin{aligned}
 \pi(0) &= \int \frac{d^4k}{(2\pi)^4} (-ie\gamma_\mu) \frac{i}{\not{k} - m_e} (-ie\gamma_\mu) \frac{-ig^{\mu\nu}}{k^2} \\
 &= -e^2 \int \frac{d^4k}{(2\pi)^4} \frac{1}{k^2(k^2 - m_e^2)} \gamma_\mu (\not{k} + m_e) \gamma^\mu \quad (3.2) \\
 &= -4e^2 m_e \int \frac{d^4k}{(2\pi)^4} \frac{1}{k^2(k^2 - m_e^2)}
 \end{aligned}$$

Figure 3.2. A Feynman diagram for electron self-energy with a one-loop photon correction.

Above this energy level, the effects of unknown physics are ignored. Typically, the Planck mass ( $M_{Pl}$ ) is used because it is the energy level where gravity is thought to become strong and QFT would not work anyway. The concept is called renormalization and there are different approaches to accomplishing it.

Doing the calculation this way leads to a logarithmic divergence. However, since the expansion can be written in terms of the electron mass itself, then this is merely a correction term. This presents an odd distinction where the electron mass used in Lagrangian formulation is not the same mass of the electron actually measured. The correction terms

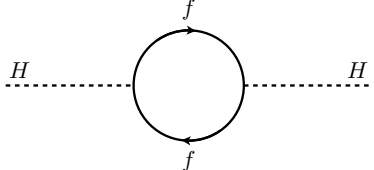
are supplied by the theory, and the electron that can be measured has already absorbed all of its correction terms.

$$\delta m_e \simeq 2 \frac{\alpha_{EM}}{\pi} m_e \log \frac{M_{Pl}}{m_e} \simeq 0.24 m_e \quad (3.3)$$

Notice that because this correction depends on the bare electron mass, then the correction would vanish if the electron had zero mass. This is known as a “natural” correction, because a symmetry is gained by setting its value equal to zero; the electron would be chiral just like the photon. Instead, the symmetry is broken because the electron has mass.

### 3.1.3 Higgs Mass

Now the same thing can be tried using the Higgs boson with a one-loop fermion correction (Figure 3.3). The same problem with the electron self-energy occurs here, but the form of the singularity is decidedly different ( $d^4k$  to  $k^{-2}$ ). Attempts can be made to renormalize as before (and generalize the number of flavors,  $n_f$ ), but this leaves a troublesome fact.



$$\begin{aligned}
 \pi(0) &= -n_f \int \frac{d^4k}{(2\pi)^4} \left[ \left( i \frac{\lambda_f}{\sqrt{2}} \right) \frac{i}{\not{k} - m_f} \right]^2 \\
 &= -2n_f \lambda_f^2 \int \frac{d^4k}{(2\pi)^4} \frac{k^2 + m_f^2}{(k^2 - m_f^2)^2} \\
 &= -2n_f \lambda_f^2 \int \frac{d^4k}{(2\pi)^4} \left[ \frac{1}{k^2 - m_f^2} + \frac{2m_f^2}{(k^2 - m_f^2)^2} \right]
 \end{aligned} \quad (3.4)$$

Figure 3.3. A Feynman diagram for Higgs self-energy with a one-loop fermion correction.

$$\delta m_H \simeq \frac{1}{8\pi} n_f m_f^2 \lambda_f^2 \quad (3.5)$$

The “correction” term does not scale logarithmically with energy and does not depend on the Higgs mass itself at all. Instead, it is quadratically divergent to the particles in the loop, which could be anything that has mass. Since new physics particles may have a huge mass, nothing really prevents the mass of the Higgs from being pulled all the way up to the maximum energy level.

However, a measurement of the Higgs mass *has* been performed, which is supposed to have all correction terms. Getting back to this known mass would require finding a way to subtract a large number from a slightly larger number ( $\sim 10^{18}$  GeV), leaving about 125 GeV for the observed Higgs mass. This is an “unnatural” situation because something other than the Higgs mass (and currently unknown) must be breaking the symmetry. It seems that physics below the 1 TeV scale is nearly or mostly natural, but the theory becomes increasingly unnatural above the Higgs VEV.

#### 3.1.4 *Fixing the Higgs Mass Problem*

This holds physics to a kind of crossroads for the time being. The idea of “fine-tuning” is undesirable, because it sounds antithetical to science to answer the question “Why are things the way they are?” with “Because they just are.” There may be something deeper at work, and hopefully it lives in a phase space that can still be accessed.

It could be that there are no fundamental scalars. The Higgs boson that was found could be a composite of confined fermions, much like the proton is not fundamental but composed of quarks as described by QCD. These new technifermions would have a new property called technicolor. The theory predicts pseudo-Goldstone bosons with masses  $\mathcal{O}(\text{TeV})$ . It is also possible that a scalar hadron with parity +1 has been overlooked as a candidate “Higgs” boson.

The SM could also break down if the Higgs interactions become strong at some energy scale. This would result in new particle resonances that could increase the EW scattering amplitudes. If gravity exists in compactified extra dimensions, the gravitational flux at higher energy scales could cause particle resonances and black hole creation.

The subject of this dissertation addresses the search for yet another possible fix for the quadratic divergence. This is called supersymmetry, and it addresses the radiative correction with a new fermion-boson symmetry. These new particles cancel the divergence, leaving a Higgs mass equal to the one measured.

Each one of these models predicts new particles at the weak scale that can be probed with the energy available at the Large Hadron Collider. One of these possibilities should present itself for study, or perhaps something even more unexpected can be found.

### 3.2 Fermion-Boson Supersymmetry

Looking back at the Periodic Table as an analogy, there is an underlying structure that makes the organization of elements work. Elements are ordered by the number of protons their atoms contain and they are grouped by their electrical properties (number of valent electrons and angular momentum). It is elementary, therefore, to ask if there is some other underlying structure to the SM than what has been discovered so far. If there was some symmetry that spontaneously breaks into fermions and bosons, that would be quite an interesting thing to find.

Supersymmetry (SUSY) starts by recognizing that Feynman diagrams with fermions have opposite signs than the corresponding diagrams with bosons. If there is a fermion-boson symmetry at work, then these diagrams would cancel (perhaps completely). Work on developing the SUSY hypothesis is extensive [4–9], but the premise that makes it plausible is presented here.

#### 3.2.1 Building SUSY

Starting simple, the minimal supersymmetric SM (MSSM) contains new particles ( $\tilde{f}$ ) and their interactions:

$$\mathcal{L} = \frac{1}{2}\tilde{\lambda}_f\phi^2(|\tilde{f}_L^2| + |\tilde{f}_R^2|) + v\tilde{\lambda}_f\phi(|\tilde{f}_L^2| + |\tilde{f}_R^2|) + \left(\frac{1}{\sqrt{2}}\lambda_f A_f\phi\tilde{f}_L\tilde{f}_R^* + h.c.\right) \quad (3.6)$$

Moving directly to the hierarchy problem at hand, the Higgs self-energy can be re-calculated using the new diagrams in Figure 3.4.

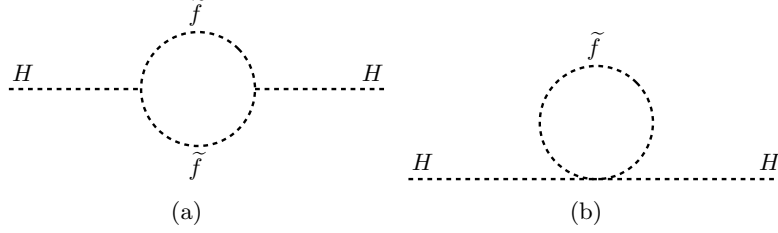


Figure 3.4. Two Feynman diagrams for Higgs self-energy with one-loop sfermion corrections with (a) cubic and (b) quartic vertices.

$$\begin{aligned}
\pi(0) = & -\tilde{\lambda}_f n_{\tilde{f}} \int \frac{d^4 k}{(2\pi)^4} \left[ \frac{1}{k^2 - m_{\tilde{f}_L}^2} + \frac{1}{k^2 - m_{\tilde{f}_R}^2} \right] \\
& + (\tilde{\lambda}_f v)^2 n_{\tilde{f}} \int \frac{d^4 k}{(2\pi)^4} \left[ \frac{1}{(k^2 - m_{\tilde{f}_L}^2)^2} + \frac{1}{(k^2 - m_{\tilde{f}_R}^2)^2} \right] \\
& + |\lambda_f A_f|^2 n_{\tilde{f}} \int \frac{d^4 k}{(2\pi)^4} \frac{1}{(k^2 - m_{\tilde{f}_L}^2)(k^2 - m_{\tilde{f}_R}^2)}
\end{aligned} \tag{3.7}$$

A couple of assumptions makes the mathematics easier to grasp. The first is that the number of right-handed and left-handed flavors is the same, and that the couplings between particles and their SUSY mirror are the same.

$$n_{\tilde{f}_L} = n_{\tilde{f}_R} = n_f \tag{3.8a}$$

$$\tilde{\lambda}_f = -\lambda_f^2 \tag{3.8b}$$

These simplifications can be plugged into the integrals:

$$\int \frac{d^4k}{i\pi^2} \frac{1}{k^2 - m^2} = m^2 \left( 1 - \log \frac{m^2}{\mu^2} \right) \quad (3.9a)$$

$$\int \frac{d^4k}{i\pi^2} \frac{1}{(k^2 - m^2)^2} = -\log \frac{m^2}{\mu^2} \quad (3.9b)$$

Another assumption is that the left-handed and right-handed masses are the same.

$$m_{\tilde{f}_L} = m_{\tilde{f}_R} = m_{\tilde{f}} \quad (3.10)$$

Combining everything together gives a nice self-energy to work with:

$$\begin{aligned} \pi(0) = & i \frac{\lambda_f^2}{16\pi^2} \left[ -2m_f^2 \left( 1 - \log \frac{m_f^2}{\mu^2} \right) + 4m_f^2 \log \frac{m_f^2}{\mu^2} \right. \\ & \left. + 2m_f^2 \left( 1 - \log \frac{m_f^2}{\mu^2} \right) - 4m_f^2 \log \frac{m_f^2}{\mu^2} \right] \\ & - |A_f|^2 \log \frac{m_f^2}{\mu^2} \end{aligned} \quad (3.11)$$

Exact cancellation can be achieved if the following assumptions are made:

$$m_{\tilde{f}} = m_f \quad (3.12a)$$

$$A_f = 0 \quad (3.12b)$$

This is just one of the ways in which SUSY can fix the hierarchy problem, but other radiative corrections are presented in Appendix C.

Particles and their SUSY partners differ by a half-integer spin. For many models, SM particles have  $R$ -parity (Section 3.4)  $+1$  and SUSY particles have  $R$ -parity  $-1$ . Partners to SM fermions are named with a prefix “s-” (sfermion, squark, slepton, selectron), while partners to SM bosons are named with a suffix “-ino” (gaugino, gluino, wino, Higgsino).



SUSY partners are indicated by a tilde ( $q$  for quark becomes  $\tilde{q}$  for squarks). A summary of these relationships is shown in Table 3.1.

Table 3.1. The particles of the MSSM

particle	spin	$R$ -parity	SUSY	spin	$R$ -parity
quark ( $q$ )	1/2	+1	squark ( $\tilde{q}$ )	0	-1
lepton ( $\ell$ )	1/2	+1	slepton ( $\tilde{\ell}$ )	0	-1
$W$	1	+1	wino ( $\tilde{W}$ )	1/2	-1
$B$	1	+1	bino ( $\tilde{B}$ )	1/2	-1
gluon ( $g$ )	1	+1	gluino ( $\tilde{g}$ )	1/2	-1
Higgs ( $H_U, H_D$ )	0	+1	Higgsino ( $\tilde{H}_U, \tilde{H}_D$ )	1/2	-1

### 3.2.2 Unification of Scales

Equally tantalizing is the idea that the gauge couplings could be unified at a high energy scale if they are now re-evaluated in the SUSY context [10–13]. The  $\beta$ -function describes how a coupling parameter ( $g$ ) changes with energy scale ( $\mu$ ).

$$\beta(g) = \frac{\partial g}{\partial \log(\mu)} \quad (3.13)$$

In EM interactions, the fine structure constant is defined as  $\alpha_{QED} \equiv e^2/4\pi$ . This is experimentally known in terms of its inverse:  $\alpha_{QED}^{-1} = 137.035999074 \pm 4.4 \times 10^{-9}$  [1]. At low energy, the loop terms are suppressed by the uncertainty principle ( $\Delta E \Delta t \geq 1/2\pi$  or  $\Delta x \Delta p \geq 1/2\pi$ ) and are called “virtual”. As energy increases, more of these extra particles now have enough energy to become real. One could imagine trying to shrink down and move closer to the electron; the charge of the electron polarizes the vacuum, virtual charges pair together and screen (partially cancel) the charge, and higher energies expose a bare charge that has less effect on the vacuum.

$$\beta(\alpha_{QED}) = \frac{2\alpha_{QED}^2}{3\pi} \quad (3.14)$$

This equation shows that the EM force gets stronger ( $\alpha_{QED}^{-1}$  decreases) with an increase in energy scale. For strong interactions, the opposite is true. In QCD, both the fermion ( $q$ ) and the gauge boson ( $g$ ) carry a color charge. The quark carries one color and the gluon is a color-anti-color pair. The polarized vacuum then augments the field instead of shielding it. Moving to higher energies would reduce this effect, which is known as asymptotic freedom [14, 15]. At low energy, perturbation theory is inadequate, and a hadronic description of QCD particles works better. When the quarks are given enough energy, the vacuum pairs can spontaneously appear, creating a shower of more hadrons.

A term similar to the fine structure constant for the strong force is  $\alpha_S \equiv g_S^2/4\pi$ . This is experimentally measured to be  $\alpha_S = 0.11856 \pm 0.0051$ .

$$\beta(\alpha_s) = - \left( 11 - \frac{2n_f}{3} \right) \frac{\alpha_s^2}{2\pi} \quad (3.15)$$

These “running” coupling constants are shown in Figure 3.5 as the energy of the interaction is increased. Without SUSY, the coupling constants converge but miss each other at high energy. If SUSY is included, they approach a single point. At a scale higher than EW, perturbation theory should still be able to provide a grand unified theory (GUT).

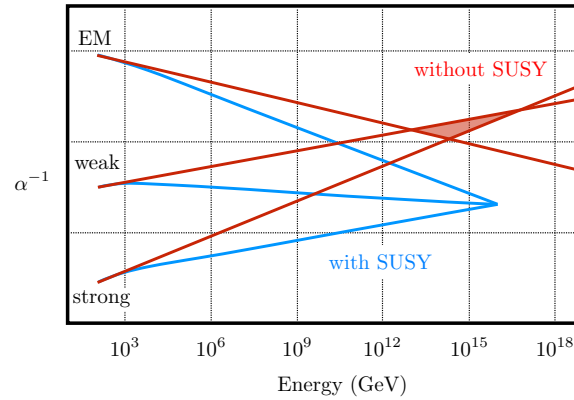


Figure 3.5. The running gauge couplings with and without SUSY.

### 3.3 Broken Supersymmetry

The assumptions in Equation 3.12 are wrong, otherwise SUSY would have been discovered long ago. There is no selectron at 511 keV with spin-0. No pairs of particles have been found at the same energy that differ only by a half-integer spin. Perhaps these new SUSY partners live at a higher mass:

$$m_f^2 = m_f^2 + \delta^2 \tag{3.16a}$$

$$\log \frac{m_f^2}{\mu^2} \simeq \log \frac{m_f^2}{\mu^2} + \frac{\delta^2}{m_f^2} \tag{3.16b}$$

$$|A_f| \ll m_f \tag{3.16c}$$

In order to save SUSY, the cancellation in Equation 3.11 should guide how much of a correction term the MSSM needs..

$$\begin{aligned} \pi(0) &= i \frac{\lambda_f^2 n_f}{16\pi^2} \left( -2\delta^2 \log \frac{m_f^2}{\mu^2} - 4\delta^2 - |A_f|^2 \log \frac{m_f^2}{\mu^2} \right) + \mathcal{O}(\delta^4, A_f^2 \delta^2) \\ &= -i \frac{\lambda_f^2 n_f}{16\pi^2} \left( 4\delta^2 + (2\delta^2 + |A_f|^2) \log \frac{m_f^2}{\mu^2} \right) + \mathcal{O}(\delta^4, A_f^2 \delta^2) \end{aligned} \tag{3.17}$$

It may be difficult to read the changes to Equation 3.11, but it means that the hierarchy problem can still be mitigated if the difference in mass between particle and sparticle is at the weak scale.

### 3.4 R-Parity

There are two Higgs doublets in the MSSM to separately describe “up”-type quarks and “down”-type quarks, giving eight degrees of freedom.

$$H_U = \begin{pmatrix} H_U^+ \\ H_U^0 \end{pmatrix} \quad H_D = \begin{pmatrix} H_D^0 \\ H_D^- \end{pmatrix} \quad (3.18)$$

Three degrees of freedom go toward EWSB and leave five Higgs bosons:  $h^0$ ,  $H^0$ ,  $H^+$ ,  $H^-$ , and  $A^0$ . The  $h^0$  particle is a Higgs boson that most closely resembles the one predicted by the SM and observed in 2012. The mixing of SM gauge bosons resulted in  $\gamma^0$ ,  $W^\pm$ , and  $Z^0$ , and a similar mixing between charge-neutral gauginos and Higgsinos results in four neutralinos:  $\tilde{\chi}_1^0$ ,  $\tilde{\chi}_2^0$ ,  $\tilde{\chi}_3^0$ ,  $\tilde{\chi}_4^0$ . For the wino and charged Higgsinos mixing, there are two charginos:  $\tilde{\chi}_1^\pm$  and  $\tilde{\chi}_2^\pm$ .

In the SM, gauge invariance leads to a conservation of baryon ( $B$ ) and lepton ( $L$ ) number for renormalizable interactions. With SUSY, because there are scalar components of quark and lepton superfields that carry  $B$  and  $L$ , it is possible to have terms that are consistent with  $SU(3) \times SU(2) \times U(1)$  symmetry that still violate this conservation.  $B$  and  $L$  conservation are well-established, as demonstrated by the remarkable stability of the proton (the lifetime measurement is  $\tau_p > 2.1 \times 10^{29}$  years [1]). To keep SUSY models consistent without wrecking this stability, the preservation of this conservation is often expected. These SUSY interactions require a new  $R$ -parity conservation (RPC) that relates  $B$  and  $L$  conservation to the new spin symmetry of SUSY [16].

$$R = (-1)^{3(B-L)+2s} \quad (3.19)$$

This leads to a very important result for a minimalistic model. Sparticles must be created in pairs, and subsequent decays of each sparticle must have an odd number of sparticles. This leaves a neutral sparticle at the end of the decay chain that will be stable, or long-lived. Such particles would be very elusive, would not interact electromagnetically, and would not interact with the SM particles of the detector ( $R$ -parity suppressed).

In RPC SUSY, each of these particles is often the lightest neutralino ( $\tilde{\chi}_1^0$ ). The term may also be called the lightest supersymmetric particle (LSP) and can be referred to as a candidate for a weakly-interactive massive particle (WIMP) as demonstrated in

Reference [17,18]. The idea of RPC is thus very appealing to an experimentalist because of such strong evidence for the existence of dark matter [19]. While trying to solve a seemingly separate problem with the SM (Section 3.1) from the EFT Lagrangian (Equation 2.49b), a prediction of dark matter particles has been found. Although  $R$ -parity-violating SUSY models do exist, this document implicitly focuses on discussing models in the RPC context.

### 3.5 Supersymmetry as a Framework

Instead of a single model that makes headlines under the presumption of proof or disproof, SUSY is a framework for models where the only rule is that a model solves the hierarchy problem with a new fermion-boson symmetry (or even more symmetries); when one model gets pushed into a corner, just move to the next one.

The success of the SM is hard to ignore, and it may barely need any kind of tweaking to fix the hierarchy problem, which is the approach taken by the MSSM [20,21]. The MSSM contains all 19 parameters of the SM. It also contains an analog to the SM Higgs mass, five real parameters of the gaugino/Higgsino sector, three  $CP$ -violating phases of the gaugino/Higgsino sector, 21 new sfermion masses, 36 real mixing angles for sfermion mass eigenstates, and 40  $CP$ -violating phases of the sfermion sector.

This means that the MSSM model has 125 parameters that need to be measured before it can be tested. With such a vast number of unknowns, the model almost has enough wiggle room to never be disproven. In fact, this has led to a contentious point about SUSY and whether it can be scientific. Even with physical evidence of new particles, it may take a few years before alternate new physics could be ruled out. However, that is also what can make a study of SUSY attractive to some. With a prosperous supply of specifics, a thorough study of the model can be performed by a steady stream of physicists.

The vast number of parameters can be reduced by constraining the model to eliminate some of its less-appealing consequences. For example, a model can propose that there is no new source for  $CP$ -violation, no FCNC, and universality of the first and second flavor

generations. This is known as the phenomenological MSSM (pMSSM [22,23]). Under these assumptions, one can reduce the 105 additional parameters to just 19:

- $\tan\beta$  - the ratio of the VEV of the two Higgs doublets
- $M_A$  - the mass of the pseudoscalar Higgs
- $\mu$  - the Higgsino mass
- $M_1$  - the bino mass
- $M_2$  - the wino mass
- $M_3$  - the gluino mass
- $m_{\tilde{q}}, m_{\tilde{u}_R}, m_{\tilde{d}_R}$  - squark masses (1st and 2nd)
- $m_{\tilde{\ell}}, m_{\tilde{e}_R}$  - slepton masses (1st and 2nd)
- $m_{\tilde{Q}}, m_{\tilde{t}_R}, m_{\tilde{b}_R}$  - squark masses (3rd)
- $m_{\tilde{L}}, m_{\tilde{\tau}_R}$  - slepton masses (3rd)
- $A_t, A_b, A_\tau$  - trilinear couplings (3rd)

One can go even further with minimal supergravity (mSUGRA [24–26]), which is also known as constrained MSSM (cMSSM). In this model, gravity finally enters into a QFT by contributing terms that spontaneously break SUSY. As the Higgs mechanism was responsible for  $SU(3) \times SU(2) \times U(1)$  symmetry breaking, the gravitino (spin-3/2 sparticle to the graviton spin-2) acquires mass and causes incomplete cancellation of the radiative corrections to sparticle mass below the gravitino scale. This model can then be predictive with just 5 parameters if the unification of Figure 3.5 is explicitly enforced:

- $m_0$  - common mass of sleptons, squarks, and Higgs at GUT scale
- $m_{1/2}$  - common mass of gauginos and Higgsinos at GUT scale
- $A_0$  - common trilinear coupling
- $\tan\beta$  - the ratio of the VEV of the two Higgs doublets
- $\text{sign}(\mu)$  - the sign of the Higgsino mass parameter

Anomaly-mediated supersymmetry breaking (AMSB [27,28]) is a special case of supergravity that treats SUSY breaking as a result of a Weyl transformation that changes the metric tensor. This is also known as a conformal anomaly.

Gauge-mediated supersymmetry breaking (GMSB [29–31]) allows the gauge interactions of the SM to break SUSY. The “hidden” sector introduces the break, which enters the “visible” sector through the gaugino at one loop and the scalar sparticles at two loops. In the scenario with a single messenger,  $\tilde{\chi}_1^0$  is actually the next-to-lightest supersymmetric particle (NLSP). If there are three messenger particles,  $\tilde{\ell}$  is the NLSP.

If SUSY still does not present a full spectrum of sparticles at the weak scale, then a split SUSY [32,33] may explain the mass split. In this case, the sfermions can be significantly heavy while the gauginos and Higgsinos must remain at the weak scale. This would also leave one scalar, neutral Higgs that would look very much like the SM Higgs, but the other Higgs bosons would be very heavy.

This is not an exhaustive list of SUSY models by any stretch of the imagination. Much of SUSY was also developed under string theory and extra-dimensions, but these concepts will not be discussed here. However, one should note that some models of extra-dimensions are phenomenologically similar to SUSY signatures and SUSY results can often be reinterpreted to these models with the same reconstruction techniques.

### 3.6 Simplified Models

Figure 3.6(a) shows how complicated these models can be with the 5 additional parameters of cMSSM. The creation of a single gluino can cascade in decay through any of the squarks with varying weighted probabilities. Some of those squarks decay to lighter squarks and then charginos. Eventually each decay path makes its way down to the neutralino, and all along the way the event is shedding hadronic jets and leptons.

Instead, the decay chain can be generalized. Figure 3.6(b) shows a simplification of the decay of a gluino. Models built from such a reduction in complexity are called simplified models (SM) and have also been referred to as simplified topologies (ST) in ATLAS publications to avoid confusion [34–36].

From this simplified view of SUSY signatures, two event topologies are considered for the analyses that follow (with neutralino indices suppressed in favor of decay indices).

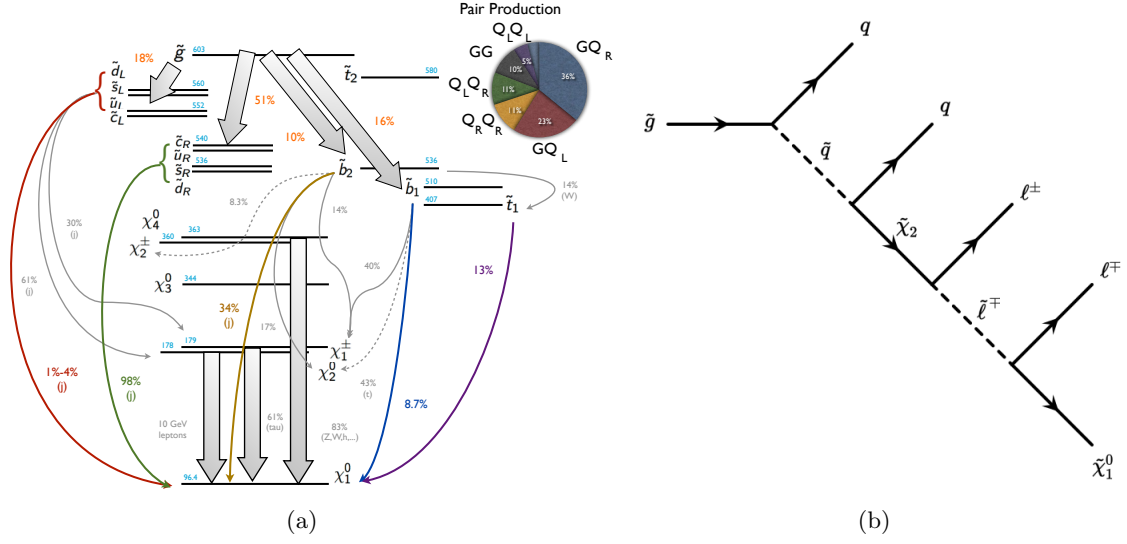


Figure 3.6. A comparison of (a) cMSSM to (b) simplified model gluino decay.

$$pp \rightarrow \tilde{q}_1 \tilde{q}_2 \rightarrow (\tilde{\chi}_1 j_1)(\tilde{\chi}_2 j_2) \quad (3.20a)$$

$$pp \rightarrow \tilde{g}_1 \tilde{g}_2 \rightarrow (\tilde{q}_1 j_{1,1})(\tilde{q}_2 j_{1,2}) \rightarrow (\tilde{\chi}_1 j_{1,1} j_{2,1})(\tilde{\chi}_2 j_{1,2} j_{2,2}) \quad (3.20b)$$

A significant criticism of simplified models is that they each assume 100% branching ratio (Section 4.3.3). If 10 signal candidates appear in excess of the background, the interpreted results can only be accurate if one takes a particular decay chain to be the dominant interaction in these events. In this way, the cumulative results of all possible decay chains should be checked to see which model best fits the excess. However, this does not provide much hope if the branching ratios are more evenly distributed. The estimation of each model assumes it would be responsible for all 10 events instead of 10 models contributing one event each.

The analysis of the events may be focused on SUSY-specific simplified models, but topological kinematic techniques may be developed that can be re-interpreted in cMSSM, pMSSM, or extra-dimensions among others. The observables may be particularly good at maximizing an excess of candidate events, even if the exclusion (and discovery) results



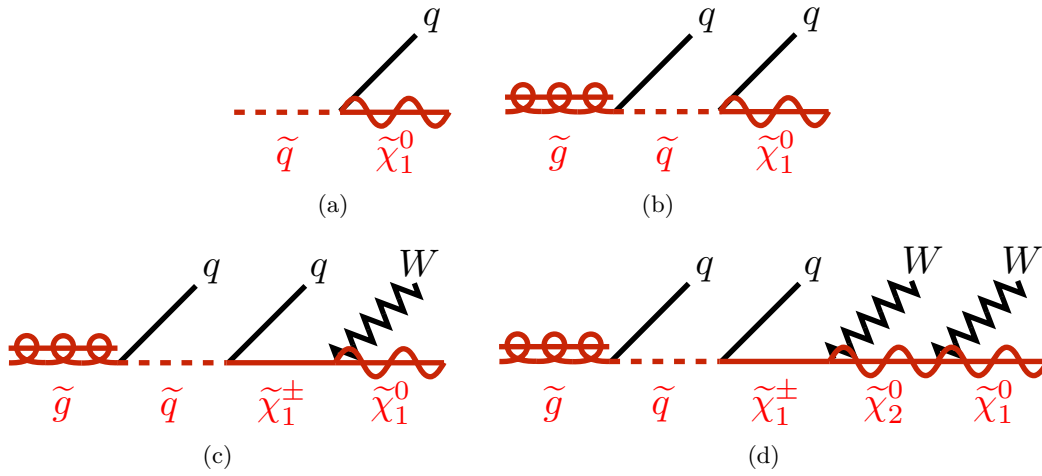


Figure 3.7. Examples of the simplified model decay of a gluino: (a) direct two-body decay  $\tilde{q} \rightarrow q \tilde{\chi}_1^0$ , (b) direct three-body decay  $\tilde{g} \rightarrow qq \tilde{\chi}_1^0$ , (c) two-step cascade  $\tilde{g} \rightarrow qqW \tilde{\chi}_1^0$ , and (d) three-step cascade  $\tilde{g} \rightarrow qqWW \tilde{\chi}_1^0$ .

should always be treated with a modicum of skepticism until refined attention arrives. Simplified models may ultimately tell us *where* to find new physics without unambiguously telling us *what* it is.

## CHAPTER 4

### Detection and Instrumentation

Having a theory to investigate and a class of models to study can go a long way toward the search for SUSY. Eventually the finely-honed beauty of the theoretical and phenomenological view of physics is tempered by the nuances of experimental reality. This shift in paradigm forces a change in perspective from that of a detached observer to one of understanding physics fundamentals in terms of a controlled interaction with them. In HEP, this means that the colliders and detectors must be studied extensively before new physics can be addressed.

This document presents details about the experimental setup at Conseil Européen pour la Recherche Nucléaire (CERN). The proton-proton collisions were provided by the Large Hadron Collider (LHC) designed for a center-of-mass (CM) energy of 14 TeV. The detector experiment used to measure these events is A Toroidal LHC Apparatus (ATLAS), which is a very large multi-purpose detector with several subcomponents. A timeline of the important milestones of the LHC and ATLAS is presented in Figure 4.1. This document discusses the data analysis and detector environment summarized by the second line of the timeline. Future upgrades to the LHC for higher luminosities (HL-LHC) and higher energy (HE-LHC) are planned, but the exact dates are subject to change.

#### 4.1 Overview of the LHC

Before the effects of particle interaction can be detected, machinery is needed to make two particles interact at a desired energy. Consequently, the search for new physics must start with the collider and the accelerators preceding it. The term “collider” or “smasher” can be misleading as it does not imply the scatter of two particles has anything to do with physical contact between the two particles (themselves having an unconfirmed physical

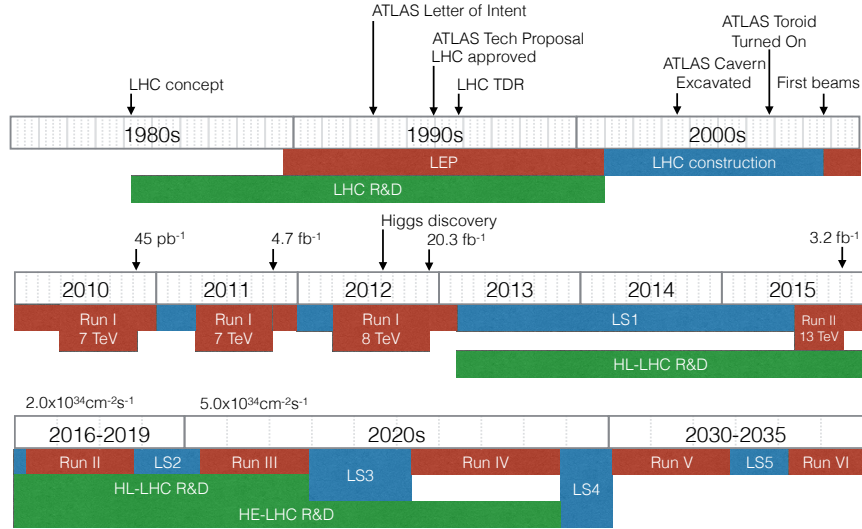


Figure 4.1. A timeline of important dates and schedule of the LHC, ATLAS, and planned upgrades.

size). Instead, the fields interfere and the inelastic change of inertial frames can be above the energetic threshold of new particle creation and spontaneously spew these particles from the available vacuum energy. A complete report of the design of the LHC can be found in Reference [37].

#### 4.1.1 Design of the LHC

Following the success of the Tevatron and the Large Electron-Positron (LEP) collider, the LHC took the place of LEP (figuratively and literally). The LHC is a circular collider with two concentric rings (one for each beam), each 26.7 km in circumference. Unlike its predecessors, the LHC does not have anti-matter in its beams. The prior choice of anti-matter was beneficial in the past because chosen matter and anti-matter particles had opposite charges and therefore curled in opposite directions when in the presence of the same magnetic field. This simplified the requirements of the preceding magnetic systems because both beams could be circulated in a single magnetic field. On the other hand, anti-matter is expensive to produce because it requires an energetic collision to create it, the creation process is slow because not every collision produces the desired anti-particles,

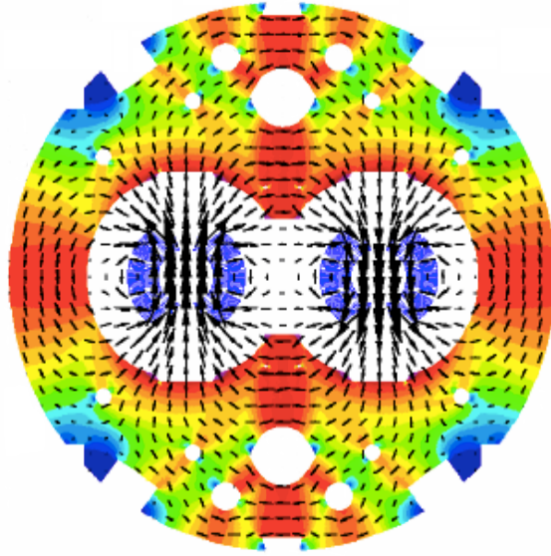


Figure 4.2. The LHC magnetic dipole field.

and it is expensive to maintain because it requires a holding ring to buffer enough particles for practical use. The cost would also extend toward time wasted by waiting for a full fill of anti-matter particles.

Instead, the LHC has a twin-bore magnetic field (Figure 4.2) that allows two magnetic fields to exist in close enough proximity to efficiently circulate two same-sign particles in opposite directions. This technological step was also useful because the existing LEP tunnel would be rather cramped if two separate rings were needed (Figure 4.3). Since each ring would need separate cryostats to keep the magnets superconductive, the compact configuration also helps by cutting the cooling and power requirements in half.

The LHC can circulate bunches of protons or bunches of lead ions. Proton collisions are suitable for BSM searches because the proton-proton collisions are much easier to model than a heavy ion collision, where the energy of a single collision is distributed among a large number of nucleons (and quarks/gluons in turn). On the other hand, heavy ions are ideal for the abundance of strong production that can allow a study of quark-gluon plasma. To keep the SUSY discussion as the primary focus in this document, the LHC will hereafter be treated as a proton-proton collision delivery machine.



Figure 4.3. A view of the LHC tunnel.

The LHC ring bends the path of the protons into a near-circular arc underneath the border between Switzerland and France by using 1232 dipole magnets that are super-cooled by liquid helium to 1.9 K to achieve a peak dipole field of 8.33 T. The beam itself is also focused, shaped, and squeezed by additional sets of quadrupole magnets (3500 total) that are likewise held at cryogenic temperatures during operation. The interaction points and collimation (cleaning) sections are shown in Figure 4.4.

#### 4.1.2 *Filling the Beams*

To reach a high number of protons in each beam, the LHC benefits from the extensive infrastructure available at CERN (Figure 4.5). Protons begin as a hydrogen gas that is ionized and accelerated in the linear gradient of Linac 2 up to 50 MeV. The protons are then injected into the circular Proton Synchrotron Booster (PSB) where they are accelerated to 1.4 GeV. These energetic protons are then injected into the Proton Synchrotron (PS) and accelerated up to 28 GeV and the Super Proton Synchrotron (SPS) raises the energy to 450 GeV by increasing electric currents in the magnets (also known as “ramping”), which is the nominal energy of the LHC. The LHC is capable of accelerating its protons up to 7 TeV per beam at design specifications.

With all of these steps, it is important that the process spends as much time at physics-ready conditions as possible rather than in downtime. When the beams are dumped,

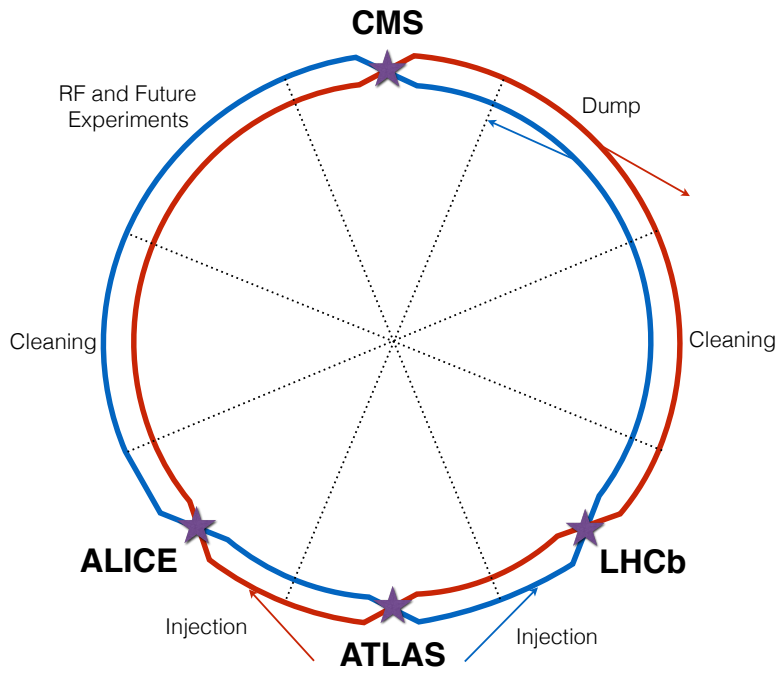


Figure 4.4. A schematic layout of the LHC components and main detectors.

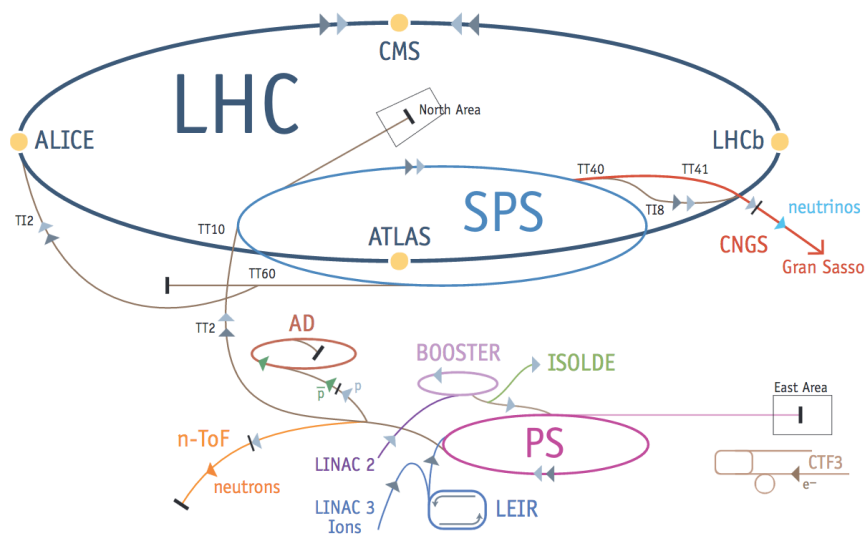


Figure 4.5. A schematic map of the accelerator facilities at CERN.

the magnets in the LHC are ramped down from 7 TeV to 450 GeV, which takes  $\sim 20$  minutes. The magnets stay at a nominal pre-injection plateau for another  $\sim 15$  minutes. A fill of the LHC requires 12 cycles of the SPS, which takes 21.6 seconds per cycle. Each cycle of the SPS requires 3 or 4 cycles of the PS at 3.6 seconds each. Allowing for inspection of the beam quality, the nominal time to fill the LHC is  $\sim 15$  minutes. Ramping the LHC magnets back to 7 TeV takes  $\sim 30$  minutes. Finally, the time needed to squeeze the beam and prepare for a physics run is another  $\sim 15$  minutes. Ideally, the turnaround should be  $\sim 95$  minutes, but due to the multiple points of failure and high level of precision needed for physics collisions, the actual turnaround time is between 3 and 10 hours.

The number of inelastic events produced by LHC collisions depends on the cross-section (Section 4.3.3) and the luminosity, which is the amount of collision data delivered per second. The cross-section for inelastic events is an expression of the probability of an event that occurs in nature and is approximated by a theoretical model. For a given energy, the true cross-section is not something that can be controlled.

$$N_{events} = L\sigma_{inelastic} \quad (4.1)$$

The total beam current is determined by the number of protons per bunch ( $N_b$ ), the number of bunches per beam ( $n_b$ ), and the frequency of beam crossings ( $f_{rev}$ ). The “brightness” of the beam is determined by  $N_b$  and the normalized transverse beam emittance ( $\epsilon_n$ ). The energy of the beam is determined by the relativistic factor ( $\gamma_r$ ) and the beam envelope at collision ( $\beta^*$ ).

$$L = \frac{N_b^2 n_b f_{rev} \gamma_r}{4\pi \epsilon_n \beta^*} F \quad (4.2)$$

The factor  $F$  is a geometric reduction due to the ability to control the interaction angle of the beams, which has the benefit of keeping the luminosity stable. As the run is ongoing, the number of protons in each beam begins to dwindle. By shallowing the crossing angle ( $\theta_c$ ) during the run, this effect can be mitigated by restoring the average number

of collisions. The geometric factor also depends on the RMS bunch length ( $\sigma_z$ ) and the transverse RMS beam size ( $\sigma^*$ ). The nominal value of these beam parameters is shown in Table 4.1.

$$F = \left[ 1 + \left( \frac{\theta_c \sigma_z}{2\sigma^*} \right) \right]^{-1/2} \quad (4.3)$$

Table 4.1. Nominal beam parameters for the LHC

$N_b$	$1.15 \times 10^{11}$
$n_b$	2808
$f_{rev}$	40.08 MHz
$\epsilon_n$	$3.75 \mu\text{m}$
$\beta^*$	0.55 m
$\theta_c$	$285 \mu\text{rad}$
$\sigma_z$	7.55 cm
$\sigma^*$	$16.6 \mu\text{m}$

An estimate of the lifetime of each beam, given intensity loss and emittance, is  $\tau_L = 14.9$  hours. Assuming that the decay happens exponentially, the integrated luminosity for a run time of  $T_{run}$  is:

$$L_{int} = L_0[1 - e^{-T_{run}/\tau_L}] \quad (4.4)$$

If the machine operated at nominal settings with 60% efficiency for 200 days per year, then the total amount of data collected would be  $\sim 100 \text{ fb}^{-1}$  (Section 4.3.3). A summary of the integrated luminosity during the years of 2011, 2012, and 2015 is shown in Figure 4.6.

#### 4.1.3 LHC Detectors

There are four large experiments located along the LHC ring (Figure 4.4). Large Hadron Collider Beauty (LHCb [38]) is a precision detector designed to measure the symmetries of interactions and look for rare decays that violate  $CP$  conservation. A Large



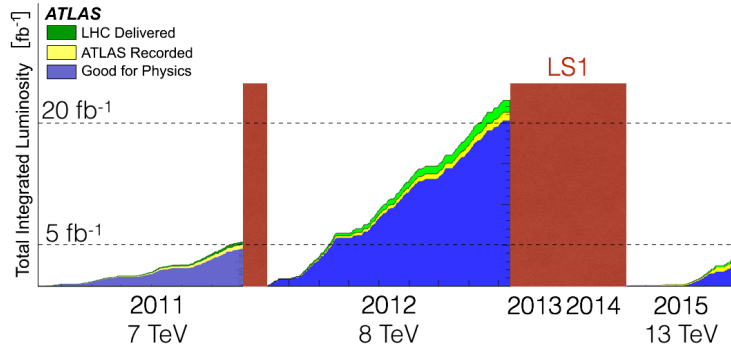


Figure 4.6. The integrated luminosity taken during 2011, 2012, and 2015. This figure is a combination of three plots that have been scaled manually to the same timescale and luminosity scale.

Ion Collider Experiment (ALICE [39]) is a heavy-ion detector that studies the nuclear reactions of lead collisions, including the asymptotic behavior of the strong force known as quark-gluon plasma. Compact Muon Solenoid (CMS [40]) and ATLAS [41] are two general-purpose detectors that are designed to search the EW sector for new physics with a peak luminosity of  $10^{34} \text{ cm}^{-2}\text{s}^{-1}$ .

Starting on 30 March 2010 and continuing through 13 February 2013, Run I of the LHC operated at 3.5 TeV and then 4 TeV per beam. Run II started on 5 April 2015 with 6.5 TeV per beam. The intervening period was known as Long Shutdown 1 (LS1) and featured several upgrades, maintenance, repair, and general assessment of the subsystems.

## 4.2 The ATLAS Detector

The basic design of a high-luminosity detector was inspired by the successes of many other detectors:

- COMPASS, Gargamelle, SHINE, ALEPH, DELPHI, L3, and OPAL at CERN
- CDF and D0 at Fermilab (Illinois, USA)
- ARGUS, OLYMPUS, H1, HERA-B, HERMES, and ZEUS at DESY (Hamburg, Germany)
- BRAHMS, PHENIX, PHOBOS, and STAR at BNL (New York, USA)

- BaBar and SLD at SLAC (Stanford, USA)
- CLEO and CUSB at Cornell (USA)
- many other historical detectors

Particles are identified by their mass. In relativistic mechanics, both the energy and momentum of a particle can be used to determine this mass. The momentum of charged particles can be measured in a magnetic field as they pass through tracking and transition materials. Energy can be measured by stopping particles through a shower of scattering interactions within calorimetry. Figure 4.7 shows how each particle can be detected in a cross-sectional view of the detector. Figure 4.8 shows how momentum and energy deposition contribute to identifying the particles in ALICE.

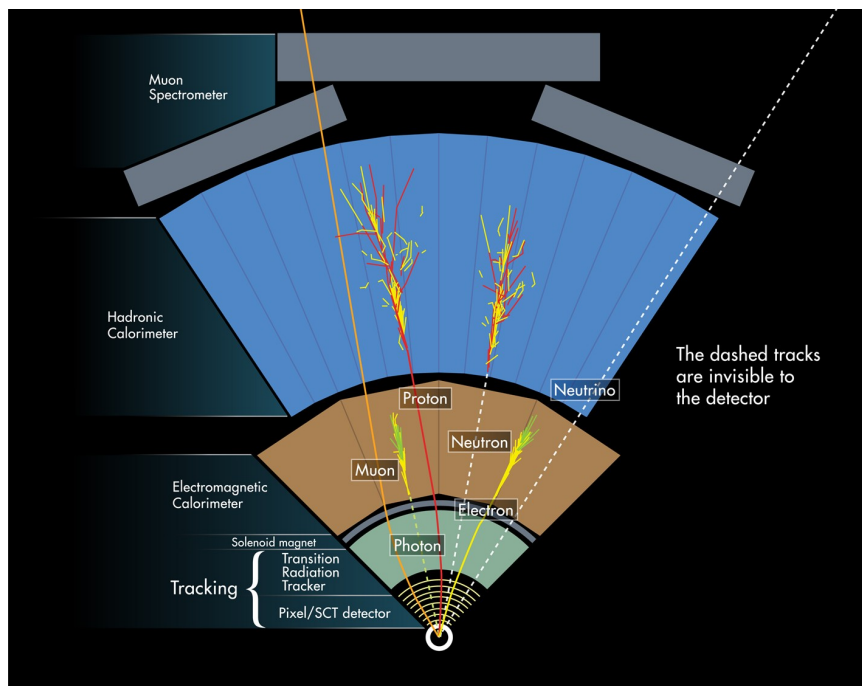


Figure 4.7. A schematic cross-section of the ATLAS detector showing how particles interact with the sub-detectors.

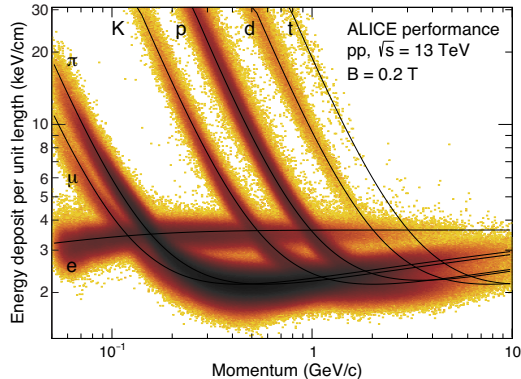


Figure 4.8. A distribution of energy deposition versus momentum used in particle identification by the ALICE collaboration.

[42]

#### 4.2.1 Design Philosophies

One of the big challenges to detector design is the elusive nature of muons. As shown in Figure 4.9, the muon momenta one would expect from LHC collisions fits into the lowest region of stopping power. This means that there is not much hope to adequately stop a high-energy muon in any calorimeter material. Low-energy muons ( $p_T < 2$  GeV) can be stopped in hadronic absorber material while calorimeters can aid in identification and calibration up to  $p_T = 5$  GeV. Inner tracking is used to determine the interaction vertex, but muon tracking can also be performed outside of the calorimetry.

Since the muon is EM charged, the measurement of muons requires tracking measurements within a magnetic volume. The radius of particle curvature is proportional to the momentum of the muon, so a high momentum will have a lower resolution of measurement. The design challenge arises when choosing a magnetic arrangement that will provide good resolution of these muons (Section 4.4). The detector can have a very strong magnetic field to tighten the track curvature (CMS) or the magnetic field can be extended to a large volume (ATLAS). The CMS design has the advantage of reducing low-energy events because the tight curvature keeps soft radiation negligible while ATLAS has the advantage of sustaining muon curvature in the larger volume. ATLAS is 44 m in length and 25 m in

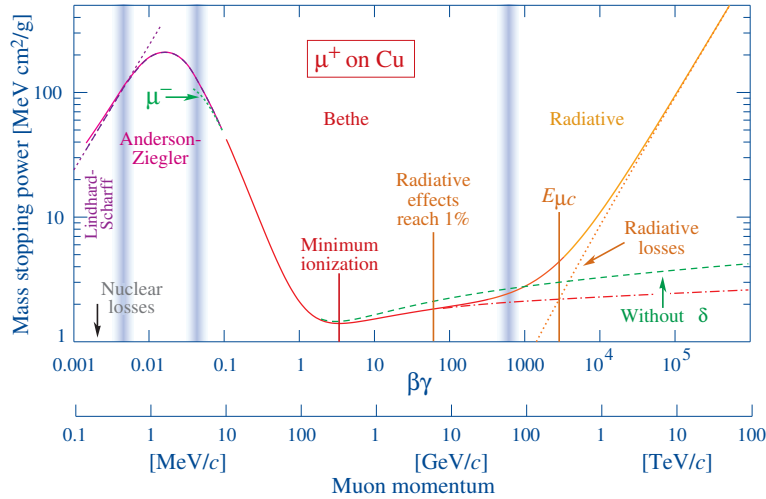


Figure 4.9. A plot of stopping power versus muon momentum. [1]

diameter while CMS is only 21.6 m long and 14.6 m in diameter. Interestingly, with a mass of 7000 t, ATLAS would float in water if it was hermetically sealed while CMS, at 12500 t, would sink.

Another motivation of the ATLAS design was to have a large acceptance (Equation 4.9) as well as full coverage in the azimuthal axis. The detector and its subsystems are segmented roughly into “transverse” and “boosted” sections that also allow cabling to run through the detector without disturbing detection volume in vital areas (Figure 4.10). For example, a subsystem may have one geometric design for the barrel region, and another boost-inspired geometry to extend coverage in the forward regions ( $|\eta| < 4.9$ ). Figure 4.11 shows what the detector looks like when the extended calorimeter is pulled out during maintenance.

#### 4.2.2 Performance of ATLAS

Measuring the numerical values of the parameters in the SM (Table 2.2) is necessary for the theory to be predictive. ATLAS has been quite successful at testing the SM during Run I and the start of Run II. In order to build trust that the machine can discover

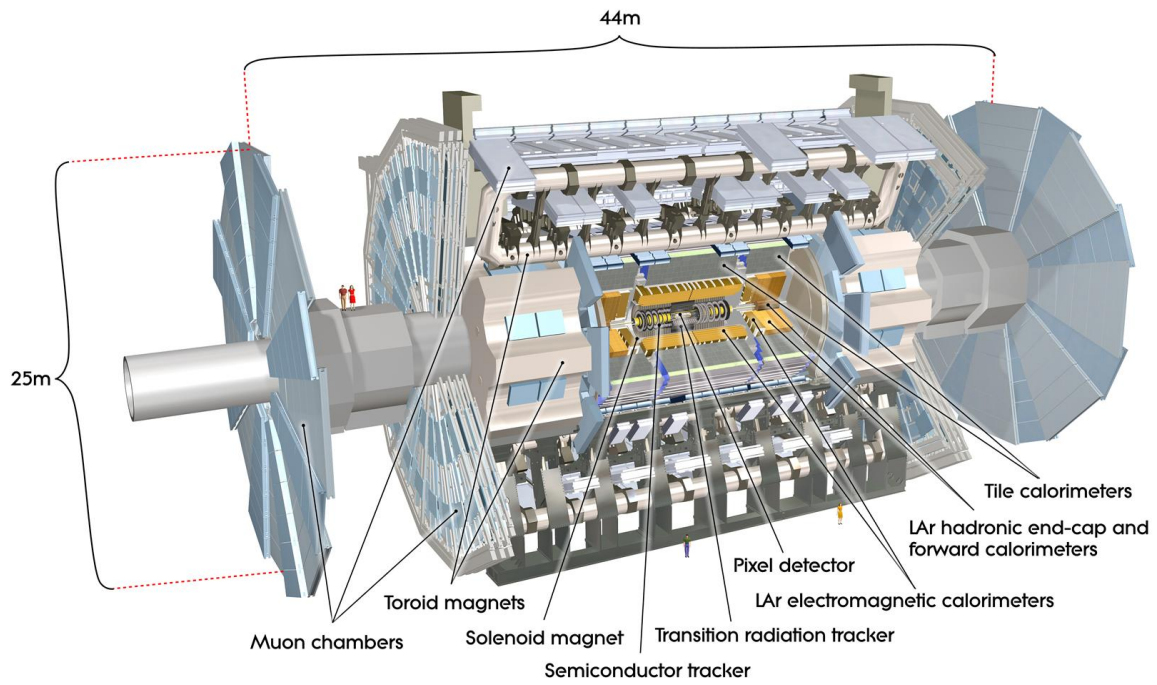


Figure 4.10. A schematic for the ATLAS detector indicating the major subsystems.

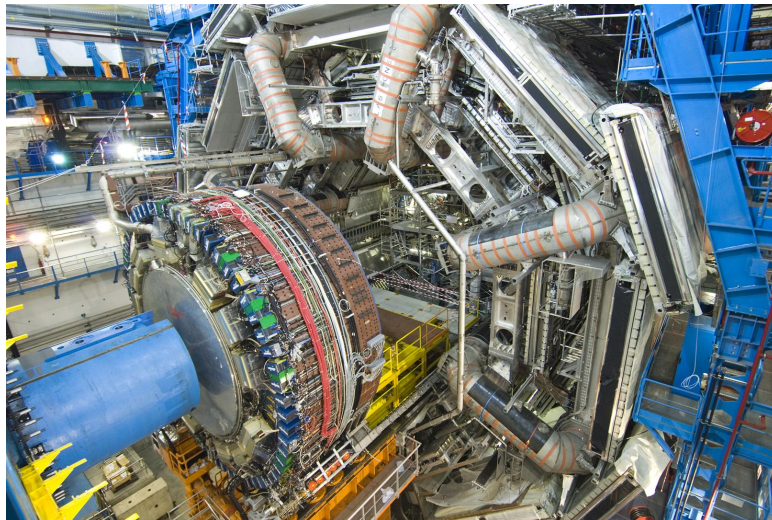


Figure 4.11. A view of the ATLAS detector with the TileCal extended barrel pulled out.

something new, it was necessary to confirm the SM to eliminate any plausible explanation for event signatures that appear to be new. Figure 4.12 shows various cross-section measurements by ATLAS compared to their theoretical predictions, and Figure 4.13 shows how cross-sections varied with the ramping of center-of-mass (CM;  $\sqrt{s}$ ) energy.

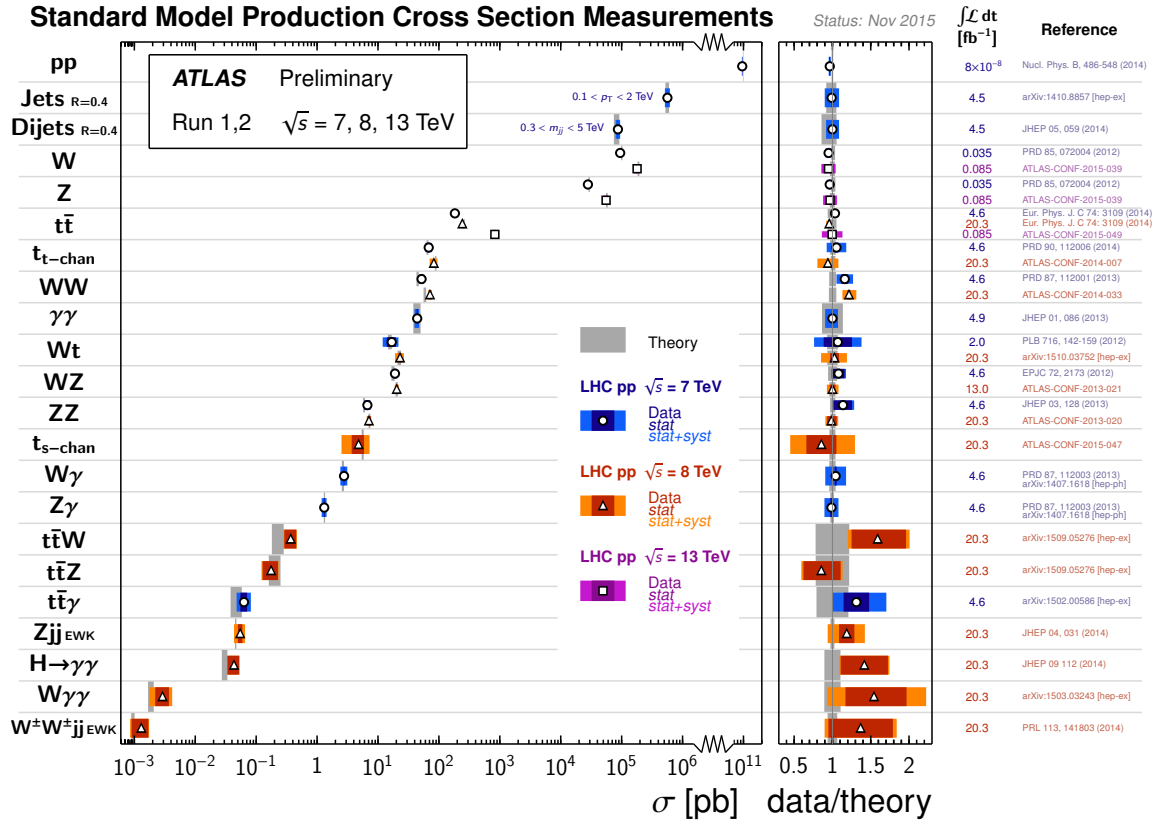


Figure 4.12. Confirmation of the SM cross-sections by ATLAS.

### 4.3 Kinematics and Measurables

The detector geometry defines a coordinate system where the positive  $x$ -axis points to the center of the LHC, the  $y$ -axis points up, and the  $z$ -axis points along the beam pipe

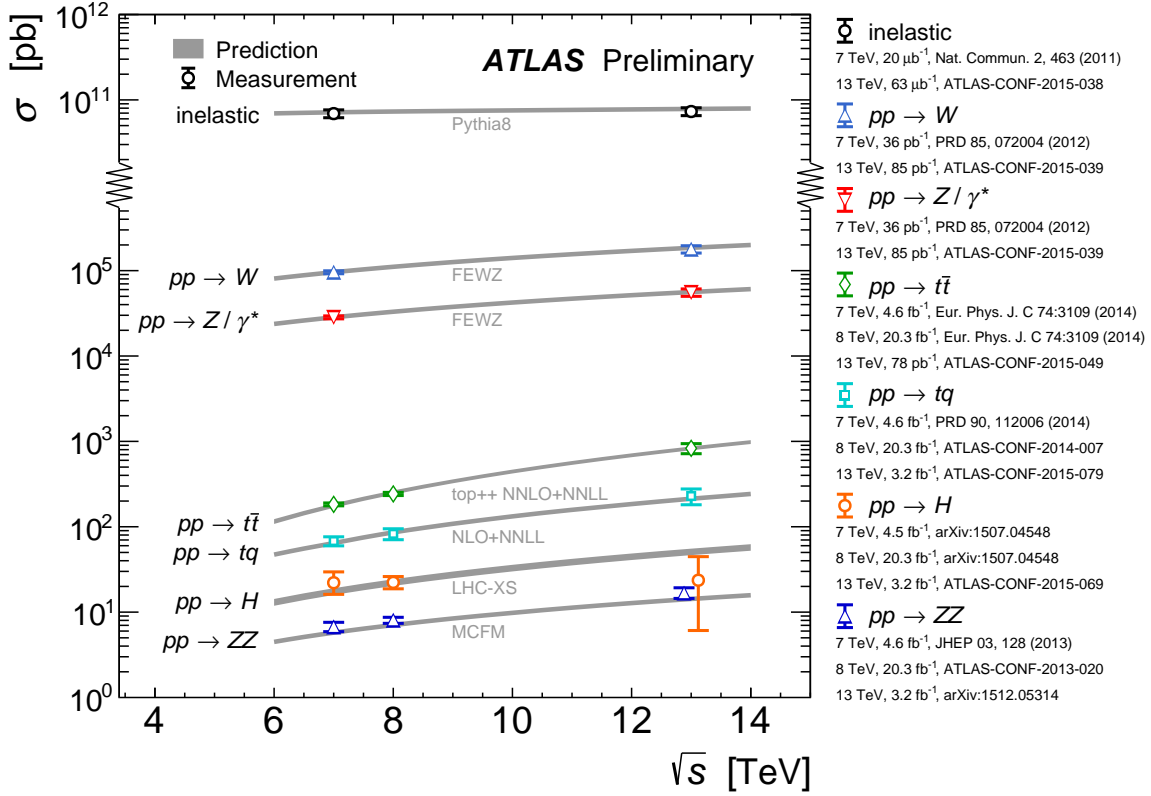


Figure 4.13. Confirmation of the SM cross-sections by ATLAS with varying  $\sqrt{s}$ .

anti-clockwise to the LHC. The azimuthal angle ( $\phi$ ) is a positive curl around the  $z$ -axis and the polar angle ( $\theta$ ) is measured from the  $z$ -axis.

The ATLAS detector has a cylindrical symmetry (Figure 4.10) where particle collisions occur along its central axis near the origin between two symmetrical halves. Hardware in the central barrel region is designated with the letter “B”, while sections “A” and “C” are end-caps on either side.

Despite how well the beams may be prepared, the CM energy is not fixed to a certain value with each collision. The energy of a proton is shared over its “parton” substructure (quarks and gluons) and it is these partons that scatter off of each other with a fraction of the total nuclear energy. Therefore, the CM frame rarely coincides with the laboratory frame.

### 4.3.1 Transverse Variables

Transverse two-vectors ( $x$  and  $y$ ) are invariant under boosts to  $z$ . Because event topology and detector acceptance introduce uncertainty to the longitudinal ( $z$ ) measurement, observables are given in terms of transverse components. These observables provide a boost-invariant plane for the event along  $\hat{z}$ . Transverse momentum is one of the most important measures used in this document:

$$\begin{aligned} p_T^2 &\equiv p_x^2 + p_y^2 \\ \vec{p}_T &\equiv \vec{p} \sin \theta \end{aligned} \tag{4.5}$$

Transverse energy is also important when constructing certain variables (Chapter 8):

$$\begin{aligned} E_T^2 &\equiv p_T^2 + m^2 \\ &= E^2 - p_z^2 \end{aligned} \tag{4.6}$$

### 4.3.2 Relativistic Boosts

Since the laboratory frame and the CM frame are not congruous, imbalances in the inelastic scattering of particles will be manifested as kinematic boosts. This way, the polar angle is quite useful in expressing observables in terms of the relativistic velocity ( $\beta = p/E$ ). Differences in the rapidity of the event is invariant under longitudinal Lorentz transformations.

$$\begin{aligned} y &\equiv \frac{1}{2} \ln \frac{E + p_z}{E - p_z} \\ &= \frac{1}{2} \ln \frac{1 + \beta \cos \theta}{1 - \beta \cos \theta} \end{aligned} \tag{4.7}$$

However, this calculation requires knowledge of  $\beta$ , which would need another detector to independently measure  $E$  and  $p$ . In the relativistic limit:



$$\beta \rightarrow 1$$

$$m \ll p_T \tag{4.8}$$

$$\cos \theta \rightarrow \tanh y$$

Using this as an approximation, the pseudo-rapidity is:

$$\begin{aligned} \eta &\equiv \frac{1}{2} \ln \frac{1 + \cos \theta}{1 - \cos \theta} \\ &= -\ln \left( \tan \frac{\theta}{2} \right) \end{aligned} \tag{4.9}$$

Particles detected at an angle  $\theta$  will all have the same pseudo-rapidity regardless of mass. If these assumptions are not accurate, longitudinal information about the event can easily be lost, which is why transverse quantities are preferred. Collectively, the transverse momentum, transverse energy, azimuthal angle, and pseudo-rapidity can combine to completely define the geometry of an event without requiring longitudinal momentum.

### 4.3.3 Consistency Checks

With a predictive theory, the model can be tested for its consistency to measurements of cross-sections, decay widths, and branching ratios. For a generic interaction between two particles, the incoming momenta can be denoted as  $p_1$  and  $p_2$  and the outgoing momenta as  $p'_1$  and  $p'_2$ . In general, the scattering matrix element takes the form:

$$\mathcal{T} = g^2 \left[ \frac{1}{(p_1 + p_2)^2 + m^2} + \frac{1}{(p_1 - p'_1)^2 + m^2} + \frac{1}{(p_1 - p'_2)^2 + m^2} \right] + \mathcal{O}(g^4) \tag{4.10}$$

The terms in this matrix element can be expressed with Lorentz scalars called Mandelstam variables:

$$\begin{aligned}
s &\equiv -(p_1 + p_2)^2 = -(p'_1 + p'_2)^2 \\
t &\equiv -(p_1 - p'_1)^2 = -(p_2 - p'_2)^2 \\
u &\equiv -(p_1 - p'_2)^2 = -(p_2 - p'_1)^2 \\
s + t + u &= m_1^2 + m_2^2 + m_{1'}^2 + m_{2'}^2
\end{aligned}
\tag{4.11}$$

The differential cross-section is a measure of the rate at which particles scatter at different separation angles:

$$\frac{d\sigma}{d\Omega} = \frac{1}{64\pi^2 s} \frac{|p'_1|}{|p_1|} |\mathcal{T}|^2
\tag{4.12}$$

The total cross-section would be a measure of how likely an interaction is. Since the cross-section is related to luminosity (Equation 4.1), the amount of data may also be expressed in terms of an inverse cross-section ( $b^{-1}$ ; “inverse barns”):

$$1 \times 10^{39} \text{ cm}^{-2} = 1 \text{ fb}^{-1}
\tag{4.13}$$

An unstable particle will decay after a lifetime duration and the uncertainty on the mass of the particle is constrained by the Heisenberg uncertainty principle. Decay widths are defined by this uncertainty in mass:

$$d\Gamma = \frac{|p'_1|}{32\pi^2 \sqrt{s} E_1} |\mathcal{T}|^2
\tag{4.14}$$

If a particle can decay by multiple channels (more than one decay chain), the width of a particular decay is called a partial decay width. Branching ratios (BR) or branching fractions (BF) calculate the ratio of partial decay width to total decay width to express the likelihood of a particular decay chain.

$$BR(i) = \frac{\Gamma_i}{\sum_i^n \Gamma_i}
\tag{4.15}$$

## 4.4 The Magnetic Systems

As explained above, the geometry of ATLAS is heavily influenced by its magnetic fields as a way to improve the momentum resolution of muons. This is also true for CMS, but the ATLAS inner detector and calorimeters were actually built inside the central toroid once it was already in place. A fairly popular photograph of the toroids was made public during construction (Figure 4.14(b)).

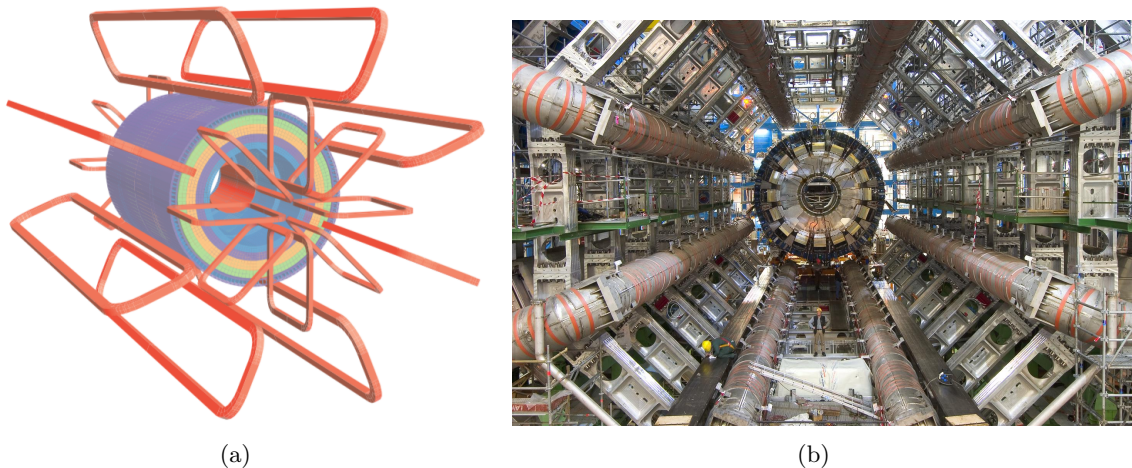


Figure 4.14. The magnetic systems of ATLAS showing (a) the geometry of the solenoid and toroids, and (b) a photograph of the toroids during construction.

CMS has taken the approach of using a strong magnetic field for track curvature that it is still powerful enough at the edges of the detector to track the muons. However, this choice also sacrifices the interaction length of the hadronic calorimeter to make space for the 4 T solenoid magnet. This causes a punch-through of hadronic energy that, although also present in ATLAS at a lower percent, was considered undesirable by the ATLAS collaboration.

On the contrary, ATLAS has a weaker solenoid magnet at 2 T (Figure 4.14(a)). At 5.8 m in length and an inner diameter of 2.46 m, the solenoid is situated around the beam pipe, between the inner detector and the calorimeters. The thickness of the solenoid and

surrounding environment is only 10 cm, which limits the amount of material a particle must pass through between the two subdetectors. The magnetic flux returns through the steel housing of the TileCal electronics (Section 4.6).

ATLAS also has toroid magnets to extend the magnetic field across the entire detector volume. The barrel toroid is 23.5 m in length, arranged in an octagonal configuration outside of the calorimeters, and has a field strength of 0.5 T. The end-cap toroids are 5 m in length, situated on either end of the calorimeters in an octagonal configuration, and have a field strength of 1 T.

#### 4.5 The Inner Detector

The inner-detector (ID [43, 44]) is a subsystem that must make precise position measurements of hundreds or thousands of particle tracks for good momentum resolution. Tracking is possible for particles with  $p_T > 0.5$  GeV and  $|\eta| < 2.5$ . The processing time of tracking algorithms prevents track identification below this  $p_T$  threshold. The ID has three main subsystems (Figure 4.15): the Pixel detector, the semiconductor tracker (SCT), and the transition radiation tracker (TRT).

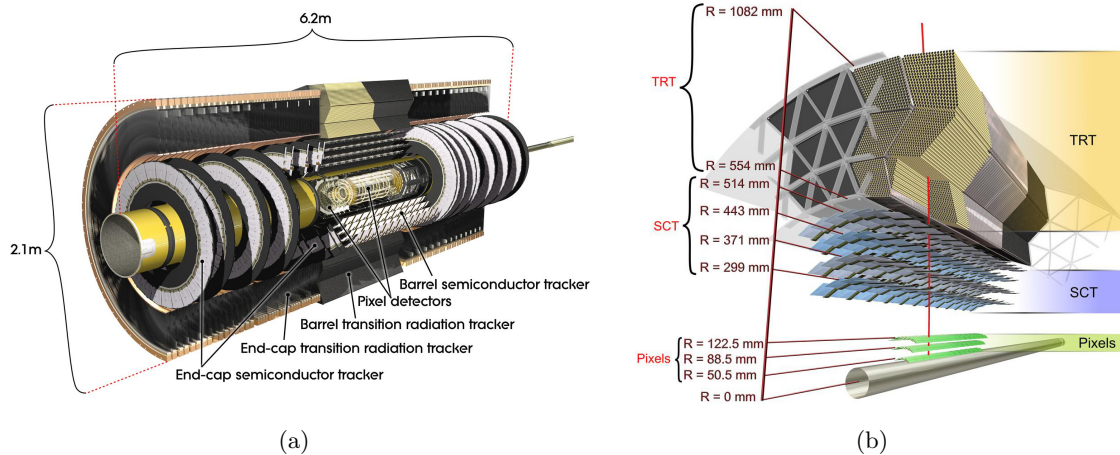


Figure 4.15. A schematic of the ID (a) components and (b) transverse cutaway.

The Pixel detector is three layers of silicon isolated into  $50 \mu\text{m} \times 400 \mu\text{m}$  pixels for fine granularity of  $\sim 10 \mu\text{m}$  in the  $r\phi$ -plane. Charged particles that pass through these pixels create electron-hole pairs, which separate due to a voltage bias and create current in the cathode. The Pixel detector has the highest number of readout channels with more than 80 million pixels. The Pixel detector is only situated along the central region and is expected to have a short lifespan due to the constant irradiation at close range.

The insertable B-layer (IBL) was added during LS1 as effectively the fourth layer of Pixel [45, 46]. This layer increases reliability of  $b$ -tagging, lowers readout inefficiencies at luminosity beyond the original design, and improves vertexing and tracking.

A particle moves through about 8 layers of silicon strips in the SCT. This detector has a resolution of about  $17 \mu\text{m}$  in the  $r\phi$ -plane. The SCT has about 6 million channels and provides a nice supplement to the Pixel detector for disentangling tracks.

TRT is comprised of 4 mm diameter drift tube “straws” made of tungsten containing xenon, oxygen, and carbon dioxide gas and a gold-plated tungsten wire. When a particle passes through the straws, it ionizes the gas, and a current spikes along the anode wire. The gas also plays a role because particles that encounter the change in dielectric constant emit x-rays at the boundary (Cherenkov radiation). The energy of the x-rays is a fairly good way to distinguish between electrons and hadrons. There are about 351k readout channels in the TRT.

## 4.6 The Calorimeters

The calorimetry has two subsystems (Figure 4.16): Liquid Argon (LAr) and Tile Calorimeter (TileCal). Particles that interact via EM tend to be stopped by low- $Z$  materials while particles that interact strongly tend to travel through low- $Z$  materials more easily, but are stopped by high- $Z$  materials. The calorimetry extends coverage to  $|\eta| < 4.9$ .

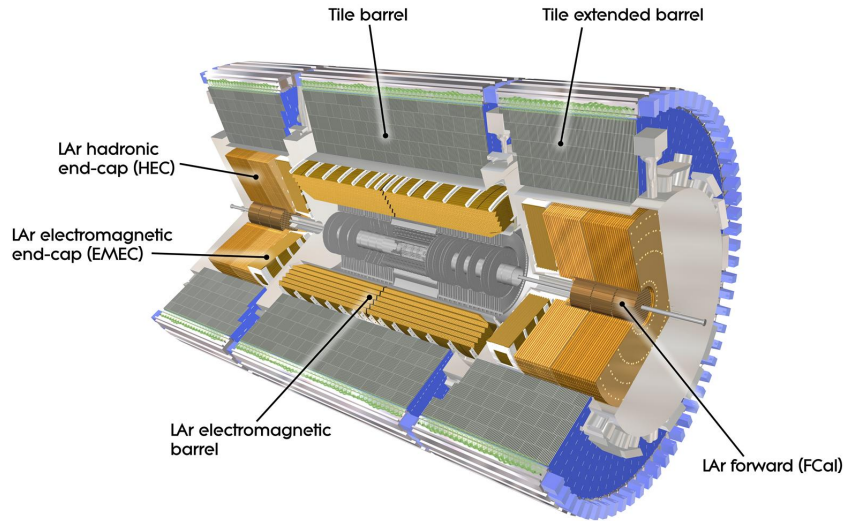


Figure 4.16. A schematic layout of the TileCal and LAr calorimeters.

#### 4.6.1 Calorimeter Principles

These calorimeters are “sampling” calorimeters because they use two types of material: an active medium and an absorber. The particles shower in the absorber material and the ionized particles from the shower are detected in the active material. EM showers are typically much shorter and narrower than hadronic showers.

A useful measure of the ability of a calorimeter to stop energetic particles is the radiation length ( $X_0$ ). This is the mean distance that a particle with energy  $E_0$  can travel before it is reduced to  $E_0/e$  (about 36.8%). The radiation length varies with the atomic number of the absorbing material and the type of incident particle. Calorimeter length is often expressed in multiples of  $X_0$  (e.g.  $10X_0 \approx 4.5 \times 10^{-5} E_0$ ).

#### 4.6.2 LAr Calorimeters

In the electromagnetic barrel (EMB; Figure 4.17), the absorber is lead and the active material is a constant flow of liquid argon with a gap between absorber plates of 4 mm. The fact that the argon is flowing means that it can avoid radiation damage. EMB is  $24X_0$  deep and has an accordion geometry to allow full coverage in  $\phi$  without having to shape

the absorber plates or leave cracks in  $\eta$ . The electrodes are placed in the middle of the gap. The electric current induced by the energy deposition is smeared by a shaping circuit into a 400 ns pulse that covers all samplings within the interaction time and its amplitude is measured after 40 ns.

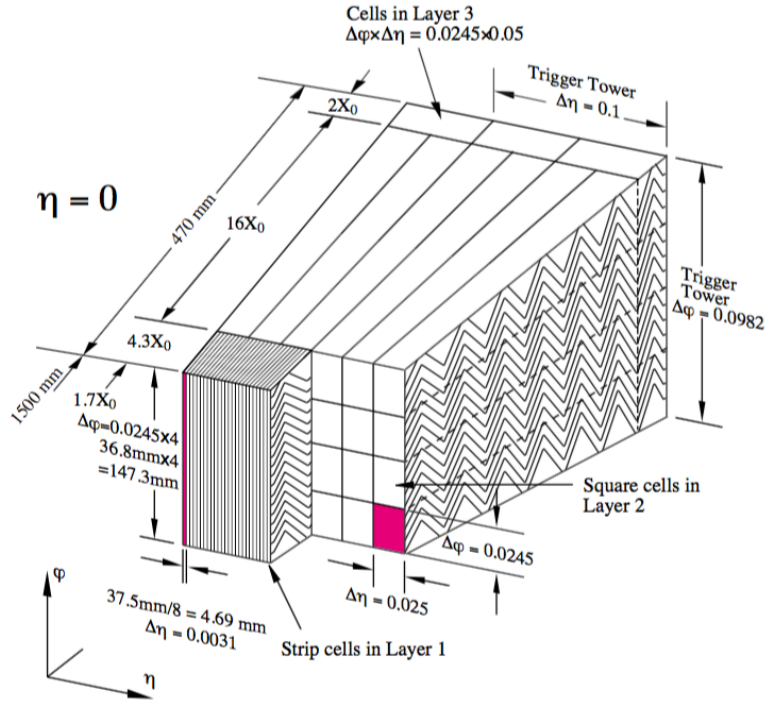


Figure 4.17. A schematic view of a barrel section of LAr.

The electromagnetic end-cap (EMEC) and the hadronic end-cap (HEC) use copper as the absorber material, while the forward calorimeter (FCAL) uses tungsten. These subdetectors use a Spanish fan geometry (or the same accordion geometry on a different axis). The LAr calorimeters have a total of about 182k readout channels.

#### 4.6.3 TileCal

TileCal is situated outside of LAr. Its active material is silicon scintillators and the absorber is steel. Although lead would have made a good absorber for TileCal as well,

TileCal also functions as physical structure and support for much of the detector and the solenoid’s magnetic flux return is assisted by its steel girders (and its steel absorbers). Lead would just be too malleable for the job at that weight and has a lower magnetic permeability.

TileCal is split into 4 sections along  $\hat{z}$ : long barrel A (LBA), long barrel C (LBC), extended barrel A (EBA), and extended barrel C (EBC). Each section is then split into 64 wedge-shaped modules along  $\phi$ . The modules are referred to by their section designation and their module numbers (e.g. LBA36). Each module is also roughly divided in  $\eta$  by cells. These cells are identified by letter (A-D starting closest to the beam pipe and moving radially) and number increasing with  $\eta$ . The exact naming of the cells is shown for two modules (barrel and end-cap) in Figure 4.18.

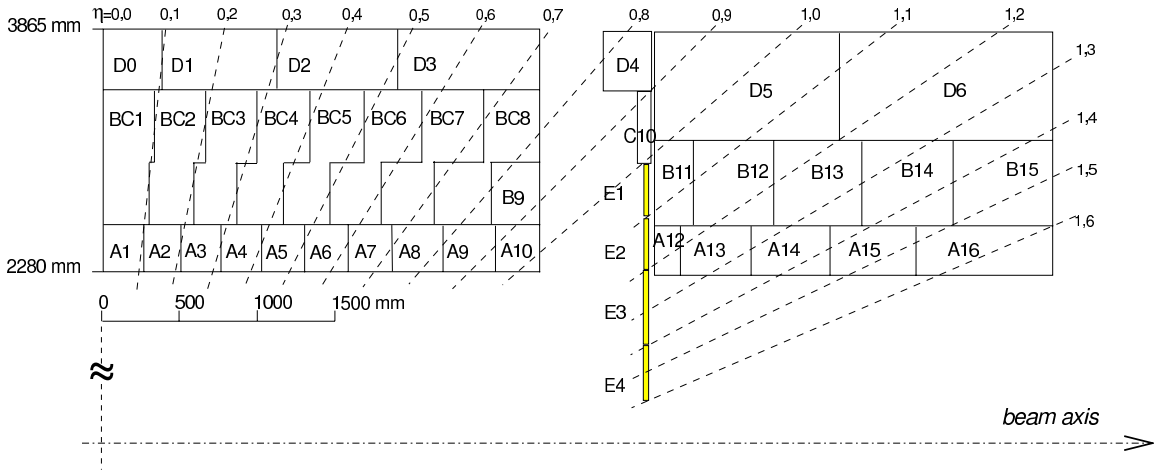


Figure 4.18. A breakdown of TileCal showing the boosted geometry of its cells.

TileCal has an inner radius of 2.28 m and an outer radius of 4.23 m ( $9X_0+$ ). The long barrel is 5.64 m long and covers  $|\eta| < 1.0$  while each extended barrel is 2.91 m long and covers  $0.8 < \eta < 1.7$ . This includes an extension called the intermediate tile calorimeter (ITC) that is intended precisely to add active volume to TileCal. These include the E cells in Figure 4.18 marked in yellow. These special cells have “crack” scintillators to provide EM



shower sampling instead of sampling particles that have passed through cabling or cryostat walls.

The absorber-active material layers are oriented longitudinally. This may seem counter-intuitive but it has a major advantage in allowing optical fibers to run radially from the cells to the steel girders that house photo-multiplier tubes (PMT) and the front-end boards (FEB; Section 5.1). The scintillators generate photons from showering hadrons, which travel along the wavelength-shifting (WLS) optical fibers, creating cascade photo-electrons in the PMT that can be measured by the FEBs. The system has two redundant PMTs for each cell.

The FEBs of each TileCal module can be pulled out of its girder housing in a single block called a super-drawer. The barrel section has 46 PMTs in each module, each extended barrel has 28 PMTs in each module, and the ITC modules contribute 3 more PMTs to each extended barrel. There are a total of 9856 readout channels for TileCal, which is the least amount for any subsystem in ATLAS.

#### 4.7 The Muon Spectrometers

The outermost parts of the detector are dedicated to the muon systems (MS [47]). The full MS can provide coverage up to  $|\eta| < 2.7$  with a dedicated trigger (Chapter 5) that covers up to  $|\eta| < 2.4$ . There are about 1 million readout channels in the MS.

Because muon energy measurement is implausibly difficult in a reasonable volume of material, one can rely on the fact that all muons have the same mass to calculate the kinetic energy. A muon that reaches the outer layers of the MS has a momentum ( $p$ ) that increases with  $\eta$ . It is important, therefore, to have a finer granularity for large  $\eta$  to keep the momentum resolution uniform. Three layers of muon spectrometers surround the barrel region at a radius of 5 m, 7.5 m, and 10 m. Three end-cap wheels are situated at 7.4 m, 10.8 m, and 21.5 m from the origin. Four types of subdetector are incorporated into the spectrometry (Figure 4.19).

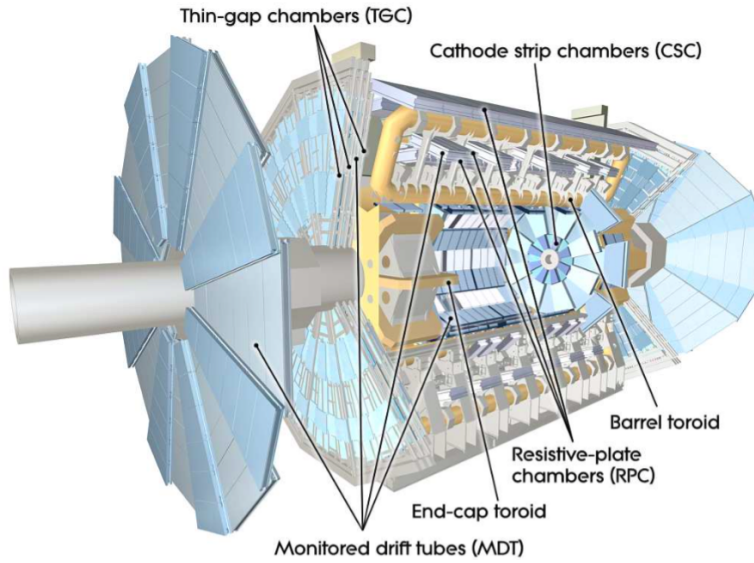


Figure 4.19. A schematic of the MS.

The monitored drift tubes (MDT) provide precision energy measurements and tracking of muons. Each tube is made of aluminum and is about 30 mm in diameter. The tubes are filled with argon and carbon dioxide gas and have a tungsten wire to detect passing muons. These detectors have a low radiation tolerance, so cathode strip chambers (CSC) are more prevalent in the forward region where they can take advantage of quick response and fine resolution. These are multi-wired chambers filled with argon, carbon dioxide, and tetrafluoromethane gas and the cathodes are oriented perpendicular to the wires to allow for two-dimensional measurement along the normal plane.

For triggering, resistive plate chambers (RPC) are used in the barrel region with  $|\eta| < 1.05$  and thin gap chambers (TGC) are used in the end-caps with  $1.05 < |\eta| < 2.4$ . For the RPC, two resistive plates with a gap of 2 mm are filled with tetrafluoroethane, isobutane, and sulfur hexafluoride gas. TGCs are similar to CSCs, but they have a reduced gap between wires and the cathode is smaller than the multi-wire spacing.

## 4.8 Forward Detectors

Three specialty detectors are located in the very forward regions and two of them do not reside in the main ATLAS cavern. These are essentially monitoring systems that detect particles from elastic diffraction.

Luminosity measurement using Cherenkov Integrating Detector (LUCID) is located 17 m down the beam pipe from the origin, putting it between two end-cap muon wheels. It is comprised of 1.5 m long aluminum tubes around the beam pipe that are filled with perfluorobutane. Cherenkov radiation from passing charged particles is collected onto PMTs to provide a real-time luminosity measurement during the run.

140 m down the beam pipe from the origin, the Zero Degree Calorimeter (ZDC) is situated where the LHC split pipes converge into a single pipe for interaction. In heavy ion collisions, the centrality of the event is highly correlated to the number of forward neutrons in the event. EM and hadronic modules use tungsten and a quartz rod matrix connected to PMTs to measure these neutrons. For proton collisions, the ZDC can only be used for low luminosity to preserve the quartz rods.

The Absolute Luminosity For ATLAS (ALFA) detector is truly isolated, as it is located 240 m down the beam pipe from the origin. Two Roman Pots situated on either side of the pipe can be moved close to the beam. 1500 scintillating fibers are able to detect protons scattered at very small angles to get an accurate measurement of luminosity. This detection still requires a higher  $\beta^*$  than would be used in physics runs, but the accurate measurement is used to calibrate LUCID.

## 4.9 Missing Momentum

The ATLAS detector is not capable of detecting every particle that is generated inside of it. Neutrinos ( $\nu_e, \nu_\mu, \nu_\tau$ ), for example, do not leave any tracks because they are neutral and they very rarely interact with anything that would leave excitation energy in the calorimetry. As a result, the ATLAS detector has no special design feature to identify the presence of neutrinos. However, the detector is fairly good at measuring nearly everything

else in an event. If a neutrino was produced by the primary proton-proton scatter, the neutrino would carry away momentum from the interaction that would not be recoverable. By assuming conservation of momentum, the neutrino can then be inferred by the missing momentum.

Unfortunately, there are still other ways to get missing momentum. The calibration of the calorimeters could be under-reporting the energy of the particles. For example, a flawed PMT in LBC46 may sporadically malfunction and report no energy from a jet. The detector is not perfectly sealed to capture every particle it should detect either. A particle could find its way into cabling rather than active detector material and lose energy in doing so. Fortunately, the detector is well-simulated on its own, so such effects are often taken into account when simulating how a signal event would be detected. A highly boosted jet with  $|\eta| > 4.9$  would be lost as longitudinal missing momentum.

If an event contained an *invisible* particle that was very heavy, the signature of missing momentum would be the recoil of visible objects. As explained in Section 4.3.1, the transverse values of momentum and energy are used because they are invariant to boosts along  $\hat{z}$ . These visible objects would be highly boosted, but a heavy invisible object may have very little recoil of its own. If the invisible object barely moves, then the visible objects may be boosted in opposite directions and appear balanced in  $z$ . The telltale recoil in the transverse plane, however, would be unaffected by the unknown boost given to the invisible particle. Taking the phenomenological perspective of a missing physical particle with momentum *and* mass, this quantity can be called the missing transverse *energy*. However, those that favor defining it by its construction – that assumes conservation of momentum – may refer to it as the missing transverse *momentum* since it is agnostic to mass. Therefore, this quantity ( $E_T^{\text{miss}}$  or MET) can be applied to the search for massless neutrinos as well as massive invisible particles.

Understanding how the detector itself biases  $E_T^{\text{miss}}$  is crucial to searching for new physics that predict weakly-interacting particles. A SUSY event with conserved  $R$ -parity, for example, has two particles that would escape detection in the final state.

#### 4.9.1 Simulated SUSY Event

In the simulated display of Figure 4.20, the ID can be recognized by the curved tracks, LAr is indicated by the smaller histograms, TileCal is represented by the larger histograms, and two muons are shown by tracks that continue past the calorimeters. Since the tracks are not very isolated (Section 6.2.2) and the energy deposition in TileCal is much greater than in LAr (Section 6.2.4), the other particles are likely “jets” of hadrons.

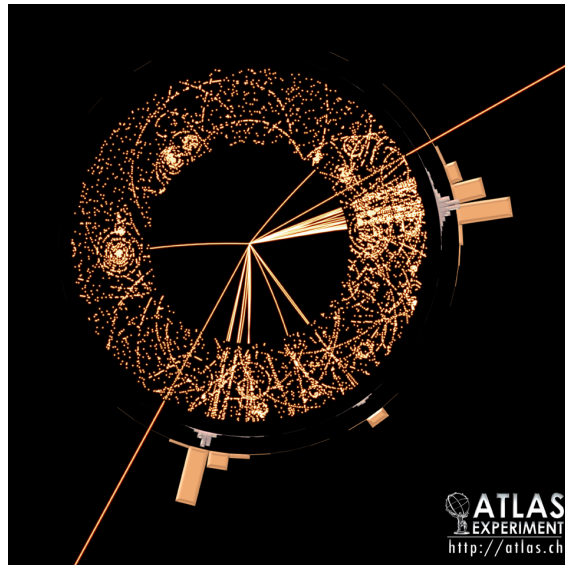


Figure 4.20. A simulation of SUSY production in an event display.

Although physics analysis is never done explicitly from such an event display anymore, they are illustrative of the kind of reconstruction (Section 6.2) that ATLAS performs. The key to reading this event is to remember that it only shows *visible* particles. Recognizing that very heavy particles are likely created near threshold energy (otherwise it might have been easier to find them at lower energy), the signature of the scatter can be characterized by the geometric symmetry of the visible particles in the plane transverse to the beam pipe.

Since this display is a view of that plane, then an event without invisible particles would exhibit near-perfect balance in the visible decay products. Instead, the display shows an event that is actually quite one-sided, suggesting that the visible particles that can be

detected are recoiling from something heavy but invisible. The large recoil is a telltale signature of a BSM event. However, realistically this is enough to label the event as “interesting” but not conclusive about being a SUSY event or otherwise if it was not already known to be simulated.

Recalling the simplified models of SUSY (Equations 3.20a and 3.20b), both final states have neutralinos. This means that the signature of interest will likely have large  $E_T^{\text{miss}}$  except for very compressed scenarios. To be more correct about the signature of the event, note that the jets (or electrons) are undifferentiated, meaning there is not enough information to determine that a particular jet (or electron) is associated to a particular decay step or  $\tilde{\chi}_1^0$ . The respective signatures that the detector can identify are shown in equation 4.16.

$$pp \rightarrow 2j + E_T^{\text{miss}} \tag{4.16a}$$

$$pp \rightarrow 4j + E_T^{\text{miss}} \tag{4.16b}$$

## CHAPTER 5

### Online Triggering

There is a landmark in Geneva, Switzerland near CERN called Jet d’Eau that is an impressive fountain of water. 500 L of water leave its nozzle every second at 200 km/h to reach an altitude of 140 m [48]. Witnessing this firsthand, one can scarcely imagine the number of 0.5 mL drops of water that are sprayed from it. However, in order to see Jet d’Eau spew 11 billion drops of water into the air, it would actually take 3 hours, 3 minutes, and 20 seconds.

Comparing the production cross-section of the Higgs boson at 14 TeV to the cross-section of any inelastic collision, roughly one in 11 billion total events could be a Higgs event (Figure 5.1). The remarkable difference between the LHC and Jet d’Eau is that the LHC, with a 40 MHz collision rate and 25 interactions per crossing, can deliver this number of events in about 11 seconds. If Jet d’Eau was capable of increasing the flow of water to achieve the same “luminosity” in drops of water, molecules of vaporized water could easily escape into space.

Now consider trying to keep 11 billion events. If only one of these was a Higgs event, then far too many non-Higgs background (BG) events with decades of experimental history already would also be kept. The computer storage would be clogged with these SM events totaling  $\mathcal{O}(\text{PB})$  (one million GB) within 15 seconds. This presents a significant challenge to analyzing all that data for new physics. Both the rate of data generation and the digital size of all the data become extremely prohibitive. To address this issue, ATLAS has a robust and systematic way of deciding which events to keep and which to reject.

Two terms are very useful to get straight before looking at the trigger and data acquisition (TDAQ) architecture. An “online” process is anything that happens at the time of data collection and automatic event reconstruction. These involve irreversible decisions

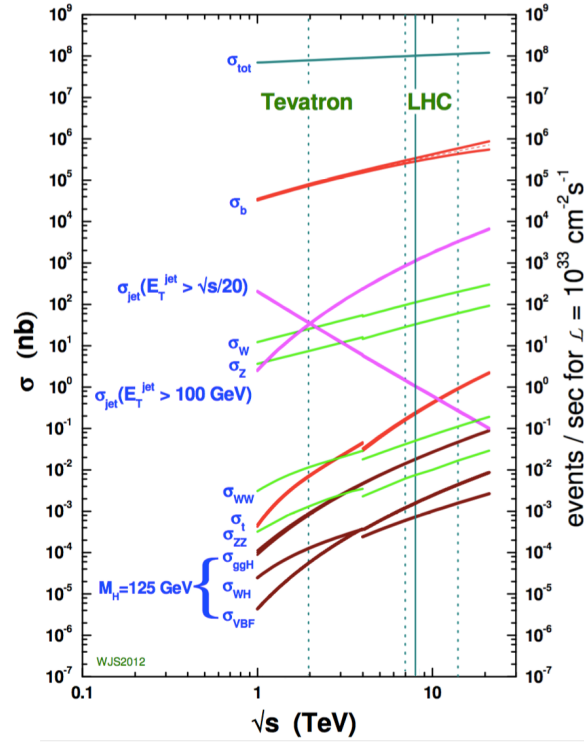


Figure 5.1. The production cross-sections of multiple processes at varying  $\sqrt{s}$ .

that must be made before the data is stored on hard drives or tape. It is vitally important to keep these decisions loose because they cannot be undone. The other term is “offline”, which is at a much more human level. These are typically analysis steps, and more information can be found in Chapter 7.

### 5.1 Calorimeter Electronics and Diagnostics

To understand how an “event” is defined in a detector, experience working in the consolidation of TileCal (Section 4.6.3) during LS1 is presented in this section. When a particle hits the absorbing material, it fragments into a shower of energy. In the active scintillator, photons are produced that typically have a high frequency. The photons illuminate wavelength shifting (WLS) optical fibers with a photofluorescent coating that transfer these photons at a lower output frequency. Each scintillator can be illuminated and each cell can have multiple scintillators. Since an individual cell may have only a few photons, the light



is directed into a PMT to amplify the generated signal. Each PMT has a locally-controlled high voltage (HV) of  $\sim 800$  V to cause the cascading photoelectric current. The output signal from the PMTs is a smooth pulse shape with a full width half maximum (FWHM) of  $\sim 15$  ns that can maintain good noise reduction even for some low-energy signals from muons.

Figure 5.2 shows the PMT response during a cesium calibration of TileCal. A thin pipe runs longitudinally through the center of each cell and a hydraulic system moves a  $^{137}\text{Cs}$   $\gamma$  source through the detector between runs or during technical stops. This source provides a steady stream of 1.176 MeV photons as it passes through the scintillators. Because TileCal is a sampling calorimeter, the apparent fluctuation in PMT current is a stochastic detail that is not as important as the cumulative effect within each cell, so the signals are either smeared into analog pulse shapes or integrated for preliminary object prototyping.

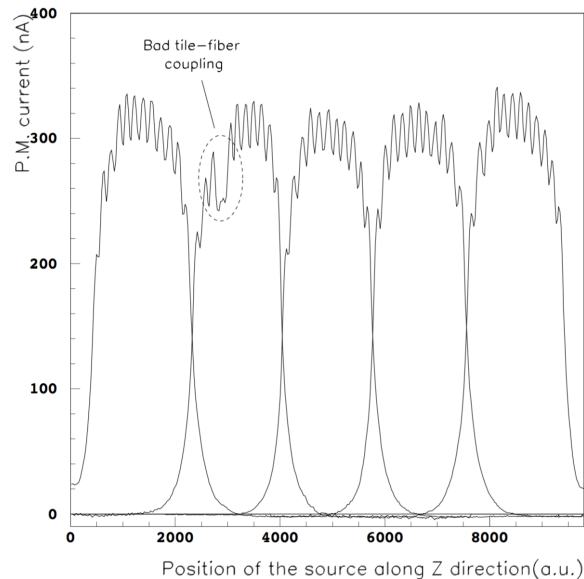


Figure 5.2. A cesium scan of TileCal showing the effect of particles traveling through alternating layers of scintillators and steel.

The PMTs are housed in an aluminum structure called a super-drawer that can be partially extracted during maintenance of TileCal (Figure 5.3). The PMTs themselves are

contained in hollowed-out cylinders within the super-drawer while the FEBs are mounted to the outside. Each PMT block also contains a 3-in-1 card for fast shaping of the signal pulse, slow integration for monitoring and calibration, and charge injection for calibration. The output of the 3-in-1 cards is split between a high-gain and low-gain amplification that is stored in a local buffer on the main FEBs and the analog trigger sums that are sent to the back-end (BE) network. A block-diagram of these components is shown in Figure 5.4. The FEBs can be configured using a controller area network (CAN) bus that is used to monitor and adjust the health of the FEBs for DCS (Section 5.3).

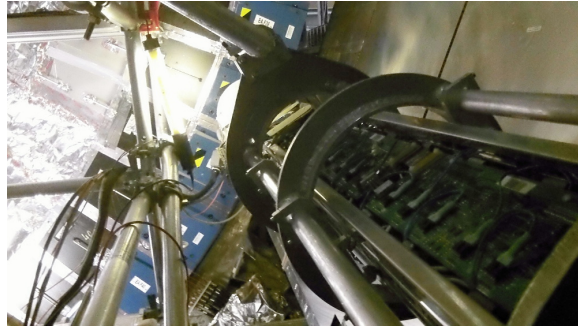


Figure 5.3. A photograph of the TileCal FEBs during maintenance. The super-drawer is rectangular in shape and is shown sitting in a temporary aluminum cradle for stability, rotation, and ease of access.

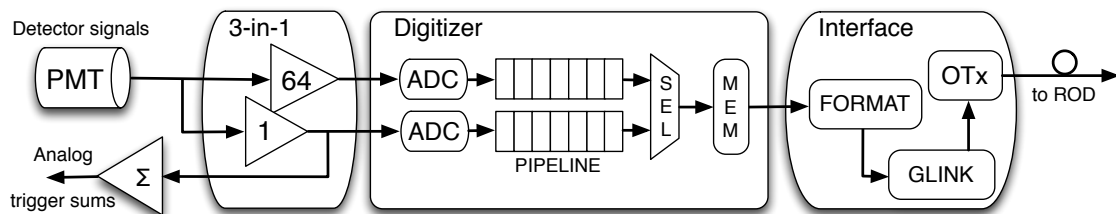


Figure 5.4. A diagram of the FEB electronics of TileCal.

The 3-in-1 cards first shape the PMT signals to extend the FWHM to a 50 ns pulse with an amplitude that is proportional to the charge of the signal (or the energy of the particle). The signals are passed through clamping amplifiers with a gain ratio of 1 (low-gain) or 64 (high-gain). The low-gain signal can be sent to the trigger summation board and then forwarded to the BE network for coarse event processing. The high-gain signal provides a high fidelity to the digital sampling in the analog-to-digital (ADC) converter which, along with a parallel low-gain signal, is stored transiently in a digital pipeline with the unique bunch-crossing identification (BCID) of the event. If the BE network requests a copy of the event through the trigger and timing control (TTC) cable, the data is transferred via a readout driver (ROD) for further processing. Otherwise, the data is allowed to expire and the digital addresses are overwritten once the buffer repeats.

#### 5.1.1 *MobiDick*

MobiDick (a corruption of “mobile DAQ”) is a portable test-bench for the diagnostic tests of the FEBs of TileCal. It is capable of simulating the processing and response of the BE network and DCS. It can be used to fully certify individual modules as documented in its historical progress [49–52].

Because the test-bench can be replicated with relative ease, it allows multiple maintenance teams to work simultaneously and cut down on the time needed for intervention and consolidation. An early version of MobiDick was based on a very heavy Versa Module Europa (VME) system ( $\sim 20$  kg) while its upgraded versions uses a field programmable gate array (FPGA) and dedicated daughterboards (Figure 5.5) and is quite light ( $\sim 4$  kg). MobiDick also includes an ethernet communication to create a client-server architecture with a graphical user interface (GUI) kept on a commercially-available laptop.

The motherboard processor includes a simple version of Linux and also contains a memory card slot that is used to load firmware onto the server. The general purpose input/output (I/O) ports allow the connection of daughterboards for communication with the FEBs and for control of a laser pulse card and HV for the PMTs. Low voltage (LV)

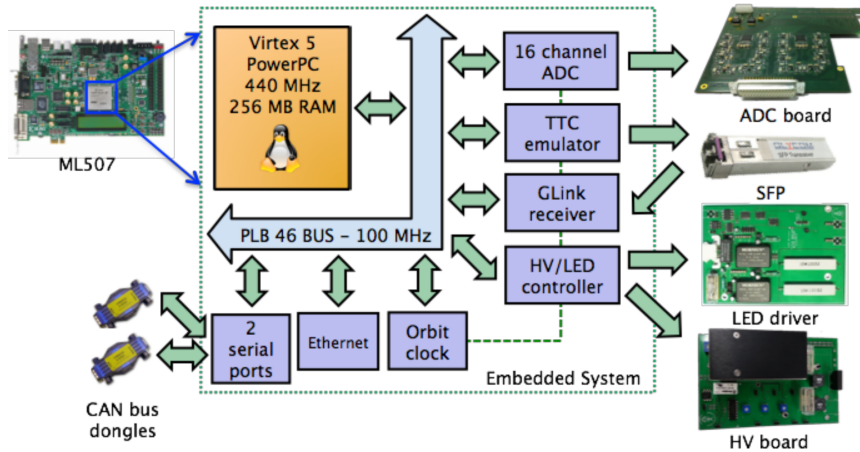


Figure 5.5. The embedded system of MobiDick uses an ML507 motherboard to process data and control daughterboards that interface with the FEBs.

power is also supplied by MobiDick to provide the 4,  $\pm 5$ , and 9 V wires needed by the FEBs. Fast communication with the FEBs is also possible through an optical small form-factor pluggable (SFP) connection. Raw data from the FEBs is passed through an (ADC) board to digitize the information. With components addressing every power and communication link needed for the operation of the FEBs, the testing procedure is kept independent of any external systems.

Several tests need to be performed to check all the components of a TileCal module. The first set of tests are for communication, identification, and configuration. `CommMB` is a test that identifies the ADC and super-drawer, then loads settings from a database and configures the subsequent tests. `DigChk` is a check of the digitizer configuration to verify that patterns of values can be written and retrieved. `CommHV` communicates with the HV boards and identifies them. `HVon/HVoff` enables or disables the HV for tests that need HV delivered to the PMTs. `Opto` is a check of all HV switches and values. `LEDon` enables the light-emitting diode (LED) pulse mode directly to the PMTs. `NominalHV` is a check of the HV value in the database that provides the pedestal bias to each PMT.

Tests designed for the digitizer diagnostics check the quality of the chips and circuits. The `Adder` test checks trigger tower summing with a test of the charge injection

system (CIS). The CIS test uses a capacitance charge to simulate a pulse in the digitizers, and **DigShape** evaluates the shape of the pulse (Figure 5.6). **DigNoise** checks the data integrity by determining the amount of noise in the digitizer and can be run in HV mode as **DigNoiseHV**. **StuckBits** rapidly changes the values in the digitizers to test the bit-flip response.

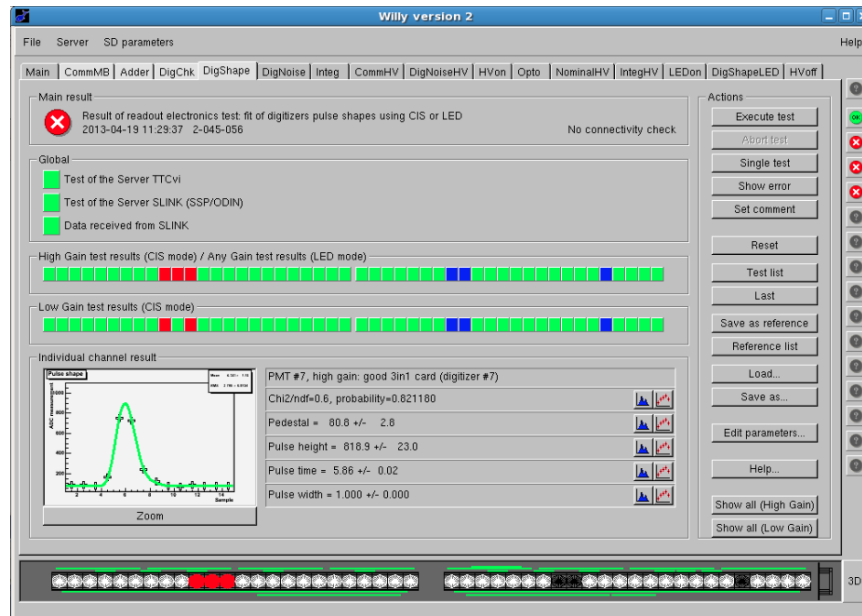


Figure 5.6. The **DigShape** test is used to fit and evaluate a pulse for each 3-in-1 and diagnose any problems with the electronics.

Lastly, some tests are aimed at PMT and 3-in-1 diagnostics. **Integ** evaluates the linearity and noise level of the integrator circuits and **IntegHV** calculates the RMS of the PMT response with the HV on. **DigShapeLED** uses an LED to directly pulse the PMTs and measure their response.

### 5.1.2 Phase I Upgrades

During LS1, the LHC was taken offline, and the ATLAS detector went under a series of upgrades, maintenance, and consolidation [53]. This opened up the detector and allowed

direct intervention to further investigate faulty cells in the TileCal modules. MobiDick was intended to directly aid in this service (Figure 5.7) and a number of issues were fixed after MobiDick was observed in its operating environment.

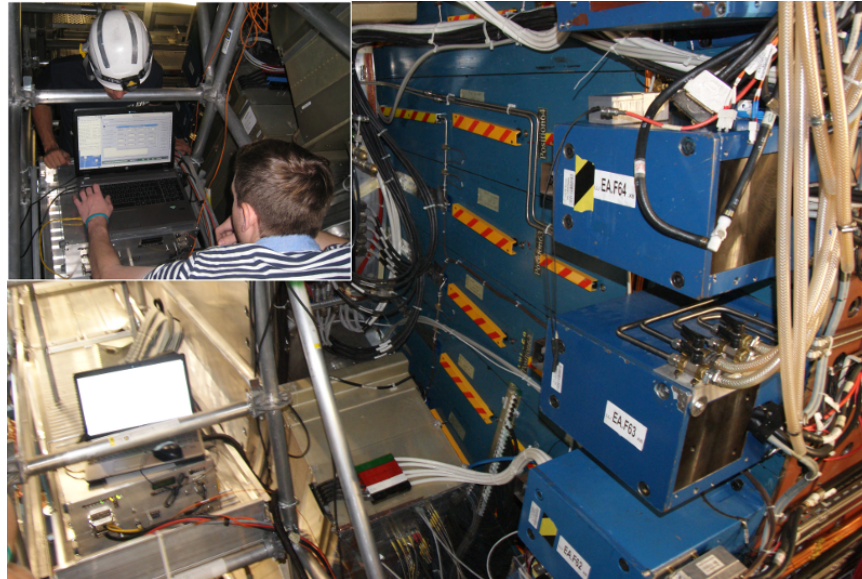


Figure 5.7. A photograph of MobiDick (lower left) in use for TileCal maintenance. The inset shows two workers reading the test results.

The first was an issue with saturation levels in noise measurements. Sampling would consistently return values of 4095, which is the 12-bit maximum value. If values are centered near the bitwise maximum, then the RMS noise reporting cannot be trusted. Furthermore, the saturation condition also meant that no energy pulse could ever be found to be in excess of the noise. Making the test fail if  $RMS = 0$  was considered, but it would supersede true results, however unlikely that might be. Secondly, values that fluctuate around the maximum would have a low RMS that would appear to be fine (Figure 5.8). The solution required that if any 12-bit saturation value was found, the test would set  $RMS = -1$  and this condition would flag the saturation error.

The second symptom appeared in the `Integ` test and gave large RMS before the CAN bus would timeout and required a manual reset. To prevent incidentally affecting the



Figure 5.8. A representation of (a) fully saturated values and (b) partially saturated values in a 12-bit sampler.

wires inside MobiDick to correct the trip, a reset button was installed on the outside of MobiDick to reset the CAN bus. The problem was traced to new minimum bias trigger system (MBTS) 3-in-1 cards in the E3 and E4 cells of the ITC that had large time constants in their integrator circuits (Figure 5.9). Because of the way stability conditions were defined in the software, it was possible for the test to start taking values before the measured values reached a plateau. Card-specific and gain-specific parameterization in databases seemed like an ineloquent idea. A plateau based on the time constant (99% value at  $4.6\tau$ ) was considered, but that lead to the next problem.

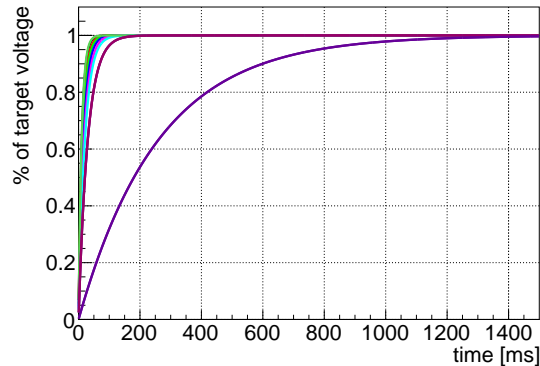


Figure 5.9. The various time constants of integrator circuits plotted to show the amount of time needed to reach a plateau value.

Lengthy test times created a tenuous situation where limited service time in certain areas of the detector led to short-changing the diagnostic cycles when numerous FEBs

needed to be checked. The `Integ` test was taking more than 11 minutes for each FEB, not to mention the time needed to extract the super-drawer and fix the problem. It was decided that the  $4.6\sigma$  requirement was too mathematically exacting. Nominal variability occurred long before the 99% plateau, and it was only the MBTS cards that were the source of the problem. The revision to the test held that the existing stability check would loop normally, wait for 1 s if it failed, and then try again. Next, saturation would result in a test failure anyway, so the test skipped sampling if any saturation values were found. This was modified to allow continued sampling if the ADC was set to zero, so that the possibility for coming down from saturation was allowed. Lastly, the database keeps a list of non-instrumented channels, so empty channels in the extended barrel could be skipped. This actually required tricking the software into running the nonlinear version of the test. After these modifications, testing time was reduced to  $\sim 5$  minutes.

Finally, the maintenance teams requested more information from the `DigShape` test to give a more complete description of an ambiguity problem. The 3-in-1 cards returned both high-gain and low-gain pulses but the test did not report which gain was being analyzed. The result gave a preference to high-gain pulses and only used the low-gain if the high-gain was saturated, but the pulse fits came back anonymously. If something was systematically causing the high-gain to saturate, this condition would not be known if the low-gain pulse passed the fit requirements. Unfortunately, the fix for this required either a large restructuring of the code or a reduction in the number of samples that could be returned in bi-gain mode as a C++ array. Due to the urgency of implementing a solution, the last sample in the array was replaced with the boolean gain value.

Upgrades to the hardware included a better 20 ns LED pulse board (and clever polarity fixes), rewiring, and better indicator lights. As shown in Figure 5.10, the upgrades to `MobiDick` were quite successful to the consolidation of `TileCal` during LS1. The percentage of masked cells in 2011, as a result of failed operation conditions, rose rapidly during 2011. Maintenance cycles in early 2012 essentially reset the percentage, but the rapid increase in masked cells continued during the 2012 portion of Run I. For Run II, a plateau at a low



percentage of masked cells can be observed. The cells that were masked may be due to the use of noisy cards pending newer replacements.

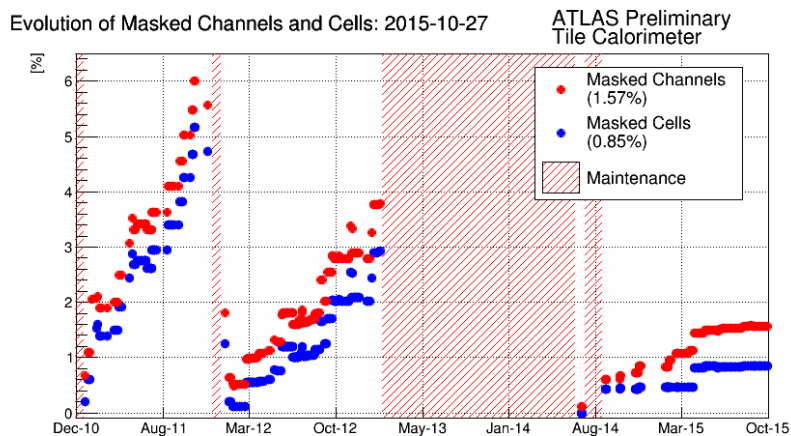


Figure 5.10. A timeline of masked cells in TileCal.

### 5.1.3 Demonstrator

An upgrade for the high-luminosity LHC (HL-LHC) is planned for  $\sim 2024$  and features a full replacement of the TileCal FEBs due to increased radiation, and vastly improved TDAQ and granularity [54]. The super-drawers will be replaced with four new mini-drawers, which feature point-to-point links rather than daisy-chains and can function independently. If there is a failure to one of the components of one mini-drawer, it does not prevent the operation of other mini-drawers downstream. This also eases serviceability, since maintenance teams can fully extract each mini-drawer in tighter spaces. The upgrade features data transfer at each bunch crossing and a continuous digitization. The data is transferred in a redundant bi-gain mode using separate transmitters with pipelines and buffers moved to the BE network. A block diagram of the upgraded FEB design is shown in Figure 5.11 [55,56]. To interface with the current system, a hybrid Demonstrator is being used to test the capabilities of the upgraded system. The block diagram for this design is shown in Figure 5.12.

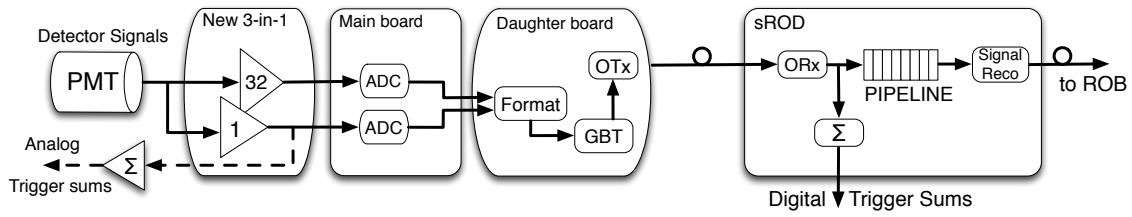


Figure 5.11. A diagram of the upgraded FEBS of TileCal.

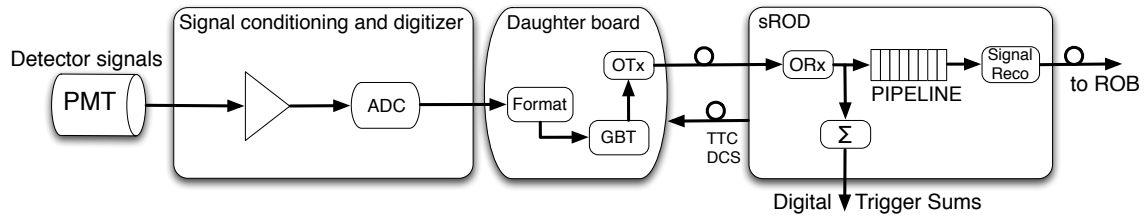


Figure 5.12. A diagram of the hybrid FEBS of the upgrade Demonstrator.

#### 5.1.4 *Prometeo*

With the upgrades to TileCal, an upgrade to MobiDick has also been under development [57–63]. The upgrade features a Xilinx VC707 board with a Virtex-7 FPGA. A block diagram of Prometeo is shown in Figure 5.13.

The software has been completely restarted from scratch and the firmware supports cross-platform compilation. Prometeo communicates through ethernet via a Very High Speed Integrated Circuit (VHSIC) module with an internet protocol bus implementation written in VHSIC hardware description language (VHDL). The client connects via user datagram protocol (UDP). Data from the mini-drawers can be collected by a C++ interface and stored in a location where an automatic analysis package written in Python can find it and process the information. Once histograms are populated, fit, evaluated, and

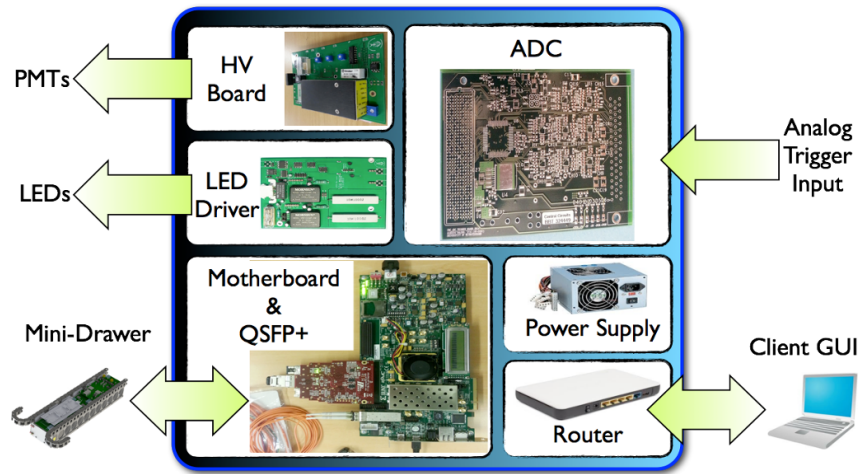


Figure 5.13. A block diagram of the Prometeo test-bench.

summarized, the results are available in graphical presentation from a webpage by any computer or mobile device with internet access and permissions.

Software tests have been categorized by components of the FEBs, which are Bias, CIS, Integ, and HV. Tests can be applied to determine linear response or the noise and stability. Control over the number of events taken allows for more statistics as well as long-term stress testing. Therefore, the basis of these tests is a 2-dimensional plot of the value of interest versus the event number (i.e. time). These 2D plots can be projected to determine a spread of events or profiled to measure the stability over time. Figure 5.14 shows the distribution for the BiasNoise test for PMT 10 high-gain results on the left and the projection fitted with a Gaussian on the right. Linearity tests would be evaluated against a linear fit from a profile plot.

The noise plot, once fitted to a Gaussian, can be used to evaluate the performance of each channel and gain (Figure 5.15). The mean values ensure that the pedestal bias does not drift over time, and the error bars are scaled to the difference between the total mean and the Gaussian mean. The  $\sigma$  value is likewise related to the RMS of the distribution and determines the resolution that can be achieved as well as determine any non-Gaussian tail

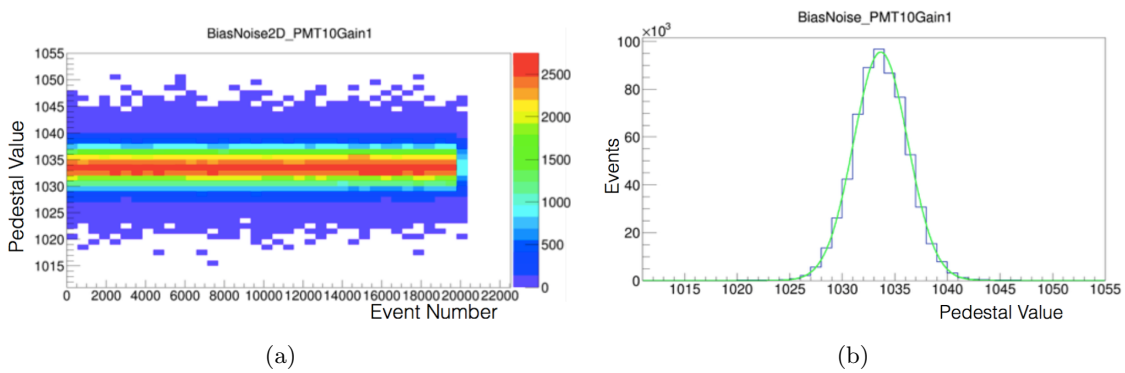


Figure 5.14. Distributions of BiasNoise for PMT 10 and high-gain presented as (a) a 2D plot versus event number and (b) the 1D projection.

events. The normalization should be constant since all channels have the same number of events, but failure to converge to a good fit can be identified from this parameter.

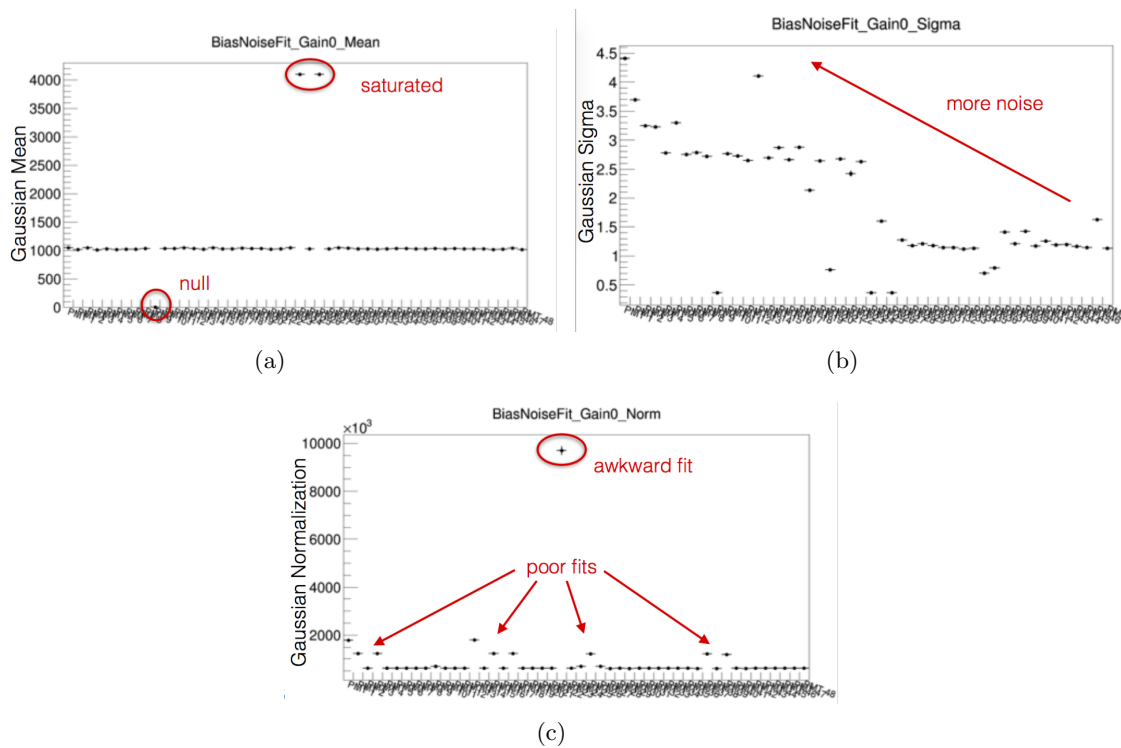


Figure 5.15. A full 48-channel summary of the Gaussian fit parameters for BiasNoise for low-gain.

Additionally, the noise can be separated into high-frequency and low-frequency because 128 samples can be taken per event. High-frequency noise is associated with the RMS of each event, while low-frequency RMS can be either the RMS of a single sample or the RMS compared to the global average. These two measures can be combined to form a frequency correlation to determine if noise is being dominated by a low-frequency effect in stress tests.

Correlations can also be extended to the integrator. In Figure 5.16, the noise of the integrator on the left shows faulty timing that leads to one sample measurement heavily influencing another. On the right, the time trend reveals that integrator data was taken without considering the time constants of the circuits.

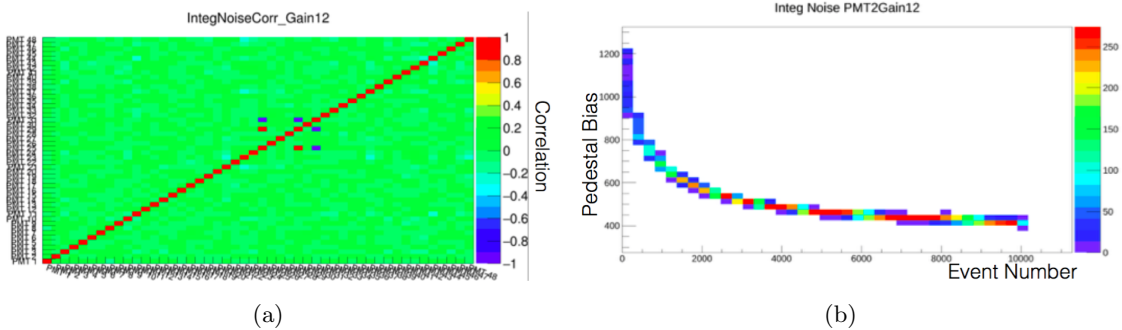


Figure 5.16. Plots of (a) the correlation of values for gain configuration 12 and (b) an unstable integrator response for PMT 2 and gain configuration 12.

The CIS pulse tests were adjusted to reflect several requested features. The parameters for pulse height, width, phase, and pedestal are defined in Figure 5.17. The pulse shape is defined by an array of values from a phase-shifted and averaged pulse shape from calibration. This shape is updated from the one used in MobiDick tests by using the parameters as a basis for the return values of the fit. Interpolation between these discrete values has been added to smooth the distribution significantly and create better fits. Negative pulse heights are now allowed, although they always represent an error state that has been

observed. Individual events are fit to the pulse shape using an array of sample values, which also allows noise and stability tests for the individual parameters,

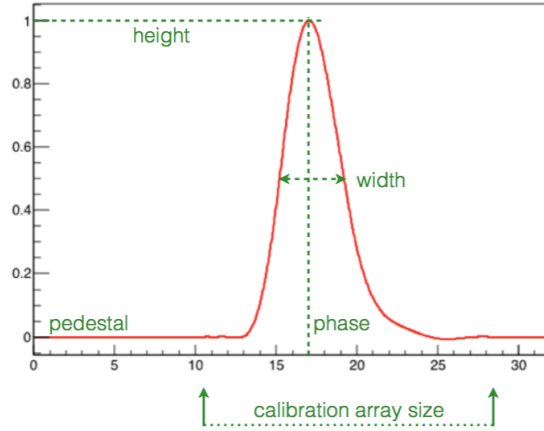


Figure 5.17. The definition of parameters used in the pulse shape fit.

## 5.2 Event Triggers

Collisions occur in ATLAS at about 40 MHz, but  $\sim 150$  million readout channels means about 1.8 MB is needed per event. This data rate ( $\sim 70$  TB/s) far exceeds any affordable design for a data server with proper cables, power, and cooling. The data servers, housed in rooms on multiple levels adjacent to the detector, need a way to reduce that rate to about 2 GB/s. Most of the excess is BG events (especially QCD) because the cross-section for new physics is very small. The rate is reduced through the use of “triggers” that establish minimum requirements that an event must meet or exceed. When a trigger “fires”, the event is recorded at a measurable rate. Multiple triggers have to share the target data rate because the event is recorded if *any* of the triggers fire. Raw events for closer inspection are selected by level 1 (L1) triggers and high-level triggers (HLT) analyze the event to ultimately decide if the event is “interesting” enough to keep. The L1 triggers approximate the reconstruction of objects in an event, which are further discussed in Section (6.2).

Because the proton-proton collision is a strong production, events are abundant in QCD BGs due to the large cross-section. A significant motivation of triggers is to reduce this background in particular. A lepton requirement can significantly reduce the QCD BG and analyses that depend on lepton signatures can often trigger on the presence of one lepton. Hadronic jet triggers are more difficult because events are swamped with jets and have to rely on the nature of these jets.

### 5.2.1 *Level 1*

The event triggers begin with the L1 system, which uses custom hardware that takes coarse information from the calorimeters and trigger chambers in the MS to reduce the event rate to  $\sim 100$  kHz. An upgrade to use FPGA hardware for topological calculations was planned during LS1, but this feature has not completed its commissioning. The L1 trigger reads the analog trigger sums from the FEBs to decide if the event is worth further investigation.

L1 triggers look for visible objects that have high  $p_T$  muons, electrons, jets, and taus decaying hadronically, as well as events with large  $E_T$  or  $E_T^{\text{miss}}$ . For muons, it collects information from RPCs and TGCs in the MS. The calorimetry is used for clusters involving electrons, jets, and taus. This also allows a very coarse measure of  $E_T$  and  $E_T^{\text{miss}}$  to be performed. The L1 trigger identifies certain features and tags regions of interest (ROI) for subsequent trigger algorithms to process.

### 5.2.2 *Common Time*

A global view of an event is needed that unites all parts of the detector and synchronizes the timing, so that the trigger acceptance can be returned to the FEBs within  $2.5 \mu\text{s}$  after the bunch crossing or the event will be lost to the rewritable buffers. Each part of the detector needs to operate on a common clock, and the alignment of electrical cables must be controlled to allow for the time delay associated with the traversing signal. TTC cables from the BE network are attached to the FEBs to provide each component with

the central LHC clock and can communicate with the FEBs to send buffered data via fast optical connection when requested by the L1 triggers.

The central trigger processor (CTP) processes the L1 muon and calorimeter triggers. It runs through a look-up table with various trigger requirements as a checklist. Each L1 trigger appears as a collective item that contains the event conditions, a mask, a priority (in case processing time is exceeded), and a prescale factor (Section 5.4). When an event passes a logical OR of all trigger items, a level 1 acceptance (L1A) is broadcast to the FEBs to request transmission of an event associated with a particular time. The data is then collected into the servers for further processing. The L1 trigger informs the subsequent algorithms about which triggers were passed and specific features or ROIs that were identified.

### *5.2.3 High-Level Trigger*

In Run I, the trigger decisions occurred at three levels: L1, level 2 (L2), and event filter (EF). In this original system, L1 merely identified ROIs at a coarse level while L2 took these ROIs and passed over them with additional algorithms and selection criteria before deciding whether to keep them. The EF system was a level where the most event-like selections could be made. This system was used simply because the status of electronics during design phase was not adequate to sift through events as quickly as necessary, and L2 allowed the breathing room to keep up with demand. CMS had only L1 and a high-level trigger (HLT = L2+EF) during Run I because the collaboration anticipated the improvement in BE network and data server technology in its design before it was actually available. By the time the detector was operational, the technology had advanced. During LS1, ATLAS upgraded its system and dropped L2 to join CMS in having only the L1 and HLT systems with new FPGA hardware.

HLT further refines the L1 trigger information to reduce the rate down to  $\sim 1$  kHz. The HLT uses the full precision and granularity of the detector and algorithms that closely resemble offline analysis selections. The improved measurements on energy deposition help with thresholds while the inclusion of tracks helps with particle identification. The L1 seed



informs the HLT about feature extraction (FEX), which identifies objects such as clusters, and hypothesis (HYPO) algorithms such as a  $p_T$ . If a trigger identifies an event with a value higher than the minimum requirement, the event is above “threshold” and is kept. L1 starts a trigger chain and several HLT triggers can inherit from it. FEX and HYPO are cached so that all HLT triggers in the chain have access to common information that leads to a reduction in transfer requests and processing time.

#### 5.2.4 Trigger Nomenclature

Triggers are named after the level of the trigger, the object(s) needed, and other selection requirements. The objects can be recognized from the trigger name following Table 5.1. The leading term in the name refers to the level of the trigger, and any objects and algorithms follow this indicator.

Table 5.1. The representation of objects in the standardized naming of triggers

signature	L1	HLT
electron	EM	e
photon	–	g
muon	MU	mu
jet	J	j
forward jet	FJ	fj
tau	TAU	tau
$E_T^{\text{miss}}$	XE	xe
$H_T$	HT	ht
$\Sigma E_T$	TE	te
jet energy	JE	je
$b$ -jet	–	b
dijet mass	M	m
$\Delta y$	DY	dy
$\Delta \eta$	DETA	deta
MBTS	MBTS	mbts

Single object triggers look for the presence of at least one object meeting a  $p_T$  threshold. A trigger such as HLT\_mu6 would require at least one muon in an event and the leading

muon  $p_T$  would have to be at least 6 GeV. Multiple objects of the same type can also be used in a trigger such as `HLT_2j100` or `HLT_j100j50`. If the objects are different, then it is referred to as a combined trigger, such as `HLT_j100_xe80`. Object definitions can also specify loose, medium, or tight selection requirements, such as `HLT_e10_medium`, to allow variations in the strictness of object definitions. Isolation from other objects can be specified to avoid triggering on fake objects, or objects that are anticipated to be removed by overlap (Section 7.3), e.g. `HLT_e20i_tight`. Reconstruction algorithms can also be specified as shown in Table 5.2 (further information can be found in Section 6.2). For physics studies, a primary trigger may be used, and supplementary or complementary triggers that benefit the analysis are called secondary triggers.

Table 5.2. The representation of algorithms in the standardized naming of triggers

term	reconstruction	algorithm	“jets”	$\Delta R$	scale
<code>a4TTem</code>	full-scan	anti- $k_t$	L1Calo towers	0.4	EM
<code>a10TTem</code>	full-scan	anti- $k_t$	L1Calo towers	1.0	EM
<code>c4ccem</code>	ROI	3-iteration	calo cells	0.4	EM
<code>c4cchad</code>	ROI	3-iteration	calo cells	0.4	EM+JES
<code>a4cchad</code>	partial-scan	anti- $k_t$	calo cells	0.4	EM+JES
<code>a2tcem</code>	full-scan	anti- $k_t$	topoclusters	0.2	EM
<code>a4tcem</code>	full-scan	anti- $k_t$	topoclusters	0.4	EM
<code>a4tchad</code>	full-scan	anti- $k_t$	topoclusters	0.4	EM+JES
<code>a4tclcw</code>	full-scan	anti- $k_t$	topoclusters	0.4	LCW
<code>a4tthad</code>	full-scan	anti- $k_t$	topotowers	0.4	EM+JES
<code>a10cem</code>	full-scan	anti- $k_t$	topoclusters	1.0	EM
<code>a10tclcw</code>	full-scan	anti- $k_t$	topotowers	1.0	LCW

### 5.3 Detector Status and Control

Information about the status and configuration of the detector is kept by the detector control system (DCS), such as high- and low-voltage settings, operating temperature, humidity, and cooling settings. This bi-directional communication allows the data to be collated with the health of the detector so that events can be rejected if they interact with

a part of the detector that exceeds its limits for good physics data. The settings for each part of the detector can be adjusted to keep everything within a healthy state, or deactivate modules that are in danger of failing.

Each data run is divided into one- or two-minute luminosity blocks (LB) to segment the data for quality inspection. An entire LB can be thrown out if something in the detector malfunctions without losing the whole run. This would be much more difficult to do if single events  $\mathcal{O}(25 \text{ ns})$  had to be inspected individually due to detector fluctuations that lasted  $\mathcal{O}(\mu\text{s})$ .

#### 5.4 Prescaling

During the lifetime of a run, luminosity and BG conditions may change and the rate of some triggers may drop as a result. This frees up some of the bandwidth for TDAQ and an optimal use of the system should have a way to keep the recording rate stable. One possibility for keeping data with loose requirements is through prescaling. If a process occurs at a rate of 100 Hz, then one in ten events could be kept to reduce this rate to 10 Hz, or one in a hundred events to reduce the rate to 1 Hz. Triggers that keep all events that they select are called unprescaled triggers. The *loosest* trigger that is unprescaled is called the *lowest* unprescaled trigger. Usually, a series of prescaled triggers vary by one parameter. For example, a series of single-jet triggers might have a leading jet  $p_T$  that varies as:

- 30 – 50 GeV in step sizes of 10 GeV,
- 100 – 200 GeV in step sizes of 50 GeV,
- and 300 – 500 GeV in step sizes of 100 GeV.

The lowest unprescaled trigger might be at 200 GeV to keep the TDAQ rate low. The triggers for 300 GeV, 400 GeV, and 500 GeV would be backup triggers in case the 200 GeV trigger rate is too high, and the lower triggers would all be prescaled.

Another idea that can be closely related to prescaling is trigger tagging. This is a common way to test the feasibility of new triggers. For instance, it may be that a special trigger needs to be tested, but it does not benefit from varying the parameters of another

trigger. However, there may be unrescaled triggers that overlap with this new trigger, and events that are kept for data are tagged as having passed or failed the new trigger. When the offline analysis is performed, a binary OR of these related triggers is used and then the performance of the new trigger can be studied using the trigger tag.

## 5.5 Trigger Efficiency

Triggers need to be efficient when selecting events for offline analyses. A low efficiency would mean that luminosity would be lost simply from a poor selection criteria that biases the inefficient events. The efficiency is calculated as the number of events selected by a tight trigger divided by the event count selected from a loose trigger. Events from the loose trigger may (or may not) appear in the tighter trigger, but all events in the tight trigger also pass the loose trigger (modulo very rare BE network failures). For L1 triggers, this is often a minimum bias trigger, which is the loosest unrescaled trigger such as special dedicated triggers for monitoring jet BG, or it can also be minimum bias enriched with random triggers to catch events with larger  $p_T$ . HLT triggers can often be compared to the L1 seeds to determine efficiency, since it is expected that the L1 triggers will become efficient before their HLT inheritors. Figure 5.18 shows what a trigger efficiency looks like for central jets at L1 and HLT for single-jet triggers.

The efficiency plot has two features to note: a turn-on and a plateau. The trigger is not perfect, and values very close to threshold are not always caught by the trigger due to dead time or mismeasurement after full reconstruction. The turn-on occurs when the tighter trigger improves at catching the events it is supposed to. The plateau occurs when the trigger is maximally efficient. The 99% efficiency level usually defines the point at which the trigger can be used to select data. If the plateau occurs at a lower level of efficiency, this factor has to be propagated to the cross-sections of any BG processes in the estimate. It is also possible to use events from the turn-on region for selecting events, which requires a good fit of the turn-on and a good understanding of the biases introduced by differing reconstruction efficiencies.

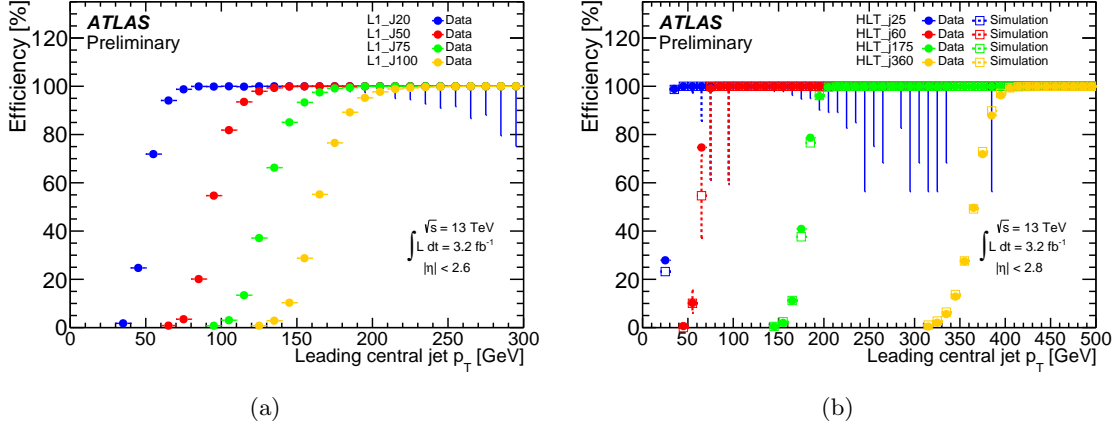


Figure 5.18. The trigger efficiency for single-jet triggers for (a) L1 with  $|\eta| < 2.6$  and (b) HLT with  $|\eta| < 2.8$ .

It is also notable to see that the uncertainty of L1\_J20 and HLT\_j25 increases with  $p_T$ . These are the lowest triggers thresholds and are required to be prescaled. L1\_J50 was anticipated to be prescaled, but it managed to stay unprescaled in 2015 with half the design luminosity. Otherwise, this trigger would most likely have the same behavior. HLT\_j60 (red on the right plot) appears to have a low plateau region threshold because it is fully efficient to its L1 seed, but this L1 trigger is not efficient until a slightly higher  $p_T$ . This is also why large errors appear in the middle of this particular efficiency plot.

Formally, the efficiency of two triggers –  $L$  (loose) and  $T$  (tight) – that are part of chain  $C$  can be calculated from boolean algebra (Appendix A.2) and a few approximations. The total trigger efficiency is:

$$P(C) = 1 - P(\bar{L})P(\bar{T}) \quad (5.1)$$

$P(T|L)$  can be counted, but the goal is to have a measurement of  $P(T)$ . Using a little probability theory:

$$\begin{aligned}
P(T) &= P(T \cap L) + P(T \cap \bar{L}) \\
&= P(T|L) \times P(L) + P(\bar{L} \cap T) \\
&= P(T|L) \times P(L) + P(\bar{L}|T)P(T) \\
&= \frac{P(T|L)}{1 - P(\bar{L}|T)}P(L)
\end{aligned} \tag{5.2}$$

Data can provide  $P(T|L)$  and  $P(\bar{L}|T)$ , but the absolute probability of  $P(L)$  needs to be estimated. If a jet in the event is triggered, the whole event is triggered. One of the triggered jets is randomly tagged and the event is probed against all jets to find the probability that a jet with a measured  $p_T$  would pass the trigger. The probability that at least one jet triggers the acceptance is:

$$P(J) = 1 - \prod_{recojets} \bar{P}_{jet}(p_T) \tag{5.3}$$

It may also be the case that an event can cause a trigger to fire from noise or a bug in reconstruction rather than from one of its jets.

$$\begin{aligned}
P(L) &= P(L \cap J) + P(L \cap \bar{J}) \\
&= P(L|J)P(J) + P(\bar{J} \cap L) \\
&= P(J) + P(\bar{J}|L)P(L) \\
&= \frac{P(J)}{1 - P(\bar{J}|L)}
\end{aligned} \tag{5.4}$$

The tag and probe method provides  $P(J)$ , and the other term can be estimated from data.

$$P(\bar{J}|L) = \frac{\text{triggered events without a triggered jet}}{\text{triggered events}} \tag{5.5}$$

## CHAPTER 6

### Simulation and Reconstruction

The type of events that the LHC can produce through strong production spans the gamut of the SM. Hadronic energy deposits are characteristic of the QCD interaction between the colliding protons, but they can also be obtained from secondary or tertiary interactions. EW interactions can result in leptons, photons, and more hadronic particles (including vector boson decays). BSM processes can also result in the full spectrum of particles. The detector itself returns data that is undifferentiated; for example, the cells cannot tell if an electron was sensed or a hadron. Because of this, the raw voltages of the detector do not imply an event came from a particular SM process or a BSM process. The objects that caused these voltages would have to be inferred using various reconstruction techniques. To understand these events, both data and a simulation of the SM phenomenology undergo the same reconstruction. A simulated chain connects the phenomenology to the raw voltages, which then get reconstructed into objects again.

#### 6.1 Monte Carlo

Monte Carlo (MC) estimation is a numerical method for estimating the integral of a distribution by taking random samples in a window around the curve and counting how many of them occupy the area under the curve. This method is used in HEP because there are a large number of variable measures representing a convolution of several complicated functions from experimental and phenomenological models. The error of other estimation techniques that attempt to form a fit around the distribution may scale with the number of dimensions, but the MC method does not.

### 6.1.1 Scatter Evolution

The simulation of a collision between two particles is a very challenging concept in a hadronic collider because its interaction with matter is essentially fractal. The precision scales with the depth of this calculation and it becomes intractable or even divergent unless it can be truncated. Figure 6.1 demonstrates a few of the processes that are involved in simulating the hadronic collision and strong decay.

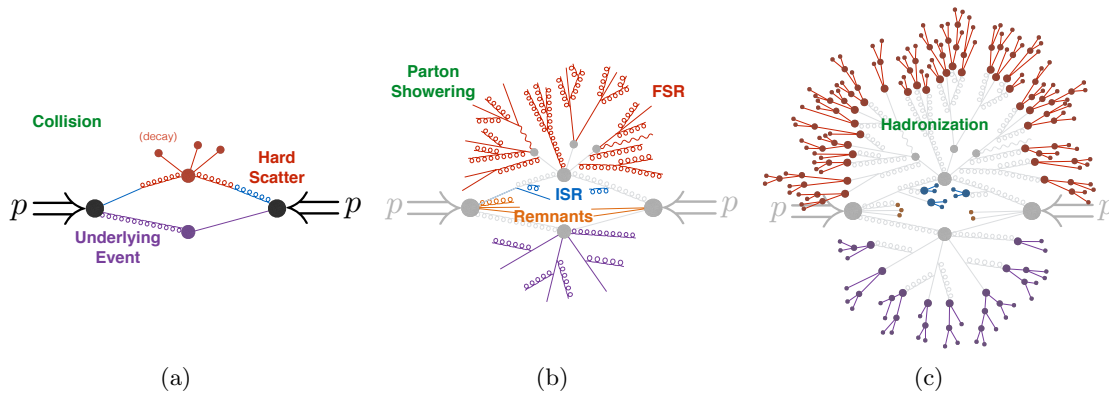


Figure 6.1. The evolution of a scatter from (a) collision to (b) parton showering and (c) hadronization. Red particles represent the evolution of a primary event, purple particles represent an underlying event, blue particles represent ISR, and orange particles represent beam remnants.

In the collision between the two protons, energy is shared among its quarks and gluons (“partons” as they are historically known). A parton distribution function (PDF) defines the probability density of a quark carrying a fraction of the total momentum. Two partons (one from each proton) may interact strongly with a momentum approximated by the PDF. If the exchange of momentum is very large, the feature is called a “hard scatter” or “primary vertex” (PV) that represents the primary collision of interest in the simulation. This scatter may also feature prompt decays or secondary vertices, and the calculations involve the matrix element of the phenomenon (including QED and EW). All of the other interactions (or non-interactions) between the remaining partons create a “glow” of energetic signatures that cloud this PV. The remaining partons from the two protons can also interact,



but with a lower momentum exchange (by classification) and the interaction represents an “underlying event” (UE).

At a factorization scale, the PDF can no longer accurately describe the interactions and the scatter proceeds with a perturbative QCD up to a renormalization scale to avoid divergences. The partons radiate into showers as the asymptotic behavior of the strong force allows the spontaneous creation of color particles. If the radiation happens before the hard scatter, it is called initial state radiation (ISR), while radiation after the hard scatter is called final state radiation (FSR). Remnant partons that did not participate in a scattering event can also be present and shower on their own. The UE also showers, and like remnant particles it also obscures some of the energy deposition from the PV.

Finally, the hard scatter and parton showering are academic notions, while the detector can only observe hadrons, which are also modeled by MC. The end of the scatter evolution is a hadronized mix of energy that gets deposited in the calorimeters. Through all of the little details, the final objects will be visible as electrons, photons, muons, and hadronic jets.

### 6.1.2 *Pileup*

Only two protons were considered in the collision in the development of the MC, but the LHC is tuned to provide many collisions simultaneously. The number of collisions per bunch crossing is called the in-time pileup (Figure 6.2). The average number of collisions per crossing is denoted as  $\langle\mu\rangle$ . These extra events present a challenge to the resolution of individual particles in the event. Considering muons that could possibly travel at velocity  $c$ , a muon created by a collision could travel about 7.5 m by the time the next crossing occurs. Noting the size of ATLAS, this means that the detector volume could easily contain three or four bunch crossings at any given time. This is called out-of-time pileup, and presents a challenge to the global timing of an event. In MC, the pileup (PU) is applied as a weighting factor to each event to scale the predictions to the number of collisions.

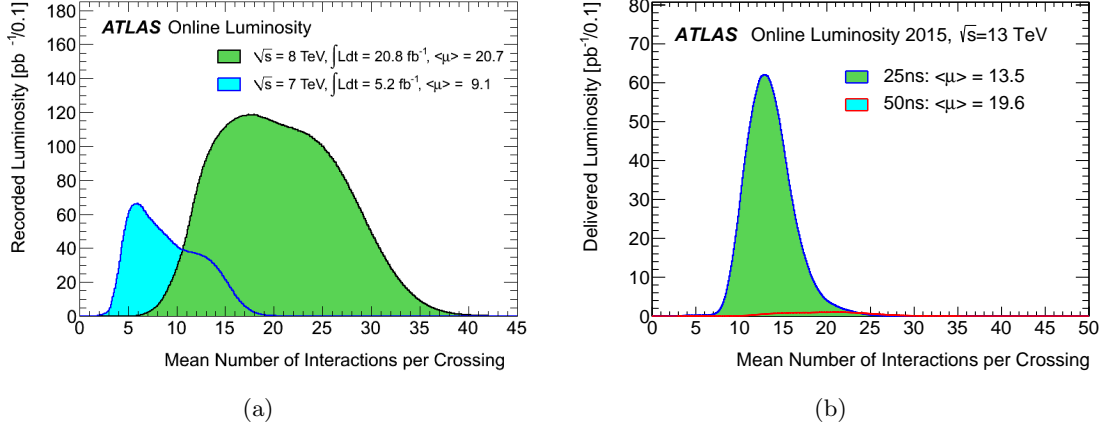


Figure 6.2. A distribution of the average number of interactions per bunch crossing for (a) 2011 and 2012 and (b) 2015.

### 6.1.3 Generators

For the PV, the matrix element can be calculated at leading order (LO; or tree-level), leading log (LL; tree-level plus corrections), next-to-leading order (NLO; loop diagrams), next-to-leading log (NLL; NLO plus corrections), and so on. Several generators are available to simulate the collisions, but there is not an overriding mandate for choosing one to model the events, although ATLAS performance groups put out recommendations based on validation data that are followed by the various working groups. More often than using a catch-all generator, one generator may provide input into another generator to account for the differing strengths of each one. Generators can also be compared side-by-side to estimate the systematic uncertainty (Section 7.4) on the predicted number of events.

For example, PYTHIA [64] may be used to provide a full event view including PV matrix elements, particle decays, UEs, parton showering, and hadronization, but only for  $2 \rightarrow 2$  processes. If more partons are desired, a generator such as MADGRAPH [65] can be interfaced to provide  $2 \rightarrow 5$  processes into the matrix element calculation. POWHEG [66] can be used to generate matrix elements that are then showered using PYTHIA. The same can be done for JIMMY [67] handing calculations over to HERWIG [68,69] that are scaled to NLO. MC@NLO [70] can be used to improve these calculations to NLO without the

need for scaling. ALPGEN [71] can be used as a specialist in calculating the matrix element for  $2 \rightarrow 6$  processes before passing the calculations to another generator for showering and hadronization. SHERPA [72] tries to do everything for up to  $2 \rightarrow 6$  processes, but only at LO, or up to  $2 \rightarrow 4$  processes at NLO.

#### 6.1.4 Detector Simulation

The view developed in the preceding sections still describe objects, which is a concept that is a step ahead of how the detector senses the presences of particles in this discussion. The simulation of the detector-level voltages induced by these particles is still necessary. The response is a specific characteristic of ATLAS and its sub-components, so a detailed modeling of the detector is used (GEANT4 [73]). This is a full simulation toolkit for modeling the passage of particles through matter. For some BSM samples, a quicker method is used that combines a generator with the calorimeter efficiency and response while simplifying tracking geometries. The fast simulation may be preferred due to frequent turnaround of data processing, but the two methods are often checked for consistency at least once to document the systematic effects and ensure that they are low. In either case, the data and MC are digitized into pulse shapes.

## 6.2 Reconstruction

Regardless of whether events represent real data or MC generation, the event processing converges at a point where the events are just a set of voltages for each channel within the detector. The reconstruction of objects from the pattern of hits and depositions is identical between the two. For MC, this is essentially walking an event back toward the phenomenological model that created it, and it is done this way to preserve the efficacy of analyzing real data in parallel.

There are hundreds of particles that could be produced by SM BG processes [1]. However, most of them have a very short lifetime ( $\tau$ ). Even if these particles traveled at the speed of light ( $c$ ), they would have to travel  $c\tau \gtrsim 500 \mu\text{m}$  in order to leave a

decent track inside a generic detector. In fact, there are only  $\sim 14$  particles that meet this criteria. ATLAS is designed to be sensitive to  $e^\pm$ ,  $\mu^\pm$ ,  $\gamma^0$ ,  $\pi^\pm$ ,  $K^\pm$ ,  $K^0$ ,  $p^\pm$ , and  $n^0$ . ATLAS may be able sense the other six particles ( $\Lambda^0$ ,  $\Sigma^\pm$ ,  $\Sigma^0$ ,  $\Xi^0$ ,  $\Xi^-$ , and  $\Omega^-$ ) but with diminished reliability and they are usually reconstructed from their decay products like all other particles.

### 6.2.1 Tracking

The ID measures the momentum of charged particles by reconstructing a continuous track from the discrete hits. The performance and recommendations of the tracking system are managed by the Inner Tracking Combined Performance Group [74]. First, clusters are built by finding hits in adjacent cells on a module, which are used to seed the tracks. Two or three points from the pixel detector are used to search for track candidates and building the likely helical trajectories that unite them. The trajectory can either be extrapolated or re-evaluated in the other layers of the ID. The candidate hits are evaluated by a quality rank to resolve the ambiguities and select the best score. The score is determined by the probability that the candidates are split or if they share hits, and includes a penalty for tracks with missing hits. Once the tracks are formed, they can be projected back into the beam pipe to locate the interaction vertex.

### 6.2.2 Electrons and Photons

The ID can reconstruct the path of electrons that may be deposited in the EM calorimeters, but photons may leave energy deposits without an associated track. The performance and recommendations for electrons and photons is managed by the EGamma Working Group [75]. EM clusters are reconstructed using a sliding window algorithm that selects cells with  $E_T > 2.5$  GeV in cluster sizes of  $3 \times 5$ ,  $3 \times 7$  (barrel), or  $5 \times 5$  (end-cap) in units of  $\eta \times \phi = 0.025 \times 0.025$  until the energy is maximized.

For electrons, the cluster energy is used to find an associated trajectory with the corresponding track  $p_T$ . Clusters are matched with tracks in the ID that are within  $\Delta R <$

0.005. For photons, the extrapolation is a straight line to find an interaction vertex. The object can be ambiguously reconstructed as both an electron and a photon that may be resolved after checking the consistency of hits in each layer of the ID.

The energy deposit formed by electrons tend to be very narrow when compared to hadronic jets. The definition of an electron can be tagged ( $el_{ID}$ ) as “loose”, “medium” or “tight” depending on the shower shape and track requirements. Defining a cone of  $\Delta R$  (Equation 6.1) around the electron is used to define an isolation term dependent on the fraction of energy in the cone ( $p_T^{cone\Delta R}/p_T$ ). Furthermore, the impact parameter (IP) is used to define a longitudinal distance between the electron and the PV along ( $|z_0 \sin \theta|$ ) and transverse ( $|d_0/\sigma_{d0}|$ ) to the beam.

$$\Delta R_{ij}^2 \equiv \Delta \phi_{ij}^2 + \Delta \eta_{ij}^2 \quad (6.1)$$

The quantities used to define electrons (with corresponding terms for photons) are as follows:

- identification:  $el_{ID}$
- momentum:  $p_T$
- pseudorapidity:  $|\eta|$
- isolation:  $p_T^{cone\Delta R}/p_T$
- PV:  $|z_0 \sin \theta|$
- IP:  $|d_0/\sigma_{d0}|$

### 6.2.3 Muons

Muons may leave traces of their presence in the detector at every level, but the tracking is the most relevant to identifying them. The performance and recommendations for muons is managed by the Muon Combined Performance Working Group [76]. The hits in the MS must be matched with tracks in the ID, but two classes arise depending on where one starts the search. The Statistical Combination (STACO) algorithm combines MDT tracks with their extrapolated counterparts in the ID, or kept if the track fit is good.

Segment-tagged muons take the opposite route, matching inner tracks with tracks in MDTs or CSCs. A muon can also have no associated central ID track and  $|\eta| > 2.5$ , representing a standalone muon that decayed in flight. Muons reconstruction with  $p_T \leq 5$  GeV are aided by identification in TileCal.

The quantities used to define muons are as follows:

- number of Pixel hits:  $N_{pix}$
- number of SCT hits:  $n_{SCT}$
- number of TRT hits:  $n_{TRT}$
- momentum:  $p_T$
- pseudorapidity:  $|\eta|$
- isolation (low- $p_T$ ):  $p_T^{cone\Delta R}$
- isolation (high- $p_T$ ):  $p_T^{cone\Delta R} / p_T$
- PV:  $|z_0 \sin \theta|$
- IP:  $|d_0 / \sigma_{d0}|$

#### 6.2.4 Jets

When a quark or a gluon hadronizes, it may leave a spray of particles in the calorimetry, which is collectively called a “jet”. The performance and recommendations for jets is managed by the Jet and Etmis Combined Performance Group [77]. Since the hadronic showers tend to be wider than electron showers, a technique needs to be developed in order to separate overlapping jets. Clusters of jets are seeded when a cell’s energy exceeds  $4\sigma$  noise levels. Contributions from  $3 \times 3 \times 3$  neighboring cells are summed with this cell. If a neighboring cell exceeds  $2\sigma$  noise level, then the adjacent contribution process is repeated. Topo-clusters represent all of these cells, plus one more single layer of cells. These are then used at the start of jet-finding algorithms.

One jet collection algorithm used often is the anti- $k_t$  algorithm. With a parameterized “jet size”  $D$ :

$$d_{ij} \equiv \min \left( \frac{1}{p_{Ti}^2}, \frac{1}{p_{Tj}^2} \right) \times \frac{\Delta R_{ij}^2}{D^2} \quad (6.2)$$

If  $d_{ij}$  is smaller than  $d_{iB}$  (with “B” for “beam”), then objects  $i$  and  $j$  are merged as if they were one jet with one four-momentum. The algorithm repeats iteratively until  $d_{ij} > d_{iB}$ , and the object is added to the list of FSR.

The quantities used to define jets are as follows:

- EM fraction ( $f_{EM}$ ): fraction of energy in the EM calorimeters
- sampling max fraction ( $f_{max}$ ): maximum energy fraction contained in a single calorimeter layer
- HEC fraction ( $f_{HEC}$ ): fraction of energy in the HEC
- LAr quality ( $LArQ$ ): fraction of energy associated with LAr cells with a large pulse shape quality factor ( $q > 4000$ )
- HEC quality ( $HECQ$ ): fraction of energy associated with HEC cells with a large pulse shape quality factor ( $q > 4000$ )
- negative energy ( $E_{neg}$ ): negative energy associated with a jet
- charge fraction ( $f_{ch}$ ): ratio of the  $\Sigma p_T^{track}$  of jets and the calibrated jet  $p_T$
- jet vertex fraction (JVF): fraction of  $\Sigma p_T^{track}$  which is carried by tracks with IPs that are consistent with the PV
- jet vertex tagger (JVT): a multivariate discriminant for determining hard-scatter events
- momentum:  $p_T$
- pseudorapidity:  $|\eta|$
- isolation (low- $p_T$ ):  $p_T^{cone\Delta R}$
- isolation (high- $p_T$ ):  $p_T^{cone\Delta R} / p_T$
- PV:  $|z_0 \sin \theta|$
- IP:  $|d_0 / \sigma_{d0}|$

For example, a `loose` jet cleaning may be defined as an `OR` of the following requirements:

- $(F_{HEC} > 0.5 \text{ AND } f_Q) \text{ OR } (|E_{neg}| > 60 \text{ GeV})$
- $f_{EM} > 0.95 \text{ AND } |f_Q| > 0.8 \text{ AND } |\eta| < 2.8$
- $f_{EM} < 0.05 \text{ AND } f_{ch} < 0.05 \text{ AND } |\eta| < 2.0$
- $f_{EM} < 0.05 \text{ AND } |\eta| \geq 2.0$
- $f_{max} > 0.99 \text{ AND } |\eta| < 2.0$

### 6.2.5 Flavor Tagging

The content of a jet may contain  $b$  quarks, often noticed by their proclivity for featuring a SV decay. The performance and recommendations for flavor tagging is managed by the Flavour Tagging Working Group [78]. The  $B$  hadron has a lifetime of  $\sim 5$  mm and features a SV that can be measured by its IP. Because the  $b$  quark is substantial in mass, the jets that recoil from it also tend to have a high  $p_T$ . A soft lepton tagger can be used for events with an electron/muon from a  $B/D$  hadron decay. Otherwise, log-likelihood estimates can determine if a jet contains  $b$  hadrons (e.g. IP3D, SV1, and JetFitter), or a neural network algorithm (e.g. MV1 and MV2c20) can be used to tag them event-by-event. The neural net uses a combination of the log-likelihood estimators to identify SVs from the ID and track IPs to determine if the jet fits criteria identified by a database of interactions with  $b$  hadrons. The flavor tag is associated with the algorithmic efficiency level for identifying  $b$  jets

### 6.2.6 Taus

Taus can decay leptonically by 35% or hadronically by 65% with a lifetime of  $87 \mu\text{m}$ . The performance and recommendations for taus is managed by the Tau Working Group [79]. Tau jets are much narrower than QCD jets. Their hadronic mode can decay through  $\pi^\pm$  or  $K^\pm$  often leaving 1 track but sometimes 3. If the decay mode goes through  $\pi^0$ , 0-2 tracks can be found. Tau jets are seeded by calo-jets using the anti- $k_t4$  algorithm with an associated track within  $\Delta R < 0.2$ . The taus are ultimately identified by a Boosted Decision Tree (BDT).



### 6.2.7 Missing Transverse Momentum

$E_T^{\text{miss}}$  is a negative vector sum of reconstructed leptons and photons that have been identified and calibrated, high- $p_T$  jets, and soft clusters and tracks. The performance and recommendations for taus is managed by the Jet and Etmis Combined Performance Group [77]. The algorithm used to determine  $E_T^{\text{miss}}$  at ATLAS includes all calibrated baseline electrons and muons in the calculation, as well as calibrated jets with  $p_T > 20$  GeV. Soft radiation not associated with reconstructed objects is taken into account via the cell-out term, which sums the contributions from standalone topological clusters. Because  $E_T^{\text{miss}}$  is sensitive to the reconstruction of all the other objects in the detector, it is smeared to approximate the effects of pileup and mismeasurement. Lepton objects entering the  $E_T^{\text{miss}}$  calculation do so prior to any smearing or scale factors have been applied.

## CHAPTER 7

### Offline Analysis

There are benefits to having an abundance of data that the LHC can provide to reduce statistical uncertainty. An analysis often comes down to finding a very small inflection point in the tail of a falling exponential distribution. The number of events in this region is usually small, so signal behavior can be lost just from a resolution effect promoting a larger number of BG events in the tail than the “true” value. Cuts (masking a range of values) in observables can be optimized to reject the number of BG events while signal events are (hopefully) left untouched. This is one way to tease out an excess related to signals, but the statistical analysis becomes harder when the relative uncertainty is high. Slight variations in the detector response could potentially wipe out any chance of finding an excess, and these systematic effects must be understood.

As a particle passes through the different subsystems of the ATLAS detector, information is collected about position, timing, momentum, and energy. The combination of all of these is used to identify and reconstruct the particles of the event. The TDAQ system and reconstruction yield a very loose definition to the identification of these particles that analysis groups may prefer to refine under their own control as needed. Analyses usually need two definitions of objects: a baseline definition and a signal definition. Baseline objects are the loosest definition that an analysis will use to discriminate objects. The other type are signal objects and inherit all selections used to define baseline objects plus some additional criteria. Baseline definitions are useful for object vetoes, where events are discarded if they contain an unwanted object. Tagging, where events are kept if an object is present, use signal definitions. A search for new physics will primarily use signal objects, although baseline events are useful in estimating BG contributions.

The data and MC samples produced and reconstructed in ATLAS hold a lot of information that is used by many different analyses. Ultimately, a single analysis may only need a small percentage of the information, but it would be inefficient for each analysis to maintain its own copies of the samples because they still occupy a lot of disk space. When a group of analyses agree to a minimum set of standards, a smaller derivation of the samples can be produced that is less burdensome on computing resources and the reduction can be managed centrally and regularly to ensure that a common source of samples is used between the groups. The reduction can “skim” the samples to keep events that pass certain triggers, “slim” the samples by requiring an event selection, and “thin” the samples by removing unused object containers. Offline analysis decisions, unlike online decisions, can be reverted by going back to the reconstructed samples or at an intermediate step of refinement.

## 7.1 Background Processes

There are two classifications of BG based on the challenges that they present to identifying the presence of a BSM signal. A reducible BG causes events that could be eliminated if the detector had a better ability to resolve the tracks and  $\phi \times \eta$  of the energy deposition. If the UE and ISR could be isolated from the PV or pileup events could be isolated from each other, this would be a tremendous help to the reconstruction and analysis of objects. On the other hand, an irreducible BG is an inescapable part of nature. The PV could be due to a SM process rather than BSM and fake the signature of leptons and hadrons predicted by BSM models. The number of BG events cannot be further reduced without affecting potential BSM events. This is how the Higgs production rate of one every 11 seconds can lead to just 5-40 Higgs events for an entire year depending on the final state particles or the classification efficiency.

The most prominent BG in a collision of hadrons is a soft QCD background with many hadronic jets. These interactions are very numerous, and triggers (Section 5.2) can be designed specifically to reject events that exhibit the behavior of the jet signatures of a QCD event. Even if there is a one in a billion chance for a QCD event to fire a dedicated

trigger, this is equivalent to keeping one thousand events in a trillion. The same trigger could reject signal models at a rate of one in a billion, but if there are only ten signal candidates that are produced, then the signal events are still being swamped by the QCD background.

This effect can often be mitigated by requiring a lepton in the event. Since the QCD events would not supply the leptons, only leptons that occur from fragmentation would be present. Requiring even a modest  $p_T$  for these electrons could eliminate a large percentage of QCD. Requiring three leptons would make the QCD contribution negligible. In that case, the BGs producing leptons would dominate the event production, such as the EW interaction involving the production of  $W$ ,  $Z$ , and dibosons. These BG events can be reduced by vetoing leptons instead at the cost of facing the QCD problem. These events can still present a hadronic signature in the form of  $W + jets$  and  $Z + jets$  at a BR of about 69%.

Events involving top quarks can present a sizable BG to both lepton tag and lepton veto analyses. The top quark lifetime is so short ( $\tau = 0.5 \times 10^{-24}$  s [1]) that it decays by weak interaction before it can hadronize almost as if it was a free quark, resulting in a  $W$  commonly accompanied by a  $b$  jet. The lepton tag or veto argument is the same as before, but the presence of a  $b$  jet suggests that a veto on  $b$  jets could reduce this BG.

More exotic BGs can also be produced, such as  $Wt$ , tribosons, and Higgs production that fill the data with a spectrum of both leptons and hadrons. These are also the signatures that are shown in Figure 3.6(b) for possible SUSY decays. Since the SUSY production occurs at small cross-sections, the goal of an offline analysis is to define a method of event reduction that reduces the number of BG events that are due to large cross-sections (Figure 7.1) while maximizing the visibility of BSM events.

## 7.2 Event Selection

ATLAS maintains a list of successful physics runs that pass preliminary data quality checks. This good runs list (GRL) allows analysts to select a common set of data from which

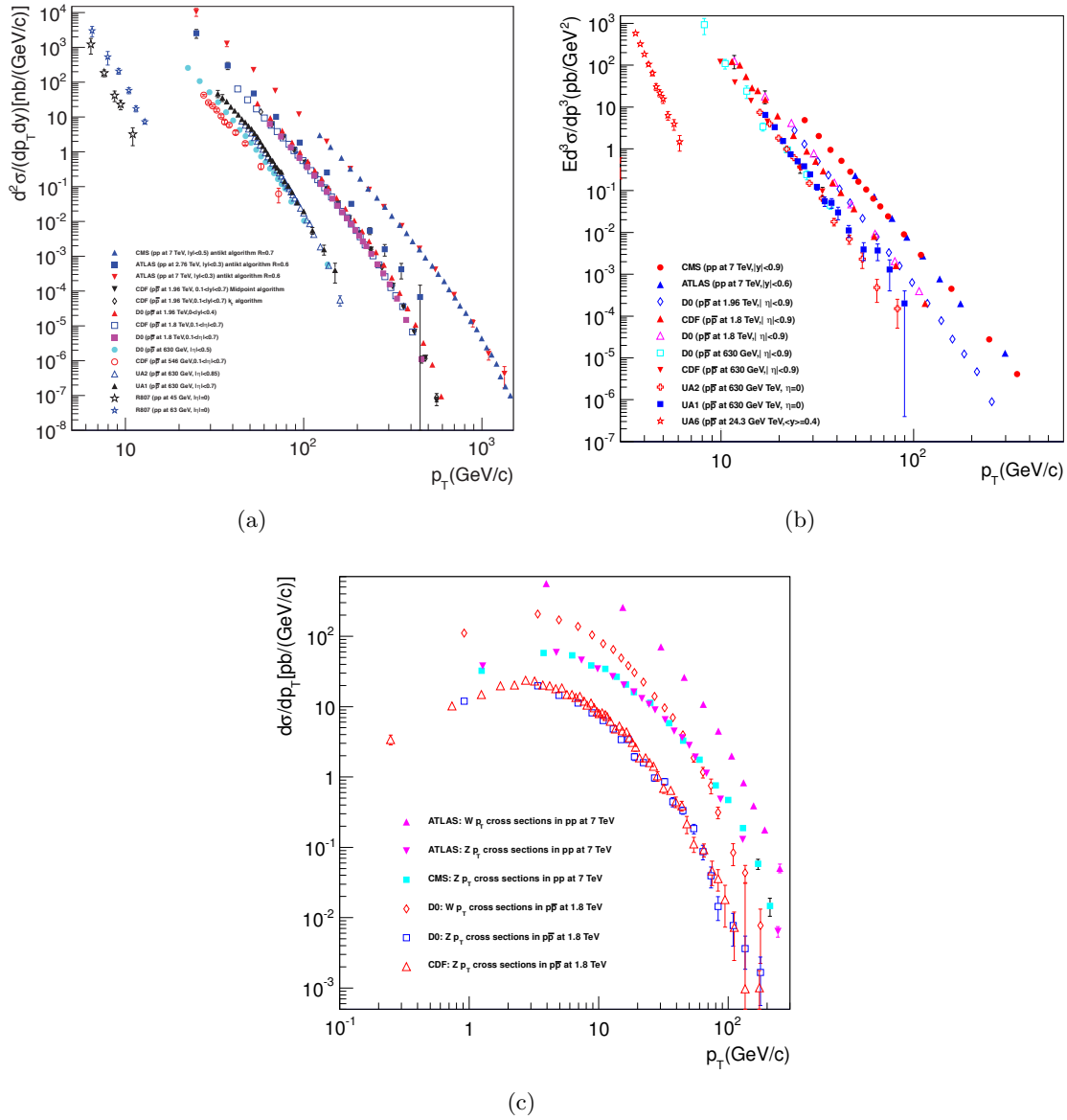


Figure 7.1. The production cross-section of (a) QCD multijets, (b) photons, and (c)  $W$  and  $Z$  BGs as estimated under various experimental production and detection conditions.

they can start with uniform quality standards. The GRL also specifies which LBs within the run are certified for quality. Sometimes good LBs or runs can be identified online, but the GRL also includes offline assessment that can be reviewed and updated later. The most updated lists are used for publication and LHC experiments usually freeze data selection during technical stops for major conferences.

SUSY analyses separate their search into channels that are associated with a particular topology by counting the number of jets, the number of heavy-flavor jets, the number of leptons, a combination of jets and leptons, a large  $E_T^{\text{miss}}$  or  $H_T$  (Equation 8.2), etc. Search channels can be further selected by requiring the decay of a top quark that leads to leptons and  $b$  jets,  $W^\pm$  to a single lepton,  $Z^0$  to two dilepton, a  $H^0$  to diphoton, etc.

Sometimes, it is necessary to remove an entire event. A few detector-level flags are used to ensure that the quality of data passes a uniform standard that can be applied offline to the whole data set. If an object's energy is reported by a hot or dead cell, the measurement of the energy deposition cannot be trusted. Rather than remove the object, the entire event is questionable, because it could affect downstream procedures such as overlap removal (Section 7.3) or  $E_T^{\text{miss}}$  calculation. The entire event is contaminated by this error, and so it is discarded.

Cosmic events are unrelated to the beam collision and are also rejected in BSM searches. Cosmic events can be recognized by muons that do not correlate to a PV in the beam pipe even though the ATLAS cavern is situated between 50 m and 92 m under molasse and limestone between Geneva and the Jura mountains. Despite having a hefty amount of dirt and rock shielding above it, ATLAS is still able to detect the cosmic showers of muons. In fact, cosmic studies only keep these events when the LHC is between runs or at a technical stop as an excellent source for calibration, momentum resolution, and muon reconstruction without a persistent high-energy collision BG.

### 7.3 Overlap Removal

The TDAQ system does not give preference to one object reconstruction over another but allows all object hypotheses from which individual analyses may sort through the ambiguities to their preferences. For this reason, a single object in data could be redundantly kept as a few different objects. It is therefore necessary to remove the extraneous objects from the reconstruction once the analysis group chooses the particle identity. However, the removal of objects is not the same as a removal of the entire event. The overlap between two

objects is usually defined by  $\Delta R$  with one object preferentially selected over another, which is discarded. The overlap removal process is sequential to avoid over-zealous removal of objects, and  $E_T^{\text{miss}}$  is usually recalculated after all objects have been resolved. The removal tests described below are fairly standard but some analyses aimed at performance may be different.

Since a photon can interact in the EM calorimeter, it is possible to misidentify a track in the ID with this energy deposit. If the energy and momentum of “electron” clusters are inconsistent with the tracks of the ID, then the “electron” is rejected in favor of the photon. A detector issue allows some “electrons” to be reconstructed that have a very small  $\Delta R$  to another “electron” object. If that is the case in an event, the “electron” with the lower  $E_T^{\text{cluster}}$  is discarded because it may be associated with the energy of the other electron.

When “electrons” and “jets” overlap, the value of  $\Delta R$  determines which object is discarded. If the “jet” and “electron” are very colinear ( $\Delta R < 0.2$ ), the energy deposit is likely due to EM leakage from the electron, and the “jet” is discarded. However, if the separation is a bit larger ( $0.2 < \Delta R < 0.4$ ), then the “electron” would be discarded. If  $\Delta R$  is large, then both objects are kept.

If a “muon” and a “jet” overlap ( $\Delta R < 0.2$ ), the “muon” is discarded. To avoid muon braking radiation resulting in a photon that is misidentified as an electron, whenever a “muon” is colinear to an “electron” ( $\Delta R < 0.1$ ), both objects are discarded.

## 7.4 Systematic Uncertainties

Raw signals from the detector must be calibrated to account for dead material that is not measured or compensated, particle leaks, sampling corrections, noise and other inefficiencies to reconstruction, and energy deposition outside of the reconstructed clusters. Varying the response of the detector or MC generation may alter the distributions of some vital observables that describe the event. Figure 7.2 demonstrates the major effects to a nominal distribution. The plot on the left shows a change in the statistical mean while the plot in the middle shows a change in uncertainty. These two effects may be coupled,

such as a change in resolution that reshapes the distribution producing a larger mean and a larger uncertainty. The plot on the right shows a normalization change, which represents a change in the number of events described by the distribution.

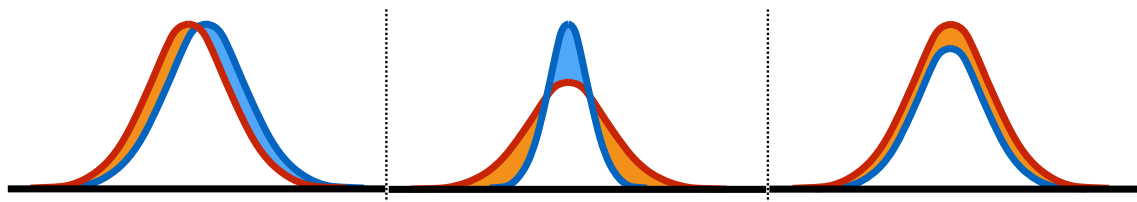


Figure 7.2. A diagram of the major effects of systematic variations on a distribution: (left) a change in mean, (middle) a change in uncertainty, and (right) a change in normalization.

The systematic alteration to a distribution shape can be quantified by considering the probability that the two distributions are samples of the same underlying process. In other words, a quantity is defined to determine how “identical” the two distributions are. For two histograms  $A$  and  $B$  each with  $n$  bins, the histograms are compared bin-by-bin to determine the log-likelihood:

$$\ln \lambda = \sum_i^n a_i \ln \left[ \frac{A(a_i + b_i)}{a_i(A + B)} \right] + b_i \ln \left[ \frac{B(a_i + b_i)}{b_i(A + B)} \right] \quad (7.1)$$

This is a simplification of an estimation technique elaborated in Section 7.9. The quantity evaluates the hypothesis that each bin contains the exact same fraction of the total number of events. This technique tests how likely a change is statistical rather than systematic. For this reason, normalization is treated under two different measures called relative change and relative difference:



$$RC = \frac{A - N}{|N|} \quad (7.2a)$$

$$RD = \left| \frac{A - B}{(A + B)/2} \right| \quad (7.2b)$$

The relative change measures the absolute difference between a distribution due to a systematic  $A$  and a distribution due to an “exact” nominal reference systematic  $N$ . If neither  $A$  or  $B$  are nominal distributions, the comparison may be better suited to a relative difference. Since even a nominal distribution is not truly “exact” either, the semantically “correct” measure should be the relative difference. However, the relative difference is bounded to  $0 \leq RD \leq 1$  and is scaled to an average of the two distributions. The relative change would be more prominent, but also indicate if the change is positive or negative.

There are many systematic uncertainties that can be attributed to the outcome of object reconstruction and algorithm efficiency in particular. The energy scale and energy resolution are discussed below because they are calorimeter effects that are applied in addition to the reconstruction.

#### 7.4.1 Energy Scale

The calorimeter energy deposits are used to reconstruct electrons, photons, and jets at the EM scale ( $p_{\text{T}}^{\text{EM}}$ ). If a jet is mostly electronic or photonic, much of the energy is deposited in the EM calorimeters and the electron energy scale (EES) is sufficient. If a jet is hadronic, then the particle shower can be degraded by its EM content and dead loss, which affects its calibration as it reaches the hadronic calorimeters. A restoration of the jet energy scale (JES) is recovered by MC corrections using one of a few algorithms.

The EM+JES calibration method parameterizes the jet  $p_{\text{T}}$  and  $\eta$  to apply a correction to EM-scale jets. The uncertainty is estimated from test beam results, track jets, dijet and photon+jet  $p_{\text{T}}$  balance, and MC comparisons. The Local Cluster Weighting (LCW) calibration applies a correction to clusters before jet finding and reconstruction occurs.

The corrections are determined by cell energy density in clusters, energy fraction in the calorimeter layers, cluster isolation, and cluster depth that are compared to a MC simulation of clusters due to pions. The jets are then reconstructed using the calibrated clusters. The Global Cell Weighting (GCW) calibration compensates for the effects of individual cells based on cell energy density and the calorimeter layer, including dead or faulty cells.

#### 7.4.2 Energy Resolution

The energy deposition in a perfect calorimeter would be a spike in voltage. The scale (magnitude) of the spike would be measured exactly and there would be no uncertainty in the measurement. In reality, the energy measurement smears a lot of the stochastic details of the particle shower into one voltage pulse. The “resolution” of the energy measurement is the amount of uncertainty introduced into the measurement of scale.

$$\frac{\sigma}{E} = \frac{S}{\sqrt{E}} \oplus \frac{N}{E} \oplus c \quad (7.3)$$

The  $\oplus$  operation indicates a quadratic sum of the individual sources of uncertainty [80]. The first term is a stochastic measurement that scales with the intrinsic fluctuations of the particle shower. Because the calorimeters in ATLAS are sampling calorimeters, the term is proportional to the thickness ( $t$ ) of the absorbing material.

$$\frac{S}{\sqrt{E}} \sim \sqrt{\frac{t}{E_0}} \quad (7.4)$$

The second term of Equation 7.3 is a noise term due to the electronics in the readout chain of the calorimeter. This term is lessened in scintillating calorimeters that use PMTs, while other attempts to reduce the electronic noise require signal shaping and filtering. The term will be small if the minimally-interacting particles (MIP) deposited more total energy in the active material than the absorbing material. The sampling fraction ( $f_{samp}$ ) would be large, which would mean the signal-to-noise ratio can also be high.

$$f_{samp} = \frac{E_{MIP}(active)}{E_{MIP}(active) + E_{MIP}(absorber)} \quad (7.5)$$

The third term in Equation 7.3 is a constant term that does not depend on the energy of the particle shower. Variations in detector geometry or readout can be easy to overcome while mechanical imperfections are much more difficult.

Measurements of the energy resolution of the calorimetry were performed with the SPS test-beam (Table 7.1). Electrons and pions were used at varying energies to measure the energy response and calibration of the calorimeters. The electron energy resolution (EER) and jet energy resolution (JER) use isolated objects to determine the nominal response to the energy deposit. The measured events are compared to this calibration to determine the sensitivity of the reconstruction to the presence of other objects in the data.

Table 7.1. The energy resolution,  $\sigma_E/E$ , of the ATLAS calorimeters

[81, 82]		
subdetector	energy term $[\sqrt{\text{GeV}}/\sqrt{E}]$	constant term
EMB	$(10.1 \pm 0.1)\%$	$(0.17 \pm 0.04)\%$
TileCal	$(52.7 \pm 0.9)\%$	$(5.7 \pm 0.2)\%$
EMEC	$(13.5 \pm 0.5)\%$	$(0.7 \pm 0.1)\%$
HEC	$(84.1 \pm 0.3)\%$	$(0.0 \pm 0.0)\%$
FCAL	$(29.3 \pm 0.7)\%$	$(3.0 \pm 0.1)\%$

The Global Sequential (GS) calibration builds on top of the EM+JES calibration to modify the resolution of jets according to the shower development. Track-Based Correction to the Jet Calibration (TBJC) assigns each jet to an ID track. The fidelity of the jet increases with the number of tracks associated to it because neutral particles tend to shower in the EM calorimeter while hadronic showers may have more charged content.

## 7.5 Jet Smearing

Despite how much effort goes into the production and validation of MC samples, they are still simulations or approximations of real empirical evidence. They are tested to ensure that they match data in regions that are well-modeled, but ultimately they are still going to be used in regions that are potentially dominated by new physics signals. It remains to be seen if these simulations are extendable for arbitrarily high values. For example, the fully hadronic description of QCD multijet events fails to accurately model events with high jet multiplicities. It certainly does not help that these events have the largest cross-section by far. Since this MC alone could be responsible for the excess due to standard statistical fluctuations, data-driven estimation methods are needed that do not rely so heavily on MC.

The jet smearing method [83] is used to select QCD events with  $E_T^{\text{miss}}$  due to jet mismeasurement and convolve their momenta according to a jet response function to provide a better prediction of the BGs in regions with large  $E_T^{\text{miss}}$  due to an invisible particle. The jet response function ( $JR$ ) quantifies the amount of fluctuation in a sample of jet  $p_T$ . It is implicitly assumed that jet mismeasurement can happen regardless of how many jets appear in the event.

$$JR = \frac{p_T^{\text{reco}}}{p_T^{\text{true}}} \quad (7.6)$$

The fluctuation is intended to describe jet mismeasurement and heavy flavor decays involving neutrinos. This function is used to scale low- $E_T^{\text{miss}}$  data events (consistent with multijet events) to get pseudo-data with large  $E_T^{\text{miss}}$ . The Gaussian component of  $JR$  can be calculated from dijet events or an event with one jet and a contralinear photon due to the steeply falling  $E_T^{\text{miss}}$  spectrum. By conservation of  $E_T$ , the fluctuation of the jet  $p_T$  can be reliably measured. The non-Gaussian tail of  $JR$  is measured from “Mercedes” events, where three jets are selected, but a relatively large  $E_T^{\text{miss}}$  is colinear with one of the jets (Figure 7.3).

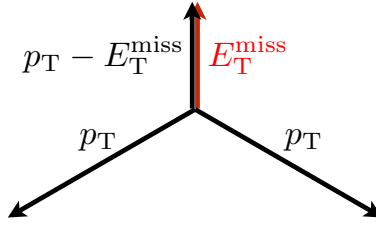


Figure 7.3. A diagram of “Mercedes” events where one of the jets is colinear with large  $E_T^{\text{miss}}$ .

This modifies the jet response function to be calculated from the reconstructed  $p_T$  of the jet associated with  $E_T^{\text{miss}}$ .

$$JR \simeq \frac{\vec{p}_{j,T} \cdot (\vec{p}_{j,T} + \vec{E}_T^{\text{miss}})}{|\vec{p}_{j,T} + \vec{E}_T^{\text{miss}}|^2} \quad (7.7)$$

The four-momenta of jets selected with low  $E_T^{\text{miss}}$  are smeared to generate pseudo-data that can have large  $E_T^{\text{miss}}$  and appear in the SR. This pseudo-data is used to generate  $\mathcal{O}(10\text{k})$  events or more for each real data event and must therefore be scaled to the correct luminosity for estimates of the QCD multijet BG. The unsmeared  $E_T^{\text{miss}}$  is corrected by the smeared jet  $p_T$ .

$$(\vec{E}_T^{\text{miss}})^{\text{smeared}} = (\vec{E}_T^{\text{miss}})^{\text{seed}} - \sum_i (\vec{p}_{ji,T})^{\text{smeared}} + \sum_i \vec{p}_{ji,T} \quad (7.8)$$

## 7.6 Variable Comparisons

A variable provides a distribution of a measurable (or a combination of measurables) from numerous events. Variables may be tied directly to the event (e.g.  $p_T$  of a visible jet) but they can also be derived as an inference from the event (e.g.  $E_T^{\text{miss}}$  due to invisible objects). Care must be taken to understand how combinations and inferences may be reliant on common descriptions of the event.

Covariance is a measure of how one variable fluctuates with another. Generic variables  $A$  and  $B$  have average values of  $\mu_A$  and  $\mu_B$  respectively. If  $A$  and  $B$  simultaneously fluctuate higher than the average, the covariance is positive. If they both fluctuate low, the covariance

is still positive. However, if one fluctuates high and the other fluctuates low, the covariance is negative. The covariance is calculated using the expected value for each point ( $E[X]$ ).

$$\text{cov}(A, B) = E[(A - \mu_A)(B - \mu_B)] \quad (7.9)$$

Covariance is sensitive to scale, meaning that the range of axes in the joint distribution can cause the covariance to have a large and unbound value. Two variables may demonstrate a similar scatter to two other variables, but the covariances may not reflect this similarity. For that reason, covariance is often scaled by the standard deviations of  $A$  and  $B$ . This correlation ( $\rho_{A,B}$ ) is preferred because its values are bound in  $-1 \leq \rho_{A,B} \leq 1$ . The covariance of Figure 7.4 is  $+0.334009$  and the correlation is  $+0.671253$ .

$$\rho_{A,B} = \frac{\text{cov}(A, B)}{\sigma_A \sigma_B} \quad (7.10)$$

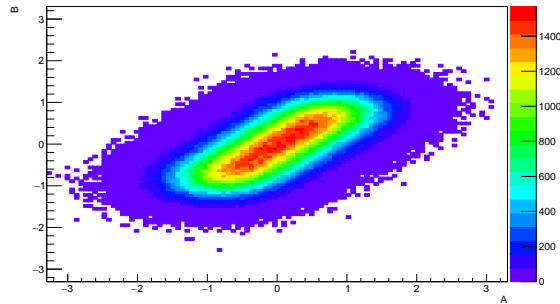


Figure 7.4. A scatter between generic variables  $A$  and  $B$  with 1 million points to illustrate covariance ( $+0.3$ ) and correlation ( $+67\%$ ).

Correlation is often used in HEP to describe the independence between two variables. If the correlation between variables is zero, the variables are thought to have very little affect on each other. For example, cuts can be applied to keep events with a high  $A$  value (such as  $B$  appearing at low  $A$  and BSM appearing at high  $A$ ), but the events lost from  $B$  may be uniformly spread from high to low (such as an undifferentiated mixture of background and

signal). However, the independence between two variables is often reported as the variables being “unrelated”, which may be a very misleading claim. Correlation just describes how well *value A* can predict *value B* (or vice versa).

To illustrate the difference between independence and *co*-relation, consider the scatter shown in Figure 7.5. The correlation between *A* and *B* is  $-0.00111085$ , which suggests that *A* and *B* are “unrelated”. This figure was drawn from a hypocycloid given by the equations (with  $r_1 = 3.8$  and  $r_2 = 1$ ):

$$\begin{aligned} A(\theta) &= (r_1 - r_2) \cos \theta + r_2 \cos \left( \frac{r_1 - r_2}{r_2} \theta \right) \\ B(\theta) &= (r_1 - r_2) \sin \theta - r_2 \sin \left( \frac{r_1 - r_2}{r_2} \theta \right) \end{aligned} \tag{7.11}$$

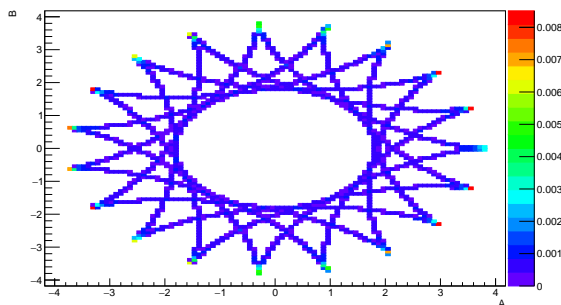


Figure 7.5. A hypocycloid ( $r_1 = 3.8$ ,  $r_2 = 1$ ) drawn with 1 million points to illustrate the difference between correlation ( $-0.1\%$ ) and mutual information ( $34\%$ ).

While it is true that *A* and *B* are independent solutions of a differential equation, the situation seems inconsistent with the claim that they are “unrelated”. The combined solution describes one circle ( $r_1 = 3.8$ ) rotating within another circle ( $r_2 = 1$ ), in which case the two solutions share the two radii and constraints. *A* and *B* seem very related under this context.

An alternative is to approach the comparison between two variables in terms of information theory where each variable contains a description of the event. The event is a transmitter of a message, each variable is a channel of that message, and a distribution is a

receiver of messages. The channel can alter the message in transit, and the entropy ( $H$ ) is the average “confusion” of the information. If  $X$  is a variable, then the entropy is calculated from its probability mass function ( $p(X)$ ):

$$H(X) = E[-\log p(X)] \quad (7.12)$$

Formally, two variables are independent if the joint probability density function ( $p(a, b)$ ) and its marginal projections ( $\rho_A(a)$  and  $\rho_B(b)$ ) have the following relationship:

$$p(a, b) = p_A(a)p_B(b) \quad (7.13)$$

Mutual information is a measure of the information common to two variables, which are related if they channel redundant messages between the event and the distributions. Mutual information is calculated as the intersect of the entropies of  $A$  and  $B$ .

$$\begin{aligned} I(A; B) &= \sum_{b \in B} \sum_{a \in A} p(a, b) \log \left( \frac{p(a, b)}{p(a)p(b)} \right) \\ &= H(A) \cap H(B) \\ &= H(A) - H(A|B) \\ &= H(B) - H(B|A) \\ &= H(A) + H(B) - H(A, B) \\ &= H(A, B) - H(A|B) - H(B|A) \end{aligned} \quad (7.14)$$

This mutual information can be scaled by the marginal entropies of the two variables so that  $0 \leq MI \leq 1$ :

$$MI(A, B) = \frac{I(A; B)}{\sqrt{H(A)H(B)}} \quad (7.15)$$

Since it is more useful to scale this value rather than leaving it unbounded, “mutual information” will refer to  $MI(A, B)$  hereafter. Mutual information describes the common-



ality of *features* used to obtain the distribution of  $A$  and  $B$ . The mutual information of Figure 7.5 is 0.338745, which suggests that  $A$  and  $B$  are indeed related. For this specific example,  $MI$  is most sensitive to the periodicity of the hypocycloid.

## 7.7 Control, Validation, and Signal Regions

After the variables are chosen, the number of predicted signal events needs to be estimated. There are data-driven methods of estimation, but a quick estimation can be made using both data and MC. The MC describes each process but can often misrepresent the magnitude or even the shape of a distribution. The data represents actual events, but has no commentary on which process created the events. The analysis needs a data-driven correction to MC that can be used as an estimate. Regions are defined where events are dominated by BG and extrapolate the estimate into a region where signals may appear.

Regions that are dominated by a particular BG, or regions where signal contamination as shown by MC is negligible, are called control regions (CR). A scale factor ( $C$ ) is calculated to normalize the MC to the data in these regions. The regions that are dominated by signal events are called signal regions (SR). Intermediate regions, called validation regions (VR), are used to check the extrapolation between CRs and SRs in a region lightly contaminated by signal.

A variable is considered discriminant if the distribution separates types of events, such as BG events populating low values and signal events populate high values (or vice versa). The CR can be fit for BG events and the extrapolation of the fit can be continued into the SR to estimate the number of BG events that could contaminate the distribution. If there are two variables that are quite good at this separation, an ABCD cut-and-count method can also be used to estimate these events. In this method, the extrapolation is calculated by transfer factors between regions. This concept can be extended to cover several SRs or to handle binned regions, as demonstrated in Figure 7.6.

In the simplified example of Figure 7.7, the CR is taken to be in the bottom left corner, two VR regions are defined at the top left and bottom right corners, and the SR is

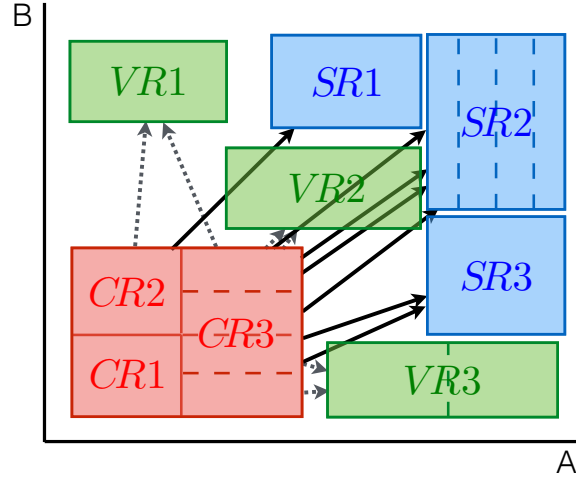


Figure 7.6. A diagram of generic CR extrapolation into VR and SR.

in the top right. The counts in each region are tabulated for both data and MC. Regions are indicated by their relative value of the variables that define them. A term such as  $D_{p_T}$  indicates a data region for low  $p_T$  and  $D^{p_T}$  indicates a region for high  $p_T$ .

$$\begin{aligned}
 n_{data}^{SR} &\approx n_{MC}^{VR,A} \times TMC_{VR,A}^{SR} \times C \\
 &= n_{MC}^{VR,A} \times TMC_{VR,A}^{SR} \times \frac{TD_{CR}^{VR,B}}{TMC_{CR}^{VR,B}} \\
 &= n_{MC}^{VR,A} \times \frac{MC_{VR,SR}}{MC_{VR,A}} \times \frac{D_{VR,B}/D_{CR}}{MC_{VR,B}/MC_{CR}}
 \end{aligned} \tag{7.16}$$

## 7.8 Event Complementarity

During the definition of regions, multiple signal models may be the target of a search and SRs can be optimized for particular points in phase space. Signal events may populate more than one SR, or one SR may be much more adept at keeping the events from a certain model than another SR. The “uniqueness” of a SR is a measure of how often an event lands in that one SR rather than the other. The overlap between SRs is a measure of how often an event lands in both. The two measures are scaled by the probability that an event lands in

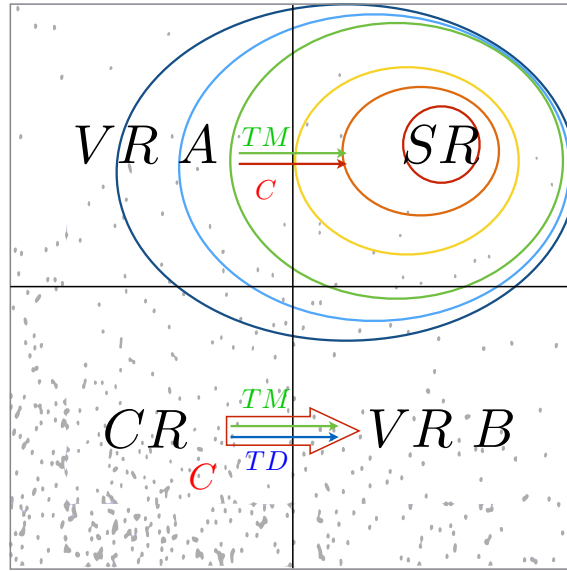


Figure 7.7. A diagram of the ABCD method. Transfer functions (TM or TD) are calculated to extrapolate the CR estimate into the SR.

either SR. A Venn diagram illustrates this difference in Figure 7.8. The relevant equations use notation described in Appendix A.2.

$$\text{unique}(A_B) = \frac{A - A \cap B}{A \cup B} \quad (7.17a)$$

$$\text{unique}(B_A) = \frac{B - A \cap B}{A \cup B} \quad (7.17b)$$

$$\text{overlap}(A, B) = \frac{A \cap B}{A \cup B} \quad (7.17c)$$

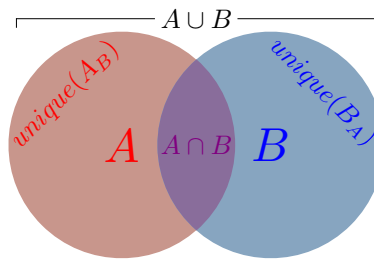


Figure 7.8. A diagram defining the complementarity between variables  $A$  and  $B$ .

## 7.9 Likelihood Function

When analyzing the statistics of a small number of events, statistical fluctuations of a nominal BG can appear in excess of the expected value. The analysis needs to estimate the number of signal events ( $S$ ) above an expected number of BG events ( $B$ ) if the number of observed events is  $n$ . The probability mass function of a discrete observable ( $x$ ) is taken to be a Poisson distribution. The MC shape of  $x$  is used to define probability density functions (PDF) for a relative mixture of  $f_S(x)$  and  $f_B(x)$ . The scale of the mixture is controlled by a parameter  $\mu$ . The BG-only hypothesis,  $\mu = 0$ , means that the statistical fluctuation of BG is entirely responsible for the number of observed events. If  $\mu = 1$ , then the full strength of the signal count is treated as responsible for the excess (signal+BG hypothesis). The parameter  $\mu$  can range between the two values (or exceed 1) to get the best estimate.

The marked Poisson model is calculated as:

$$\begin{aligned} \mathcal{P}(n|\mu) &= (\mu S + B)^n \frac{e^{-(\mu S + B)}}{n!} \left[ \prod_{i=1}^n \frac{\mu S f_S(x_i) + B f_B(x_i)}{\mu S + B} \right] \\ &= L(\mu) \end{aligned} \quad (7.18)$$

If the logarithm of this equation is taken, the new equation is called the extended maximum likelihood fit.

$$\begin{aligned} -\ln L(\mu) &= -n \ln(\mu S + B) + (\mu S + B) + \ln n! - \sum_{i=1}^n \ln \left[ \frac{\mu S f_S(x_i) + B f_B(x_i)}{\mu S + B} \right] \\ &= (\mu S + B) + \ln n! - \sum_{i=1}^n \ln[\mu S f_S(x_i) + B f_B(x_i)] \end{aligned} \quad (7.19)$$

The PDFs can be modified by parameters that shape and modify rates, as well as apply systematic variation as nuisance parameters ( $\lambda(\mu, \theta)$ ). If the distribution shape is given by histograms with a value  $\lambda_{b_i}(\mu, \theta)$  at bin  $b_i$  with a corresponding width  $\Delta_{b_i}$ , then the PDFs can be written as:

$$f_B(x_i) = \frac{\lambda_{bi}^B(\mu, \theta)}{B\Delta_{bi}} \quad (7.20a)$$

$$f_S(x_i) = \frac{\lambda_{bi}^S(\mu, \theta)}{S\Delta_{bi}} \quad (7.20b)$$

The histograms are normalized, so:

$$S = \sum_b \lambda_b^{sig}(\mu, \theta) \quad (7.21a)$$

$$B = \sum_b \lambda_b^{BG}(\mu, \theta) \quad (7.21b)$$

This defines the marked Poisson model that estimates the number of events as:

$$\mathcal{P}(n|\mu, \theta) = (\mu S + B)^n \frac{e^{-(\mu S + B)}}{n!} \left[ \prod_b \frac{\mu \lambda_b^{sig}(\mu, \theta) + \lambda_b^{BG}(\mu, \theta)}{\mu S + B} \right] \quad (7.22)$$

## 7.10 Exclusions and Discovery

The question that still remains is how an analysis can define a discovery or a lack of discovery, and what conclusions can be drawn from fluctuations and excesses. The null hypothesis is considered first, which in this case is called the BG-only hypothesis. The Poisson distribution of the number of events ( $n$ ) has a peak, but it also has tails where a large  $n$  compared to the average can still represent BG-only fluctuations. The confidence interval (CI) or confidence level (CL) defines a measure of how unlikely the occurrence of this situation is.

In Figure 7.9, the BG-only hypothesis is shown in red. The value of  $n$  becomes more discriminant, so the larger it is, the less compatible it would be to the hypothesis. If  $n$  events are observed (the dashed line on the right), then the integral of events above this limit represents the probability that events could fluctuate this high. In the figure, only 5% of events ( $p = 0.05$ ) could fluctuate if this number of events were observed. 95% of

BG-only events would result in less than  $n$  events ( $CL_B$ ). Since this also corresponds to the signal+BG distribution near the mean, this can be interpreted as a 95% confidence in discovery.

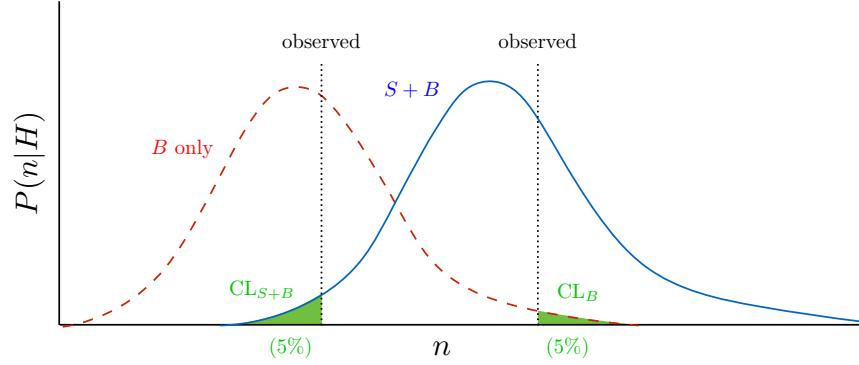


Figure 7.9. A demonstration of the 95% CL for the hypothesis tests of BG-only and signal+BG.

The observed line on the left of the figure illustrates  $CL_{S+B}$ . The shaded portion represents the number of events that are predicted by the signal+BG model. The chance that this model could fluctuate that low is only 5%. Seeing that the BG-only hypothesis peaks near this interval, this says that the signal model is excluded to 95% confidence. The  $p$ -value is an inverse of the confidence ( $1 - CL$ ) and is commonly represented in multiples of the standard deviation ( $m\sigma$ ) of a Gaussian distribution. The first five  $\sigma$  values are shown in Table 7.2.

$$\begin{aligned}
 p &\equiv 2 \int_{m\sigma+\mu}^{\infty} \frac{1}{\sigma\sqrt{2\pi}} e^{-\frac{(x-\mu)^2}{2\sigma^2}} dx \\
 &= \operatorname{erf}\left(\frac{m\sigma}{\sqrt{2}\sigma}\right) \\
 m &= \sqrt{2} \operatorname{erf}^{-1}(p)
 \end{aligned} \tag{7.23}$$

There is also a danger of a strong downward fluctuation in both the BG-only hypothesis and the signal+BG hypothesis (Figure 7.10). This can result in 95% confidence in the exclusion of the true count of  $S$ , and yet it also appears to be a discovery at 95% confidence.

Table 7.2. A table of  $p$ -values as a significance of fluctuation. The  $p$ -value is given in units of a Gaussian  $\sigma$  and the equivalent confidence level

$p$ -value	CL
$1\sigma$	68.2689%
$2\sigma$	95.4500%
$3\sigma$	99.7300%
$4\sigma$	99.9937%
$5\sigma$	99.9999%

This motivates using  $CL_S \equiv CL_{S+B}/CL_B$  (which is *not* a probability) to allow exclusion only if  $CL_S < 5\%$ .

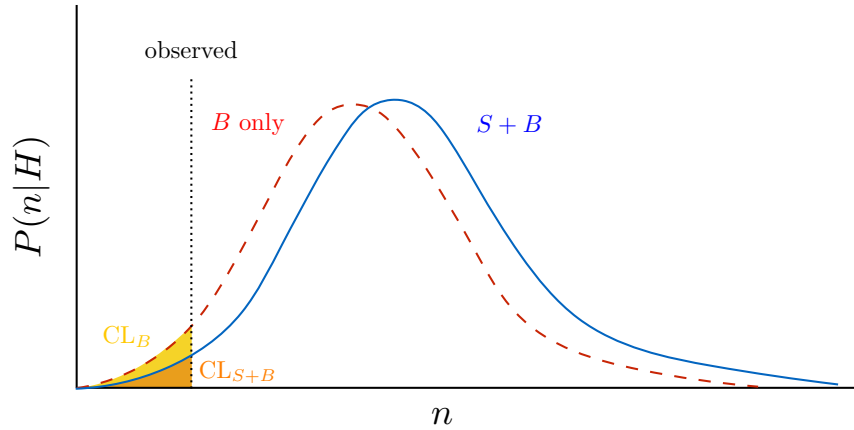


Figure 7.10. A demonstration of the 95% CL sensitivity issue.

There is always a way to find fluctuation by looking at inherently probabilistic event counts. Cutting down the number of events from  $\mathcal{O}(10^{15})$  triggered events to  $\mathcal{O}(10)$  events in a SR should cause some concern in that respect because an analysis may be biased just from the statistical fluctuations. Since hypotheses are tested multiple times, a  $p$ -value of  $1/n$  is likely occur after  $n$  tests (the “look-elsewhere” effect). This problem is dealt with by defining a threshold determined by the Likelihood ratio of signal+BG to BG-only hypotheses:

$$q(x) = \frac{L(S(x) + B)}{L(B)} \quad (7.24)$$

Figure 7.11 shows a fit of BG events on the top plot using one PDF for the BG and another for an excess. Since  $q$  is allowed to vary with some observable  $x$ , this test slides along the axis and evaluates the Likelihood at each step. The test statistic is shown in the bottom plot and shows that three excesses can be found above threshold in the top plot.

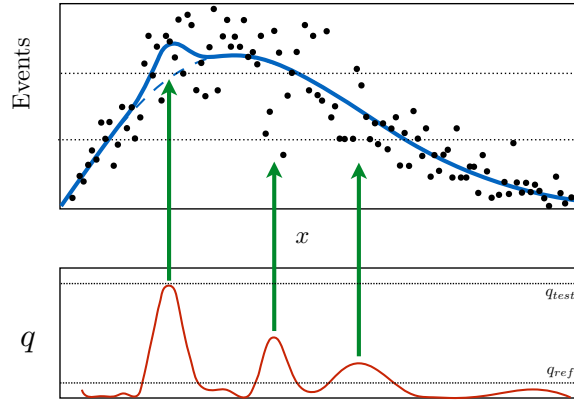


Figure 7.11. The look-elsewhere effect of data excess using a Likelihood ratio test statistic.

Using this plot, a global  $p$ -value is defined that describes all excesses:

$$p_0^{global} \simeq p_0^{local} + \langle n(q_{ref}) \rangle e^{-(q_{test} - q_{ref})/2} \quad (7.25)$$

The plot shown in Figure 7.11 demonstrates the fit of the most prominent excess, but it is not the only one. One may hastily claim to see three discoveries unless a threshold  $p$ -value is agreed on to prevent such bold practice. SUSY exclusions are optimized for  $2\sigma$  and SUSY discoveries are optimized for  $3\sigma$ . The Higgs boson search in 2012 had to meet a  $5\sigma$  criteria before the results were widely accepted [84, 85]. In simple terms,  $5\sigma$  is a “one-in-a-million” chance, while dealing a royal flush in 5-card poker is about 3 in 200k.



## 7.11 HistFitter

HistFitter [86] is a software framework that provides the statistical calculations used extensively in the ATLAS collaboration. It is the standard for statistical interpretation of SUSY searches in ATLAS and has also been used in exotics and Higgs searches. HistFitter can scale the normalization and transfer functions of a large number of samples independently. It enables analyses to include multiple signal and BG samples, parameterize systematic effects ( $\theta$ ), calculate statistical uncertainties bin-by-bin, combine multiple channels, and correlate all parameters of the final fit. Results for fitting, exclusion, and discovery can be displayed graphically.

## CHAPTER 8

### Global and Topological Variables

Many BSM models involve the creation of one or more heavy particles that the detector is unable to reconstruct. A large amount of momentum can “disappear” in ways that are associated with these invisible particles. However, this  $E_T^{\text{miss}}$  can become negligible if the invisible particles moves in offsetting directions, and  $E_T^{\text{miss}}$  can be faked by faulty measurement of the visible objects in the event. SUSY events involving invisible decay products would look like Figure 8.1, where  $j/\ell$  are visible and  $\chi$  is invisible. Event decays involving two invisible particles are highly under-constrained. The unknown  $m_{\tilde{\chi}_1^0}$  masses are common to all events, but there are eight unknowns from the four-momenta corresponding to each  $m_{\tilde{\chi}_1^0}$ . There are only six constraints on the system:

$$[p(j_1) + p(\tilde{\chi}_{11}^0)]^2 = [p(j_2) + p(\tilde{\chi}_{12}^0)]^2 = m_{\tilde{q}}^2 \quad (8.1a)$$

$$[p(\tilde{\chi}_{11}^0)]^2 = [p(\tilde{\chi}_{12}^0)]^2 = m_{\tilde{\chi}_1^0}^2 \quad (8.1b)$$

$$\vec{p}_T(\tilde{\chi}_{11}^0) + \vec{p}_T(\tilde{\chi}_{12}^0) = \vec{E}_T^{\text{miss}} \quad (8.1c)$$

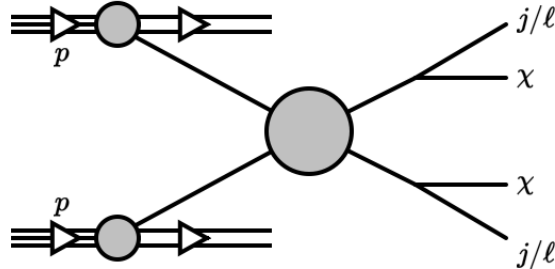


Figure 8.1. A diagram showing a signature involving pair production and subsequent decay to jets/leptons and invisible particles.

Therefore, four degrees of freedom need to be generated from the visible particles somehow to completely solve the kinematics of the event. Even if MC simulation masses can be chosen for  $m_{\tilde{q}}$  and  $m_{\tilde{\chi}_1^0}$ , there are still two more degrees of freedom in the system.

Several variables have been used to search for SUSY.  $H_T$  (Equation 8.2) has been a fairly common measure of the hadronic energy in an event for decades and  $M_{\text{eff}}$  (Equation 8.3) just adds  $E_T^{\text{miss}}$  to it. The adoption of transverse mass (Equation 8.5 [87]) coincided with a study of semi-leptonic events involved in the  $W$  and  $Z$  mass and the semi-invisible transverse mass (Equation 8.6 [88]) was a natural extension to it. A contranverse variable (Equation 8.14 [89]) were built on the idea of measuring events with pairs of invisible particles. Each of these variables is sensitive to the visible energy in the event. The distributions tend to feature a peak at a mass scale of the particles or a mass-splitting scale of the decay with a falling exponential tail.

A different class of variables were developed in parallel starting with the study of the energy shape of hadronic showers (Section 8.2 [90]). Just prior the the LHC operation, a ratio between energy scales was used to define  $\alpha_T$  (Equation 8.17 [91]) for dijet events. These variables describe the energy structure of the event. They are classification variables that attempt to distinguish QCD from BSM based on the fact that QCD events tend to be very isotropic and  $E_T^{\text{miss}}$  can come from jet mismeasurement.

The third class has mostly been untouched, which is the missing energy scale of the event – summarily encapsulated in just one variable –  $E_T^{\text{miss}}$ . Hybrid variables that combine these different variable classes have been ubiquitous. For example,  $E_T^{\text{miss}}/\sqrt{H_T}$  is commonly used in ATLAS SUSY as a measure of  $E_T^{\text{miss}}$  significance. Several variables corresponding to these classes are presented in sections below.

This document also includes research and development of the Razor and Super Razor reconstruction techniques (Section 8.5) and the Recursive Jigsaw reconstruction technique (Section 8.6) to design search strategies for SUSY searches. These techniques attempt to construct complementary variables that represent energy scale, missing energy scale, energy structure, and hybrid measures all in one design philosophy.

## 8.1 Energy Scale Variables

### 8.1.1 Hadronic Momentum

SUSY searches often place a lot of importance on  $E_T^{\text{miss}}$  because of the heavy and invisible particles an event would produce. In signatures with hard jets (especially for 0-lepton channels), the total hadronic transverse momentum is also quite important because visible jets recoil from  $E_T^{\text{miss}}$ :

$$H_T(n) \equiv \sum_{i=1}^n p_T(j_i) \quad (8.2)$$

The variable  $n$  can be equal to the total number of hadronic jets that pass selection criteria or it can also be limited to a desired number of jets. If a SUSY event had perfectly balanced visible jets, then  $E_T^{\text{miss}}$  would be zero. Conversely, if the jets were very unbalanced, the  $E_T^{\text{miss}}$  would be high. The measure presented in 0-lepton SUSY searches is often  $E_T^{\text{miss}} / \sqrt{H_T}$  to relate these two measures as a “significance” of the  $E_T^{\text{miss}}$  signature.

### 8.1.2 The Effective Mass

The effective mass is uses a definition of  $H_T$  that includes only the first four leading jets (to avoid soft radiation) in an event for calculation but all of the leptons and the  $E_T^{\text{miss}}$ .

$$M_{\text{eff}} \equiv H_T(4) + \sum_{k=1}^m p_T(\ell_k) + E_T^{\text{miss}} \quad (8.3)$$

This is an approximate representation of the energetic activity of an event. The effective mass distribution peaks at the mass of pair-produced (s)particles, providing a mass scale for the physics of the event. Other combinations of  $H_T$  and  $M_{\text{eff}}$  are also used in analyses to sharpen the definition of the mass scale. For example, the  $E_T^{\text{miss}} / M_{\text{eff}}$  ratio would provide a measure of how much of the energetic activity goes to the transverse sum of the two  $\tilde{\chi}_1^0$  in the event.

### 8.1.3 Dijet Invariant Mass

The remaining energy scale variables will take inspiration from the analysis of dijet events.

$$M_{jj}^2 \equiv m_{j_1}^2 + m_{j_2}^2 + 2[E_T(j_1) E_T(j_2) - \vec{p}_T(j_1) \cdot \vec{p}_T(j_2)] \quad (8.4)$$

### 8.1.4 Transverse Mass

Another variable that has been useful, particularly for BGs involving neutrinos, is the transverse mass. This replaces one of the jets in the dijet mass with an invisible particle ( $\chi$ ):

$$M_T^2 \equiv m_j^2 + m_{\tilde{\chi}_1^0}^2 + 2[E_T(j) E_T(\chi) - \vec{p}_T(j) \cdot \vec{p}_T(\chi)] \quad (8.5)$$

In most cases, this variable assumes that  $E_T^{\text{miss}}$  is from an invisible particle that has zero mass. This would be the case for a decay such as  $W \rightarrow e\nu$ , and the distribution would have a kinematic edge at  $M_T \leq m_W$ . Particles involving a massive  $\tilde{\chi}_1^0$  would have a distribution skewed toward large  $M_T$ .

### 8.1.5 Stransverse Mass

When there are *two* invisible particles in the event, then there are two transverse masses that can be calculated from separate decay chains. The two masses are calculated by minimizing the maximum  $M_T$  for all combinatorics of the split  $E_T^{\text{miss}}(1)$  and  $E_T^{\text{miss}}(2)$  that still sum up to  $E_T^{\text{miss}}$  total.

$$(M_{T2})^2 \equiv \max \{ M_T^2[\vec{p}_T(j_1), \vec{p}_T^{\text{miss}}(1)], M_T^2[\vec{p}_T(j_2), \vec{p}_T^{\text{miss}}(2)] \} \quad (8.6)$$

The minimization in the  $M_{T2}$  procedure preferentially decides which jet corresponds to one side of the decay tree to put a lower limit on SUSY pair production ( $M_{T2} \leq m_{\tilde{q}}$ ). A

distribution of  $M_{T2}$  is shown in Figure 8.2 and demonstrates how a SUSY signature appears quite distinguishable compared to QCD.

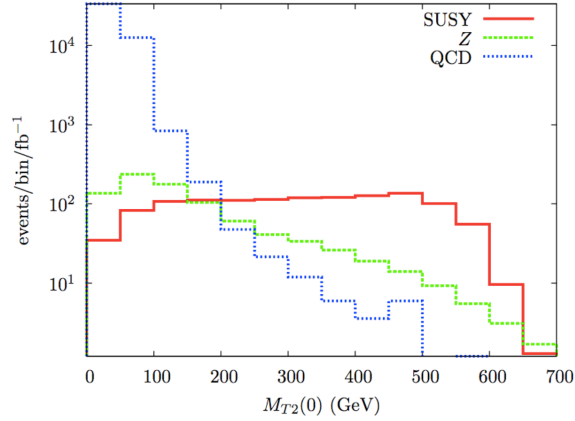


Figure 8.2. A distribution of  $M_{T2}$  for SUSY,  $Z$ , and QCD events.

## 8.2 Event Shape

The pair-production of heavy SUSY particles is expected to occur near threshold energy, meaning that the available energy goes into the creation of rest energy with very little to spare for the kinetic energy because of the large invisible masses. As a result, the events should have a mostly spherical event shape from the cascading decay, but only the visible jets recoiling from  $E_T^{\text{miss}}$  can be observed.

### 8.2.1 Delta Phi

If the azimuthal angle between a jet and  $E_T^{\text{miss}}$  is very small, then  $E_T^{\text{miss}}$  could be indicating the mismeasurement of a jet. High values of  $\Delta\phi(\vec{p}_T, \vec{E}_T^{\text{miss}})$  can indicate that the jet  $p_T$  is not mismeasured as  $E_T^{\text{miss}}$ , but maybe one of the other jets could be responsible for it. For that reason, more jets can be analyzed such as  $\Delta\phi(\vec{p}_T(j_1, j_2), \vec{E}_T^{\text{miss}})$ , where the two jets can be used to define a single cut or the cut can be applied to a minimum  $\Delta\phi$  from the two jets. In general, a large jet multiplicity can obscure this variable because an increase in

the number of jets increases the chance that a random jet can point in the same direction as  $E_T^{\text{miss}}$ .

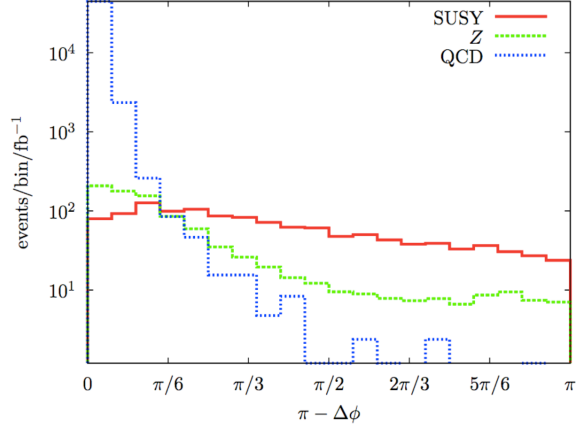


Figure 8.3. A distribution of  $\Delta\phi(\vec{p}_T, \vec{E}_T^{\text{miss}})$  for SUSY,  $Z$ , and QCD events.

A distribution of  $\Delta\phi(\vec{p}_T, \vec{E}_T^{\text{miss}})$  is shown in Figure 8.3 and demonstrates that QCD events tend to peak at low  $\Delta\phi(\vec{p}_T, \vec{E}_T^{\text{miss}})$  while SUSY signatures are flat.

### 8.2.2 Sphericity

A matrix of correlated jet momenta describes the hadronic shower shape of an event:

$$\mathcal{M} \equiv \sum_i \begin{pmatrix} p_{xi} \\ p_{yi} \\ p_{zi} \end{pmatrix} \begin{pmatrix} p_{xi} & p_{yi} & p_{zi} \end{pmatrix} \quad (8.7)$$

This matrix is used to describe the balance, or spherical nature, of the event. Its eigenvalues can be used to define the sphericity (Equation 8.8), the transverse sphericity (Equation 8.9), and aplanarity (Equation 8.10).

$$S \equiv \frac{3}{2}(\lambda_2 + \lambda_3) \quad (8.8)$$

$$S_T \equiv \frac{2\lambda_2}{\lambda_1 + \lambda_2} \quad (8.9)$$

$$A \equiv \frac{3}{2}\lambda_3 \quad (8.10)$$

A QCD dijet event (small  $E_T^{\text{miss}}$ ) is dominated by back-to-back jets and has  $S_T \sim 0$  while SUSY events (large  $E_T^{\text{miss}}$ ) have  $S_T \sim 1$ . SUSY events can be further discriminated by the aplanarity, which is a measure of the activity that lies outside of the plane defined by the two leading jets. Events with  $A \sim 0$  are planar while  $A \sim 1/2$  events are spherical.

Since the behavior of the third jet can characterize the shape of a dijet event, then its strength compared to the dijet defines another variable:

$$y_{23} \equiv \frac{p_T^2(j_3)}{H_T^2(2)} \quad (8.11)$$

This variable is limited to values  $0 \leq y_{23} < 1/4$  and may be presented as  $\ln y_{23}$ .

### 8.2.3 Jet Thrust

A “thrust” axis for the jets is defined as the normal axis ( $\hat{n}$ ) that minimizes  $H_T$  (Figure 8.4).

$$T_{\perp} \equiv \max \left( \frac{\sum_i \vec{p}_T(j_i) \cdot \hat{n}}{H_T} \right) \quad (8.12)$$

To keep the definitions consistent with values near zero for dijet events, the thrust is often presented as  $\tau_{\perp} \equiv 1 - T_{\perp}$ . The thrust axis and the beam axis define the event plane, and the total  $p_T$  out of this plane is given by the minor component of  $T_{\perp}$ .

$$T_{m,\perp} \equiv \frac{\sum_i |\vec{p}_T(j_i) \times \hat{n}|}{H_T} \quad (8.13)$$



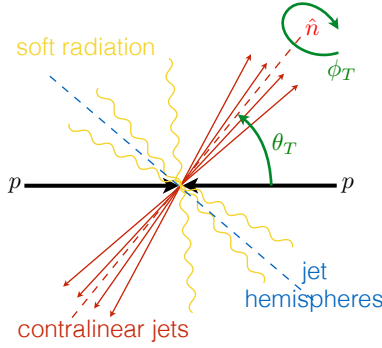


Figure 8.4. A diagrammatic representation of thrust variables.

### 8.3 Cotransverse and Contranverse Mass

If dijet events are contralinear (back-to-back), then they are subject to boosts that are equal and opposite. The quantity  $p_{j1} + p_{j2}$  is invariant under boosts if the particles are subjected to the same boost (colinear). If the particles are moved to contralinear frames, this quantity is not invariant and a method is needed to calculate such boosts. The invariant dijet (contranverse) mass is defined as:

$$\begin{aligned}
 M_{CT}^2 &\equiv [E_T(j_1) + E_T(j_2)]^2 - [\vec{p}_T(j_1) - \vec{p}_T(j_2)]^2 \\
 &= m_{j_1}^2 + m_{j_2}^2 + 2[E_T(j_1) E_T(j_2) + \vec{p}_T(j_1) \cdot \vec{p}_T(j_2)]
 \end{aligned}
 \tag{8.14}$$

If the two jets are massless, then this can be reduced even further:

$$\begin{aligned}
 \lim_{m_{j_1, j_2} \rightarrow 0} M_{CT}^2 &\sim 2 p_T(j_1) p_T(j_2) (1 + \cos \Delta\phi_{j_1, j_2}) \\
 &= (E_T^{\text{miss}})^2 - [p_T(j_1) - p_T(j_2)]^2
 \end{aligned}
 \tag{8.15}$$

The kinematic edge to  $M_{CT}$  is quite different from the mass scale of pair-produced  $\tilde{q}\tilde{q}$ . In fact, it is helpful to define a mass-splitting scale based on the distribution of this variable:

$$M_{CT} \leq \frac{m_{\tilde{q}}^2 - m_{\tilde{\chi}_1^0}^2}{m_{\tilde{q}}}
 \tag{8.16}$$

Unfortunately, if the mass difference between  $m_{\tilde{q}}$  and  $m_{\tilde{\chi}_1^0}$  is less than  $m_W$ , this variable is not as effective as a discriminating distribution.

#### 8.4 Alpha T

The previous variables are heavily influenced by  $E_T^{\text{miss}}$ , which is calculated once all objects are reconstructed from tracking, calorimetry, and MS. This makes them particularly sensitive to both beam conditions and detector performance. In a hadronic collider with high luminosity, MC may fail to precisely predict the kinematics and cross-sections of multijet events. By focusing on the energy and angles of visible objects, a variable can be defined to avoid jet mismeasurement.

$$\begin{aligned}
 \alpha_T &\equiv \frac{p_T(j_2)}{M_{jj}} \\
 &= \frac{1}{2} \frac{H_T - \Delta H_T}{\sqrt{H_T^2 - (E_T^{\text{miss}})^2}} \\
 &= \frac{1}{2} \frac{1 - (\Delta H_T / H_T)}{\sqrt{1 - (E_T^{\text{miss}} / H_T)^2}}
 \end{aligned} \tag{8.17}$$

For contralinear dijets, the distribution (Figure 8.5) peaks near  $\alpha_T = 0.5$  and an imbalance results in a lower value that can be used to isolate events with jet mismeasurement because  $E_T^{\text{miss}}$  is correlated with  $\Delta H_T$ . Unbounded quantities above this value come from events that are not contralinear but recoiling from large  $E_T^{\text{miss}}$ , and dijet event counts fall rapidly as the relative sensitivity to mismeasurement vanishes. For SUSY events, the dropoff is not as severe, and the correlation is less.

#### 8.5 Razor and Super-Razor

Four main ideas should be apparent now in defining the previous topological variables:

- Variables are constructed to exploit differences between SUSY signals and QCD BGs.
- If heavy, invisible particles are created, then the shape of the event can be tied to  $E_T^{\text{miss}}$ .

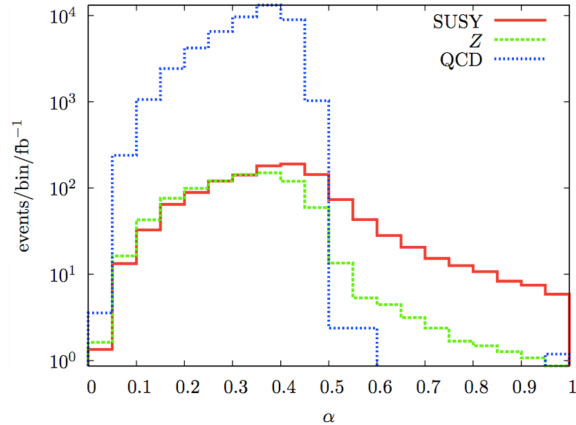


Figure 8.5. A distribution of  $\alpha_T$ .

- A mass scale or mass-splitting scale is used to estimate the sparticle masses.
- The lack of longitudinal information is a challenge for Lorentz invariance.

The second and third points seem to suggest that a variable such as  $T_{m,\perp}$  should be paired with  $M_{CT}$ , since  $T_{m,\perp}$  can be used to study the transverse shape of the event while  $M_{CT}$  can be used to estimate the masses involved. However, the variables are ultimately still calculated in an inclusive way and avoid the explicit inclusion of  $E_T^{\text{miss}}$  that appears anyway in correlations. Essentially, a cut to one variable would bias the distribution of the other, resulting in a loss of event acceptance.

Also note that  $\vec{E}_T^{\text{miss}}$  or  $\vec{p}_T^{\text{miss}}$  are only two-vectors and cannot provide longitudinal information. Therefore, calculations that do not correct for this are not Lorentz-invariant approaches. Because the events come from the collision of protons, the collision itself has a boost uncertainty, which is why transverse observables were chosen for measurement. The unaccounted boost affects the reconstruction of every level of the decay tree.

A search would benefit from variables constructed by complementary measures of both the event shape and the mass scale. The unknown degrees of freedom are resolved by algorithms that enforce boost invariance and mass minimization. By approximating the event in different frames, we aim to construct a variable from independent measures of mass and angles that are largely uncorrelated (or correlated in an easily-understood way).

Such a set of variables is the subject of the Razor and Super-Razor techniques described in Reference [92, 93].

The variables that have been defined so far take inspiration from how a QCD dijet event (with  $E_T^{\text{miss}}$  from jet mismeasurement) would be kinematically different from a SUSY event (with  $E_T^{\text{miss}}$  from invisible particles). The pair-production of  $\tilde{\ell}^\pm \tilde{\ell}^\mp \rightarrow \ell^\pm \ell^\mp \tilde{\chi}_1^0 \tilde{\chi}_1^0$  is often used to justify this construction because the leptons can be a relatively clean signature. However, the cross-section for dilepton pair-production is considerably lower than disquark or digluino for  $\sqrt{s} = 8$  TeV in hadronic collisions (Figure 8.6).

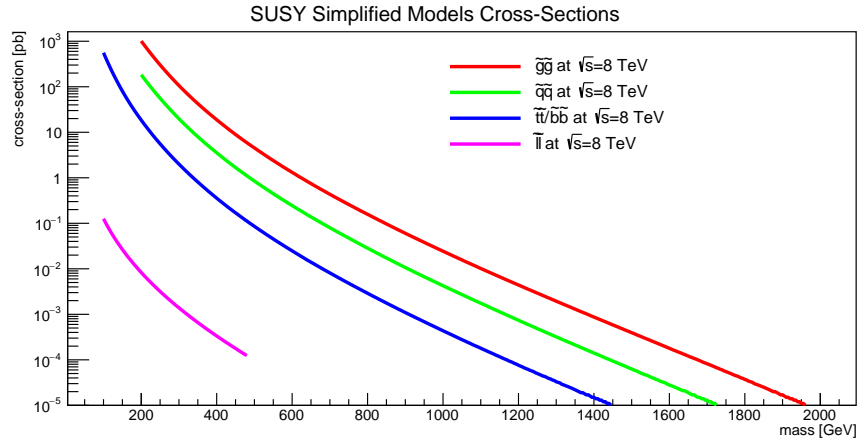


Figure 8.6. The cross-section for SUSY pair-production at  $\sqrt{s} = 8$  TeV. [94, 95]

Strong SUSY production would increase the number of QCD dijet events as well as increase the number of jets in most events, presenting a huge background of QCD multijet events. These events would not have to be contralinear or planar, and could easily contaminate any cuts designed to maximize SUSY events. Each jet could be subject to mismeasurement contributing to  $E_T^{\text{miss}}$ . Luckily, the cross-section for strong production increases by a substantial amount as  $\sqrt{s}$  is increased (Figure 8.7) for all masses of SUSY pair-production as dijet masses of equivalent size decrease (Figure 5.1).

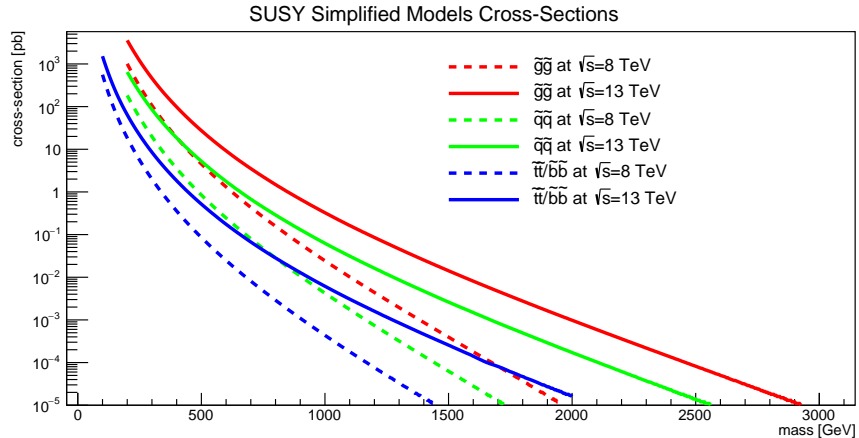


Figure 8.7. The cross-sections for SUSY production at  $\sqrt{s} = 8$  TeV (dashed lines) and  $\sqrt{s} = 13$  TeV (solid lines).

[94, 95]

### 8.5.1 Event Frames

There are four frames of interest in the direct two-body decay of a generic pair production  $PP \rightarrow V_a I_a V_b I_b$ :

- the laboratory frame of the detector from which measurements are made,
- the CM frame where  $PP$  production occurs at rest,
- and the two decay frames

$$\begin{aligned}
 & - P_a \rightarrow V_a I_a \\
 & - P_b \rightarrow V_b I_b
 \end{aligned}$$

The frames are related by boosts and Figure 8.8 identifies the  $R$  and  $R + 1$  frames that approximate them as well as introduce the notation of the transformations involved.

If the pair-production is truly created at threshold, then the CM and decay frames ( $R$  and  $R + 1$ ) are the same frame and the Razor technique is sufficient for the purpose of approximating the event. Otherwise, the Super-Razor technique is followed.

### 8.5.2 Razor

Instead of dijets, we focus on constructing variables using megajets. These are collections of jets that are treated as a single jet with a four-momentum defined as the sum

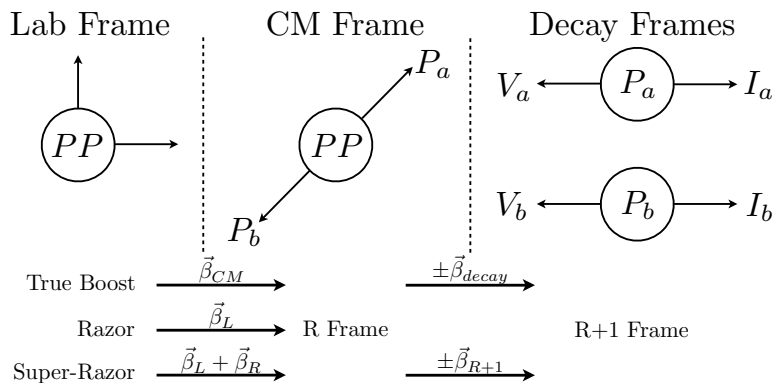


Figure 8.8. The definition of  $R$  and  $R + 1$  frames by approximate boosts.

total of its constituent four-momenta. The two “hemispheres” of jets have no overlap but include all visible jets. The rest-frame of the visible system is first determined by the four-momentum sum of all visible objects. The combinatorics are checked for the partition that maximizes  $p_{V_a}^V + p_{V_b}^V$ . This sets a thrust axis in the visible frame where the masses have been minimized:

$$M_{V_i} = \sqrt{p_{V_i}^2} \quad (8.18)$$

It is true that this does not force jets into the true branches of the decay tree, but we accept the mass minimization as a reasonable assumption to make when trying to approximate the true decay. The first boost ( $\beta_L$ ) is defined by taking the frame where the two megajets have equal and opposite  $p_z$ .

$$\beta_L \equiv \frac{p_{V_{a,z}}^2 + p_{V_{b,z}}^2}{E_{V_a} + E_{V_b}} \quad (8.19)$$

As this value increases, signal events appear more distinguished because BG events do not have kinematics from this frame above  $M_\Delta \sim m_W$ . In this frame,  $M_\Delta \approx 2E_{V_a} \approx 2E_{V_b}$ . We can calculate a new version of  $M_{CT}$  in this frame:

$$M_R \equiv (E_{V_a} + E_{V_b})^2 - (p_{V_{a,z}} + p_{V_{b,z}})^2 \quad (8.20)$$

The distribution of  $M_R$  will have its kinematic edge around  $M_\Delta$ , but BG events are not expected to have any features at this scale. This variable approximates the longitudinal measure of the event, so we also construct a transverse variable from  $E_T^{\text{miss}}$  and  $p_T$  with information unused by  $M_R$ :

$$(M_T^R)^2 \equiv \frac{1}{2} \left[ E_T^{\text{miss}}(p_{V_{a,T}} + p_{V_{b,T}}) - \vec{E}_T^{\text{miss}} \cdot (\vec{p}_{V_{a,T}} + \vec{p}_{V_{b,T}}) \right] \quad (8.21)$$

$M_T^R$  also falls sharply at  $M_\Delta$ . We introduce the dimensionless variable  $R$  as the ratio of these two approximately orthogonal quantities:

$$R \equiv \frac{M_T^R}{M_R} \quad (8.22)$$

This represents an event shape with  $R \sim 1$  for SUSY and  $R \sim 0$  for QCD.  $M_R$  and  $R$  have a strong hyperbolic correlation for BGs but are nearly uncorrelated for signals (Figure D.8). In the limit where  $M_P$  and  $M_I$  are degenerate, signals start to look like BG. However, the transition is gradual and generally opens sensitivity to regions with low  $M_\Delta$ .

### 8.5.3 Super-Razor

Now consider if we collect all transverse momenta in an event:

$$\vec{J}_T = -(\vec{E}_T^{\text{miss}} + \vec{p}_{V_{a,T}} + \vec{p}_{V_{b,T}}) \quad (8.23)$$

We need an additional boost to recoil from ISR contamination, which was not taken into account by the original Razor formulation. After the longitudinal boost  $\vec{\beta}_L$ , we construct this new boost from an approximation to the CM energy ( $\sqrt{s_R}$ ):

$$\vec{\beta}_R \equiv \frac{\left\{ -\vec{J}_T, p_z^R \right\}}{\sqrt{J_T^2 + (p_z^R)^2 + s_R}} \quad (8.24)$$

This boost is systematically larger than  $\vec{\beta}_{CM}$ . We assume that the invariant mass of  $V$  is now equal to the invariant mass of  $I$ . We also assume that the longitudinal boost is accurate enough to discard  $p_z^R$  from the calculation ( $\partial\sqrt{s_R}/\partial p_z^R = 0$ ).

$$s_R \equiv 2 \left[ M_R^2 + \vec{J}_T \cdot (\vec{p}_{V_a} + \vec{p}_{V_b}) + M_R \sqrt{M_R^2 + J_T^2 + 2\vec{J}_T \cdot (\vec{p}_{V_a} + \vec{p}_{V_b})} \right] \quad (8.25)$$

This variable is now a jet-corrected version of  $M_R$  that scales to  $M_\Delta$  and  $\sqrt{s}$ . The value of  $\sqrt{s_R}$  is systematically less than  $\sqrt{s}$  because it assumes the energy is evenly split between  $V$  and  $I$ .

We can then approximate the boost to the decay frames since the two frames should be contralinear:

$$\vec{\beta}_{R+1} \equiv \frac{p_{V_a}^R - p_{V_b}^R}{E_{V_a}^R + E_{V_b}^R} \quad (8.26)$$

This last boost and  $\sqrt{s_R}$  should be related to  $M_\Delta$  because only the visible objects are used.

$$M_\Delta^R \equiv \frac{\sqrt{s_R}}{2\gamma_{R+1}} \quad (8.27)$$

$M_\Delta^R$  is therefore the hyperbolic contour in the  $\sqrt{s_R}$  and  $\gamma_{R+1}$  plane. QCD jets tend to exist along these contour lines rather than populating regions dominated by SUSY events. If a point in this plane represents a QCD event, contralinear jets tend to have small mass scale while jet mismeasurement tends to increase the mass scale while reducing the appearance of a decay boost. The effect of these QCD uncertainties is to “slide” along the contours rather than move independently around the plane.

We can also revisit  $s_R$  to greatly simplify the notation:

$$\frac{1}{4}s_R = (M_\Delta^R)^2 + (p_{V_a.T}^R + p_{V_b.T}^R)^2 + (E_{V_a}^R - E_{V_b}^R)^2 \quad (8.28)$$



So far we have only looked at mass variables. If we can approximate the decays, then we can also approximate the decay angles. The azimuthal angle between  $\vec{\beta}_R$  and  $(p_{V_a,T}^R + p_{V_b,T}^R)$  is designated as  $\Delta\phi_{R,\beta}$  and contains information about the ratio between  $M_P$  and  $M_I$  to complement  $M_\Delta^R$ . If  $\vec{\beta}_R$  consistently over-boosts to the CM frame, the visible particles will be contralinear to the boost. Therefore, for large  $M_I$ , this distribution peaks around  $\pi$ . Thus, we gain a discriminant between neutrinos and neutralinos.

Using the energy difference of  $V_a$  and  $V_b$ , we construct another angle between  $\vec{\beta}_R$  and  $V_i$  in the  $R + 1$  frame.

$$\begin{aligned} |\cos\theta_{R+1}|^2 &\equiv \frac{(E_{V_a}^R - E_{V_b}^R)^2}{\frac{1}{4}s_R - (M_\Delta^R)^2} \\ &= \frac{\frac{1}{4}s_R - (M_\Delta^R)^2 - (p_{V_a,T}^R + p_{V_b,T}^R)^2}{\frac{1}{4}s_R - (M_\Delta^R)^2} \end{aligned} \quad (8.29)$$

In the CM frame, there is no reason to expect a strong correlation between  $E_{V_a}$  and  $E_{V_b}$  and the distribution should be flat in SUSY events. For large  $m_{\tilde{\chi}_1^0}$ , the distribution starts to skew toward  $\pi$ . The production of  $W^+W^-$  would demonstrate the existence of a polarization correlation between  $V_a$  and  $V_b$  by peaking at 0.

CMS has had considerably more enthusiasm than ATLAS for using both Razor [96–102] and Super-Razor [103–110]. Fermilab has produced a study on Razor sensitivity in dark matter searches [111] and CMS also performed such a search [112]. CMS has also published a search for Higgs using the Super-Razor [113].

## 8.6 Recursive Jigsaw Reconstruction

Since Super-Razor is like a Razor analysis extended to more boost frames, a technique has been developed to extend the reconstruction to an arbitrary number of decay frames that carry Lorentz invariance. If an event has decay structure remaining up to the  $R + N$  frame, then it can become trivial to compare it to events that only last up to  $R + N - 1$ . For example, a noisy QCD multijet event effectively has many decay frames, but a  $W \rightarrow e\nu$

event exhausts its phase space much quicker. RJ reconstruction was developed along with the 2015 SUSY search [114] and parts of it are summarized below.

The Recursive Jigsaw (RJ) reconstruction technique preferentially rebuilds an event to look like a desired decay tree as much as possible. This gives a set of masses and decay angles for the final states and any intermediate states. The idea is to take something that looks like Equation. 4.16 and reconstruct it as something that looks like Equation. 3.20 again.

This would be a perfect method for real signal events while real BG events should show some sign of incomplete reconstruction or else demonstrate an over-(under-)abundance bias in the distribution of observables that could be quantified. By carefully studying the appropriate MC backgrounds, one could then exploit the differences to build an analysis with these observables as discriminants.

### 8.6.1 Inclusive Disparticle Reconstruction

The first decay tree we consider is the pair-production of  $P_a$  and  $P_b$  that decay into visible particles ( $V_a$  and  $V_b$ ) and invisible particles ( $I_a$  and  $I_b$ ) (Figure 8.9). The first Jigsaw algorithm partitions the visible jets by minimizing the masses of the megajet four-momenta. The unknown degrees of freedom are tied to their association with  $E_T^{\text{miss}}$ . The algorithm first addresses the mass of any invisible particles present in the event. We assume that the CM frame pair-produces two particles with equal mass, and the two constituents take symmetric paths through their decays.

$$M_I^2 = M_V^2 - 4M_{V_a}M_{V_b} \quad (8.30)$$

The longitudinal momentum is resolved by boosting into a frame where the visible system and the invisible system have the same rapidity, which essentially minimizes  $M_{V+I}$ . This keeps the entire decay tree boost invariant.

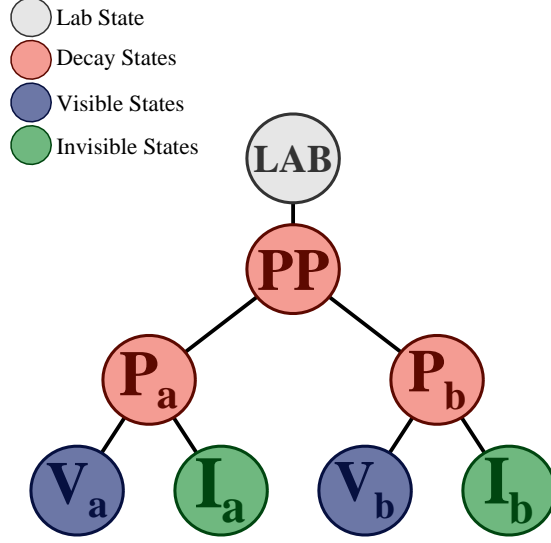


Figure 8.9. The decay tree used for reconstructing  $pp \rightarrow \tilde{q}\tilde{q} \rightarrow qq \tilde{\chi}_1^0 \tilde{\chi}_1^0$ .

$$\vec{\beta}_{PP}^{Lab} \equiv \frac{\vec{p}_{PP}^{Lab}}{E_{PP}^{Lab}} = \frac{\vec{p}_V^{Lab} + \vec{p}_I^{Lab}}{E_V^{Lab} + \sqrt{(p_I^{Lab})^2 + M_I^2}} \quad (8.31)$$

Moreover, with an invariance tied to the minimization of masses, the variables remain largely independent in construction through each step of the decay.

$$M_{P_i} = \frac{M_{P_i}^2 - M_{I_i}^2 + M_{V_i}^2}{2M_P} \quad (8.32)$$

This constraint is used to solve for the mass of each particle using only the visible objects. The distribution of this variable has its kinematic end-point near  $M_\Delta$  (Figure 8.10).

$$M_P \equiv \frac{M_{V_a}^2 - M_{V_b}^2}{2(E_{V_a}^{P_a} - E_{V_b}^{P_b})} \quad (8.33)$$

If the sparticles are produced at threshold, the sum of the masses should be equal to the mass of the production frame. Therefore, the approximate relativistic factor is calculated by the ratio of the masses.

$$M_{PP} \equiv 2\sqrt{M_P^2 + (\vec{p}_{P_i}^{PP})^2} \quad (8.34)$$

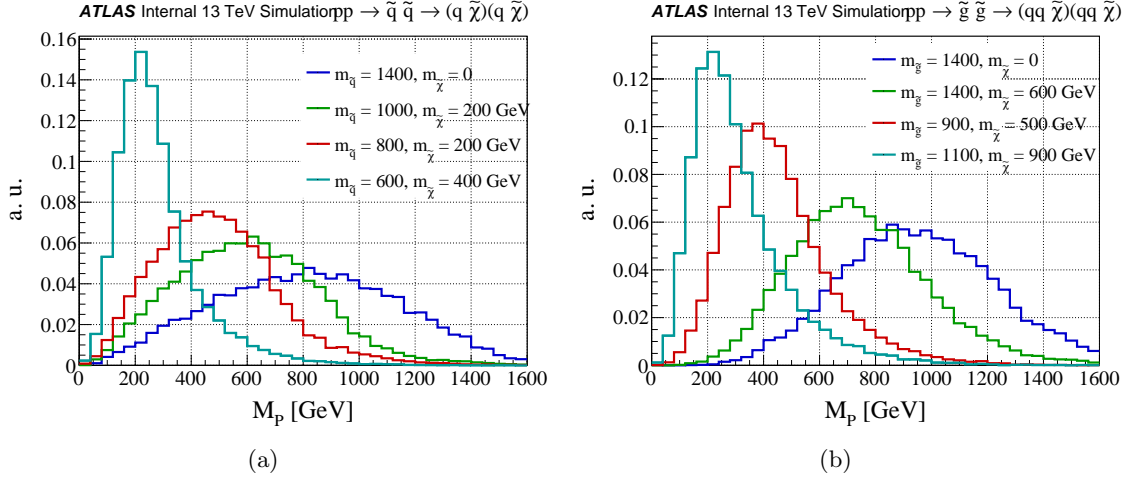


Figure 8.10. A distribution of  $M_P$  for (a)  $\tilde{q}\bar{\tilde{q}} \rightarrow qq \tilde{\chi}_1^0 \tilde{\chi}_1^0$  and (b)  $\tilde{g}\bar{\tilde{g}} \rightarrow qq qq \tilde{\chi}_1^0 \tilde{\chi}_1^0$ .

$$\gamma_P^{PP} \equiv \frac{M_{PP}}{2M_P} \quad (8.35)$$

The distribution of this variable (Figure 8.11) has no features related to  $M_\Delta$ . Instead, it is sensitive to the mass of each  $V_i$  and how much momentum imbalance they have in the  $PP$  frame.

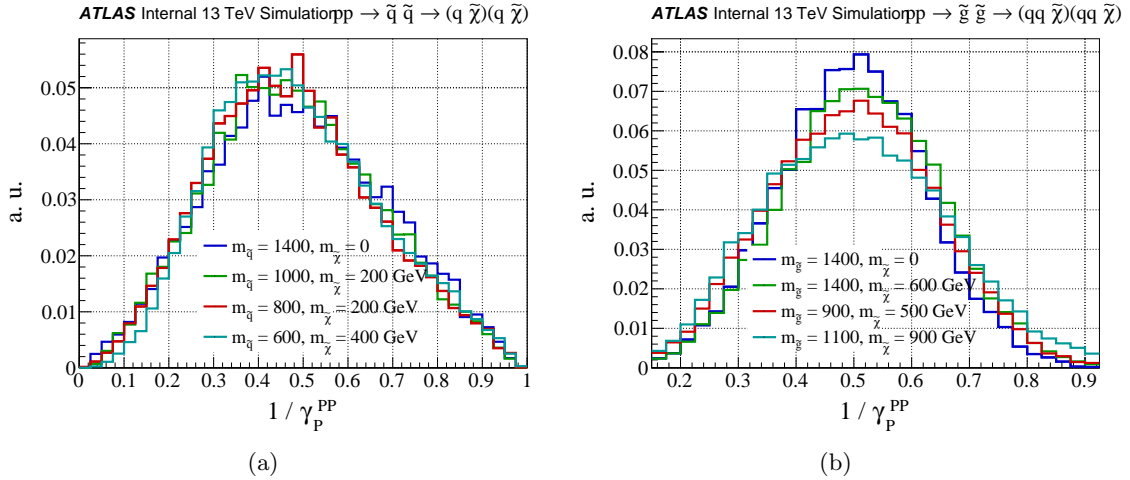


Figure 8.11. A distribution of  $1/\gamma_P^{PP}$  for (a)  $\tilde{q}\bar{\tilde{q}} \rightarrow qq \tilde{\chi}_1^0 \tilde{\chi}_1^0$  and (b)  $\tilde{g}\bar{\tilde{g}} \rightarrow qq qq \tilde{\chi}_1^0 \tilde{\chi}_1^0$ .

To use this variable as a background discriminant, we note that QCD multijets would also be sensitive to  $V_i$  but not the momentum imbalance. We refer to this as the transverse visible shape. Colinear events have  $1/\gamma_P^{PP} \sim 1$  while contralinear events have  $1/\gamma_P^{PP} \sim 0$ . This distribution does show slight sensitivity to gluino events because the decay is a three-body decay where some of the available energy is taken by masses rather than momentum (Figure 8.12).

$$VS_{PP} \equiv \frac{\sqrt{2(p_{V_a}^{PP} p_{V_b}^{PP} + \vec{p}_{V_a}^{PP} \cdot \vec{p}_{V_b}^{PP})}}{p_{V_a}^{PP} + p_{V_b}^{PP}} \quad (8.36)$$

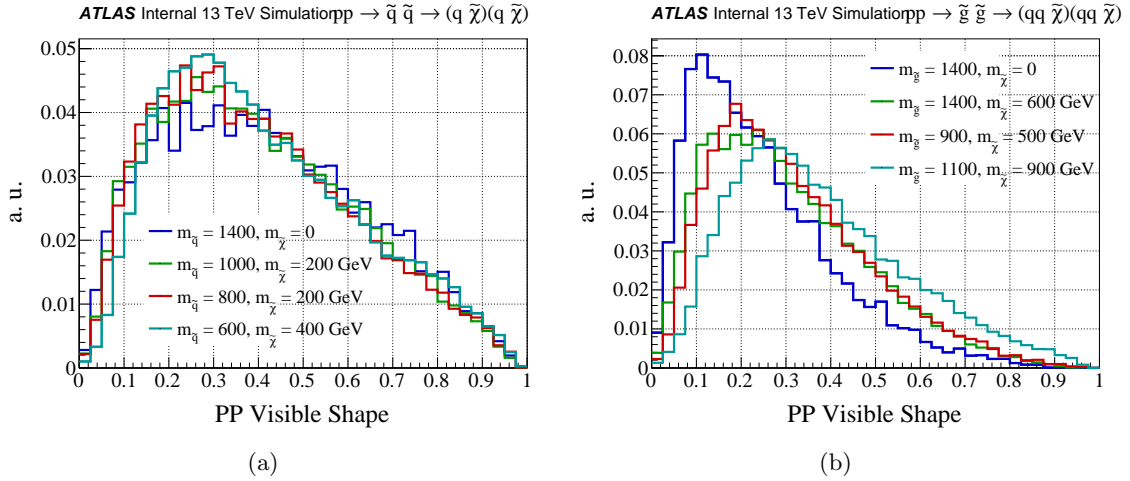


Figure 8.12. A distribution of  $VS_{PP}$  for (a)  $\tilde{q}\tilde{q} \rightarrow qq \tilde{\chi}_1^0 \tilde{\chi}_1^0$  and (b)  $\tilde{g}\tilde{g} \rightarrow qq qq \tilde{\chi}_1^0 \tilde{\chi}_1^0$ .

$VS_{PP}$  and  $\sqrt{s_R}$  replace the  $R$  and  $M_R$  of the original Razor formulation, where we now use  $\sqrt{s_R} \equiv M_{V+I}$ . We note that backgrounds still have a hyperbolic correlation between these two variables, which we explicitly use to define a contour in this plane:

$$M_{\Delta}^R \equiv VS_{PP} M_{V+I} \quad (8.37)$$

The distribution of this variable is quite good at suppressing the high-rate backgrounds and forms the basis of a trigger proposed and accepted for Run II (Section 8.7).

We note that this contour also represents the relative jet mismeasurement in QCD events similar to its function in the Super-Razor formulation. The correlation vanishes for large  $M_\Delta$ , which is also the average value for these events.

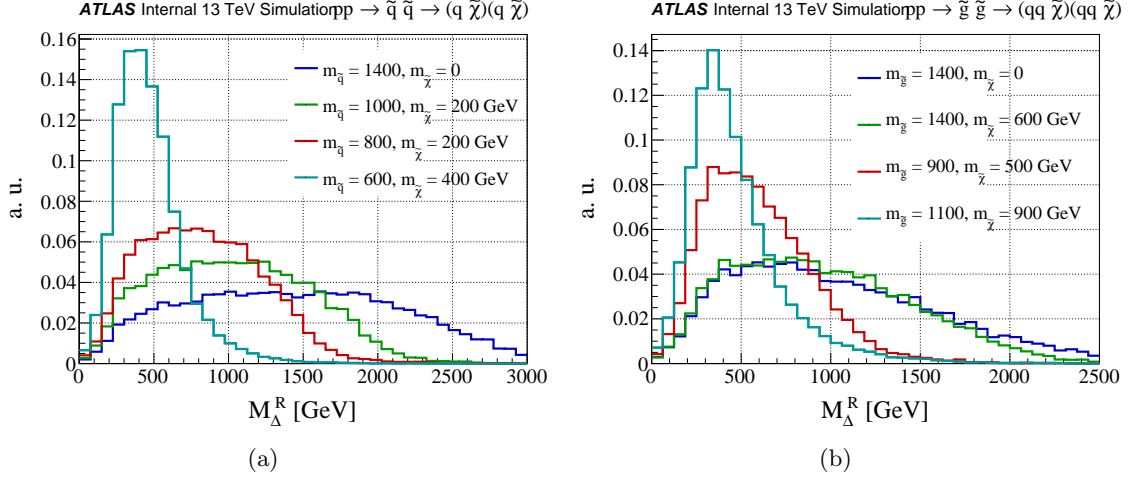


Figure 8.13. A distribution of  $M_\Delta^R$  for (a)  $\tilde{q}\tilde{q} \rightarrow qq \tilde{\chi}_1^0 \tilde{\chi}_1^0$  and (b)  $\tilde{g}\tilde{g} \rightarrow qqqq \tilde{\chi}_1^0 \tilde{\chi}_1^0$ .

Working directly from the decay tree also allows us to define a decay angle of the  $PP$  system:

$$\cos \theta_{PP} \equiv \hat{p}_{Pa}^{PP} \cdot \hat{p}_{PP}^{lab} \quad (8.38)$$

If the  $PP$  decay axis aligns with the beam axis, the distribution peaks at  $\pm 1$  (Figure 8.14).

We define an angle for the subsequent decays in a similar way:

$$\cos \theta_P \equiv \hat{p}_{Ia}^{Pa} \cdot \hat{p}_{Pa}^{PP} \quad (8.39)$$

The distribution of this variable is quite different between  $\tilde{q}$  and  $\tilde{g}$  (Figure 8.15), which is again due to the three-body masses in the phase space.

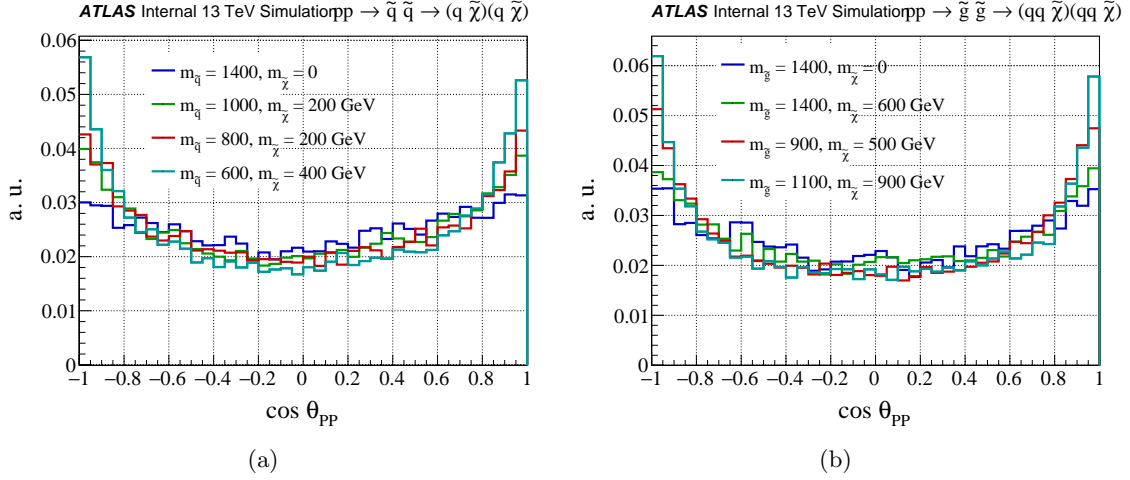


Figure 8.14. A distribution of  $\cos \theta_{PP}$  for (a)  $q\bar{q} \rightarrow q\bar{q} \tilde{\chi}_1^0 \tilde{\chi}_1^0$  and (b)  $g\tilde{g} \rightarrow qq\bar{q}q \tilde{\chi}_1^0 \tilde{\chi}_1^0$ .

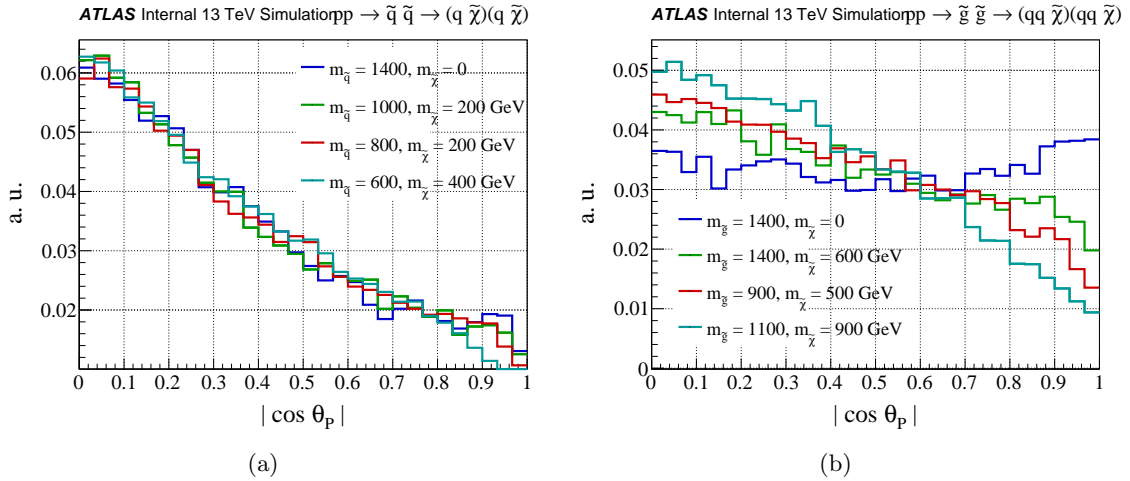


Figure 8.15. A distribution of  $\cos \theta_P$  for (a)  $q\bar{q} \rightarrow q\bar{q} \tilde{\chi}_1^0 \tilde{\chi}_1^0$  and (b)  $g\tilde{g} \rightarrow qq\bar{q}q \tilde{\chi}_1^0 \tilde{\chi}_1^0$ .

We also define the azimuthal difference between the  $\vec{p}_T$  of the visible particles in the laboratory and  $PP$  frames:

$$\Delta\phi_{PP,V} \equiv \Delta\phi(\vec{p}_{PP}^{Lab}, \vec{p}_V^{PP}) \quad (8.40)$$

The azimuthal difference can also be examined for  $\vec{p}_T$  in the  $PP$  and  $P_i$  frames:

$$\Delta\phi_{VP} \equiv \Delta\phi(\vec{p}_V^{PP}, \vec{p}_{Pa}^{PP}) \quad (8.41)$$

Both  $\Delta\phi_{PP,V}$  and  $\Delta\phi_{VP}$  are expected to be flat (Figures 8.16 and 8.17), although the discontinuity in the distribution of  $\Delta\phi_{VP}$  for  $\tilde{q}\tilde{q}$  is due to the combinatoric choice that  $M_{Va} > M_{Vb}$ .

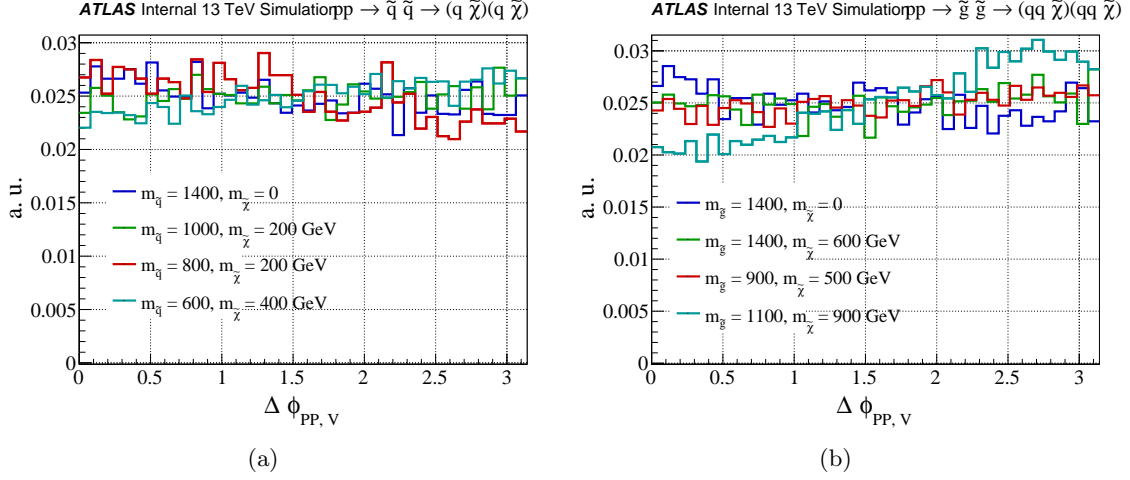


Figure 8.16. A distribution of  $\Delta\phi_{PP,V}$  for (a)  $\tilde{q}\tilde{q} \rightarrow qq \tilde{\chi}_1^0 \tilde{\chi}_1^0$  and (b)  $\tilde{g}\tilde{g} \rightarrow qq qq \tilde{\chi}_1^0 \tilde{\chi}_1^0$ .

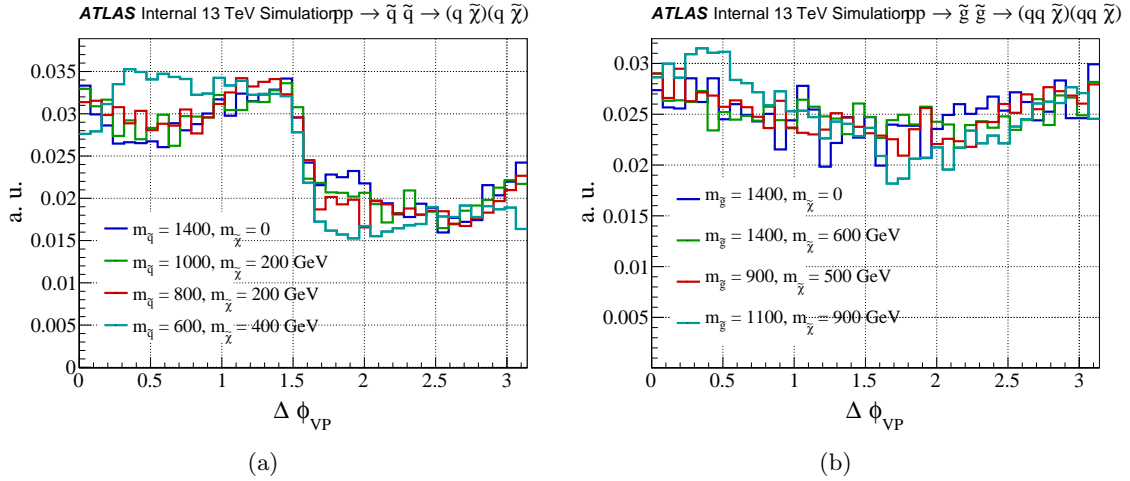


Figure 8.17. A distribution of  $\Delta\phi_{VP}$  for (a)  $\tilde{q}\tilde{q} \rightarrow qq \tilde{\chi}_1^0 \tilde{\chi}_1^0$  and (b)  $\tilde{g}\tilde{g} \rightarrow qq qq \tilde{\chi}_1^0 \tilde{\chi}_1^0$ .



### 8.6.2 Digluino Reconstruction

In  $\tilde{g}\tilde{g}$  decays, there is an additional structure to each leg of the inclusive reconstruction. We apply the Jigsaw technique *recursively* to the frame that extends a two-body decay into a three-body decay by binary separation into child frames. In this case, we now have a decay with child decay frames ( $C_a$  and  $C_b$ ) and at least four visible objects ( $V_{1a}, V_{2a}, V_{1b}, V_{2b}$ ; see Figure 8.18). Variables from the substructure of hemispheres should allow methods that can distinguish  $\tilde{g}\tilde{g}$  from  $\tilde{q}\tilde{q}$ .

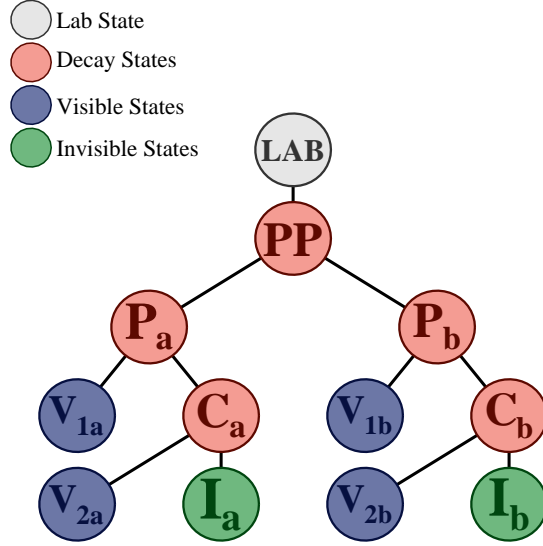


Figure 8.18. The decay tree used for reconstructing  $pp \rightarrow \tilde{g}\tilde{g} \rightarrow qq \tilde{q}\tilde{q} \rightarrow qq qq \tilde{\chi}_1^0 \tilde{\chi}_1^0$ .

The invariant mass distribution of the sequential decay presents an end-point that looks like a different form of  $M_\Delta$ :

$$M_V^2 \leq \frac{(M_P^2 - M_C^2)(M_C^2 - M_I^2)}{M_C^2} \quad (8.42)$$

All variables used in the inclusive disparticle construction can also be used in the digluino approach along with some dedicated variables. We now have access to the azimuthal

angle between  $C$  and  $P$  frames. The correlations in this distribution are used to identify BG processes that look like dijet events (Figure 8.19).

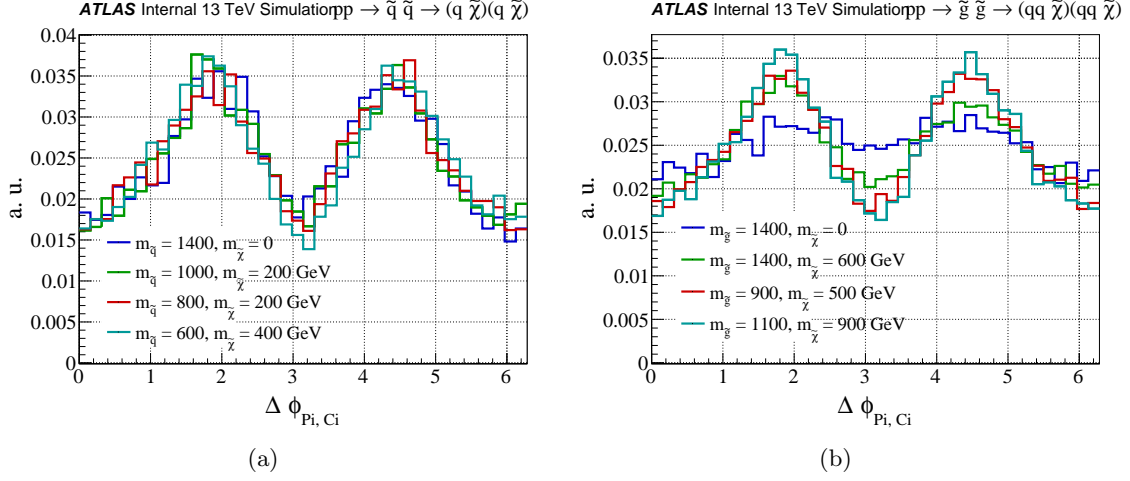


Figure 8.19. A distribution of  $\Delta\phi_{P_i, C_i}$  for (a)  $\tilde{q}\bar{\tilde{q}} \rightarrow qq \tilde{\chi}_1^0 \tilde{\chi}_1^0$  and (b)  $\tilde{g}\tilde{g} \rightarrow qq qq \tilde{\chi}_1^0 \tilde{\chi}_1^0$ .

The particles have to share the available momentum between  $V_{2i}$  and  $I_i$ :

$$R_{P_{I_i}}^{P_i} \equiv \frac{2P_{I_i}}{P_{I_i} + P_{V_{1i}} + P_{V_{2i}}} \quad (8.43)$$

If  $V_{2i}$  gets all the momentum, then  $R_{P_{I_i}}^{P_i} \sim 0$ . Otherwise if  $I_i$  gets all the momentum, then  $R_{P_{I_i}}^{P_i} \sim 1$ . This distribution is shown in Figure 8.20.

This variable can be applied to both sides of the decay. Multiple jets associated with BG events can be spuriously assigned to one leg in the decay chain over the other. If an event had an odd number of jets, it might seem that the last jet would be assigned arbitrary to one side instead of another. To address this concern, the plane  $R_{P_{I_a}}^{P_a}$  versus  $R_{P_{I_b}}^{P_b}$  is used to examine the structure of each jet and reject BGs that look like two-body decays (e.g.  $Z \rightarrow \nu\nu + jets$ ).

Similar to  $VS_{PP}$ , we can define a shape for each sparticle with a distribution corresponding to Figure 8.21:

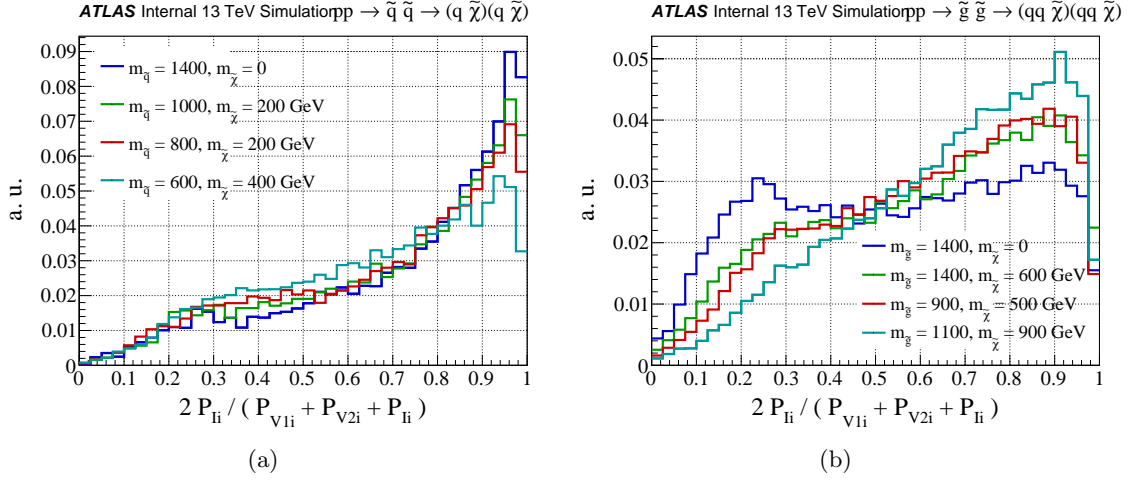


Figure 8.20. A distribution of  $R_{P_i}^{P_i}$  for (a)  $q\bar{q} \rightarrow qq \tilde{\chi}_1^0 \tilde{\chi}_1^0$  and (b)  $g\bar{g} \rightarrow qq\bar{q}\bar{q} \tilde{\chi}_1^0 \tilde{\chi}_1^0$ .

$$VSP \equiv \frac{\sqrt{2(p_{V1i}^{P_i} p_{V2i}^{P_i} + \vec{p}_{V1i}^{P_i} \cdot \vec{p}_{V2i}^{P_i})}}{p_{V1i}^{P_i} + p_{V2i}^{P_i}} \quad (8.44)$$

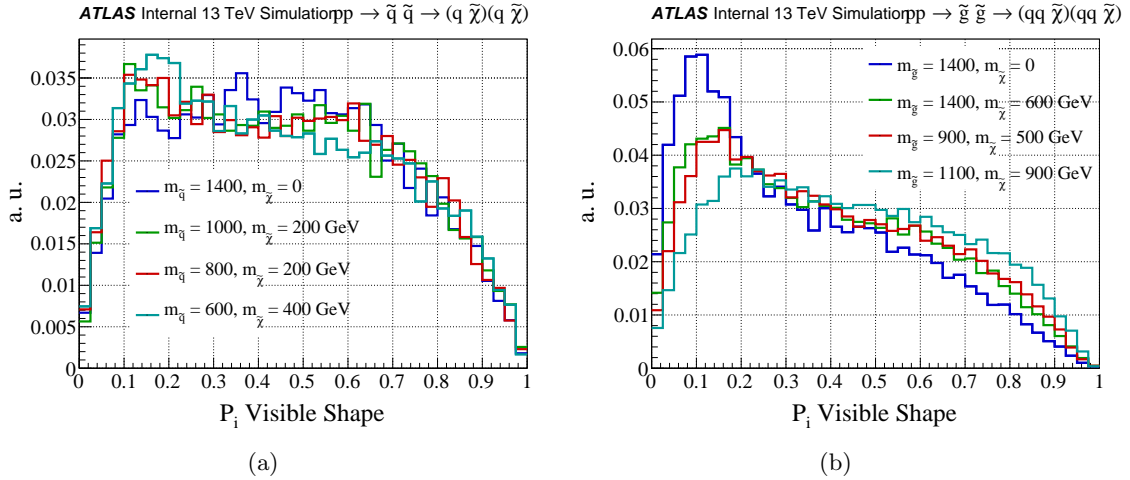


Figure 8.21. A distribution of  $VSP$  for (a)  $q\bar{q} \rightarrow qq \tilde{\chi}_1^0 \tilde{\chi}_1^0$  and (b)  $g\bar{g} \rightarrow qq\bar{q}\bar{q} \tilde{\chi}_1^0 \tilde{\chi}_1^0$ .

It is also beneficial to look at the distribution of the two sides in the  $VSP_a$  versus  $VSP_b$  plane, which is used to identify events without much transverse shape. In top events

with a missing lepton, the imbalance in shape can be measured by taking the difference between the visible shape and the decay angle  $|\frac{2}{3} \Delta\phi_{V,P}^{PP} - \frac{1}{3} \cos\theta_P|$ .

### 8.6.3 Compressed Sparticle Reconstruction

Compressed (or degenerate) SUSY spectra, where  $m_{\tilde{\chi}_1^0} \lesssim m_{\tilde{q}}$  or  $m_{\tilde{\chi}_1^0} \lesssim m_{\tilde{g}}$ , is a difficult region of the phase space to target because the decay is soft and swamped by ISR. Scale variables are very detrimental to searches in this regions, so a unique set of RJ variables are used for the compressed scenarios. The decay tree used in the RJ reconstruction is shown in Figure 8.22.

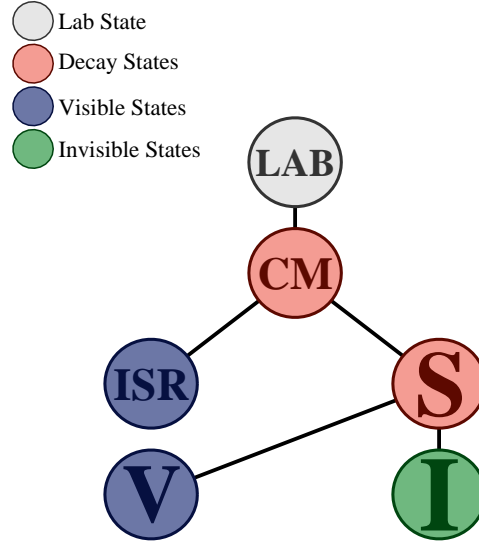


Figure 8.22. The decay tree used for reconstructing compressed SUSY points.

The magnitude of the ISR transverse momenta is  $p_{TS}^{ISR}$ . Compressed SUSY events are expected to have large values of  $m_{\tilde{\chi}_1^0}/m_{\tilde{q}}$  or  $m_{\tilde{\chi}_1^0}/m_{\tilde{g}}$  but BGs rarely do, so  $\vec{p}_I^{CM} \cdot \hat{p}_{TS}^{CM}/p_{TS}^{CM}$  is taken to approximate these measures (Figure 8.23). Familiar variables are also used in the boost-invariant RJ context with  $M_{TS}$  as the new transverse mass,  $\Delta\phi_I^{CM}$  as the new  $\Delta\phi$ , and  $N_{jet}^V$  to only count the number of jets that are not associated with ISR.

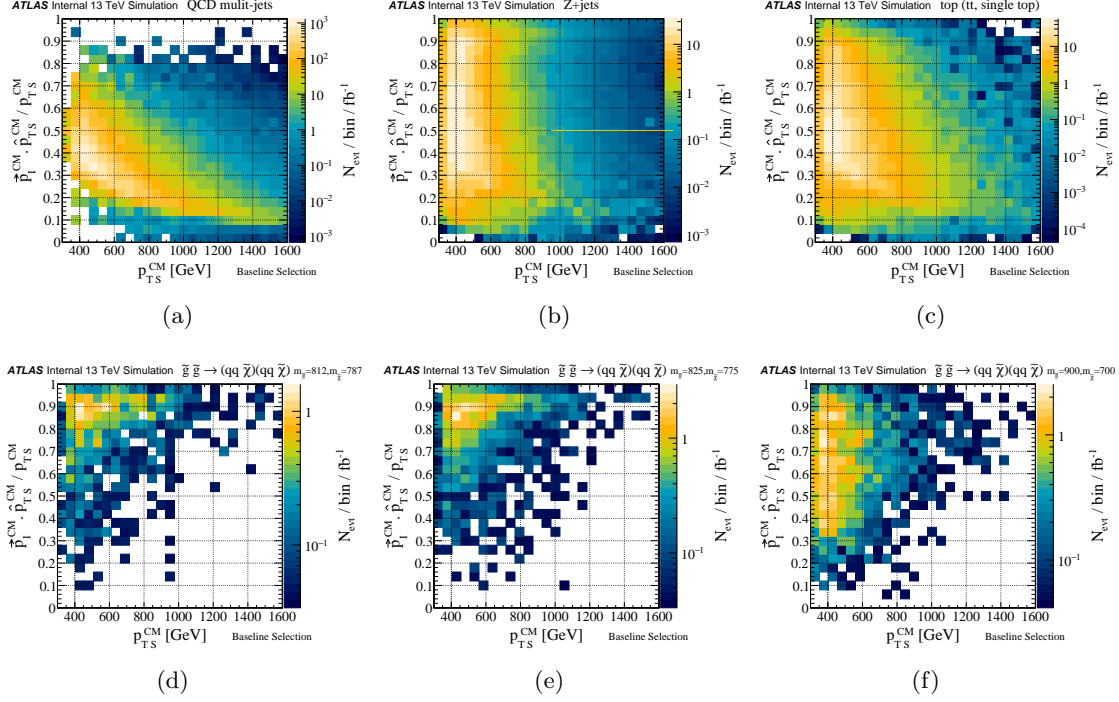


Figure 8.23. Correlation between  $\vec{p}_I^{CM} \cdot \hat{p}_{TS}^{CM} / p_{TS}^{CM}$  and  $p_{TS}^{ISR}$  for (top) BG and (bottom) signal. The BG processes are (a) QCD multijets, (b)  $ZS$ +jets, and (c) top. The signal models are  $\tilde{g}$  events with (d)  $m_{\tilde{g}} = 812$  GeV and  $m_{\tilde{\chi}_1^0} = 787$  GeV, (e)  $m_{\tilde{g}} = 825$  GeV and  $m_{\tilde{\chi}_1^0} = 7775$  GeV, and (f)  $m_{\tilde{g}} = 900$  GeV and  $m_{\tilde{\chi}_1^0} = 700$  GeV.

#### 8.6.4 Hadronic Scale Reconstruction

With a rest-frame approximated for each level of the decay tree, we find it useful to appropriate the use of  $H_T$  (although not necessarily limited to transverse quantities). Since the technique describes an *event* reconstruction rather than an *object* reconstruction, the mass estimations above are sensitive to any QCD excesses such as UE and ISR that can also create large decay angles. Hadronic scale variables are designed to measure the shape and balance of events once they have been reconstructed via RJ. Whereas Sections 8.6.1-8.6.3 describe methods of targeting individual signal grid points, these hadronic scale signals are used as the primary method of reducing BGs.

The notation specifies the frame ( $F$ ) in which the calculation is performed, the number of visible objects used ( $n$ ), and the number of invisible particles assumed ( $m$ ). Variables

involving  $n = 2$  define a disquark-inspired inclusive reconstruction while  $n = 4$  is appropriate for digluino reconstruction. Any extra jets are summed according to the mass-minimization Jigsaw used to construct the decay tree.

$$H_{n,m}^F = \sum_i^n |\vec{p}_{V_i}^F| + \sum_j^m |\vec{p}_{I_j}^F| \quad (8.45)$$

By increasing the number of visible objects in this calculation, large jet multiplicities can be selected by reducing events with low jet multiplicity. On the other hand,  $H_{1,1}^{PP}$  can be used to measure momentum imbalance independently from a measure of jet multiplicity. The transverse value can also be specified in the subscript. For example, the original definition of  $H_T$  and  $M_{\text{eff}}$  would be represented in this notation for 0-lepton if they are calculated in the laboratory frame (Equation 8.46). If these values are boosted to the  $PP$  frame they would essentially be invariant versions of their original definitions. Examples of the variables used in disquark and digluino searches are shown in Figures 8.24 and 8.25.

$$H_{Tn,0}^{Lab} = H_T(n) \quad (8.46a)$$

$$H_{T4,1}^{Lab} = M_{\text{eff}} \quad (8.46b)$$

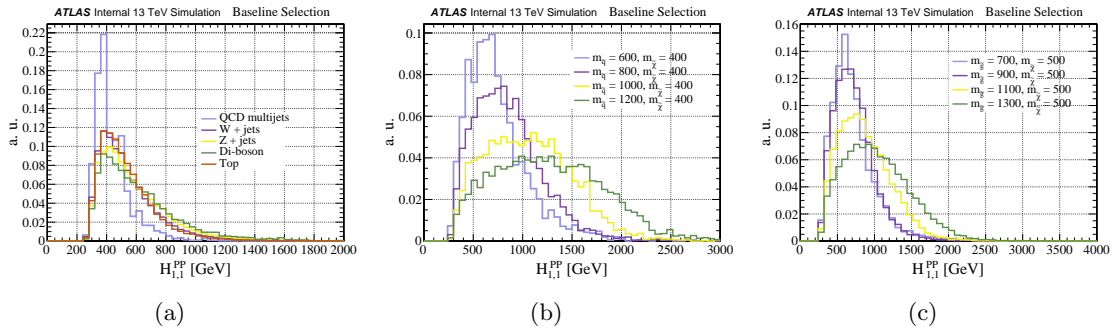


Figure 8.24. A distribution of  $H_{1,1}^{PP}$  for (a) BG, (b) disquark, and (c) digluino.

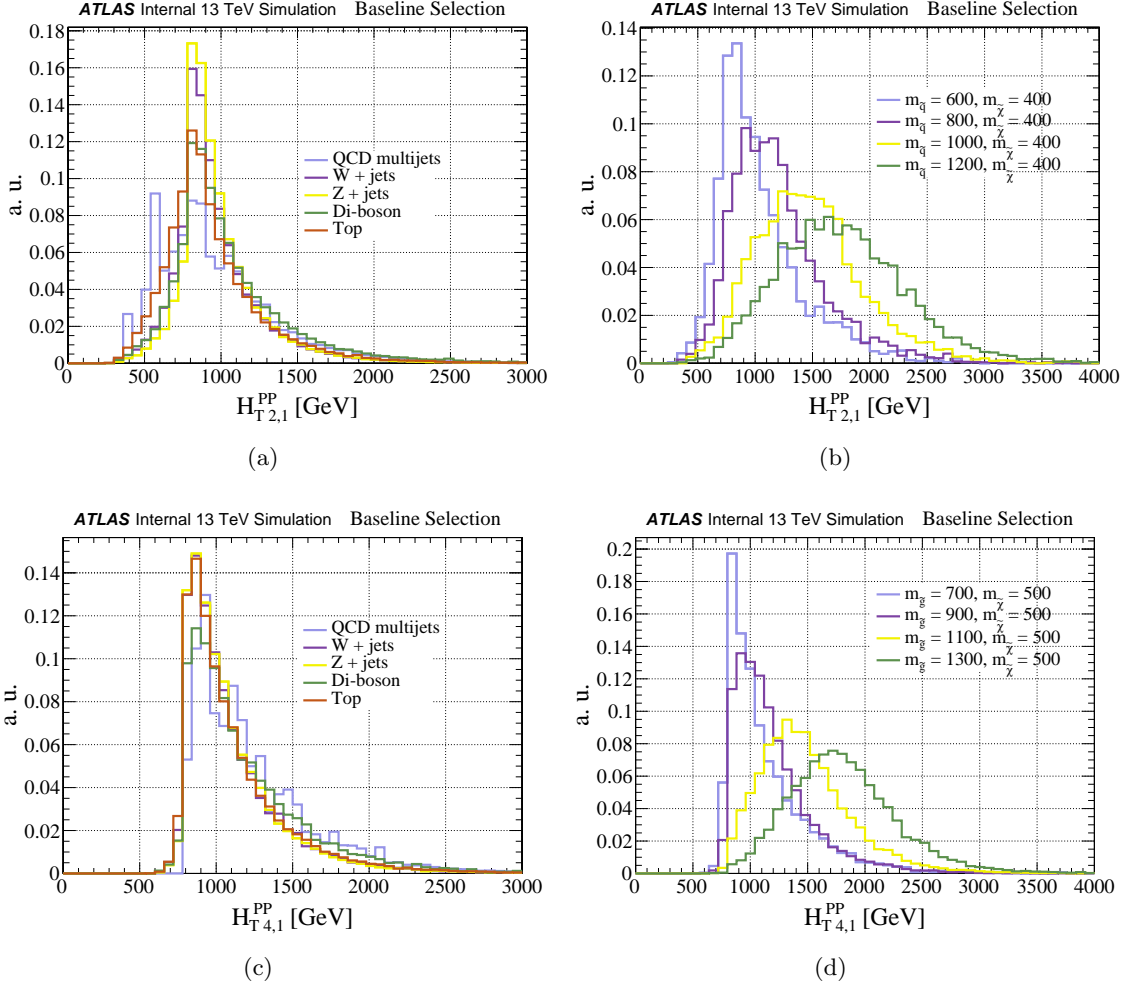


Figure 8.25. A distribution of (top)  $H_{T,1}^{PP}$  and (bottom)  $H_{T,4,1}^{PP}$  for (left) BG, (b) disquark, and (d) digluino.

Ratios of these variables present a scale-less discriminant when constructing SRs. An arbitrary number of measures could be formed, but the variables used in the context of Chapter 11 are explained here.

$H_{1,1}^{PP} / H_{2,1}^{PP}$  (Figure 8.26) and  $H_{1,1}^{PP} / H_{4,1}^{PP}$  (Figure 8.27) can observe an imbalance in event shape where the scale is determined by one large jet  $p_T$  or  $E_T^{\text{miss}}$ . The imbalance from a comparison to  $p_z^{\text{Lab}}$  is described by  $p_z^{\text{Lab}} / (p_z^{\text{Lab}} / H_{T,1}^{PP})$  (Figure 8.28) and  $p_z^{\text{Lab}} / (p_z^{\text{Lab}} / H_{T,4,1}^{PP})$  (Figure 8.29). A measure of the transverse scale of gluino events is  $H_{T,4,1}^{PP} / H_{4,1}^{PP}$  (Figure 8.30). Because  $Z + jets$  events tend to feature one jet that has a much higher  $p_T$  than

another, the ratio  $p_{Tj_2}^{PP} / H_{T2,1}^{PP}$  (Figure 8.31) can test this visible jet balance. For gluino events, targeting  $Z \rightarrow \nu\nu$  means that additional jets may not have similar momenta, so  $\min(p_{Tj_2}^{PP} / H_{T2,1}^{PP})$  (Figure 8.32) is defined to select the minimum from each hemisphere. The jet momenta in each hemisphere can be tested for balance with  $\max(H_{1,0}^P / H_{2,0}^P)$ .

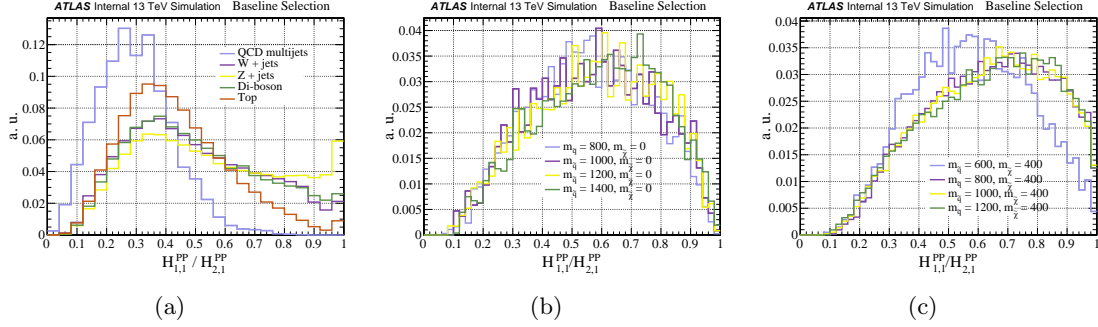


Figure 8.26. A distribution of  $H_{1,1}^{PP} / H_{2,1}^{PP}$  for (a) BG, (b) large mass-splitting disquark, and (c) intermediate mass-splitting disquark.

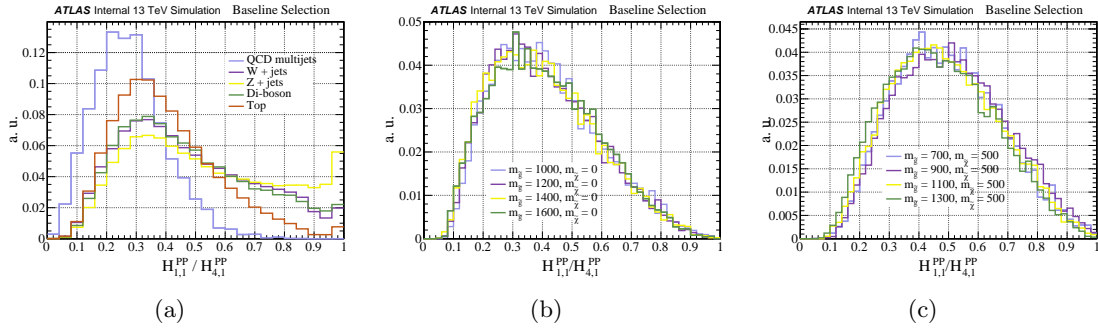


Figure 8.27. A distribution of  $H_{1,1}^{PP} / H_{4,1}^{PP}$  for (a) BG, (b) large mass-splitting digluino, and (c) intermediate mass-splitting digluino.



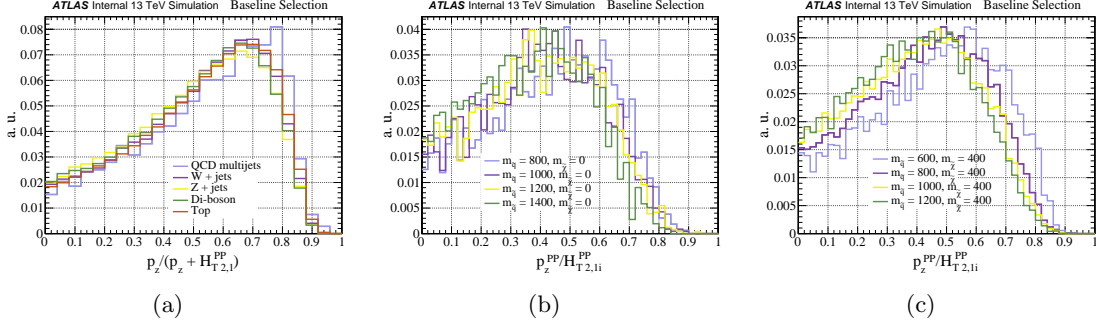


Figure 8.28. A distribution of  $p_z^{Lab} / (p_z^{Lab} / H_{T2,1}^{PP})$  for (a) BG, (b) large mass-splitting disquark, and (c) intermediate mass-splitting disquark.

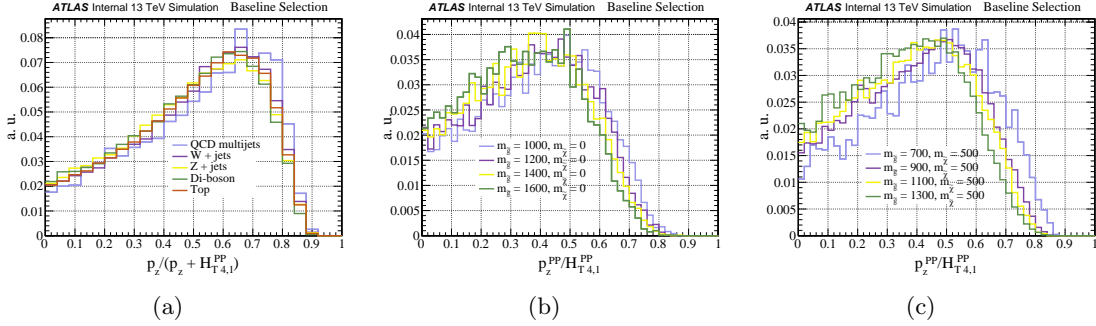


Figure 8.29. A distribution of  $p_z^{Lab} / (p_z^{Lab} / H_{T4,1}^{PP})$  for (a) BG, (b) large mass-splitting digluino, and (c) intermediate mass-splitting digluino.

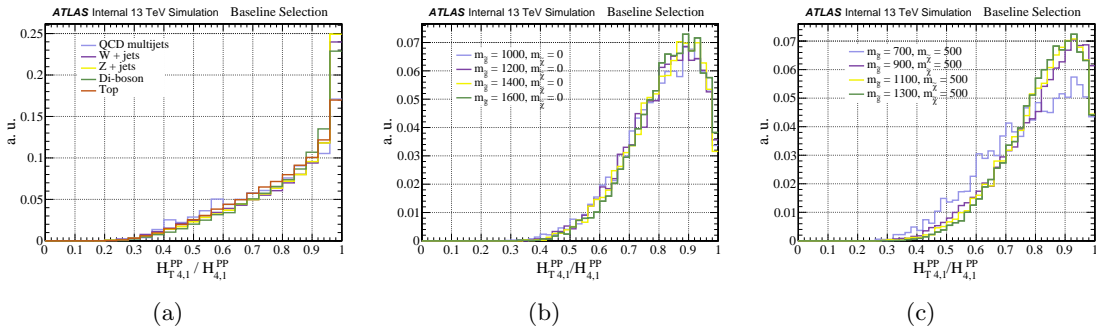


Figure 8.30. A distribution of  $H_{T4,1}^{PP} / H_{4,1}^{PP}$  for (a) BG, (b) large mass-splitting digluino, and (c) intermediate mass-splitting digluino.

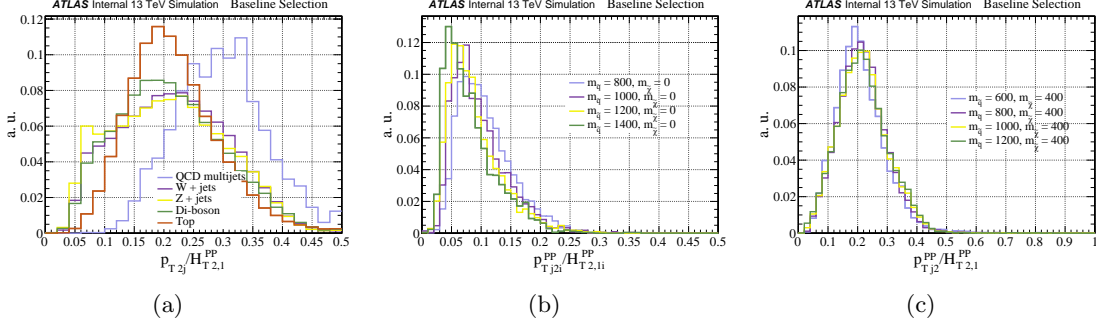


Figure 8.31. A distribution of  $p_{Tj_2}^{PP} / H_{T2,1}^{PP}$  for (a) BG, (b) large mass-splitting disquark, and (c) intermediate mass-splitting disquark.

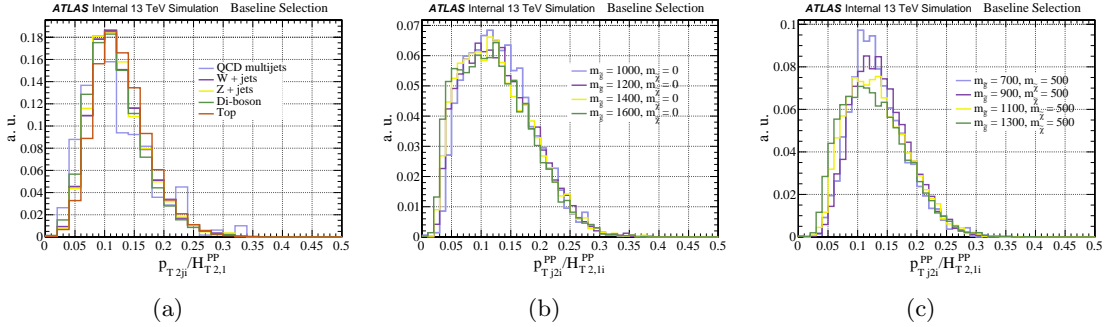


Figure 8.32. A distribution of  $p_{Tj_2}^{PP} / H_{T2,1}^{PP}$  for (a) BG, (b) large mass-splitting digluino, and (c) intermediate mass-splitting digluino.

### 8.6.5 QCD Multijet Rejection Method

To illustrate RJ effectiveness to isolate BG events, we consider compressed SUSY scenarios that appear nearly identical to the abundant QCD background. Particle interactions are inherently probabilistic and can populate the SRs despite attempts to approximate the complete system. Two types of QCD multijet background events contribute to this contamination. The first (Type A) are jets that are mismeasured, producing  $E_T^{\text{miss}}$  because the total energy is not measured well. The second (Type B) are jets that do not lie within a good acceptance range, producing  $E_T^{\text{miss}}$  because the total momenta is not known.

The standard approach to Type A events is to cut on  $\Delta\phi(\vec{p}_T, \vec{E}_T^{\text{miss}})$ . If  $E_T^{\text{miss}}$  points in the same direction as a jet, then it could indicate that the jet was mismeasured. The problem with this approach is that it is phenomenologically indiscriminate because it is

possible for a signal event to have jets randomly distributed in the same direction as  $E_T^{\text{miss}}$  or because several jets are equally mismeasured. This effect becomes worse as the number of jets increases and cutting on  $\Delta\phi(\vec{p}_T, \vec{E}_T^{\text{miss}})$  begins to look like a cut on the jet multiplicity. For signal regions that have many jets,  $\Delta\phi(\vec{p}_T, \vec{E}_T^{\text{miss}})$  is relaxed to avoid this conflict. An alternative is to only calculate  $\Delta\phi(\vec{p}_T, \vec{E}_T^{\text{miss}})$  using the first few jets in the event, but this becomes ineffective for events with many soft jets. This method has no answer to Type B events, which presents an unaccounted source of  $E_T^{\text{miss}}$  in most analyses.

Taking inspiration from the RJ method, we instead construct another set of observables aimed at determining how much an event looks like a BG-only hypothesis. We construct a self-assembling decay tree that has jets and  $E_T^{\text{miss}}$ . The Jigsaw algorithm dissects the event into binary branches that minimize the masses of intermediate jets to create a decay tree of association with  $E_T^{\text{miss}}$ .

For a dijet event, one can think of  $E_T^{\text{miss}}$  as due to one of three possibilities (Figure 8.33): (a) mismeasurement of  $p_T(j_1)$ , (b) mismeasurement of  $p_T(j_2)$ , or (c) an invisible particle. The signature involving an invisible particle is the type of event we want to keep while the other signatures could potentially be reduced.

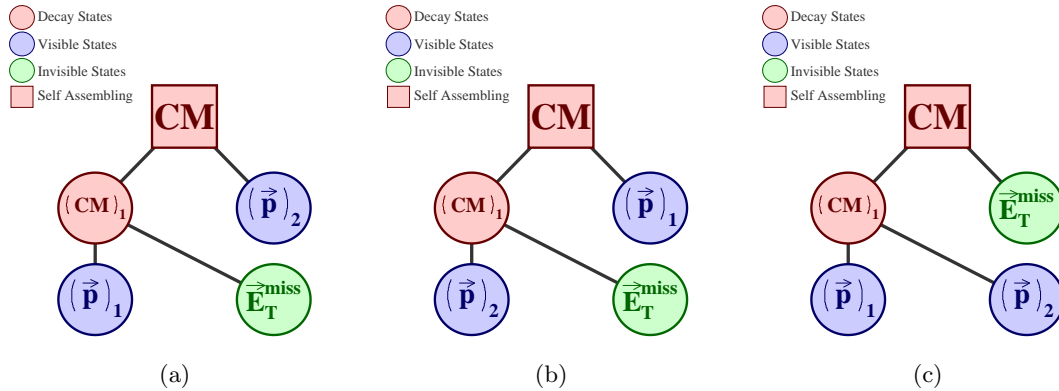


Figure 8.33. Three possible decay trees for reconstructing  $pp \rightarrow 2j + E_T^{\text{miss}}$ .

We label these diagrams by the association with  $E_T^{\text{miss}}$ . The source of  $E_T^{\text{miss}}$  comes from a parent frame and, if the decays are binary, the visible jet from the same parent is a

“sibling” to  $E_T^{\text{miss}}$ . In Figure 8.33, the siblings to  $E_T^{\text{miss}}$  are (a)  $p_T(j_1)$ , (b)  $p_T(j_2)$ , and (c) the parent frame of both jets. The event can even look far more complicated for an 8-jet event (Figure 8.34), but the principles are still the same.

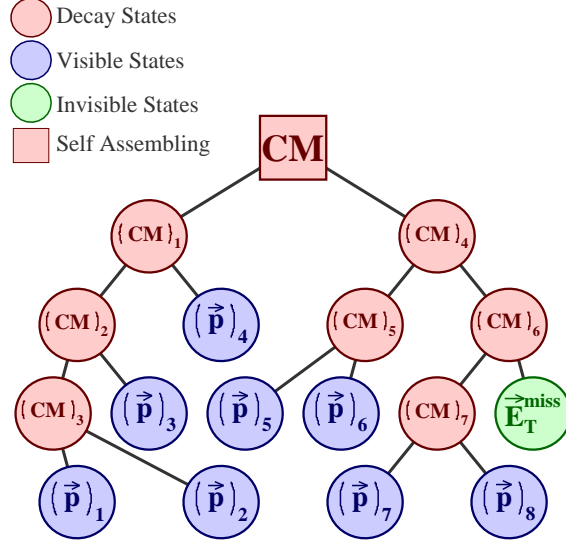


Figure 8.34. An example of a decay tree for reconstructing  $pp \rightarrow 8j + E_T^{\text{miss}}$ .

The ambiguities in kinematic and combinatoric quantities are resolved by a choice of Jigsaw algorithms. We determine if events have a large  $p_T$  or  $p_z$  relative to the mass of the system:

$$R_{p_T^{PP}, M_{PP}} \equiv \frac{p_{PP,T}^{\text{Lab}}}{p_{PP,T}^{\text{Lab}} + \frac{1}{4}M_{PP}} \quad (8.47)$$

$$R_{p_z^{PP}, M_{PP}} \equiv \frac{p_{PP,z}^{\text{Lab}}}{p_{PP,z}^{\text{Lab}} + \frac{1}{4}M_{PP}} \quad (8.48)$$

In the distribution of these variables (Figures 8.35 and 8.36), we note that they peak at different values for SUSY events:  $R_{p_T^{PP}, M_{PP}} \sim 0$  and  $R_{p_z^{PP}, M_{PP}} \sim 1$ .

By projecting  $E_T^{\text{miss}}$  onto the “sibling” jet momentum, we can calculate the fraction of  $E_T^{\text{miss}}$  that is associated with a particular jet.

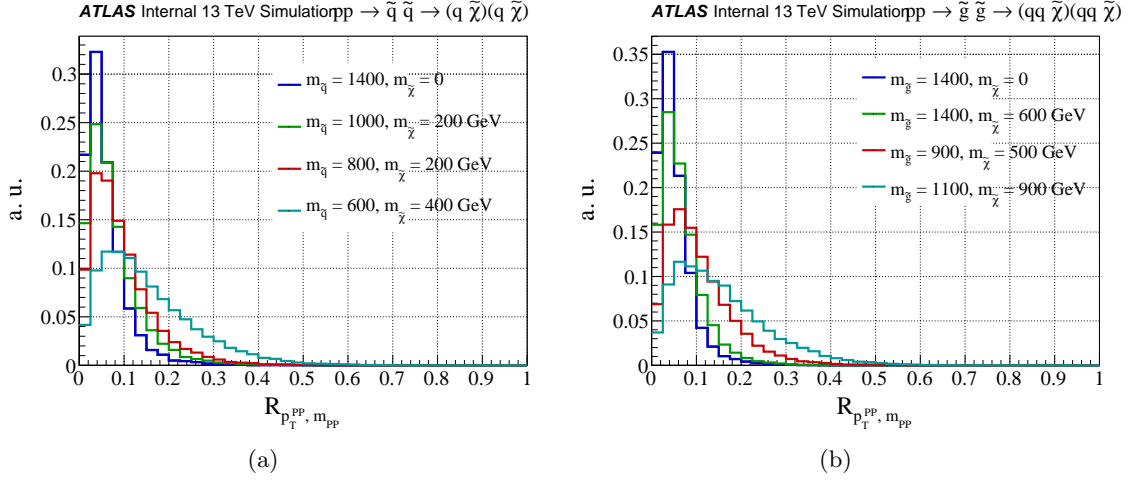


Figure 8.35. A distribution of  $R_{p_T^{PP}, M_{PP}}$  for (a)  $\tilde{q} \rightarrow q \tilde{\chi}_1^0$  and (b)  $\tilde{g} \rightarrow qq \tilde{\chi}_1^0$ .

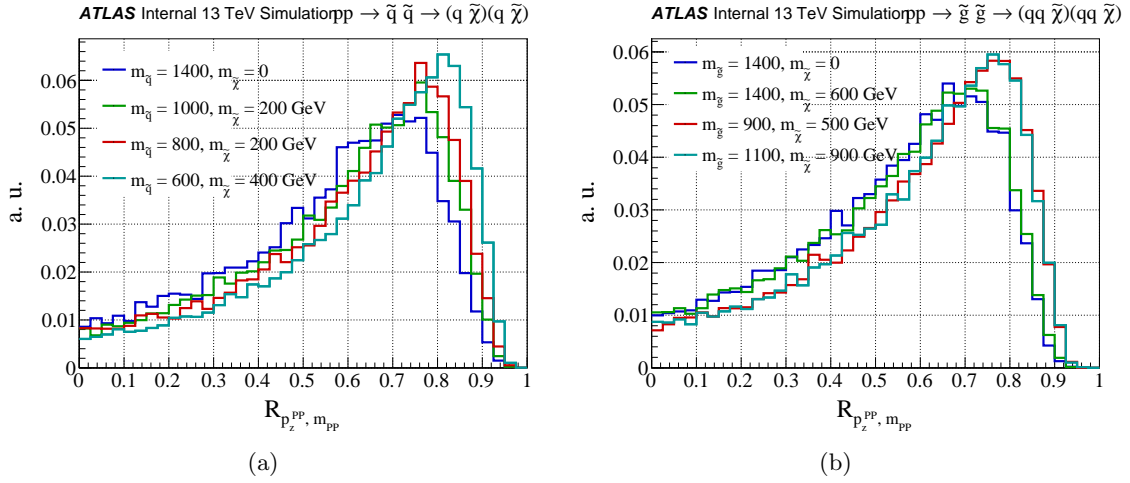


Figure 8.36. A distribution of  $R_{p_z^{PP}, M_{PP}}$  for (a)  $\tilde{q} \rightarrow q \tilde{\chi}_1^0$  and (b)  $\tilde{g} \rightarrow qq \tilde{\chi}_1^0$ .

$$R_{p_{sib}, E_T^{\text{miss}}} \equiv \frac{\vec{p}_{sib} \cdot \hat{E}_T^{\text{miss}}}{\vec{p}_{sib} \cdot \hat{E}_T^{\text{miss}} + E_T^{\text{miss}}} \quad (8.49)$$

We can also look at the decay angle by boosting into the sibling rest-frame:

$$\vec{\beta}_{sib, \text{miss}}^{Lab} \equiv \frac{\vec{p}_{sib} + \vec{E}_T^{\text{miss}}}{E_{sib} + E_T^{\text{miss}}} \quad (8.50)$$

$$\cos \theta_{p_{sib}, E_T^{\text{miss}}} \equiv \vec{\beta}_{sib, \text{miss}}^{Lab} \cdot \hat{p}_{sib}^{sib+\text{miss}} \quad (8.51)$$

Rather than attempt to analyze events with these variables that are highly correlated with each other, we look at their relative difference:

$$\Delta_{QCD} \equiv \frac{1 + \cos \theta_{p_{sib}, E_T^{\text{miss}}} - 2 R_{p_{sib}, E_T^{\text{miss}}}}{1 + \cos \theta_{p_{sib}, E_T^{\text{miss}}} + 2 R_{p_{sib}, E_T^{\text{miss}}}} \quad (8.52)$$

Each jet is compared to its sibling (“sibling rivalry”) to decide if the  $E_T^{\text{miss}}$  signature is due to the mismeasurement of either jet or if they are merely cousins to  $E_T^{\text{miss}}$ . If the jet is mismeasured such that the sibling system has a momentum colinear to  $E_T^{\text{miss}}$ , then  $R_{p_{sib}, E_T^{\text{miss}}} \sim 1$  and  $\Delta_{QCD} < 0$ . The correlation of these two variables can be found in Figure D.20.

For type B QCD events, the visible objects recoil from an unmeasured object, but this object is likely an object that we should be able to reconstruct if we knew its  $p_T$ .

$$p_{PP, T}^{Lab} = \vec{E}_T^{\text{miss}} + p_{V, T}^{Lab} \quad (8.53)$$

We use this “virtual” object as another object in the event to induce a correlation to the sum of visible momenta in the  $PP$  frame. An over-boost results in contralinear correlation while an under-boost is colinear. For this reason, QCD events tend to feature an accumulation of events with  $\Delta\phi_{PP, V} \sim 0$  or  $\Delta\phi_{PP, V} \sim 1$ , especially if a cut to  $R_{p_T^{PP}, M_{PP}}$  is applied first. This correlation is presented in Figure D.21.

## 8.7 Trigger Evolution

Because of the strong correlation between  $H_T$  and  $M_R$  for SUSY events (Figure D.6), it was assumed that an HLT trigger based on  $H_T$  would be appropriate for the 2011 Razor search (Chapter 9). This reasoning also carried into the 2012 Razor search (Chapter 10), but the performance for compressed models in the 0-lepton channel motivated a second trigger based on  $E_T^{\text{miss}}$ . It was hoped that one mass-scale trigger that was correlated to a

longitudinal variable would complement a trigger that was correlated to a transverse variable (Figure D.7). However, cuts designed to make either of these triggers efficient would bias the approximate boosts and induce complicated correlations that are not well-understood. To cover the phase space that would be lost, a trigger based on  $M_{\Delta}^R$  was proposed (Figure 8.37). Due to the timing of the work that went into the proposal, it was given the obsolete name of ‘‘Razor’’ trigger.

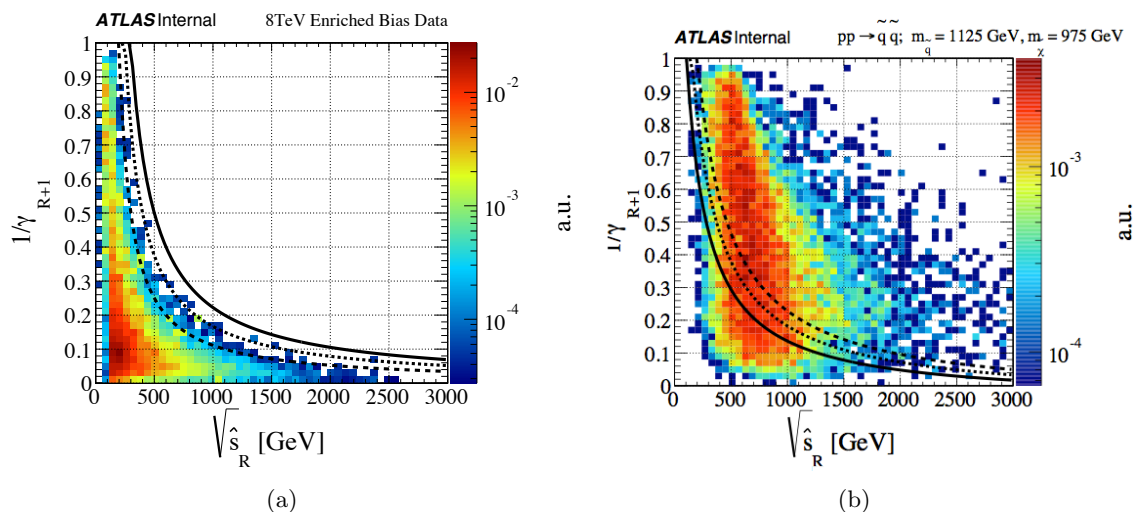


Figure 8.37. The trigger is based on the  $M_{\Delta}^R$  contours of the Super-Razor analysis plane (a) determined by the hyperbolic shape of enriched bias data and (b) discriminant to compressed SUSY.

The Razor trigger was designed for an improved HLT system that resulted in online variables that very closely resemble their offline counterparts (Figure 8.38). A Razor trigger for L1 was investigated, but the mass-minimization algorithm would limit the number of objects included too severely and possibly introduce unrecoverable biases that affect the RJ calculations.

### 8.7.1 L1 Seed

A preliminary L1 seed for the HLT Razor was HT200. Studies of the effect of  $H_T$  on  $M_{\Delta}^R$  (called  $\bar{\Pi}$  at the time) presented several problems. The first is that the offline efficiency

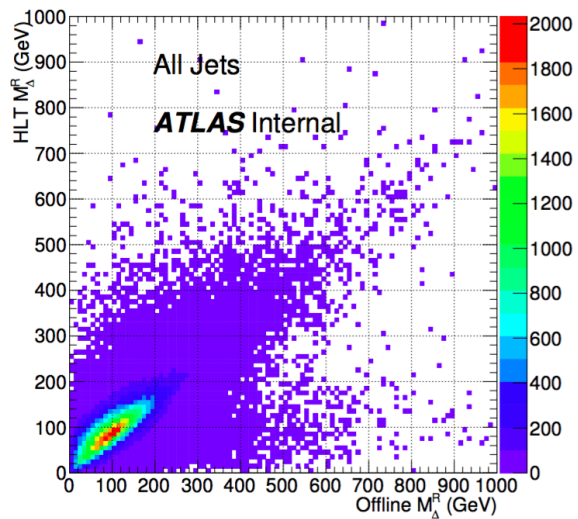


Figure 8.38. The correlation between HLT and offline definitions of  $M_{\Delta}^R$ .

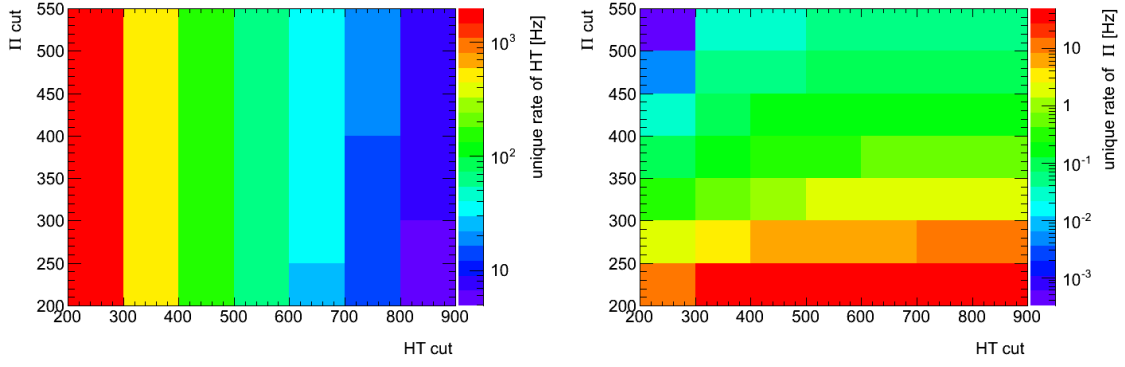
cuts for  $H_T$  needed to be very high (ultimately they exceeded  $H_T > 1000$  GeV) and events unique to lower  $\bar{\Pi}$  cuts could be kept if the  $H_T$  requirement was ignored. In fact, the two cuts seemed to have an orthogonal sensitivity as demonstrated by the overlapping rate (Figure 8.39).

The second problem was what happens to a typical measure of SUSY events such as  $E_T^{\text{miss}} / \sqrt{H_T}$ . The variable  $H_T$  does appear in this significance measurement, but it is not very sensitive to this scale in the low- $E_T^{\text{miss}}$  region of minimum bias events. Control over the trigger rate is achieved by cutting events across the spectrum. Instead,  $\bar{\Pi}$  cuts demonstrate a nice turn-on curve where the rate reduction is achieved by cutting events with low  $E_T^{\text{miss}} / \sqrt{H_T}$  similar to what an offline analysis would make anyway (Figure 8.40).

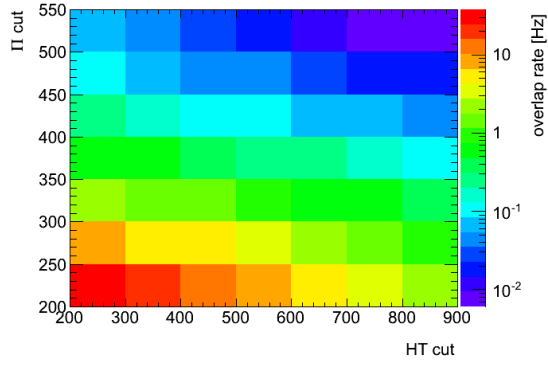
Lastly, cuts to  $H_T$  tended to remove a lot of acceptance and efficiency for SUSY models with large  $m_{\tilde{\chi}_1^0}$ . Considering the fact that the cut shown for  $H_T$  is actually quite low compared to the eventual conditions in the months to follow, this was one of the most compelling reasons to search for a new L1 seed (Figure 8.41).

The turn-on behavior of  $E_T^{\text{miss}} / \sqrt{H_T}$  suggests itself as a possible seed, but it is not necessary to have that much reconstructed information at L1. The RJ technique really only needs two jets and some  $E_T^{\text{miss}}$  to calculate all variables. Therefore, we requested a new



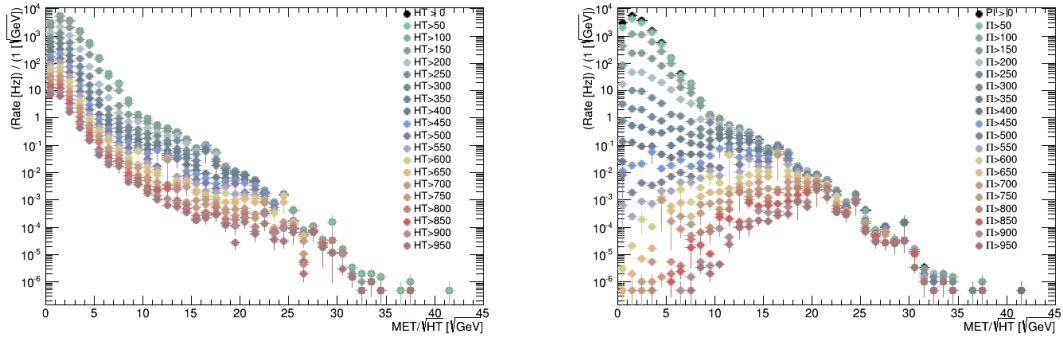


(a) (b)



(c)

Figure 8.39. A comparison of the rates after various  $H_T$  and  $\bar{\Pi}$  cuts expected for (a) unique events selected by  $H_T$ , (b) unique events selected by  $\bar{\Pi}$ , and (c) an overlap of events.



(a) (b)

Figure 8.40. A comparison of the rates of  $E_T^{\text{miss}} / \sqrt{H_T}$  of various cuts to (a)  $H_T$  and (b)  $\bar{\Pi}$ .

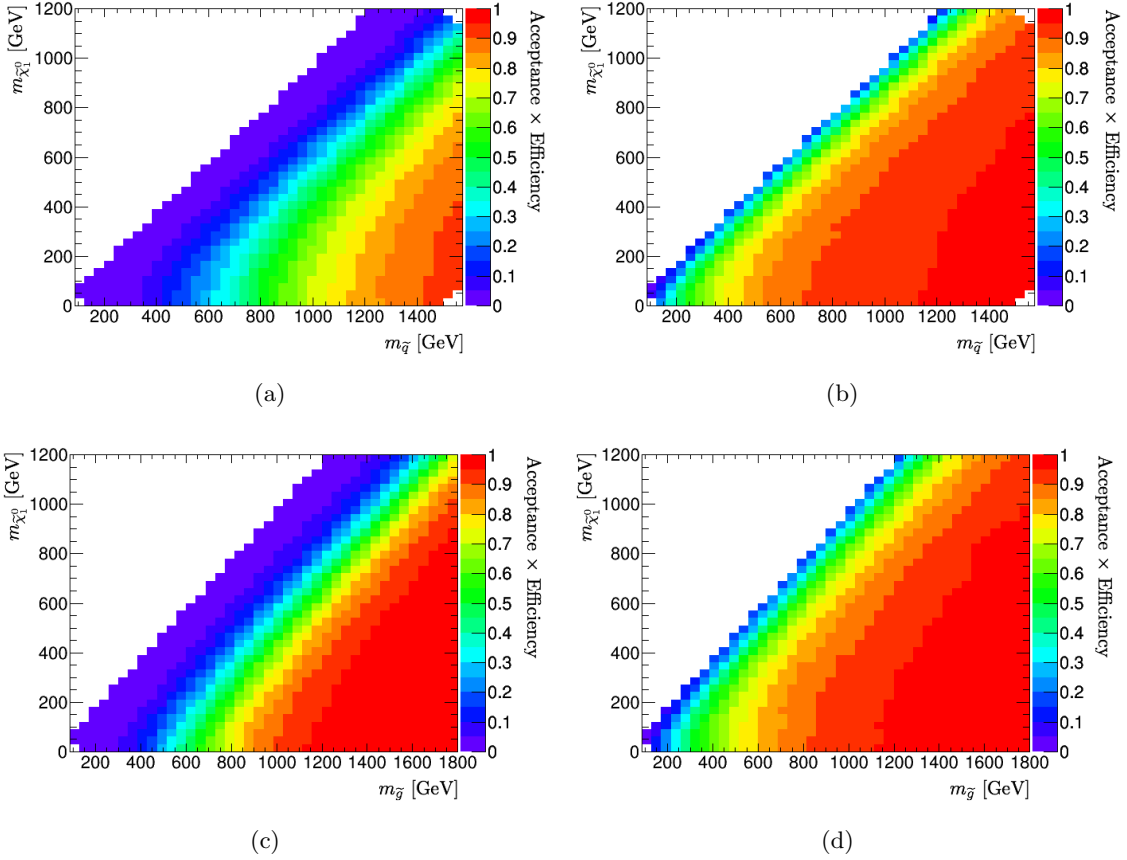


Figure 8.41. A comparison of the rates of acceptance  $\times$  efficiency after applying cuts (left)  $H_T > 800$  GeV and (right)  $\bar{\Pi} > 250$  GeV for (top)  $\tilde{q} \rightarrow q \tilde{\chi}_1^0$  and (bottom)  $\tilde{g} \rightarrow qq \tilde{\chi}_1^0$ .

L1 seed of 2J15\_XE55. The rate for this L1 seed was calculated to be  $976 \pm 13$  Hz at a luminosity of  $2 \times 10^{34} \text{ cm}^{-2}\text{s}^{-1}$ . Currently, only the Razor triggers use this seed.

### 8.7.2 Predictions of Performance

To predict the performance of a Razor trigger before validation samples were available, we built our own enriched bias using prescaled single-jet triggers in ranged  $p_T$  bins to form a smooth distribution in both  $p_T$  and  $E_T^{\text{miss}}$  (Figure 8.42). Note that the  $E_T^{\text{miss}}$  distribution shows a long exponential tail after the weak scale due to neutrino activity. The points that appear in excess of the overall sloping trend in both distributions come from individual

and isolated statistical fluctuations in the tail of an exponential drop but receive the full prescale weight that exceeds the (probably) true weight.

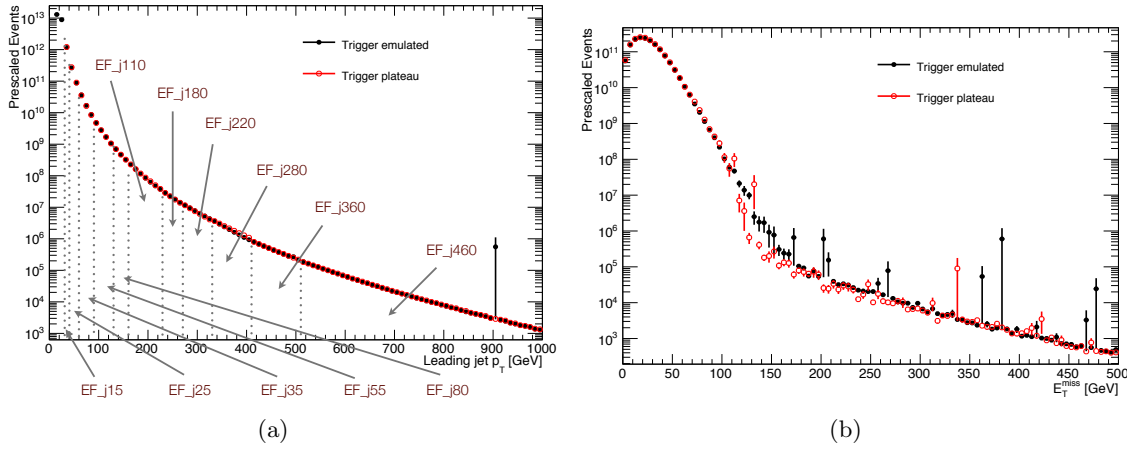
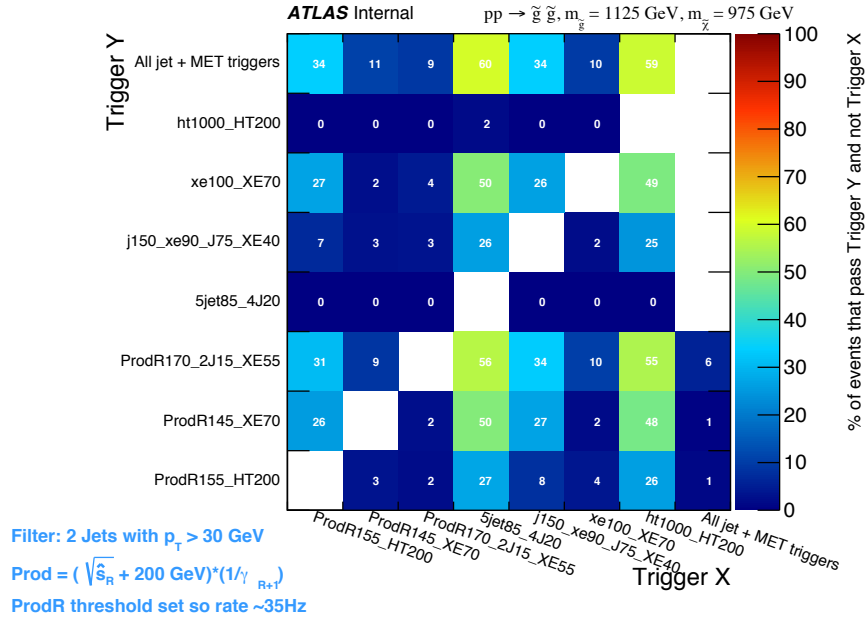


Figure 8.42. A distribution of the reconstructed prescaled data for (a)  $p_T$  and (b)  $E_T^{\text{miss}}$  for a preliminary validation of the trigger.

The Razor trigger was grouped with the jet+MET trigger category, which included an  $H_T$  trigger, an  $E_T^{\text{miss}}$  trigger, a single jet  $p_T + E_T^{\text{miss}}$  trigger, and a multijet trigger. In Figure 8.43, the unique rate of the Razor trigger (ProdR170) to select compressed  $\tilde{g}$  events out-performs an inclusive OR of all the other triggers by 6%. However, an analysis would not search for SUSY in such a disjointed mixture of  $p_T$ ,  $H_T$ , and  $E_T^{\text{miss}}$  requirements, but would separate them into different SRs. The most competitive trigger in the group is **xe100** at 10%. Also note that the HLT trigger based on HT200 ended up being **ht1000** and loses luminosity compared to the Razor trigger by 55%.

Therefore, it was necessary to demonstrate how a SUSY search would benefit from including the Razor trigger as compared to **xe100**. To present the trigger community with information to aid their decisions in keeping rate limits in check, we offered the sensitivity plots of Figure 8.44. In this figure, we present both a competing and a complementing look at the sensitivity. In the plots on the left, the two rates are compared as if **xe100** would be discarded. In compressed regions, the Razor trigger has  $\sim 30\%$  better sensitivity than



xe100 for  $\tilde{q}$  models and  $\sim 25\%$  for  $\tilde{g}$  models. On the right side of the figure, the compressed sensitivity doubles in both  $\tilde{q}$  and  $\tilde{g}$  models if both triggers are used to select SUSY events.

### 8.7.3 Trigger Validation

Once the trigger was proposed and accepted to the trigger menu for Run II by the collaboration, simulated samples were produced for the purposes of validating the behavior of every trigger. For the Razor trigger, we looked at a minimum bias sample, two  $t\bar{t}$  samples pertinent to the 2015 data (one for 50 ns bunch crossing and the other for 25 ns), and a direct-decay disquark sample with a squark mass of 1200 GeV and a  $\tilde{\chi}_1^0$  mass of 1050 GeV.

Prior to validation, it was suspected that the online and offline calculations of  $M_{\Delta}^R$  would not match due to refined object definitions during the triggering process. Initial estimates of the trigger efficiency used an offline definition for all objects and found an efficiency plateau of approximately 95%. The  $M_{\Delta}^R$  calculation requires at least two jets but the online acceptance range extends to  $|\eta| < 3.2$ , which is larger than our offline definition

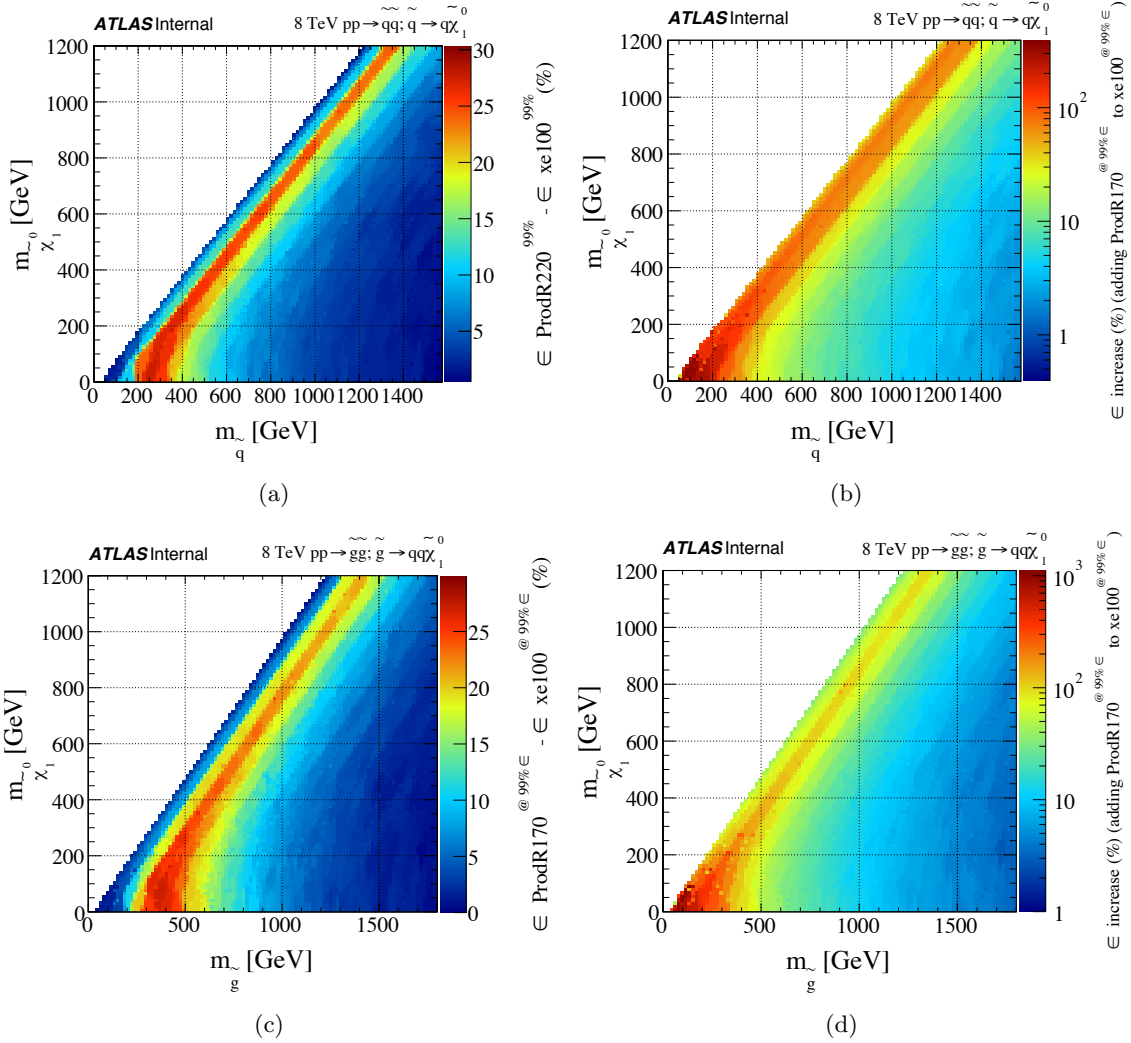


Figure 8.44. The acceptance  $\times$  efficiency increase if **xe100** and **razor170** (left) compete for rate and (right) complement each other for (top)  $\tilde{q} \rightarrow q\tilde{\chi}_1^0$  and (bottom)  $\tilde{g} \rightarrow qq\tilde{\chi}_1^0$ .

( $|\eta| < 2.5$ ). For validation, we then opened the range of our jet definition to include jets out to  $|\eta| < 3.2$ . Muons were not included in online definitions of  $E_T^{\text{miss}}$  so we also looked at removing muons from the offline definition.

Our first set of triggers were as follows:

- HLT\_j30\_xe10\_razor100
- HLT\_j30\_xe10\_razor170
- HLT\_j30\_xe10\_razor185

- HLT\_j30\_xe10\_razor195

The jet  $p_T$  requirement keeps the algorithm infrared-safe and the trigger rate under control. A limit of 10 jets can be analyzed by the mass-minimization algorithm while keeping the processing time low enough to function at the HLT timescale. A bug exists in the 2015 version of the trigger that needs a multijet trigger to catch events that have more than 10 jets.  $M_{\Delta}^R$  is systematically under-valued when events with more than 10 jets are limited to calculating only the leading 10, and the effect is not negligible (Figure 8.45).

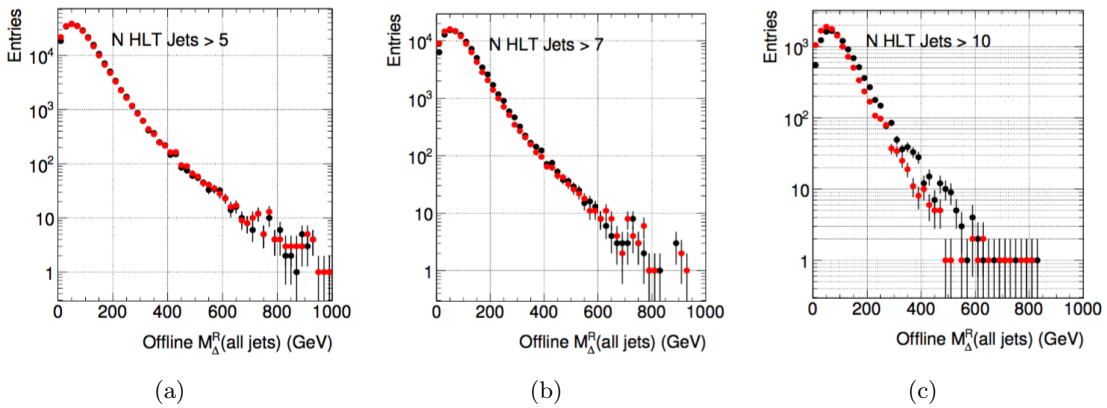


Figure 8.45. The distribution of  $M_{\Delta}^R$  using (black) all jets as compared to (red) only the leading  $N$  jets: (a)  $N > 5$  (b)  $N > 7$  (c)  $N > 10$ .

The 2016 version plans to treat these many-jet events as pass-through without running the full algorithm. The  $E_T^{\text{miss}}$  requirement was kept lower than the L0ne seed to avoid placing additional  $E_T^{\text{miss}}$  cuts at HLT. The lowest unprescaled trigger is intended to be **razor170** with a prescaled **razor100** and backups **razor185** and **razor195**.

From Figure 8.46, it was realized that the 5% inefficiency could be due to events indicated by the discontinuity with  $M_{\Delta}^R \sim 250$  GeV. These are events that pass the L1 seed but do not pass the HLT trigger. The distribution has an end-point at  $E_T^{\text{miss}} \sim 100$  GeV, which corresponds to  $E_T^{\text{miss}} \sim 60$  GeV at L1. For this reason, a revised set of triggers with **xe60** were requested.

- HLT\_j30\_xe60\_razor100

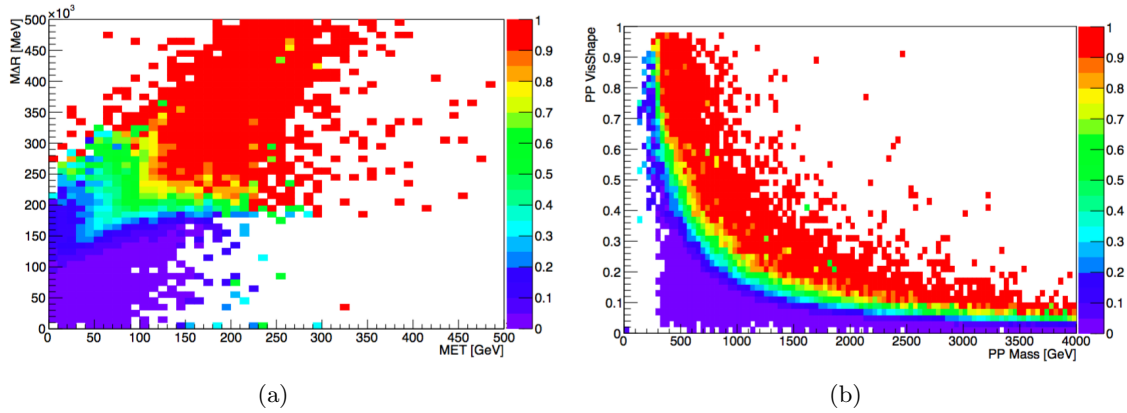


Figure 8.46. The efficiency of `razor170` in the (a) the  $M_{\Delta}^R$  versus  $E_T^{\text{miss}}$  plane and (b) the  $M_{PP}$  versus  $V_{S_{PP}}$  plane.

- `HLT_j30_xe60_razor170`
- `HLT_j30_xe60_razor185`
- `HLT_j30_xe60_razor195`

For offline analyses, a  $E_T^{\text{miss}} > 100$  GeV cut is recommended. This sharpened the turn-on curve without altering the efficiency point (Figure 8.47). Furthermore, it took the plateau from 95% to 100%. The reduction in low- $E_T^{\text{miss}}$  events had a significant improvement in trigger rate without placing additional requirements on  $M_{\Delta}^R$ .

The turn-ons of the other Razor triggers and `xe100` are shown in Figure 8.48 with a  $E_T^{\text{miss}} > 100$  GeV cut applied to the Razor triggers. The Razor triggers significantly out-perform `xe100` efficiency in the  $M_{\Delta}^R$  distribution. The difference in the cut required corresponds to a sensitivity increase of  $\Delta m_{\tilde{\chi}_1^0} \sim 100$  GeV. In the  $E_T^{\text{miss}}$  distribution,  $M_{\Delta}^R$  is not particularly sensitive to the  $E_T^{\text{miss}}$  efficiency, but `razor170` does have improved efficiency at  $\sim 120$  GeV.

#### 8.7.4 Trigger Performance

It was decided that an OR of the `razor170` and `xe100` would provide the best sensitivity (Figure 8.49). The acceptance  $\times$  efficiency plot shows good sensitivity in gluino production across the phase space except for the most compressed scenarios.

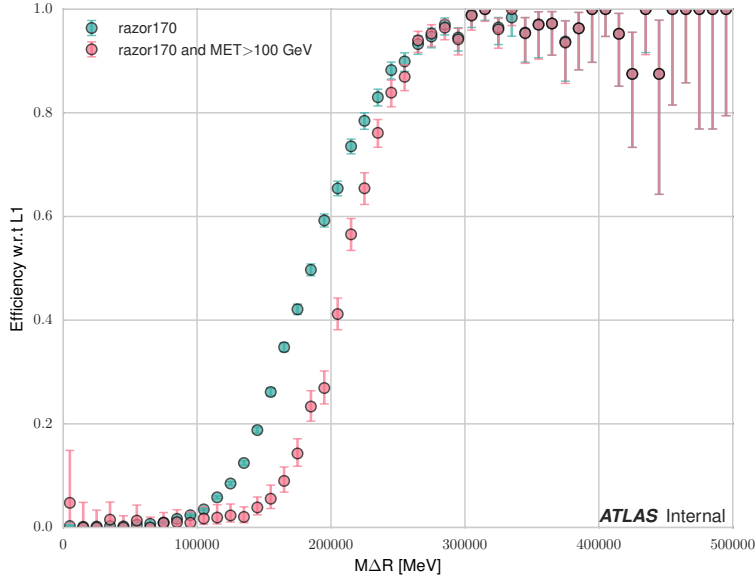


Figure 8.47. The efficiency of `razor170` with and without a  $E_T^{\text{miss}} > 100$  GeV cut.

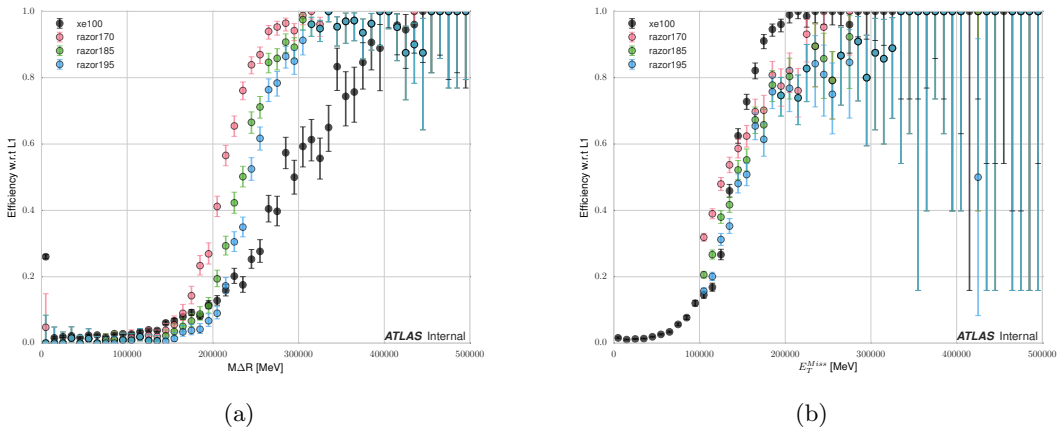


Figure 8.48. The efficiency of Razor and `xe100` triggers.

These triggers were validated with  $80.4 \text{ pb}^{-1}$  of integrated luminosity from 13 TeV data at 25 ns. The absolute rate for `razor170` was found to be  $\sim 20$  Hz at a luminosity of  $1 \times 10^{34} \text{ cm}^{-2}\text{s}^{-1}$ . For comparison, `j100_xe80` had an absolute rate  $\sim 40$  Hz and `xe100` was  $\sim 15$  Hz. The unique rate for `razor170` was lower at  $\sim 8$  Hz at  $1 \times 10^{34} \text{ cm}^{-2}\text{s}^{-1}$  and  $\sim 10$  Hz at  $2 \times 10^{34} \text{ cm}^{-2}\text{s}^{-1}$ .



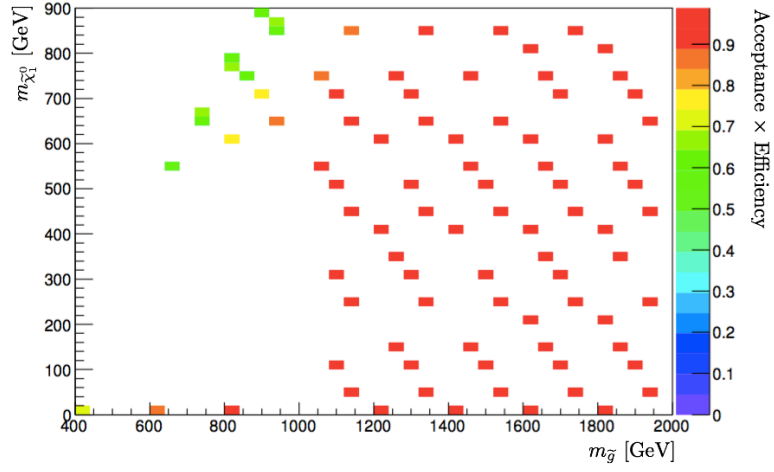


Figure 8.49. The acceptance  $\times$  efficiency of razor170 OR xe100 for  $\tilde{g} \rightarrow qq \tilde{\chi}_1^0$ .

## CHAPTER 9

### 2011 Razor Analysis

Now that all the supporting material is established, the multi-channel search for SUSY from the 2011 Run I of the LHC is presented in this chapter. This analysis was performed after the original Razor paper [92] and contributed to a few updates to the technique. Lessons learned in its implementation led to improvements that were incorporated into the Super Razor technique (Section 8.5). From 13 March 2011 to 30 October 2011 the LHC was configured for collisions with proton beams at 3.5 TeV per beam ( $\sqrt{s} = 7$  TeV) with 50 ns bunch spacing and 1380 bunches per beam. ATLAS was able to record  $4.7 \text{ fb}^{-1}$  of physics data. The results of this analysis were published in Reference [115] and parts of it are summarized below. The outline also includes references to the “standard” analyses in Reference [116–118].

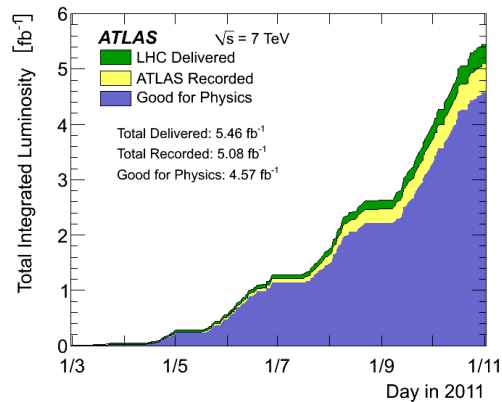


Figure 9.1. Timeline of integrated luminosity during 2011 data-taking run.

## 9.1 Trigger Choice

The trigger used for the 0-lepton channels was `EF_j100_a4tc_EFFS_ht400`. It requires at least one jet defined by the anti- $k_t$  algorithm with  $D = 0.4$  and a leading  $p_T > 100$  GeV and  $H_T > 400$  GeV formed at the EF level as the scalar sum of all jet  $p_T > 30$  GeV and  $|\eta| < 3.2$ . The efficiency of this trigger was tested using prescaled single-jet EF triggers (Figure 9.2). For SM BGs, the turn-on was steeper with increasing  $R$ , but the turn-on for SUSY was not altered significantly. This means that the trigger efficiency requirements can be adjusted based on the CR and SR requirements on  $R$ .

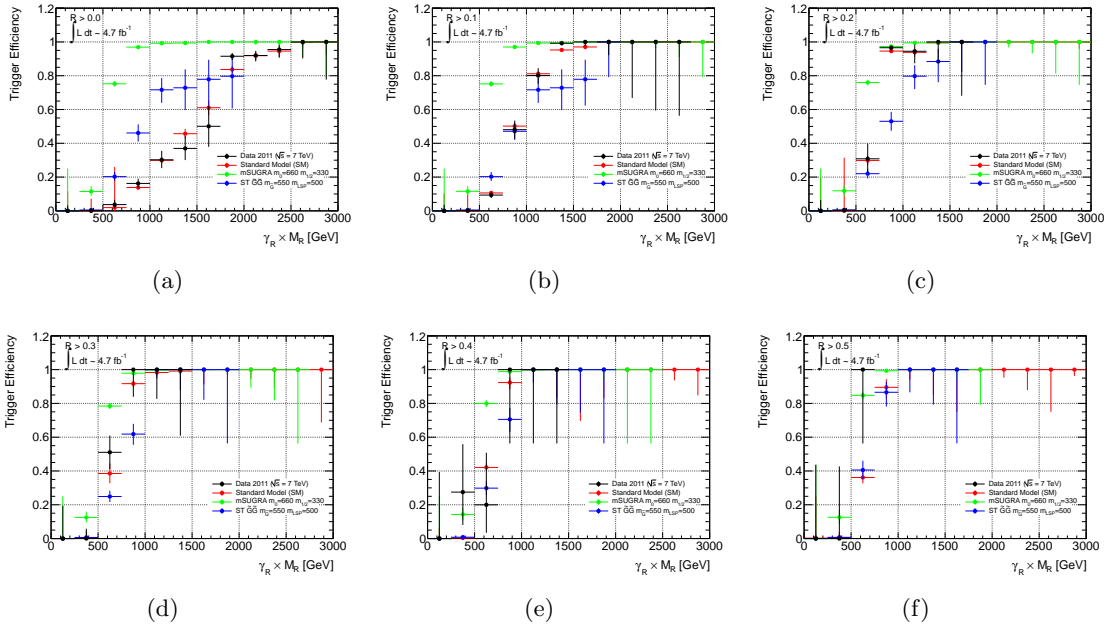


Figure 9.2. The efficiency of `EF_j100_a4tc_EFFS_ht400` for increasing  $R$ : (a)  $R > 0.0$ , (b)  $R > 0.1$ , (c)  $R > 0.2$ , (d)  $R > 0.3$ , (e)  $R > 0.4$ , (f)  $R > 0.5$ .

The triggers used for 1- and 2-lepton were the lowest unprescaled single-lepton triggers active during 2011. The electron trigger used for periods A-J was `e20_medium`. It requires at least one electron with  $p_T > 20$  GeV, which was increased to  $p_T > 22$  GeV for period K due to an increase in instantaneous luminosity. Periods L-M introduced a hadronic core isolation (`vh`) requirement that was combined with `e45_medium1` as recommended by the

electron trigger experts. The muon trigger used for period A-I was `mu18`, which requires at least one muon with  $p_T > 18$  GeV. Because of the increased rate, periods J-M used a `medium` definition with a higher L1  $p_T$  threshold as input to the HLT algorithms. These triggers were 100% efficient to the offline event selection without further cuts. The trigger selection is summarized in Table 9.1.

Table 9.1. Trigger selection for the 2011 analysis

trigger	integrated luminosity [ $\text{fb}^{-1}$ ]	periods
<code>e20_medium</code>	$1.69 \pm 0.07$	A-J
<code>e22_medium</code>	$0.59 \pm 0.02$	K
<code>e22_medium OR e45_medium1</code>	$2.43 \pm 0.09$	L-M
<code>mu18</code>	$1.46 \pm 0.06$	A-I
<code>mu18</code>	$3.24 \pm 0.13$	J-M
<code>j100_a4tc_EFFS_ht400</code>	$4.70 \pm 0.18$	A-M

## 9.2 Object Definitions and Event Selection

Electrons were defined following the recommendations of the EGamma group (Table 9.2). Muons were defined following the recommendations of the Muon Combined Performance group (Table 9.3). The electron  $\eta$  threshold used in the standard 0-lepton analysis was  $|\eta| < 2.5$ , but this was reduced to  $|\eta| < 2.4$  for this analysis to harmonize the definition between channels. Jets were defined following the recommendations of the Jet Performance group (Table 9.4). The JVF cut prevents photons without corresponding tracks from being classified as signal jets but these photons were not rejected. Recommendations from the  $b$ -tagging group lead to the definitions for  $b$ -jets.  $E_T^{\text{miss}}$  is calculated during the overlap process, but its definitions are listed in Table 9.5.

Once the objects were selected, overlap removal and event selection were applied:

1. If an event did not have a vertex, the event was discarded.
2. If an event had  $n_{\text{track}} < 5$  and  $p_T^{\text{track}} < 150$  MeV, the event was discarded.

Table 9.2. Summary of the electron definitions used in the 2011 analysis

Baseline Electron	
trigger	e20_medium (A-J) e22_medium (K) e22vh_medium1 (L-M) e45_medium1 (L-M) must have L2 seed match
algorithm	egamma
acceptance	$p_T > 10$ GeV if $S_i$ hits $> 3$ : $ \eta^{track}  < 2.47$ else: $ \eta^{cluster}  < 2.47$
quality	medium++
Signal Electron	
acceptance	if leading $e$ is leading $\ell$ : $p_T > 25$ GeV
quality	tight++
isolation	$p_T^{cone20}/p_T < 0.1$

Table 9.3. Summary of the muon definitions used in the 2011 analysis

Baseline Muons	
trigger	mu18 (A-I) mu18_medium (J-M) must have L2 seed match
algorithm	STACO
acceptance	$p_T > 10$ GeV $ \eta  < 2.4$
Signal Muons	
acceptance	if leading $\mu$ is leading $\ell$ : $p_T > 20$ GeV
quality	tight++
isolation	$p_T^{cone20}/p_T < 0.1$

3. If an event appeared to be cosmic ( $|z| > 10$  cm), the event was discarded.
4. If the event was flagged with a LAr hole veto (dead FEBS), the event was discarded.
5. If a baseline muon missed the PV by  $|d_0^{PV}| > 0.2$  mm and  $|z_0^{PV}| > 1$  mm, the event was discarded.
6. If a baseline muon was badly measured ( $\Delta_{q/p}/|q/p| \geq 0.2$ ), the event was discarded.

Table 9.4. Summary of the jet definitions used in the 2011 analysis

Baseline Jets	
trigger	j100_a4tc_EFFS_ht400
algorithm	anti- $k_t$ with $D = 0.4$ at EM scale calibrated with EM+JES scheme
acceptance	$p_T > 20$ GeV $ \eta  < 4.5$
quality	larError==0 tileError==0
Signal Jets	
acceptance	$ \eta  < 2.5$
track quality	$JVF > 0.75$
$b$ -Jets	
algorithm	JetFitter $\epsilon = 60\%$

Table 9.5. Summary of the  $E_T^{\text{miss}}$  definition used in the 2011 analysis

algorithm	Simplified20_Reffinal
baseline electrons	$E_T > 20$ GeV
baseline muons	includes non-isolated muons
baseline jets	EM+JES $p_T > 20$ GeV
CellOut	unaffiliated topo-clusters calibrated at EM scale

7. If two baseline electrons were within  $\Delta R_{\text{cone}} < 0.1$ , the electron with lowest  $E_T^{\text{cl}}$  was discarded.
8. If a baseline jet and a baseline electron were within  $\Delta R < 0.2$ , the jet was discarded.
9. If a baseline electron and a baseline jet were within  $\Delta R < 0.4$ , the electron was discarded.
10. If a baseline muon had  $p_T > 250$  GeV and was within  $\Delta R < 0.2$  of a baseline jet with  $p_T > 500$  GeV (punch-through), the muon was discarded.
11.  $E_T^{\text{miss}}$  and Razor variables were calculated.
12. If a baseline muon and a baseline jet were within  $\Delta R < 0.4$ , the muon was discarded.
13. If a baseline electron and a baseline muon were within  $\Delta R_{\text{cone}} < 0.1$ , both objects were discarded.

14. If the event contains a “very loose” bad jet or “ugly” jet with  $p_T > 20$  GeV, the event was discarded.
15. If an event does not have an MC event record, the event was discarded.
16. If an event was on a list for a GEANT4 energy non-conservation bug, the event was discarded.

### 9.3 Monte Carlo Samples

Data was compared to MC generator samples that pass through full simulation. For QCD, samples were separated by  $p_T$  for the hard  $2 \rightarrow 2$  scatter and the nine individual samples were then combined according to their cross-section as reported by PYTHIA. For the  $W + jets$ ,  $Z + jets$ , and top BGs, the samples were divided by the number of partons in the final state and were re-summed according to their cross-section as reported by ALPGEN, and k-factors were applied to scale the LO cross-sections. The mSUGRA grid was generated using HERWIG with a dense population of points at low mass. NLO cross-sections were generated for each point using PROSPINO. Three simplified models were considered:

- $\tilde{g} \rightarrow q \tilde{\chi}_1^0$  (only used in the 0-lepton channel)
- $\tilde{g} \rightarrow q \tilde{\chi}_1^\pm \rightarrow W \tilde{\chi}_1^0$  ( $m_{\tilde{\chi}_1^\pm} = (m_{\tilde{g}} + m_{\tilde{\chi}_1^0})/2$ )
- $\tilde{g} \rightarrow tt \tilde{\chi}_1^0$

For the 2-lepton channel, tau-enriched GMSB samples were used for the lepton-rich FSR. A summary of MC generators used in the analysis are shown in Figure 9.6.

### 9.4 Systematic Uncertainties

The standard systematic uncertainties (Sections 6.2 and 7.4) were applied to MC with a few details:

- JES - assumes an even mixture of quarks and gluons with no knowledge of the true flavor
- JER - each jet was smeared by a Gaussian distribution, and was considered as a one-sided systematic because MC resolution was always better than data

Table 9.6. Summary of MC generators used in the 2011 analysis

process	generators	cross-section [pb]	k-factor
QCD	PYTHIA	$9.86 \times 10^9$	–
$t\bar{t}$	ALPGEN + MC@NLO	166.8	–
$W + jets$	ALPGEN	$6.92 \times 10^3$	1.20
$WW + bb + jets$	ALPGEN	3.34	1.20
$Z + jets$	ALPGEN	$6.68 \times 10^2$	1.25
single top	MC@NLO	7.59	–
$tW$	MC@NLO	15.74	–
$WW$	HERWIG + ALPGEN	11.5	1.48
$WZ$	HERWIG + ALPGEN	3.46	1.60
$ZZ$	HERWIG + ALPGEN	0.972	1.30
mSUGRA	HERWIG + PROSPINO	various	–
ST	MADGRAPH + PROSPINO	various	–
GMSB	HERWIG + PROSPINO	various	–

- $b$ -tagging - variations to efficiency of light-quark mis-tagging, charm-quark tagging and mis-tagging, and  $b$ -quark tagging
- JVF - implemented as event weights: 1.02 for each passing jet, 0.8 for each failing jet
- $E_T^{\text{miss}}$  - included cell-out components and PU

The total uncertainty on the top cross-section, as recommended by the top group, was an asymmetric  $^{+16.5}_{-17.8}$  pb. Shape variations to the semi-leptonic top distributions were determined by variations to matching scale and factorization scale as recommended by the 1-lepton group. MC@NLO samples were used to cross-check for consistency. The cross-section uncertainty was conservatively estimated to be  $\pm 21$  pb. Shape variations to  $t\bar{t}$  were tested with ACERMC with ISR and FSR tuning, but very little difference was observed.

The  $W$  and  $Z$  cross-sections from the SUSY group were reported to be  $\pm 0.52$  pb. The diboson samples used a conservative 7% uncertainty. The production of  $W$  with heavy flavor were scaled by 1.63 for  $W + bb$ , 1.63 for  $W + cc$ , and 1.11 for  $W + c$ . The uncertainties for the production were  $^{+1.63}_{-0.76}$  for  $W + bb$ ,  $^{+1.63}_{-0.76}$  for  $W + cc$ ,  $^{+1.11}_{-0.35}$  for  $W + c$  and  $\pm 55\%$  for  $Z + bb$ . The  $p_T$  of  $Z$  bosons was mis-modeled in ALPGEN, so this value was reweighted



at the truth level according to SHERPA samples. The uncertainty was taken as half of the applied weight.

Electrons and jets can be faked by a failure in the reconstruction of jets. The matrix elements and identification efficiency are used to estimate “fake factors” from the fraction of jets that pass the loose selection criteria of leptons that also pass tighter selection.

For signal models, uncertainty starts with the calculation of statistical uncertainties at each point. This uncertainty varied greatly, but was typically  $\mathcal{O}(10\%)$ . Renormalization and factorization scales in the PROSPINO PDFs caused variations as well. They were typically the largest uncertainties, reaching  $\sim 30\%$ - $40\%$ . For the simplified models, the uncertainty from modeling ISR was taken to grow linearly from 0% at  $m_{heavy} > 400$  GeV to 20% at  $m_{heavy} = 200$  GeV, and from 0% at  $m_{heavy} - m_{\tilde{\chi}_1^0} > 150$  GeV to 20% at  $m_{heavy} = m_{\tilde{\chi}_1^0}$  (i.e. the maximum was 40% uncertainty). Lastly, the uncertainty on luminosity, which was 3.9%, was taken from the luminosity group recommendations.

## 9.5 Definition of Signal Regions

The 0-lepton channel was defined as having zero events with baseline leptons. Electrons with  $p_T < 10$  GeV and muons  $p_T < 10$  GeV can still be accepted into this channel, as can 25 GeV and 20 GeV if the lepton leads in  $p_T$  as described above). This channel could also include taus, because the definition of “lepton” as used in the channel selections only includes electrons and muons. The 1-lepton channel has only one baseline lepton and the 2-lepton channel has two. Events with high- $p_T$  leptons that were non-isolated do not fall into any channel.

There were two signal points chosen for the optimization of the 0-lepton SRs:

- mSUGRA  $A_0 = 0, \tan \beta = 10, \mu > 0$ 
  - $m_0 = 660$  GeV,  $m_{1/2} = 330$  GeV
- ST  $\tilde{g}\tilde{g} \rightarrow qq\tilde{\chi}_1^0\tilde{\chi}_1^0$ 
  - $m_{\tilde{g}} = 550$  GeV,  $m_{\tilde{\chi}_1^0} = 500$  GeV

There were four signal points chosen for the optimization of the 1-lepton SRs:

- mSUGRA  $A_0 = 0$ ,  $\tan \beta = 10$ ,  $\mu > 0$ 
  - $m_0 = 580$  GeV,  $m_{1/2} = 300$  GeV
  - $m_0 = 500$  GeV,  $m_{1/2} = 600$  GeV
  - $m_0 = 500$  GeV,  $m_{1/2} = 480$  GeV
- ST  $\tilde{g}\tilde{g} \rightarrow WW \tilde{\chi}_1^0 \tilde{\chi}_1^0$ 
  - $m_{\tilde{g}} = 665$  GeV,  $m_{\tilde{\chi}_1^\pm} = 385$  GeV,  $m_{\tilde{\chi}_1^0} = 105$  GeV

There were two signal points chosen for the optimization of the 2-lepton SRs:

- mSUGRA  $A_0 = 0$ ,  $\tan \beta = 10$ ,  $\mu > 0$ 
  - $m_0 = 340$  GeV,  $m_{1/2} = 330$  GeV
- GMSB  $\Lambda = 40$  TeV,  $\tan \beta = 15$

The 0- and 1-lepton channels use  $b$ -tagging to define a total of four distinct SRs. The 2-lepton channel was also distinct, but uses the sign of the leptons to define SRs: opposite sign (OS) and same sign (SS). The definitions are summarized in Table 9.7.

Table 9.7. SR definitions for 0-, 1-, and 2-lepton in 2011

leptons	jets	selection	$R$	$M_R$ [GeV]
0	$> 5$	$b$ -veto	$> 0.7$	$> 600$
		$b$ -tag	$> 0.4$	$> 900$
1	$> 0$	$b$ -veto	$> 0.55$	$> 500$
		$b$ -tag	$> 0.35$	$> 1000$
2	–	SS	$> 0.25$	$> 500$
		OS	$> 0.4$	$> 600$

The 0-lepton estimated number of counts in each SR is shown in Table 9.8. Dominant BGs in the  $b$ -veto SR were  $W$ +jets and  $Z$ +jets, although they were still quite low compared to the simulated signals. In the  $b$ -tag SR, the dominant BGs were multijets and  $t\bar{t}$  at a fairly significant count despite the multijet requirement of more than 5 jets.

The 1-lepton channel has a jet requirement because at least two objects are needed for the Razor calculations. The 1-lepton estimated number of counts in each SR is shown

Table 9.8. Estimated number of events in each signal region for 0-lepton in 2011

	SR0 $b$ -veto	SR0 $b$ -tag
multijets	$0.18 \pm 0.18$	$14.19 \pm 10.32$
$W$ +jets	$3.61 \pm 1.21$	$1.09 \pm 0.64$
$Z$ +jets	$1.87 \pm 0.63$	$0.25 \pm 0.25$
single top	$0.23 \pm 0.23$	$0.11 \pm 0.14$
$t\bar{t}$	$0.65 \pm 0.53$	$7.24 \pm 1.64$
diboson	$0.04 \pm 0.03$	$0.03 \pm 0.02$
total BG	$6.58 \pm 1.49$	$22.90 \pm 10.47$
mSUGRA 660, 330	$3.60 \pm 0.54$	$21.75 \pm 1.31$
ST $\tilde{g}\tilde{g}$ 550, 500	$8.40 \pm 1.89$	$1.30 \pm 0.75$

in Tables 9.9 and 9.10. Dominant BGs in both the  $b$ -veto and  $b$ -tag SRs were  $W \rightarrow e\nu$  and  $t\bar{t}$  at a comparable count to the simulated signals. A significant BG also comes from fake jets and electrons cause by a failure in the reconstruction of jets.

Table 9.9. Estimated number of events in each signal region for 1- $e$  in 2011

	SR1 $b$ -veto	SR1 $b$ -tag
fakes	$0.28 \pm 0.28$	$0.65 \pm 0.46$
$W \rightarrow e\nu$	$2.43 \pm 1.00$	$1.63 \pm 0.82$
$W \rightarrow \mu\nu$	$0.00 \pm 0.00$	$0.00 \pm 0.00$
$W \rightarrow \tau\nu$	$0.00 \pm 0.00$	$0.00 \pm 0.00$
$W$ +HF	$0.00 \pm 0.00$	$0.00 \pm 0.00$
$Z \rightarrow ee$	$0.00 \pm 0.00$	$0.00 \pm 0.00$
$Z \rightarrow \mu\mu$	$0.00 \pm 0.00$	$0.00 \pm 0.00$
$Z \rightarrow \tau\tau$	$0.00 \pm 0.00$	$0.00 \pm 0.00$
$t\bar{t}$	$2.91 \pm 1.31$	$5.50 \pm 1.43$
single top	$0.00 \pm 0.00$	$1.05 \pm 0.40$
diboson	$0.01 \pm 0.01$	$0.07 \pm 0.04$
total BG	$5.62 \pm 1.67$	$8.90 \pm 1.76$
mSUGRA 580, 300	$5.18 \pm 1.17$	$9.26 \pm 1.54$
mSUGRA 500, 600	$0.11 \pm 0.02$	$0.36 \pm 0.03$
mSUGRA 500, 480	$0.55 \pm 0.10$	$1.83 \pm 0.18$
ST $\tilde{g}\tilde{g}$ 1-step 665, 385, 105	$6.90 \pm 0.73$	$0.67 \pm 0.24$

Table 9.10. Estimated number of events in each signal region for  $1\text{-}\mu$  in 2011

	SR1 $b$ -veto	SR1 $b$ -tag
fakes	$0.00 \pm 0.00$	$0.00 \pm 0.00$
$W \rightarrow e\mu$	$0.00 \pm 0.00$	$0.00 \pm 0.00$
$W \rightarrow \mu\nu$	$2.11 \pm 0.95$	$1.07 \pm 0.65$
$W \rightarrow \tau\nu$	$0.00 \pm 0.00$	$0.49 \pm 0.49$
$W$ +HF	$0.00 \pm 0.00$	$0.45 \pm 0.45$
$Z \rightarrow ee$	$0.00 \pm 0.00$	$0.00 \pm 0.00$
$Z \rightarrow \mu\mu$	$0.00 \pm 0.00$	$0.00 \pm 0.00$
$Z \rightarrow \tau\tau$	$0.14 \pm 0.00$	$0.00 \pm 0.00$
$t\bar{t}$	$1.92 \pm 0.10$	$6.06 \pm 1.61$
single top	$0.26 \pm 0.19$	$0.37 \pm 0.25$
diboson	$0.01 \pm 0.01$	$0.02 \pm 0.01$
total BG	$4.45 \pm 1.47$	$8.46 \pm 1.88$
mSUGRA 580, 300	$6.92 \pm 1.44$	$7.93 \pm 1.50$
mSUGRA 500, 600	$0.09 \pm 0.02$	$0.34 \pm 0.03$
mSUGRA 500, 480	$0.46 \pm 0.18$	$1.67 \pm 0.18$
ST $\tilde{g}\tilde{g}$ 1-step 665, 385, 105	$5.54 \pm 0.66$	$0.34 \pm 0.17$

The 2-lepton estimated number of counts in each SR is shown in Tables 9.11-9.13. Dominant BGs in the SS SR were fakes and  $t\bar{t}$ . Dominant BGs in the OS SR were fakes and single top at a comparable count to the simulated signals.

Table 9.11. Estimated number of events in each signal region for  $e\text{-}e$  in 2011

	SR2 SS	SR2 OS
fakes	$3.65 \pm 1.21$	$1.16 \pm 0.66$
$Z \rightarrow ee$	$0.29 \pm 0.29$	$0.38 \pm 0.27$
$Z \rightarrow \mu\mu$	$0.00 \pm 0.00$	$0.00 \pm 0.00$
$Z \rightarrow \tau\tau$	$0.00 \pm 0.00$	$1.04 \pm 0.35$
$t\bar{t}$	$1.72 \pm 0.27$	$7.01 \pm 0.61$
single top	$0.00 \pm 0.00$	$1.35 \pm 0.39$
$WW$	$0.05 \pm 0.05$	$0.37 \pm 0.11$
$ZZ$	$0.05 \pm 0.03$	$0.07 \pm 0.04$
$WZ$	$0.24 \pm 0.08$	$0.21 \pm 0.07$
total BG	$5.99 \pm 1.28$	$11.59 \pm 1.08$
GMSB L40, T15	$14.80 \pm 1.15$	$10.02 \pm 0.97$
mSUGRA 340, 330	$2.20 \pm 0.75$	$3.93 \pm 0.99$

Table 9.12. Estimated number of events in each signal region for  $\mu\text{-}\mu$  in 2011

	SR2 SS	SR2 OS
fakes	$3.36 \pm 1.59$	$1.32 \pm 1.07$
$Z \rightarrow ee$	$0.00 \pm 0.00$	$0.00 \pm 0.00$
$Z \rightarrow \mu\mu$	$0.00 \pm 0.00$	$0.00 \pm 0.00$
$Z \rightarrow \tau\tau$	$0.00 \pm 0.00$	$1.00 \pm 0.33$
$t\bar{t}$	$0.07 \pm 0.05$	$8.29 \pm 0.62$
single top	$0.00 \pm 0.00$	$0.95 \pm 0.31$
$WW$	$0.00 \pm 0.00$	$0.42 \pm 0.12$
$ZZ$	$0.02 \pm 0.02$	$0.06 \pm 0.04$
$WZ$	$0.19 \pm 0.07$	$0.13 \pm 0.06$
total BG	$3.63 \pm 1.60$	$12.17 \pm 1.32$
GMSB L40 T15	$13.18 \pm 1.11$	$7.45 \pm 0.84$
mSUGRA 340, 330	$4.16 \pm 0.96$	$3.28 \pm 0.86$

Table 9.13. Estimated number of events in each signal region for  $e\text{-}\mu$  in 2011

	SR2 SS	SR2 OS
fakes	$10.59 \pm 2.54$	$0.57 \pm 0.40$
$Z \rightarrow ee$	$0.00 \pm 0.00$	$0.00 \pm 0.00$
$Z \rightarrow \mu\mu$	$0.00 \pm 0.00$	$0.00 \pm 0.00$
$Z \rightarrow \tau\tau$	$0.00 \pm 0.00$	$1.26 \pm 0.37$
$t\bar{t}$	$0.62 \pm 0.44$	$20.84 \pm 2.644$
single top	$0.00 \pm 0.00$	$1.67 \pm 0.41$
$WW$	$1.18 \pm 0.11$	$0.47 \pm 0.12$
$ZZ$	$0.00 \pm 0.00$	$0.04 \pm 0.03$
$WZ$	$0.36 \pm 0.10$	$0.10 \pm 0.05$
charge flip	$1.11 \pm 0.05$	$0.00 \pm 0.00$
total BG	$13.87 \pm 2.59$	$24.96 \pm 2.73$
GMSB L40, T15	$25.70 \pm 1.56$	$13.52 \pm 1.13$
mSUGRA 340, 330	$4.36 \pm 1.03$	$7.98 \pm 1.40$

## 9.6 Definition of Control and Validation Regions

Multijet CRs were defined from the 0-lepton channel with more than 5 jets, where QCD events were abundant, and were split into  $b$ -veto and  $b$ -tag regions. A table defining these regions is shown in Table 9.14.  $W + jets$  CRs were defined from the 1-lepton channel  $b$ -veto regions where  $W \rightarrow \ell\nu$  events were abundant. A table defining these regions is shown in Table 9.15.  $Z + jets$  CRs were defined from the 2-lepton channel where  $Z \rightarrow \ell\ell$  events were abundant. Charge flip BGs were also included. A table defining these regions is shown in Table 9.16. Top CRs were defined from the 1- 2-lepton channels with  $b$ -tag where  $t \rightarrow \ell b$  events were abundant. The validation regions were split between a semi-leptonic region with 1-lepton and two fully-leptonic regions with 2-leptons. A table defining these regions is shown in Table 9.17. Diagrammatic representations of all regions are shown in Figures 9.3-9.5.

Table 9.14. Multijet CR and VR definitions in 2011

region	$b$ -jets	leptons	$n_{jet}$	$R$	$M_R$ [GeV]
CR1	0	0	$> 5$	$0.3 < R < 0.4$	$800 < M_R < 2000$
CR2	$\geq 1$			$0.2 < R < 0.3$	$1000 < M_R < 2000$
VR1	0	0	$> 5$	$0.4 < R < 0.6$	$800 < M_R < 2000$
VR2	$\geq 1$			$0.3 < R < 0.4$	$1100 < M_R < 2000$

Table 9.15.  $W \rightarrow jets$  CR and VR definitions in 2011

region	$b$ -jets	leptons	$n_{jet}$	$M_R$ [GeV]
CR1	0	$e$	$> 5$	$300 < M_R < 400$
CR2		$\mu$		
VR	0	1	$> 5$	$400 < M_R < 550$

Table 9.16.  $Z \rightarrow jets$  CR definitions in 2011

region	leptons	$R$
CR1	$e^+e^-$	$R < 0.4$
CR2	$\mu^+\mu^-$	$R < 0.25$
charge flip	$e^\pm e^\pm$	$R < 0.25$

Table 9.17. Top CR and VR definitions in 2011

region	$b$ -jets	leptons	$n_{jet}$	$R$	$M_R$ [GeV]
CR1	$\geq 1$	$e$	$> 5$	-	$400 < M_R < 650$
CR2		$\mu$			
CR3		$e^+e^-$	-		
CR4		$\mu^+\mu^-$			
CR5		$e^\pm\mu^\mp$			
semi-lep VR	$\geq 1$	1	$> 5$	-	$700 < M_R < 850$
fully-lep VR1		$e^+e^-$ or $\mu^+\mu^-$	-	$0.3 < R < 0.4$	$400 < M_R$
fully-lep VR2		$e^\pm\mu^\mp$	-		-

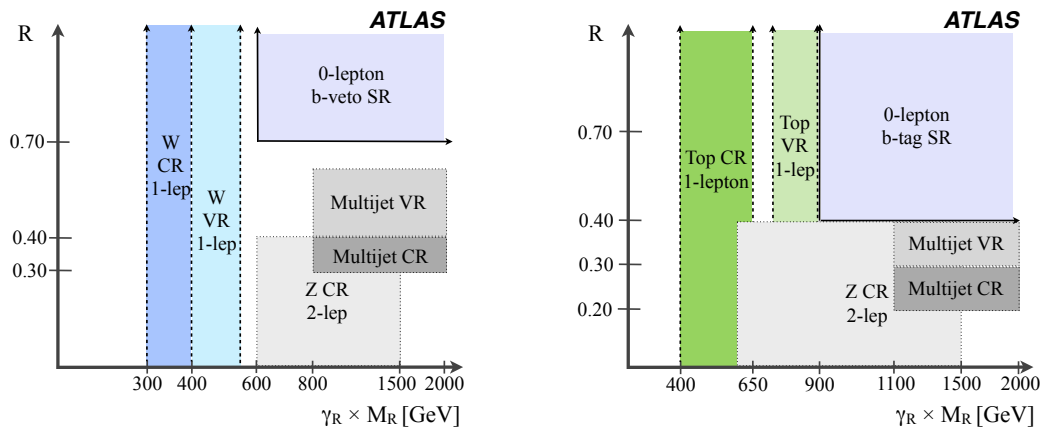


Figure 9.3. Schematic of CR, VR, and SR configurations used in the fit for 0-lepton in 2011.

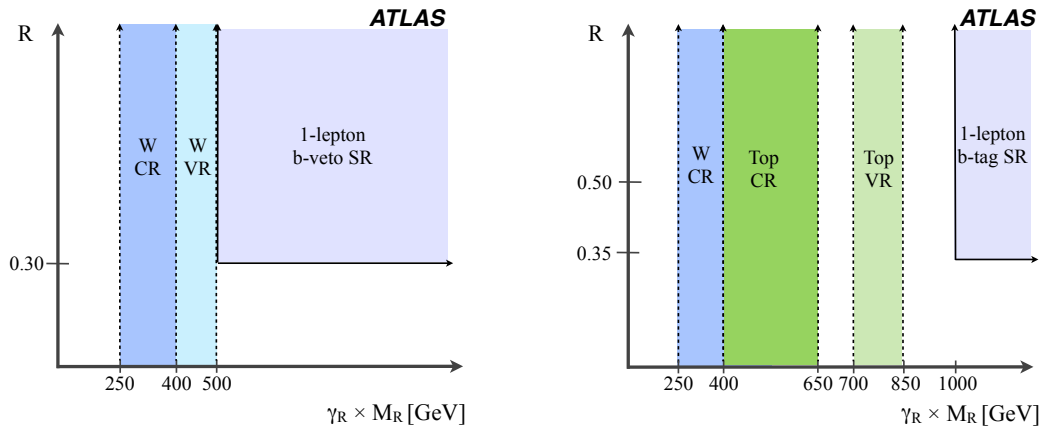


Figure 9.4. Schematic of CR, VR, and SR configurations used in the fit for 1-lepton in 2011.

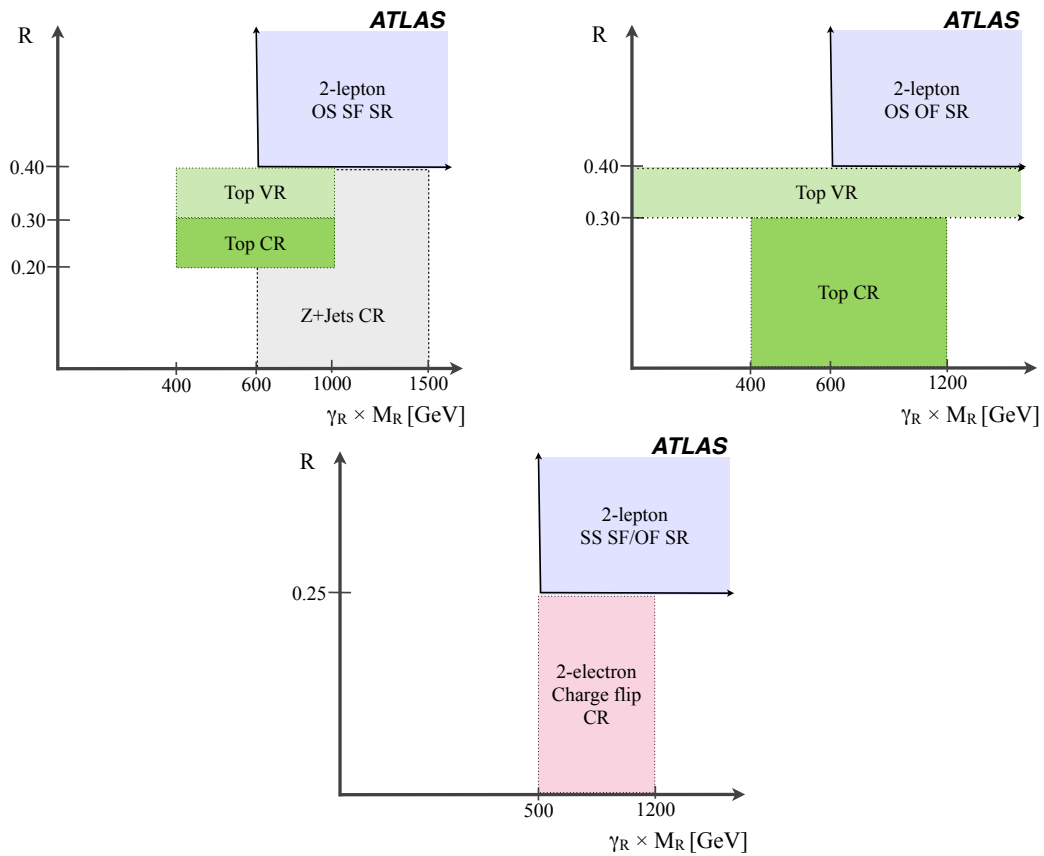


Figure 9.5. Schematic of CR, VR, and SR configurations used in the fit for 2-lepton in 2011.



## 9.7 Prescaled Data Validation

The 0-lepton  $b$ -veto had the most statistics, but the estimated number of QCD multijets that leak into the SR was  $0.18 \pm 0.18$  (Table 9.8). There were no ways to really get a perfect count of zero, but this is one of the ways to express “zero”. Even with a 100% uncertainty, there was predicted to be less than one QCD multijet BG in this SR. However, QCD MC is not exactly trustworthy due to the inexactness of a perturbative description of a purely hadronic event, and was not expected to closely reproduce large jet multiplicities found in data. For this reason, it was requested that other estimation methods be explored since our regions required more than 5 jets.

### 9.7.1 CMS Data-Driven Estimate

A method described by the original Razor paper explains the origin of its namesake. A distribution of  $M_R$  can be cut or “shaved” with the Razor variable  $R$ . This cut has the effect of sharpening the distribution of  $M_R$  (Figure 9.6).

This distribution was fit with a turn-on modeled by an asymmetric Gaussian plus an exponential tail. This piecewise definition was explicitly written as:

$$f(M_R) = \begin{cases} f_1(M_R) = N_1 \exp\left(-\frac{(M_R - \mu)^2}{2\sigma_1^2}\right) & M_R \leq \mu \\ f_2(M_R) = N_2 \exp\left(-\frac{(M_R - \mu)^2}{2\sigma_2^2}\right) & \mu < M_R < \nu \\ f_3(M_R) = N_3 \exp(S M_R) & M_R \geq \nu \end{cases} \quad (9.1)$$

The slope ( $S$ ) of the tail for each value of  $R$  was then plotted over an  $R^2$  axis. This relationship turns out to be linear, and the number of events can be extrapolated into the high- $M_R$  region. The estimate of the number of BG events was modeled by the piecewise function with all parameters set from the BG fit.

This type of method would not be allowed in ATLAS publications, because it is not data-blinded. The cuts were given as thresholds rather than exclusive bins (e.g.  $0.2 \leq R < 0.3$ ). As a result, all events up to a high- $R$  and high- $M_R$  (the SR) were being included in this

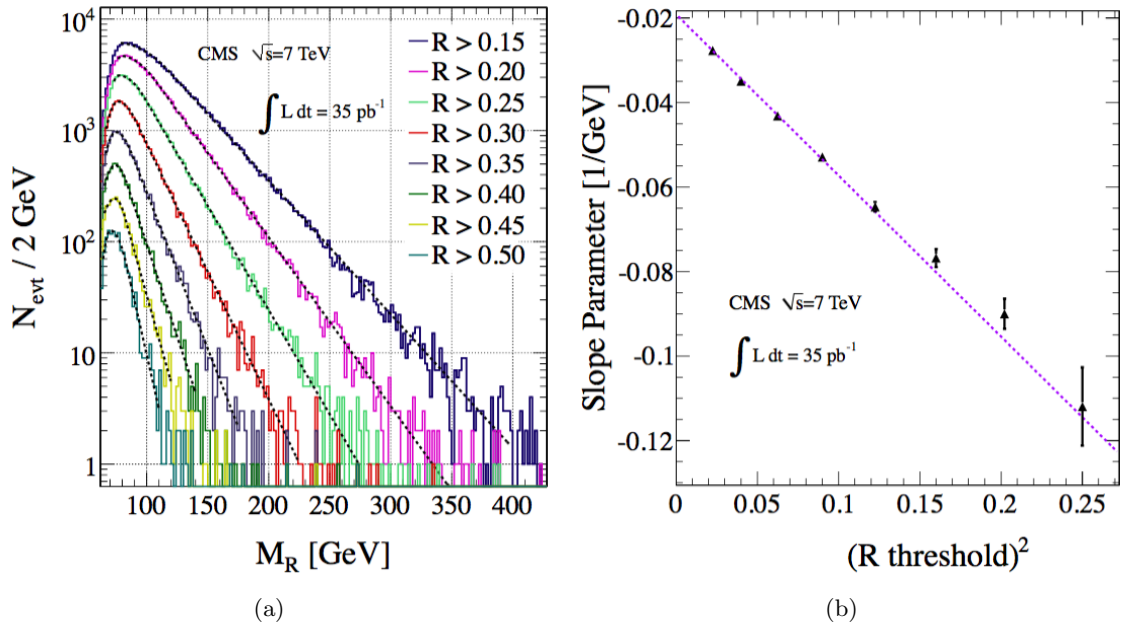


Figure 9.6. The QCD multijet estimate employed by CMS. In (a), the distribution of  $M_R$  is shown for increasing  $R$  cuts and (b) the slope of the exponential decay is plotted as a function of  $R^2$ .

[92]

estimate. The possible contamination is not something that can be ignored. For example, by including high- $M_R$  values while simultaneously making an inclusive cut of  $R > 0.5$ , this was essentially fitting signal events as if they were BGs.

### 9.7.2 Prescaled Data

Instead, a new method for this analysis was the use of prescaled data constructed from single-jet triggers with low- $p_T$  thresholds. At the start of designing this method, no such study had been performed. The single-jet triggers were binned in  $p_T$  so that they were at least 99% efficient as determined by the jet trigger group, but no two trigger bins overlap (Table 9.18).

The prescaled data was validated according to the  $p_T$  spectrum, which should appear smooth (Figure 9.7).

Table 9.18. Prescaled triggers and their 99% efficiency bins in  $p_T$

trigger	jet $p_T$ bin [GeV]
EF_j10_a4tc_EFFS	$37.5 \leq p_T < 50$
EF_j15_a4tc_EFFS	$50 \leq p_T < 60$
EF_j20_a4tc_EFFS	$60 \leq p_T < 72.5$
EF_j30_a4tc_EFFS	$72.5 \leq p_T < 202.5$
EF_j100_a4tc_EFFS	$p_T \geq 202.5$

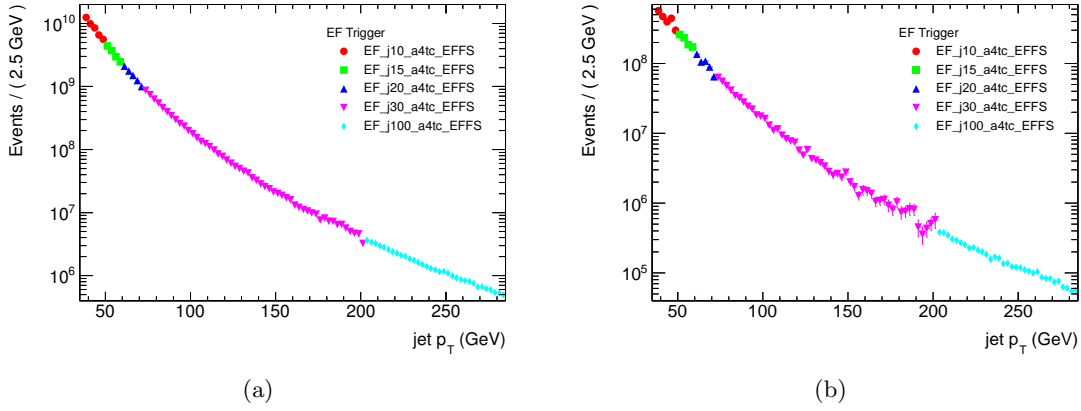


Figure 9.7. The  $p_T$  spectrum built from prescaled single-jet triggers for (a)  $b$ -veto and (b)  $b$ -tag.

This prescaled data could then represent a QCD-rich BG to vastly increase the number of statistics available to estimate the events that appear in the SR. This sample of low- $R$ , low- $M_R$ , and low- $n_{jet}$  data would have to be projected into a modified 3-dimensional version of the ABCD method to estimate the count in a high- $R$ , high- $M_R$ , and high- $n_{jet}$  SR.

### 9.7.3 Modified ABCD

The agreement between prescaled data and unprescaled trigger data was determined from these two types of efficiency plots. The best points were:

- $b$ -veto:  $M_R > 996$  GeV
- $b$ -tag:  $M_R > 908$  GeV

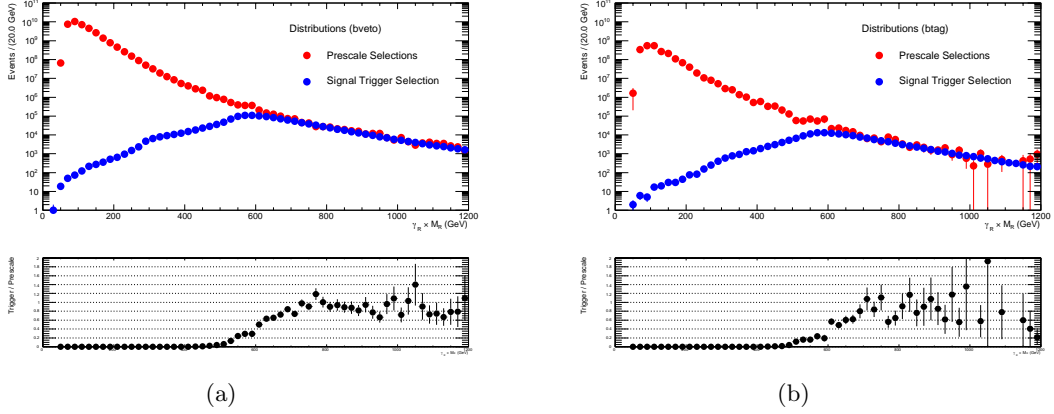


Figure 9.8. The  $M_R$  spectrum comparing single-jet trigger preselections with the 0-lepton signal trigger for (a)  $b$ -veto and (b)  $b$ -tag.

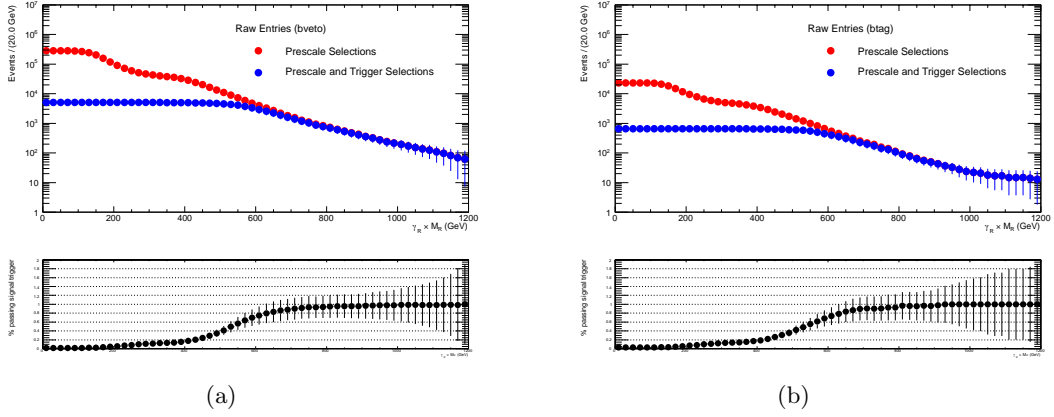


Figure 9.9. The percentage of events passing the 0-lepton signal trigger compared to the single-jet trigger preselections for (a)  $b$ -veto and (b)  $b$ -tag.

A combined data set was used where the  $M_R$  values below these points came from prescaled data, and events above this value came from triggered events that had better statistics in the tails. Two QCD CRs were defined as they appear in Table 9.19.

Table 9.19. A CR using prescaled data designed for QCD multijets

$b$ -jets	$M_R$ [GeV]	$R$	$n_{jet}$
veto	$120 \leq M_R \leq 600$	$0.2 \leq R \leq 0.4$	$2 \leq n_{jet} \leq 5$
tag	$120 \leq M_R \leq 1100$		

With three variables, this approach needed to modify the ABCD method. It was rather tricky to choose the transfer region, where the MC was scaled to data. In certain regions, such as high- $R$ , low- $M_R$ , and high- $n_{jet}$ , there were simply no data events with which to compare. Therefore, it was not a three-step transfer as was originally thought, but relied on the distributions to support a diagonal transfer from low- $R$  to high- $R$  in separate planes of  $n_{jet}$ . A diagrammatic explanation of this complication is shown in Figure 9.10.

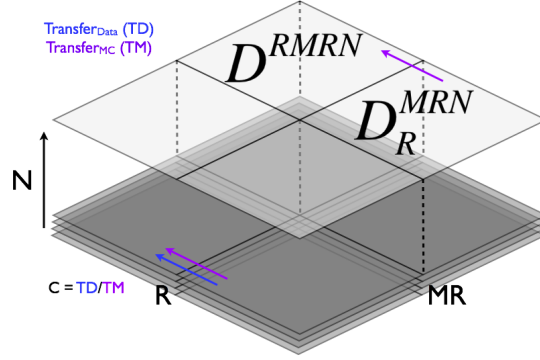


Figure 9.10. A validation of the prescaled data estimate of multijet BG events using a modified ABCD method.

The number of data events expected in the high- $R$ , high- $M_R$ , high- $n_{jet}$  SR ( $D^{R,MR,N}$ ) were estimated using the number of events in a low- $R$ , high- $M_R$ , high- $n_{jet}$  data CR ( $D_R^{MR,N}$ ) with a transfer factor from MC simulation ( $TM^{MR,N}$ ). This estimate was corrected by the ratio of transfer factors from regions of low- $M_R$  and low- $n_{jet}$  in data ( $TD_{MR,N}$ ) and MC simulation ( $TM_{MR,N}$ ).

$$\begin{aligned}
 D^{R,MR,N} &= D_R^{MR,N} \times TM^{MR,N} \times C_{MR,N} \\
 &= D_R^{MR,N} \times TM^{MR,N} \times \frac{TD_{MR,N}}{TM_{MR,N}} \\
 &= D_R^{MR,N} \times \frac{MC^{R,MR,N}}{MC_R^{MR,N}} \times \frac{D_{R,MR,N}/D_{MR,N}^R}{MC_{R,MR,N}/MC_{MR,N}^R}
 \end{aligned} \tag{9.2}$$

#### 9.7.4 MC Cleaning

Spikes in the MC distribution were identified by fitting the distribution to a double Gaussian. Events were inspected and removed if it was determined that they lay outside of an acceptable fit. Table 9.20 shows how this cleaning affected the estimated number of multijet events in the 0-lepton CRs.

Table 9.20. Estimated number of multijet events in the 0-lepton SRs with and without MC cleaning

	without cleaning	with cleaning
$b$ -veto	$0.0895 \pm 0.0955$	$0.0900 \pm 0.0960$
$b$ -tag	$15.489 \pm 11.672$	$4.141 \pm 1.128$

#### 9.7.5 Data Scaling

It was assumed that the prescaled region was dominated by QCD multijet events, but the other regions used in the fit were not checked for their QCD-richness. The percentage of MC multijet events in each region was used to scale the data as an estimate of how many data points actually came from this BG. A Table of the scale factors is provided in Table 9.21.

Table 9.21. Data scale factors used for the estimate of multijet events in the 0-lepton SR

	$b$ -veto	$b$ -tag
$D_{R,MR,N}$	0.9995	0.9995
$D_{MR,N}$	0.5947	0.0059
$D_R^{MR,N}$	0.7604	0.9665

With this data scaling applied, the estimate was repeated once more, and the results are shown in Table 9.22.

Table 9.22. Estimated number of multijet events in the 0-lepton SR with and without data scaling

	without scaling	with scaling
$b$ -veto	$0.0895 \pm 0.0955$	$0.0522 \pm 0.0594$
$b$ -tag	$15.489 \pm 11.672$	$11.7338 \pm 8.9891$

### 9.7.6 Comparison to Other Methods

A bit of a conundrum exists when a validation method needs to be validated because it's new. Ultimately, the HistFitter package became available and it was decided that a HistFitter approach (Figure 9.11) or alternate generator was needed to check for consistency.

Table 9.23. Estimations of multijet event counts in SRs by various methods

method	$b$ -veto	$b$ -tag	notes
HistFitter	$0.25 \pm 0.12$	$11.9 \pm 5.9$	–
prescaled triggers	$0.09 \pm 0.09$	$15.5 \pm 11.7$	without cleaning
prescaled triggers	$0.09 \pm 0.09$	$4.1 \pm 1.1$	with cleaning
split PYTHIA	$0.27 \pm 0.15$	$8.3 \pm 6.8$	–
$n_{jet}$ fit	$0.23 \pm 0.13$	$5.7 \pm 2.7$	–
jet smearing	$0.41 \pm 0.06$	$9.5 \pm 0.3$	statistical uncertainties
ALPGEN	0.0	$15.3 \pm 3.7$	–

As can be seen from Table 9.23, there were indeed several ways to say “zero” events for the  $b$ -veto region. The estimate using prescaled data sets an ambitiously low estimate but still has  $\sim 100\%$  uncertainty. The estimate for  $b$ -tag was fairly reasonable (with cleaning) but it was also the lowest estimate. Ultimately, the lack of statistics after the required  $n_{jet}$  cut doomed this method.

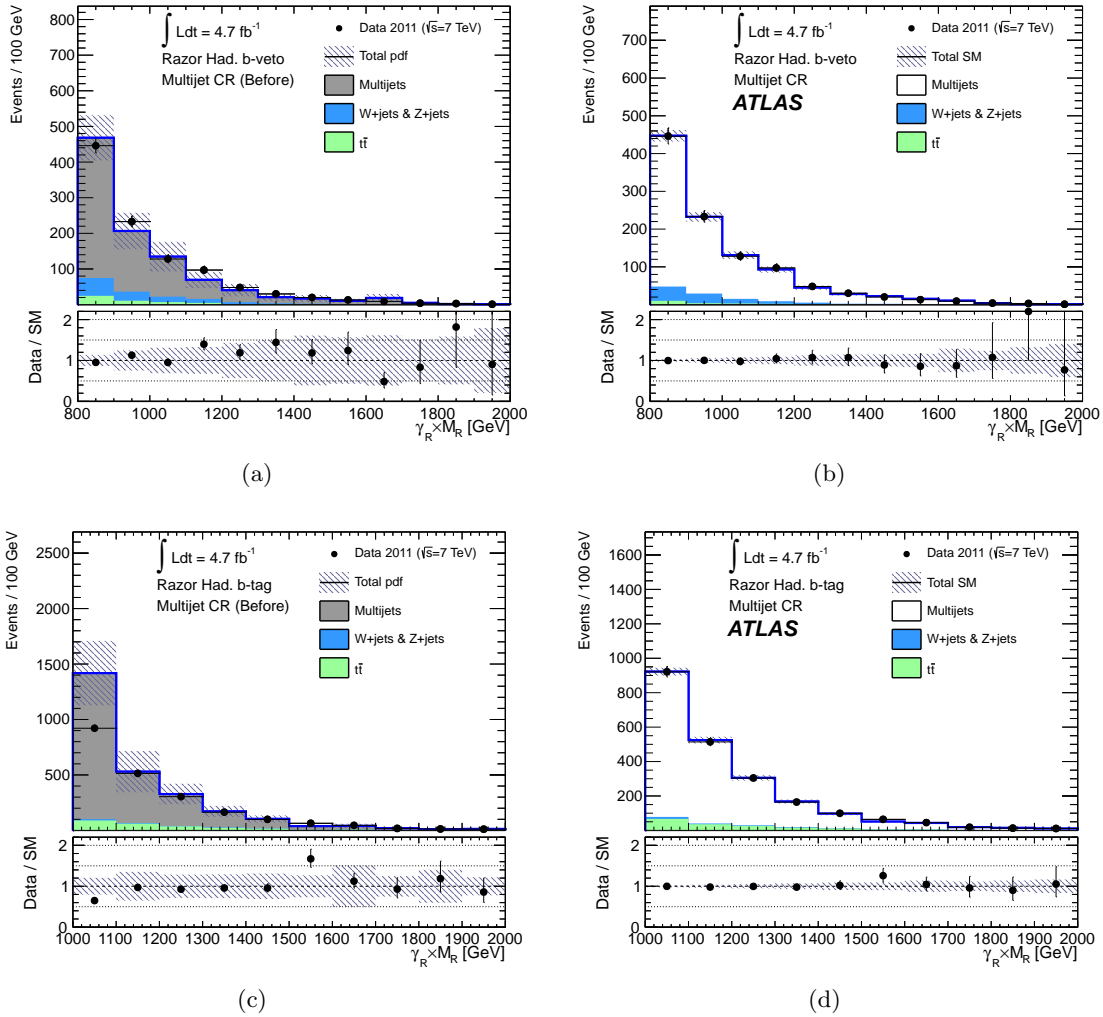


Figure 9.11. The BG estimate of the multijet CRs (left) before and (right) after fit for (top) *b*-veto and (bottom) *b*-tag.

## 9.8 Background CR Fit

The CR BG fit estimation used a variety of methods, which are given in Table 9.24. Where applicable, the HistFitter results before and after the CR BG fit are shown in Figures 9.12-9.17.

A count of MC expectation and BG fit for the number of events in each region is shown in Tables 9.25 and 9.26.



Table 9.24. Estimation methods used in the BG fit in 2011

BG	0-lepton	1-lepton	2-lepton
multijets	MJ CRs	matrix method	matrix method
$W \rightarrow \ell\nu$	$W$ CRs	$W$ CRs	matrix method
$Z \rightarrow \ell\ell$	$Z$ CRs	$Z$ CRs	$Z$ CRs
$\gamma + jets$	$Z$ CRs	$Z$ CRs	$Z$ CRs
$Z \rightarrow \nu\nu$	$Z$ CRs	matrix method	matrix method
$t\bar{t}$	$t\bar{t}$ CRs	$t\bar{t}$ CRs	$t\bar{t}$ CRs
single top	$t\bar{t}$ CRs	$t\bar{t}$ CRs	$t\bar{t}$ CRs
$WW$	MC	MC	MC
other dibosons	$Z$ CRs	$Z$ CRs	$Z$ CRs

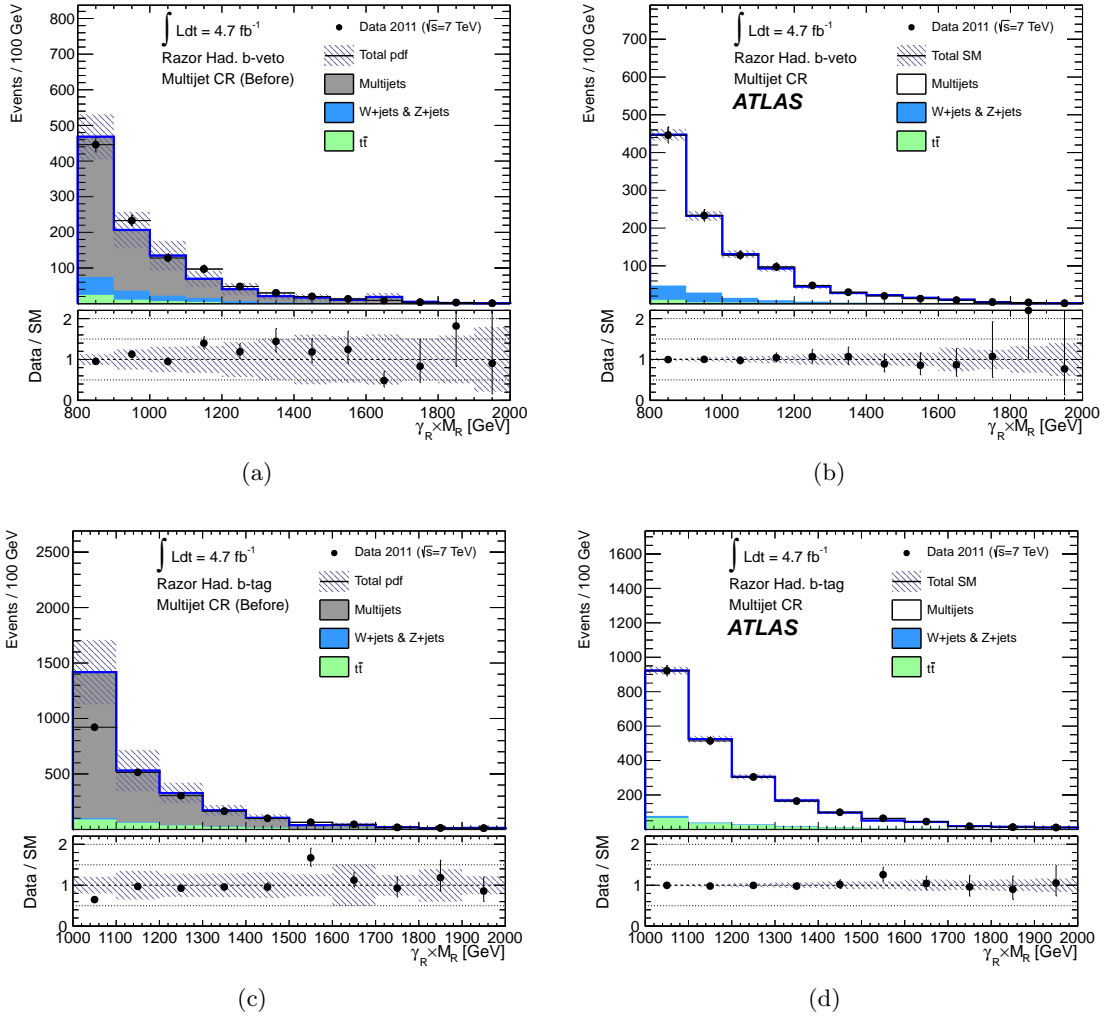


Figure 9.12. A comparison of MC to data in multijet CRs for (top)  $b$ -veto and (bottom)  $b$ -tag (left) before and (right) after the CR BG fit.

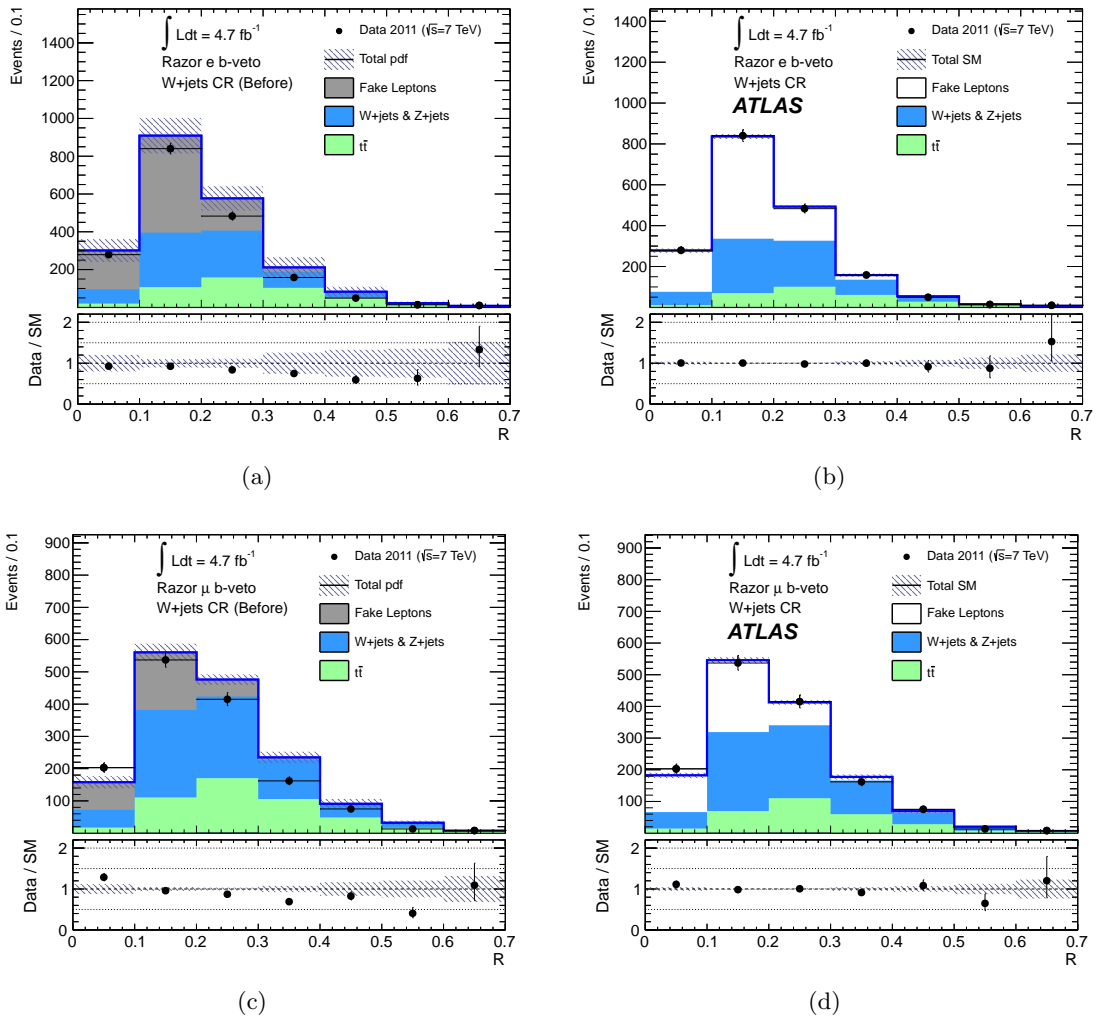


Figure 9.13. A comparison of MC to data in  $W + jets$   $b$ -veto CRs for (top)  $e$  and (bottom)  $\mu$  (left) before and (right) after the CR BG fit.

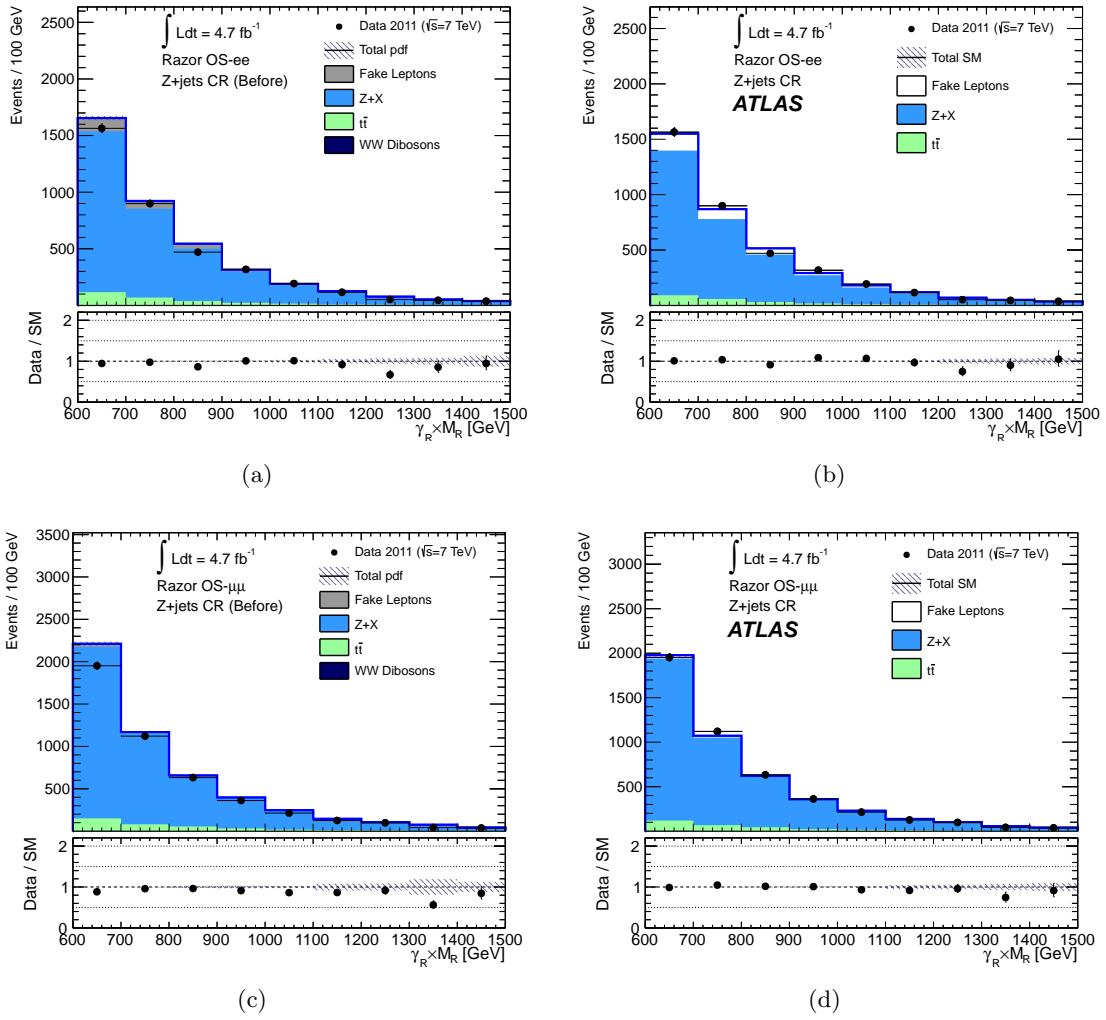
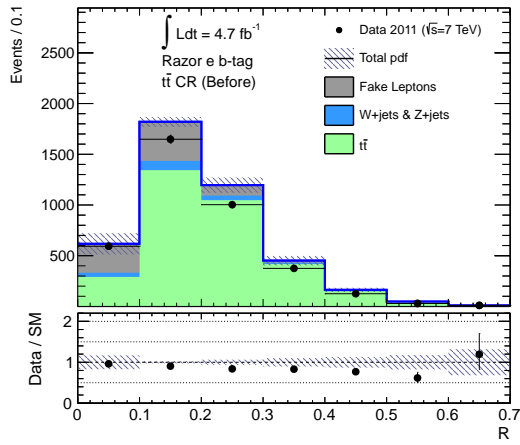
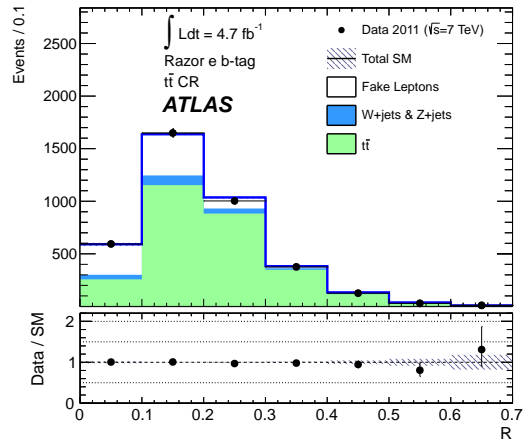


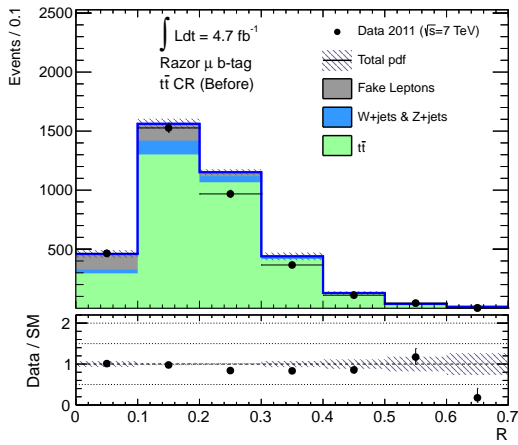
Figure 9.14. A comparison of MC to data in  $Z + jets$   $b$ -tag CRs for (top)  $e$  and (bottom)  $\mu$  (left) before and (right) after the CR BG fit.



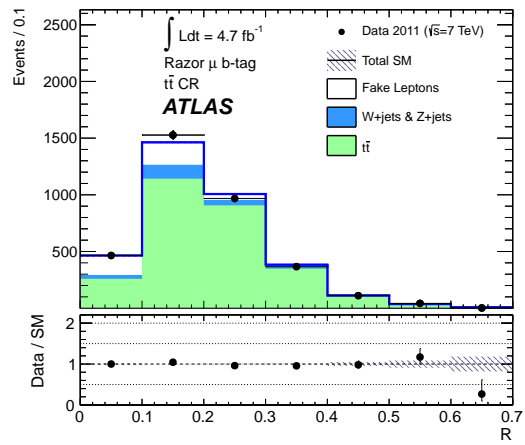
(a)



(b)



(c)



(d)

Figure 9.15. A comparison of MC to data in  $t\bar{t}$   $b$ -tag CRs for (top)  $e$  and (bottom)  $\mu$  (left) before and (right) after the CR BG fit.

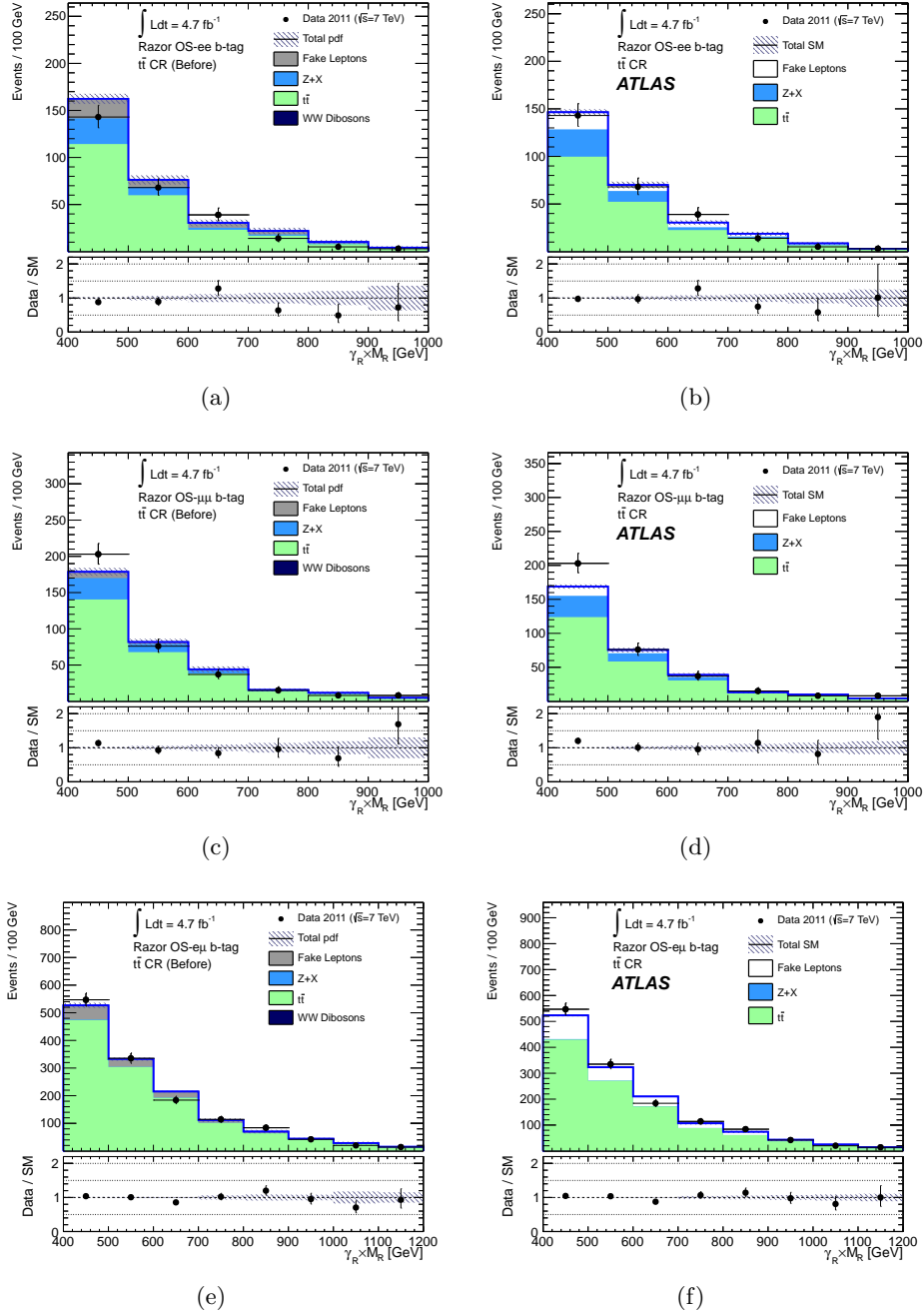


Figure 9.16. A comparison of MC to data in  $t\bar{t}$   $b$ -tag CRs for (top)  $e$  and (bottom)  $\mu$  (left) before and (right) after the CR BG fit.

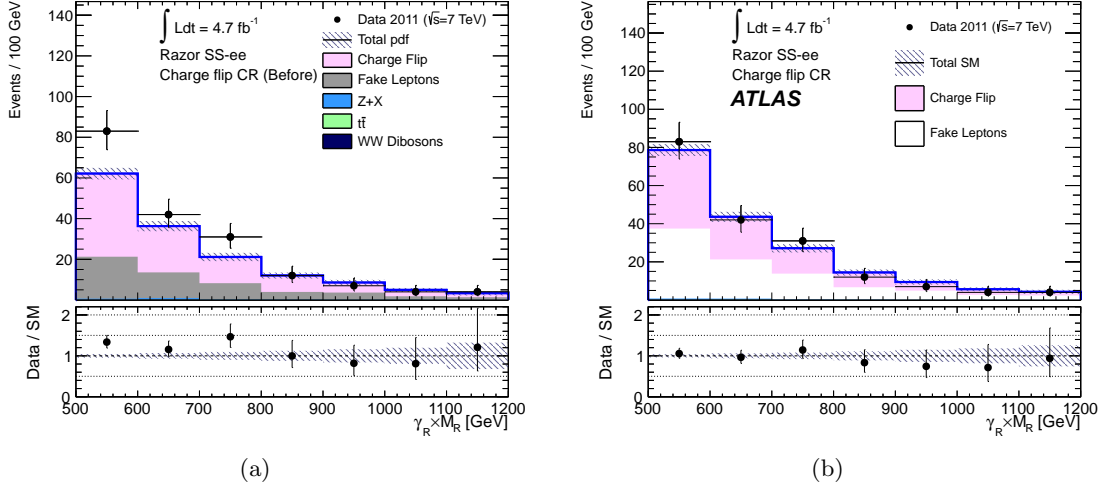


Figure 9.17. A comparison of MC to data in a charge-flip  $ee$  CR for (left) before and (right) after the CR BG fit.

Table 9.25. BG fit result for 0- and 1-lepton for 2011

	$b$ -veto multijet	$b$ -tag multijet	$eW + jets$	$\mu W + jets$	$e\bar{t}\bar{t}$	$\mu\bar{t}\bar{t}$
MC W/Z	110	28	740	760	200	220
MC WW	0.61	0.18	4.6	4.6	1.4	1.1
MC top	52	245	450	470	3300	3250
charge flip	0	0	0	0	0	0
fake lepton	0	0	910	330	800	310
BG expected	900	2670	2110	1560	4300	3790
$W/Z$ fit	$90 \pm 10$	$26 \pm 4$	$670 \pm 40$	$690 \pm 50$	$210 \pm 20$	$240 \pm 30$
WW fit	$0.54 \pm 0.18$	$0.14 \pm 0.05$	$4.2 \pm 1.8$	$4.5 \pm 1.9$	$1.2 \pm 0.5$	$1.0 \pm 0.4$
top fit	$21 \pm 7$	$170 \pm 19$	$280 \pm 30$	$290 \pm 30$	$2800 \pm 60$	$2800 \pm 60$
charge flip fit	$0 \pm 0$	$0 \pm 0$	$0 \pm 0$	$0 \pm 0$	$0 \pm 0$	$0 \pm 0$
fake lepton fit	$0 \pm 0$	$0 \pm 0$	$890 \pm 50$	$430 \pm 40$	$810 \pm 70$	$440 \pm 60$
BG fit	$1030 \pm 30$	$2150 \pm 50$	$1840 \pm 40$	$1410 \pm 30$	$3820 \pm 60$	$3470 \pm 50$
observed	1032	2153	1833	1413	3783	3479

Table 9.26. BG fit result for 2-lepton for 2011

	$e\bar{e}t\bar{t}$	$\mu\bar{\mu}t\bar{t}$	$e\bar{\mu}t\bar{t}$	$eeZ$	$\mu\mu Z$	$ee$ charge flip
MC W/Z	41	47	3.1	3360	4600	1.14
MC WW	0.21	0.09	1.2	6	8	1.2
MC top	225	276	1220	278	357	0.094
charge flip	0	0	0	0	0	94
fake lepton	39	13	120	270	80	51
BG expected	305	336	1340	3920	5050	148
$W/Z$ fit	$45 \pm 4$	$51 \pm 5$	$3.5 \pm 0.3$	$3090 \pm 90$	$4220 \pm 80$	$1.06 \pm 0.11$
$WW$ fit	$0.22 \pm 0.08$	$0.10 \pm 0.15$	$1.3 \pm 0.5$	$6 \pm 3$	$8 \pm 5$	$1.2 \pm 0.6$
top fit	$198 \pm 7$	$237 \pm 8$	$1090 \pm 30$	$220 \pm 9$	$281 \pm 11$	$0.104 \pm 0.011$
charge flip fit	$0 \pm 0$	$0 \pm 0$	$0 \pm 0$	$0 \pm 0$	$0 \pm 0$	$94 \pm 14$
fake lepton fit	$34 \pm 15$	$22 \pm 8$	$220 \pm 40$	$360 \pm 100$	$80 \pm 50$	$87 \pm 19$
BG fit	$277 \pm 14$	$310 \pm 10$	$1320 \pm 30$	$3670 \pm 60$	$4590 \pm 70$	$183 \pm 13$
observed	272	347	1340	3688	4579	183

## 9.9 Signal Region Extrapolation

The combined fit extrapolations into the SRs are shown in Figures 9.18-9.20.

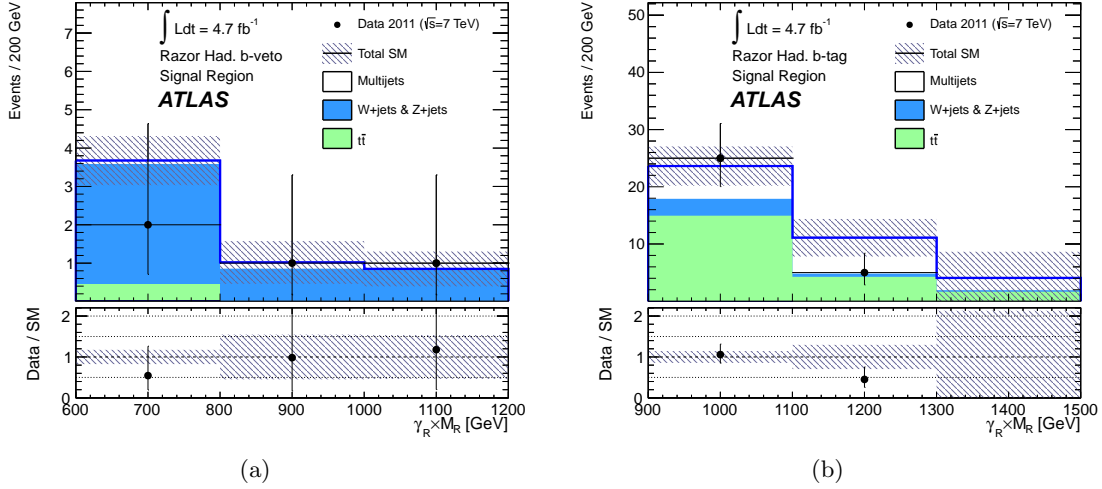


Figure 9.18. A distribution of  $M_R$  in the 0-lepton channel for (a)  $b$ -veto and (b)  $b$ -tag SRs after the combined fit comparing data and MC.

A count of MC expectation and combined fit for the number of events in each SR is shown in Tables 9.25 and 9.26.

Table 9.27. SR extrapolation result for 0- and 1-lepton for 2011

	hadronic $b$ -veto	hadronic $b$ -tag	$e + b$ -veto	$e + b$ -tag	$\mu + b$ -veto	$\mu + b$ -tag
MC W/Z	5.62	4.02	8.48	1.75	6.13	0.53
MC WW	0.04	0.046	0.01	0.000	0.012	0.010
MC top	0.88	30.28	5.73	6.26	3.35	4.55
charge flip	0	0	0	0	0	0
fake lepton	0	0	0.28	0.45	0	0
BG expected	6.74	55.09	14.49	8.46	9.49	5.08
$W/Z$ fit	$4.85 \pm 1.34$	$3.80 \pm 0.66$	$7.16 \pm 1.67$	$1.17 \pm 0.47$	$3.84 \pm 1.34$	$0.62 \pm 0.54$
$WW$ fit	$0.03 \pm 0.02$	$0.029 \pm 0.010$	$0.01 \pm 0.02$	$0.000 \pm 0.009$	$0.001 \pm 0.008$	$0.001 \pm 0.005$
top fit	$0.40 \pm 0.14$	$20.82 \pm 2.61$	$2.68 \pm 0.93$	$4.97 \pm 1.25$	$1.69 \pm 0.56$	$3.73 \pm 1.14$
charge flip fit	$0 \pm 0$	$0 \pm 0$	$0 \pm 0$	$0 \pm 0$	$0 \pm 0$	$0 \pm 0$
fake lepton fit	$0 \pm 0$	$0 \pm 0$	$0.28 \pm 0.44$	$0.45 \pm 0.57$	$0 \pm 0$	$0 \pm 0$
BG fit	$5.54 \pm 1.50$	$38.77 \pm 7.03$	$10.12 \pm 2.35$	$6.58 \pm 1.65$	$5.53 \pm 1.70$	$4.36 \pm 1.30$
observed	4	30	6	13	9	4



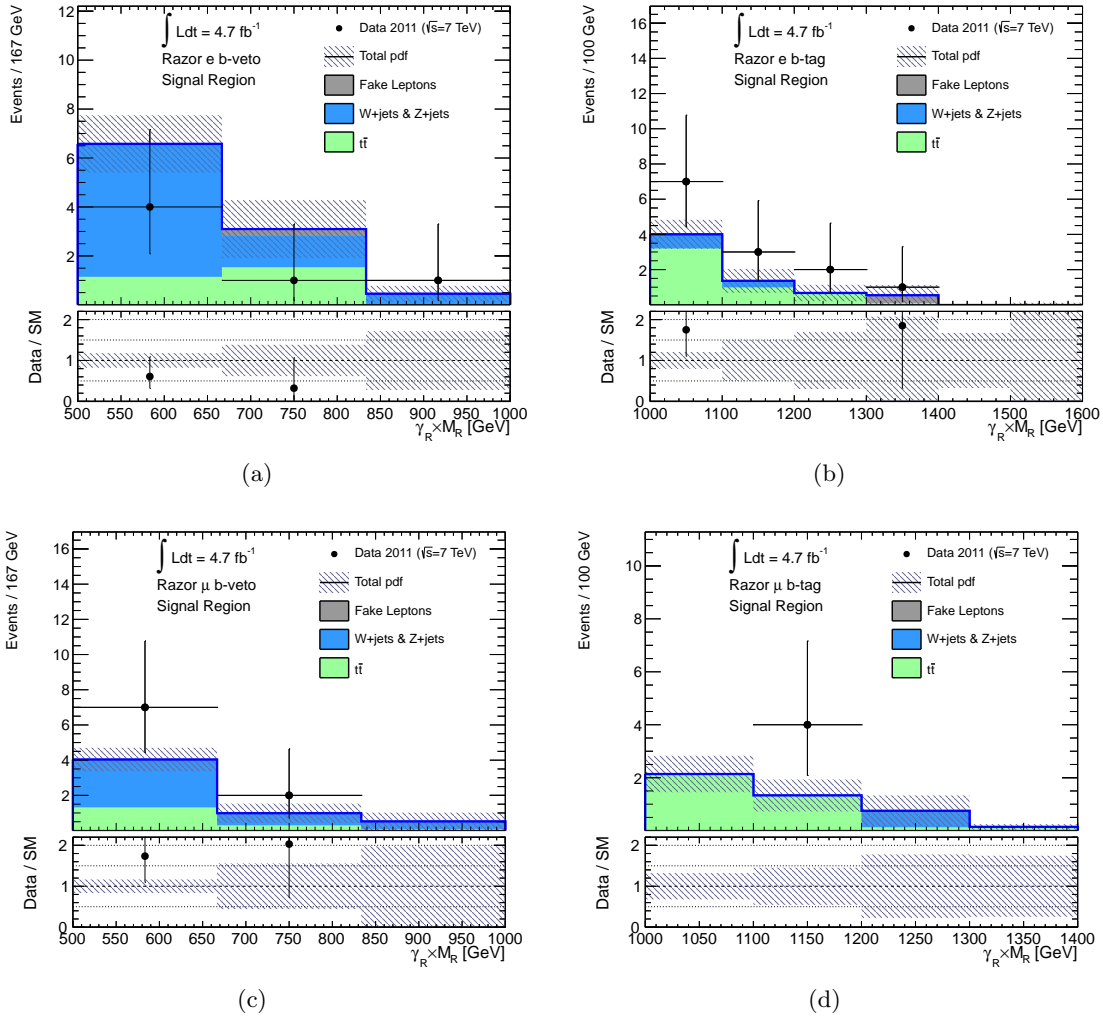


Figure 9.19. A distribution of  $M_R$  in the 1-lepton channel for (top)  $e$  and (bottom)  $\mu$  SRs with (left)  $b$ -veto and (right)  $b$ -tag comparing data and MC.

The combined fit uses a variety of scales and parameters to enable the combined fit of all channels and samples with systematic variations. These parameters are shown in Table 9.29. The free-floating parameters can be set by the combined fit to best adjust the BG distributions. For a good fit quality, the evaluation of these parameters at each step should be independent, which is shown in the correlation matrix of Figure 9.21. Once all the systematic parameters and scale factors were set by the combined fit, the amount of “pull” that each had on the MC estimate gave a measure of how vital the variation was

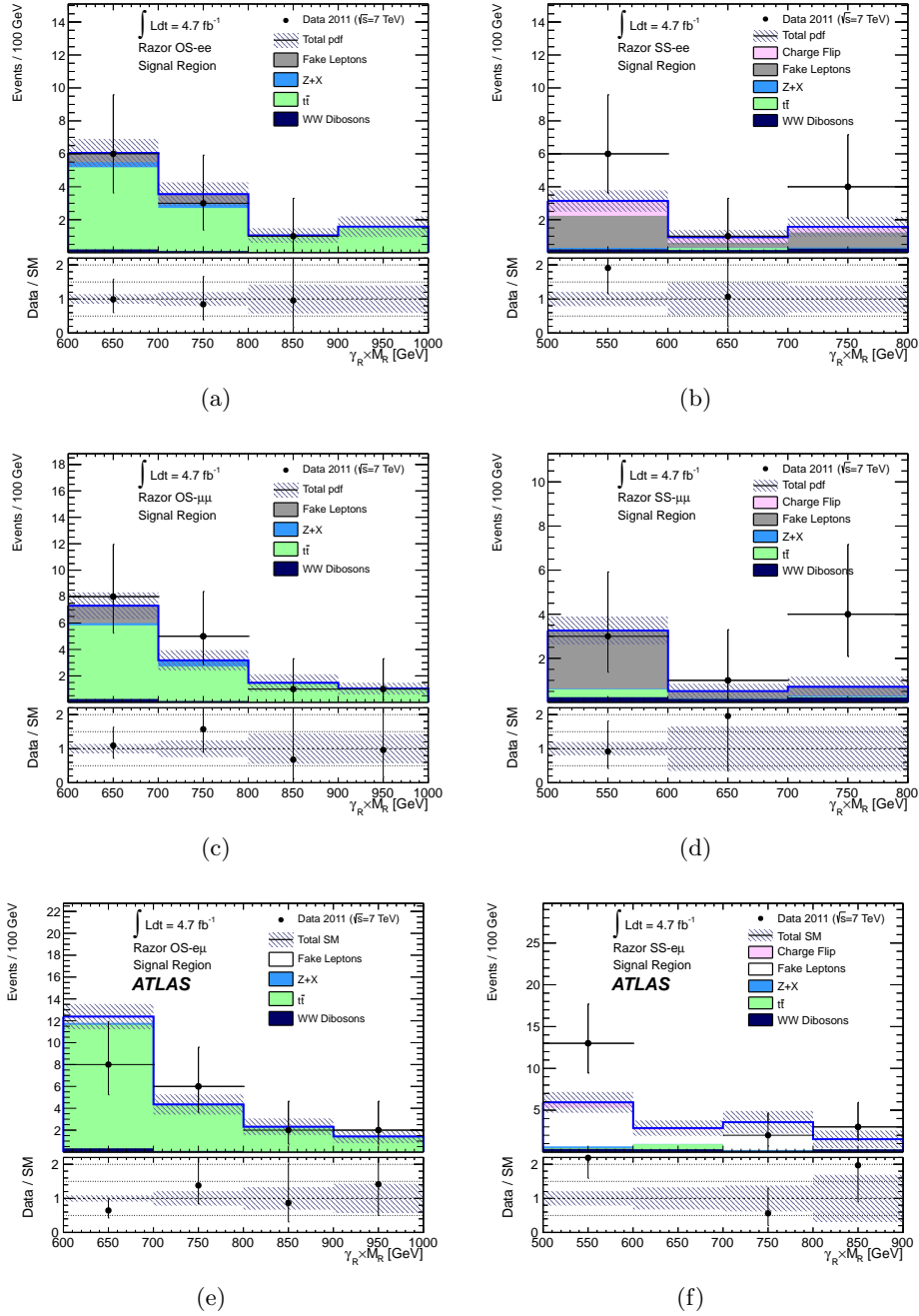


Figure 9.20. A distribution of  $M_R$  in the 2-lepton channel for (top)  $ee$ , (middle)  $\mu\mu$ , and (bottom)  $e\mu$  SRs with (left) OS and (right) SS comparing data and MC.

Table 9.28. SR extrapolation result for 2-lepton for 2011

	OS $ee$	OS $\mu\mu$	SS $ee$	SS $\mu\mu$	OS $e\mu$	SS $e\mu$
MC W/Z	0.67	0.44	0.19	0.21	0.27	0.36
MC WW	0.38	0.42	0.68	0.66	0.47	1.19
MC top	13.06	14.71	0.13	0.49	22.86	0.62
charge flip	0	0	1.59	0	0	1.04
fake lepton	1.16	1.32	3.15	3.36	0.57	10.60
BG expected	15.27	16.89	5.75	4.71	24.17	13.81
W/Z fit	$0.54 \pm 0.10$	$0.62 \pm 0.17$	$0.16 \pm 0.04$	$0.10 \pm 0.04$	$0.26 \pm 0.04$	$0.33 \pm 0.07$
WW fit	$0.36 \pm 0.38$	$0.36 \pm 0.51$	$0.63 \pm 0.31$	$0.63 \pm 0.47$	$0.47 \pm 0.97$	$1.18 \pm 0.73$
top fit	$10.16 \pm 1.53$	$10.69 \pm 1.59$	$0.12 \pm 0.04$	$0.39 \pm 0.17$	$19.14 \pm 2.32$	$0.70 \pm 0.21$
charge flip fit	$0 \pm 0$	$0 \pm 0$	$1.58 \pm 0.39$	$0 \pm 0$	$0 \pm 0$	$1.06 \pm 0.22$
fake lepton fit	$1.16 \pm 1.26$	$1.32 \pm 1.10$	$3.15 \pm 3.61$	$3.36 \pm 2.66$	$0.57 \pm 0.57$	$10.60 \pm 7.96$
BG fit	$12.22 \pm 2.20$	$13.00 \pm 2.22$	$5.64 \pm 3.76$	$4.48 \pm 2.87$	$20.44 \pm 2.70$	$13.87 \pm 8.14$
observed	10	15	11	8	18	18

to the analysis. Figure 9.22, for example, shows that  $b$ -tagging was a crucial part of this analysis and had a large effect.

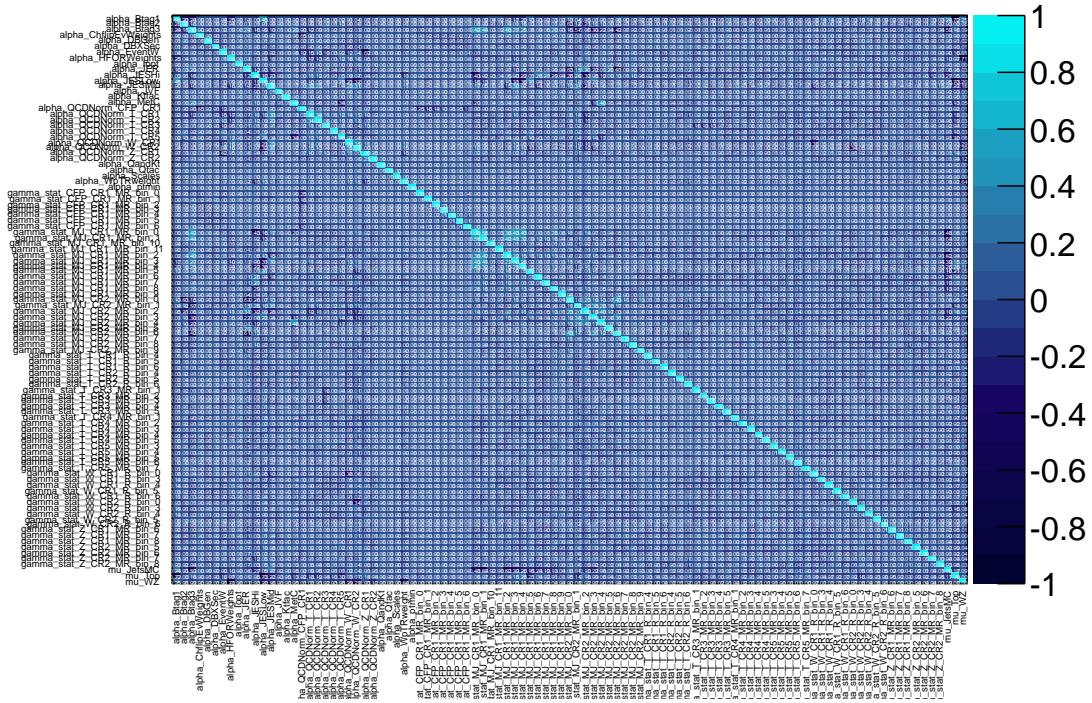


Figure 9.21. A correlation matrix of all free-floating parameters used in the combined fit.

Table 9.29. The free-floating parameter values after the BG combined fit for 2011

floating parameter	final value	floating parameter	final value
alpha_Btag1	1.4790e+00 ± 5.10e-01	gamma_stat_MJ_CR1_MR_bin_0	9.7416e-01 ± 9.34e-02
alpha_Btag2	-8.0578e-02 ± 8.18e-01	gamma_stat_MJ_CR1_MR_bin_1	1.0311e+00 ± 9.67e-02
alpha_Btag3	-3.7510e-01 ± 5.19e-01	gamma_stat_MJ_CR1_MR_bin_10	1.1681e+00 ± 3.24e-01
alpha_ChflipEvWeights	-2.3353e-02 ± 9.68e-01	gamma_stat_MJ_CR1_MR_bin_11	9.6073e-01 ± 3.28e-01
alpha_DBGen	-4.6754e-02 ± 7.63e-01	gamma_stat_MJ_CR1_MR_bin_2	8.3340e-01 ± 9.09e-02
alpha_DBXSec	4.6296e-03 ± 9.88e-01	gamma_stat_MJ_CR1_MR_bin_3	1.2635e+00 ± 1.60e-01
alpha_EventW	-1.7215e-01 ± 8.48e-01	gamma_stat_MJ_CR1_MR_bin_4	1.2271e+00 ± 1.91e-01
alpha_HFORWeights	9.2674e-01 ± 8.40e-01	gamma_stat_MJ_CR1_MR_bin_5	1.0224e+00 ± 1.00e-01
alpha_Iopt	0.0000e+00 ± 9.93e-01	gamma_stat_MJ_CR1_MR_bin_6	9.6604e-01 ± 1.06e-01
alpha_JER	-5.8115e-01 ± 2.86e-01	gamma_stat_MJ_CR1_MR_bin_7	9.5878e-01 ± 1.23e-01
alpha_JESHi	-3.5298e-01 ± 1.50e-01	gamma_stat_MJ_CR1_MR_bin_8	5.5720e-01 ± 1.73e-01
alpha_JESLow	-2.0945e-01 ± 1.74e-01	gamma_stat_MJ_CR1_MR_bin_9	1.0178e+00 ± 2.28e-01
alpha_JESMid	-2.8779e-01 ± 3.51e-01	gamma_stat_MJ_CR2_MR_bin_0	8.7957e-01 ± 2.01e-01
alpha_JVF	-5.4342e-04 ± 2.91e-02	gamma_stat_MJ_CR2_MR_bin_1	7.6003e-01 ± 8.12e-02
alpha_Ktfac	0.0000e+00 ± 9.93e-01	gamma_stat_MJ_CR2_MR_bin_2	9.6984e-01 ± 1.03e-01
alpha_MetC	1.0969e+00 ± 6.74e-01	gamma_stat_MJ_CR2_MR_bin_3	8.5686e-01 ± 8.32e-02
alpha_QCDNorm_CFP_CR1	3.4285e-01 ± 1.93e-01	gamma_stat_MJ_CR2_MR_bin_4	1.1130e+00 ± 1.56e-01
alpha_QCDNorm_T_CR1	2.6646e-02 ± 1.49e-01	gamma_stat_MJ_CR2_MR_bin_5	1.0754e+00 ± 7.24e-02
alpha_QCDNorm_T_CR2	1.3452e+00 ± 6.07e-01	gamma_stat_MJ_CR2_MR_bin_6	1.2513e+00 ± 2.43e-01
alpha_QCDNorm_T_CR3	-1.9118e-01 ± 5.41e-01	gamma_stat_MJ_CR2_MR_bin_7	9.9130e-01 ± 9.65e-02
alpha_QCDNorm_T_CR4	1.0161e+00 ± 9.00e-01	gamma_stat_MJ_CR2_MR_bin_8	9.7260e-01 ± 1.22e-01
alpha_QCDNorm_T_CR5	1.3193e+00 ± 5.69e-01	gamma_stat_MJ_CR2_MR_bin_9	1.0097e+00 ± 1.23e-01
alpha_QCDNorm_W_CR1	-3.7199e-02 ± 8.48e-02	gamma_stat_CFP_CR1_MR_bin_0	1.0157e+00 ± 5.64e-02
alpha_QCDNorm_W_CR2	1.2766e+00 ± 5.50e-01	gamma_stat_CFP_CR1_MR_bin_1	9.9043e-01 ± 7.06e-02
alpha_QCDNorm_Z_CR1	4.3897e-01 ± 5.42e-01	gamma_stat_CFP_CR1_MR_bin_2	1.0394e+00 ± 9.26e-02
alpha_QCDNorm_Z_CR2	-5.8879e-03 ± 8.65e-01	gamma_stat_CFP_CR1_MR_bin_3	9.6225e-01 ± 1.12e-01
alpha_QandKt	0.0000e+00 ± 9.93e-01	gamma_stat_CFP_CR1_MR_bin_4	9.3332e-01 ± 1.42e-01
alpha_Qfac	0.0000e+00 ± 9.93e-01	gamma_stat_CFP_CR1_MR_bin_5	9.3700e-01 ± 1.73e-01
alpha_Scales	0.0000e+00 ± 9.93e-01	gamma_stat_CFP_CR1_MR_bin_6	9.7551e-01 ± 2.56e-01
alpha_WpTRweight	-5.1084e-01 ± 9.29e-01	mu_JetsMC	1.2743e+00 ± 1.16e-01
alpha_ptmin	0.0000e+00 ± 9.93e-01	mu_Top	8.1436e-01 ± 3.78e-02
gamma_stat_W_CR1_R_bin_0	1.0055e+00 ± 4.69e-02	mu_WZ	9.3975e-01 ± 8.79e-02
gamma_stat_W_CR1_R_bin_3	1.0005e+00 ± 4.63e-02	gamma_stat_W_CR1_R_bin_4	9.6693e-01 ± 7.20e-02
gamma_stat_W_CR1_R_bin_5	9.5198e-01 ± 1.29e-01	gamma_stat_W_CR1_R_bin_6	1.2459e+00 ± 2.54e-01
gamma_stat_W_CR2_R_bin_0	1.0752e+00 ± 5.26e-02	gamma_stat_W_CR2_R_bin_3	9.5524e-01 ± 4.41e-02
gamma_stat_W_CR2_R_bin_4	1.0401e+00 ± 7.11e-02	gamma_stat_W_CR2_R_bin_5	8.7282e-01 ± 1.07e-01
gamma_stat_W_CR2_R_bin_6	1.1140e+00 ± 2.51e-01	gamma_stat_Z_CR1_MR_bin_6	9.3955e-01 ± 5.15e-02
gamma_stat_Z_CR1_MR_bin_7	9.7456e-01 ± 6.39e-02	gamma_stat_Z_CR1_MR_bin_8	1.0121e+00 ± 7.52e-02
gamma_stat_Z_CR2_MR_bin_5	9.6272e-01 ± 4.70e-02	gamma_stat_Z_CR2_MR_bin_6	9.8244e-01 ± 5.49e-02
gamma_stat_Z_CR2_MR_bin_7	9.0900e-01 ± 6.50e-02	gamma_stat_Z_CR2_MR_bin_8	9.6309e-01 ± 8.65e-02
gamma_stat_T_CR1_R_bin_4	9.8039e-01 ± 4.45e-02	gamma_stat_T_CR1_R_bin_5	9.3694e-01 ± 7.91e-02
gamma_stat_T_CR1_R_bin_6	1.1126e+00 ± 1.99e-01	gamma_stat_T_CR2_R_bin_4	9.9314e-01 ± 4.98e-02
gamma_stat_T_CR2_R_bin_5	1.0720e+00 ± 9.52e-02	gamma_stat_T_CR2_R_bin_6	8.1161e-01 ± 1.45e-01
gamma_stat_T_CR3_MR_bin_1	9.9098e-01 ± 5.97e-02	gamma_stat_T_CR3_MR_bin_2	1.0999e+00 ± 1.00e-01
gamma_stat_T_CR3_MR_bin_3	9.1806e-01 ± 1.09e-01	gamma_stat_T_CR3_MR_bin_4	9.0124e-01 ± 1.40e-01
gamma_stat_T_CR3_MR_bin_5	1.0029e+00 ± 2.45e-01	gamma_stat_T_CR4_MR_bin_1	1.0028e+00 ± 5.57e-02
gamma_stat_T_CR4_MR_bin_2	9.8651e-01 ± 7.67e-02	gamma_stat_T_CR4_MR_bin_3	1.0308e+00 ± 1.18e-01
gamma_stat_T_CR4_MR_bin_4	9.5315e-01 ± 1.40e-01	gamma_stat_T_CR4_MR_bin_5	1.1728e+00 ± 2.13e-01
gamma_stat_T_CR5_MR_bin_3	1.0214e+00 ± 4.81e-02	gamma_stat_T_CR5_MR_bin_4	1.0423e+00 ± 5.79e-02
gamma_stat_T_CR5_MR_bin_5	9.9326e-01 ± 7.15e-02	gamma_stat_T_CR5_MR_bin_6	9.6093e-01 ± 8.14e-02
gamma_stat_T_CR5_MR_bin_7	1.0007e+00 ± 1.10e-01		

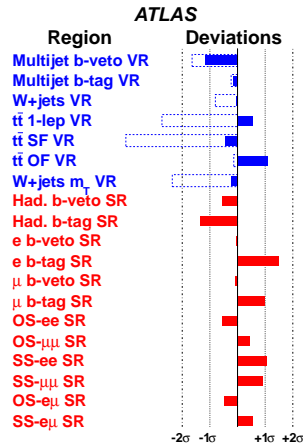


Figure 9.22. The pull on BG weights after the combined fit.

## 9.10 Exclusion Results

The combined analysis set limits in the mSUGRA models (Figure 9.23), the  $\tilde{g} \rightarrow t\bar{t}\tilde{\chi}_1^0$  models (Figure 9.24), and the  $\tilde{q} \rightarrow q\bar{q}W\tilde{\chi}_1^0$  plane (Figure 9.25). The 2-lepton analysis set limits to GMSB models (Figure 9.26).

Table 9.30. SR exclusion for 0- and 1-lepton after the combined fit

	hadronic <i>b</i> -veto	hadronic <i>b</i> -tag	<i>e</i> + <i>b</i> -veto	<i>e</i> + <i>b</i> -tag	$\mu$ + <i>b</i> -veto	$\mu$ + <i>b</i> -tag
$M_R$ [GeV]	600	1100	600	1100	600	1100
BG events	$6.2 \pm 1.8$	$13 \pm 3$	$5.3 \pm 1.6$	$2.4 \pm 1.0$	$2.4 \pm 1.0$	$1.9 \pm 0.8$
observed	4	5	5	6	2	4
<i>p</i> -value	0.72	0.91	0.53	0.07	0.54	0.16

Table 9.31. SR exclusion for 2-lepton after the combined fit

	OS <i>ee</i>	OS $\mu\mu$	SS <i>ee</i>	SS $\mu\mu$	OS <i>eμ</i>	SS <i>eμ</i>
<i>p</i> -value	0.71	0.32	0.15	0.18	0.68	0.29

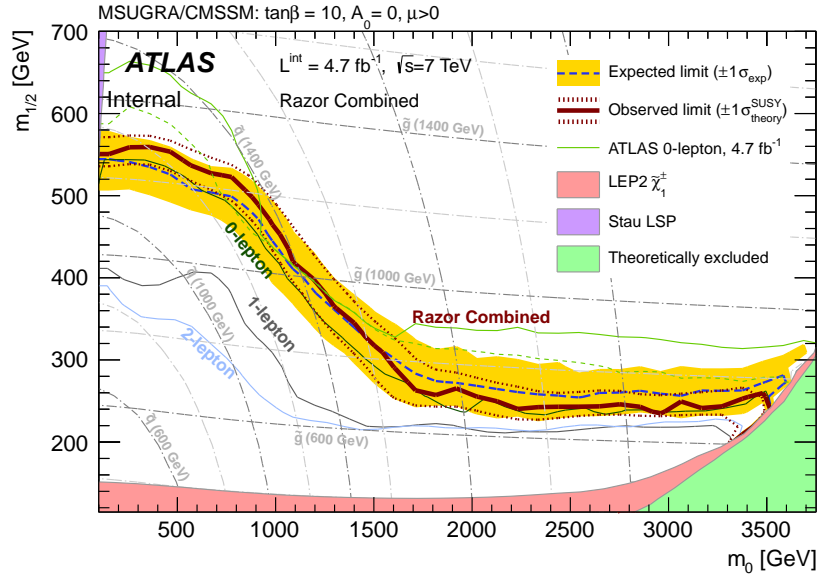


Figure 9.23. An exclusion plot in the  $m_{1/2}$  versus  $m_0$  plane in the mSUGRA model.

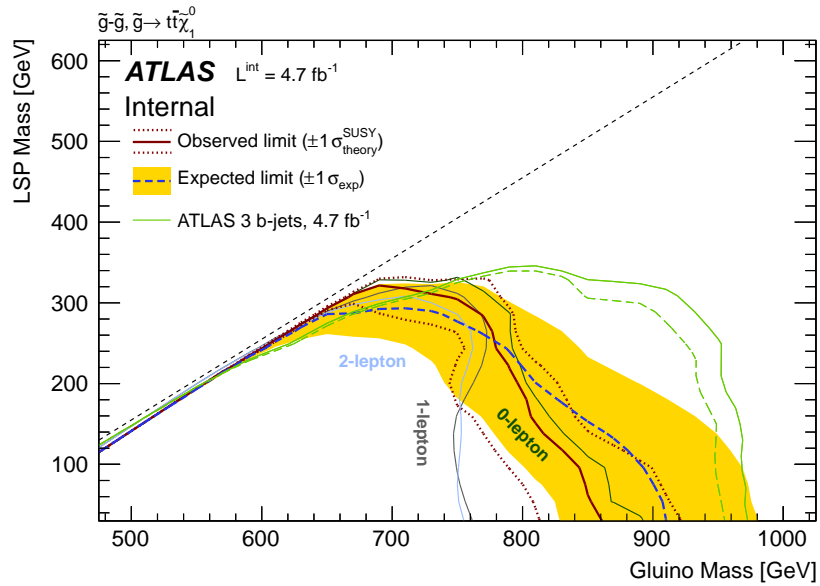


Figure 9.24. An exclusion plot in the  $m_{\tilde{\chi}_1^0}$  versus  $m_{\tilde{g}}$  plane in the  $\tilde{g} \rightarrow t\bar{t}\tilde{\chi}_1^0$  simplified model.

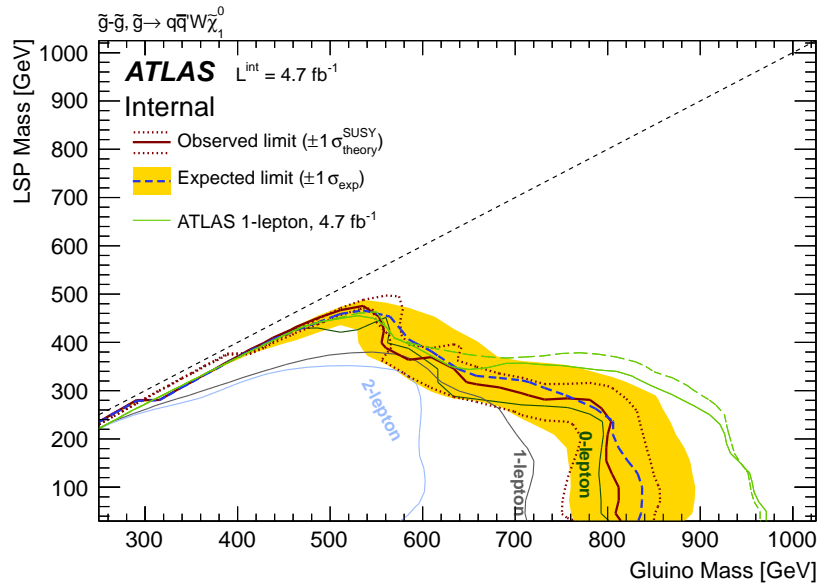


Figure 9.25. An exclusion plot in the  $m_{\tilde{\chi}_1^0}$  versus  $m_{\tilde{g}}$  plane in the  $\tilde{g} \rightarrow q\bar{q}W\tilde{\chi}_1^0$  simplified model.

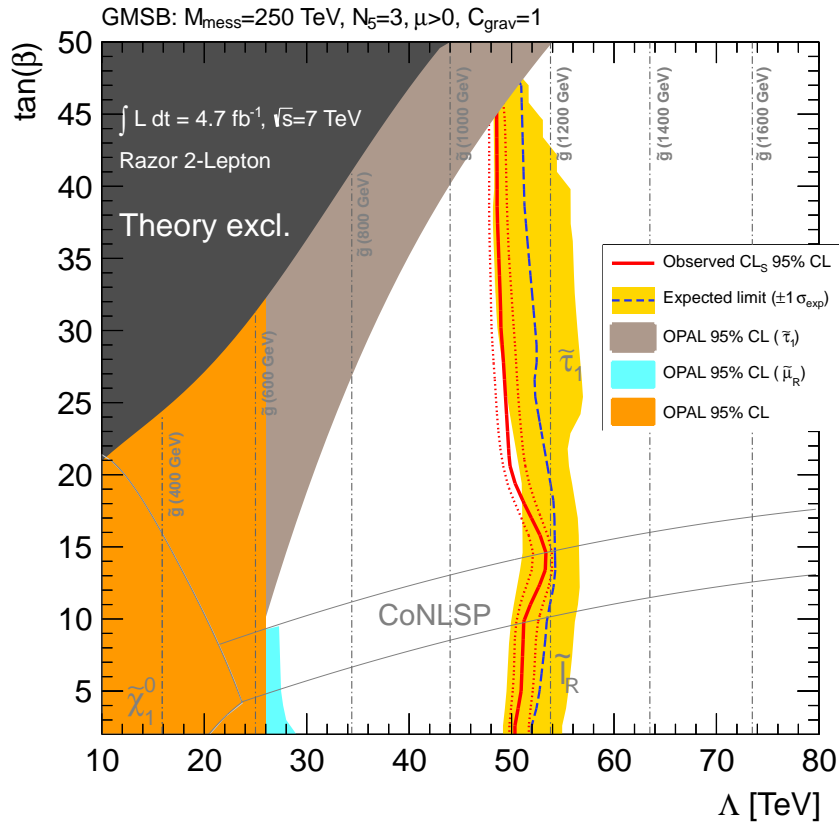


Figure 9.26. An exclusion plot in the  $\tan\beta$  versus  $\Lambda$  plane in the GMSB model.

## 9.11 Comments on the 2011 Analysis

This was the first attempt at putting together an analysis for ATLAS using the Razor reconstruction technique. Much of our effort went toward understanding the variable distributions involved and their correlation to some of the more standard variables used in analyses. We were able to accomplish a lot considering that this was a multi-channel search, which would normally be a combined effort from more than a hundred people. Instead, we had a fresh graduate student and a post-doctoral researcher working on 0-lepton, a doctoral candidate working on 1-lepton, and a doctoral student and post-doctoral researcher working on 2-lepton.

The individual exclusions underperformed the reach of the standard analyses, but the combined limits were still competitive. A major influence on the sensitivity of the analysis was due to the choice of trigger. Not much was known about the sensitivity of Razor at the start and it was assumed that the correlation between  $M_R$  and  $H_T$  made the  $H_T$  trigger look like an ideal choice. However, the requirement of having at least 5 jets for 0-lepton heavily influenced events that could be found in each SR, which was a reactionary attempt to reduce the multijet BG.

On top of the efficiency requirements, the analysis plane used orthogonal cuts on  $R$  and  $M_R$ . In order to reduce the BG contamination of each SR, these cuts tended to be quite high. Furthermore, the optimization was done manually with a coarse increase in cuts. Since the relationship in this plane was actually hyperbolic, we lost a lot of potential signal events in the process at lower mass-scale. Our claim to viability was the exclusion plot of 1-lepton scaled to show the fractional mass-splitting ( $m_{frac}$  or  $x$ ):

$$m_{frac} \equiv \frac{m_{\tilde{\ell}^\pm} - m_{\tilde{\chi}}}{m_{\tilde{g}} - m_{\tilde{\chi}}} \quad (9.3)$$

In the exclusion plot of  $m_{frac}$  versus  $m_{\tilde{g}}$  (Figure 9.27), the 0-lepton Razor exclusion actually sets a higher limit than the standard 1-lepton analysis for high  $m_{\tilde{g}}$  and high  $m_{frac}$ . In addition, there were regions where each Razor exclusion sets the highest limit for the



Razor-combined analysis. 1- and 2-lepton underperform the overall limit everywhere, but the complementarity at least suggests that the channels have different strengths that can be exploited in a multi-channel search.

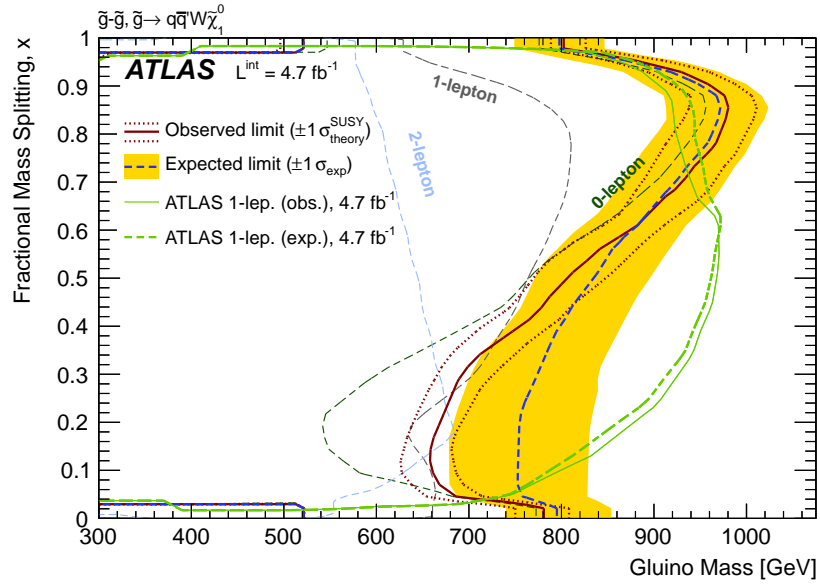


Figure 9.27. An exclusion plot in the  $m_{frac}$  versus  $m_{\tilde{g}}$  plane.

## CHAPTER 10

### 2012 Razor Analysis

The 2011 Razor analysis was soon followed by another Razor analysis for Run I in 2012. This time, the effort was split such that the analysis in this chapter was only directed toward the 0-lepton channel, although the analysis was coordinated with 2-lepton+jets  $Z$ -veto (Reference [119]) and EW 2/3-lepton+ $E_T^{\text{miss}}$  (Reference [120]). The development of the Super Razor occurred late during this analysis and is not featured in this chapter. From 5 April 2012 to 6 December 2012 the LHC was configured for collisions with proton beams at 4 TeV per beam ( $\sqrt{s} = 8$  TeV) with 50 ns bunch spacing and 1380 bunches per beam. A total of  $20.3 \text{ fb}^{-1}$  of physics data from ATLAS was used for this analysis. The results of this analysis were documented in Reference [121] and parts of it are summarized below. The outline also includes references to the “standard” analysis in Reference [122].

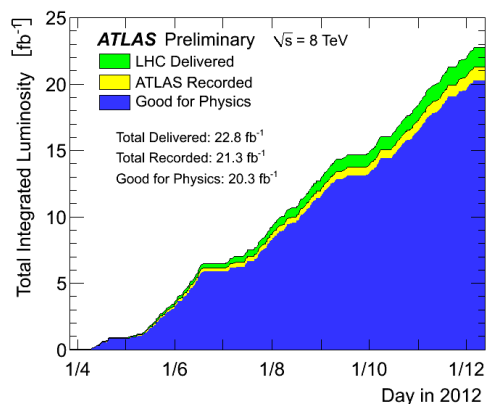


Figure 10.1. Timeline of integrated luminosity during 2012 data-taking run.

## 10.1 Trigger Choice

Following the results of the 2011 analysis (Chapter 9), it was decided that a complementary signal trigger was needed. The two triggers would be used to define SRs from their disparate strengths. The  $H_T$  trigger revealed a good sensitivity toward high mass-scales while a new  $E_T^{\text{miss}}$  strategy would be sensitive to low mass-scales. The  $H_T$  trigger selects BGs with low  $R$  and high  $M_R$  while the  $E_T^{\text{miss}}$  trigger selects high  $R$  and low  $M_R$ . An overlap at high  $R$  and high  $M_R$  would mean that these two triggers could work cooperatively to use this BG split-sensitivity as a powerful discriminant (Figure 10.2).

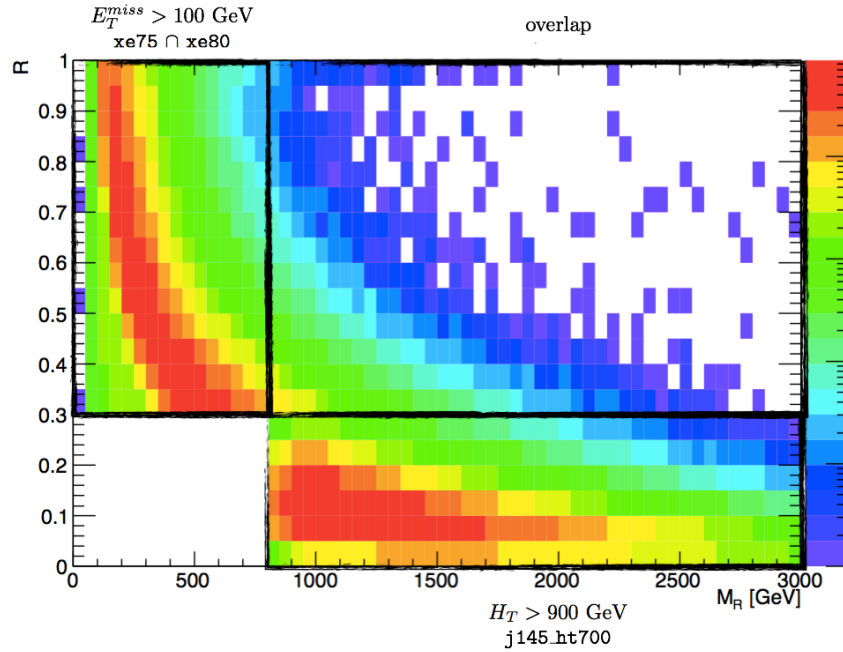


Figure 10.2. The complementary coverage of a  $E_T^{\text{miss}}$  trigger and an  $H_T$  trigger.

The xe75 trigger was the lowest unrescaled trigger in period A, but the threshold was raised to xe80 for the remaining periods of data (Table 10.2). Therefore, the trigger was applied as a binary OR of both triggers to catch the data for all periods. The  $H_T$  trigger appeared to have nearly the same sensitivity at high mass scales as the  $E_T^{\text{miss}}$  trigger. However, the  $E_T^{\text{miss}}$  trigger also showed an ability to reach sensitivity in the compressed

Table 10.1. Trigger selection for the 2012 analysis

trigger	L2 chain	L1 seed
EF_mu24i_tight	L2_mu24i_tight	L1_MU15
EF_e24vhi_medium1	L2_e24vhi_medium1	L1_EM18VH
EF_e60_medium1	L2_e60_medium1	L1_EM30
EF_xe75_tclcw	L2_xe55	L1_XE50
EF_xe80_tclcw	L2_xe55	L1_XE50
EF_j145_a4tchad_ht700_L2FS	L2_j95	L1_J75

region that the  $H_T$  trigger (with an efficiency requirement of  $H_T > 900$  GeV) could not cover. It was ultimately dropped as a signal trigger but was retained just to study the effects of these differing triggers. Instead, the  $E_T^{\text{miss}}$  strategy was altered to target a loose SR and a tight SR.

Table 10.2. Luminosity from individual periods for the 2012 analysis

period	runs	integrated luminosity [ $\text{fb}^{-1}$ ]
A	200804-201557	0.7940
B	202660-205114	5.0947
C	206248-207398	1.4060
D	207447-209026	3.2884
E	209074-210309	2.5263
G	211522-212273	1.2748
H	212619-213360	1.4449
I	213431-213820	1.0163
J	213900-215092	2.5963
L	215414-215644	0.8398
total	–	20.2815

A study of trigger efficiency in  $E_T^{\text{miss}}$  for increasing  $R$  cuts is shown in Figure 10.3. The 99% efficiency plateau was determined to stabilize around  $E_T^{\text{miss}} > 160$  GeV when  $R$  is increased.

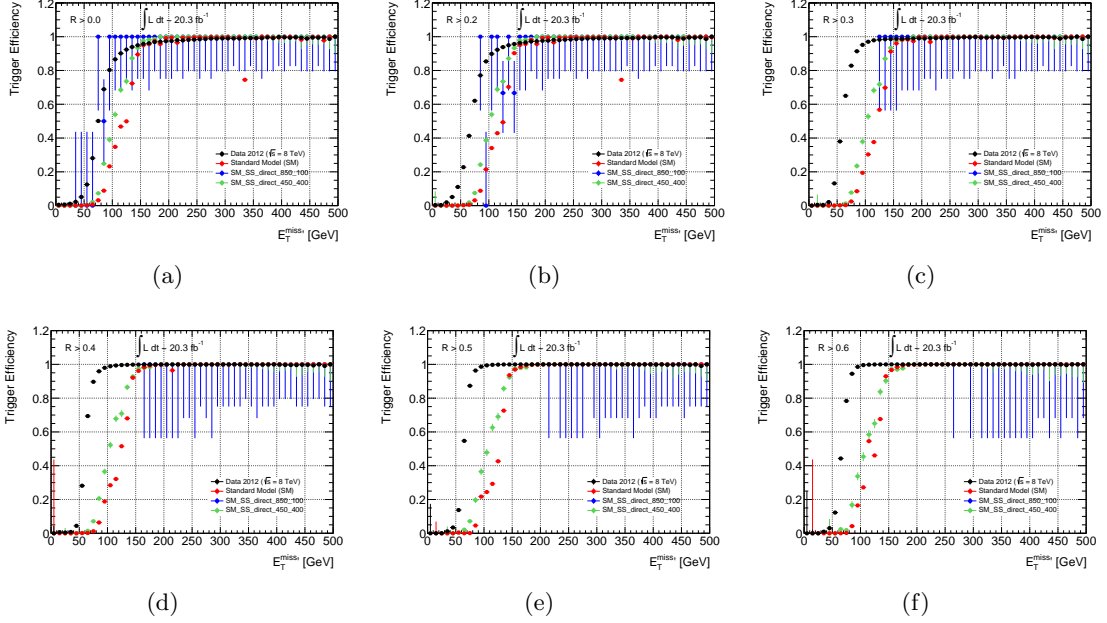


Figure 10.3. The efficiency of `EF_xe75_tclcw` OR `EF_xe80_tclcw` for increasing cuts on  $R$ : (a)  $R > 0.0$ , (b)  $R > 0.2$ , (c)  $R > 0.3$ , (d)  $R > 0.4$ , (e)  $R > 0.5$ , and (f)  $R > 0.5$ .

## 10.2 Object Definitions and Event Selections

Electrons were defined following the recommendations of the EGamma working group (Table 10.3). Muons were defined following the recommendations of the Muon Combined Performance group (Table 10.4). Jets were defined according to the recommendations of the Jet Performance group (Table 10.5). Recommendations from the Flavor Tagging group lead to the definitions for  $b$ -jets.

Once the objects were selected, overlap removal and event selection were applied:

1. If a baseline electron and a baseline jet were within  $R < 0.2$ , the jet was discarded.
2. If a baseline electron and a baseline jet were found within  $0.2 \leq R < 0.4$ , the electron was discarded.
3. If a baseline muon and a baseline jet were found within  $R < 0.4$ , the muon was discarded.
4. If a baseline muon and a baseline electron were found within  $R < 0.1$ , both objects were discarded.

Table 10.3. Summary of the electron definitions used in the 2012 analysis

Baseline Electrons	
algorithm	<b>AuthorElectron</b>
acceptance	$p_T > 10$ GeV $ \eta^{cl}  < 2.47$
quality	<b>medium++</b>
Signal Electrons	
acceptance	$p_T > 25$ GeV
quality	<b>tight++</b>
isolation	$p_{T\text{cone}20} / p_T < 0.10$ $ d_0^{PV}  < 1$ mm $ z_0^{PV}  < 2$ mm

Table 10.4. Summary of the muon definitions used in the 2012 analysis

Baseline Muons	
algorithm	<b>STACO</b>
acceptance	$p_T > 10$ GeV $ \eta  < 2.4$
quality	<b>loose</b> $\geq 1$ $m_{pixel}$ hit or $n_{pixel}^{dead}$ $\geq 5$ $n_{SCT}$ $n_{pixel}^{holes} + n_{SCT}^{holes} < 3$ $\geq 1$ $b$ -layer hit when expected if $0.1 \eta  < 1.9$ : $n_{TRT} \geq 6$ if $n_{TRT} \geq 6$ : $n_{TRT}^{outliers} < 0.9n_{TRT}$
Signal Muons	
isolation	$\Sigma p_T < 1.8$ GeV in $\Delta R = 0.2$
cosmics	$ z_\mu - z_{PV}  < 1$ mm $d_0 < 0.2$ mm

5. If the PV had less than 5 tracks, the event was discarded.
6. If `larError`  $\neq 0$  and `tileError`  $== 2$  and `coreFlag0&x4000`  $\neq 0$ , the event was discarded.
7. If there were **Looser** bad jets with  $p_T > 20$  GeV, the event was discarded.
8. If there were two jets with  $p_T > 100$  GeV and
  - $chf < 0.02$  AND  $|\eta| < 2.0$

Table 10.5. Summary of the jet definitions used in the 2012 analysis

Baseline Jets	
algorithm	<b>AntiKt4Topo</b>
acceptance	$p_T > 20 \text{ GeV}$ $ \eta^{cl}  < 4.5$
quality	reject very loose bad jets
Signal Jets	
acceptance	$p_T > 45 \text{ GeV}$ $ \eta  < 2.5$

- or  $chf < 0.05$  AND  $emf > 0.9$  AND  $|\eta| < 2.0$

the event was discarded.

9. If the energy-weighted mean time of  $N$  jets was  $\langle t \rangle > 4 \text{ ns}$ , the event was discarded.
10. If a jet was near LBC28 with  $E_{layer2}/E_{jet} > 0.6$ , the event was discarded.
11. If a jet was near  $\eta = -0.1$  and  $\phi = 2, 3$  with  $chf < 0.3$  and  $emfrac < 0.2$ , the event was discarded.
12. If  $((E_T^{\text{miss}})^{CellOut} / E_T^{\text{miss}}) \times \cos [\phi(E_T^{\text{miss}})^{CellOut} - \phi(E_T^{\text{miss}})] > 0.5$ , the event was discarded.
13. If any jet with  $p_T > 40 \text{ GeV}$  and  $BCH\_CORR\_JET > 5\%$ , the event was discarded.
14. If a CR muon had  $|\mu\_staco\_z0\_exPV| \geq 1$  or  $|\mu\_staco\_d0\_exPV| \geq 0.2$ , the event was discarded.
15. If a muon had  $\sqrt{\mu\_staco\_cov\_qoverp\_exPV} / |\mu\_staco\_qoverp\_exPV| \geq 0.2$ , the event was discarded
16. If  $((E_T^{\text{miss}})^{CellOut} / E_T^{\text{miss}}) \times \cos [\phi(E_T^{\text{miss}})^{CellOut} - \phi(E_T^{\text{miss}})] > 0.5$ , the event was discarded.
17. If an electron or muon had  $p_T > 10 \text{ GeV}$ , the event was discarded.

### 10.3 Monte Carlo Samples

The vector boson samples contained massive  $c$  and  $b$  quarks that were split by jet content and  $p_T$ . Simplified models were used to simulate  $\tilde{q}\tilde{q} \rightarrow qq \tilde{\chi}_1^0 \tilde{\chi}_1^0$  using MADGRAPH

interfaced with PYTHIA, and the cross-sections were calculated at NLO+NLL. Samples were reweighted for PU using minimum bias generated with PYTHIA. The  $\langle \mu \rangle$  value was scaled by 1.11 following the recommendations of the tracking performance group to keep MC in agreement with data.

Table 10.6. Summary of MC generators used in the 2012 analysis

process	generator
multijets	PYTHIA
$W + jets$	SHERPA(massive $c$ and $b$ )
$Z + jets$	SHERPA(massive $c$ and $b$ )
$\gamma + jets$	SHERPA(massive $c$ and $b$ )
$t\bar{t}$	POWHEG+PYTHIA
single top	MC@NLO+ACERMC
$t\bar{t} + V$	MADGRAPH+PYTHIA
diboson	SHERPA(massive $c$ and $b$ )
ST $\tilde{q}\tilde{q}$	MADGRAPH+PYTHIA

#### 10.4 Systematic Uncertainties

The standard systematic uncertainties (Sections 6.2 and 7.4) were applied to MC with a few details:

- JES - assumes an even mixture of quarks and gluons with no knowledge of the true flavor
- JER - each jet was smeared by a Gaussian distribution, and was considered as a one-sided systematic because MC resolution was always better than data
- $b$ -tagging - variations to efficiency of light-quark mis-tagging, charm-quark tagging and mis-tagging, and  $b$ -quark tagging
- JVF - implemented as event weights: 1.02 for each passing jet, 0.8 for each failing jet
- $E_T^{\text{miss}}$  - included cell-out components and PU
- luminosity - set to  $\pm 2.8\%$



Vector boson uncertainties in the renormalization, factorization, and matching scales were applied using ALPGEN variations to SHERPA samples with truth jets. A 50% uncertainty was assigned to the PDF variations. In the  $W$ ,  $Z$ , and  $\gamma$  samples, the  $c$  and  $b$  quarks are massless, but they are massive in the other samples. A 7% uncertainty is applied to the theoretical cross-section. The  $t\bar{t}$  weights are binned by  $p_T$ :

- $p_T < 40$  GeV
- $40 \leq p_T < 170$  GeV
- $170 \leq p_T < 340$  GeV
- $p_T > 340$  GeV

The weights decrease by bin from  $\sim 1.0$  to  $\sim 0.57$ . Renormalization and factorization scales were varied by factors of 2 to estimate the uncertainty. The MC generator variation was estimated as the difference to ALPGEN generation, and parton shower was estimated from the difference between PYTHIA and JIMMY. ISR and FSR uncertainty used ACERMC to vary parton showering. These variations were also applied to the single top samples, but  $t\bar{t} + V$  was given a flat estimate of  $\pm 22\%$ . Signal samples varied renormalization, factorization, and  $\alpha_S$  scales by a factor of 2, and a systematic associated to ISR used the following factor:

$$\delta = A \left( 1 - \frac{\Delta m}{300} \right)$$

$$\text{if } m_{heavy} \geq 300 \text{ GeV} : A = \sqrt{0.0725} \tag{10.1}$$

$$\text{else} : A = \frac{1}{4} \sqrt{0.0725} \left( 1 - \frac{m_{heavy} - 200}{100} \right)$$

## 10.5 Definition of Signal Regions

The 2012 analysis was only focused on the 0-lepton channel. Two signal points from the simplified decay  $\tilde{q}\tilde{q} \rightarrow qq \tilde{\chi}_1^0 \tilde{\chi}_1^0$  were chosen for optimization:

- $m_{\tilde{q}} = 850$  GeV,  $m_{\tilde{\chi}_1^0} = 100$  GeV
- $m_{\tilde{q}} = 450$  GeV,  $m_{\tilde{\chi}_1^0} = 400$  GeV

MC was normalized to 0.53 for  $W + jets$ , 0.82 for  $Z + jets$ , and 0.78 for top. Estimations of the significance of signal events used preliminary CRs rather than iteratively running through the entire HistFitter process. The test statistic used for optimization was its  $z$ -score:

$$z = \frac{S}{\sqrt{B + \sigma_{BG}^2 + \sigma_{sig}^2}} \quad (10.2)$$

For optimization, an 8% relative uncertainty for BG events was estimated and the uncertainty for signal was taken as the ISR uncertainty. The potential for exclusion limits was drawn wherever  $z = 2$  for  $\tilde{q}\tilde{q}$  production. A comparison to HistFitter results showed good agreement to this approximation. High- $M_R$  values were suitable for high  $m_{\tilde{q}}$  but decreased sensitivity along the diagonal of compressed points. High- $R$  values also tended to reduce sensitivity to large  $m_{\tilde{\chi}_1^0}$ . The best cuts for optimization are shown in Table 10.7.

Table 10.7. SR definitions for loose and tight regions in 2012

	SRloose	SRtight
$E_T^{\text{miss}}$ [GeV]	> 160	
$p_T(j_1, j_2)$ [GeV]	> 150	> 200
$\Delta\phi(\vec{p}_T(j_1, j_2), \vec{E}_T^{\text{miss}})$	> 0.4	> 1.4
$R$	> 0.5	> 0.6
$M_R$ [GeV]	> 700	> 900

## 10.6 Definition of Control and Validation Regions

Multijet CRs were defined from the 0-lepton channel where QCD events were abundant. Two regions for CRQ were chosen based on their relationship to SRloose and SRtight. A table defining these regions is shown in Table 10.8.  $W + jets$  CRs were defined from the 1-lepton channel with  $b$ -veto where  $W \rightarrow \ell\nu$  events were abundant. A table defining these regions is shown in Table 10.9.  $Z + jets$  CRs were defined from the 2-lepton channel where

$Z \rightarrow \ell\ell$  events were abundant. These events were also used to mimic  $Z \rightarrow \nu\nu$  as a source of  $E_T^{\text{miss}}$ . A table defining these regions is shown in Table 10.10. Top CRs were defined from the 1-lepton channel with  $b$ -tag, where  $t \rightarrow \ell b$  events were abundant. A table defining these regions is shown in Table 10.11. Diagrammatic representations of all regions are shown in Figures 10.4-10.5.

Table 10.8. CR and VR definitions for QCD loose and tight regions in 2012

	CRQloose	CRQtight	VRQloose	VRQtight
$n_\ell$	= 0			
$p_T(j1, j2)$ [GeV]	> 150	> 200	> 150	> 200
$E_T^{\text{miss}}$ [GeV]	> 160			
$\Delta\phi(p_T(j_2), E_T^{\text{miss}})$	< 0.2		< 0.4	< 1.4
$R$	$0.35 < R < 0.45$	$0.5 < R < 0.55$	$0.45 < R < 0.5$	$0.54 < R < 0.6$
$M_R$ [GeV]	> 1000		> 900	

Table 10.9. CR and VR definitions for  $W + jets$  in 2012

	CRW	VRW
$n_\ell$	$e$ or $\mu$	
$b$ -jets	= 0	
interpret	$\ell$ as $j$	
$R$	$0.3 < R < 0.55$	$0.55 < R < 1.0$
$M_R$ [GeV]	> 800	$400 < M_R < 1000$

Table 10.10. CR and VR definitions for  $Z + jets$  in 2012

	CRZ	VRZ
$n_\ell$	$e^\pm e^\mp$ or $\mu^\pm \mu^\mp$	
$m_{\ell\ell}$ [GeV]	$66 < m_{\ell\ell} < 116$	
interpret	$E_T^{\text{miss}} =  E_T^{\text{miss}} + p_T(\ell\ell) $	
$R$	$0.3 < R < 0.55$	$0.55 < R < 1.0$
$M_R$ [GeV]	> 800	$400 < M_R < 1000$

Table 10.11. CR and VR definitions for  $t\bar{t}$  in 2012

	CRT	VRT
$n_\ell$ $b$ -jets interpret	$e$ or $\mu$ $= 0$ $\ell$ as $j$	
$R$ $M_R$ [GeV]	$0.3 < R < 0.55$ $> 800$	$0.55 < R < 1.0$ $400 < M_R < 1000$

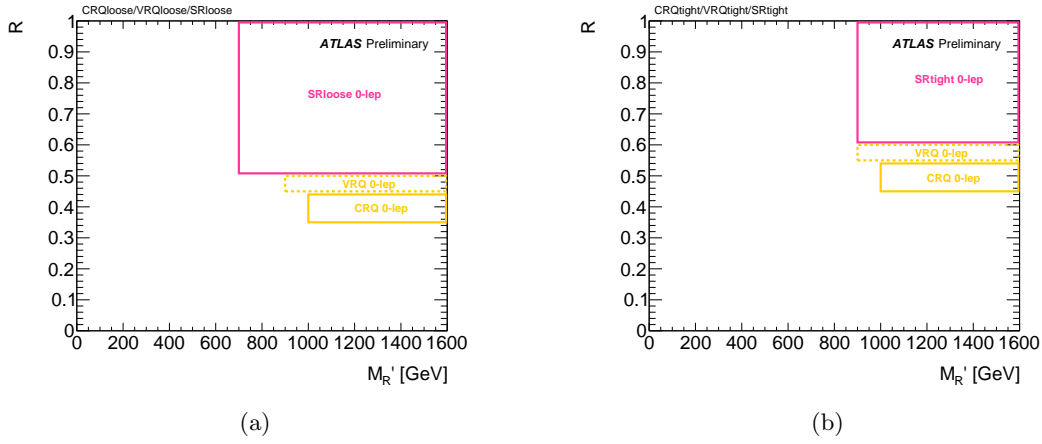


Figure 10.4. Schematic of CR, VR, and SR configurations for the (a) loose and (b) tight regions.

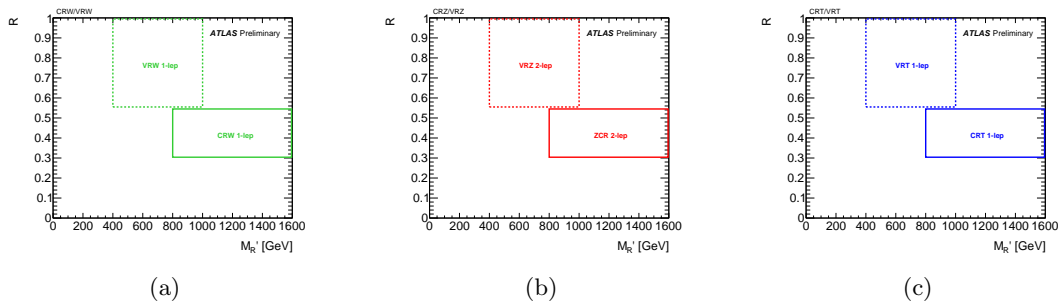


Figure 10.5. Schematic of CR and VR configurations for (a)  $W + jets$ , (b)  $Z + jets$ , and (c) top regions.

## 10.7 QCD MC Cleaning

A distribution of the QCD multijet MC clearly shows that some events appeared to spike above the smooth distribution. These were events at the tail of the individual sample distributions where the statistics were low but the weight was high. Figure 10.6 shows the individual samples (JZ0-JZ7) stacked on top of each other. It became apparent that JZ0 could not be salvaged, which was a shared preliminary recommendation from the BG group, but they also recommended the removal of JZ1. This figure shows that some of the JZ1 events could be kept if the overweighted spikes were removed.

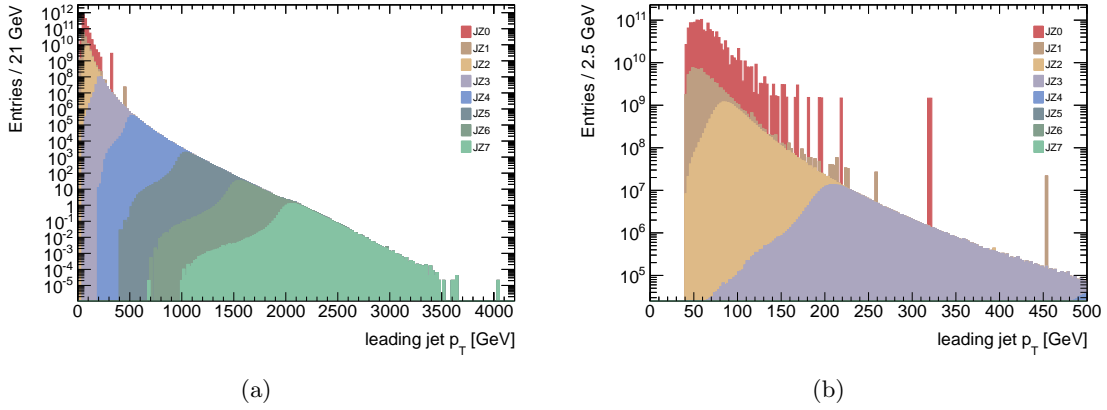


Figure 10.6. Stacked distributions of QCD multijet BG for (a) the full range of  $p_T$  and (b) low  $p_T$ .

### 10.7.1 Nested Exponential Model

Previous attempts at a fit of this background used a double exponential, but this did not accurately model the “dip” in the distribution where most of the problematic events occurred. Instead, a model was derived to consider a steep exponential slope that asymptotically approached a shallow slope.

$$f(x) = \exp\left(ae^{bx} + cx\right) \tag{10.3}$$

$$a > 0; b, c < 0$$

Attempting to fit this function to the histograms resulted in some lackluster results. Fitting the logarithm of this distribution was considered, which would exhibit more linear behavior, but unbinned fits could not be used because of the limitations of logarithms:

$$\ln(x_1 + x_2) \neq \ln(x_1) + \ln(x_2) \quad (10.4)$$

Instead, binned fits would have to suffice. The automatic fitting procedure did not converge well because the range and starting values of the parameters had a large effect on the outcome, although an ocular method had much better fits. Three methods to automate the fit parameters were developed.

### 10.7.2 Three Fit Methods

The first was a push-pull method where the number of bins is varied. The fit was performed over each step from 2 bins to 500 bins. The lower number of bins set the approximately linear behavior of the fit while the higher number of bins targeted the problematic “dip” region (Figure 10.7). The fit parameters at this step “pushed” or “pulled” at the fit to make this correction according to its derivatives.

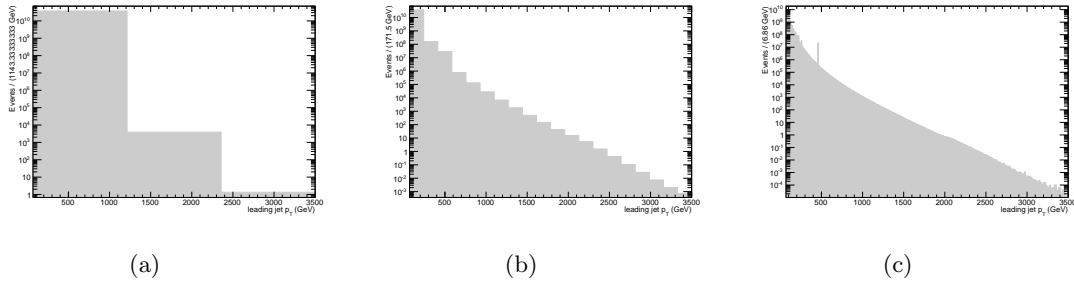


Figure 10.7. The distribution of QCD multijet events while varying the number of bins from (a) 3 bins to (b) 20 bins and (c) 500 bins.

$$\frac{\partial f}{\partial c} = x f \quad (10.5a)$$

$$\frac{\partial f}{\partial a} = f e^{bx} \quad (10.5b)$$

$$\frac{\partial f}{\partial b} = a \frac{\partial f}{\partial c} e^{bx} \quad (10.5c)$$

$$\frac{\partial f}{\partial x} = ab \frac{\partial f}{\partial a} + cf \quad (10.5d)$$

An unbinned fit is like a binned fit with an infinite number of bins. A second fit method involved a “1.5” dimensional fit that fakes this behavior by allowing the individual samples to overlap like a multi-valued function. Each individual sample defines a mean value and an uncertainty (RMS) for a total of only 7 points, which would make fitting easier. The error on the fit would be related to the RMS of each individual sample. In Figure 10.8 shows this behavior in a 2-dimensional plane on the left while the distribution on the right shows this behavior from a higher dimension.

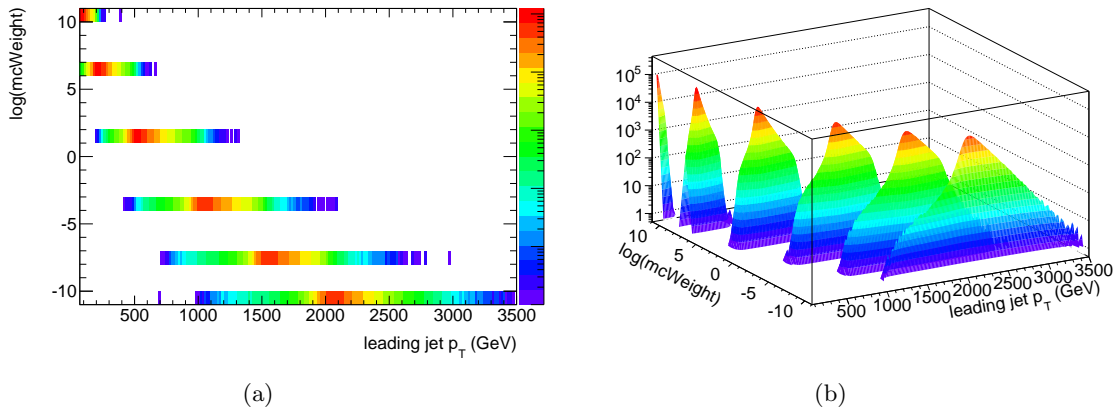


Figure 10.8. A “1.5” dimensional fit of mean values with uncertainty determined by distributions shown in (a) a 2D histogram and (b) a 3D perspective.

The final method used was a bootstrap method that iteratively refined the parameter ranges and starting values until they began to converge. The exponential tail was mostly isolated in the high jet  $p_T$  region, so the parameter of  $c$  was set to best approximate this

feature. Parameter  $a$  was guessed initially and  $b$  was held constrained. The function was fit to obtain a better parameter for  $a$ . Then a guess for  $b$  was set and  $a$  was held constrained. A second fit resulted in a better parameter for  $b$ . This fit refinement was repeated until the parameters had converged. The performance of this fit is shown in Figure 10.9.

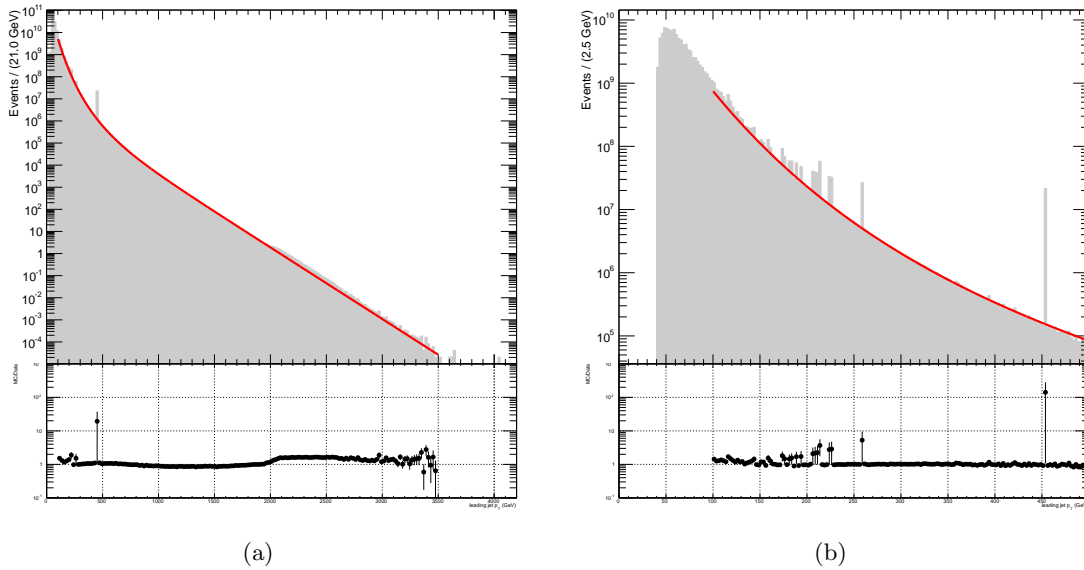


Figure 10.9. A bootstrapped fit of the jet  $p_T$  distribution for (a) the full spectrum and (b) a windowed view. The ratio is an MC count divided by the fit.

An unintended consequence of this method was the discovery of the “bump” at  $p_T \sim 2000$  GeV visible in the ratio plot on the left of the figure, which represents an excess of the distribution above the fit. Since the tail parameter was held constant in the fit, the ratio still plateaus, but this bump indicates that the distribution has an excess above the fit. Upon further inspection, this bump was only coming from the J7 sample that appeared as if it had peaked too low in  $p_T$ . Instead, it was due to a change in the recommended cross-sections of each sample, but the J7 sample had not been updated with the new weights. The effect was caught by software we developed to document all the metadata of all samples, including consistency between updates, and it was capable of making quality checks and displaying them graphically.



### 10.7.3 Removing Spikes

The various fits were in a strong agreement to the parameters of the fit. The variance of the different methods was considered to be a systematic error. Events that stood out from this fit and above the range between methods were cleaned from the QCD multijet BG. JZ1 had 3914 simulated events, but this combined fit only required the removal of 21 entries.

$$a = 11.5355 \pm 0.06 \quad (10.6a)$$

$$b = -0.0044 \pm 0.004 \quad (10.6b)$$

$$c = -0.0074 \pm 0.0001 \quad (10.6c)$$

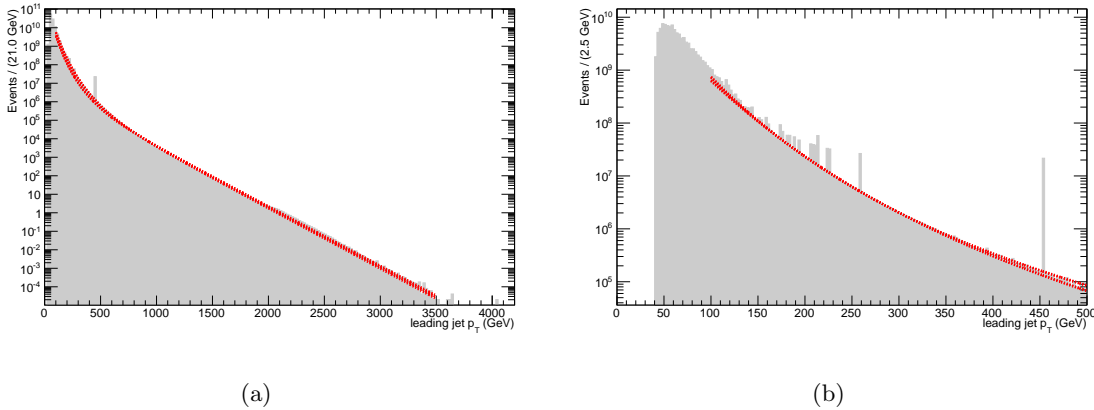


Figure 10.10. A combination of fits showing the strong agreement between push-pull, “1.5D”, and bootstrap methods for the (a) full view and (b) a windowed view.

Ultimately, it was decided to compare the samples at truth level. The truth samples had a cleaner  $p_T$  spectra without all the resolution effects of a detector-corrected MC. The individual samples had a much sharper cutoff in their assigned  $p_T$  bins (Table 10.12).

The promotion of events into tails with large weights came from a minimum bias overlay on the hard scatter. The jet group recommended keeping events if:

Table 10.12. Bins for the truth jet  $p_T$  used in the 2012 analysis

sample	true jet $p_T$ [GeV]
JZ0	0-20
JZ1	20-80
JZ2	80-200
JZ3	200-500
JZ4	500-1000
JZ5	1000-1500
JZ6	1500-2000
JZ7	2000+

$$0.6 < \frac{p_T^{avg}}{p_T^{truth}(j_1)} < 1.4 \quad (10.7)$$

The average  $p_T$  was calculated from the two leading reconstructed jets:

$$p_T^{avg} = \frac{1}{2}(p_T^{reco}(j_1) + p_T^{reco}(j_2)) \quad (10.8)$$

The sample weights were scaled to correct for the apparent inefficiency after events were removed. A comparison before and after this cut is shown in Figure 10.11.

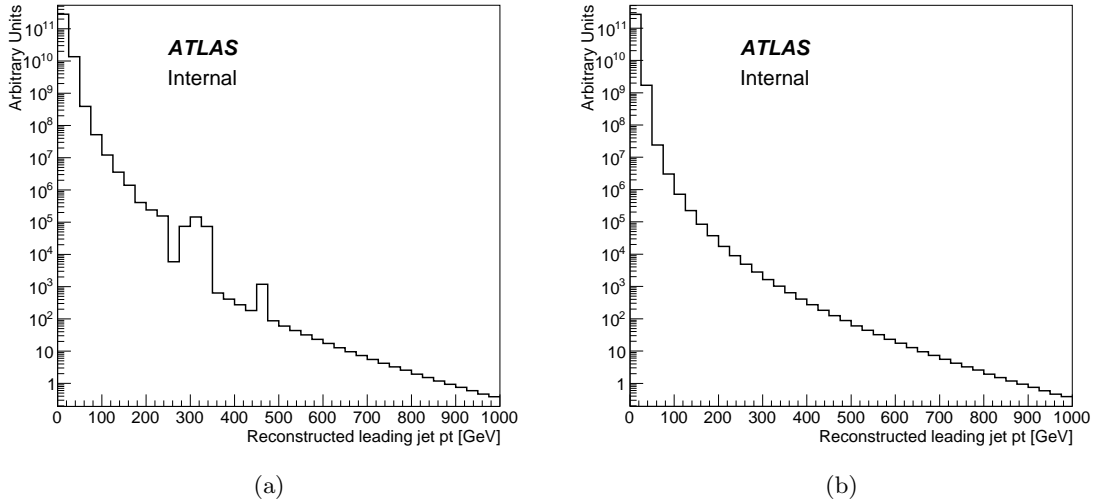


Figure 10.11. A comparison of the leading jet  $p_T$  spectrum (a) before and (b) after truth cleaning.

## 10.8 Background CR Fit

The CR BG fit estimation used a variety of methods, which are given in Table 10.13. Where applicable, the HistFitter results before and after the CR BG fit are shown in Figures 10.12-10.14.

Table 10.13. Estimation methods used in the BG fit in 2012

BG	0-lepton	1-lepton	2-lepton
multijets	MJ CRs	matrix method	matrix method
$W \rightarrow l\nu$	$W$ CRs	CR fit	MC
$Z \rightarrow \ell\ell$	$Z$ CRs	MC	CR fit
$t\bar{t}$	$t\bar{t}$ CRs	CR fit	MC
single top	MC	MC	MC
$t\bar{t} + V$	MC	MC	MC
dibosons	MC	MC	MC
$\gamma + jets$	MC CRs	MC	MC

A count of MC expectation and BG fit for the number of events in each region is shown in Tables 10.14 and 10.15.

Table 10.14. BG fit result for SRloose

	CRQ	CRW	CRZ	CRT	SRloose
MC multijets	1265.16	0	0	0	17.95
MC ZX	67.49	252.90	97.62	16.87	761.85
MC WX	154.92	2.14	3654.91	484.45	793.62
MC $t\bar{t}$	48.04	24.27	293.15	1152.05	137.74
MC single top	14.06	2.16	73.26	208.81	23.90
MC $t\bar{t}V$	0.88	1.24	4.59	19.95	4.71
MC diboson	20.05	21.85	266.64	56.54	111.74
MC fakes	0	1.55	73.41	83.15	0
MC DY	4.81	0	0.76	0.29	0.04
BG expected	1575.43	306.11	4464.41	2022.14	1851.59
multijets fit	$974.96 \pm 64.04$	$0 \pm 0$	$0 \pm 0$	$0 \pm 0$	$13.92 \pm 13.26$
ZX fit	$63.80 \pm 27.05$	$205.59 \pm 20.47$	$91.24 \pm 40.93$	$15.91 \pm 7.68$	$618.19 \pm 76.41$
WX fit	$97.39 \pm 52.14$	$1.22 \pm 0.83$	$2125.73 \pm 170.02$	$302.88 \pm 171.25$	$454.41 \pm 39.87$
$t\bar{t}$ fit	$45.76 \pm 2.99$	$25.12 \pm 4.46$	$296.11 \pm 42.63$	$964.50 \pm 164.87$	$117.31 \pm 21.66$
single top fit	$13.27 \pm 1.32$	$2.49 \pm 0.82$	$71.72 \pm 13.09$	$198.31 \pm 22.74$	$24.85 \pm 2.57$
$t\bar{t}V$ fit	$0.62 \pm 0.20$	$1.23 \pm 0.28$	$3.98 \pm 1.11$	$17.22 \pm 4.21$	$3.68 \pm 1.04$
diboson fit	$17.14 \pm 8.93$	$17.44 \pm 9.39$	$228.83 \pm 119.89$	$48.55 \pm 25.37$	$93.46 \pm 48.98$
fake fit	$0 \pm 0$	$1.61^{+1.86}_{-1.61}$	$73.72 \pm 31.51$	$77.48 \pm$	$0 \pm 0$
DY fit	$4.61 \pm 0.91$	$0 \pm 0$	$0.67 \pm 0.07$	$0.30 \pm 0.01$	$0.06 \pm 0.06$
BG fit	$1217.59 \pm 35.54$	$254.71 \pm 16.13$	$2892.06 \pm 59.38$	$1612.17 \pm 45.51$	$1325.91 \pm 83.54$
observed	1217	255	2892	1623	1322

Table 10.15. BG fit result for SRTight

	CRQ	CRW	CRZ	CRT	SRloose
MC multijets	42.71	0	0	0	2.64
MC ZX	7.35	252.90	97.62	16.87	57.66
MC WX	21.09	2.14	3654.91	484.45	48.93
MC $t\bar{t}$	4.03	24.27	293.15	1152.05	1.81
MC single top	1.88	2.16	73.26	208.81	1.62
MC $t\bar{t}V$	0.11	1.24	4.59	19.95	0.22
MC diboson	1.55	21.85	266.64	56.54	10.18
MC fakes	0	1.55	73.41	83.15	0
MC DY	1.39	0	0.76	0.29	0
BG expected	80.11	306.11	4464.41	2022.14	123.05
multijets fit	$38.90 \pm 10.21$	$0 \pm 0$	$0 \pm 0$	$0 \pm 0$	$2.40 \pm 2.39$
ZX fit	$7.96 \pm 3.88$	$202.79 \pm 19.67$	$107.92 \pm 60.81$	$19.19 \pm 11.64$	$45.06 \pm 6.12$
WX fit	$14.14 \pm 6.20$	$1.28 \pm 0.75$	$2079.26 \pm 164.46$	$316.59 \pm 148.21$	$27.04 \pm 2.98$
$t\bar{t}$ fit	$4.10 \pm 0.80$	$24.34 \pm 3.72$	$287.79 \pm 40.05$	$931.20 \pm 140.87$	$1.65 \pm 0.49$
single top fit	$2.09 \pm 0.95$	$1.83 \pm 0.66$	$69.47 \pm 12.19$	$204.30 \pm 23.46$	$1.81 \pm 0.34$
$t\bar{t}V$ fit	$0.11 \pm 0.03$	$1.23 \pm 0.28$	$4.32 \pm 1.19$	$19.32 \pm 4.61$	$0.20 \pm 0.07$
diboson fit	$1.72 \pm 0.87$	$21.51 \pm 10.20$	$268.32 \pm 125.47$	$58.08 \pm 27.20$	$9.99 \pm 4.70$
fake fit	$0 \pm 0$	$1.65^{+1.89}_{-1.65}$	$74.16 \pm 31.71$	$77.10 \pm 21.24$	$0 \pm 0$
DY fit	$0.35^{+0.72}_{-0.35}$	$0 \pm 0$	$0.69 \pm 0.08$	$0.29 \pm 0.01$	$0 \pm 0$
BG fit	$69.31 \pm 8.26$	$254.63 \pm 15.97$	$2891.98 \pm 53.85$	$1626.09 \pm 44.09$	$88.15 \pm 7.85$
observed	70	255	2892	1623	74

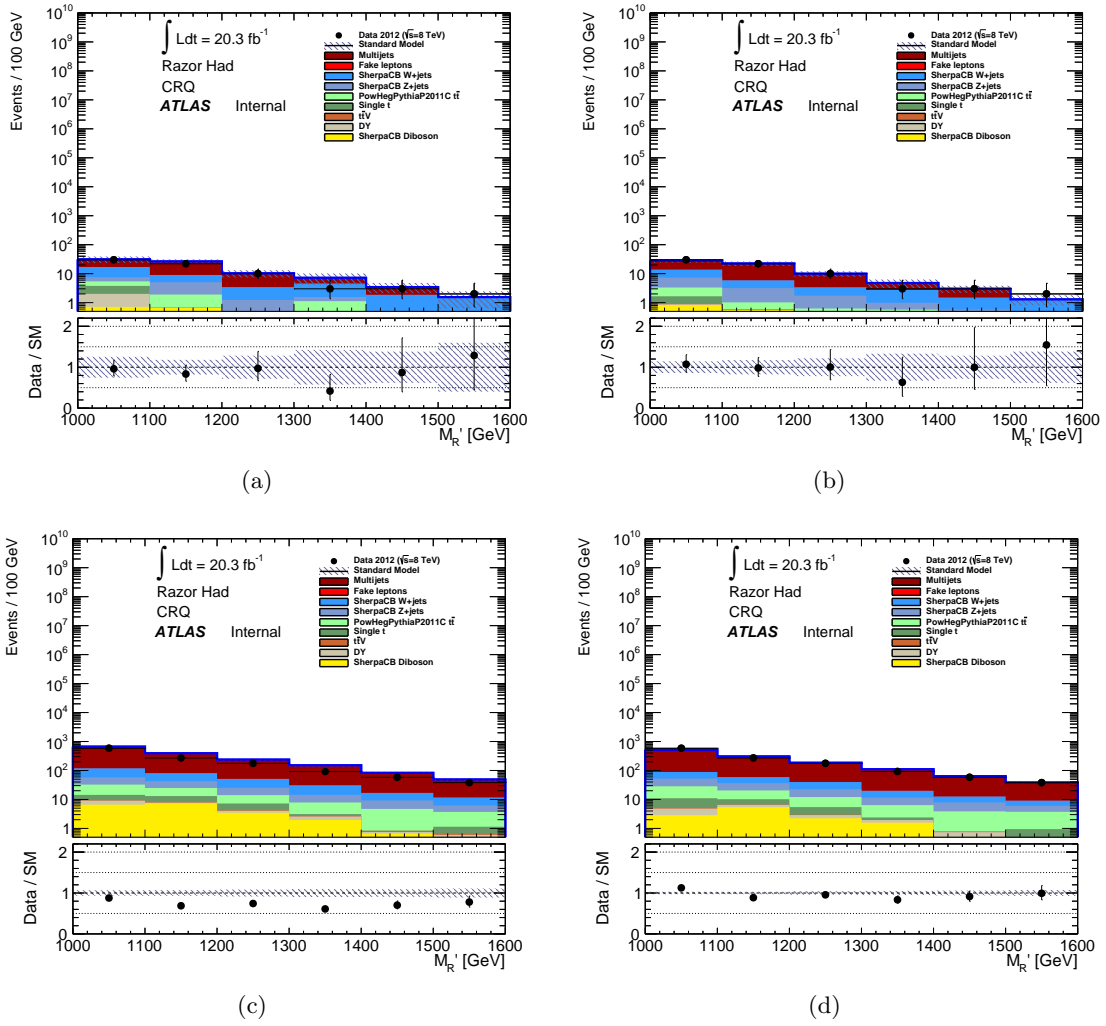


Figure 10.12. A comparison of MC to data in multijet CRs (left) before and (right) after the fit for (top) CR<sub>tight</sub> and (bottom) CR<sub>loose</sub>.

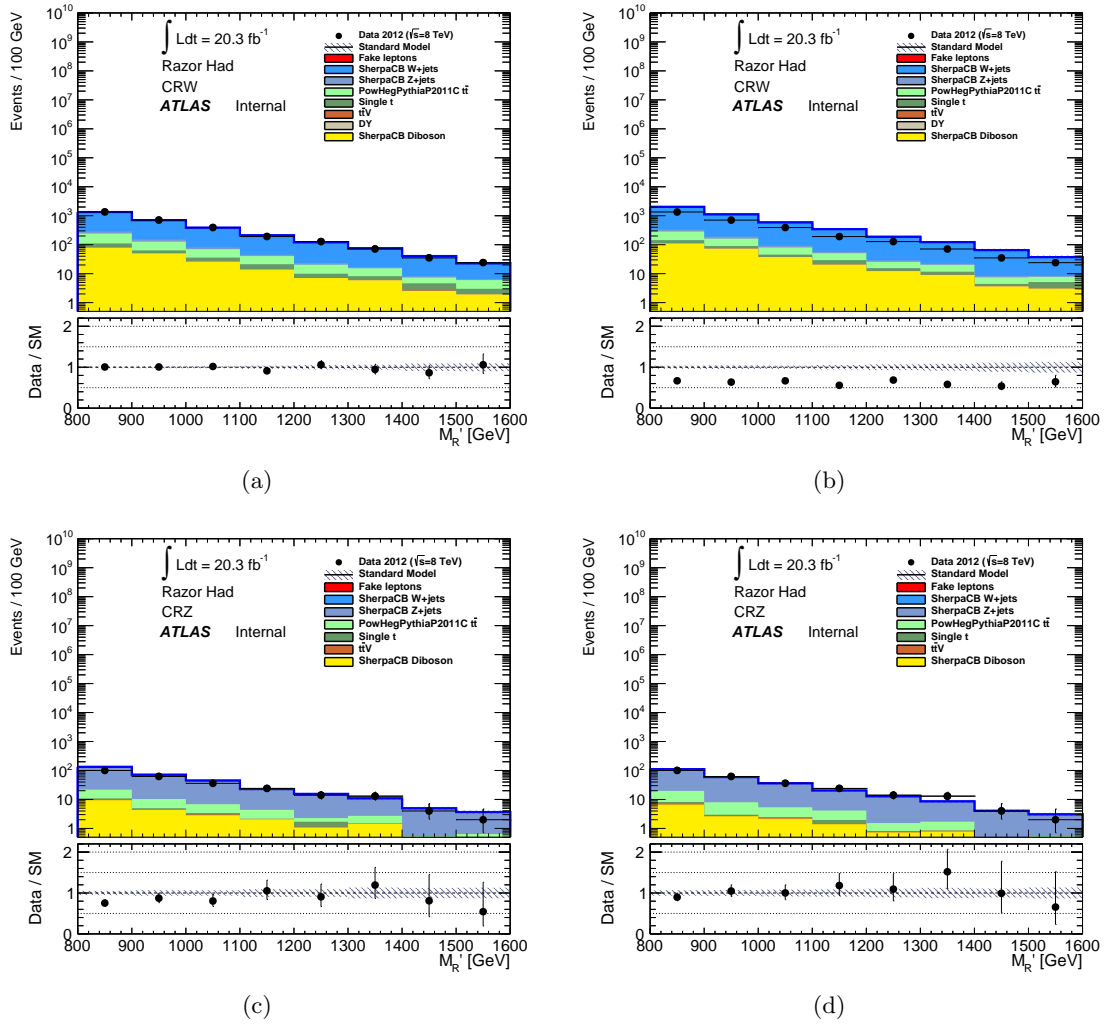


Figure 10.13. A comparison of MC to data (left) before and (right) after the fit for (top)  $W$  and (bottom)  $Z$  CRs.

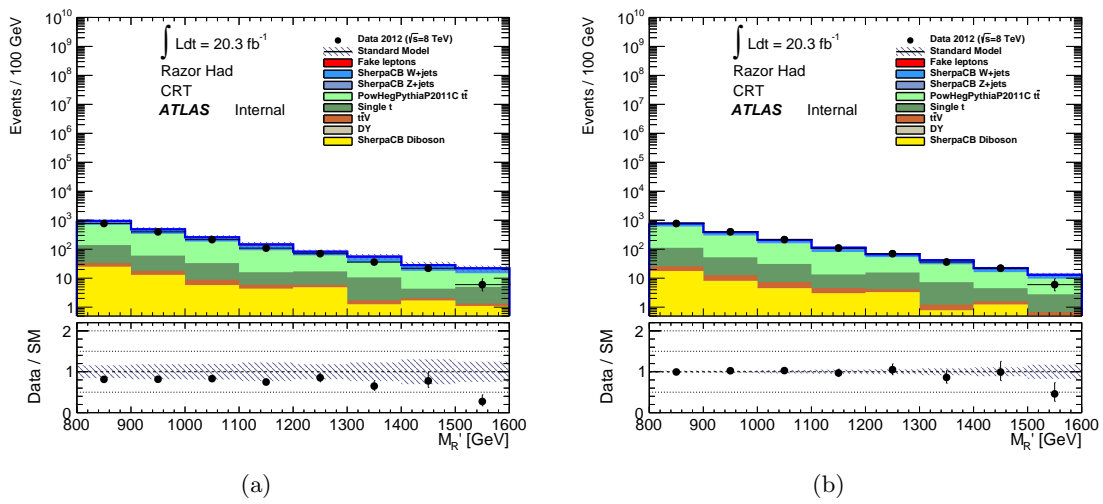


Figure 10.14. A comparison of MC to data (left) before and (right) after the fit for top CRs.

## 10.9 Signal Region Extrapolation

The combined fit used a variety of scales and parameters to enable the combined fit of all channels and samples with systematic variations. These parameters are shown in Tables 10.16 and 10.17. The free-floating parameters were set by the combined fit to best adjust the BG distributions. For a good fit quality, the evaluation of these parameters at each step should be independent, which is shown in the correlation matrices of Figures 10.16 and 10.17. Once all the systematic parameters and scale factors were set by the combined fit, the amount of “pull” that each has on the MC estimate gave a measure of how vital the variation was to the analysis. Figure 10.18, for example, shows that  $b$ -tagging was again a crucial part of this analysis and had a large effect.



Table 10.16. Systematic uncertainties of SRloose

uncertainty	SRloose
mu_ZX	$\pm 63.07$
alpha_theoryDiboson	$\pm 49.40$
alpha_Z_ktScale	$\pm 43.35$
mu_WX	$\pm 36.33$
mu_ttbar	$\pm 20.06$
alpha_theoSysQCD	$\pm 13.23$
alpha_EtaIntercalibration_Modelling	$\pm 8.19$
alpha_JER	$\pm 6.54$
alpha_WZDBXSec	$\pm 6.51$
alpha_W_qScale	$\pm 5.16$
alpha_EffectiveNP_2	$\pm 4.72$
alpha_Z_qScale	$\pm 3.92$
alpha_Btag1	$\pm 3.67$
alpha_STXSec	$\pm 1.68$
alpha_EffectiveNP_1	$\pm 1.53$
alpha_W_ktScale	$\pm 1.06$
mu_QCD	$\pm 0.92$
alpha_BJes	$\pm 0.90$
alpha_TTWXSec	$\pm 0.81$
alpha_PileupRhoTopology	$\pm 0.77$
alpha_FlavorCompUncert	$\pm 0.75$
alpha_FlavorResponseUncert	$\pm 0.59$
alpha_SCALEST	$\pm 0.34$
alpha_EventW	$\pm 0.21$
alpha_RESOST	$\pm 0.20$
alpha_st_PDF	$\pm 0.00$
alpha_ttbar_RScales	$\pm 0.00$
alpha_ZX_PDF	$\pm 0.00$
alpha_Diboson_PDF	$\pm 0.00$
alpha_ttbar_PDF	$\pm 0.00$
alpha_ttbar_FScales	$\pm 0.00$
alpha_WX_PDF	$\pm 0.00$
alpha_ttbarV_PDF	$\pm 0.00$
BG expectation	1325.91
BG systematic	$\pm 6.30\%$

Table 10.17. Systematic uncertainties of SRtight

uncertainty	SRtight
alpha_theoryDiboson	$\pm 4.69$
mu_ZX	$\pm 4.48$
alpha_Z_ktScale	$\pm 3.39$
alpha_theoSysQCD	$\pm 2.28$
mu_WX	$\pm 2.14$
alpha_EventW	$\pm 0.84$
alpha_EffectiveNP_1	$\pm 0.80$
mu_QCD	$\pm 0.70$
alpha_WZDBXSec	$\pm 0.69$
alpha_W_qScale	$\pm 0.51$
alpha_Z_qScale	$\pm 0.38$
alpha_EtaIntercalibration_Modelling	$\pm 0.33$
mu_ttbar	$\pm 0.25$
alpha_BJes	$\pm 0.22$
alpha_EffectiveNP_2	$\pm 0.22$
alpha_W_ktScale	$\pm 0.22$
alpha_SCALEST	$\pm 0.20$
alpha_Btag1	$\pm 0.19$
alpha_STXSec	$\pm 0.12$
alpha_JER	$\pm 0.10$
alpha_TTWXSec	$\pm 0.04$
alpha_RESOST	$\pm 0.04$
alpha_PileupRhoTopology	$\pm 0.03$
alpha_FlavorCompUncert	$\pm 0.02$
alpha_FlavorResponseUncert	$\pm 0.00$
alpha_ttbar_RScales	$\pm 0.00$
alpha_ZX_PDF	$\pm 0.00$
alpha_Diboson_PDF	$\pm 0.00$
alpha_ttbar_PDF	$\pm 0.00$
alpha_st_PDF	$\pm 0.00$
alpha_ttbar_FScales	$\pm 0.00$
alpha_WX_PDF	$\pm 0.00$
alpha_ttbarV_PDF	$\pm 0.00$
BG expectation	88.15
BG systematic	$\pm 8.91\%$

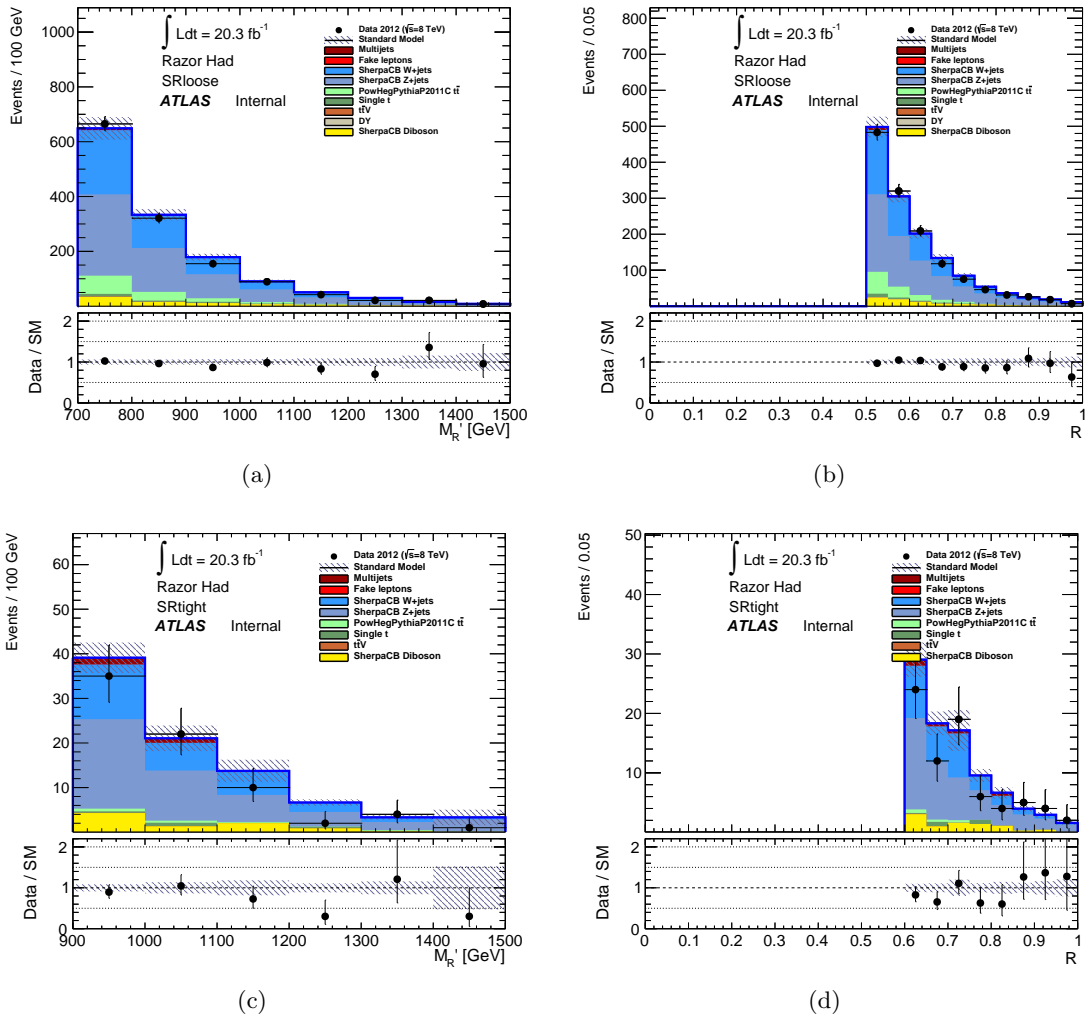


Figure 10.15. A distribution of (left)  $M_R$  and (right)  $R$  in (top) SRloose and (bottom) SRTight after the combined fit comparing data and MC.

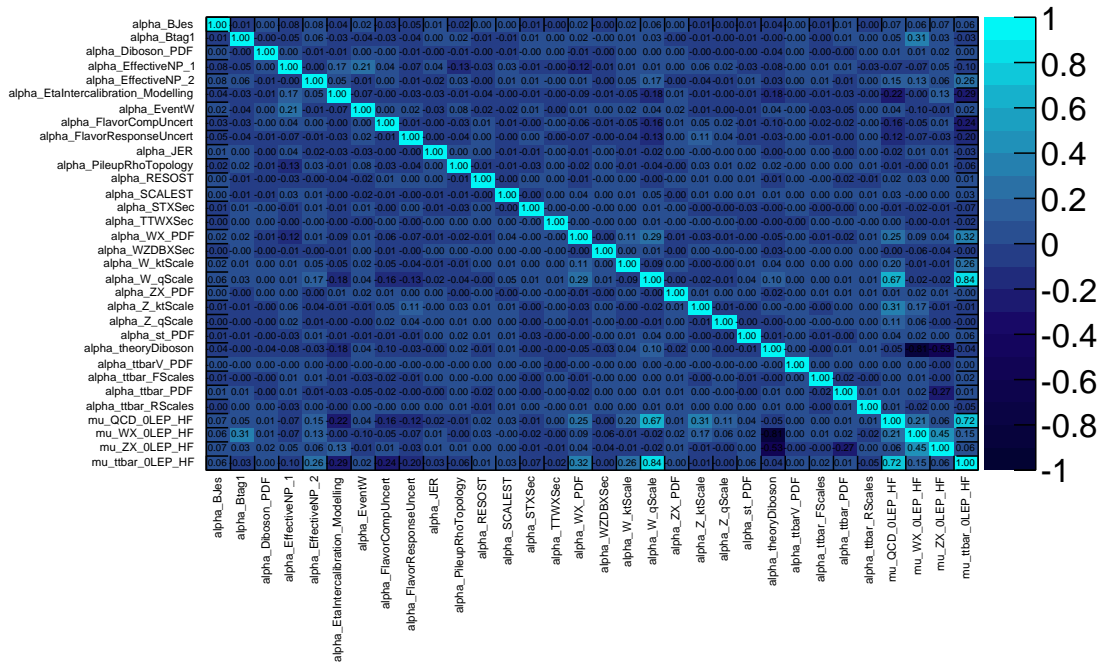


Figure 10.16. A correlation matrix of all free-floating parameters used in the combined fit for SRloose.

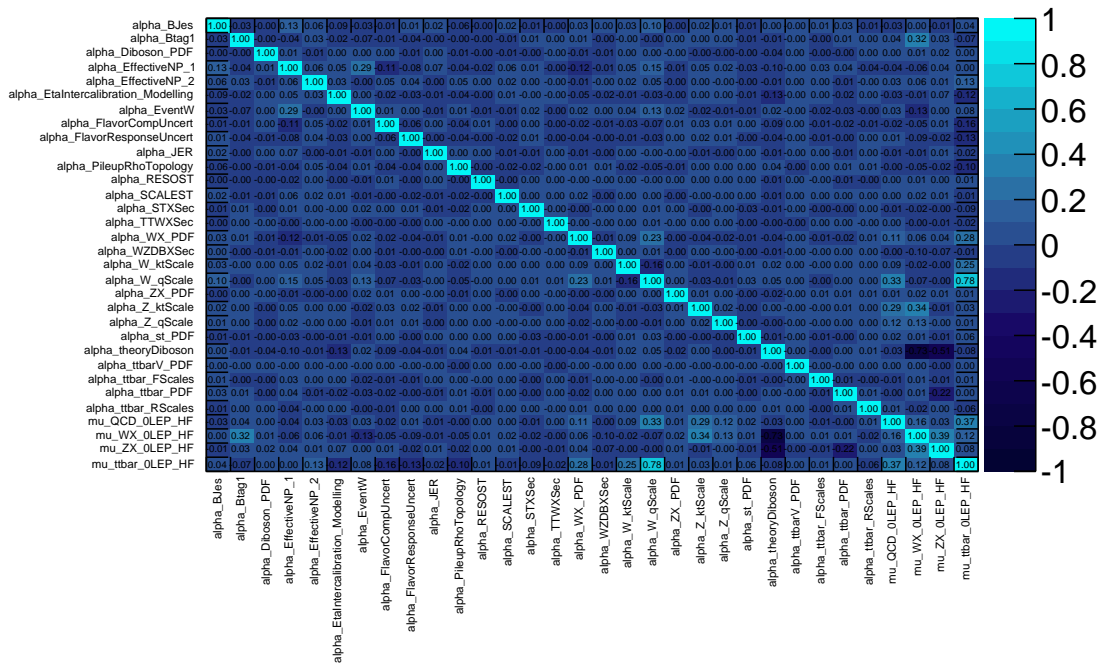


Figure 10.17. A correlation matrix of all free-floating parameters used in the combined fit for SRtright.

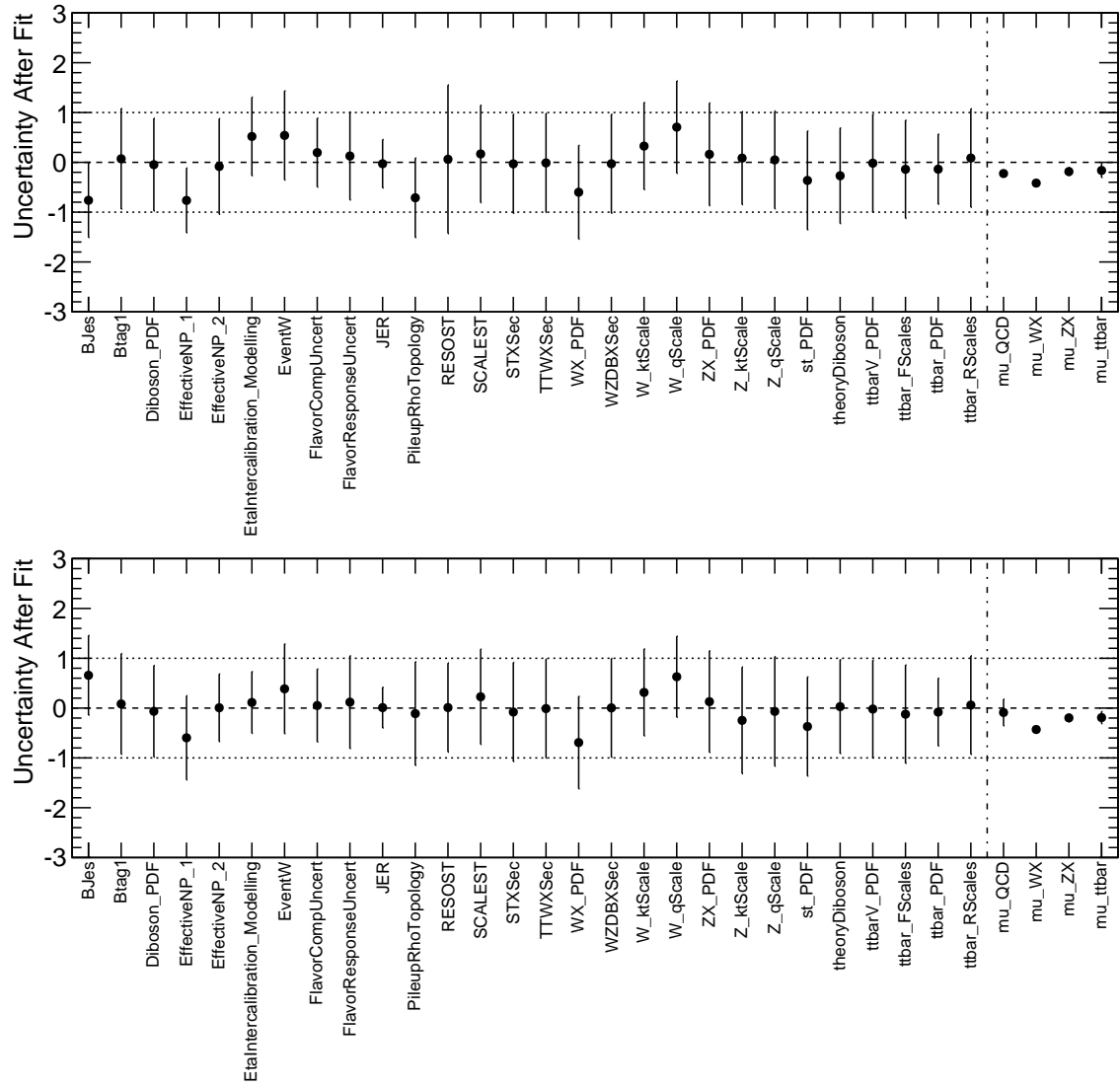
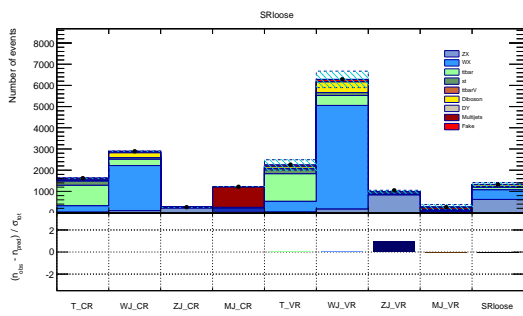
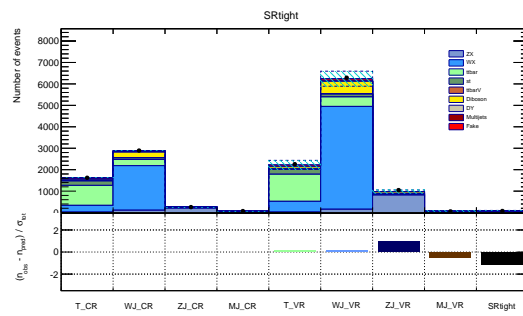


Figure 10.18. The systematic variation after the combined fit for (a) SRloose and (b) SRtight.



(a)



(b)

Figure 10.19. The pull on BG weights after the combined fit for (a) SRloose and (b) SRright.

## 10.10 Exclusion Results

The combined analysis set limits in the  $\tilde{q}\tilde{q} \rightarrow qq \tilde{\chi}_1^0 \tilde{\chi}_1^0$  models (Figure 10.20). The cross-section excluded at 95% is shown along the  $z$ -axis. Compared to the standard analysis, the exclusion limit for large  $m_{\tilde{q}}$  is competitive, but the exclusion for  $m_{\tilde{\chi}_1^0}$  shows advantages to the Razor analysis. In fact, splitting the exclusion by region (Figure 10.21) demonstrates how the separate effects are due to loose and tight requirements. It's interesting to note that the exclusion limits set by SRtight are similar to what a search using  $H_T$  would reach.

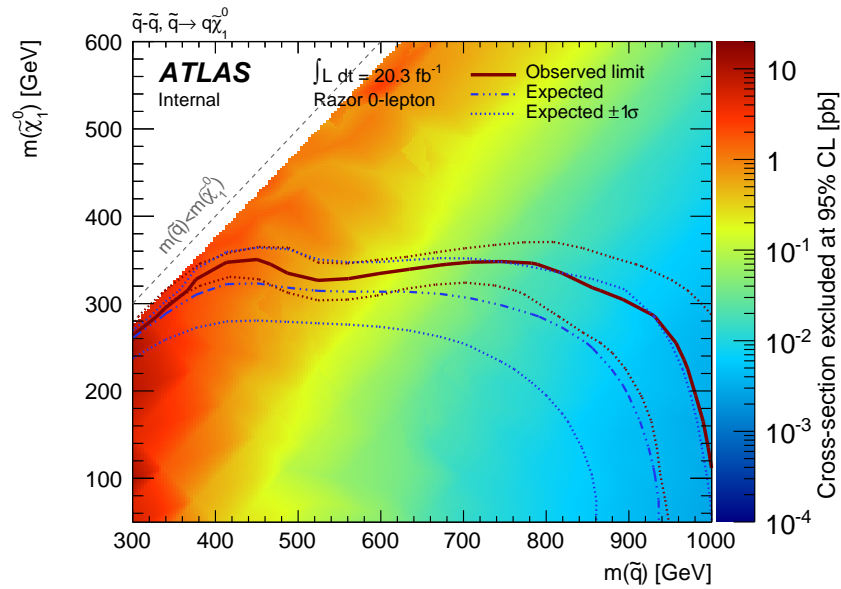


Figure 10.20. The combined exclusion results for the  $m_{\tilde{\chi}_1^0}$  versus  $m_{\tilde{q}}$  in the  $\tilde{q}\tilde{q}$  direct decay simplified model.



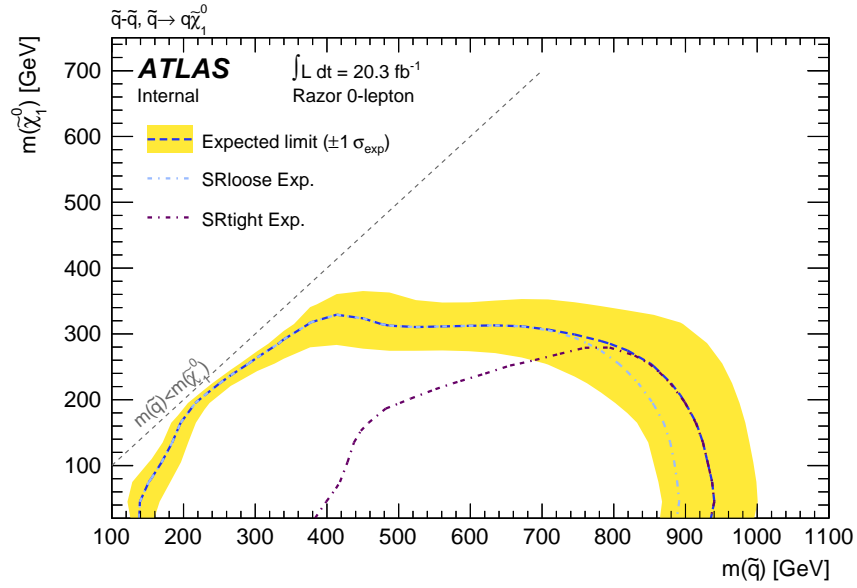


Figure 10.21. The component exclusion results for the  $m_{\tilde{\chi}_1^0}$  versus  $m_{\tilde{q}}$  in the  $\tilde{q}\tilde{q}$  direct decay simplified model.

### 10.11 Event Overlap

The standard analysis defined four SRs as shown in Table 10.18. To demonstrate the idea that the Razor analysis selects different events, the overlap between SRs is shown in Figure 10.22. SRs shown on the  $y$ -axis contain  $z\%$  of the events in SR  $x$ . The most competitive standard region is SR<sub>meff\_4jm</sub>, which has a reduction of  $\sim 5 - 7\%$  of the events that Razor picks up.

Table 10.18. Standard SR definitions for 2012

	SRmeff_2jm	SRmeff_2jt	SRmeff_4jl	SRmeff_4jm
$E_T^{\text{miss}}$ [GeV]	> 160			
$p_T(j_1)$ [GeV]	> 130			
$p_T(j_2)$ [GeV]	> 60			
$p_T(j_3)$ [GeV]	-		> 60	
$p_T(j_4)$ [GeV]	-		> 60	
$E_T^{\text{miss}} / \sqrt{H_T}$ [GeV <sup>1/2</sup> ]	> 15		> 10	-
$E_T^{\text{miss}} / M_{\text{eff}}$	> 1200	> 1600	> 1000	-
$M_{\text{eff}}$	-			> 1300
$\Delta\phi(\vec{p}_T(j_1, j_2), \vec{E}_T^{\text{miss}})$	> 0.4			
$\Delta\phi(p_T(j_3), E_T^{\text{miss}})$	-		> 0.4	
$\Delta\phi(p_T(j_4), E_T^{\text{miss}})$	-			> 0.2
$n_{jet}(p_T > 40 \text{ GeV})$	> 1		> 3	

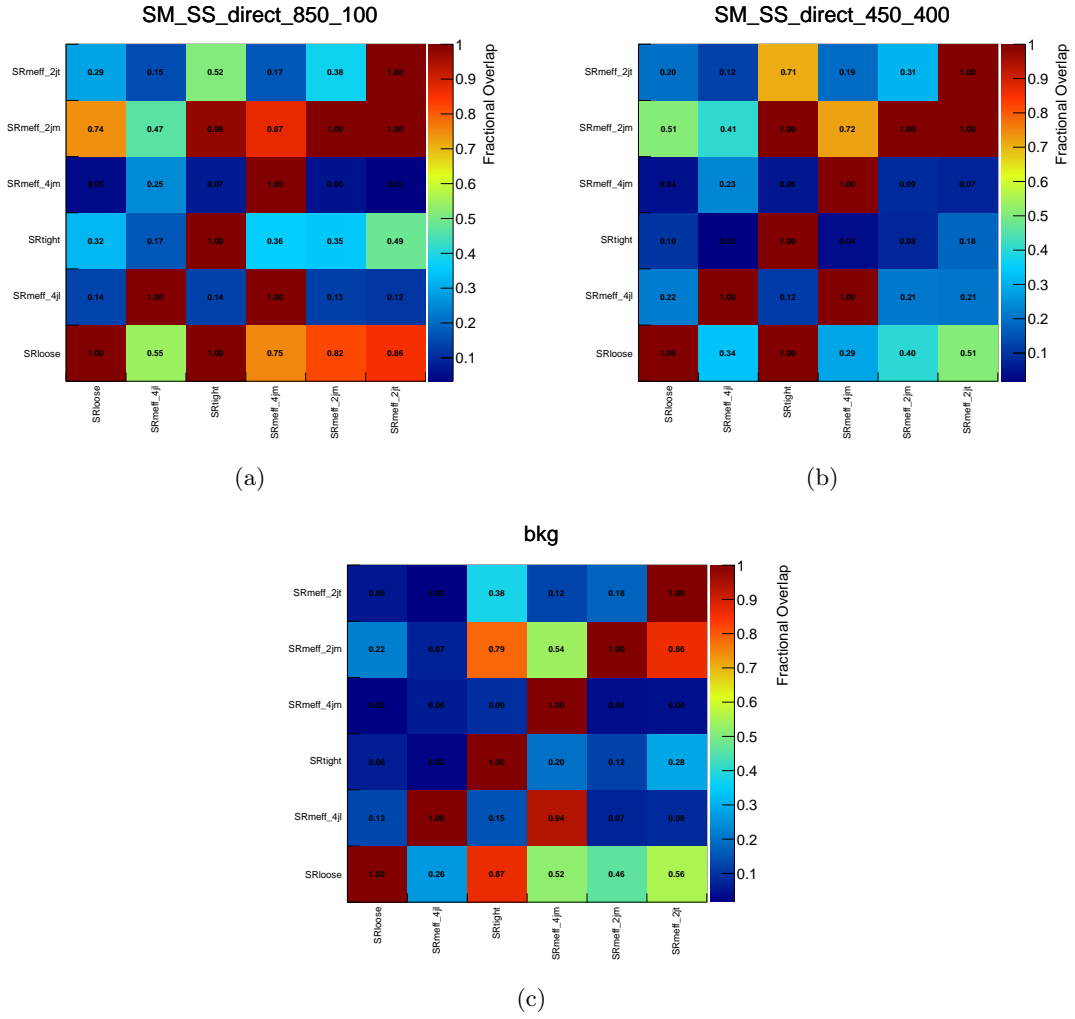


Figure 10.22. A study of event overlap between SRs for (a)  $m_{\tilde{q}} = 850$  GeV  $m_{\tilde{\chi}_1^0} = 100$  GeV (b)  $m_{\tilde{q}} = 450$  GeV  $m_{\tilde{\chi}_1^0} = 400$  GeV, and (c) BG.

## 10.12 Comments on 2012 Analysis

The 2011 results (Chapter 9) were an interesting first step. For the 2012 analysis, we were encouraged to join the much larger inclusive squark/gluino subgroup and contribute to common tasks such as the evaluation of object definition, event selection, sample quality, and cutflow. Ultimately, it was intended that Razor could be added as an independently-motivated SR to the standard 0-lepton analysis. We were advised against complicating the search by taking it as a multi-channel search again, but ironically the BG estimate required 1- and 2-lepton analysis anyway, even if no SRs were designed for these channels.

The trigger choice started with the  $H_T$  trigger as the next evolution of the trigger used in the 2011 analysis. However, knowing that we could be biased against massive neutralinos, a complementary  $E_T^{\text{miss}}$  trigger was chosen. Many of the cuts used to define SRs were required by the subgroup to better align with their preference of performance and cleaning cuts. Cuts to  $M_{\text{eff}}$ ,  $E_T^{\text{miss}}/\sqrt{H_T}$ , and aplanarity were substituted with cuts on  $R$  and  $M_R$ .

Unfortunately, the prescribed cuts by the subgroup to energy scale  $p_T(j_1)$ ,  $p_T(j_2)$ , and the structure cut  $\Delta\phi(\vec{p}_T(j_1, j_2), \vec{E}_T^{\text{miss}})$  are aimed at maximizing squark and gluino events with a *massless* neutralino. This greatly biased the events that can be reconstructed in the Razor plane and actively limited our  $E_T^{\text{miss}}$  search strategy because of the deleterious requirement on  $R$  once  $\Delta\phi(\vec{p}_T(j_1, j_2), \vec{E}_T^{\text{miss}})$  cuts were applied (Figures D.3 and D.5). The increasing  $R$  requirement would then translate to an insensitivity to signal models (Figure D.7). The  $H_T$  search strategy essentially aligned with the standard analysis because  $R$  and  $M_R$  would be strongly correlated after these cuts.

It was realized that the sensitivity of  $M_\Delta^R$  could provide a powerful discriminant between signal and BG, and Phase I upgrades to the trigger system made it possible to create a new trigger based on it (Section 8.7). The Recursive Jigsaw technique (Section 8.6) was also under development as the generalization of the Razor technique to an indefinite number of boosted decay frames. Its most appealing feature was that it could potentially be used to completely describe the event without the need for traditional variables beyond

$p_T$  and  $E_T^{\text{miss}}$ . It was hoped that another attempt at the analysis with greater control over the cuts that affect us would yield the results we had aspired to all along.

## CHAPTER 11

### 2015 Recursive Jigsaw Analysis

LS1 provided a long break in the analysis to assess the status of the Razor analysis. Significant advancements were made by introducing a new trigger (Section 8.7) and the full-scale research and development that went into the creation of the Recursive Jigsaw technique (Section 8.6). From August 2015 to 4 November 2015 the LHC was configured for collisions with proton beams at 6.5 TeV per beam ( $\sqrt{s} = 13$  TeV) with 25 ns bunch spacing and 2760 bunches per beam. ATLAS was able to record 3.7 fb<sup>1</sup> of physics data. The results of this analysis were documented in Reference [114] and parts of it are summarized below. The outline also includes references to the “standard” analysis in Reference [123].

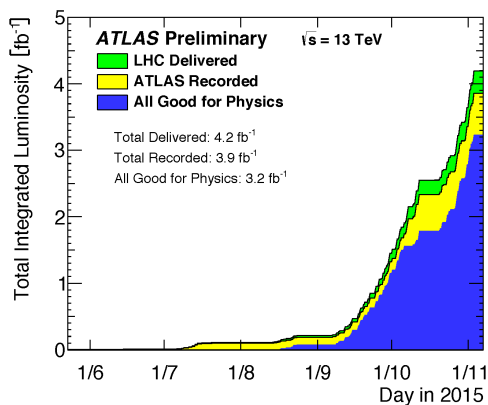


Figure 11.1. Timeline of integrated luminosity during 2015 data-taking run.

#### 11.1 Trigger Choice

The Razor triggers were implemented specifically because they benefitted the search for new physics, but they were designed with a luminosity of  $2 \times 10^{34}$ . During 2015, the luminosity peaked at about half of that amount. With less pressure on the TDAQ system,

some triggers that were expected to be prescaled were able to remain unrescaled. The `razor170` trigger was optimized to compete with `xe100`, but `xe70` was available as an unrescaled trigger. This trigger was also studied during the creation of the Razor trigger and it delivers a (mostly) superset of events compared to the Razor trigger. Furthermore, this trigger was expected to have a lower  $E_T^{\text{miss}}$  threshold and none of the  $n_{jet} > 10$  problems identified in the Razor trigger. Therefore, the trigger used to select data was `HLT_xe70`.

During LS1, the volume of file storage presented a concern for the analyses, which were encouraged to find ways of reducing the disk space used by the collaboration. This effort targeted the indefinite retention of large files but it also included self-imposed event selections. Under a “factory” production of both data and MC samples, analyses formed groups by common interest to define a set of filter selections. These factory samples could be centrally produced and re-run every  $\sim 2$  weeks. Both the standard analysis and the RJ search used the same factory filter:

- $M_{\text{eff}} > 800 \text{ GeV}$
- $E_T^{\text{miss}} > 150 \text{ GeV}$
- $p_T(j_1) > 100 \text{ GeV}$

These cuts are not ideal for the RJ technique, but they are adequate for a couple of reasons. First, the  $M_{\text{eff}}$  and  $E_T^{\text{miss}}$  requirements mean that an implicit  $H_T$  requirement of 650 GeV is a maximum cut only reserved for low  $E_T^{\text{miss}}$  events. This does sacrifice some sensitivity toward compressed points at very low mass scale. However, it is still possible to recognize the contribution of dijet events with such a large  $H_T$ . The cuts are aimed at increasing sensitivity to signal points with zero  $m_{\tilde{\chi}_1^0}$ , but we can still define satisfactory SRs with a reasonable reduction in the number of events to analyze. Secondly, the RJ technique still needed to prove its lofty claim to improve sensitivity over the standard analysis. The standard analysis could define CRs after these cuts, so it made sense that we would also be able to carve out useful regions. The secondary triggers for CR enrichment are shown in Table 11.1.

Table 11.1. Trigger selection for the 2015 analysis

trigger	regions
HLT_xe70	SR
HLT_mu24_loose_L1MU15	CRW, CRT, CRZ
HLT_mu50	CRW, CRT, CRZ
HLT_e24_medium_loose_L1EM20VH	CRW, CRT, CRZ
HLT_e24_medium_loose_L1Mu1SVH	CRW, CRT, CRZ
HLT_e60_lhmedium	CRW, CRT, CRZ
HLT_e120_lhloose	CRW, CRT, CRZ
HLT_g120_loose	CRY

### 11.2 Object Definitions and Event Selections

Object definitions are summarized in Tables 11.2-11.5 following the recommendations of performance and working groups. Calorimeter-based and non-baseline muons were ignored in the analysis, including the recalculation of  $E_T^{\text{miss}}$ . The transverse momenta of all physics objects and all tracks and/or calorimeter energy clusters not associated with these objects were used to calculate  $E_T^{\text{miss}}$ .

Table 11.2. Summary of the electron definitions used in the 2015 analysis

Baseline Electron	
algorithm	<b>AuthorElectron</b>
acceptance	$p_T > 10 \text{ GeV}$ $ \eta^{\text{clust}}  < 2.47$
quality	<b>LooseLH</b>
Signal Electron	
quality	<b>TightLH</b>
isolation	<b>GradientLoose</b> $ z_0^{PV}  < 0.5 \text{ mm}$ $ d_0^{PV} /\sigma(d_0^{PV}) < 5$

Once the objects were selected, overlap removal and event selection was applied. For the steps that involve photons, the removal was only applied to photon CRs.

1. If an “electron” and a “muon” shared the same ID track, the “electron” was discarded.



Table 11.3. Summary of the photon definitions used in the 2015 analysis

Baseline Photons	
acceptance	$p_T > 25 \text{ GeV}$ $ \eta  < 2.37$
quality	<b>Loose</b>
Signal Photons	
quality	<b>Tight</b>
isolation	<b>FixedCutLoose</b>

Table 11.4. Summary of the muon definitions used in the 2015 analysis

Baseline Muons	
acceptance	$p_T > 15 \text{ GeV}$ $ \eta  < 2.7$
quality	<b>Medium</b>
Signal Muons	
isolation	<b>GradientLoose</b> $ z_0^{PV} \sim \theta  < 0.5 \text{ mm}$ $ d_0^{PV} /\sigma(d_0^{PV}) < 3$

Table 11.5. Summary of the jet definitions used in the 2015 analysis

Baseline Jets	
algorithm	<b>anti-<math>k_t</math>4Topo</b>
acceptance	$p_T > 20 \text{ GeV}$ $ \eta  < 2.8$
quality	<b>LooseBad</b> $p_T > 20 \text{ GeV}$
hard-scatter	$ JVT  > 0.59$ or $p_T > 60$ or $ \eta  > 2.4$
<i>b</i> -Jets	
algorithm	<b>MV2c20</b> at $\epsilon = 77\%$
acceptance	$p_T > 20 \text{ GeV}$ $ \eta  < 2.5$

Table 11.6. Summary of the event preselections used in the 2015 analysis

trigger PV	HLT_xe70 leading PV with tracks > 2
jet cleaning	no LooseBad jets with $p_T > 20$ GeV no leading TightBad jets no jets in dead Tile region
cosmics cleaning	$ z_0^{PV}  > 1$ mm $ d_0^{PV}  > 0.2$
muon cleaning	$E_T^{\text{miss}}(\mu) / E_T^{\text{miss}} \times \cos[\phi(E_T^{\text{miss}} \mu) - \phi E_T^{\text{miss}}] < 0.5$
leptons	baseline leptons = 0
$E_T^{\text{miss}}$	> 200 GeV
$p_{j1,T}$	> 130 GeV
$p_{j2,T}$	> 50 GeV

2. If a “photon” and an “electron” were within  $\Delta R < 0.4$ , the “photon” was discarded.
3. If a “photon” and a “muon” were within  $\Delta R < 0.4$ , the “photon” was discarded.
4. If an “electron” and a “jet” that was not  $b$ -tagged were within  $\Delta R < 0.2$ , the “jet” was discarded.
5. If an “electron” and a “jet” that passed the JVT selection were within  $0.2 \leq \Delta R < 0.4$ , the “electron” was discarded.
6. If a “photon” and a “jet” were within  $\Delta R < 0.2$ , the “jet” was discarded if:
  - $N_{\text{track}} < 3$  with  $p_T > 500$  MeV
  - or  $p_T(\mu) > 0.7 \sum p_T^{\text{track}}$  AND  $p_T(j) < 0.5 p_T(\mu)$
7. If a “muon” and a “jet” that passed the JVT selection were within
  - $\Delta R < \min(0.4, 0.04 + 10 \text{ GeV} / p_T(\mu))$
the “muon” was discarded.
8. If the PV had less than 3 tracks, the event was discarded.
9. If the event had LooseBad jets with  $p_T > 20$  GeV, the event was discarded.
10. If the event had a leading TightBad jet, the event was discarded.
11. If the event had muons with:
  - $|z_0^{PV}| > 1$  mm
  - or  $|d_0^{PV}| > 0.2$  mm

the event was discarded.

12. If  $((E_T^{\text{miss}})^{\text{CellOut}} / E_T^{\text{miss}}) \times \cos [\phi(E_T^{\text{miss}})^{\text{CellOut}} - \phi(E_T^{\text{miss}})] > 0.5$ , the event was discarded.
13. If the event had leptons with  $p_T > 10$  GeV, the event was discarded.

### 11.3 Monte Carlo Samples

CT10 was used to generate the PDFs. Contributions from  $W + jets$  and  $Z + jets$  bosons were simulated using the SHERPA generator. Matrix elements were calculated for up to two partons at NLO and four partons at LO using the COMIX and OPENLOOPS matrix element generators that were showered in SHERPA. The generation of  $t\bar{t}$  and single-top processes in the  $Wt$  and s-channel used POWHEG. The decay is modeled by MADSPIN and showering, fragmentation, and UE were modeled in PYTHIA. Dibosons were simulated in SHERPA using COMIX and OPENLOOPS to calculate the matrix element and PYTHIA was used for multijet samples. Signal samples were simplified models for the direct squark and direct gluino decays. which were generated with MADGRAPH interfaced with PYTHIA. Table 11.7 summarizes these generators.

Table 11.7. Summary of MC generators used in the 2015 analysis

process	generators	cross-section [pb]	k-factor
$W + jets$	SHERPA	$6.63e + 04$	0.91
	MADGRAPH + PYTHIA	$5.02e + 04$	
$Z + jets$	SHERPA	$6.88e + 03$	0.90
	MADGRAPH + PYTHIA + EVTGEN	$5.12e + 03$	1.239
$\gamma + jets$	SHERPA	$1.24e + 04$	0.91
	SHERPA	$3.83e + 04$	1.00
top	POWHEG + PYTHIA + EVTGEN	$5.93e + 02$	1.00
multiboson	SHERPA	$1.50e + 02$	1.00
$t\bar{t} + V$	MADGRAPH + PYTHIA + EVTGEN	$8.23e - 01$	various
$\tilde{q} \rightarrow q \tilde{\chi}_1^0$	MADGRAPH + PYTHIA	various	–
$\tilde{g} \rightarrow qq \tilde{\chi}_1^0$	MADGRAPH + PYTHIA	various	–
$\tilde{g} \rightarrow W \tilde{\chi}_1^0$	MADGRAPH + PYTHIA	various	–

## 11.4 Systematic Uncertainties

Table 11.8. Summary of MC systematics used in the 2015 analysis

process	systematic	generators	cross-section [pb]	k-factor
$W + jets$	generator	MADGRAPH + PYTHIA	$9.26e + 03$	1.2283
	generator	MADGRAPH + PYTHIA	$3.14e + 03$	1.00
top	radiation generator	MC@NLO + HERWIG	$1.19e + 03$	1.00
		POWHEG + PYTHIA	$4.52e + 02$	
	parton shower	POWHEG + HERWIG	$9.04e + 02$	
POWHEG + PYTHIA				
multiboson	st subtraction	POWHEG + PYTHIA	$6.80e + 01$	1.00
	generator	POWHEG + PYTHIA	$9.02e + 01$	

## 11.5 Definition of Signal Regions

SRs were classified into three groups following the reconstruction sensitivity described in Sections 8.6.1-8.6.5. To optimize the regions, at least one BG event was required with all MC scaled to  $4 \text{ fb}^{-1}$ . The optimization used a toolkit for multivariate data analysis (TMVA [124]), which is a neural network, with a test statistic determined by  $z$ -score (Equation 10.2). We found that an increase in mass-scale cuts led to an increase in sensitivity to large mass-splitting, while scaleless cuts performed well in the region of intermediate mass-splitting. The strategy for targeting simplified model mass-splittings is shown in Table 11.9.

Table 11.9. SR target mass-splittings for the 2015 analysis

SR number	SRS	SRG	SRC
1	200 – 400 GeV	200 – 500 GeV	25 GeV
2	400 – 600 GeV	500 – 800 GeV	50 GeV
3	> 600 GeV	> 800 GeV	100 GeV
4/5	–	–	200 GeV

The cuts defining the disparticle inclusive regions are shown in Table 11.10. The cuts defining the digluino regions are shown in Table 11.11. The cuts defining the compressed regions are shown in Table 11.12.

Table 11.10. SR definitions for  $\tilde{q}$ -like events for the 2015 analysis

	SRS1A	SRS1B	SRS2A	SRS2B	SRS3A	SRS3B
$H_{1,1}^{PP} / H_{2,1}^{PP}$	$\geq 0.6$		$\geq 0.55$		$\geq 0.5$	
$H_{1,1}^{\dot{P}P} / H_{2,1}^{\dot{P}P}$	$\leq 0.95$		$\leq 0.96$		$\leq 0.98$	
$p_z^{Lab} / (p_z^{Lab} + H_{T2,1}^{PP})$	$\leq 0.55$		$\leq 0.6$		$\leq 0.63$	
$p_{Tj_2}^{PP} / H_{T2,1}^{PP}$	$\geq 0.16$		$\geq 0.15$		$\geq 0.13$	
$H_{T2,1}^{PP}$ [GeV]	$> 1000$	$> 1200$	$> 1300$	$> 1450$	$> 1600$	$> 1800$
$H_{1,1}^{\dot{P}P}$ [GeV]	$> 900$		$> 1200$		$> 1500$	

Table 11.11. SR definitions for  $\tilde{g}$ -like events for the 2015 analysis

	SRG1A	SRG1B	SRG2A	SRG2B	SRG3A	SRG3B
$H_{1,1}^{PP} / H_{4,1}^{PP}$	$\geq 0.35$		$\geq 0.25$		$\geq 0.2$	
$H_{T4,1}^{PP} / H_{4,1}^{PP}$	$\geq 0.8$		$\geq 0.75$		$\geq 0.65$	
$p_z^{Lab} / (p_z^{Lab} + H_{T4,1}^{PP})$	$\leq 0.5$		$\leq 0.55$		$\leq 0.6$	
$\min(p_{Tj_2}^{PP} / H_{T2,1}^{PP})$	$\geq 0.125$		$\geq 0.11$		$\geq 0.09$	
$\max(H_{1,0}^{PP} / H_{2,0}^{PP})$	$\leq 0.95$		$\leq 0.97$		$\leq 0.98$	
$ \frac{2}{3} \Delta\phi_{V,P}^{PP} - \frac{1}{3} \cos\theta_P $	$\leq 0.6$		-			
$H_{T4,1}^{PP}$ [GeV]	$> 1000$	$> 1200$	$> 1400$	$> 1800$	$> 2200$	$> 2500$
$H_{1,1}^{\dot{P}P}$ [GeV]	$> 550$		$> 750$		$> 850$	

Questions were posed about the complex mixture of variables used to define the SRs. For example,  $M_{\Delta}^R$  is a powerful discriminator and it was suggested for us to use a higher  $M_{\Delta}^R$  cut with more traditional cuts to  $p_T(j_1, j_2)$  and  $\Delta\phi(\vec{p}_T(j_1, j_2), \vec{E}_T^{\text{miss}})$  because they were approved for QCD reduction. It was our opinion that the mixture of boosted and unboosted variables would be antithetical to the technique. Each one of the RJ variables is a tool for cutting up regions to target different points. Tempered cuts on mass-scale variables can

Table 11.12. SR definitions for compressed spectra for the 2015 analysis

	SRC1	SRC2	SRC3	SRC4	SRC5
$\vec{p}_I^{CM} \cdot \hat{p}_{TS}^{CM} / p_{TS}^{CM}$	$\geq 0.9$	$\geq 0.85$	$\geq 0.8$	$\geq 0.75$	$\geq 0.70$
$M_{TS}$	$\geq 100$	$\geq 200$	$\geq 500$		
$\Delta\phi_I^{CM}$	$\geq 3.1$	$\geq 3.07$	$\geq 2.95$		
$\Delta\phi(\vec{p}_T(j_1), \vec{E}_T^{\text{miss}})$	–			$\min\Delta\phi \geq 0.4$	
$\Delta\phi(\vec{p}_T(j_2), \vec{E}_T^{\text{miss}})$					
$p_{TS}^{ISR}$	$\geq 800$		$\geq 700$		
$N_{jet}^V$	$\geq 1$		$\geq 2$		$\geq 3$

allow shape variables to do their job. When carving a statue from a block of marble, the sledge hammer has a powerful usefulness that doesn't replace the suitability of a chisel.

## 11.6 QCD Multijet Rejection

In addition to the cuts defining the SR, the QCD multijet rejection described in Section 8.6.5 was used to further reduce the contributions from QCD BG. In Figure 11.2, a contour cut is shown in red to indicate events that come from type A multijets. The rectangular cuts in Figure 11.3 reduce the type B multijets. Neither of these are appropriate for the compressed region because those regions are also defined by event imbalance.

The performance of these cuts is presented in the receiver operating characteristic (ROC) curves of Figure 11.4. These figures compare the signal efficiency on the  $y$ -axis to the BG rejection on the  $x$ -axis. The rejection for BG can be quite high without sacrificing many signal events using this rejection method, which outperforms the  $\Delta\phi(\vec{p}_T, \vec{E}_T^{\text{miss}})$  cuts.

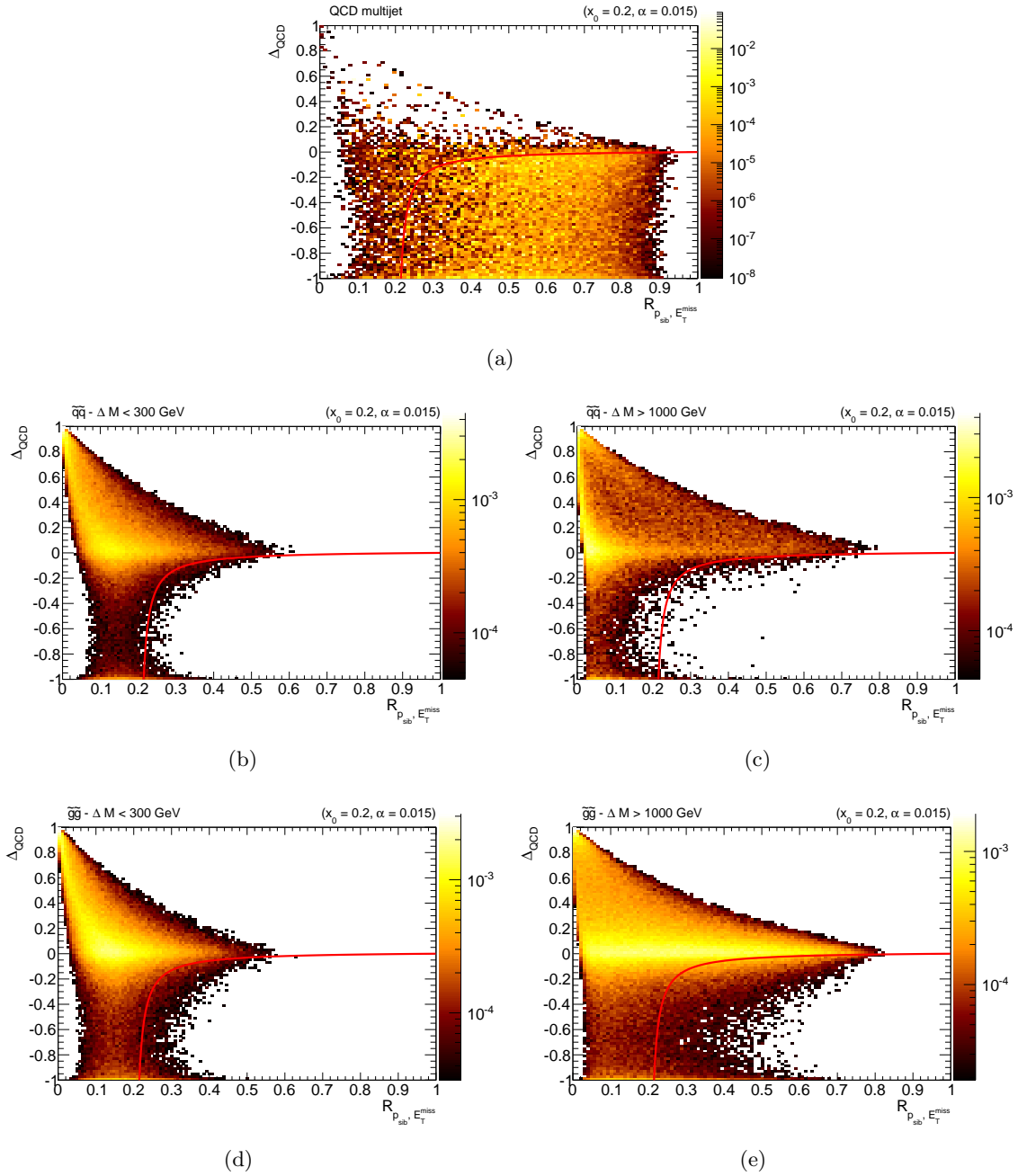


Figure 11.2. The distribution of  $\Delta_{QCD}$  versus  $R_{p_{sib}, E_T^{miss}}$  for (top) QCD multijets, (middle)  $\tilde{q}$ , and (bottom)  $\tilde{g}$  decays with (left)  $M_{Delta} < 300 \text{ GeV}$  and (right)  $M_{\Delta} > 1000$ .



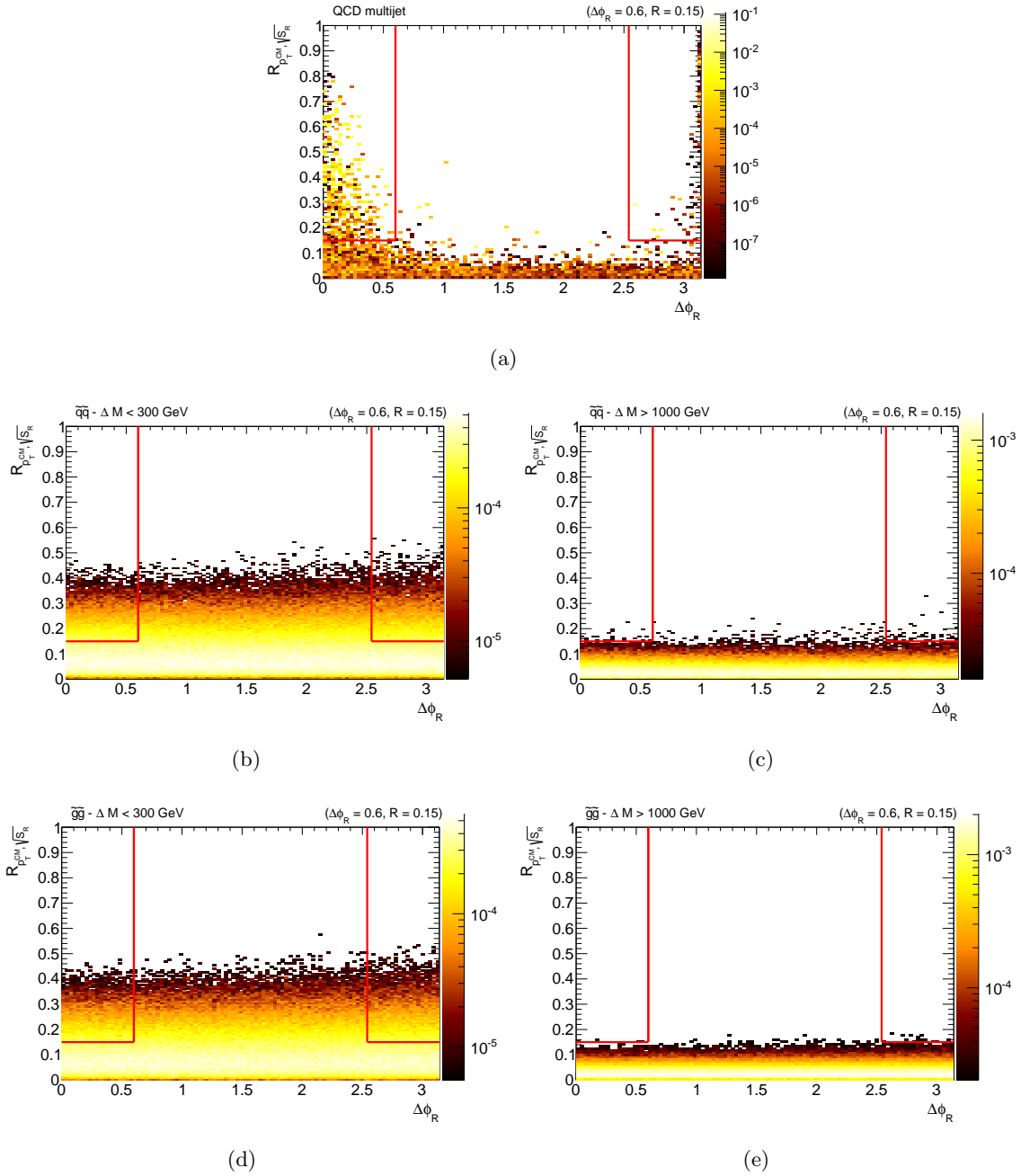


Figure 11.3. The distribution of  $R_{p_{T,V}}^{cM}$  versus  $\Delta\phi_{PP,V}$  for (top) QCD multijets, (middle)  $\tilde{q}$ , and (bottom)  $\tilde{g}$  decays with (left)  $M_{Delta} < 300 \text{ GeV}$  and (right)  $M_{\Delta} > 1000$ .

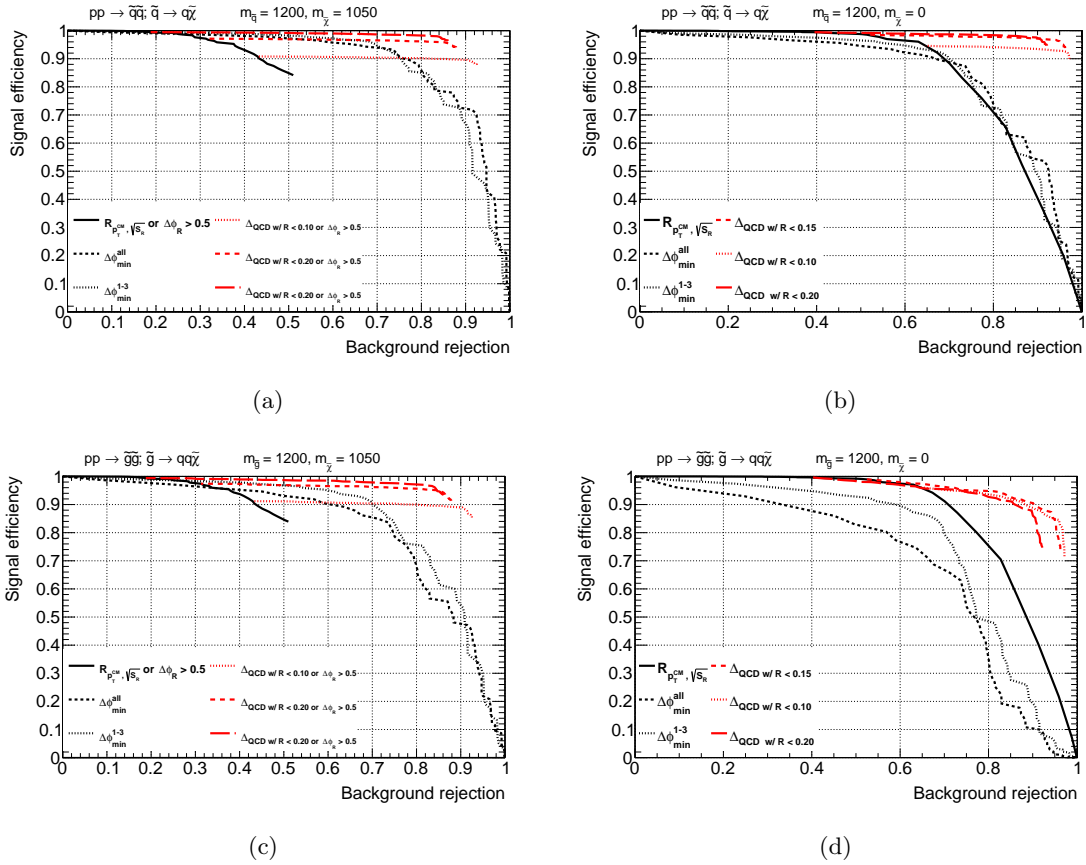


Figure 11.4. ROC curves for the BG rejection method for (top) squark and (bottom) gluino with (left) intermediate and (right) large mass splittings.

### 11.7 Definition of Control and Validation Regions

The contribution of the  $Z \rightarrow \nu\nu$  process is estimated using a data-driven method of the  $Z + jets$  BG using event reweighting of CRY events. To quantify the degree at which MC misrepresents the ratio between  $Z + jets$  and  $\gamma + jets$ , a  $\kappa$  factor is defined as:

$$\kappa = \left( \frac{N_{CRYVL}^{\gamma+jets,data}}{N_{CRZVL}^{Z\ell,data}} \right) \bigg/ \left( \frac{N_{CRYVL}^{\gamma+jets,MC}}{N_{CRZVL}^{Z\ell,MC}} \right) \quad (11.1)$$

To align with the standard analysis, we use  $\kappa = 1.55 \pm 0.1$  except we can define looser control regions to accommodate the difference for SRS-type events (Tables 11.15 and 11.16).

Table 11.13. CR definitions for the 2015 analysis

	CRW	CRT	CRQ	CRY
$n_b$	= 0	> 0		-
$n_\ell$	= 1	= 1		-
$n_\gamma$	-			> 0 ( $p_T > 130$ )
interpretation	treat $\ell$ as $j$			$E_T^{\text{miss}} = \vec{p}_T(\gamma) + \vec{E}_T^{\text{miss}}$
$H_{1,1}^{PP}$	> 550 (SRS)			
$H_{1,1}^{PP}$	> 900 GeV (SRG)			
$H_{T2,1}^{PP}$	> 1000 (SRS)			
$H_{T4,1}^{PP}$	> 800 (SRG)			
$M_{TS}$	> 0 (SRC)			
$\Delta_{QCD}$	< 0			
$H_{1,1}^{PP} / H_{2,1}^{PP}$	invert SRS			
$H_{1,1}^{PP} / H_{4,1}^{PP}$	invert SRG			
$ \frac{2}{3} \Delta\phi_{V,P}^{PP} - \frac{1}{3} \cos\theta_P $	> 0.5 (SRG1)			

Table 11.14. VR definitions

	VRWa	VRTa	VRWb	VRTb	VRZ	VRQ
$n_b$	= 0	> 0	= 0	> 0	-	
$n_\ell$	= 1				> 1 OS $p_T(1) > 25$ $p_T(2) > 10$	
interpretation	treat lepton as jet				treat dilepton as $E_T^{\text{miss}}$	
$H_{1,1}^{PP}$	-		> 550 for SRS > 550 (SRG)			-
$H_{T2,1}^{PP}$	> 1100 (SRS)		-			
$H_{T4,1}^{PP}$	> 800 (SRG)		-			
$M_{TS}$	-		> 0 (SRC)			
$\Delta_{QCD}$						< 0
$H_{1,1}^{PP} / H_{2,1}^{PP}$	-					invert SRS
$H_{1,1}^{PP} / H_{4,1}^{PP}$	-					invert SRG
$ \frac{2}{3} \Delta\phi_{V,P}^{PP} - \frac{1}{3} \cos\theta_P $						< 0.5

Table 11.15. CR loose definitions for SRS in the 2015 analysis

	CRYL and CRZL
$p_z^{Lab} / (p_z^{Lab} + H_{N,1}^{PP})$	< 0.55
$p_{Tj_2}^{PP} / H_{T2,1}^{PP}$	> 0.16
$p_{Tj_2}^{PP}$	> 100 GeV
$H_{1,1}^{PP}$	> 900 GeV
$H_{2,1}^{PP}$	> 1000 GeV

Table 11.16. CR loose definitions for SRG in the 2015 analysis

	CRYL and CRZL
$p_z^{Lab} / (p_z^{Lab} + H_{N,1}^{PP})$	$< 0.55$
$\min(p_{Tj_2}^{PP} H_{T2,1}^{PP})$	$> 0.09$

### 11.8 Background CR Fit

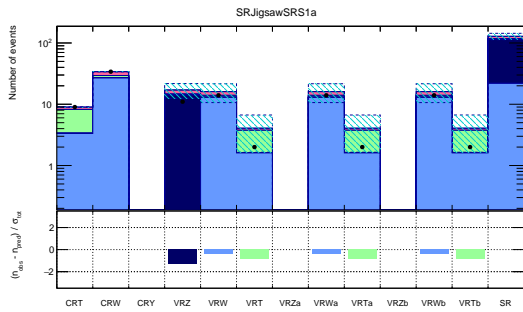
A count of MC expectation and BG fit from HistFitter for the number of events in each region is shown in Table 11.17.

Table 11.17. BG fit result for 2015

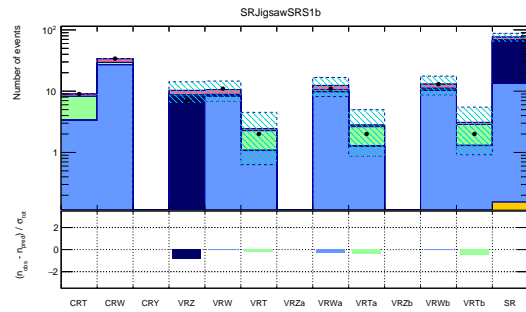
	CRT	CRW	CRY	CRQ
MC multijets	$0.00 \pm 0.00$	$0.00 \pm 0.00$	$0.00 \pm 0.00$	$10.64 \pm 4.84$
MC $W + jets$	$9.47 \pm 2.28$	$48.87 \pm 3.80$	$1.14 \pm 1.00$	$0.37 \pm 0.19$
MC $Z + jets$	$0.08 \pm 0.03$	$0.28 \pm 0.14$	$0.03^{+0.03}_{-0.03}$	$0.06 \pm 0.04$
MC $\gamma + jets$	$0.00 \pm 0.00$	$0.00 \pm 0.00$	$39.91 \pm 1.77$	$0.00 \pm 0.00$
MC top	$20.05 \pm 1.10$	$5.40 \pm 0.88$	$0.26 \pm 0.22$	$0.90^{+1.00}_{-0.90}$
MC diboson	$1.24 \pm 0.20$	$4.46 \pm 1.40$	$0.01 \pm 0.00$	$0.05^{+0.09}_{-0.05}$
BG expected	$30.84 \pm 2.70$	$59.01 \pm 4.51$	$41.35 \pm 2.10$	$12.02 \pm 5.56$
multijets fit	$0.00 \pm 0.00$	$0.00 \pm 0.00$	$0.00 \pm 0.00$	$4.57 \pm 2.81$
$W + jets$ fit	$6.50 \pm 2.50$	$33.52 \pm 7.48$	$0.78 \pm 0.75$	$0.25 \pm 0.15$
$Z + jets$ fit	$0.12 \pm 0.05$	$0.42 \pm 0.22$	$0.05^{+0.05}_{-0.05}$	$0.09 \pm 0.06$
$\gamma + jets$ fit	$0.00 \pm 0.00$	$0.00 \pm 0.00$	$60.79 \pm 7.91$	$0.00 \pm 0.00$
top fit	$24.17 \pm 6.48$	$6.52 \pm 2.27$	$0.31 \pm 0.28$	$1.06^{+1.22}_{-1.06}$
diboson fit	$1.24 \pm 0.20$	$4.48 \pm 1.40$	$0.01 \pm 0.00$	$0.05^{+0.09}_{-0.05}$
BG fit	$32.03 \pm 5.66$	$44.94 \pm 6.70$	$61.94 \pm 7.87$	$6.02 \pm 2.46$
observed	32	45	62	6

### 11.9 Signal Region Extrapolation

Once all the systematic parameters and scale factors were set by the combined fit, the amount of “pull” that each has on the MC estimate can give a measure of how vital the variation is to the analysis (Figure 11.5-11.14).

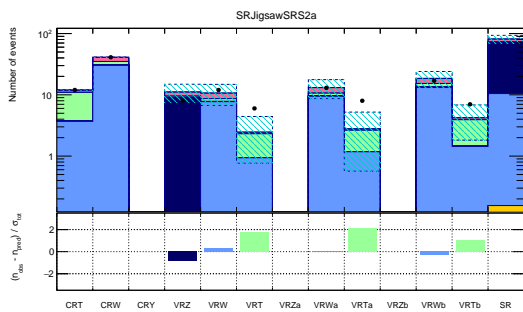


(a)

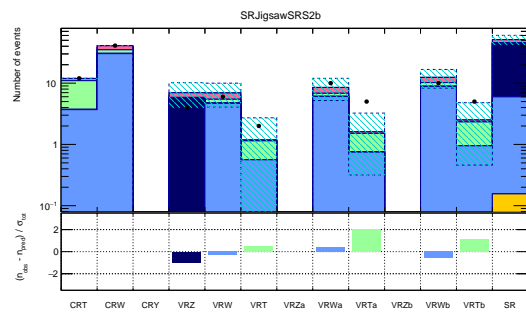


(b)

Figure 11.5. Pull plots after the combined fit to SRS1.

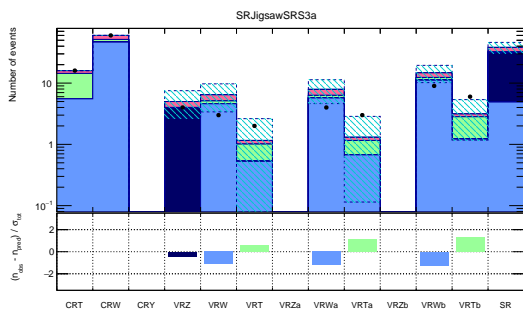


(a)

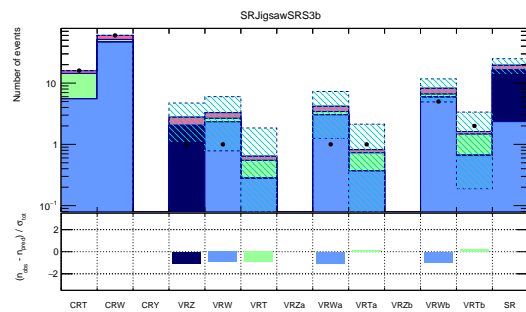


(b)

Figure 11.6. Pull plots after the combined fit to SRS2.



(a)



(b)

Figure 11.7. Pull plots after the combined fit to SRS3.

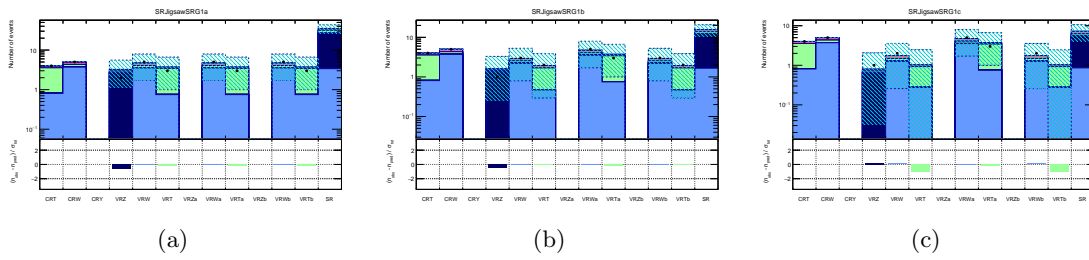


Figure 11.8. Pull plots after the combined fit to SRG1.

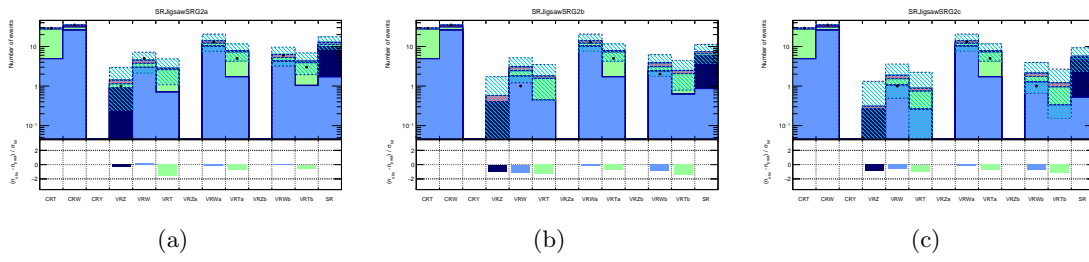


Figure 11.9. Pull plots after the combined fit to SRG2.

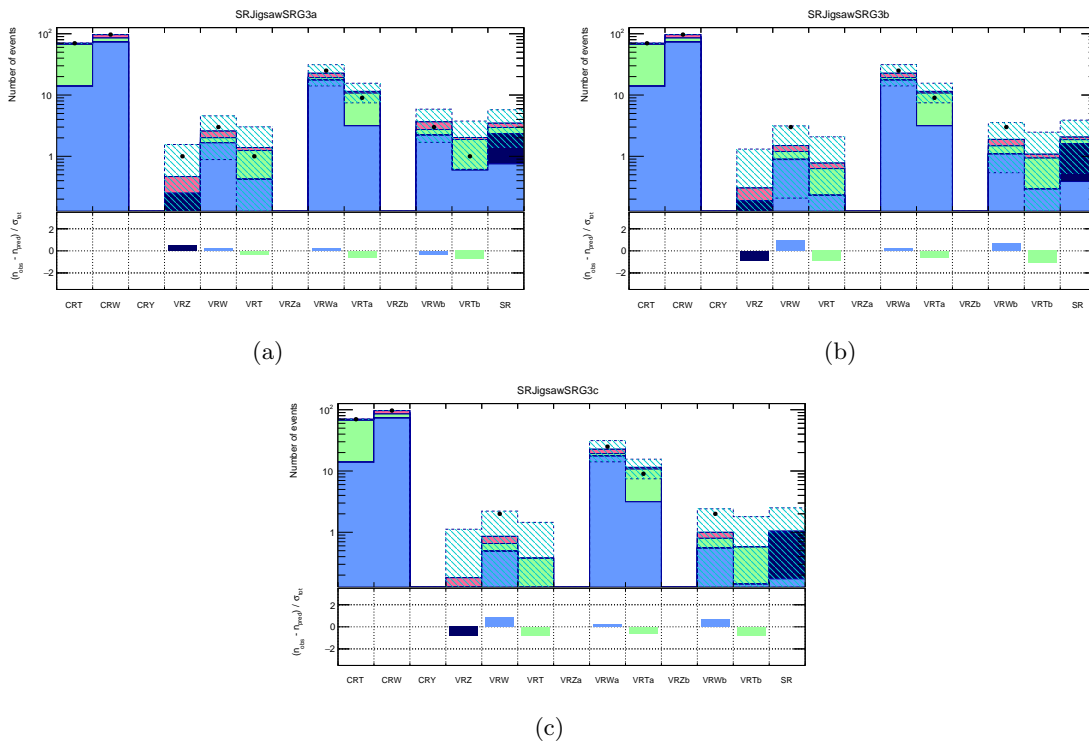


Figure 11.10. Pull plots after the combined fit to SRG3.

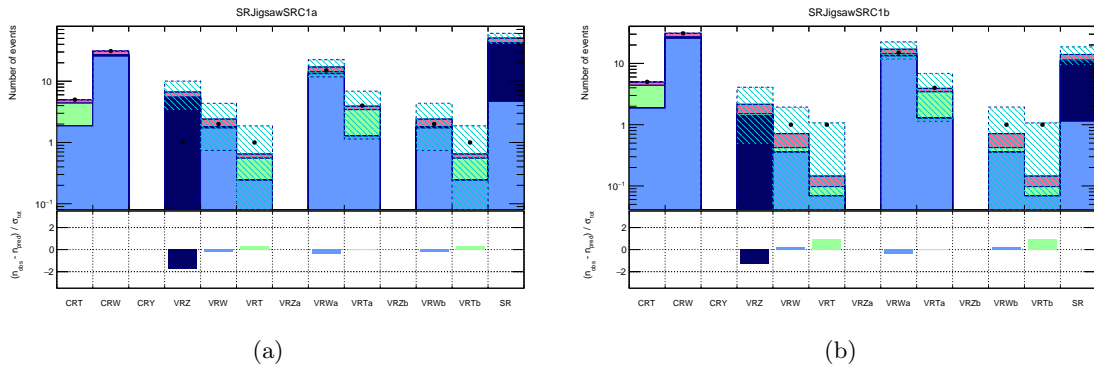


Figure 11.11. Pull plots after the combined fit to SRC1.

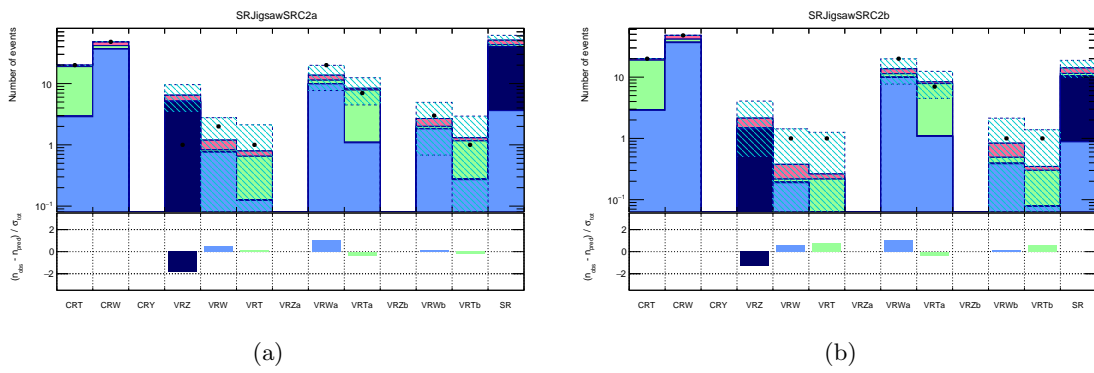


Figure 11.12. Pull plots after the combined fit to SRC2.

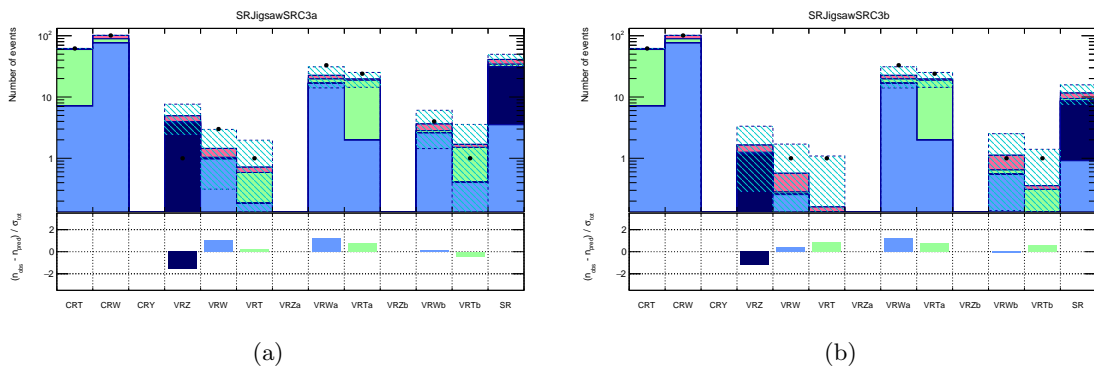
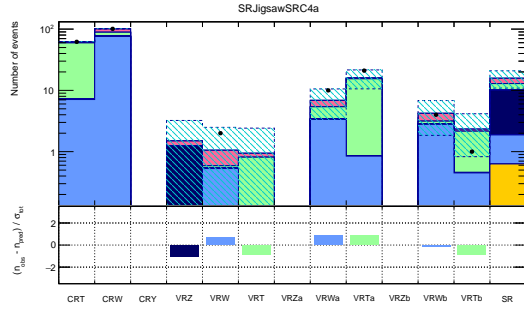
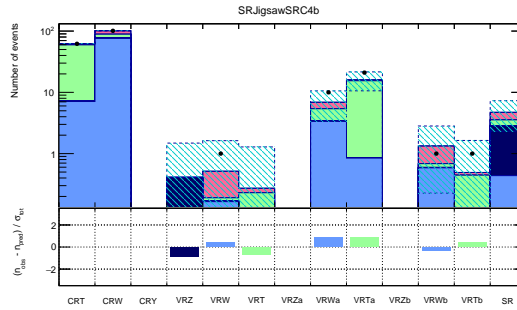


Figure 11.13. Pull plots after the combined fit to SRC3.



O

(a)



(b)

Figure 11.14. Pull plots after the combined fit to SRC4.

### 11.10 $M_{\text{eff}}$ Comparisons

There were a few barriers to the data recorded in 2015 that prevented the completion of the RJ analysis for the 2015 data. The run started with 50 ns data that ultimately did not produce enough data to reach the exclusion limits already set by 2012 analyses. The 25 ns data was also delayed and it was determined that recommendations for the combination to the 50 ns data would not be ready in time. We were encouraged, instead, to treat the 50 ns data as validation in preparation for the 25 ns data. The standard  $M_{\text{eff}}$  analysis was able to push forward with a result for 2015 data while RJ was not granted unblinding. Since we contributed to the  $M_{\text{eff}}$  analysis as well, the results of this reach are shown here with comments about how RJ compared to it. The standard analysis defined seven SRs as shown in Tables 11.18 and 11.19.

Overall, the RJ analysis does best in the intermediate mass-splitting regions that it targets for the improved sensitivity to massive neutralinos. Across both the disquark (Figure



Table 11.18. Standard 2 jet SR definitions for 2015

	2jl	2jm	2jt
$E_T^{\text{miss}}$ [GeV]	> 200		
$p_{j1,T}$ [GeV]	> 200	> 300	> 200
$p_{j2,T}$ [GeV]	> 200	> 50	> 200
$\Delta\phi_{\min}(jet_{1,2,(3)}, E_T^{\text{miss}})$	> 0.8	> 0.4	> 0.8
$E_T^{\text{miss}} H_T$ [GeV <sup>1/2</sup> ]	> 15	> 15	> 20
$M_{\text{eff}}$ [GeV]	> 1200	> 1600	> 2000

Table 11.19. Standard 3+ jet SR definitions for 2015

	4jt	5j	6jm	6jt
$E_T^{\text{miss}}$ [GeV]	> 200			
$p_{j1,T}$ [GeV]	> 200			
$p_{j2,T}$ [GeV]	> 100			
$p_{j3,T}$ [GeV]	> 100			
$p_{j4,T}$ [GeV]	> 100			
$p_{j5,T}$ [GeV]	–	> 50		
$p_{j6,T}$ [GeV]	–	> 50		
$\Delta\phi_{\min}(jet_{1,2,(3)}, E_T^{\text{miss}})$	> 0.4			
aplanarity	> 0.04			
$E_T^{\text{miss}} / M_{\text{eff}}$	> 0.2	> 0.25	> 0.2	
$M_{\text{eff}}$ [GeV]	> 2200	> 1600	> 2000	

11.15) and digluino (Figure 11.16) simplified model planes, RJ has its most significant uniqueness of intermediate mass-splitting event rates compared to the  $M_{\text{eff}}$  analysis, while the two techniques overlap for high-scale, massless neutralino grid points.

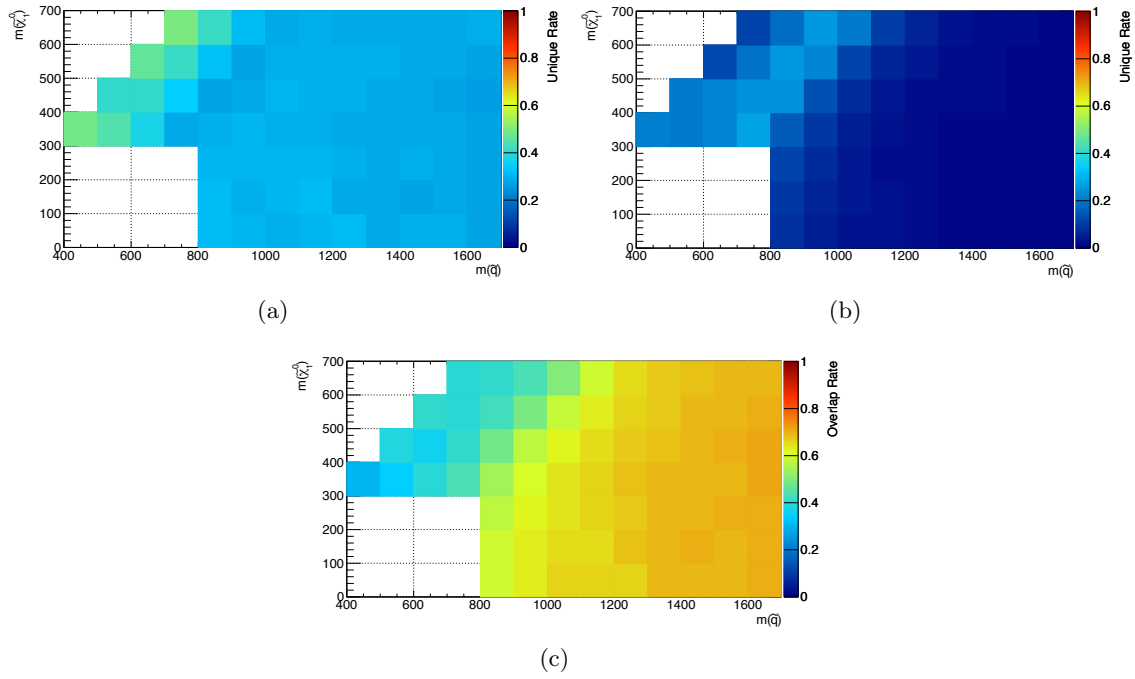


Figure 11.15. SR complementarity between  $M_{\text{eff}}$  and RJ for all squark grid points showing (a) unique rate for  $M_{\text{eff}}$ , (b) unique rate for RJ, and (c) overlapping rate.

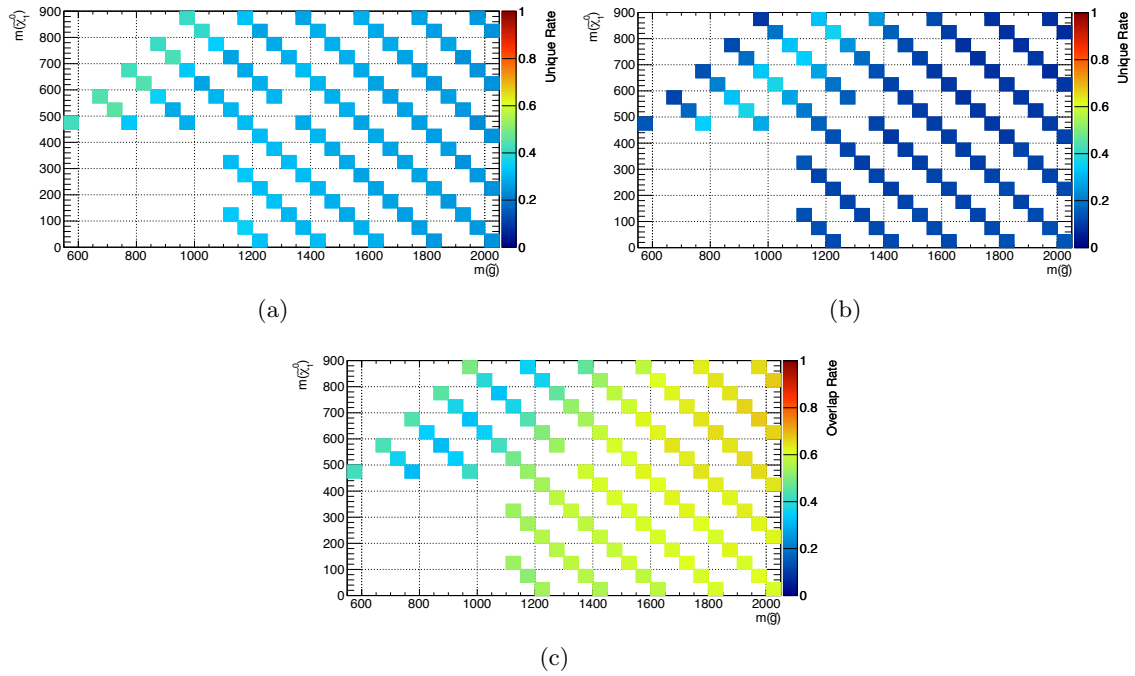


Figure 11.16. SR complementarity between  $M_{\text{eff}}$  and RJ for all gluino grid points showing (a) unique rate for  $M_{\text{eff}}$ , (b) unique rate for RJ, and (c) overlapping rate.

### 11.10.1 SR Overlap

To demonstrate the idea that the RJ analysis selects different events, the complementarity between SRs is shown in Figures 11.17-11.22 with the left plots showing the overlap rate between SRS while the right plot shows the unique rates. For the unique rates, the plot is read as “SR X has Z events that do not pass SR Y” or “SR Y is missing Z events from SR X”. For QCD (Figure 11.17) shows that  $M_{\text{eff}}$  defines a few regions that use an identical set of events with a similar definition of QCD, while RJ can adjust its definition of QCD for each region. Figures 11.18 and 11.19 show the complementary rate for squark models for intermediate and large mass-splitting (respectively). Figures 11.20-11.22 show the complementarity rate for gluino models for compressed, intermediate, and large mass-splitting (respectively). The compressed points are difficult to target for both analyses. For the intermediate region and have a similar ability to select signal events. The SRS and SRG regions show their ability to discriminate between squark and gluino events, while  $M_{\text{eff}}$  has often creates SRs by selecting very inclusive events between squark and gluino. For the large mass-splitting, the analyses again return to a similar sensitivity, which plays to the design strength of  $M_{\text{eff}}$ .

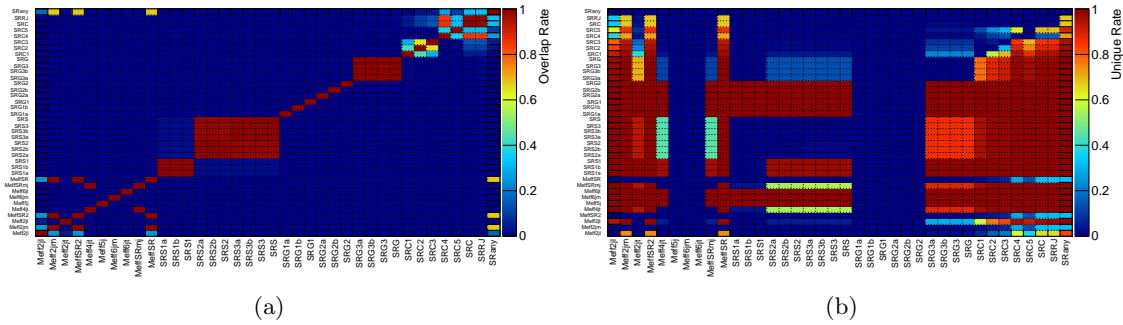


Figure 11.17. SR complementarity between  $M_{\text{eff}}$  and RJ for QCD BG showing (a) overlapping rate and (b) unique rate.

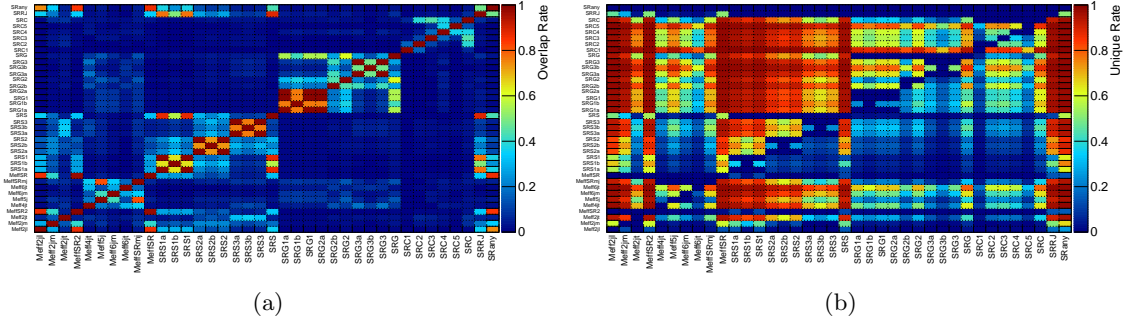


Figure 11.18. SR complementarity between  $M_{\text{eff}}$  and RJ for an intermediate mass-splitting squark simplified model showing (a) overlapping rate and (b) unique rate.

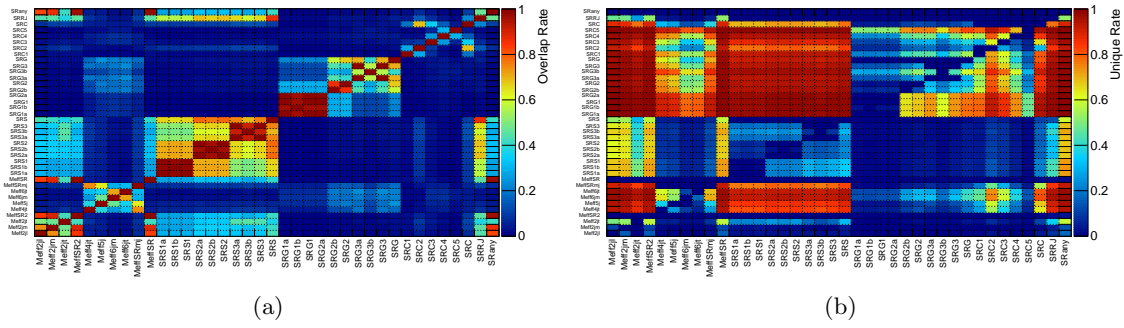


Figure 11.19. SR complementarity between  $M_{\text{eff}}$  and RJ for a large mass-splitting squark simplified model showing (a) overlapping rate and (b) unique rate.

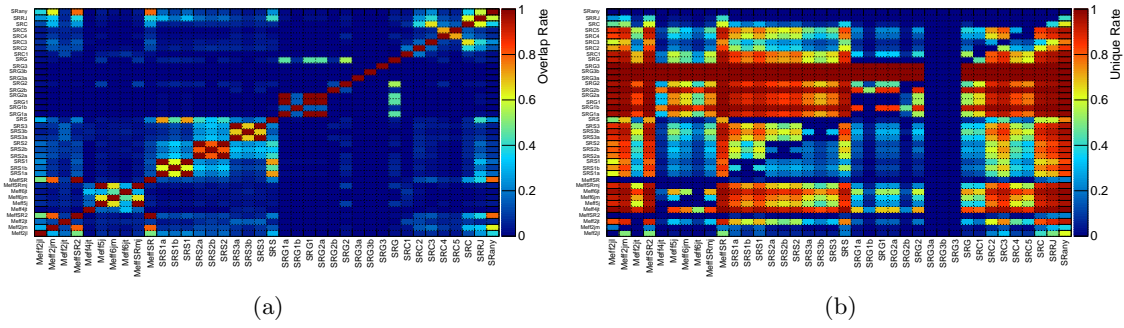


Figure 11.20. SR complementarity between  $M_{\text{eff}}$  and RJ for a compressed mass-splitting gluino simplified model showing (a) overlapping rate and (b) unique rate.

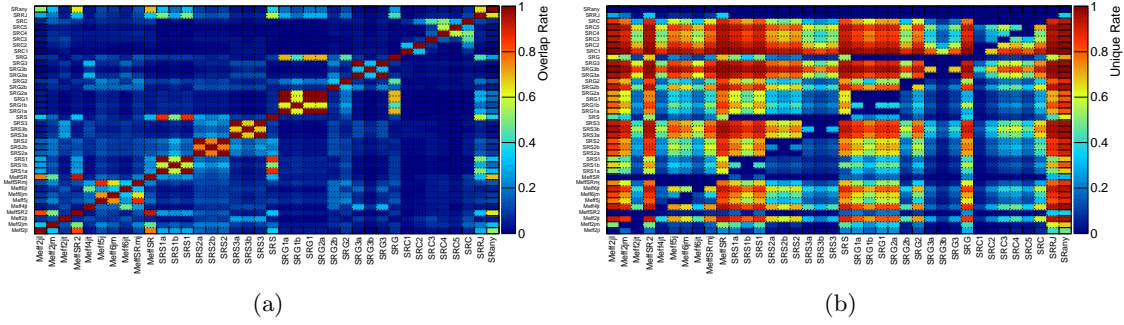


Figure 11.21. SR complementarity between  $M_{\text{eff}}$  and RJ for an intermediate mass-splitting gluino simplified model showing (a) overlapping rate and (b) unique rate.

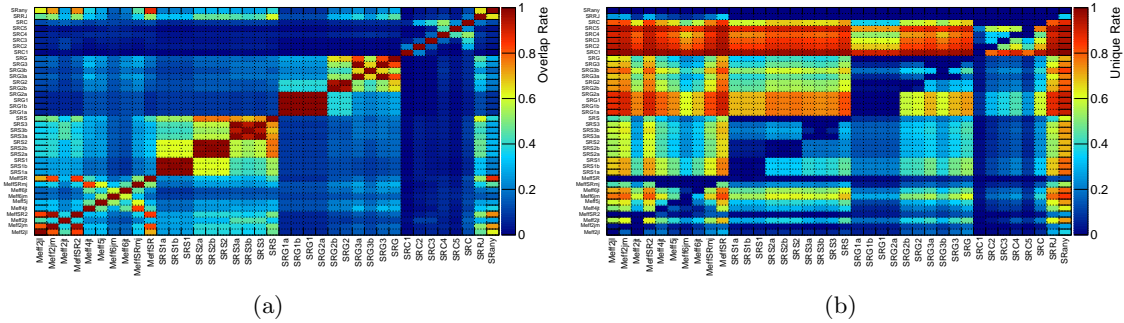


Figure 11.22. SR complementarity between  $M_{\text{eff}}$  and RJ for a large mass-splitting gluino simplified model showing (a) overlapping rate and (b) unique rate.

### 11.10.2 Variable Relations

The variables that describe SUSY events can have different strengths between  $M_{\text{eff}}$  and RJ. Figures 11.23-11.28 present the correlation between variables on the left and their mutual information on the right. The BG and signal models are the same as the previous subsection. These figures demonstrate that the collection of  $M_{\text{eff}}$  variables tend to have common features in their definitions. RJ variables tend to have less commonality, while a cross-purpose mixing of the two sets also tends to have low commonality.

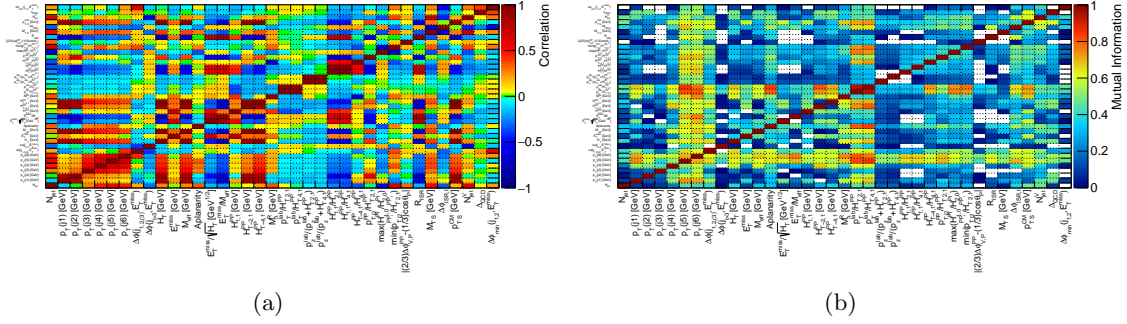


Figure 11.23. Variable (a) correlation and (b) mutual information used for  $M_{\text{eff}}$  and RJ analyses for QCD BG.

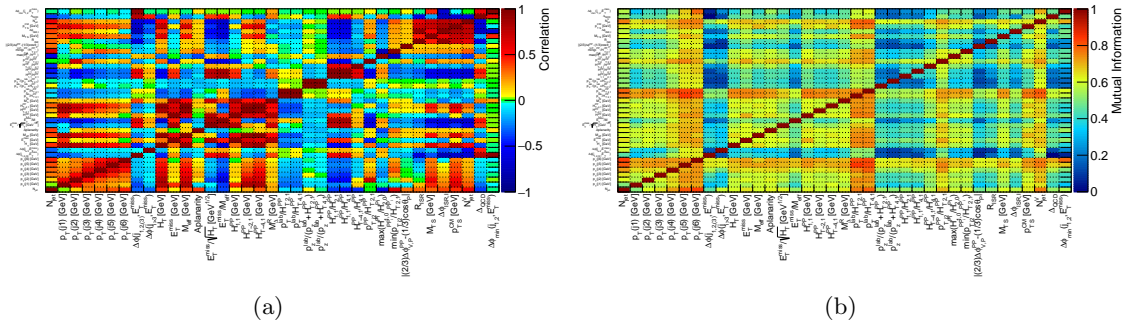


Figure 11.24. Variable (a) correlation and (b) mutual information used for  $M_{\text{eff}}$  and RJ analyses for an intermediate mass-splitting squark simplified model.

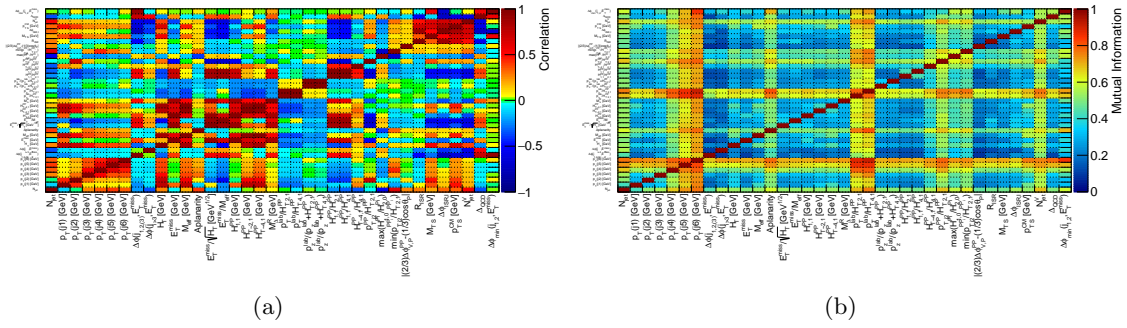


Figure 11.25. Variable (a) correlation and (b) mutual information used for  $M_{\text{eff}}$  and RJ analyses for a large mass-splitting squark simplified model.



### 11.10.3 Systematic Variations

The systematic variations can have a large effect on the distribution of variables. Since the RJ technique is designed to be sensitive to the composition of each event, this is where the sensitivity suffers from variations. To understand how the numerous effects alter the numerous distributions, the shape log-likelihood to a null hypothesis and normalization change are shown in Figures 11.29-11.34. The shape of QCD events affected the shape of  $M_{\text{eff}}$  variables while RJ variables were largely unaffected by these variations. However, upon normalization, the normalization change greatly increased the total number of these events in RJ without having much affect on the  $M_{\text{eff}}$  regions. The signal models (Figures 11.30-11.34) are much less sensitive to the changes while compressed points are (again) complicated to analyze. The largest systematic variation comes from JER.

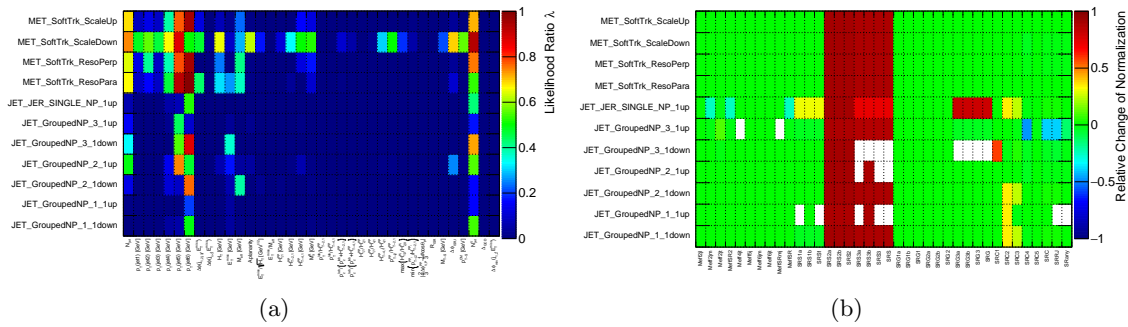


Figure 11.29. Systematic variations to (a) shape and (b) normalization used for  $M_{\text{eff}}$  and RJ analyses for QCD BG.

The choice of BG CRs can affect the BG systematics to the point that the choice alone tends to dominate the reach of the RJ exclusions. The targeted reduction of BGs has the unintended effect of reducing the statistics of events in the final SRs, so the statistical error can greatly increase under systematic variations. For the future of the analysis, it is hoped that RJ variables applied at the filter level or upgrades to the detector precision can mitigate the systematic barrier to RJ analysis.





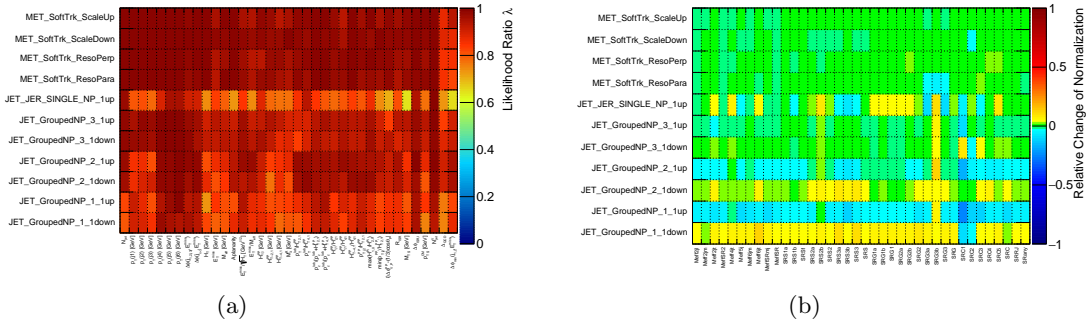


Figure 11.33. Systematic variations to (a) shape and (b) normalization used for  $M_{\text{eff}}$  and RJ analyses for an intermediate mass-splitting gluino simplified model.

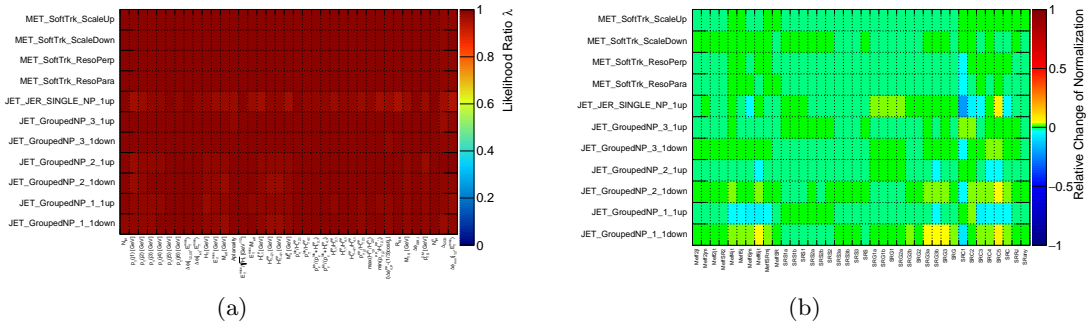


Figure 11.34. Systematic variations to (a) shape and (b) normalization used for  $M_{\text{eff}}$  and RJ analyses for a large mass-splitting gluino simplified model.

### 11.11 Exclusion Reach

The combined analysis projected exclusion and discovery limits to the  $\tilde{q} \rightarrow q \tilde{\chi}_1^0$  and  $\tilde{g} \rightarrow qq \tilde{\chi}_1^0$  models (Figures 11.35 and 11.36). The limits presented are a comparison between the  $M_{\text{eff}}$  analysis on the left and the RJ analysis on the right. These limits show that the RJ analysis *does* outperform the standard analysis if the BG systematics are estimated on an equal standing of 10%. The  $M_{\text{eff}}$  analysis optimization targeted a projected  $4 \text{ fb}^{-1}$  of data while the RJ analysis was optimized to  $3 \text{ fb}^{-1}$ . If the two analyses had been optimized to the same luminosity, we suspect that the limits for high mass scale would have been nearly identical. For very compressed points along the diagonal, the two analyses were also very similar in reach. For intermediate points, however, RJ outperforms the standard analysis, which is expected to be true even if the points were optimized to the

same integrated luminosity. The expected exclusion and observation results for squark and gluino are shown in Figure 11.37.

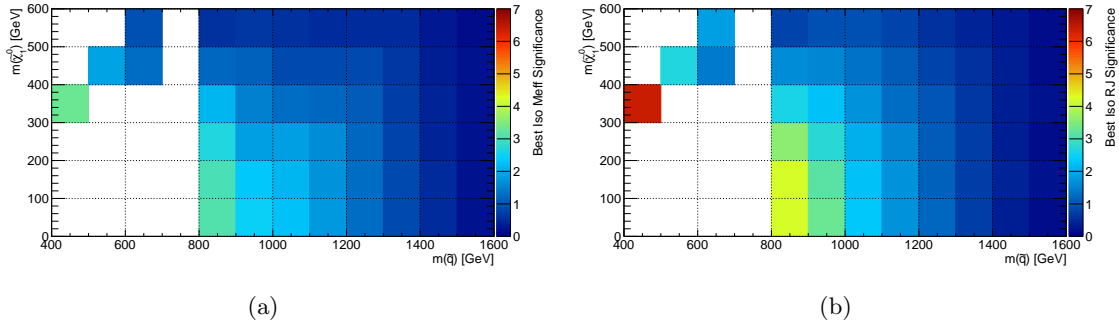


Figure 11.35. Expected exclusion sensitivity to the  $\tilde{q}$  direct decay mass plane comparing the most performant (left)  $M_{\text{eff}}$  SRs and (right) RJ SRs.

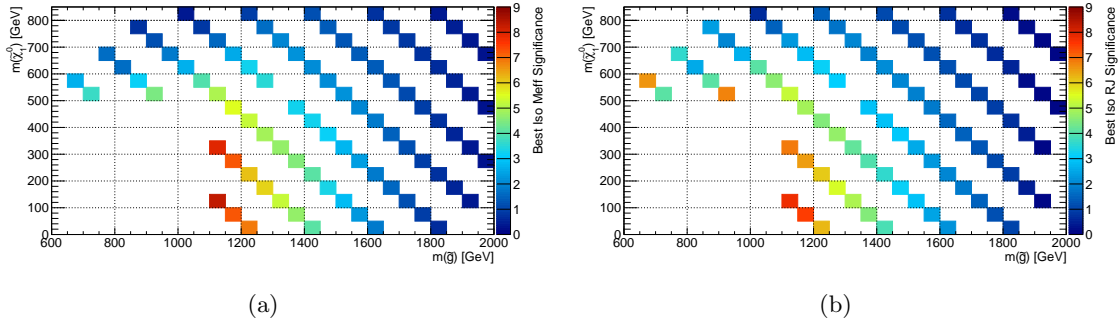


Figure 11.36. Expected exclusion sensitivity to the  $\tilde{g}$  direct decay mass plane comparing the most performant (left)  $M_{\text{eff}}$  SRs and (right) RJ SRs.

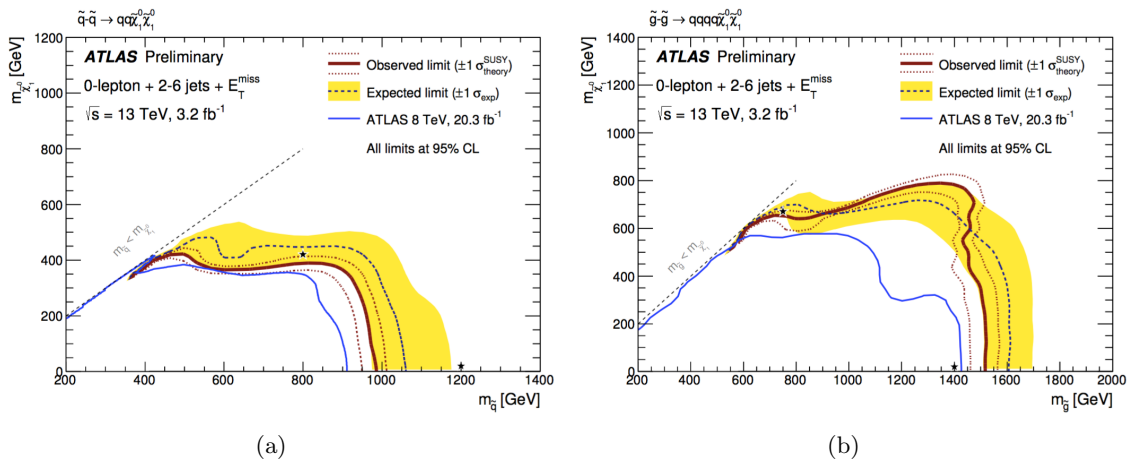


Figure 11.37. Expected and observed limits of the 2015  $M_{\text{eff}}$  analysis for (left) squark and (right) gluino simplified models.

## CHAPTER 12

### Conclusions

A summary of the search for supersymmetry using boosted decay tree topologies was presented. The context motivating this search is a description of nature that can correct for the problems of the (still) highly successful Standard Model. Under the supersymmetric framework, the requirement of heavy partners to each Standard Model particle provides an opportunity to search for new particles. The LHC has demonstrated its ability to deliver the energy necessary for the search, and the ATLAS detector is similarly capable of studying the signatures of these events.

The ATLAS experiment needs to provide an accurate description of inelastic scattering within its volume. Research into the upgrades to the diagnostic tools used in the maintenance of the detector for performance was presented. An upgrade to the electronics and future diagnostics was also presented.

Distinguishing background particles is also a concern to the search for supersymmetric particles. The detector itself must use triggers to select data worth recording and analyses need good topological variables. The development of these variables was outlined, and new variables based on the boosted decay tree of a signal event were presented. A new trigger based on this analysis philosophy was also presented.

Three searches from three different years of operation of the LHC were presented to show the progress and performance of these techniques. In each year, the strength of the boosted decay tree strategy has been its ability to select unique events. The sensitivity of the analysis can be optimized to target the low mass-splitting regions of compressed supersymmetry points that other analyses have difficulty reaching. The new observables introduced by these techniques can complement the standard practices of analysis efforts,

or they can offer a “cover-to-cover” description of how a supersymmetric event is identified and analyzed.

The status of these boosted decay trees looks promising. Due to the large number of pieces that can contribute to the technique at large, a sizable workforce would be best when moving forward with the analysis. There is also significant progress being made toward repurposing the multivariate technique into a project for artificial intelligence because of the ability for these variables to provide multiple opportunities to find discernment between signal and background. Individual events could be evaluated by their properties and assigned a weighted probability of matching a particular model against a set of competing models.

## REFERENCES

- [1] Particle Data Group Collaboration, K. A. Olive et al., *Review of Particle Physics*, Chin. Phys. **C38** (2014) 090001.
- [2] R. Barbieri and G. F. Giudice, *Upper Bounds on Supersymmetric Particle Masses*, Nucl. Phys. B **306** (1988) 63.
- [3] B. de Carlos and J. A. Casas, *One loop analysis of the electroweak breaking in supersymmetric models and the fine tuning problem*, Phys. Lett. B **309** (1993) 320–328, arXiv:hep-ph/9303291 [hep-ph].
- [4] Yu. A. Golfand and E. P. Likhtman, *Extension of the Algebra of Poincare Group Generators and Violation of  $p$  Invariance*, JETP Lett. **13** (1971) 323–326. [Pisma Zh. Eksp. Teor. Fiz.13,452(1971)].
- [5] D. V. Volkov and V. P. Akulov, *Is the Neutrino a Goldstone Particle?*, Phys. Lett. B **46** (1973) 109–110.
- [6] J. Wess and B. Zumino, *Supergauge Transformations in Four-Dimensions*, Nucl. Phys. B **70** (1974) 39–50.
- [7] J. Wess and B. Zumino, *Supergauge Invariant Extension of Quantum Electrodynamics*, Nucl. Phys. B **78** (1974) 1.
- [8] S. Ferrara and B. Zumino, *Supergauge Invariant Yang-Mills Theories*, Nucl. Phys. B **79** (1974) 413.
- [9] A. Salam and J. A. Strathdee, *Supersymmetry and Nonabelian Gauges*, Phys. Lett. B **51** (1974) 353–355.
- [10] N. Sakai, *Naturalness in Supersymmetric Guts*, Z. Phys. C **11** (1981) 153.
- [11] S. Dimopoulos, S. Raby, and F. Wilczek, *Supersymmetry and the Scale of Unification*, Phys. Rev. D **24** (1981) 1681–1683.

- [12] L. E. Ibanez and G. G. Ross, *Low-Energy Predictions in Supersymmetric Grand Unified Theories*, Phys. Lett. B **105** (1981) 439.
- [13] S. Dimopoulos and H. Georgi, *Softly Broken Supersymmetry and SU(5)*, Nucl. Phys. B **193** (1981) 150.
- [14] H. D. Politzer, *Reliable Perturbative Results for Strong Interactions?*, Phys. Rev. Lett. **30** (1973) 1346–1349.
- [15] D. J. Gross and F. Wilczek, *Ultraviolet behavior of non-Abelian gauge theories*, Phys. Rev. Lett. **30** (1973) 1343–1346. <http://cds.cern.ch/record/1027326>.
- [16] G. R. Farrar and P. Fayet, *Phenomenology of the Production, Decay, and Detection of New Hadronic States Associated with Supersymmetry*, Phys. Lett. B **76** (1978) 575–579.
- [17] H. Goldberg, *Constraint on the Photino Mass from Cosmology*, Phys. Rev. Lett. **50** (1983) 1419. [Erratum: Phys. Rev. Lett.103,099905(2009)].
- [18] J. R. Ellis, J. S. Hagelin, D. V. Nanopoulos, K. A. Olive, and M. Srednicki, *Supersymmetric Relics from the Big Bang*, Nucl. Phys. B **238** (1984) 453–476.
- [19] K. Garrett and G. Duda, *Dark Matter: A Primer*, Tech. Rep. arXiv:1006.2483, Jun, 2010. <http://cds.cern.ch/record/1271843>. Comments: 26 pages, 6 figures.
- [20] P. Fayet, *Supersymmetry and Weak, Electromagnetic and Strong Interactions*, Phys. Lett. B **64** (1976) 159.
- [21] P. Fayet, *Spontaneously Broken Supersymmetric Theories of Weak, Electromagnetic and Strong Interactions*, Phys. Lett. B **69** (1977) 489.
- [22] MSSM Working Group Collaboration, A. Djouadi et al., *The Minimal supersymmetric standard model: Group summary report*, in *GDR (Groupement De Recherche) - Supersymetrie Montpellier, France, April 15-17, 1998*. 1998. arXiv:hep-ph/9901246 [hep-ph].  
[https://inspirehep.net/record/481987/files/arXiv:hep-ph\\_9901246.pdf](https://inspirehep.net/record/481987/files/arXiv:hep-ph_9901246.pdf).
- [23] C. F. Berger, J. S. Gainer, J. L. Hewett, and T. G. Rizzo, *Supersymmetry Without Prejudice*, JHEP **02** (2009) 023, arXiv:0812.0980 [hep-ph].



- [24] A. H. Chamseddine, R. L. Arnowitt, and P. Nath, *Locally Supersymmetric Grand Unification*, Phys. Rev. Lett. **49** (1982) 970.
- [25] R. Barbieri, S. Ferrara, and C. A. Savoy, *Gauge Models with Spontaneously Broken Local Supersymmetry*, Phys. Lett. B **119** (1982) 343.
- [26] G. L. Kane, C. F. Kolda, L. Roszkowski, and J. D. Wells, *Study of constrained minimal supersymmetry*, Phys. Rev. D **49** (1994) 6173–6210, [arXiv:hep-ph/9312272](#) [hep-ph].
- [27] G. F. Giudice, M. A. Luty, H. Murayama, and R. Rattazzi, *Gaugino mass without singlets*, JHEP **12** (1998) 027, [arXiv:hep-ph/9810442](#) [hep-ph].
- [28] L. Randall and R. Sundrum, *Out of this world supersymmetry breaking*, Nucl. Phys. B **557** (1999) 79–118, [arXiv:hep-th/9810155](#) [hep-th].
- [29] M. Dine and W. Fischler, *A Phenomenological Model of Particle Physics Based on Supersymmetry*, Phys. Lett. B **110** (1982) 227.
- [30] L. Alvarez-Gaume, M. Claudson, and M. B. Wise, *Low-Energy Supersymmetry*, Nucl. Phys. B **207** (1982) 96.
- [31] C. R. Nappi and B. A. Ovrut, *Supersymmetric Extension of the  $SU(3) \times SU(2) \times U(1)$  Model*, Phys. Lett. B **113** (1982) 175.
- [32] G. F. Giudice and A. Romanino, *Split supersymmetry*, Nucl. Phys. B **699** (2004) 65–89, [arXiv:hep-ph/0406088](#) [hep-ph]. [Erratum: Nucl. Phys. B706,65(2005)].
- [33] N. Arkani-Hamed and S. Dimopoulos, *Supersymmetric unification without low energy supersymmetry and signatures for fine-tuning at the LHC*, JHEP **06** (2005) 073, [arXiv:hep-th/0405159](#) [hep-th].
- [34] J. Alwall, M.-P. Le, M. Lisanti, and J. G. Wacker, *Searching for Directly Decaying Gluinos at the Tevatron*, Phys. Lett. B **666** (2008) 34–37, [arXiv:0803.0019](#) [hep-ph].
- [35] J. Alwall, P. Schuster, and N. Toro, *Simplified Models for a First Characterization of New Physics at the LHC*, Phys. Rev. D **79** (2009) 075020, [arXiv:0810.3921](#) [hep-ph].

- [36] LHC New Physics Working Group Collaboration, D. Alves, *Simplified Models for LHC New Physics Searches*, J. Phys. G **39** (2012) 105005, arXiv:1105.2838 [hep-ph].
- [37] L. Evans and P. Bryant, *LHC Machine*, Journal of Instrumentation **3** (2008) no. 08, S08001. <http://stacks.iop.org/1748-0221/3/i=08/a=S08001>.
- [38] LHCb Collaboration, *The LHCb Detector at the LHC*, Journal of Instrumentation **3** (2008) no. 08, S08005. <http://stacks.iop.org/1748-0221/3/i=08/a=S08005>.
- [39] ALICE Collaboration, *The ALICE experiment at the CERN LHC*, Journal of Instrumentation **3** (2008) no. 08, S08002. <http://stacks.iop.org/1748-0221/3/i=08/a=S08002>.
- [40] CMS Collaboration, *The CMS experiment at the CERN LHC*, Journal of Instrumentation **3** (2008) no. 08, S08004. <http://stacks.iop.org/1748-0221/3/i=08/a=S08004>.
- [41] ATLAS Collaboration, *The ATLAS Experiment at the CERN Large Hadron Collider*, Journal of Instrumentation **3** (2008) no. 08, S08003. <http://stacks.iop.org/1748-0221/3/i=08/a=S08003>.
- [42] ALICE Collaboration, *First results of the ALICE detector performance at 13 TeV*, . <http://cds.cern.ch/record/2047855>.
- [43] ATLAS Collaboration, *ATLAS inner detector: Technical Design Report, 1*. Technical Design Report ATLAS. CERN, Geneva, 1997. <http://cds.cern.ch/record/331063>.
- [44] ATLAS Collaboration, S. Haywood, L. Rossi, R. Nickerson, and A. Romaniouk, *ATLAS inner detector: Technical Design Report, 2*. Technical Design Report ATLAS. CERN, Geneva, 1997. <http://cds.cern.ch/record/331064>.
- [45] M. Capeans, G. Darbo, K. Einsweiler, M. Elsing, T. Flick, M. Garcia-Sciveres, C. Gemme, H. Pernegger, O. Rohne, and R. Vuillermet, *ATLAS Insertable B-Layer Technical Design Report*, Tech. Rep. CERN-LHCC-2010-013. ATLAS-TDR-19, CERN, Geneva, Sep, 2010. <http://cds.cern.ch/record/1291633>.

- [46] ATLAS Collaboration, *ATLAS Insertable B-Layer Technical Design Report Addendum*, Tech. Rep. CERN-LHCC-2012-009. ATLAS-TDR-19-ADD-1, CERN, Geneva, May, 2012. <http://cds.cern.ch/record/1451888>. Addendum to CERN-LHCC-2010-013, ATLAS-TDR-019.
- [47] ATLAS Collaboration, *ATLAS muon spectrometer: Technical Design Report*. Technical Design Report ATLAS. CERN, Geneva, 1997. <http://cds.cern.ch/record/331068>.
- [48] Micheloud and Cie, *Geneva's liquid asset*, Online. <http://switzerland.isyours.com/e/guide/geneva/jetdeau.html>.
- [49] F. Martin, *Description of the test bench for the ATLAS hadronic tile front end electronics*, Tech. Rep. ATL-TILECAL-2003-003, CERN, Geneva, Dec, 2002. <http://cds.cern.ch/record/685438>.
- [50] R. Bonnefoy, D. Calvet, R. Chadelas, M. Crouau, and F. Martin, *MobiDICK: a mobile test bench for the TileCal super-drawers*, Tech. Rep. ATL-TILECAL-2004-003, CERN, Geneva, Aug, 2003. <http://cds.cern.ch/record/681350>.
- [51] D. Calvet, *Test system for the production of the ATLAS Tile Calorimeter front- end electronics*, Nucl. Instrum. Methods Phys. Res., A **518** (2004) 509–510. <http://cds.cern.ch/record/802341>.
- [52] V. Giangiobbe and D. Calvet, *Performance of the TileCal super-drawers from a global analysis of the MobiDICK tests*, Tech. Rep. ATL-TILECAL-PUB-2008-007. ATL-COM-TILECAL-2007-010, CERN, Geneva, Apr, 2007. <http://cds.cern.ch/record/1026732>.
- [53] ATLAS Collaboration, *Letter of Intent for the Phase-I Upgrade of the ATLAS Experiment*, Tech. Rep. CERN-LHCC-2011-012. LHCC-I-020, CERN, Geneva, Nov, 2011. <http://cds.cern.ch/record/1402470>.

- [54] ATLAS Collaboration, *Letter of Intent for the Phase-II Upgrade of the ATLAS Experiment*, Tech. Rep. CERN-LHCC-2012-022. LHCC-I-023, CERN, Geneva, Dec, 2012. <https://cds.cern.ch/record/1502664>. Draft version for comments.
- [55] P. Moreno Marti, F. Carrio Argos, and A. Valero, *Firmware Development for the ATLAS TileCal sROD*, Tech. Rep. ATL-TILECAL-PROC-2015-006, CERN, Geneva, Jun, 2015. <https://cds.cern.ch/record/2023908>.
- [56] A. Valero, *A new read-out architecture for the ATLAS Tile Calorimeter Phase-II Upgrade*, Tech. Rep. ATL-TILECAL-PROC-2015-025, CERN, Geneva, Dec, 2015. <https://cds.cern.ch/record/2117093>.
- [57] P. Moreno, J. Alves, D. Calvet, F. Carrio, M. Crouau, K. Hee Yeun, I. Minashvili, S. Nemececk, G. Quin, V. Schettino, C. Solans, G. Usai, and A. Valero, *A new portable test bench for the ATLAS Tile Calorimeter front-end electronics*, Tech. Rep. ATL-TILECAL-PROC-2012-010, CERN, Geneva, Nov, 2012. <https://cds.cern.ch/record/1493086>.
- [58] J. Alves, F. Carri, K. Hee Yeun, I. Minashvili, P. Moreno, G. Qin, R. Reed, V. Schettino, A. Shalyugin, C. Solans, J. Sousa, G. Usai, and A. Valero, *A new portable test bench for the ATLAS Tile Calorimeter front-end electronics certification*, Tech. Rep. ATL-TILECAL-PROC-2013-005, CERN, Geneva, May, 2013. <https://cds.cern.ch/record/1551920>.
- [59] C. Solans, F. Carrio, H. Y. Kim, P. Moreno, R. Reed, C. Sandrock, X. Ruan, A. Shalyugin, V. Schettino, J. Souza, G. Usai, and A. Valero, *Computing challenges in the certification of ATLAS Tile Calorimeter front-end electronics during maintenance periods*, Tech. Rep. ATL-TILECAL-PROC-2013-015, CERN, Geneva, Oct, 2013. <https://cds.cern.ch/record/1621927>.
- [60] F. Carrio, H. Y. Kim, P. Moreno, R. Reed, C. Sandrock, A. Shalyugin, V. Schettino, J. Souza, C. Solans, G. Usai, and A. Valero, *Design of an FPGA-based embedded system for the ATLAS Tile Calorimeter front-end electronics test-bench*, tech. rep., CERN.

- [61] H. Y. Kim, H. Akerstedt, F. Carrio, P. Moreno, T. Masike, R. Reed, C. Sandrock, V. Schettino, A. Shalyugin, C. Solans, J. Souza, R. Suter, G. Usai, and A. Valero, *Design of a Portable Test Facility for the ATLAS Tile Calorimeter Front-End Electronics Verification*, Tech. Rep. ATL-TILECAL-PROC-2013-018, CERN, Geneva, Nov, 2013. <https://cds.cern.ch/record/1628746>.
- [62] F. Carrio, V. Castillo, A. Ferrer, L. Fiorini, Y. Hernandez, E. Higon, B. Mellado, L. March, P. Moreno, R. Reed, C. Solans, A. Valero, and J. A. Valls, *The sROD Module for the ATLAS Tile Calorimeter Phase-II Upgrade Demonstrator*, tech. rep., CERN.
- [63] D. Bullock, F. Carrio, M. Govender, I. Hofsjager, B. Mellado, P. Moreno, R. Reed, X. Ruan, C. Sandrock, C. Solans, R. Suter, G. Usai, and A. Valero, *Prometeo: A portable test-bench for the upgraded front-end electronics of the ATLAS Tile calorimeter*, Tech. Rep. ATL-TILECAL-PROC-2014-012, CERN, Geneva, Jun, 2014. <https://cds.cern.ch/record/1710332>.
- [64] T. Sjstrand, S. Ask, J. R. Christiansen, R. Corke, N. Desai, P. Ilten, S. Mrenna, S. Prestel, C. O. Rasmussen, and P. Z. Skands, *An Introduction to PYTHIA 8.2*, *Comput. Phys. Commun* **191** (Oct, 2014) 159–177. 45 p.  
<http://cds.cern.ch/record/1955026>. Comments: 45 pages.
- [65] J. Alwall, R. Frederix, S. Frixione, V. Hirschi, F. Maltoni, O. Mattelaer, H. S. Shao, T. Stelzer, P. Torrielli, and M. Zaro, *The automated computation of tree-level and next-to-leading order differential cross sections, and their matching to parton shower simulations*, *J. High Energy Phys.* **07** (May, 2014) 079. 158 p.  
<http://cds.cern.ch/record/1699128>. Comments: 158 pages, 27 figures; a few references have been added.
- [66] S. Frixione, P. Nason, and C. Oleari, *Matching NLO QCD computations with Parton Shower simulations: the POWHEG method*, *JHEP* **11** (2007) 070, [arXiv:0709.2092](https://arxiv.org/abs/0709.2092) [hep-ph].

- [67] J. Butterworth, J. R. Forshaw, and M. H. Seymour, *Multiparton interactions in photoproduction at HERA*, *Z. Phys. C* **72** (Jan, 1996) 637–646. 22 p.  
<http://cds.cern.ch/record/295247>.
- [68] M. Bahr, S. Gieseke, M. A. Gigg, D. Grellscheid, K. Hamilton, O. Latunde-Dada, S. Platzer, P. Richardson, M. H. Seymour, A. Sherstnev, and B. R. Webber, *Herwig++ Physics and Manual*, *Eur. Phys. J. C* **58** (Mar, 2008) 639–707. 143 p.  
<http://cds.cern.ch/record/1093062>.
- [69] J. Bellm, S. Gieseke, D. Grellscheid, S. Pltzer, M. Rauch, C. Reuschle, P. Richardson, P. Schichtel, M. H. Seymour, A. Sidmok, A. Wilcock, N. Fischer, M. A. Harrendorf, G. Nail, A. Papaefstathiou, and D. Rauch, *Herwig 7.0 / Herwig++ 3.0 Release Note*, Tech. Rep. arXiv:1512.01178. CERN-PH-TH-2015-289. MAN-HEP-2015-15. IFJPAN-IV-2015-13. HERWIG-2015-01. KA-TP-18-2015. DCPT-15-142. MCNET-15-28. IPPP-15-71, Dec, 2015.  
<http://cds.cern.ch/record/2110873>. Comments: 8 pages. Herwig is available from <https://herwig.hepforge.org>.
- [70] S. Frixione and B. R. Webber, *Matching NLO QCD computations and parton shower simulations*, *JHEP* **06** (2002) 029, arXiv:hep-ph/0204244 [hep-ph].
- [71] M. L. Mangano, M. Moretti, F. Piccinini, R. Pittau, and A. Polosa, *ALPGEN, a generator for hard multiparton processes in hadronic collisions*, *J. High Energy Phys.* **07** (Jun, 2002) 001. 35 p. <http://cds.cern.ch/record/565290>.
- [72] T. Gleisberg, S. Hoeche, F. Krauss, M. Schonherr, S. Schumann, F. Siegert, and J. Winter, *Event generation with SHERPA 1.1*, *JHEP* **02** (2009) 007, arXiv:0811.4622 [hep-ph].
- [73] ATLAS Collaboration, *The ATLAS Simulation Infrastructure*, *Eur. Phys. J. C* **70** (May, 2010) 823–874. 53 p. <http://cds.cern.ch/record/1267853>.
- [74] Inner Tracking Combined Performance Group Collaboration.  
<https://twiki.cern.ch/twiki/bin/view/AtlasProtected/InDetTrackingWG>.

- [75] EGamma Working Group Collaboration.  
<https://twiki.cern.ch/twiki/bin/view/AtlasProtected/ElectronGamma>}.
- [76] Muon Combined Performance Working Group Collaboration.  
<https://twiki.cern.ch/twiki/bin/view/AtlasProtected/MuonPerformance>}.
- [77] Jet and Etmiss Combined Performance Group Collaboration.  
<https://twiki.cern.ch/twiki/bin/view/AtlasProtected/JetEtMiss>}.
- [78] Flavour Tagging Working Group Collaboration.  
<https://twiki.cern.ch/twiki/bin/view/AtlasProtected/FlavourTagging>}.
- [79] Tau Working Group Collaboration.  
<https://twiki.cern.ch/twiki/bin/view/AtlasProtected/TauWG>}.
- [80] ATLAS Collaboration, *Jet energy resolution in proton-proton collisions at  $\sqrt{s} = 7$  TeV recorded in 2010 with the ATLAS detector*, Eur. Phys. J. C **73** (Oct, 2012) 2306. 26 p. <http://cds.cern.ch/record/1489592>. Comments: 13 pages plus author list (26 pages total), 15 figures, 1 table, submitted to European Physical Journal C.
- [81] ATLAS Collaboration Collaboration, S. Jzquel, *The electromagnetic calorimeter of ATLAS and its performances*, Nucl. Instrum. Methods Phys. Res., A **409** (Oct, 1997) 589–592. 6 p. <http://cds.cern.ch/record/342038>.
- [82] Y. A. Kulchitskii and V. B. Vinogradov, *Performances of the ATLAS Hadronic Tile Calorimeter Modules for Electrons and Pions*, Tech. Rep. ATL-TILECAL-2004-013. ATL-COM-TILECAL-2004-009. CERN-ATL-COM-TILECAL-2004-009, CERN, Geneva, 2004. <http://cds.cern.ch/record/799443>.
- [83] S. Owen, *Data-driven estimation of the QCD multijet background to SUSY searches with jets and missing transverse momentum at ATLAS using jet smearing*, Tech. Rep. ATL-PHYS-INT-2012-008, CERN, Geneva, Feb, 2012.  
<https://cds.cern.ch/record/1423310>.
- [84] ATLAS Collaboration, *Observation of a new particle in the search for the Standard Model Higgs boson with the ATLAS detector at the LHC*, Phys. Lett. B **716** (Aug,

- 2012) 1–29. 39 p. <http://cds.cern.ch/record/1471031>. Comments: 24 pages plus author list (38 pages total), 12 figures, 7 tables, revised author list.
- [85] ATLAS Collaboration, *Combined search for the Standard Model Higgs boson in pp collisions at  $\sqrt{s} = 7$  TeV with the ATLAS detector*, Phys. Rev. D **86** (Jul, 2012) 032003. 32 p. <http://cds.cern.ch/record/1459149>. Comments: 19 pages plus author list (32 pages total), 10 figures, 4 tables.
- [86] M. Baak, G. J. Besjes, D. Cote, A. Koutsman, J. Lorenz, and D. Short, *HistFitter software framework for statistical data analysis*, Eur. Phys. J. C **75** (Oct, 2014) 153. 35 p. <http://cds.cern.ch/record/1953093>. Comments: 35 pages (excluding appendix) and 10 figures. Code publicly available at: <http://cern.ch/histfitter>.
- [87] D. J. Summers, *Transverse mass as a means of measuring the W width at the Tevatron*, Phys. Lett. B **392** (Aug, 1996) 216–222. 13 p. <http://cds.cern.ch/record/308850>.
- [88] C. G. Lester and D. J. Summers, *Measuring masses of semi-invisibly decaying particles pair produced at hadron colliders*, Phys. Lett. B **463** (1999) no. hep-ph/9906349. CAVENDISH-HEP-99-07. 1, 99–103. <http://cds.cern.ch/record/390377>.
- [89] D. R. Tovey, *On measuring the masses of pair-produced semi-invisibly decaying particles at hadron colliders*, J. High Energy Phys. **04** (Feb, 2008) 034. 13 p. <http://cds.cern.ch/record/1090251>. Comments: 13 pages, 4 .eps figures, JHEP3 style.
- [90] SPS Collaboration, *Jet measures and hadronic event shapes at the CERN  $\bar{p}p$  collider*, Z. Phys. C **36** (Apr, 1987) 175–187. 27 p. <http://cds.cern.ch/record/178313>.
- [91] L. Randall and D. Tucker-Smith, *Dijet Searches for Supersymmetry at the LHC*, Phys. Rev. Lett. **101** (2008) 221803, arXiv:0806.1049 [hep-ph].



- [92] C. Rogan, *Kinematical variables towards new dynamics at the LHC*, Tech. Rep. arXiv:1006.2727. CALT 68-2790, Jun, 2010.  
<https://cds.cern.ch/record/1272065>.
- [93] M. R. Buckley, J. D. Lykken, C. Rogan, and M. Spiropulu, *Super-Razor and Searches for Sleptons and Charginos at the LHC*, Phys. Rev. **D89** (2014) no. 5, 055020, arXiv:1310.4827 [hep-ph].
- [94] Kr tech. rep.
- [95] C. Borschensky, M. Krmer, A. Kulesza, M. Mangano, S. Padhi, T. Plehn, and X. Portell, *Squark and gluino production cross sections in pp collisions at  $\sqrt{s} = 13, 14, 33$  and  $100$  TeV*, Eur. Phys. J. C **74** (Jul, 2014) 3174. 22 p.  
<http://cds.cern.ch/record/1744356>. Comments: 22 pages, 16 figures. arXiv admin note: substantial text overlap with arXiv:1206.2892.
- [96] CMS Collaboration, *Inclusive search for squarks and gluinos at  $\sqrt{s} = 7$  TeV*, Tech. Rep. CMS-PAS-SUS-10-009, CERN, Geneva, 2011.  
<http://cds.cern.ch/record/1338577>.
- [97] CMS Collaboration, *Searches for supersymmetry in hadronic final states with the CMS detector*, Tech. Rep. CMS-CR-2011-211, CERN, Geneva, Oct, 2011.  
<http://cds.cern.ch/record/1399479>.
- [98] CMS Collaboration, *Search for supersymmetry with the razor variables at CMS*, Tech. Rep. CMS-PAS-SUS-11-008, CERN, Geneva, 2011.  
<http://cds.cern.ch/record/1404167>.
- [99] CMS Collaboration, *Search for supersymmetry with the razor variables at CMS*, Tech. Rep. CMS-PAS-SUS-11-024, CERN, Geneva, 2012.  
<http://cds.cern.ch/record/1459813>.
- [100] CMS Collaboration, *Search for supersymmetry with the razor variables at CMS*, Tech. Rep. CMS-PAS-SUS-12-005, CERN, Geneva, 2012.  
<http://cds.cern.ch/record/1430715>.

- [101] CMS Collaboration, *A search for the decays of a new heavy particle in multijet events with the razor variables at CMS in pp collisions at  $\sqrt{s} = 7$  TeV*, Tech. Rep. CMS-PAS-SUS-12-009, CERN, Geneva, 2012.  
<http://cds.cern.ch/record/1459812>.
- [102] CMS Collaboration, *Search for supersymmetry with taus using the razor variables*, Tech. Rep. CMS-PAS-SUS-11-029, CERN, Geneva, 2012.  
<http://cds.cern.ch/record/1493504>.
- [103] CMS Collaboration, *Search for supersymmetry with photons in pp collisions at  $\sqrt{s} = 8$  TeV*, Phys. Rev. D **92** (Jul, 2015) 072006. 38 p.  
<http://cds.cern.ch/record/2033174>. Comments: Replaced with published version. Added journal reference and DOI.
- [104] CMS Collaboration, *Search for supersymmetry in two-photons+jet events with razor variables in pp collisions at  $\sqrt{s} = 8$  TeV*, Tech. Rep. CMS-PAS-SUS-14-008, CERN, Geneva, 2014. <http://cds.cern.ch/record/1749154>.
- [105] CMS Collaboration, *Exclusion limits on gluino and top-squark pair production in natural SUSY scenarios with inclusive razor and exclusive single-lepton searches at 8 TeV.*, Tech. Rep. CMS-PAS-SUS-14-011, CERN, Geneva, 2014.  
<http://cds.cern.ch/record/1745586>.
- [106] J. Duarte, *Search for natural Supersymmetry in events with 1 b-tagged jet using razor variables at 8 TeV*, Tech. Rep. arXiv:1409.4466, Sep, 2014.  
<http://cds.cern.ch/record/1756029>. Comments: LHCP Conference 2014.
- [107] CMS Collaboration, *Search for supersymmetry using razor variables in events with b-jets in pp collisions at 8 TeV*, Tech. Rep. CMS-PAS-SUS-13-004, CERN, Geneva, 2013. <http://cds.cern.ch/record/1596446>.
- [108] CMS Collaboration, *Search for supersymmetry in pp collisions at  $\sqrt{s} = 8$  TeV in final states with boosted W bosons and b jets using razor variables*, Tech. Rep. CERN-EP-2016-008. CMS-SUS-14-007-003, CERN, Geneva, Feb, 2016.  
<http://cds.cern.ch/record/2130623>.

- [109] CMS Collaboration, *Inclusive search for supersymmetry using the razor variables at  $\sqrt{s} = 13$  TeV*, Tech. Rep. CMS-PAS-SUS-15-004, CERN, Geneva, 2015.  
<http://cds.cern.ch/record/2114815>.
- [110] CMS Collaboration, *Search for supersymmetry using razor variables in events with  $b$ -tagged jets in  $pp$  collisions at  $\sqrt{s} = 8$  TeV*, Phys. Rev. D **91** (Feb, 2015) 052018. 45 p. <http://cds.cern.ch/record/1984165>. Comments: Submitted to Phys. Rev. D.
- [111] P. J. Fox, R. Harnik, R. Primulando, and C.-T. Yu, *Taking a Razor to Dark Matter Parameter Space at the LHC*, Tech. Rep. arXiv:1203.1662. FERMILAB-PUB-12-066-T, Mar, 2012. <http://cds.cern.ch/record/1430414>. Comments: 25 pages, 10 figures.
- [112] CMS Collaboration, *Search for dark matter direct production using razor variables in events with two or more jets in  $pp$  collisions at 8 TeV*, Tech. Rep. CMS-PAS-EXO-14-004, CERN, Geneva, 2015.  
<http://cds.cern.ch/record/2002861>.
- [113] CMS Collaboration, *Search for SUSY with Higgs in the diphoton final state using the razor variables*, Tech. Rep. CMS-PAS-SUS-14-017, CERN, Geneva, 2015.  
<http://cds.cern.ch/record/2047472>.
- [114] D. Bullock, O. Dale, A. Farbin, L. Heelan, P. Jackson, T. J. Khoo, L. Lee, D. Miller, A. Petridis, A. Qureshi, C. S. Rogan, R. Smith, G. Stark, E. Tolley, and M. White, *Search for Squarks and Gluinos in Run II Using the Recursive Jigsaw Technique in  $0$ -Lepton Final States*, Tech. Rep. ATL-COM-PHYS-2015-1340, CERN, Geneva, Nov, 2015. <https://cds.cern.ch/record/2064407>.
- [115] T. Bain, D. Bullock, A. Farbin, L. Heelan, E. Kuwertz, R. Lafaye, and Z. Marshall, *Multi-channel search for squarks and gluinos in  $\sqrt{s} = 7$  TeV  $pp$  collisions with the ATLAS detector*, Tech. Rep. ATL-PHYS-INT-2013-001, CERN, Geneva, Jan, 2013.  
<https://cds.cern.ch/record/1503509>.

- [116] ATLAS Collaboration, *Search for squarks and gluinos with the ATLAS detector in final states with jets and missing transverse momentum using  $4.7 \text{ fb}^{-1}$  of  $\sqrt{s} = 7 \text{ TeV}$  proton-proton collision data*, Phys. Rev. D **87** (Aug, 2012) 012008. 36 p.  
<https://cds.cern.ch/record/1472021>. Comments: 23 pages plus author list (36 pages total), 15 figures, 5 tables, submitted to Physical Review D.
- [117] ATLAS Collaboration, *Further search for supersymmetry at  $\sqrt{s} = 7 \text{ TeV}$  in final states with jets, missing transverse momentum and one isolated lepton*, Tech. Rep. ATLAS-CONF-2012-041, CERN, Geneva, Mar, 2012.  
<https://cds.cern.ch/record/1435195>.
- [118] I. Santoyo Castillo, C. Clement, G. Conti, J. Firmino da Costa, J. Dietrich, A. Floderus, S. Fratina, S. French, B. Gjelsten, E. Gramstad, M. Hamer, C. Hensel, E. Hines, B. Jackson, T. Kono, F. Legger, C. Lester, M. Medinnis, B. Meirose, A. S. Mete, H. Okawa, F. Ould-Saada, M. Pedersen, F. Salvatore, A. Taffard, E. Thomson, B. Toggerson, R. Ueno, S. Williams, and J. Wittkowski, *Searching for direct gaugino production and direct slepton production with two leptons and missing transverse momentum at  $\sqrt{s} = 7 \text{ TeV}$  (supporting INT note)*, Tech. Rep. ATL-COM-PHYS-2011-1721, CERN, Geneva, Dec, 2011.  
<https://cds.cern.ch/record/1408807>.
- [119] E. S. Kuwertz, Z. L. Marshall, A. Chitan, V. Tudorache, N. Kanaya, and A. Koutsman, *Search for strongly produced supersymmetric particles in decays with at least two leptons at  $\sqrt{s} = 8 \text{ TeV}$  with the ATLAS detector*, Tech. Rep. ATL-COM-PHYS-2013-1539, CERN, Geneva, Nov, 2013.  
<https://cds.cern.ch/record/1627071>.
- [120] D. J. Antrim, K. Brendlinger, C. Clement, A. De Santo, D. Gerbaudo, Z. Gecse, M. Hirose, O. Jinnouchi, P. Klimek, A. Kourkoumeli-Charalampidi, R. Nagai, A. S. Mete, C. Potter, A. Petridis, P. F. Salvatore, I. Santoyo Castillo, D. Schaefer, C. Y. Shehu, A. Taffard, and S. Williams, *Search for supersymmetry in compressed scenarios with two and three leptons and missing transverse momentum in the final*

- state in  $21 \text{ fb}^{-1}$   $pp$  collisions at  $\sqrt{s} = 8 \text{ TeV}$  with the ATLAS detector, Tech. Rep. ATL-COM-PHYS-2014-959, CERN, Geneva, Aug, 2014.  
<https://cds.cern.ch/record/1747483>.
- [121] D. Bullock, A. Farbin, L. Heelan, A. Kravchenko, Z. Marshall, and M. Purohit, *Search for direct squark and gluino pair production using the Razor kinematical variables with  $\sqrt{s} = 8 \text{ TeV}$   $pp$  collisions at the ATLAS detector*, Tech. Rep. ATL-COM-PHYS-2014-1107, CERN, Geneva, Sep, 2014.  
<https://cds.cern.ch/record/1752911>.
- [122] ATLAS Collaboration, *Search for squarks and gluinos with the ATLAS detector in final states with jets and missing transverse momentum using  $\sqrt{s} = 8 \text{ TeV}$  proton-proton collision data*, J. High Energy Phys. **09** (May, 2014) 176. 52 p.  
<http://cds.cern.ch/record/1705530>. Comments: 36 pages plus author list + cover pages (54 pages total), 13 figures, 5 tables, submitted to JHEP, All figures including auxiliary figures are available at  
<https://atlas.web.cern.ch/Atlas/GROUPS/PHYSICS/PAPERS/SUSY-2013-02/>.
- [123] S. Adachi, D. Bullock, G. Conti, I. Deigaard, L. Duflot, G. T. Fletcher, L. Heelan, S. Henrot-Versille, M. Hodgkinson, P. Jackson, L. Lee JR, N. Makovec, Y. Minami, H. J. Moss, Y. Nakahama, B. Petersen, A. Petridis, M. Ronzani, Z. Rurikova, R. Smith, A. Strubig, D. Tovey, M. Vranjes Milosavljevic, T. Yamanaka, J. Mamuzic, B. Abeloos, G.-J. Besjes, O. Dale, and C. S. Rogan, *Search for squarks and gluinos with the ATLAS detector in final states with jets and missing transverse momentum using  $\sqrt{s}=13 \text{ TeV}$  proton-proton collision data: supporting documentation*, Tech. Rep. ATL-COM-PHYS-2015-381, CERN, Geneva, May, 2015.  
<https://cds.cern.ch/record/2015060>.
- [124] P. Speckmayer, A. Hocker, J. Stelzer, and H. Voss, *The toolkit for multivariate data analysis: TMVA 4*, J. Phys.: Conf. Ser. **219** (2010) 032057.  
<http://cds.cern.ch/record/1270192>.

APPENDIX A  
Mathematical Notation

## A.1 Matrices

An identity matrix of arbitrary size  $n \times n$  is denoted as  $I(n)$ . Wherever the size of the identity matrix can be inferred, it can be written as  $I$ . A matrix is “Hermitian” if it is equal to its conjugate transpose (adjoint).

$$H = H^\dagger \tag{A.1}$$

A matrix is “unitary” if its inverse is equal to its adjoint. A unitary matrix of size  $n \times n$  is denoted as  $U(n)$ . If the determinant of the matrix is equal to unity, the matrix is called a “special” unitary matrix and is denoted as  $SU(n)$ .

$$\begin{aligned} U^{-1} &= U^\dagger \\ U^\dagger U &= U U^\dagger = I \end{aligned} \tag{A.2}$$

A term such as  $x^\mu$  denotes a column vector while  $x_\mu$  denotes a row vector. Column vectors and row vectors are related by the transpose property. The number of parameters are shown in the superscript or subscript, such as  $A'_\mu$  in a  $2 \times 2$  matrix or  $\epsilon^{\mu\nu\sigma}$  in a  $3 \times 3$  matrix.

When a matrix equation uses repeated indices, a summation is implied:

$$\begin{aligned} ax^\mu &= \sum_\mu ax^\mu \\ &= ax^0 + ax^1 + ax^2 + ax^3 + \dots \end{aligned} \tag{A.3}$$

## A.2 Boolean Algebra

When an outcome of a term is “true” or “false”, the boolean numbers 1 and 0 are used. This can simplify the equations because variables can be expressed as being 1 or NOT(1). If variable  $A$  contains a boolean value, then the inverse of its boolean value is denoted as  $\bar{A}$ , which is the same as NOT( $A$ ).

Probabilities may also benefit from boolean expressions because they represent counting statistics. An outcome could land in  $A$  or it could not land in  $A$ . The cumulative effect of this binary selection process determines the probability. If an outcome lands in  $A$  but it also lands in  $B$ , then the combined outcome is a logical AND of  $A$  and  $B$ , which is denoted as  $A \cap B$  and called an “intersect” between the two probabilities. If an outcome lands somewhere in either  $A$  or  $B$  (exclusively  $A$ , exclusively  $B$ , or both  $A$  and  $B$ ), the outcome is a logical OR of  $A$  and  $B$ , which is denoted as  $A \cup B$  and called a “union” between the two probabilities.

### A.3 Poincaré Group

The Poincaré group is the symmetry group of the SM (Section 2.2.1). This group is a semi-direct product of the translation and Lorentz groups. The translation matrix transforms a position vector ( $x^\mu$ ) by a velocity vector ( $v^\mu$ ).

$$\begin{aligned} x'^\mu &= T_\mu^\nu x^\nu \\ &= x^\nu + v^\nu \end{aligned} \tag{A.4}$$

This matrix has the form (including the time component):

$$T^{\mu\nu} = \begin{pmatrix} 1 & 0 & 0 & v_x \\ 0 & 1 & 0 & v_y \\ 0 & 0 & 1 & v_z \\ 0 & 0 & 0 & 1 \end{pmatrix} \tag{A.5}$$

Spacetime coordinates in the Lorentz group are given by:

$$x^\mu = \begin{pmatrix} ct \\ x \\ y \\ z \end{pmatrix} \tag{A.6}$$



These coordinates are transform a position vector by relativistic boosts:

$$x'^{\mu} = \Lambda^{\mu}_{\nu} x^{\nu} \quad (\text{A.7})$$

This equation is independent of the choice of coordinates, but one can always choose orthogonal axes and align the  $x$ -axis along the boost direction. In that case, the Lorentz matrix has the form:

$$\Lambda^{\mu\nu} = \begin{pmatrix} \gamma & -\gamma\beta & 0 & 0 \\ -\gamma\beta & \gamma & 0 & 0 \\ 0 & 0 & 1 & 0 \\ 0 & 0 & 0 & 1 \end{pmatrix} \quad (\text{A.8})$$

The Lorentz transformation has an quantity ( $I$ ) that is invariant in any reference frame:

$$\begin{aligned} I &= (x^0)^2 - (x^1)^2 - (x^2)^2 - (x^3)^2 \\ &= (x'^0)^2 - (x'^1)^2 - (x'^2)^2 - (x'^3)^2 \end{aligned} \quad (\text{A.9})$$

In order to write this in a compact form, the relative + and – signs are collected into the Minkowski metric:

$$g^{\mu\nu} = \begin{pmatrix} 1 & 0 & 0 & 0 \\ 0 & -1 & 0 & 0 \\ 0 & 0 & -1 & 0 \\ 0 & 0 & 0 & -1 \end{pmatrix} \quad (\text{A.10})$$

Since this metric is diagonal, it is often expressed by a simpler notation:

$$g^{\mu\nu} = (+, -, -, -) \quad (\text{A.11})$$

In some HEP texts, this metric is inverted. In the theoretical derivations presented in this document, the metric will be applied as shown here. The invariant can now be expressed as:

$$\begin{aligned} I &= g_{\mu\nu}x^\mu x^\nu \\ &= x_\mu x^\mu \end{aligned} \tag{A.12}$$

The metric also enables column vectors to be written in terms of row vectors (and vice versa):

$$\begin{aligned} x_\mu &= g_{\mu\nu}x^\nu \\ x^\mu &= g^{\mu\nu}x_\nu \end{aligned} \tag{A.13}$$

#### A.4 Pauli Matrices

There are 3 generators of the  $SU(2)$  group known as the Pauli matrices ( $\sigma$ ):

$$\sigma_1 \equiv \begin{pmatrix} 0 & 1 \\ 1 & 0 \end{pmatrix} \quad \sigma_2 \equiv \begin{pmatrix} 0 & -i \\ i & 0 \end{pmatrix} \quad \sigma_3 \equiv \begin{pmatrix} 1 & 0 \\ 0 & -1 \end{pmatrix} \tag{A.14}$$

These three matrices are related by the commutation and anticommutation relations:

$$[\sigma_a, \sigma_b] = 2i\epsilon_{abc}\sigma_c \tag{A.15a}$$

$$\sigma_a \sigma_b = 2\delta_{ij} \tag{A.15b}$$

The  $\epsilon_{abc}$  term is an antisymmetric tensor called the Levi-Civita tensor given by:

$$\epsilon_{abc} = \begin{cases} +1 & \text{even permutation of } a, b, c \\ -1 & \text{odd permutation of } a, b, c \end{cases} \tag{A.16}$$

## A.5 Gell-Mann Matrices

There are 8 generators of the  $SU(3)$  group known as the Gell-Mann matrices ( $\lambda$ ):

$$\begin{aligned}
 \lambda_1 &\equiv \begin{pmatrix} 0 & 1 & 0 \\ 1 & 0 & 0 \\ 0 & 0 & 0 \end{pmatrix} & \lambda_2 &\equiv \begin{pmatrix} 0 & -i & 0 \\ i & 0 & 0 \\ 0 & 0 & 0 \end{pmatrix} & \lambda_3 &\equiv \begin{pmatrix} 1 & 0 & 0 \\ 0 & -1 & 0 \\ 0 & 0 & 0 \end{pmatrix} \\
 \lambda_4 &\equiv \begin{pmatrix} 0 & 0 & 1 \\ 0 & 0 & 0 \\ 1 & 0 & 0 \end{pmatrix} & \lambda_5 &\equiv \begin{pmatrix} 0 & 0 & -i \\ 0 & 0 & 0 \\ i & 0 & 0 \end{pmatrix} & \lambda_6 &\equiv \begin{pmatrix} 0 & 0 & 0 \\ 0 & 0 & 1 \\ 0 & 1 & 0 \end{pmatrix} & (A.17) \\
 \lambda_7 &\equiv \begin{pmatrix} 0 & 0 & 0 \\ 0 & 0 & -i \\ 0 & i & 0 \end{pmatrix} & \lambda_8 &\equiv \frac{1}{\sqrt{3}} \begin{pmatrix} 1 & 0 & 0 \\ 0 & 1 & 0 \\ 0 & 0 & -2 \end{pmatrix}
 \end{aligned}$$

These eight matrices are related by the commutation and anticommutation relations:

$$[\lambda_a, \lambda_b] = 2if_{abc}\lambda_c \quad (A.18a)$$

$$\lambda_a, \lambda_b = 2d_{abc}\lambda_c + \frac{4}{3}\delta_{ab} \quad (A.18b)$$

The  $f_{abc}$  term is an antisymmetric tensor called a field structure given by:

- $f_{123} = 1$
- $f_{147} = 1/2$
- $f_{156} = -1/2$
- $f_{246} = 1/2$
- $f_{257} = 1/2$
- $f_{356} = 1/2$
- $f_{367} = -1/2$
- $f_{458} = \sqrt{3}/2$
- $f_{678} = \sqrt{3}/2$

- $f_{abc} = 0$  otherwise

The  $d_{abc}$  term is an antisymmetric tensor called a Casimir operator given by:

- $d_{118} = 1/\sqrt{3}$
- $d_{146} = 1/2$
- $d_{157} = 1/2$
- $d_{228} = 1/\sqrt{3}$
- $d_{247} = -1/2$
- $d_{256} = 1/2$
- $d_{338} = 1/\sqrt{3}$
- $d_{344} = 1/2$
- $d_{355} = 1/2$
- $d_{366} = -1/2$
- $d_{377} = -1/2$
- $d_{448} = -1/2\sqrt{3}$
- $d_{558} = -1/2\sqrt{3}$
- $d_{668} = -1/2\sqrt{3}$
- $d_{778} = -1/2\sqrt{3}$
- $d_{888} = -1/\sqrt{3}$

## A.6 Dirac Matrices

The transformation of spinors depends on the particular field involved. The definitions first need a definition of Dirac Matrices ( $\gamma^0$ ,  $\gamma^1$ ,  $\gamma^2$ , and  $\gamma^3$ ) and auxiliary matrices ( $\gamma^5$ ,  $\Sigma$ , and  $\sigma^{\mu\nu}$ ):

$$\gamma^0 \equiv \begin{pmatrix} I & 0 \\ 0 & -I \end{pmatrix} \quad \gamma^i \equiv \begin{pmatrix} 0 & \sigma^i \\ -\sigma^i & 0 \end{pmatrix} \quad (\text{A.19a})$$

$$\gamma^5 \equiv i\gamma^0\gamma^1\gamma^2\gamma^3 \quad (\text{A.19b})$$

$$\Sigma \equiv \begin{pmatrix} \sigma & 0 \\ 0 & \sigma \end{pmatrix} \quad (\text{A.19c})$$

$$\sigma^{\mu\nu} \equiv \frac{1}{2}i(\gamma^\mu\gamma^\nu - \gamma^\nu\gamma^\mu) \quad (\text{A.19d})$$

These matrices are related by the commutation and anticommutation relations:

$$\gamma^\mu, \gamma^\nu = 2g^{\mu\nu} \quad (\text{A.20a})$$

$$\gamma^\mu, \gamma^5 = 0 \quad (\text{A.20b})$$

A useful notation to avoid clutter is the Dirac “slashed” notation:

$$\not{p} \equiv p_\mu\gamma^\mu \quad (\text{A.21})$$

These matrices are useful for defining how a Dirac spinor transforms under the fields.

Table A.1. Definitions for spinor transformations using Dirac matrices

term	notation	components
scalar	$\bar{\psi}\psi$	1
pseudoscalar	$\bar{\psi}\gamma^5\psi$	1
vector	$\bar{\psi}\gamma^\mu\psi$	4
pseudovector	$\bar{\psi}\gamma^\mu\gamma^5\psi$	4
tensor	$\bar{\psi}\sigma^{\mu\nu}\psi$	6

Scalars are magnitudes and remain invariant under both rotation and parity. Vectors have a direction, so rotations and parity can alter this direction. Tensors can have multiple directions and thus are not so tidy to describe in terms of parity. The cross product between two vectors is a pseudovector. For example, consider angular momentum:

$$\vec{L} = \vec{r} \times \vec{p} \tag{A.22}$$

The two vectors change sign under parity transformation, but the angular momentum does not – which makes it a pseudovector. A similar contradiction occurs in the volume formula:

$$V = \vec{a} \cdot (\vec{b} \times \vec{c}) \tag{A.23}$$

The volume is a scalar, but under parity transformations of the vectors, it changes sign – which makes it a pseudoscalar. Scalars should never be placed on equal footing with pseudoscalars, nor should vectors be placed on equal footing with pseudovectors. The Lorentz force correctly sums a vector ( $E$ ) with a pseudovector ( $B$ ) by crossing the pseudovector with another vector ( $v$ ):

$$\vec{F} = q(\vec{E} + v \times \vec{B}) \tag{A.24}$$

### A.7 CKM Matrix

Because quarks exhibit parity violation in quarks but not leptons, a basis is defined such that the quarks can mix such that EW interactions can be written in terms of doublets. This mixing is represented as:

$$\begin{pmatrix} d' \\ s' \\ b' \end{pmatrix} = \begin{pmatrix} V_{ud} & V_{us} & V_{ub} \\ V_{cd} & V_{cs} & V_{cb} \\ V_{td} & V_{ts} & V_{tb} \end{pmatrix} \tag{A.25}$$

The form of the CKM matrix is:

$$V_{CKM} = \begin{pmatrix} c_{12}c_{13} & s_{12}c_{13} & s_{13}\exp(-i\delta) \\ -s_{12}c_{23} - c_{12}s_{23}s_{13}\exp(i\delta) & c_{12}c_{23} - s_{12}s_{23}s_{13}\exp(i\delta) & s_{23}c_{13} \\ s_{12}s_{23} - c_{12}c_{23}s_{13}\exp(i\delta) & -s_{23}c_{12} - s_{12}c_{23}s_{13}\exp(i\delta) & c_{23}c_{13} \end{pmatrix} \quad (\text{A.26})$$

Unitarity of the CKM matrix requires:

$$\sum_i V_{ij}V_{ik}^* = \delta_{jk} \quad (\text{A.27a})$$

$$\sum_j V_{ij}V_{kj}^* = \delta_{ik} \quad (\text{A.27b})$$

Six triangles in the complex plane can be formed from the combinations that vanish. The largest triangle (Figure A.1)) is used for the  $CP$ -violating interaction in  $B\bar{B}$  events, and is obtained from the following relationship:

$$V_{ud}^*V_{ub} + V_{cd}^*V_{cb} + V_{td}^*V_{tb} = 0 \quad (\text{A.28})$$

In order to scale the triangle so that one of its sides ranges from (0, 0 to (1, 0), each side is divided by  $V_{cd}V_{cb}^*$ . The angles of the triangle are then:

$$\begin{aligned} \alpha &= \arg\left(-\frac{V_{td}V_{td}^*}{V_{ud}V_{ub}^*}\right) \\ \beta &= \arg\left(-\frac{V_{cd}V_{cb}^*}{V_{td}V_{tb}^*}\right) \\ \gamma &= \arg\left(-\frac{V_{ud}V_{ub}^*}{V_{cd}V_{cb}^*}\right) \end{aligned} \quad (\text{A.29})$$

If one side of the CKM triangle is fixed along one axis, the measurement can be parameterized by the coordinate of the third point. This is called Wolfenstein parameterization:

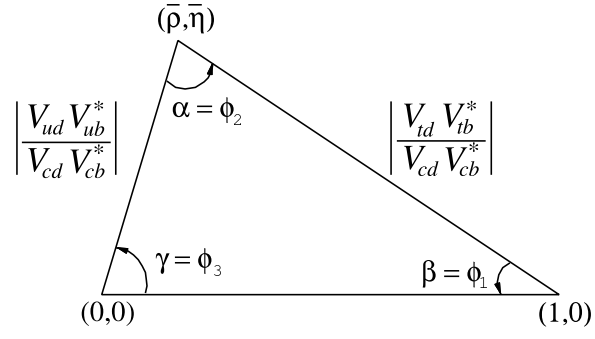


Figure A.1. A CKM triangle commonly used to study  $CP$  violation in  $B\bar{B}$  events.

$$\bar{\rho} + i\bar{\eta} = -\frac{V_{ud}V_{ub}^*}{V_{cd}V_{cb}^*} \quad (\text{A.30})$$



## APPENDIX B

### Feynman Rules for the Standard Model

## B.1 External Lines

Table B.1. Feynman rules for external lines


spin	particle in	antiparticle in	particle out	antiparticle out
0	–	–	–	–
1/2	$u$	$\bar{v}$	$\bar{u}$	$v$
1	$\epsilon_\mu$	$\epsilon_\mu$	$\epsilon_\mu^*$	$\epsilon_\mu^*$

## B.2 Propagators




$$= \frac{i(\not{p} + m_f)}{p^2 - m_f^2 + i\epsilon} \quad (\text{B.1})$$

Figure B.1. The Feynman rule for the fermion propagator.



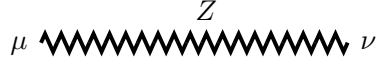
$$= -i \left[ \frac{g_{\mu\nu}}{p^2 + i\epsilon} - (1 - g_e) \frac{p_\mu p_\nu}{(p^2)^2} \right] \quad (\text{B.2})$$

Figure B.2. The Feynman rule for the photon propagator.



$$= -i \frac{1}{p^2 - m_W^2 + i\epsilon} \left[ g_{\mu\nu} - (1 - g_W) \frac{p_\mu p_\nu}{p^2 - g_W m_W^2} \right] \quad (\text{B.3})$$

Figure B.3. The Feynman rule for the weak (charged) propagator.



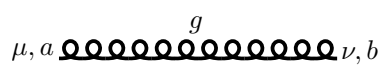
$$= -i \frac{1}{p^2 - m_Z^2 + i\epsilon} \left[ g_{\mu\nu} - (1 - g_Z) \frac{p_\mu p_\nu}{p^2 - g_Z m_Z^2} \right] \quad (\text{B.4})$$

Figure B.4. The Feynman rule for the weak (neutral) propagator.



$$= \frac{i}{p^2 - m_H^2 + i\epsilon} \quad (\text{B.5})$$

Figure B.5. The Feynman rule for the Higgs propagator.



$$= -i\delta_{ab} \left[ \frac{g_{\mu\nu}}{p^2 + i\epsilon} - (1 - \xi_G) \frac{p_\mu p_\nu}{(p^2)^2} \right] \quad (\text{B.6})$$

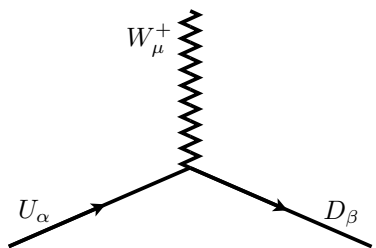
Figure B.6. The Feynman rule for the gluon propagator.

### B.3 Vertex Factors



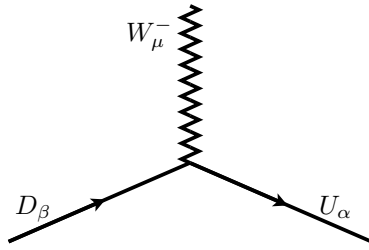
$$= -ig_e\gamma^\mu \quad (\text{B.7})$$

Figure B.7. The Feynman rule for the  $ff\gamma^0$  vertex.



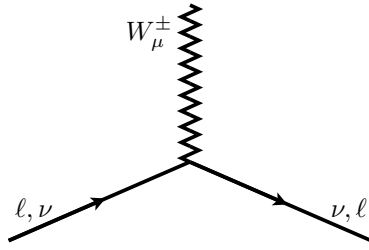
$$= -i\frac{g_W}{2\sqrt{2}}\gamma^\mu(1 - \gamma^5)V_{ij} \quad (\text{B.8})$$

Figure B.8. The Feynman rule for the  $qqW^+$  vertex.



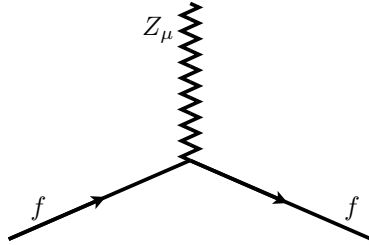
$$= -i \frac{g_W}{2\sqrt{2}} \gamma^\mu (1 - \gamma^5) V_{ij}^* \quad (\text{B.9})$$

Figure B.9. The Feynman rule for the  $qqW^-$  vertex.



$$= -i \frac{g_W}{2\sqrt{2}} \gamma^\mu (1 - \gamma^5) \quad (\text{B.10})$$

Figure B.10. The Feynman rule for the  $\ell\nu W^\pm$  vertex.



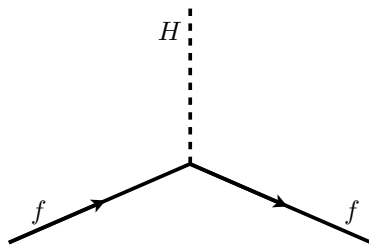
$$= -i \frac{g_Z}{2} \gamma^\mu (c_V^f - c_A^f \gamma^5) \quad (\text{B.11a})$$

$$(\text{B.11b})$$

Figure B.11. The Feynman rule for the  $ffZ^0$  vertex.

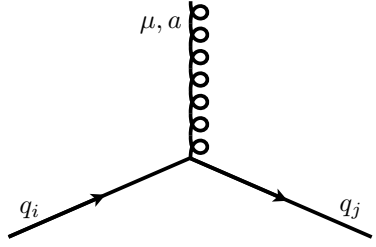
Table B.2.  $c_V$  and  $c_A$  factors for the Feynman rule for the  $ffZ^0$  vertex

$f$	$c_V$	$c_A$
$\nu_e, \nu_\mu, \nu_\tau$	$\frac{1}{2}$	$\frac{1}{2}$
$e, \mu, \tau$	$-\frac{1}{2} + 2 \sin^2 \theta_W$	$-\frac{1}{2}$
$u, c, t$	$\frac{1}{2} - \frac{4}{3} \sin^2 \theta_W$	$\frac{1}{2}$
$d, s, b$	$-\frac{1}{2} + \frac{2}{3} \sin^2 \theta_W$	$-\frac{1}{2}$



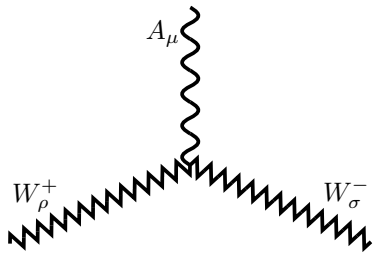
$$= -i \frac{g}{2} \frac{m_f}{m_W} \quad (\text{B.12})$$

Figure B.12. The Feynman rule for the  $ffH$  vertex.



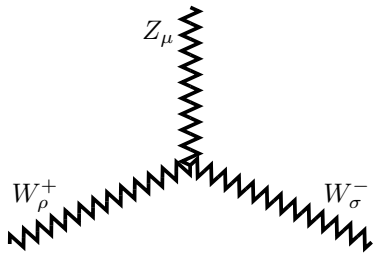
$$= i \frac{g_s}{2} \lambda^a \gamma^\mu \quad (\text{B.13})$$

Figure B.13. The Feynman rule for the  $qqg$  vertex.



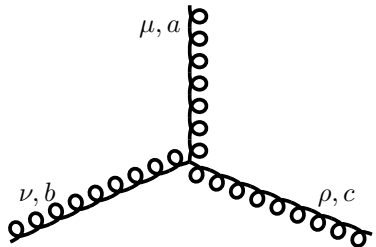
$$= -ig_e [g_{\sigma\rho}(p_- - p_+)_\mu + g_{\rho\mu}(p_+ - k)_\sigma + g_{\mu\sigma}(k - p_-)_\rho] \quad (\text{B.14})$$

Figure B.14. The Feynman rule for the  $\gamma^0 W^\pm W^\mp$  vertex.



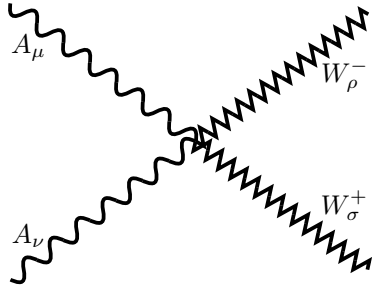
$$= -ig_W \cos \theta_W [g_{\sigma\rho}(p_- - p_+)_\mu + g_{\rho\mu}(p_+ - k)_\sigma + g_{\mu\sigma}(k - p_-)_\rho] \quad (\text{B.15})$$

Figure B.15. The Feynman rule for the  $W^\pm W^\mp Z^0$  vertex.



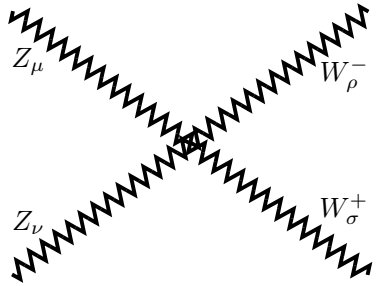
$$= -g_s f^{abc} [g^{\mu\nu}(p_1 - p_2)_\rho - g^{\nu\rho}(p_2 - p_3)_\mu - g^{\rho\mu}(p_3 - p_1)_\nu] \quad (\text{B.16})$$

Figure B.16. The Feynman rule for the  $ggg$  vertex.



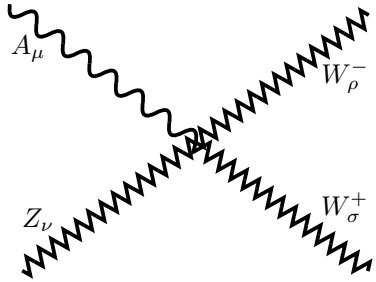
$$= -ig_e^2 (2g_{\sigma\rho}g_{\mu\nu} - g_{\sigma\mu}g_{\rho\nu} - g_{\sigma\nu}g_{\rho\mu}) \quad (\text{B.17})$$

Figure B.17. The Feynman rule for the  $\gamma^0\gamma^0W^\pm W^\mp$  vertex.



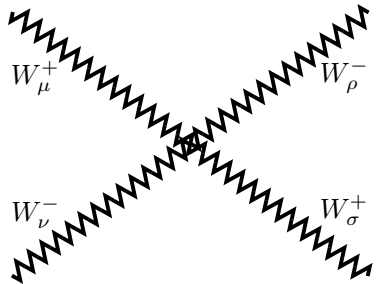
$$= ig_W^2 \cos^2 \theta_W (2g_{\sigma\rho}g_{\mu\nu} - g_{\sigma\mu}g_{\rho\nu} - g_{\sigma\nu}g_{\rho\mu}) \quad (\text{B.18})$$

Figure B.18. The Feynman rule for the  $W^\pm W^\mp Z^0 Z^0$  vertex.



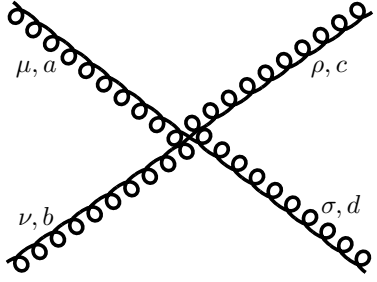
$$= -ig_e g_W \cos \theta_W (2g_{\sigma\rho}g_{\mu\nu} - g_{\sigma\mu}g_{\rho\nu} - g_{\sigma\nu}g_{\rho\mu}) \quad (\text{B.19})$$

Figure B.19. The Feynman rule for the  $\gamma^0 W^\pm W^\mp Z^0$  vertex.



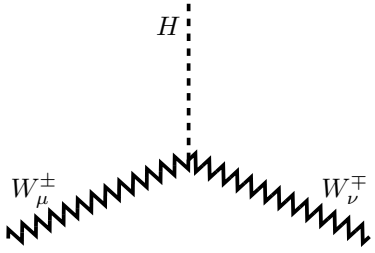
$$= ig_W^2 (2g_{\sigma\mu}g_{\rho\nu} - g_{\sigma\rho}g_{\mu\nu} - g_{\sigma\nu}g_{\rho\mu}) \quad (\text{B.20})$$

Figure B.20. The Feynman rule for the  $W^\pm W^\mp W^\pm W^\mp$  vertex.



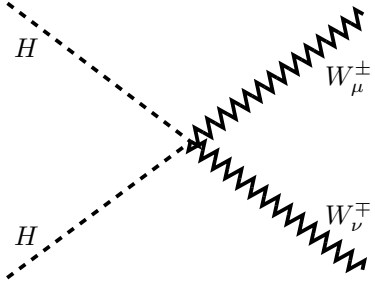
$$\begin{aligned}
 &= -i f^{ead} f^{ebc} (g_{\mu\nu} g_{\rho\sigma} - g_{\mu\rho} g_{\nu\sigma}) \\
 &\quad - i f^{eac} f^{edb} (g_{\mu\sigma} g_{\rho\nu} - g_{\mu\nu} g_{\rho\sigma}) \\
 &\quad - i f^{eab} f^{ecd} (g_{\mu\rho} g_{\nu\sigma} - g_{\mu\sigma} g_{\nu\rho})
 \end{aligned} \tag{B.21}$$

Figure B.21. The Feynman rule for the  $gggg$  vertex.



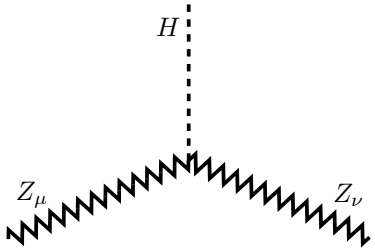
$$= i g m_W g_{\mu\nu} \tag{B.22}$$

Figure B.22. The Feynman rule for the  $HW^+W^-$  vertex.



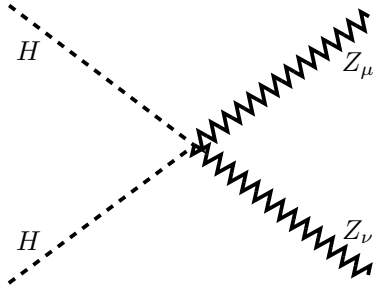
$$= \frac{i}{2} g^2 g_{\mu\nu} \tag{B.23}$$

Figure B.23. The Feynman rule for the  $HHW^+W^-$  vertex.



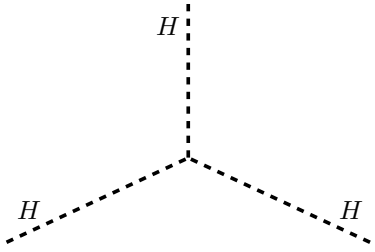
$$= i \frac{g}{\cos \theta_W} m_Z g_{\mu\nu} \tag{B.24}$$

Figure B.24. The Feynman rule for the  $HZ^0Z^0$  vertex.



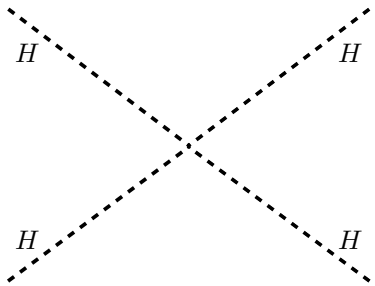
$$= \frac{i}{2} \frac{g^2}{\cos^2 \theta_W} g^{\mu\nu} \quad (\text{B.25})$$

Figure B.25. The Feynman rule for the  $HHZ^0 Z^0$  vertex.



$$= -\frac{3}{2} ig \frac{m_h^2}{m_W} \quad (\text{B.26})$$

Figure B.26. The Feynman rule for the  $HHH$  vertex.



$$= -\frac{3}{4} ig^2 \frac{m_h^2}{m_W^2} \quad (\text{B.27})$$

Figure B.27. The Feynman rule for the  $HHHH$  vertex.

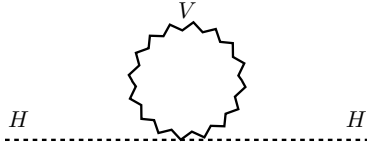


## APPENDIX C

### Radiative Corrections in SUSY

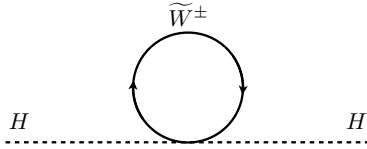
The cancellation of the quadratic divergence of the Higgs self-energy was explicitly demonstrated for the fermion loop in equations 3.7 through 3.12. This appendix applies the SUSY interactions to other radiative corrections of the Higgs boson. The diagrams are grouped according to similar terms or divergence.

### C.1 Correction Group 1



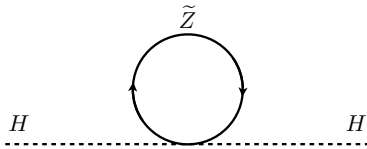
$$\pi(0) = 3g^2 \int \frac{d^4k}{(2\pi)^4} \frac{1}{k^2 - m_W^2} \quad (\text{C.1})$$

Figure C.1. A Feynman diagram for Higgs self-energy with a one-loop quartic  $W^\pm$  or  $Z^0$  correction.



$$\pi(0) = -2g^2 \int \frac{d^4k}{(2\pi)^4} \left[ \frac{1}{k^2 - 2m_W^2} + \frac{4m_W^2}{(k^2 - 2m_W^2)^2} \right] \quad (\text{C.2})$$

Figure C.2. A Feynman diagram for Higgs self-energy with a one-loop quartic  $\widetilde{W}$  correction.



$$\pi(0) = -g^2 \int \frac{d^4k}{(2\pi)^4} \left[ \frac{1}{k^2 - m_W^2} + \frac{2m_W^2}{(k^2 - m_W^2)^2} \right] \quad (\text{C.3})$$

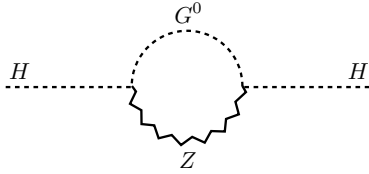
Figure C.3. A Feynman diagram for Higgs self-energy with a one-loop quartic  $\widetilde{Z}$  correction.

Figure C.1 cancels with the sum of Figures C.2 and C.3

## C.2 Correction Group 2

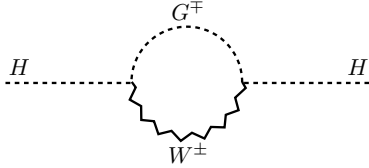
The Higgs coupling needs to be specified since the Higgs doublets could interact with Goldstone bosons.

$$\begin{aligned}
 V_D &= \frac{1}{8}g^2 \left[ (H_i^* \sigma_1^{ij} H_j)^2 + (H_i^* \sigma_2^{ij})^2 + (H_i^* \sigma_3^{ij} H_j)^2 \right] \\
 &= \frac{1}{8}g^2 \left[ \frac{1}{2}(\phi + v)^2 + \frac{1}{2}(G^0)^2 + |G^-|^2 \right]^2
 \end{aligned} \tag{C.4}$$



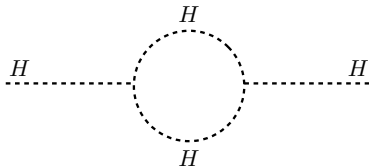
$$\pi(0) = -\frac{g^2}{4} \int \frac{d^4k}{(2\pi)^4} \frac{k^2}{(k^2 - m_W^2)^2} \tag{C.5}$$

Figure C.4. A Feynman diagram for Higgs self-energy with a one-loop  $Z^0$  and a Goldstone  $G^0$  correction.



$$\pi(0) = -\frac{g^2}{2} \int \frac{d^4k}{(2\pi)^4} \frac{k^2}{(k^2 - m_W^2)^2} \tag{C.6}$$

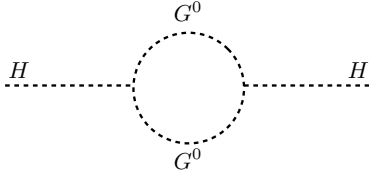
Figure C.5. A Feynman diagram for Higgs self-energy with a one-loop  $W^\pm$  and a Goldstone  $G^\mp$  correction.



$$\pi(0) = \frac{3}{8}g^2 \int \frac{d^4k}{(2\pi)^4} \frac{1}{k^2 - m_H^2} \tag{C.7}$$

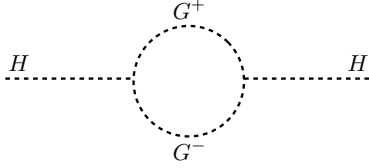
Figure C.6. A Feynman diagram for Higgs self-energy with a one-loop Higgs correction.

The sum of Figures C.4 and C.5 cancels with the sum of Figures C.6, C.7, and C.8.



$$\pi(0) = \frac{1}{8}g^2 \int \frac{d^4k}{(2\pi)^4} \frac{1}{k^2 - m_W^2} \quad (\text{C.8})$$

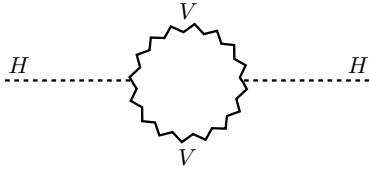
Figure C.7. A Feynman diagram for Higgs self-energy with a one-loop Goldstone  $G^0$  correction.



$$\pi(0) = \frac{1}{4}g^2 \int \frac{d^4k}{(2\pi)^4} \frac{1}{k^2 - m_W^2} \quad (\text{C.9})$$

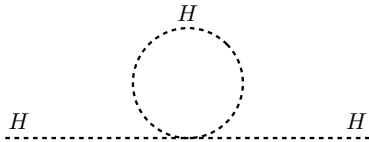
Figure C.8. A Feynman diagram for Higgs self-energy with a one-loop Goldstone  $G^\pm$  correction.

### C.3 Correction Group 3



$$\pi(0) = 6g^2 m_W \int \frac{d^4k}{(2\pi)^4} \frac{1}{(k^2 - m_W^2)^2} \quad (\text{C.10})$$

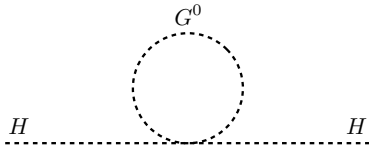
Figure C.9. A Feynman diagram for Higgs self-energy with a one-loop  $W^\pm$  or  $Z^0$  correction.



$$\pi(0) = \frac{9}{8}g^2 M_W^2 \int \frac{d^4k}{(2\pi)^4} \frac{1}{(k^2 - m_h^2)^2} \quad (\text{C.11})$$

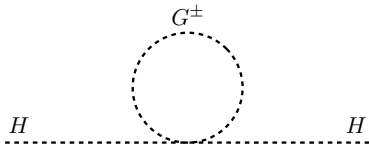
Figure C.10. A Feynman diagram for Higgs self-energy with a one-loop quartic Higgs correction.

Figures C.9, C.10, C.11, and C.12 are only logarithmically divergent.



$$\pi(0) = \frac{1}{8} g^2 M_W^2 \int \frac{d^4 k}{(2\pi)^4} \frac{1}{(k^2 - m_W^2)^2} \quad (\text{C.12})$$

Figure C.11. A Feynman diagram for Higgs self-energy with a one-loop quartic Goldstone  $G^0$  correction.



$$\pi(0) = \frac{1}{4} g^2 M_W^2 \int \frac{d^4 k}{(2\pi)^4} \frac{1}{(k^2 - m_W^2)^2} \quad (\text{C.13})$$

Figure C.12. A Feynman diagram for Higgs self-energy with a one-loop quartic Goldstone  $G^\pm$  correction.

APPENDIX D

Variable Correlations

## D.1 Razor Correlations

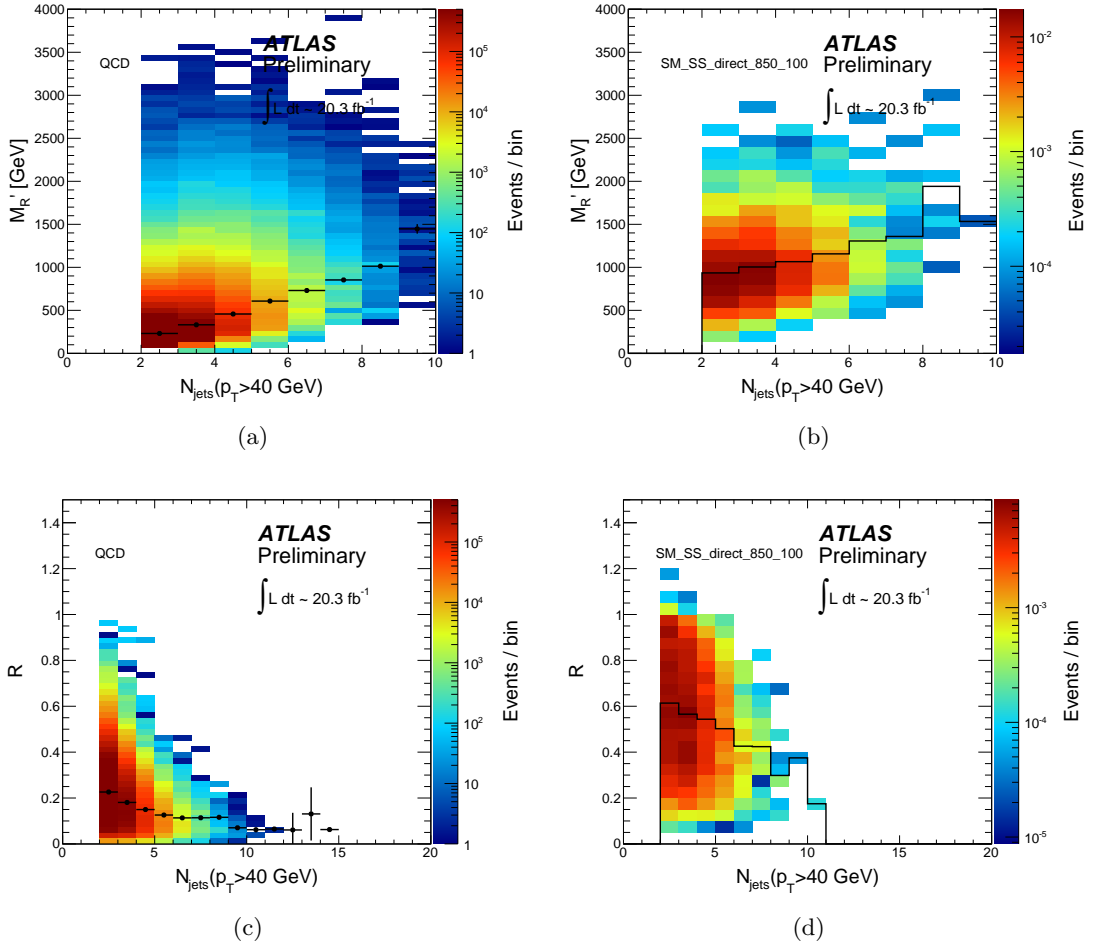


Figure D.1.  $n_{jet}$  correlation to (top)  $M_R$  and (bottom)  $R$  for (left) QCD multijets and (right)  $\tilde{q}(850), \tilde{\chi}(100)$ .

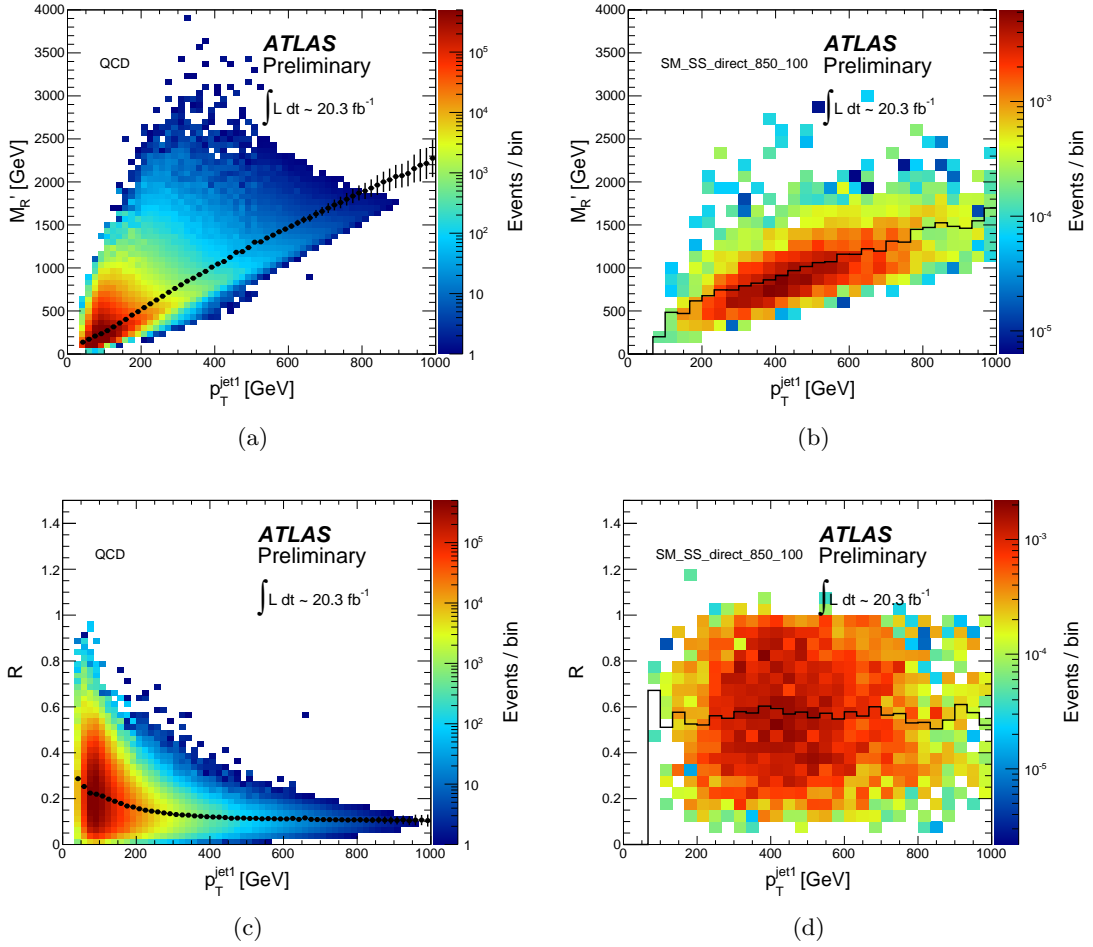


Figure D.2. Leading jet  $p_T$  correlation to (top) MR and (bottom) R for (left) QCD multijets and (right)  $\tilde{q}(850)$ ,  $\tilde{\chi}(100)$ .



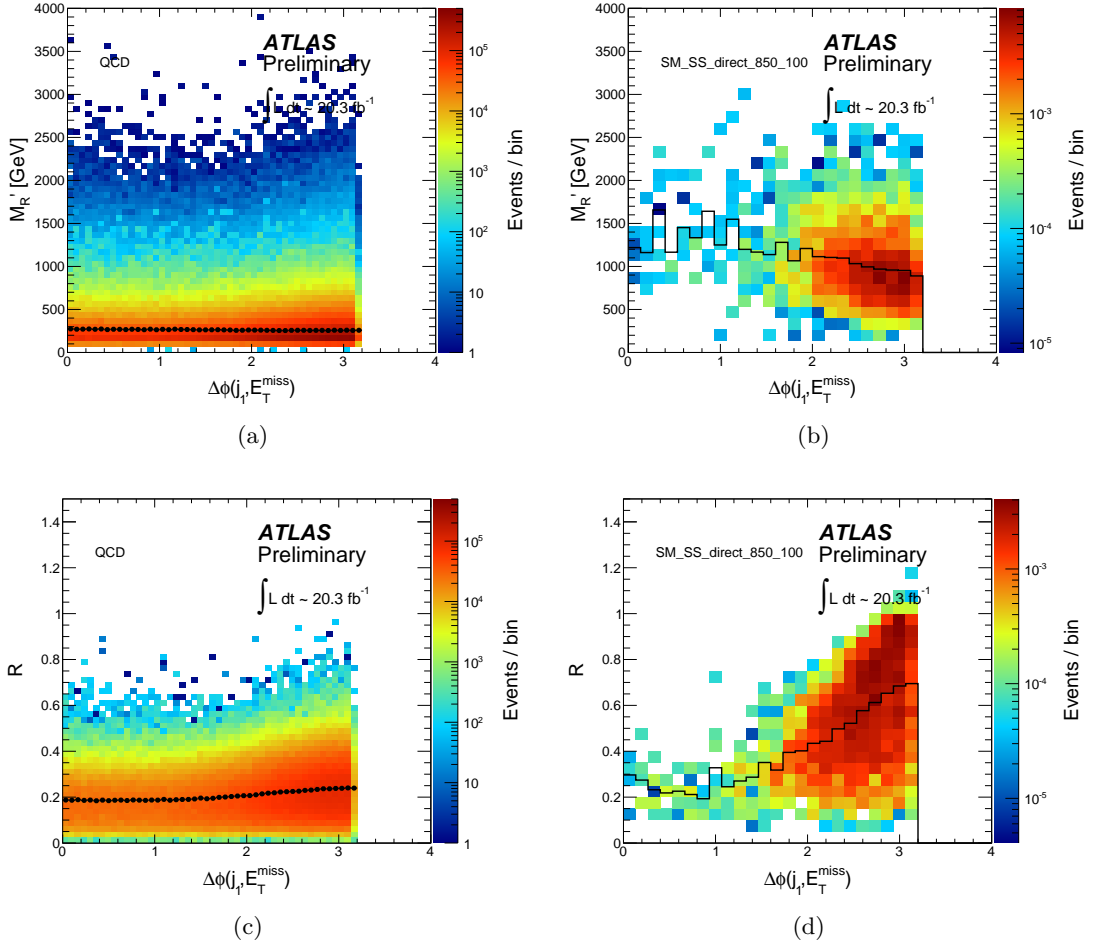


Figure D.3.  $\Delta\phi(j_1, E_T^{\text{miss}})$  correlation to (top) MR and (bottom) R for (left) QCD multijets and (right)  $\tilde{q}(850), \tilde{\chi}(100)$ .

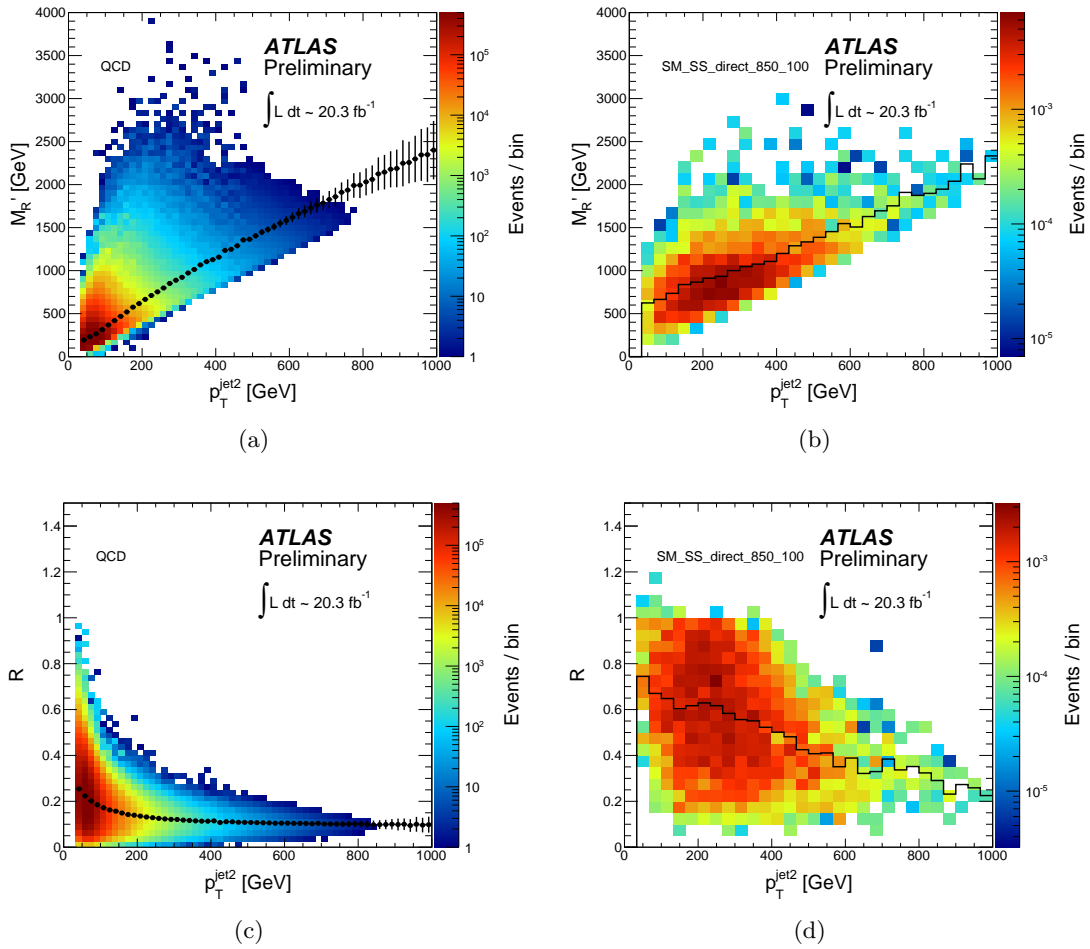


Figure D.4. Sub-leading jet  $p_T$  correlation to Razor variables for background and signal.

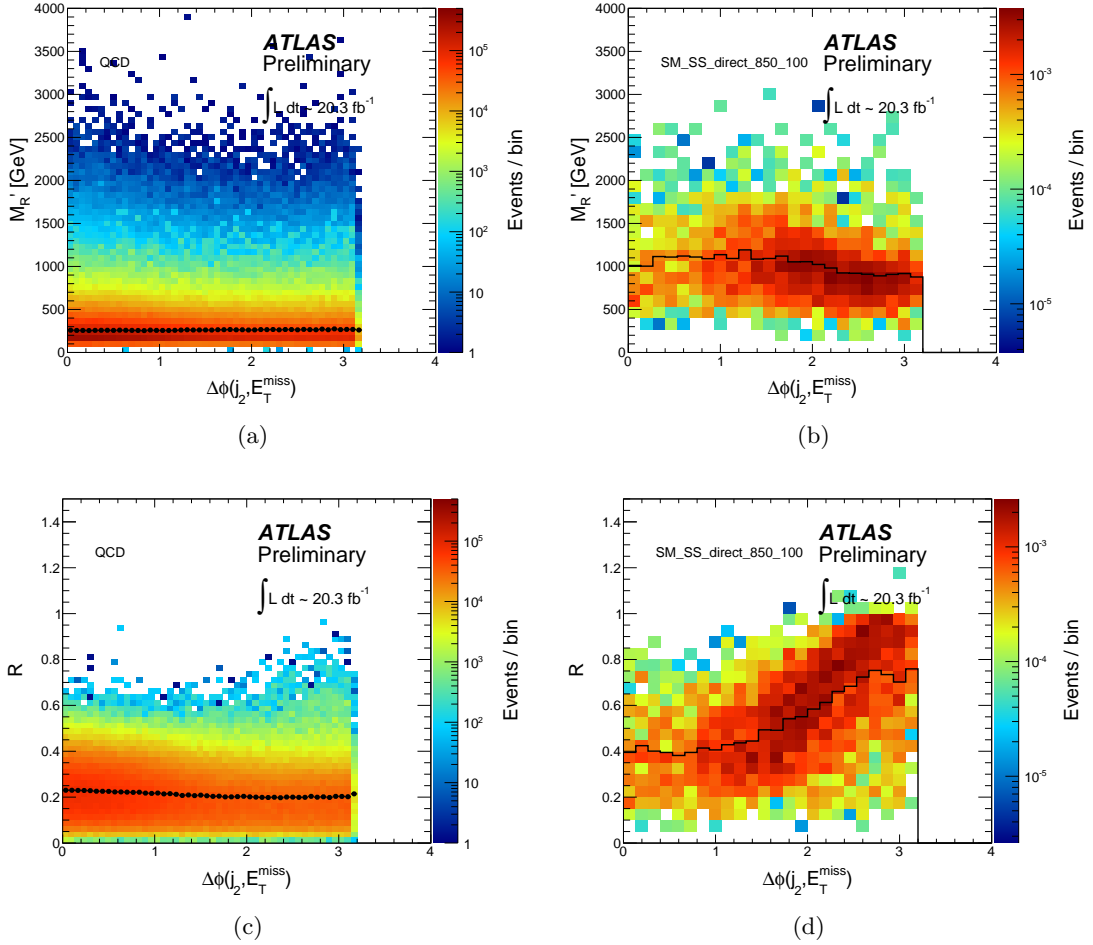


Figure D.5.  $\Delta\phi(j_2, E_T^{\text{miss}})$  correlation to (top) MR and (bottom) R for (left) QCD multijets and (right)  $\tilde{q}(850), \tilde{\chi}(100)$ .

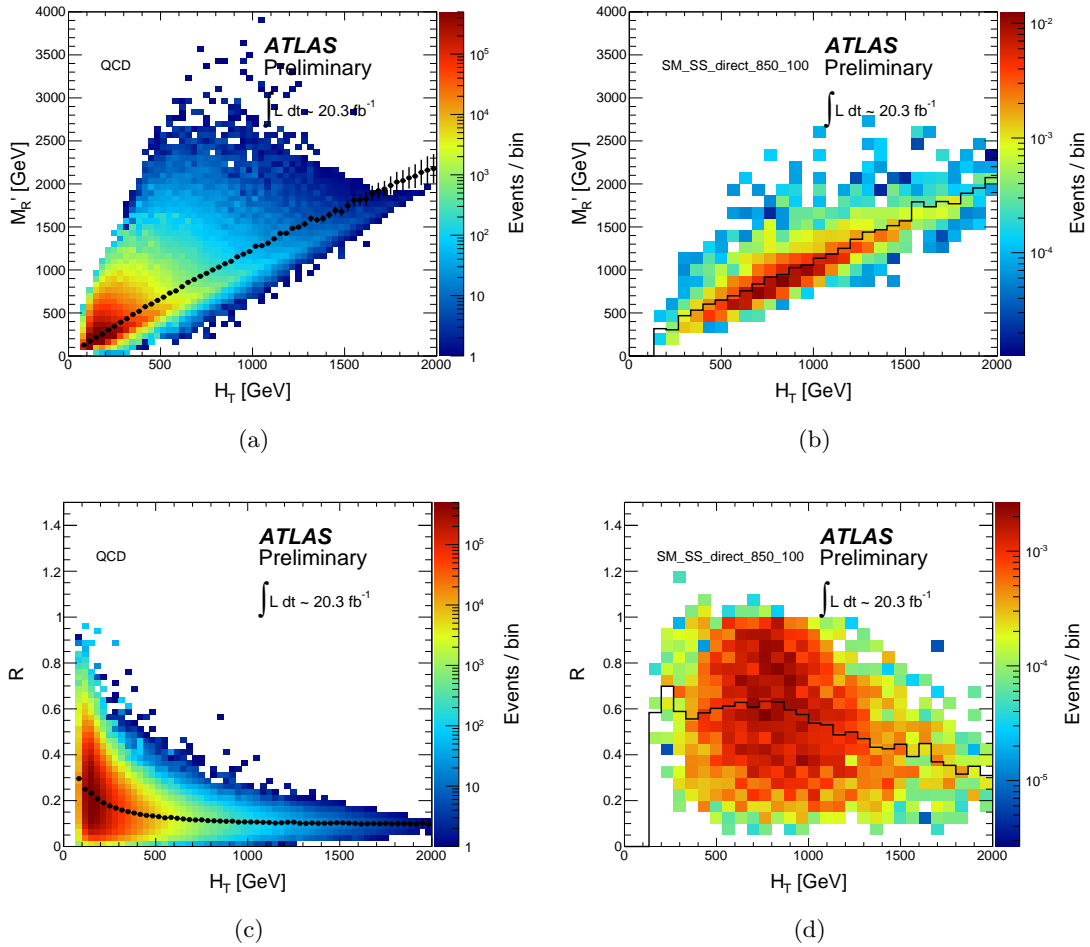


Figure D.6.  $H_T$  correlation to (top) MR and (bottom) R for (left) QCD multijets and (right)  $\tilde{q}(850), \tilde{\chi}(100)$ .

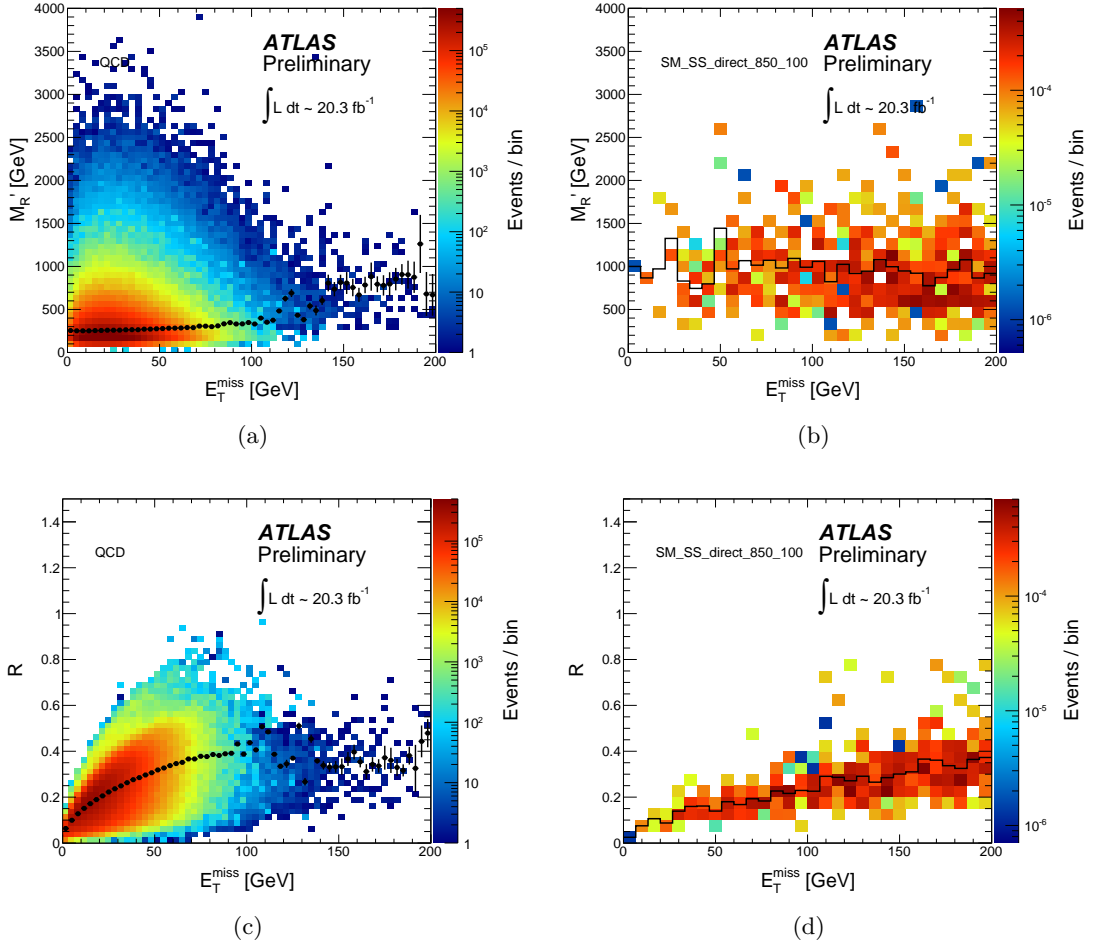


Figure D.7.  $E_T^{\text{miss}}$  correlation to (top) MR and (bottom) R for (left) QCD multijets and (right)  $\tilde{q}(850), \tilde{\chi}(100)$ .

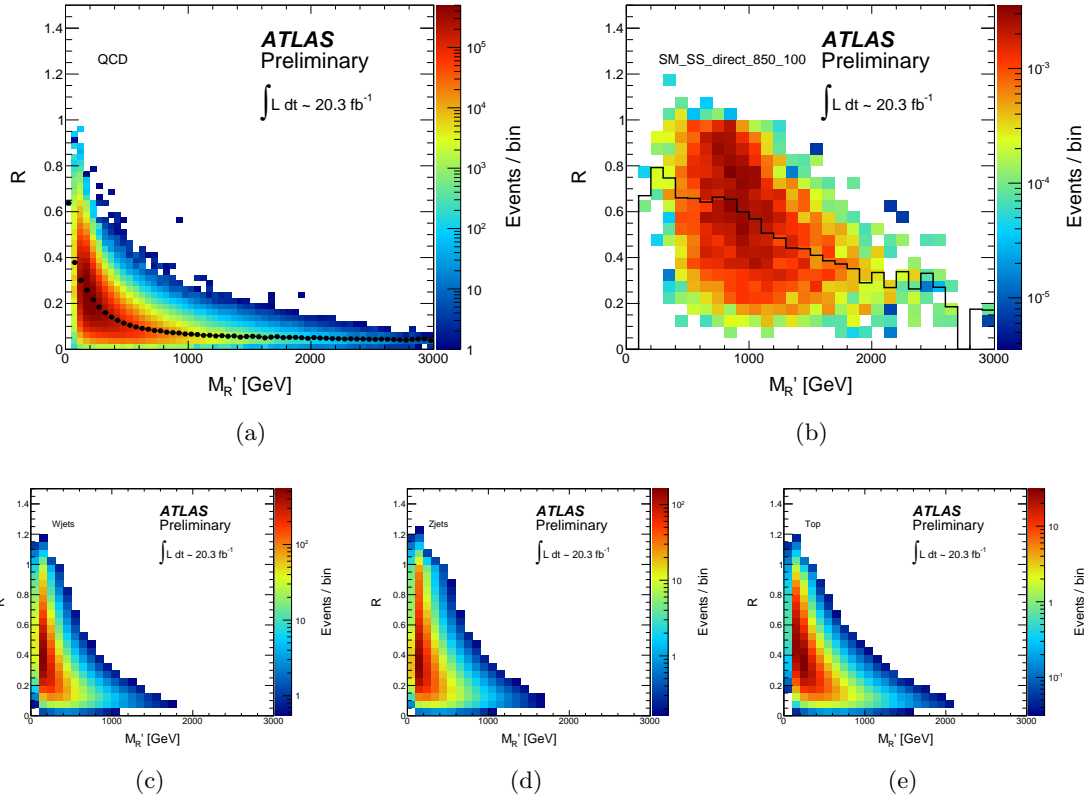


Figure D.8. Razor variable MR and R correlations for (a) QCD multijets (b)  $\tilde{q}(850), \tilde{\chi}(100)$ , (c)  $W + jets$ , (d)  $Z + jets$  and (e) top.

## D.2 Recursive Jigsaw Correlations

In these correlations, cuts are applied to target SUSY with large mass scale. These cuts are:

- $M_{eff} > 800$  GeV
- $E_T^{\text{miss}} > 140$  GeV
- $M_{\Delta}^R > 300$  GeV

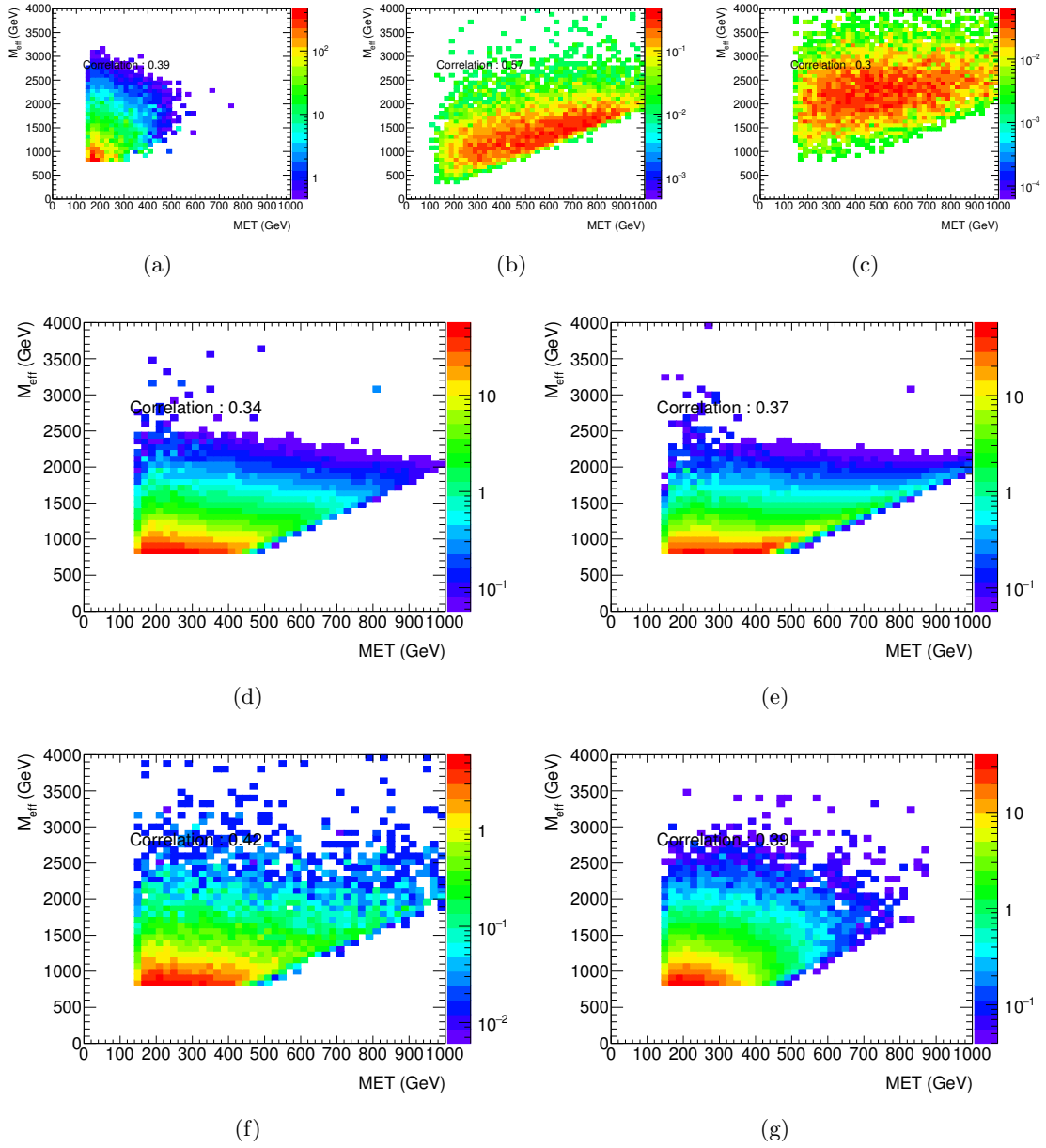


Figure D.9.  $E_T^{miss}$  and  $M_{eff}$  correlation for (a) QCD multijets, (b)  $\tilde{q}(900), \tilde{\chi}(0)$ , and (c)  $\tilde{g}(1400), \tilde{\chi}(0)$ , (d)  $W + jets$ , (e)  $Z + jets$ , (f) Diboson, and (g) Top.



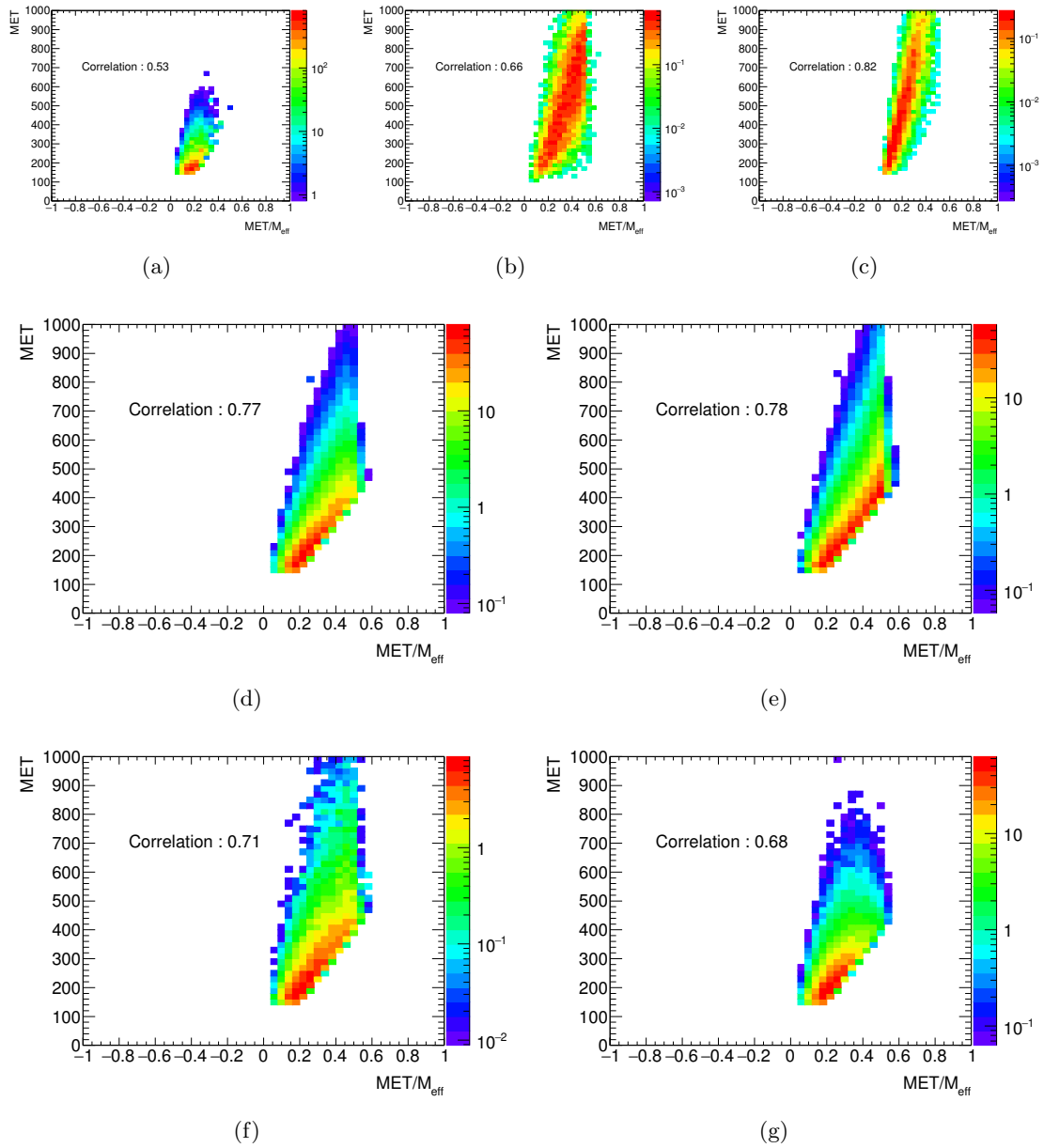


Figure D.10.  $E_T^{miss}/M_{eff}$  and  $E_T^{miss}$  correlation for (a) QCD multijets, (b)  $\tilde{q}(900), \tilde{\chi}(0)$ , and (c)  $\tilde{g}(1400), \tilde{\chi}(0)$ , (d)  $W + jets$ , (e)  $Z + jets$ , (f) Diboson, and (g) Top.

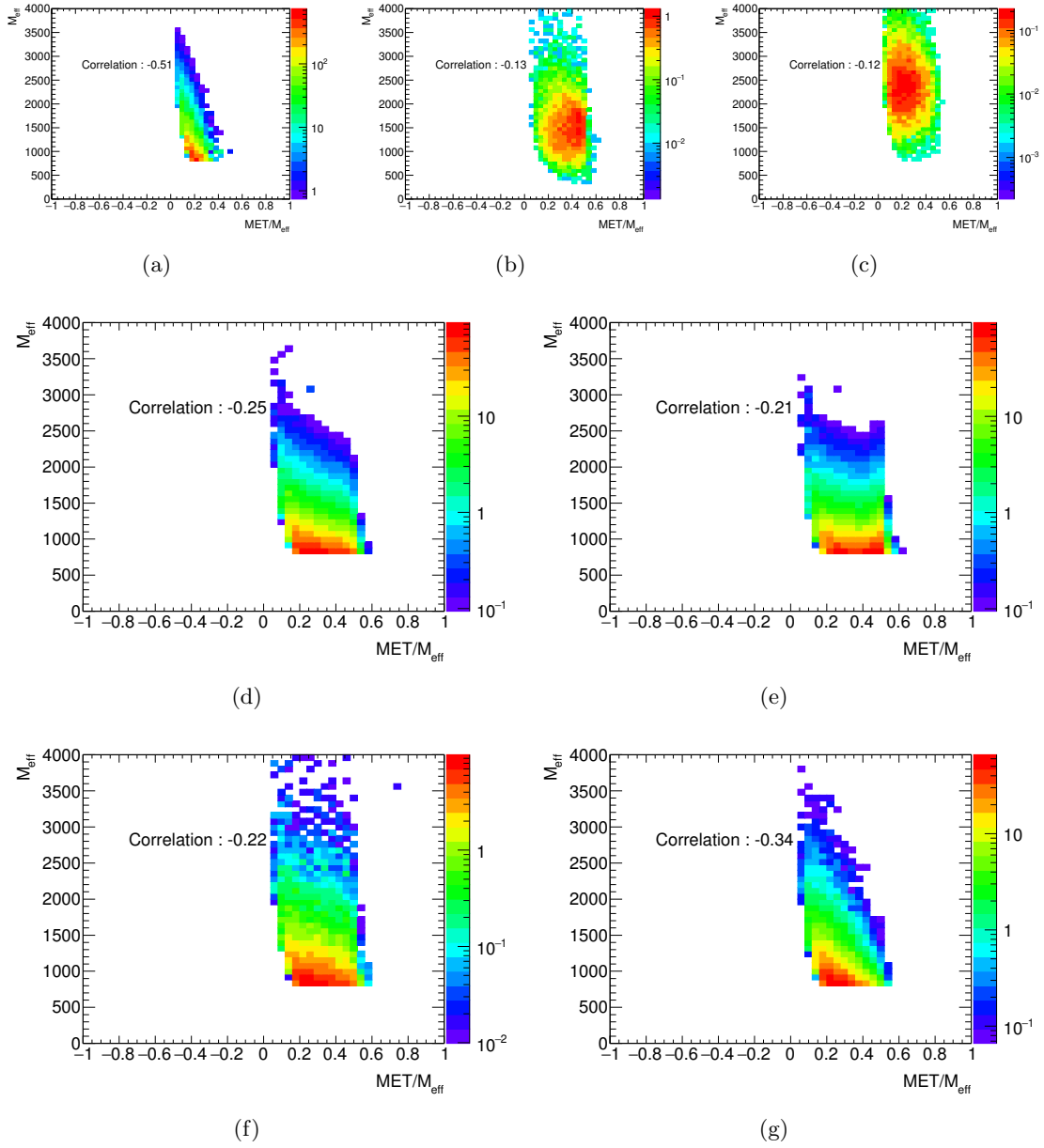


Figure D.11.  $E_T^{\text{miss}}/M_{\text{eff}}$  and  $M_{\text{eff}}$  correlation for (a) QCD multijets, (b)  $\tilde{q}(900), \tilde{\chi}(0)$ , and (c)  $\tilde{g}(1400), \tilde{\chi}(0)$ , (d)  $W + jets$ , (e)  $Z + jets$ , (f) Diboson, and (g) Top.

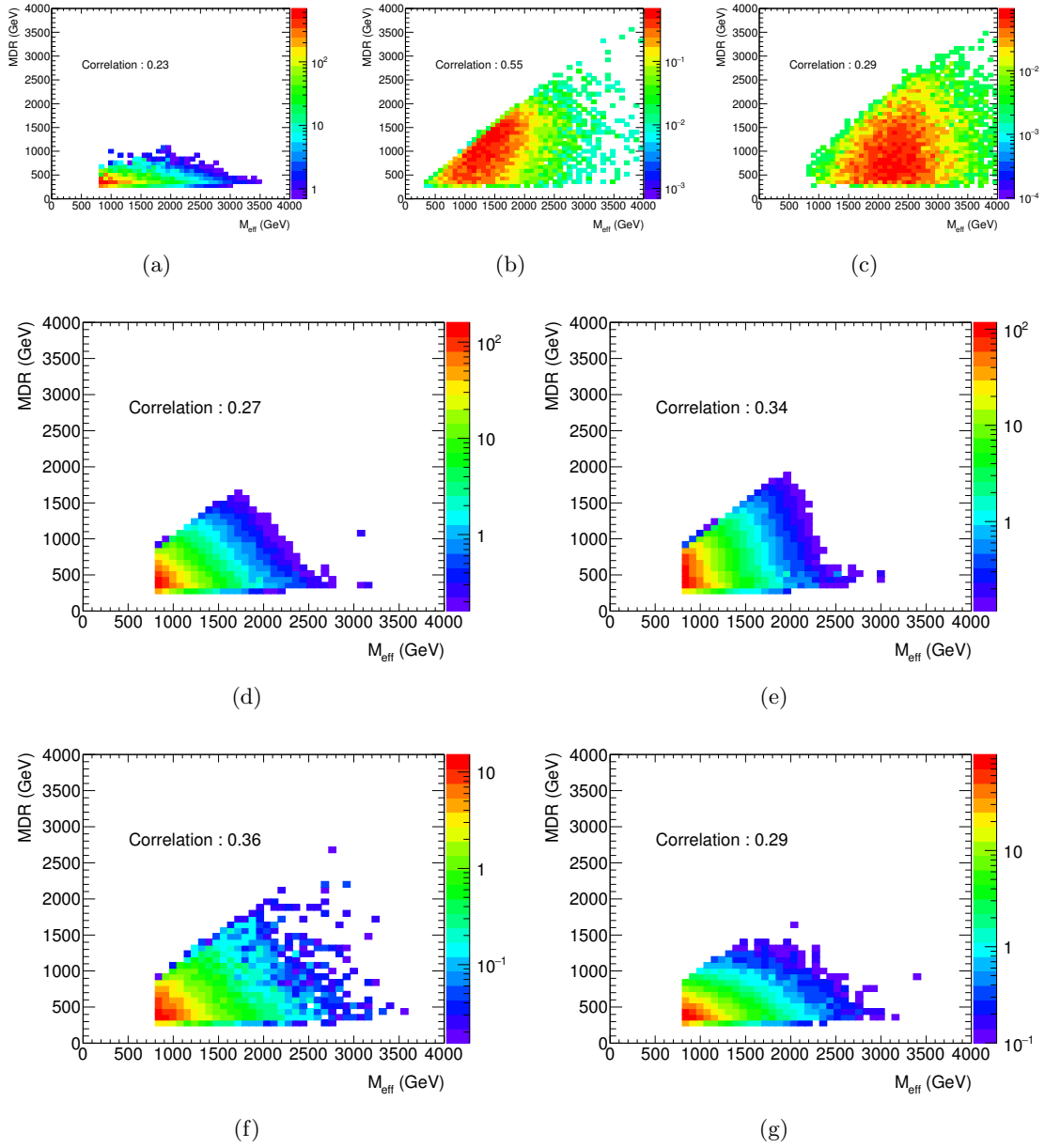


Figure D.12.  $M_{\text{eff}}$  and  $M_{\Delta}^R$  correlation for (a) QCD multijets, (b)  $\tilde{q}(900), \tilde{\chi}(0)$ , and (c)  $\tilde{g}(1400), \tilde{\chi}(0)$ , (d)  $W + jets$ , (e)  $Z + jets$ , (f) Diboson, and (g) Top.

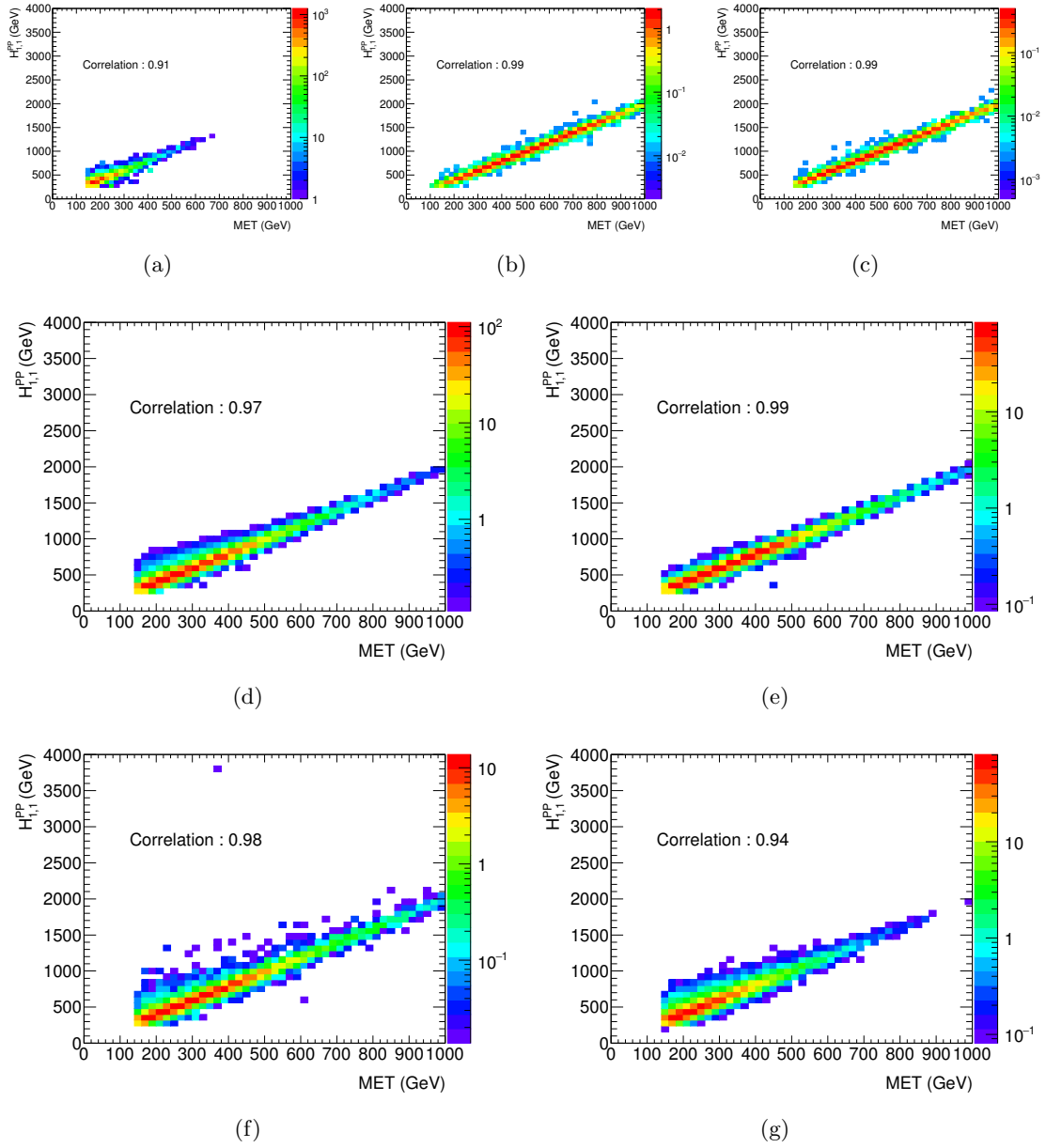


Figure D.13.  $E_T^{miss}$  and  $H_2^{PP}$  correlation for (a) QCD multijets, (b)  $\tilde{q}(900), \tilde{\chi}(0)$ , and (c)  $\tilde{g}(1400), \tilde{\chi}(0)$ , (d)  $W + jets$ , (e)  $Z + jets$ , (f) Diboson, and (g) Top.

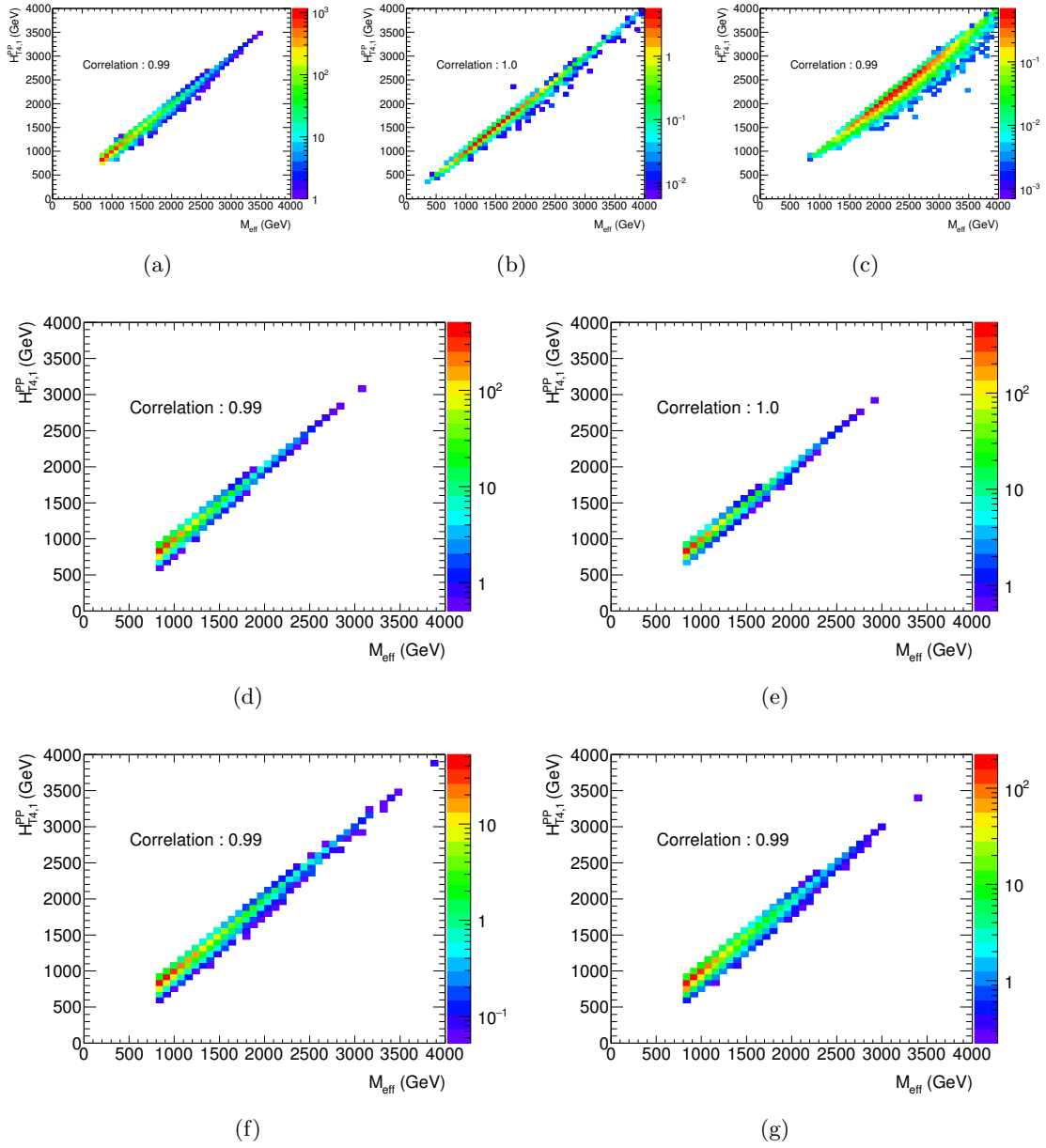


Figure D.14.  $M_{eff}$  and  $H_T^{PP}$  correlation for (a) QCD multijets, (b)  $\tilde{q}(900), \tilde{\chi}(0)$ , and (c)  $\tilde{g}(1400), \tilde{\chi}(0)$ , (d)  $W + jets$ , (e)  $Z + jets$ , (f) Diboson, and (g) Top.

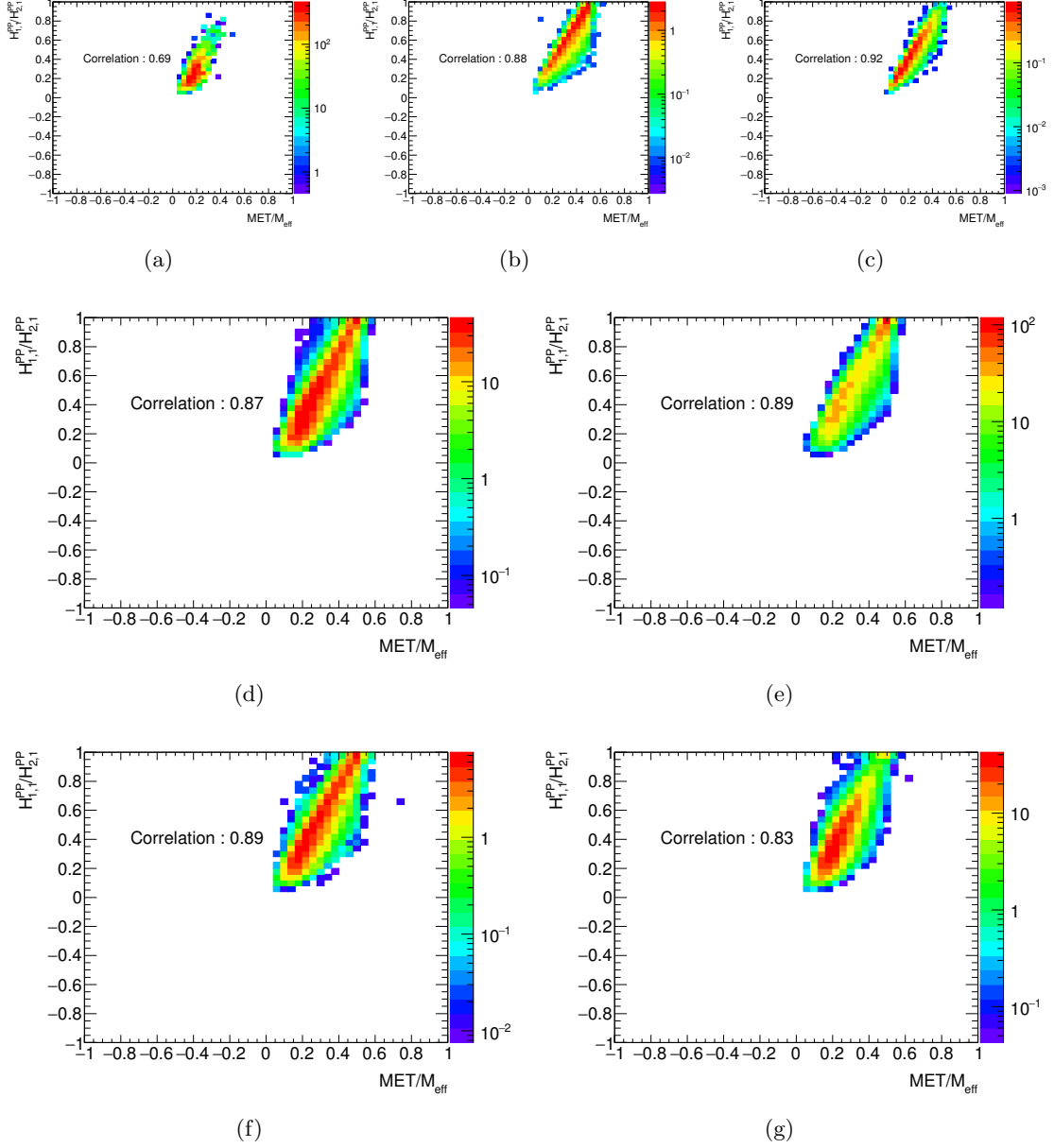


Figure D.15.  $E_T^{miss}/M_{eff}$  and  $H_2^{PP}/H_3^{PP}$  correlation for (a) QCD multijets, (b)  $\tilde{q}(900), \tilde{\chi}(0)$ , and (c)  $\tilde{g}(1400), \tilde{\chi}(0)$ , (d)  $W + jets$ , (e)  $Z + jets$ , (f) Diboson, and (g) Top.

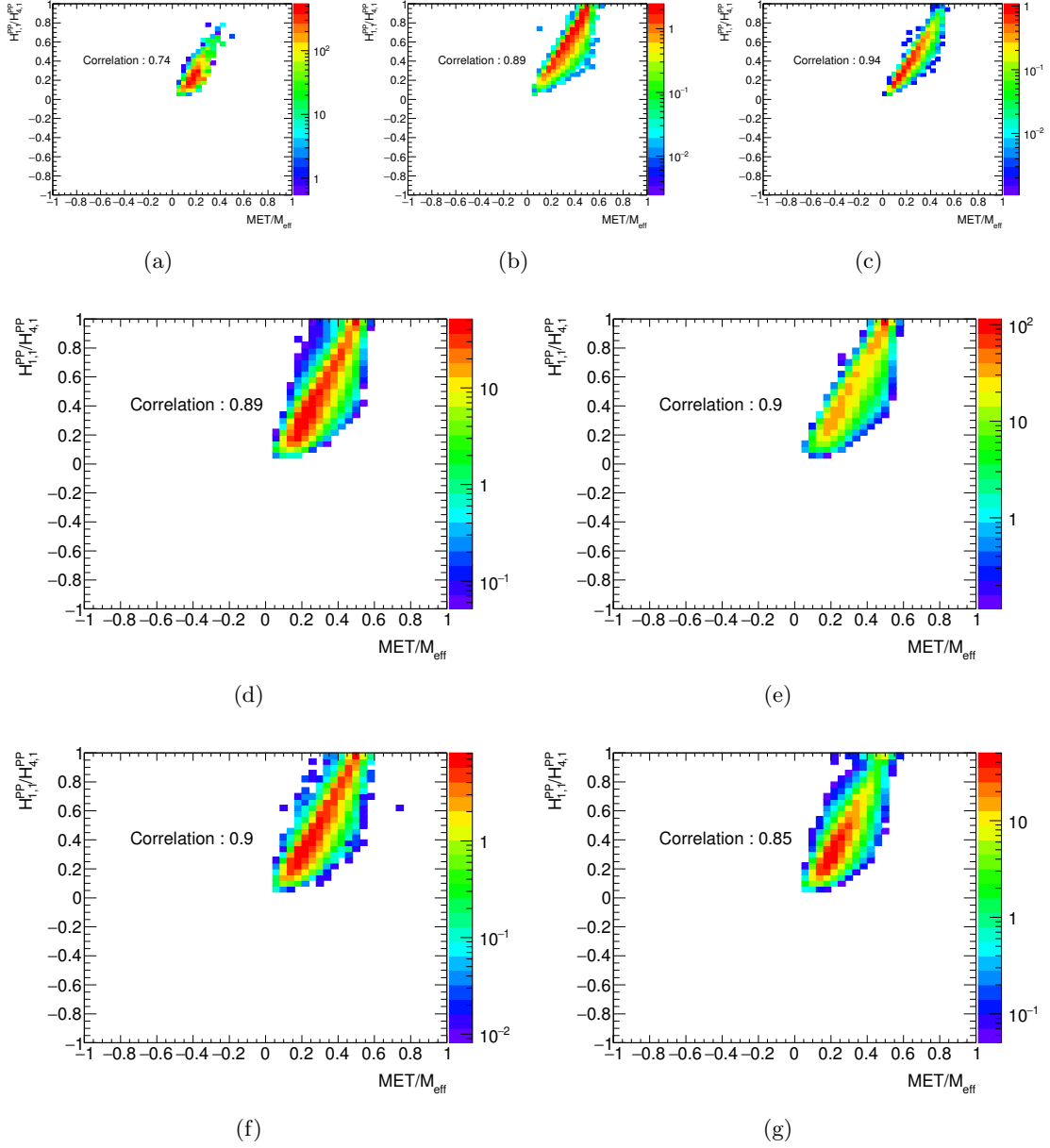


Figure D.16.  $E_T^{miss}/M_{eff}$  and  $H_2^{PP}/H_5^{PP}$  correlation for (a) QCD multijets, (b)  $\tilde{q}(900)$ ,  $\tilde{\chi}(0)$ , and (c)  $\tilde{g}(1400)$ ,  $\tilde{\chi}(0)$ , (d)  $W + jets$ , (e)  $Z + jets$ , (f) Diboson, and (g) Top.

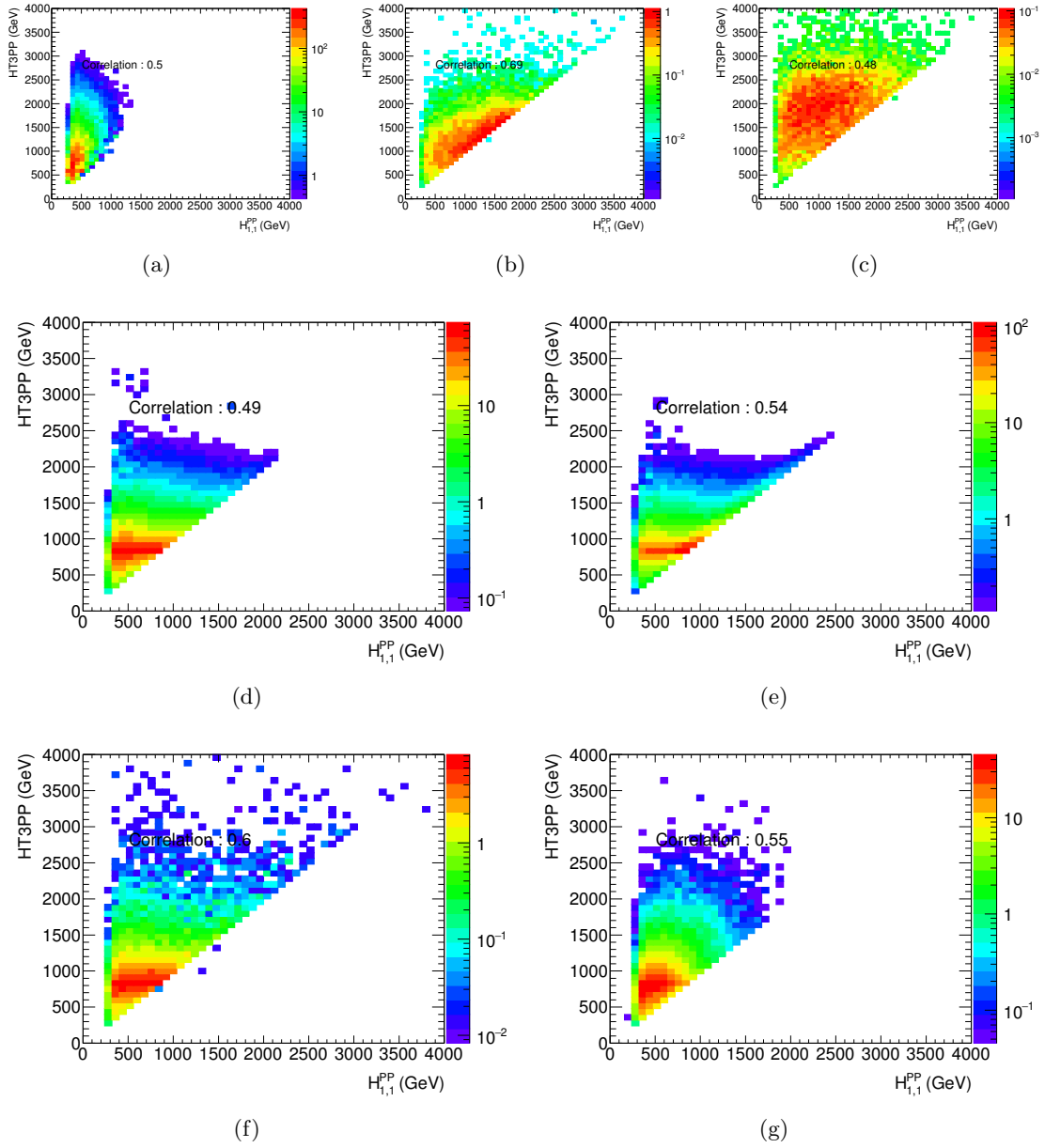


Figure D.17.  $H_2^{PP}$  and  $H_T^3$  correlation for (a) QCD multijets, (b)  $\tilde{q}(900), \tilde{\chi}(0)$ , and (c)  $\tilde{g}(1400), \tilde{\chi}(0)$ , (d)  $W + jets$ , (e)  $Z + jets$ , (f) Diboson, and (g) Top.



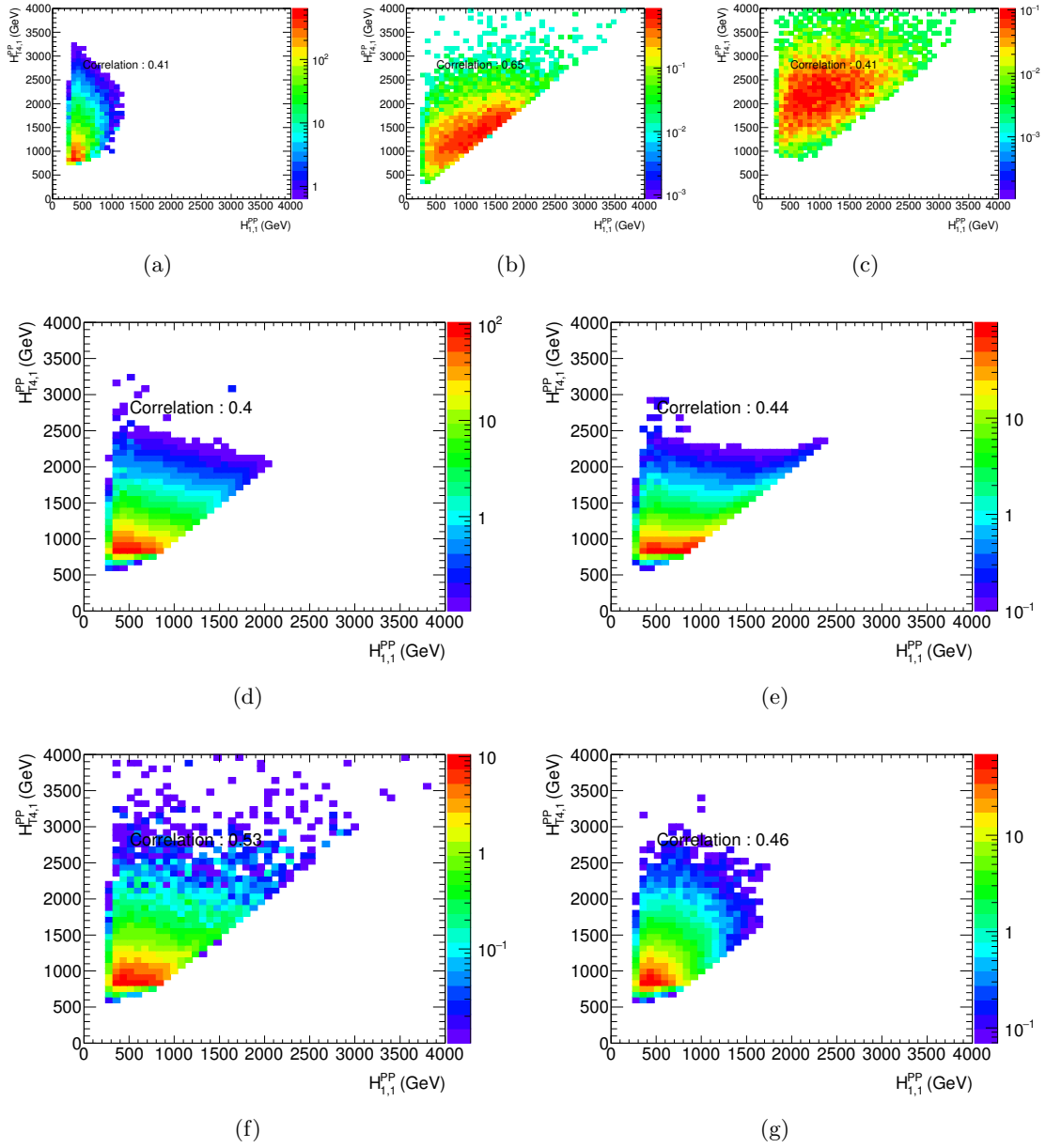


Figure D.18.  $H_2^{PP}$  and  $H_T^{PP}$  correlation for (a) QCD multijets, (b)  $\tilde{q}(900), \tilde{\chi}(0)$ , and (c)  $\tilde{g}(1400), \tilde{\chi}(0)$ , (d)  $W + jets$ , (e)  $Z + jets$ , (f) Diboson, and (g) Top.

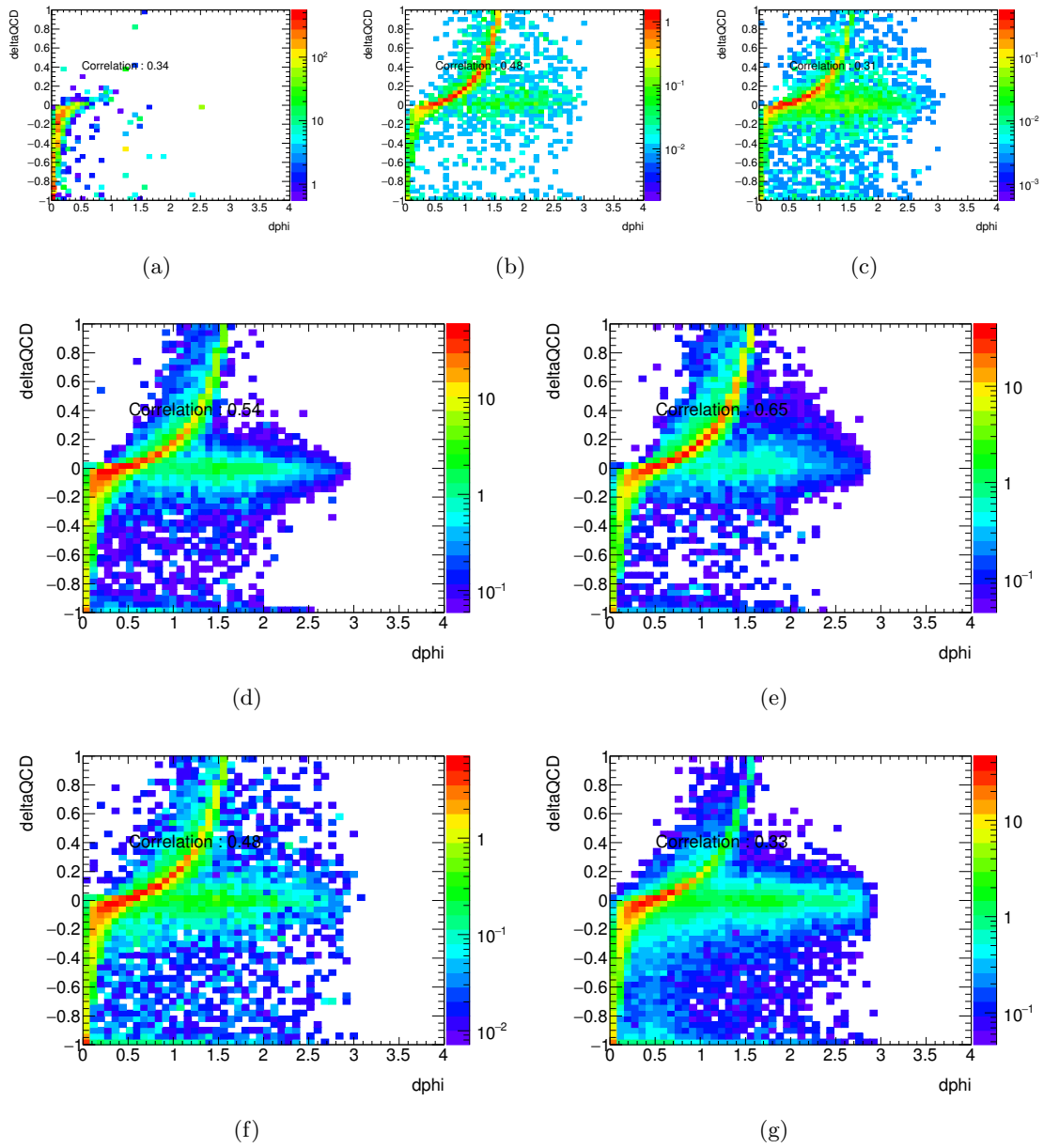


Figure D.19.  $\Delta\phi$  and  $\Delta_{QCD}$  correlation for (a) QCD multijets, (b)  $\tilde{q}(900), \tilde{\chi}(0)$ , and (c)  $\tilde{g}(1400), \tilde{\chi}(0)$ , (d)  $W + jets$ , (e)  $Z + jets$ , (f) Diboson, and (g) Top.

### D.3 QCD Rejection Correlations

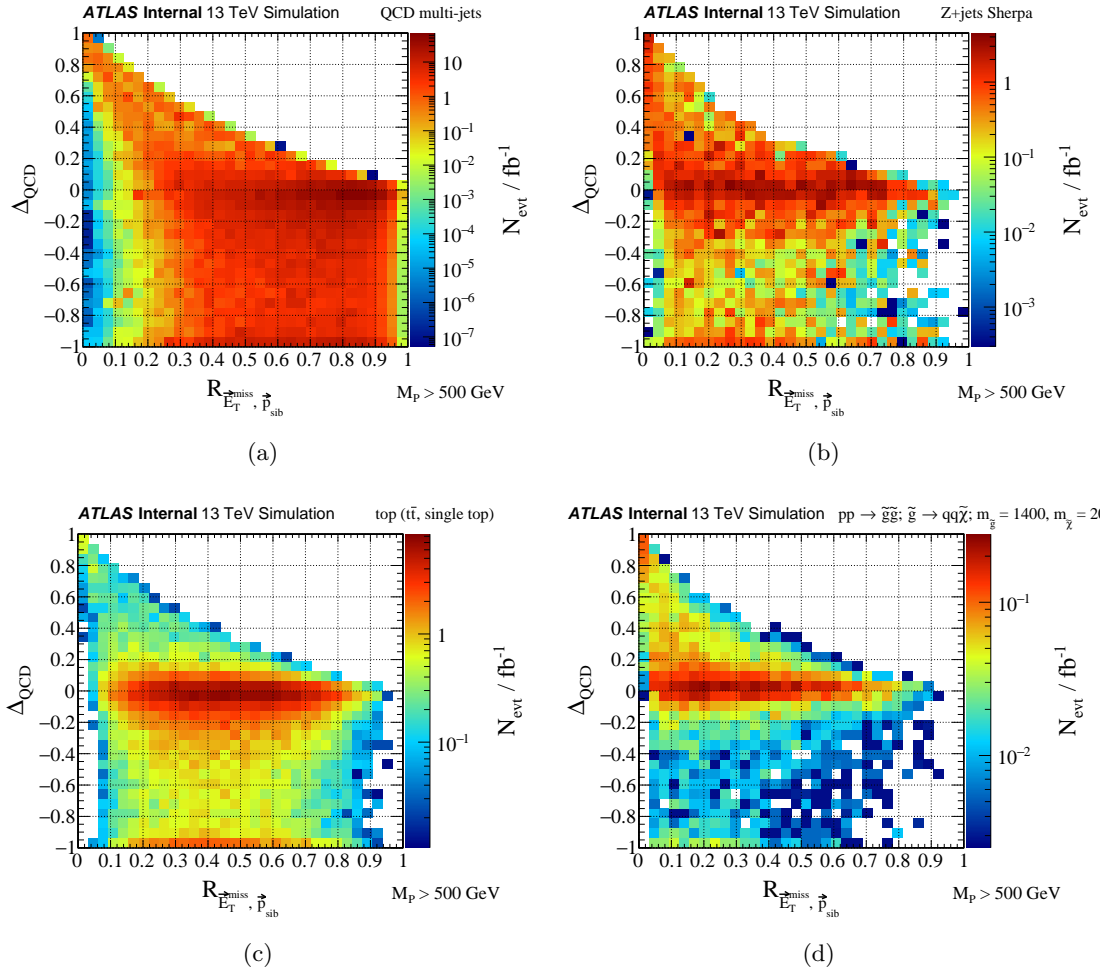


Figure D.20.  $R_{p_{sib}, E_T^{miss}}$  and  $\Delta_{QCD}$  correlation for (a) QCD multijets, (b)  $Z + jets$ , (c) Top, and (d)  $\tilde{g}(1400), \tilde{\chi}(200)$ .

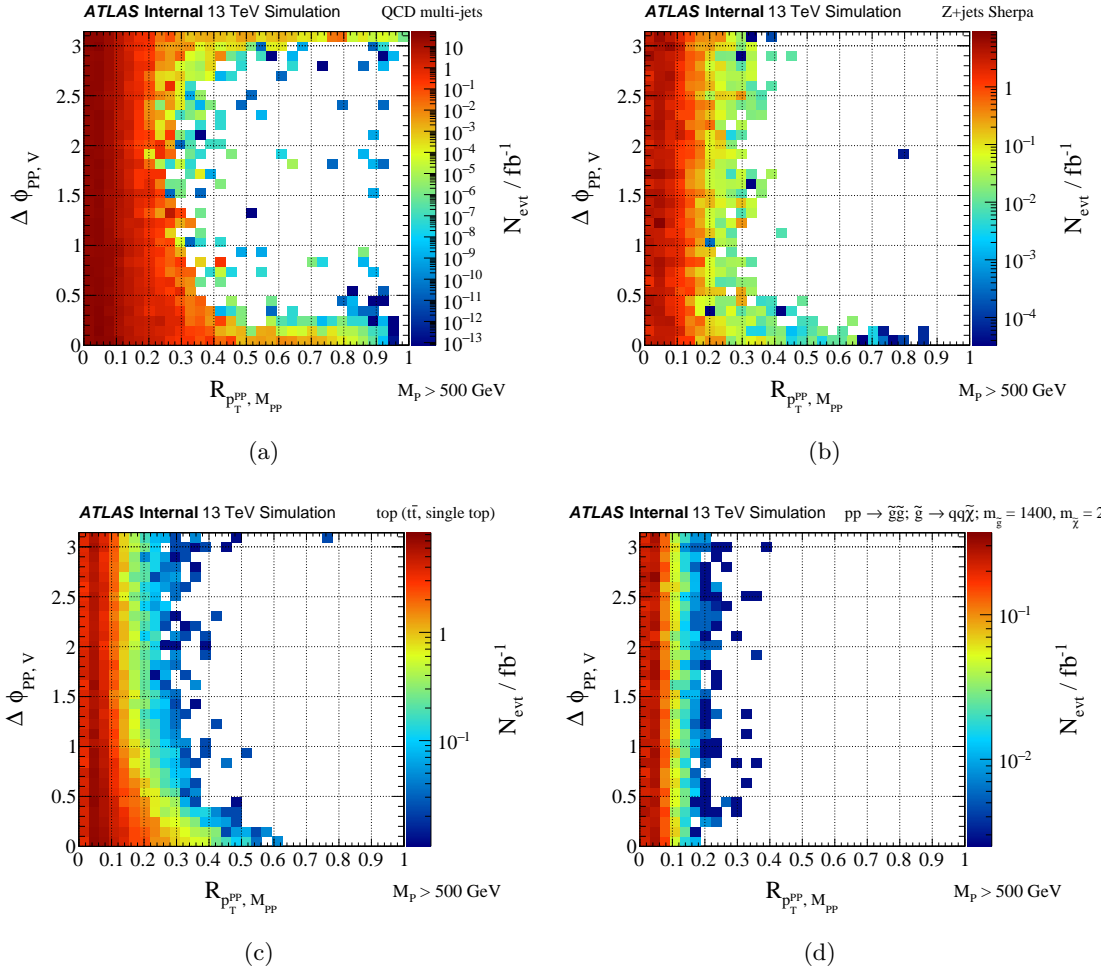


Figure D.21.  $R_{psib, E_T^{miss}}$  and  $\Delta_{QCD}$  correlation for (a) QCD multijets, (b)  $Z + jets$ , (c) Top, and (d)  $\tilde{g}(1400), \tilde{\chi}(200)$ .